

PROCEEDINGS
of the

1995



***Battlefield
Atmospherics
Conference***

**White Sands Missile Range, New Mexico
5 - 7 December 1995**

**U.S. Army Research Laboratory
Battlefield Environment Directorate
White Sands Missile Range
New Mexico**

Approved for Public Release; Distribution is unlimited

19980909 024

DTIC QUALITY INSPECTED 1

NOTICES

Disclaimers

The findings in this report are not to be construed as an official Department of the Army position, unless so designed by other authorized documents.

The citation of trade names and names of manufacturers in this report is not to be construed as official Government endorsement or approval of commercial products or services referenced herein.

DESTRUCTION NOTICE

When this document is no longer needed, destroy it by any method that will prevent disclosure of its contents or reconstruction of the document.

**Proceedings
of the
1995 Battlefield Atmospherics Conference**

5 - 7 December 1995

Sponsor

**Battlefield Environment Directorate
U.S. Army Research Laboratory
White Sands Missile Range, New Mexico**

Conference Chairman

**Dr. James Gillespie
Mr. Edward D. Creegan
Mr. John R. Elrick**

U.S. Army Research Laboratory

CONTENTS

Preface.....	vii
--------------	-----

SESSION I: OPERATIONAL WEATHER

Technical Validation of the Battlescale Forecast Model David I. Knapp and Robert Dumais, Jr., U.S. Army Research Laboratory	3
A Statistical Verification of the U.S. Army Battlescale Forecast Model: Case Study of Ft. Irwin, CA, April 1994 Robert E. Dumais, Jr., U.S. Army Research Laboratory	12
Real-Time PC Interface and Applications of AWDS Bruce L. Bauer, M. Noah and T. Myers, Mission Research Corporation R.M. Cox, Defense Nuclear Agency	22
Further Assessment of the Meteorological Office Mesoscale Model for the Prediction of Artillery Ballistic Messages, and the Development of an Artillery Meteorological Package for Forecasters Peter F. Davies, Defence Projects, The Meteorological Office, United Kingdom	31

SESSION II: BATTLE WEATHER INTEGRATION

UAV Dropsondes: A Target Area System Dr. James L. Cogan, U.S. Army Research Laboratory Thomas Greenling, S.A. Lucas and James Thomas, Physical Sciences Laboratory	42
The Battle Weather Test Bed: A System for Product Development for the Integrated Meteorological System John R. Elrick, U.S. Army Research Laboratory	52
Battlescale Forecast Model Application to Artillery Meteorology Dr. Teizi Henmi and Abel Blanco U.S. Army Research Laboratory John Spalding, Physical Sciences Laboratory	57
Validation of a Mass Consistency Wind Model at White Sands Missile Range John Sontowski, Science Applications International Robert M. Cox, Defense Nuclear Agency Cathy Dougherty, Science Applications International Richard N. Fry, Jr., HQ, Defense Group Inc.	64
Weather Impact Decision Aids for Electro-Optical (E-O) Weapons Support Lt. Col. Joe P. Alleca, Phillips Laboratory/Geophysics Directorate	77
The Processing, Databasing, and Displaying of AVHRR and DMSP Data for the Integrated Meteorological System Stephen F. Kirby, U.S. Army Research Laboratory	83
Automated Thermal Injury Risk Assessment for the Dismounted Soldier Gary B. McWilliams and Eugene S. Barnes, U.S. Army Research Laboratory William T. Matthew, U.S. Army Research Institute of Environmental Medicine	93

Selection of the Theater Forecast Model	100
Bruce L. Bauer and C. Tremback, Mission Research Corporation	
R.M. Cox, Defense Nuclear Agency	

SESSION III: BOUNDARY LAYER RESEARCH

Atmospheric Transport Over White Sands Missile Range	114
Maj Robert M. Cox, Defense Nuclear Agency	
John Sontowski, Science Applications Corporation	
Richard N. Fry, Defense Group Inc.	
Cathy Dougherty, Science Applications Corporation	
Analysis of Condensation Nuclei Counter Measurements in the Arabian Gulf and the Gulf of Oman	126
Andreas K. Goroch, Marine Meteorology Division, Naval Research Laboratory	
John W. Raby, U.S. Army Research Laboratory	
Measured Parameters of Puff Dispersion	134
Max Bleiweiss, U.S. Army Research Laboratory	
Kenneth C. Payne and Donald Stogden, Physical Sciences Laboratory	
Christopher D. Padilla, U.S. Army Research Laboratory	
High Resolution Wind Field Simulations Run Real-Time and with Other Inputs to Optimize Model Output	144
Ronald M. Cionco and John Byers, U.S. Army Research Laboratory	
Forecasting Atmospheric Optical Turbulence Neutral Events - Part II	153
Gail Tirrell Vaucher and Robert W. Endlich, U.S. Army Research Laboratory	
The NOAA Boulder Atmospheric Observatory Boundary Layer Study - Clear Air or Not?	163
John R. Hines, U.S. Army Research Laboratory	
C. Riese, Radian Corporation	
F. Eaton and W. Hatch, U.S. Army Research Laboratory	
S. McLaughlin, Radian Corporation	
Modelling and Measurements of Optical Turbulence Over Land	173
D.L. Hutt, Defence Research Establishment, Valcartier, Canada	
D. Stryckman, Universite Laval, Quebec, Canada	

SESSION IV: ATMOSPHERIC PHYSICS

Center for Geoscience Overview of DoD Sponsored Research at the Cooperative Institute for Research in the Atmosphere (CIRA)	184
Kenneth E. Eis, Thomas H. Vonder Haar and Donald L. Reinke, Cooperative Institute for Research in the Atmosphere (CIRA)	
Bi-Fractal Analysis of Atmospheric Signals Illustrated with Cloud Data	194
Anthony Davis and Alexander Marshak, NASA-Goddard Space Flight Center	
Obscurant Mass Extinction Coefficient Determination by Least Absolute Deviation	211
Brian R. Bullard and Roger E. Davis, Science and Technology Corporation	
Walter E. Klimek, U.S. Army Research Laboratory	

The Number of Laser Wavelengths Limit Biodetection in Fluorescence Lidar	223
David L. Rosen and James B. Gillespie, U.S. Army Research Laboratory	

SESSION V: ATMOSPHERIC SIMULATION AND ANALYSIS

Multifractal Characterization as an Analytical Tool for Atmospheric Research	237
Thelma Chenault, Max P. Bleiweiss, Rene Smith and Martin Bayang, U.S. Army Research Laboratory	
Climatological and Historical Analysis of Cloud for Environmental Simulations (CHANCES) - Applications to Battlefield Atmospherics	247
Donald L. Reinke, Thomas H. Vonder Haar and Kenneth E. Eis, STC-METSAT	
Prediction of Infrared Scenes Using Artificial Neural Networks	257
Peter Soliz, Applied Sciences Laboratory Inc.	
Joseph Eicher, Air Force Phillips Laboratory	
George C. Koenig, Cold Regions Research and Engineering Laboratory	
Scene Generation Including Multiply-Scattered Diffuse Radiance From Finite Clouds	266
Donald W. Hoock, Jr., U.S. Army Research Laboratory,	
Sean G. O'Brien, John C. Giever and Steven J. McGee, Physical Sciences Laboratory	
Evaluation of WAVES Using Image Statistics	276
Patti Gillespie, U.S. Army Research Laboratory	
Michael Rollins, Science and Technology Corporation	
David Tofsted, U.S. Army Research Laboratory.	
A Hybrid GIS and 3D Infrared Target/Background Modeling System	295
Guy P. Seeley, Radex Inc.	
Steve A. Luker USAF Phillips Laboratory/Geophysics Directorate	
Texture Generation for Use in Synthetic Scenes	305
Clem Z. Ota and J. Michael Rollins, Science and Technology Corporation	
Max P. Bleiweiss, U.S. Army Research Laboratory	
Atmospheric Effects Interpolation Algorithm	315
Glenn J. Higgins, Melanie J. Gouveia, Paul.D. Hestand and Michael S. Seablom, TASC	
DYBETA - A Practical Tool for Battlefield Environment Analysis	324
Shlomit Grossman, A. Katz, G. Sagi and D. Elial, Hancal-Systems Engineering Division	
TAAS-Israel Industries Ltd.	
Temporal Behavior of Natural Terrain Radiance at Infrared Wavelengths	334
Max P. Bleiweiss and Chistopher D. Padilla, U.S. Army Research Laboratory	
Acoustic Sensors and Systems in the Real World: Modeling the Effects of the Environment on Acoustic Propagation	344
David H. Marlin, U.S. Army Research Laboratory	

A High Spatial and Temporal Resolution Database for Synthetic Scene Generation and Validation	354
--	------------

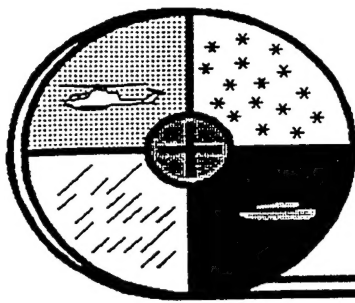
Max P. Bleiweiss, U.S. Army Research Army Laboratory
Thomas Cassidy and Forrest Scott, Sensor Concepts and Applications, Inc.
George G. Koenig, U.S. Army Cold Regions Research and Engineering Laboratory
James P. Welsh, SWOE JT&E Program Office

Atmospheric Experiments with an Imaging Spectral Radiometer	364
Patti Gillespie, Samuel Crow and David Tofsted, U.S. Army Research Laboratory	

Cross-Platform Demonstration of Combic Graphical User Interface (GUI)	372
Karen M. McLaughlin and Melanie M. Coakley, SPARTA, Inc.	

APPENDICES

Appendix A: Agenda	375
Appendix B: List of Attendees	380
Author Index	405



Battlefield Atmospherics Conference

The genesis of the Battlefield Atmospherics Conference (BAC) was the analysis of the 1973 Israeli War and the effective use of smoke by the Israeli forces to defeat electro-optical systems. On March 16, 1978, Dr. William Perry, then the Under-Secretary of Defense for Research and Engineering, sent a memorandum to the Services giving the initial DoD plan for Atmospheric Transmission Research and Development. The Army was assigned tasks to:

- (1) Measure and model atmospheric propagation conditions for battlefield conditions;
- (2) Develop models describing natural and man-made dust, smoke, and chemicals and their propagation characteristics; and
- (3) Develop battlefield diffusion models to relate propagation conditions to meteorology.

The Electro-Optical Systems Atmospheric Effects Library (EOSAEL) was developed in response to this tasking, and EOSAEL Conferences were held annually beginning in 1980. With the increased use of computers by FORSCOM in their MICROFIX program, the Corps of Engineers in their Airland Battlefield Environment Program, Tactical Weather Intelligence (TWI) was conceived to provide automated decision aids for Commanders and their staffs. The annual conference became the EOSAEL/TWI Conference. The conference continued to grow in breadth of subject matter and number of attendees.

In 1991, in an effort to encompass additional aspects of battlefield atmospheric effects such as acoustic transmission, the conference became known as the Battlefield Atmospherics Conference. This year the conference will be held at the White Sands Missile Range

Session I

OPERATIONAL WEATHER

Technical Validation of the Battlescale Forecast Model

David I. Knapp and Robert E. Dumais, Jr.
Battlefield Environment Directorate
U.S. Army Research Laboratory
White Sands Missile Range, NM 88002-5501, USA

ABSTRACT

Results of preliminary technical validation of the Battlescale Forecast Model (BFM) are presented for 17 winter and spring 1995 cases from the Colorado Region centered near Colorado Springs. Mean Absolute Errors are used to compare BFM output at 10km and 5km horizontal resolutions with the Global Spectral Model (GSM) output from Air Force Global Weather Central. Comparisons of surface data are made using raw observations from 19 locations spread across the varied terrain of the BFM domain. Calculations are made in 3-hour increments from BFM forecast 0-hour to 12-hour. Upper-level data comparisons are limited to the 12-hour BFM forecast time and to the sole RAOB location in the BFM domain at Denver. Model output of wind, temperature, and dew point variables are compared to reported values at the surface and six upper-levels to 500mb. Surface data comparisons prove the BFM to be a far superior model than the GSM. Upper-level data comparisons, however, are far less conclusive as the differences between both models are generally small. The lack of a wide variety of verifying RAOB locations may be significantly contributing to these inconclusive upper-level data results.

1. INTRODUCTION

The Battlescale Forecast Model (BFM) is a hydrostatic, quasi-Boussinesq mesoscale model developed primarily to forecast boundary layer processes over complex terrain. Diurnal effects due to radiational heating/cooling and surface forcing are included. Thus, flows such as mountain/valley upslope and downslope winds and coastal sea and land breezes can be resolved. Current model capabilities include running at horizontal resolutions as fine as 2.5km. Complete documentation of this model can be found in Yamada (1982), Mellor and Yamada (1982), Yamada and Bunker (1988, 1989), and Henmi, et. al. (1995).

The BFM has been selected as the first generation mesoscale model for the U.S. Army's Integrated Meteorological System (IMETS). BFM output will be used by battlefield forecasters and numerous IMETS automated tactical decision aids to provide commanders and other decision-makers with fine-scale weather data at required Army resolutions. Technical validation of the BFM is driven by two goals:

1. To compare BFM 12-hour forecast accuracy with the current state-of-the-art model output being supplied by Air Force Global Weather Central's (AFGWC) Global Spectral Model (GSM).
2. To discover specific model tendencies based on location, terrain, and synoptic situation.

Data from six different climatological regions in the Northern Hemisphere are being compiled for the model comparisons. These are summarized in Table 1. Model output data (BFM and GSM) are being compared

to raw surface and upper air observations in each region for the 500km x 500km grid area surrounding each region's center point. The goal is to collect between fifteen and twenty cases in each region, accounting for all seasons and for both static and dynamic synoptic events. Case collection will cover all seasons from Winter 1995 to Winter 1996.

Table 1. Summary of BFM Regions Studied

<u>REGION</u>	<u>Center Point</u>
Colorado	38.8N 104.7W
New England	40.8N 72.8W
Florida	28.0N 81.0W
Ft. Irwin, California	35.2N 116.4W
Korea	37.5N 127.0E
Bosnia	43.9N 18.4E

2. COLORADO REGION BFM CONFIGURATION

Comparisons have been completed thus far for the Colorado region during late winter and spring situations. The following also applies to future verification work for the other five regions. Horizontal grid resolutions for the BFM were verified at 10km and 5km. Terrain following vertical levels were staggered in such a way that maximum resolution was maintained near the surface allowing for boundary layer processes to be better captured by the model physics. The model top is rigid, set at 7000m above the highest terrain grid point in the model domain.

Large scale forcing during the 12-hour forecast period is supplied to the BFM by the 12-hour and 24-hour gridded forecast fields provided by the GSM's 2.5° lat x 2.5° lon output. These forecast grids mimic the real-world availability of data for timely BFM runs. The 12-hour GSM fields are used as first-guess analysis guidance for the BFM which also merges upper air sounding data and surface data to create a three-dimensional initial data field. GSM and RAOB data cover the BFM domain and extend another 1000km beyond. Surface data is used from only the BFM domain.

Large scale forcing is incorporated into the BFM using four dimensional data assimilation via the Newtonian relaxation or nudging method (Yamada and Bunker, 1989). Nudging is applied to the prognostic variables (u, v, potential temperature, and mixing ratio) at all grid points above 100m AGL. This allows large scale synoptic forcing and boundary layer mesoscale forcing to interact more realistically. Hourly nudging data files are created by linearly interpolating in time between GSM 12-hour and 24-hour forecast data.

In the BFM, the pressure gradient above 1000m AGL is assumed to be equal to the large scale pressure gradient given by the GSM. Below 1000m AGL, the pressure gradient is calculated using the thermal wind method described by Yamada (1981) based on the wind and potential temperature at 1000m AGL. This allows pressure gradients to be generated near the surface due to diurnal forcing mechanisms such as radiational heating and cooling of sloped surfaces.

3. VERIFICATION STATISTICS AND VARIABLES

To compare BFM and GSM model results, calculations of the Mean Absolute Error (MAE) are used to show the average error between forecast model output and observed data. Variables verified were u, v, wind speed, temperature, and dew point. Model output for both the BFM and GSM were taken directly for comparisons at applicable levels, or interpolated to the verified levels when necessary. Levels studied were the surface, 250m,

500m, 1000m, and 1500m AGL, plus 700mb and 500mb. Surface data observation locations used for the comparisons in the Colorado region are shown in Fig 1.

Surface data verification was accomplished in three-hour increments from model 0-hour to the 12-hour point. BFM output was directly read for each increment, and GSM output (available only in 12-hour increments) was linearly time-interpolated to the BFM 3-hour increments. Only one RAOB location is found in the BFM domain (Denver), and comparisons for model output aloft are applied only to this location at BFM times 0-hour and 12-hour, corresponding to the 00 UTC and 12 UTC RAOBs, respectively.

4. VERIFICATION RESULTS

Surface and upper-level data verification results are compiled showing the MAEs for the combined data set of surface observations from the Colorado region for the cases listed in Table 2. These cases represent verification work completed thus far, analyzing late winter and spring season cases. Another 13 cases have been collected for future study which examine summer, fall, and early winter events in the Colorado region.

Table 2. Listing of 17 Colorado region BFM vs. GSM 1995 case studies listed by BFM base time

00Z	12Z
5 APR	24 MAR
13 APR	28 MAR
14 APR	30 MAR
21 APR	12 APR
22 APR	13 APR
3 MAY	20 APR
4 MAY	21 APR
5 MAY	22 APR
	4 MAY

4a. Surface Data Verification

GSM grid point data were interpolated to the BFM grid points at 5- and 10km resolutions, then both models' output were interpolated to the actual raw data surface observation locations to compile the verification parameters. Statistics for the five time periods studied, in three-hour increments, are presented to show trends for each variable and resolution in Tables 3 and 4. Shading in the tables highlights the model and resolution with the lowest MAE for each variable verified. Forecast 0-hour in the tables corresponds to BFM 0-hour and the GSM's 12-hour forecast used to initialize the BFM at its 0-hour. Thus, comparisons of 0-hour MAE values should not be considered as valid since raw surface and upper-air observations were used to initialize the BFM at 0-hour, supplemented with GSM 12-hour forecast gridded data used as a "first guess" analysis for boundary conditions. Since the 12-hour GSM grids are used as analysis fields at BFM 0-hour, comparisons at this time are suspect and show an expectedly large difference in favor of the BFM.

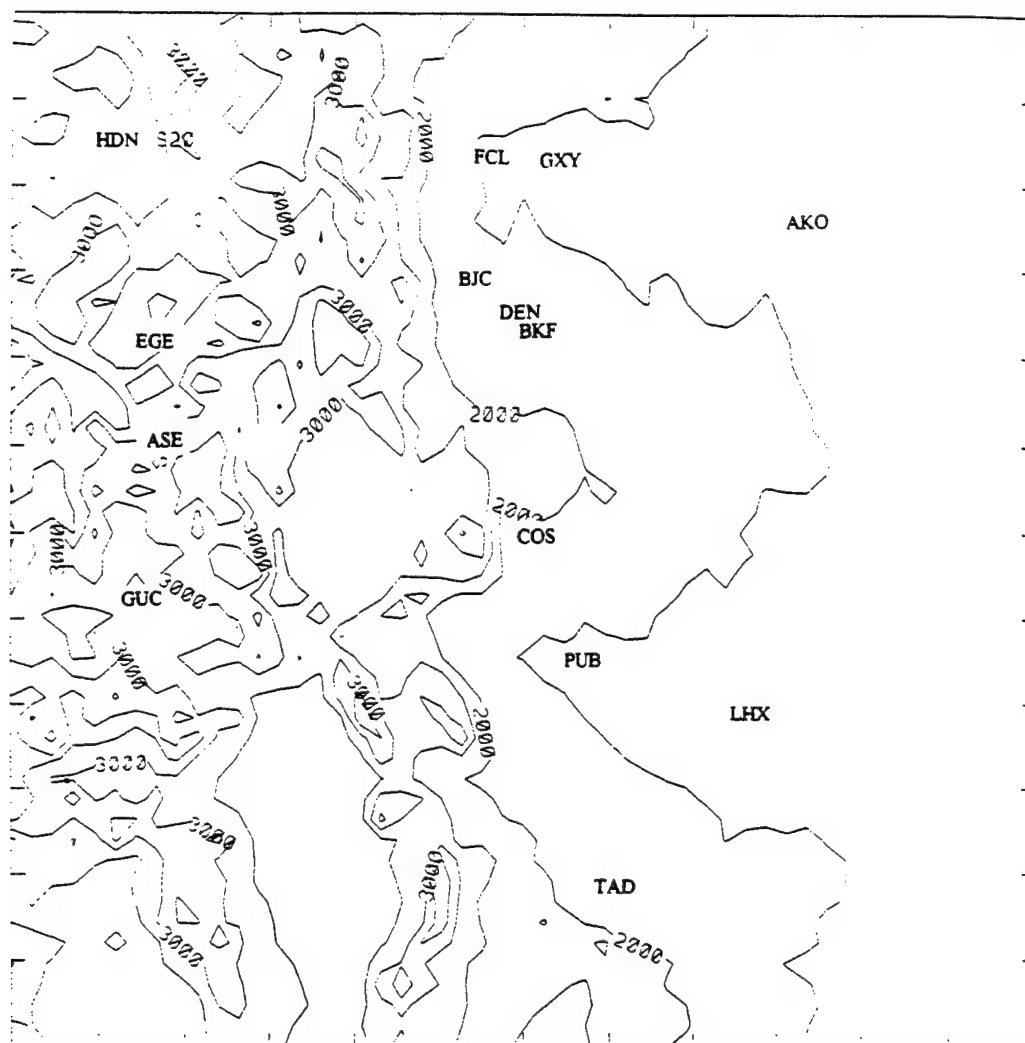


Figure 1. Colorado Region BFM surface and upper-level observation verification network. Location at Denver (DEN) is the only RAOB station used for upper-level verification. All others (DEN included) are surface data observation sites. Solid contours show MSL height in 1000m intervals taken from the BFM's terrain database.

Table 3. Mean Absolute Error statistics for Colorado region BFM vs. GSM surface wind data. Variables shown are u=u-wind component, v=v-wind component, and spd=wind speed. All values in ms^{-1} .

Model	Resolution	Variable	BFM Forecast Hour				
			0	3	6	9	12
BFM	5	u	.48	2.83	2.86	3.31	3.30
GSM	5	u	4.52	4.10	5.13	5.23	5.17
BFM	10	u	.71	2.48	2.48	3.05	2.73
GSM	10	u	3.91	3.58	4.44	4.45	4.64
BFM	5	v	.56	2.78	2.59	3.08	3.44
GSM	5	v	5.26	4.71	4.83	5.42	6.65
BFM	10	v	.72	2.61	2.80	2.84	3.16
GSM	10	v	4.97	4.47	4.82	4.96	5.99
BFM	5	spd	.65	2.43	2.33	2.01	2.26
GSM	5	spd	3.89	3.10	4.11	3.97	4.39
BFM	10	spd	.92	2.18	2.04	1.93	1.90
GSM	10	spd	3.84	3.06	3.55	3.70	4.33

Table 4. Mean Absolute Error statistics for Colorado region BFM vs. GSM surface temperature and dew point data. All values in $^{\circ}\text{C}$.

Model	Resolution	Variable	BFM Forecast Hour				
			0	3	6	9	12
BFM	5	Temp	2.46	3.19	3.97	3.75	3.22
GSM	5	Temp	6.24	2.64	2.99	4.32	4.72
BFM	10	Temp	2.50	2.69	3.72	3.27	2.87
GSM	10	Temp	5.51	2.52	3.64	5.55	5.08
BFM	5	Dewpt	3.67	3.38	3.46	3.29	4.29
GSM	5	Dewpt	4.57	4.40	4.81	5.17	6.30
BFM	10	Dewpt	3.18	3.71	3.54	3.36	3.70
GSM	10	Dewpt	3.46	3.63	4.10	4.48	5.35

Ignoring the 0-hour comparisons, Tables 3 and 4 show the BFM outperforming the GSM in virtually all surface data comparisons. The BFM wind forecasts produce MAEs 42% lower than the GSM at both resolutions, with average 10km BFM MAE for u, v, and speed of 2.7, 2.9, and 2.0 ms^{-1} , respectively. BFM MAEs gradually increase with each forecast hour, except the 10km speed MAE which gradually decreases with time. Temperature comparisons in Table 4 show the BFM producing MAEs 19% lower than the GSM at both resolutions. BFM 10km temperature and dew point MAE values of 3.1 and 3.6 $^{\circ}\text{C}$, respectively, are the best of both models and resolutions studied. The BFM's 10km temperature calculations at hours 3 and 6 were worse than the GSM's but this trend was reversed and MAEs were lower than the GSM's at hours 9 and 12. This indicates that the BFM may take up to six hours of forecast spinup time to better depict the temperature fields. Similar findings occur for the BFM's 10km dew point calculations, but these MAE values are higher than the GSM's only at hour 3.

4b. Upper-air Data Verification

Only one RAOB location, Denver, was located within the BFM grid for the Colorado region. As with surface data, GSM grid point data were interpolated to the BFM grid points at 5- and 10km resolutions, then both models' output were interpolated to the Denver RAOB location to compile the verification parameters. Statistics for the six upper levels studied are

presented for the BFM's 12-hour forecast vs. GSM 24-hour forecast to show differences for each resolution in Tables 5 and 6. Shading in the tables highlights the model and resolution with the lowest MAE for each variable and level verified.

Table 5. Mean Absolute Error statistics for Denver RAOB location BFM 12-hour forecast vs. GSM 24-hour forecast upper level wind data

Model	Resolution	Variable	Level (Heights AGL and Pressure)					
			250m	500m	1000m	1500m	700mb	500mb
BFM	5	u	7.03	6.93	4.80	3.24	3.52	3.42
GSM	5	u	5.10	5.45	4.25	3.21	3.18	3.91
BFM	10	u	5.31	6.09	4.62	3.93	3.96	3.73
GSM	10	u	5.39	5.68	4.17	3.44	3.61	4.12
BFM	5	v	6.08	6.50	6.76	5.85	5.97	4.47
GSM	5	v	6.82	6.85	6.64	5.88	5.94	4.79
BFM	10	v	7.04	6.84	6.74	6.40	6.45	5.22
GSM	10	v	7.35	7.01	6.80	6.33	6.45	5.58
BFM	5	spd	5.79	5.06	5.13	3.64	3.78	2.56
GSM	5	spd	3.89	4.03	4.35	3.66	3.73	2.56
BFM	10	spd	4.62	4.76	4.88	4.77	4.54	2.82
GSM	10	spd	4.06	4.11	4.71	4.43	4.47	3.06

Table 6. Mean Absolute Error statistics for Denver RAOB location BFM 12-hour forecast vs. GSM 24-hour forecast upper level temperature and dew point data

Model	Resolution	Variable	Level (Heights AGL and Pressure)					
			250m	500m	1000m	1500m	700mb	500mb
BFM	5	Temp	3.16	3.73	2.9	3.05	2.61	1.58
GSM	5	Temp	4.19	4.27	3.40	3.31	2.90	1.68
BFM	10	Temp	2.77	2.98	2.43	2.19	2.72	1.46
GSM	10	Temp	3.91	3.52	2.65	2.35	2.92	1.57
BFM	5	Dewpt	2.7	2.9	4.08	4.9	4.52	6.03
GSM	5	Dewpt	4.27	4.13	4.59	4.83	4.55	5.28
BFM	10	Dewpt	3.24	3.11	3.2	4.57	4.58	7.19
GSM	10	Dewpt	4.39	4.24	4.68	4.93	5.06	6.76

Results of upper-level wind comparisons show the GSM performed better than the BFM by an average of 5% (Table 5). Both model's MAEs decrease with height, indicating the GSM's strong influence in the free atmosphere above the boundary layer. The BFM's v-component does perform better than the GSM in the boundary layer at both resolutions and averaging MAE values of 5.9 and 6.5ms⁻¹ for 5- and 10km output, respectively.

Temperature and dew point contrasts (Table 6) show the BFM averaging 13% lower MAEs than the GSM at both resolutions. The lowest MAEs occurred for the temperatures at 10km resolution (2.4°C) and dew points at 5km (4.1°C). A significant increase in the dew point MAEs at 500mb reveals the GSM's weakness in depicting mid-level moisture which is also reflected in the BFM output.

4c. Verification Overview

Table 7 is a summary showing which model had the lowest MAE for each surface parameter, resolution, and forecast time for the surface stations used in the verification. Similarly, Table 8 shows the best model for each upper-level, resolution, and parameter using the Denver RAOB location for

verification.

For surface data forecasts, the BFM outperforms the GSM in most cases (Table 7). Upper-level comparisons tell a slightly different story (Table 8), with the GSM outperforming the BFM for u-component and speed variables, but only by $.4\text{ms}^{-1}$. The BFM's v-component, temperature, and dew point MAE's averaged $.2\text{ms}^{-1}$, $.5^{\circ}\text{C}$, and $.4^{\circ}\text{C}$ better, respectively.

Table 7. Summary comparison showing the model with the lowest Mean Absolute Error statistics of BFM vs. GSM (shaded) surface data forecasts by forecast time and parameter (compare with Tables 3 and 4).

Parameter	5km Output Comparisons					10km Output Comparisons				
	Forecast Hour					Forecast Hour				
	0	3	6	9	12	0	3	6	9	12
u	BFM	BFM	BFM	BFM	BFM	BFM	BFM	BFM	BFM	BFM
v	BFM	BFM	BFM	BFM	BFM	BFM	BFM	BFM	BFM	BFM
spd	BFM	BFM	BFM	BFM	BFM	BFM	BFM	BFM	BFM	BFM
Temp	BFM	GSM	GSM	BFM	BFM	BFM	GSM	GSM	BFM	BFM
Dewpt	BFM	BFM	BFM	BFM	BFM	BFM	GSM	BFM	BFM	BFM

Table 8. Summary comparison showing the model with the lowest Mean Absolute Error statistics of BFM vs. GSM (shaded) Denver RAOB location upper-level data forecasts valid at BFM 12-hour forecast time. Ties are highlighted. Compare with Tables 5 and 6.

Parameter	5km Output Comparisons						10km Output Comparisons					
	Level (Height AGL and Pressure)											
	250m	500m	1000m	1500m	700mb	500mb	250m	500m	1000m	1500m	700mb	500mb
u	GSM	GSM	GSM	GSM	GSM	BFM	BFM	GSM	GSM	GSM	GSM	BFM
v	BFM	BFM	GSM	BFM	GSM	BFM	BFM	BFM	BFM	GSM	TIE	BFM
spd	GSM	GSM	GSM	BFM	GSM	TIE	GSM	GSM	GSM	GSM	GSM	BFM
Temp	BFM	BFM	BFM	BFM	BFM	BFM	BFM	BFM	BFM	BFM	BFM	BFM
Dewpt	BFM	BFM	BFM	BFM	BFM	BFM	BFM	BFM	BFM	BFM	BFM	BFM

The question of which BFM resolution to use is addressed in Table 9. Forecasters using the fielded IMETS and running the BFM will have their choice of model resolutions to run. Obviously, the smaller the grid resolution chosen, the longer the model will take to run across the same domain size. The question arises as to the usefulness of running the BFM at 5km for higher resolution, smaller domain, and presumably more accurate output.

Table 9. Summary comparison showing model resolution with the lowest Mean Absolute Error statistics of 5km BFM (shaded) vs. 10km BFM output for Colorado surface data and Denver RAOB location upper-level data forecasts.

Parameter	Surface Data					Upper-level Data					
	Forecast Hour					Level (Height AGL and Pressure)					
	0	3	6	9	12	250m	500m	1000m	1500m	700mb	500mb
u	5	10	10	10	10	10	10	10	5	5	5
v	5	10	5	10	10	5	5	10	5	5	5
spd	5	10	10	10	10	10	10	10	5	5	5
Temp	5	10	5	5	5	10	10	10	10	5	10
Dewpt	10	5	5	5	10	5	5	10	10	5	5

For surface data, 5km resolution is best at 0- and 6-hours, whereas 10km resolution is better at 3-, 9-, and 12-hours. 10km output is better for winds and 5km is best for temperature and dew point. Upper-level calculations show 10km the preferred resolution for the boundary layer, with 5km preferred at and above the 1500m level. Upper-level variable calculations show that 5km resolution is best for depicting v-component and dew point, 10km output best for temperatures, and calculations of u-component and speed a toss-up.

5. SUMMARY AND FUTURE WORK

BFM verification performance has been compared to the GSM's across the Colorado region for 17 late winter and spring 1995 cases. Surface observation data from 19 stations in the region were used to verify model surface data output. The BFM showed significant improvement over the GSM's capability to forecast all surface parameters studied. This is directly attributable to the enhanced boundary layer physics used by the BFM. Over complex terrain as in the Colorado region, the surface temperature, dew point, and wind fields are closely tied together, thus model results are physically consistent.

BFM improvement is less evident when examining upper-level data verification. Each model seems to have its own upper-level strengths and weaknesses, yet these results should be considered inconclusive at this time. Only one RAOB location was available for use in the upper-level verification process. The location of the Denver site is in complex terrain subject to a wide variety of fine-scale forcings which the BFM probably can't accurately depict given the initialization resolution of the GSM gridded data fields. By comparison, even though there were surface stations located in rough terrain, the sample size of surface observations and locations used for verification was much greater than that for the upper-level verification. In the future, more RAOB and wind profiler locations would be desired to increase the location diversity of upper-level verification sites, thus providing a database and sampling large enough to provide better conclusions about the BFM's upper-level forecast depiction capabilities.

Another probable reason for less than desirable upper-level BFM results is that the model was run with nudging at each grid point in the vertical as well as horizontal. Thus, GSM forcings aloft tended to significantly influence the BFM's free atmosphere output. Future comparisons will include model runs without BFM-domain nudging of the data aloft, allowing the mesoscale forcings of the BFM to react with much less GSM influence. The lack of an adequate BFM convective parameterization may also be contributing to the upper-level errors.

Limited across-the-board improvement in BFM forecasts run at the lower 5km resolution reveals that better resolution of terrain forced local phenomena will require very fine resolution topographical data and/or improved resolution from the model used for BFM initialization and boundary

conditions. As these higher resolution regional models with improved physics packages become available to the IMETS in the future, the BFM will incorporate these forecast data as boundary conditions to better depict large-scale forcing. These improvements should further reduce the MAEs of both models, and lead to a truly accurate BFM at resolutions which meet the Army's requirements.

Future work includes the following:

- a. Completion of analyses from the remaining 13 cases collected for the Colorado region.
- b. Re-running the 30 cases at 10km resolution with these options:
 - i) Nudging at all interior points throughout the forecast cycle, with no nudging at the surface.
 - ii) Same as above with surface nudging damped exponentially with time.
 - iii) Nudging at all points and levels during model spin-up to 0-hour with all nudging in the BFM domain shut off after 0-hour. Nudging will only continue at the lateral boundaries.

REFERENCES

- Henmi, T., M.E. Lee, and T.J. Smith, 1995: Battlescale Forecast Model and its evaluation using White Sands Missile Range meteorological data. ARL-TR-569, Army Research Laboratory, WSMR, NM 88002-5501.
- Mellor, G.L., and T. Yamada, 1982: Development of a turbulence closure model for geophysical problems. *Rev. Geophys. Space Phys.*, **20**, 851-875.
- Yamada, T., 1981: A numerical simulation of octurnal drainage flow. *Journal of the Meteor. Society of Japan*, **59**, 108-122
- , 1982: A numerical model study of turbulent airflow in and above a forest canopy. *Journal of the Meteor. Society of Japan*, **60**, 439-454.
- , and S.S. Bunker, 1988: development of a nested grid, second moment turbulence closure model and application to the 1992 ASCOT Brush Creek data simulation. *Journal of Applied Meteor.*, **27**, 562-578.
- , and S. Bunker, 1989: A numerical model study of nocturnal drainage flows with strong wind and temperature gradients. *Journal of Applied Meteor.*, **28**, 545-554.

**A Statistical Verification of the
U.S. Army Battlescale Forecast Model:
Case Study of Ft. Irwin, California,
April, 1994.**

**Robert E. Dumais, Jr.
Battlefield Environment Directorate
U.S. Army Research Laboratory
White Sands Missile Range, NM, 8802-5501, USA**

ABSTRACT

Surface meteorological data collected as part of Operation Desert Capture II will be used to statistically analyze the performance of the Battlescale Forecast Model, which was run for several 12-hr periods within the time frame of the exercise. The exercise took place at Ft. Irwin, California during April, 1994. The model was run at two horizontal resolutions (5 km and 2.5 km), and was initialized with only gridded forecast data from the U.S.A.F. Global Spectral Model. The Global Spectral Model also provided the time-dependent lateral boundary conditions, with a Newtonian nudging technique applied. No upper air or surface observations were used in initializing the model, allowing for a comparison of the Battlescale Forecast Model and Global Spectral Model forecast fields.

1.0 INTRODUCTION

The U.S. Army Battlescale Forecast Model (BFM) is a hydrostatic, quasi-Boussinesq mesoscale meteorological model that was developed primarily to forecast boundary layer processes over complex terrain. Diurnal effects due to radiational heating/cooling surface forcing are included, so that flows such as mountain/valley upslope and downslope winds and coastal sea and land breezes can be resolved. The model is capable of running at horizontal resolutions as fine as 2.5 km, although it runs much quicker at 5 and 10 km resolution. Complete documentation of this model can be found in Yamada (1982), Yamada and Bunker (1988,1989), Mellor and Yamada (1982), and Henmi et al (1995). This model has been selected as the interim mesoscale model for the U.S. Army Integrated Meteorological System (IMETS), until it is replaced by the U.S. Naval Research Laboratory's nonhydrostatic COAMPS model when it becomes available.

During April 1994, surface automated meteorological sensor (SAMS) data was collected routinely around the U.S. Army National Training Center, Ft. Irwin, California as part of the Operation Desert Capture II (ODCII) exercise. Data from ten 12-hour periods was compiled at the Army Research Lab (ARL) Battlefield Environment Directorate so that 12-hr BFM forecasts could be statistically analyzed for validation and verification. In addition, since the U.S. Air Force Global Spectral Model (GSM) forecasts are currently used by the BFM to supply the large-scale meteorological forcing (ie: lateral boundary conditions), a statistical verification of this model's performance can also be made for comparison with BFM.

2.0 Model Configuration

The BFM orthogonal grid was centered at 35.283°N and 116.633°W, near Bicycle Lake, and within the National Training Center (Dumais, 1995). Two different grid configurations were used: 51x51x16 at 2.5 km horizontal resolution and 27x27x16 at 5 km horizontal resolution. Since the model time steps must be small enough to satisfy the Courant-Friedrichs-Levy criteria (Haltiner and Williams, 1980), the speed of a BFM 12-hour forecast depends on the horizontal resolution, thermal stratification, and large scale wind flow. On an HP-755 workstation running Unix 9.0, a 12-hour BFM forecast for a 51x51x16 grid (at 5 km resolution) is typically one hour.

The terrain following vertical levels are staggered in such a way that maximum resolution is maintained near the surface, so that boundary layer processes can be better captured by the model physics. The model top is rigid and is set at 7000 meters above ground level.

3.0 Large Scale Forcing and Lateral Boundary Conditions

Large scale forcing during the 12-hr forecast period is supplied to the BFM by the 12-hr and 24-hr gridded forecast fields provided by the GSM at 380 km resolution. This is not an ideal approach, since 0-hr and 12-hr forecasts generated by a regional scale model such as the Naval Research Laboratory's NORAPS or Limited-Area Numerical Weather Prediction Model (Harms et al, 1992) would be the most suitable as boundary conditions for the BFM.

At the moment the current IMETS configuration provides only the gridded GSM forecast fields routinely via the Automated Weather Data System (AWDS), which is the reason the BFM uses the approach mentioned above. As regional forecast model data becomes available through IMETS, the BFM will adjust accordingly. The use of 12-hr and 24-hr forecast fields from the previous global/regional forecast model run as opposed to the 0-hr and 12-hr fields from the current run is necessitated by the long time lag encountered before the gridded forecast files are actually transmitted to the IMETS.

For example, a BFM 12-hr forecast initialized at 1200 UTC on day 1 will use the GSM's 12-hr forecast from 0000 UTC on day 1 as initial conditions, and the GSM's 24-hr forecast from 0000 UTC on day 1 as its 12-hr boundary conditions. This is because the GSM 1200 UTC day 1 forecast products would not be available to the BFM

until around 1700 or 1800 UTC.

Although in this paper only the GSM gridded forecast data is used to initialize the BFM, in general the BFM merges GSM data, upper air sounding data, and surface data (such as SAMS) to create a three-dimensional initial data field.

The large scale forcing is incorporated into the BFM by using a four dimensional data assimilation method called Newtonian relaxation or nudging (Yamada and Bunker, 1989). A nudging factor of 0.0003 is used, and nudging is applied to the prognostic variables (u-wind, v-wind, potential temperature, and mixing ratio) at all grid points above 100 magl. This is done with the intent of allowing large scale synoptic forcing and boundary layer mesoscale forcing to interact more realistically. Hourly nudging data files are created by linearly interpolating in time between the GSM 12-hr forecast data and the 24-hr forecast data.

In the BFM, the pressure gradient above 1000 magl is assumed to be equal to the large scale pressure gradient given by the GSM. Below 1000 magl, the pressure gradient is calculated using the thermal wind method described by Yamada (1981) based on the wind and potential temperature at 1000 magl. This will allow pressure gradients to be generated near the surface due to diurnal radiational forcing mechanisms (such as radiational heating and cooling of sloped surfaces).

4.0 Statistics Used in Verification

To compare BFM and GSM model results, the following statistics were selected for analysis:

Correlation Coefficient

$$\sum_{i=1}^{NOBS} (O_i - \bar{O}) * (M_i - \bar{M}) / \sqrt{(\sum_{i=1}^{NOBS} (O_i - \bar{O})^2) * (\sum_{i=1}^{NOBS} (M_i - \bar{M})^2)}$$

Root Mean Square Error

$$\sqrt{(\sum_{i=1}^{NOBS} (M_i - O_i)^2) / NOBS}$$

Mean Bias

$$\bar{M} - \bar{O}$$

Table 3.0 Mean absolute error of 10 magl
v- wind component in m/s

Site	Elev(m)	Lat (n)	Lon (w)	5 km BFM	2.5 km BFM	5 km GSM	2.5 km GSM
Bike Lk	725	35.28	116.65	NA	NA	NA	NA
247- Pad	760	35.27	116.68	1.80	1.89	5.61	5.84
Granite	1200	35.42	116.57	2.81	2.69	4.67	4.95
Nelson Lk	940	35.42	116.76	3.80	3.88	6.42	6.74
Live Fire	1080	35.48	116.49	3.65	3.68	4.46	4.93
Red Pass	670	35.26	116.37	3.77	3.91	7.09	7.46
4 Corners	758	35.35	116.59	2.35	2.37	6.27	6.52
East Gate	800	35.38	116.36	2.60	2.82	5.59	5.70
Gary Owen	1220	35.52	116.78	4.03	4.60	5.97	6.16
Avawatz	1670	35.52	116.37	5.94	6.87	5.35	5.53

Table 4.0 Mean absolute error of 10 magl
wind speed in m/s

Site	Elev(m)	Lat (n)	Lon (w)	5 km BFM	2.5 km BFM	5 km GSM	2.5 km GSM
Bike Lk	725	35.28	116.65	NA	NA	NA	NA
247- Pad	760	35.27	116.68	2.02	1.97	3.84	3.86
Granite	1200	35.42	116.57	2.13	2.22	3.14	3.15
Nelson Lk	940	35.42	116.76	2.79	2.82	4.10	4.03
Live Fire	1080	35.48	116.49	1.86	1.87	3.18	3.32
Red Pass	670	35.26	116.37	3.86	3.68	3.65	3.52
4 Corners	758	35.35	116.59	1.85	1.89	3.94	4.01
East Gate	800	35.38	116.36	3.10	3.16	3.55	3.28
Gary Owen	1220	35.52	116.78	2.50	2.43	3.02	3.06
Avawatz	1670	35.52	116.37	3.24	3.54	3.89	3.89

Table 5.0 Mean absolute error of 2 magl
temperature in degrees celsius

Site	Elev(m)	Lat (n)	Lon (w)	5 km BFM	2.5 km BFM	5 km GSM	2.5 km GSM
Bike Lk	725	35.28	116.65	4.58	4.67	6.58	6.72
247- Pad	760	35.27	116.68	4.80	4.83	6.57	6.62
Granite	1200	35.42	116.57	4.14	3.64	4.41	4.75
Nelson Lk	940	35.42	116.76	3.72	3.89	6.89	7.00
Live Fire	1080	35.48	116.49	3.89	3.48	5.07	5.14
Red Pass	670	35.26	116.37	5.21	4.99	5.88	6.00
4 Corners	758	35.35	116.59	4.36	4.47	6.35	6.50
East Gate	800	35.38	116.36	5.00	5.04	5.48	6.03
Gary Owen	1220	35.52	116.78	3.32	2.95	4.50	4.69
Avawatz	1670	35.52	116.37	3.67	2.83	2.62	2.49

Relative Scatter

$$\left(\left(\sum_{i=1}^{NOBS} (O_i - M_i)^2 \right) / NOBS \right) / |(\bar{O} - \bar{M})|$$

Factor 2

Fraction of cases $i=1$ to $NOBS$ where

$$0.5 \leq O_i / M_i \leq 2.0$$

Mean of Absolute Residuals

$$\left(\sum_{i=1}^{NOBS} |(O_i - M_i)| \right) / NOBS$$

Standard Deviation of Absolute Residuals

$$\sqrt{\left(\sum_{i=1}^{NOBS} (|O_i - M_i| - \left(\left(\sum_{i=1}^{NOBS} |O_i - M_i| \right) / NOBS \right))^2 \right) / (NOBS - 1)}$$

where in all equations

$$\bar{O} = \left(\sum_{i=1}^{NOBS} (O_i) \right) / NOBS$$

$$\bar{M} = \left(\sum_{i=1}^{NOBS} (M_i) \right) / NOBS$$

NOBS = total number of observations/model forecasts
 i = individual observation/model forecast.

Statistics were done in two ways; averaged over all cases and forecast times (10 cases x 13 forecast periods) by station or averaged over all cases by forecast time and station. Because of publication restrictions, only averages over all cases and forecast times by station will be displayed in this paper. The variables analyzed are surface u wind component, v wind component, wind speed, wind direction and temperature at each hourly interval throughout the 12 hour forecast cycle. Since the SAMS data was collected in 15 minute intervals, hourly observations have been averaged using the five 15-minute observations between 30 minutes before the hour and 30 minutes after the hour.

5.0 Statistical Results

This section reviews the statistical results compiled from the following ten 12-hr BFM forecast periods, initialized at the times listed in Table 1.0. As mentioned previously, the statistics shown here were taken from a sample over all ten cases and thirteen forecast periods (0hr, 1hr, 2hr,....12hr) , by each individual SAMS site. Tables 2.0 through 9.0 display some of the more interesting statistical findings from the study.

Table 1.0 Initialization times for the
ten forecast periods

Date	UTC
4-07-94	1200
4-11-94	0000
4-12-94	1200
4-14-94	0000
4-14-94	1200
4-17-94	0000
4-18-94	1200
4-19-94	0000
4-20-94	1200
4-21-94	0000

Table 2.0 Mean absolute error of 10 magl
u- wind component in m/s

Site	Elev(m)	Lat (n)	Lon(w)	5 km BFM	2.5 km BFM	5 km GSM	2.5 km GSM
Bike Lk	725	35.28	116.65	NA	NA	NA	NA
247- Pad	760	35.27	116.68	2.33	2.35	2.39	2.40
Granite	1200	35.42	116.57	2.52	2.51	1.86	1.97
Nelson Lk	940	35.42	116.76	2.80	2.70	3.43	3.43
Live Fire	1080	35.48	116.49	1.47	1.52	2.06	2.10
Red Pass	670	35.26	116.37	3.21	3.03	3.21	3.26
4 Corners	758	35.35	116.59	1.94	1.88	2.61	2.68
East Gate	800	35.38	116.36	3.14	3.21	3.10	3.04
Gary Owen	1220	35.52	116.78	1.97	2.16	2.32	2.36
Avawatz	1670	35.52	116.37	2.38	2.36	3.00	2.99

Table 6.0 Standard deviation of absolute error
of 10 magl u- wind component in m/s

Site	Elev(m)	Lat (n)	Lon (w)	5 km BFM	2.5 km BFM	5 km GSM	2.5 km GSM
Bike Lk	725	35.28	116.65	NA	NA	NA	NA
247- Pad	760	35.27	116.68	1.94	1.82	1.81	1.83
Granite	1200	35.42	116.57	1.64	1.59	1.97	2.00
Nelson Lk	940	35.42	116.76	2.18	2.12	1.97	2.00
Live Fire	1080	35.48	116.49	1.24	1.15	1.85	1.91
Red Pass	670	35.26	116.37	2.52	2.52	2.39	2.34
4 Corners	758	35.35	116.59	1.64	1.63	1.63	1.62
East Gate	800	35.38	116.36	2.55	2.73	2.63	2.58
Gary Owen	1220	35.52	116.78	1.82	1.74	2.23	2.25
Avawatz	1670	35.52	116.37	1.78	1.76	2.31	2.36

Table 7.0 Standard deviation of absolute error
of 10 magl v- wind component in m/s

Site	Elev(m)	Lat (n)	Lon (w)	5 km BFM	2.5 km BFM	5 km GSM	2.5 km GSM
Bike Lk	725	35.28	116.65	NA	NA	NA	NA
247- Pad	760	35.27	116.68	1.44	1.38	2.11	2.01
Granite	1200	35.42	116.57	2.39	2.10	2.76	2.76
Nelson Lk	940	35.42	116.76	2.66	2.71	2.68	2.78
Live Fire	1080	35.48	116.49	3.14	3.17	2.86	2.93
Red Pass	670	35.26	116.37	2.43	2.52	3.77	4.29
4 Corners	758	35.35	116.59	1.58	1.52	2.30	2.42
East Gate	800	35.38	116.36	1.36	1.42	2.97	3.07
Gary Owen	1220	35.52	116.78	3.02	3.26	3.13	3.24
Avawatz	1670	35.52	116.37	4.51	5.32	2.82	2.86

Table 8.0 Standard deviation of absolute error
of 10 magl wind speed in m/s

Site	Elev(m)	Lat (n)	Lon (w)	5 km BFM	2.5 km BFM	5 km GSM	2.5 km GSM
Bike Lk	725	35.28	116.65	NA	NA	NA	NA
247- Pad	760	35.27	116.68	1.60	1.52	2.50	2.58
Granite	1200	35.42	116.57	1.72	1.56	2.29	2.34
Nelson Lk	940	35.42	116.76	2.71	2.59	2.56	2.57
Live Fire	1080	35.48	116.49	1.51	1.50	2.43	2.26
Red Pass	670	35.26	116.37	2.99	2.91	2.42	2.41
4 Corners	758	35.35	116.59	1.65	1.57	2.38	2.44
East Gate	800	35.38	116.36	2.34	2.41	2.45	2.59
Gary Owen	1220	35.52	116.78	2.21	1.97	2.36	2.36
Avawatz	1670	35.52	116.37	2.71	2.82	2.25	2.28

Table 9.0 Standard deviation of absolute error
of 2 magl temperature in degrees celsius

Site	Elev(m)	Lat(n)	Lon(w)	5 km BFM	2.5 km BFM	5 km GSM	2.5 km GSM
Bike Lk	725	35.28	116.65	2.50	2.59	4.51	4.62
247- Pad	760	35.27	116.68	2.72	2.71	4.63	4.66
Granite	1200	35.42	116.57	2.13	2.20	2.97	3.04
Nelson Lk	940	35.42	116.76	2.11	2.03	4.29	4.36
Live Fire	1080	35.48	116.49	2.30	2.23	3.50	3.40
Red Pass	670	35.26	116.37	2.63	2.59	4.43	4.39
4 Corners	758	35.35	116.59	2.44	2.49	4.52	4.64
East Gate	800	35.38	116.36	2.62	2.83	4.09	4.20
Gary Owen	1220	35.52	116.78	2.11	1.94	2.70	2.84
Avawatz	1670	35.52	116.37	2.98	2.27	1.70	1.62

It should be noted from Table 1.0 that an equal number of cases were initialized at each base time: 1200 and 0000 UTC. These times corresponded to 0500 and 1700 local time, thus we were able to simulate both daytime and nighttime scenarios adequately. Large scale flow was generally quite strong early in the period and much weaker towards the end.

The residuals data in the tables above reveal a couple of things about the BFM behavior. Most noticeable is the significant reduction in error the BFM provided to surface wind speed, v-component magnitude, and temperature forecasts when compared to the 12 to 24 hour GSM forecast for the same period. Apparently the BFM is capable of initializing from the GSM 12-hr forecast fields and then upgrading the GSM forecast over the following 12 hour forecast period. Ongoing three-dimensional BFM studies at ARL are indicating that the significant improvements to the GSM are near the surface and that above the first hundred meters little difference between BFM and GSM forecasts is seen (except where BFM initialization has been enhanced by surface and upper air observations). This is expected due to the four dimensional data assimilation scheme discussed earlier. The tables also indicate that at least over the terrain spectra of the National Training Center, little if any improvement is shown by running the BFM at 2.5 km resolution as opposed to 5 km resolution.

6.0 Conclusions

The data obtained from the BFM simulations during the ODC II exercise at Ft. Irwin, California clearly indicate that the model is capable of initializing from only a 12-hr GSM forecast and then generating an improved forecast of the surface fields of wind and temperature over the following twelve hour period. Particular improvement is seen in the forecast magnitude of the surface v-wind components. One would expect even more dramatic improvements when upper air and surface observations are used to enhance the BFM initialization, and regional scale models with full physics are used to assimilate the time-dependent larger scale forcing.

Fluctuations from the basic state (u-wind component) zonal wind flow in the mid-latitudes is generally due to synoptic and mesoscale phenomena such as polar cyclogenesis, mesoscale convective complexes, etc. However, at the lower end of the mesoscale spectrum, terrain forcing plays a significant role in deviation from a basic state flow.

Since the GSM runs at such a coarse resolution, it can not properly resolve mesoscale-forced perturbations in the flow adequately, if at all. Although the BFM is not capable of physically simulating mesoscale phenomena missed by the GSM that are forced by precipitation microphysics, latent heat releasing, symmetrical instabilities, etc., it is able to generate flow patterns driven by the local topography. In the Ft. Irwin area, this capability of the BFM is shown clearly by the improvement in the surface v-wind component forecasts over the period of the ODC II exercise.

Additionally, the BFM yielded much better forecasts of surface temperature than the GSM during the exercise. This is almost certainly due to the enhanced boundary layer physics used by the BFM. Over complex terrain the surface temperature and wind fields are closely tied together, thus the BFM results are physically consistent.

The lack of substantial improvement in BFM forecasts run at 2.5 km horizontal resolution as opposed to 5 km horizontal resolution may indicate that better resolution of terrain forced, local mesobeta phenomena will require very fine resolution topographical data. Another possibility for this finding is that some of the SAMS sites may be located in regions whose surface meteorology is characterized by very complicated topographical features, resolved only at resolutions less than 2 km. For instance, the only site where the BFM wind forecasts degraded some from the GSM was at Avawatz, at an elevation of 1670 meters in a complex region of mountainous terrain. When contoured at both 5km and 2.5 km resolution, the overall geometry of the slopes look identical. However, when contoured at a resolution of 100 meters a completely different geometry presents itself, with complex and varied slope patterns the rule.

Regardless of what the true reason for this finding is in this particular exercise, the important thing it illustrates is that running any mesoscale model at a finer horizontal resolution doesn't necessarily correlate with better forecast output. McQueen et al (1995) report similar findings in their research with the Regional Atmospheric Modeling System (RAMS) over the Susquehanna River valley in Pennsylvania.

As higher resolution regional models with more complete physics packages become available to IMETS in the future, the BFM will incorporate their forecast data as boundary conditions for the purpose of large scale forcing. By using the four dimensional data assimilation method of Newtonian nudging, a quasi-nesting scheme with no interactive feedback is accomplished. The BFM is also capable of generating low stratus layers and fogs, so better resolution of three dimensional moisture fields will also be necessary.

Acknowledgements

The author extends special thanks to John Ligon and Kira Dumais for their assistance in processing the SAMS data.

References

- Dumais Jr., R.E., 1995: Performance of the US Army Battlescale Forecast Model during Operation Desert Capture II. *Proceedings of the 1994 Battlefield Atmospherics Conference*, Army Research Laboratory, WSMR, NM, 88002-5501.
- Haltiner, G.J., and R.T. Williams, 1980: Numerical Prediction and Dynamic Meteorology, John Wiley and Sons, Inc., Pg. 118.
- Harms D.E., K.D. Sashegyi, R.V. Madala, and S. Raman, 1992: Four-dimensional data assimilation of GALE data using a multivariate analysis scheme and a mesoscale model with diabatic initialization. *NRL/MR/4223-92-7147*, Naval Research Laboratory, Washington, DC, 20375-5320.
- Henmi, T., M.E. Lee, and T.J. Smith, 1995: Battlescale Forecast Model and its evaluation using White Sands Missile Range meteorological data. *ARL-TR-569*, Army Research Laboratory, WSMR, NM, 88002-5501.
- Mellor, G.L., and T. Yamada, 1982: Development of a turbulence closure model for geophysical problems. *Rev. Geophys. Space Phys.*, **20**, 851-875.
- McQueen, J.T., R.R. Draxler, and G.D. Rolph, 1995: Influence of grid size and terrain resolution on wind field predictions from an operational mesoscale model. *Journal of Applied Meteor.*, **34**, 2166-2181.
- Yamada, T., 1981: A numerical simulation of nocturnal drainage flow. *Journal of the Meteor. Society of Japan*, **59**, 108-122.
- , 1982: A numerical model study of turbulent airflow in and above a forest canopy. *Journal of the Meteor. Society of Japan*, **60**, 439-454.
- , and S.S. Bunker, 1988: Development of a nested grid, second moment turbulence closure model and application to the 1992 ASCOT Brush Creek data simulation. *Journal of Applied Meteor.*, **27**, 562-578.
- , and S. Bunker, 1989: A numerical model study of nocturnal drainage flows with strong wind and temperature gradients. *Journal of Applied Meteor.*, **28**, 545-554.

REAL-TIME PC INTERFACE AND APPLICATIONS OF AWDS

B. L. Bauer, M. Noah, and T. Myers
Mission Research Corporation
Huntsville, Alabama and Nashua, New Hampshire

R. M. Cox
Defense Nuclear Agency
Alexandria, Virginia

ABSTRACT

As part of its Hazard Prediction and Assessment Capability Program, the Defense Nuclear Agency (DNA) has developed software that provides real-time communication between a personal computer (PC) and the Air Force Automated Weather Distribution System (AWDS). Previously users who wanted to use real-meteorological data through the AWDS Command and Control (C2) port were restricted to relatively expensive UNIX based workstations. Using a relatively low cost Windows based personal computer (PC) will make this data available to more applications. The DNA PC to AWDS C2 port software interface now provides this capability in theater or in any military command post with AWDS access.

PC_WXSYNC is based on the WXSYNC interface program that was developed by and obtained from the AWDS Program Office. The requirement to obtain AWDS data on a PC lead initially to the development of LINUX based version. The LINUX version of the interface allowed cost effective development of software to convert the AWDS Appendix 30/150 data to input data for HPAC applications. DNA currently uses an older 386 PC as the AWDS server, freeing a workstation of this task.

DNA hazard prediction models are being ported from workstations to notebook computers for on-site support to tactical operations. While the LINUX version of the interface could support these models it would be cumbersome for many users. To support these users a Windows version of the interface was developed.

The various PC versions of the WXSYNC interface provide a very flexible and cost effective means of tapping the utility of the AWDS meteorological data.

1. INTRODUCTION

1.1 Scope of Effort

The DNA hazard prediction models require extensive meteorological data entry. Mission Research Corporation has developed an interface between the DNA models and the AWDS system:

- To facilitate data entry of meteorological conditions, and
- To allow for the atmospheric dispersion predictions to be calculated in near real-time.

The first task was a proof of concept that the AWDS Appendix 30 Weather Products can be extracted onto the PC architecture. Figure 1 illustrates the basic system components developed by the 14 April 1995 Task 1 deadline.

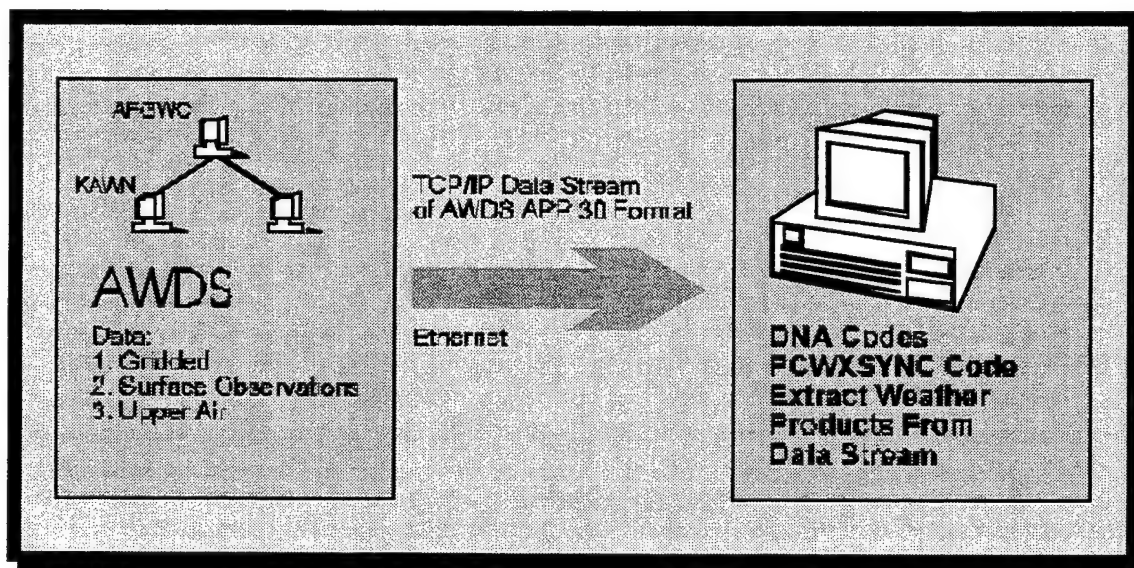


Figure 1: The Task 1 Proof of Concept (Completed 14 April 1995). Prototype programs PCWXSUNC, for LINUX, and WINSUNC, for MS-Windows, were developed to act as servers for extracting AWDS Appendix 30 Weather Products from the TCP/IP data stream.

The second task resulted in a completed MS-Windows and LINUX software package for extracting Appendix 30 weather products and preprocessing them into input files for the DNA Hazard Assessment codes. The second task required the creation of programs to 1) interpret the binary data, performing byte-swapping if necessary; 2) sort the data by product type, and 3) preprocess the data into DNA code input file format. The

preprocessors include unit conversion utilities to reformat the weather data in appropriate units. Figure 2 illustrates the Task 2 effort completed in August of 1995. The resulting product is now called "WOW" for "Weather On Windows" and will run under either MS-Windows or Linux.

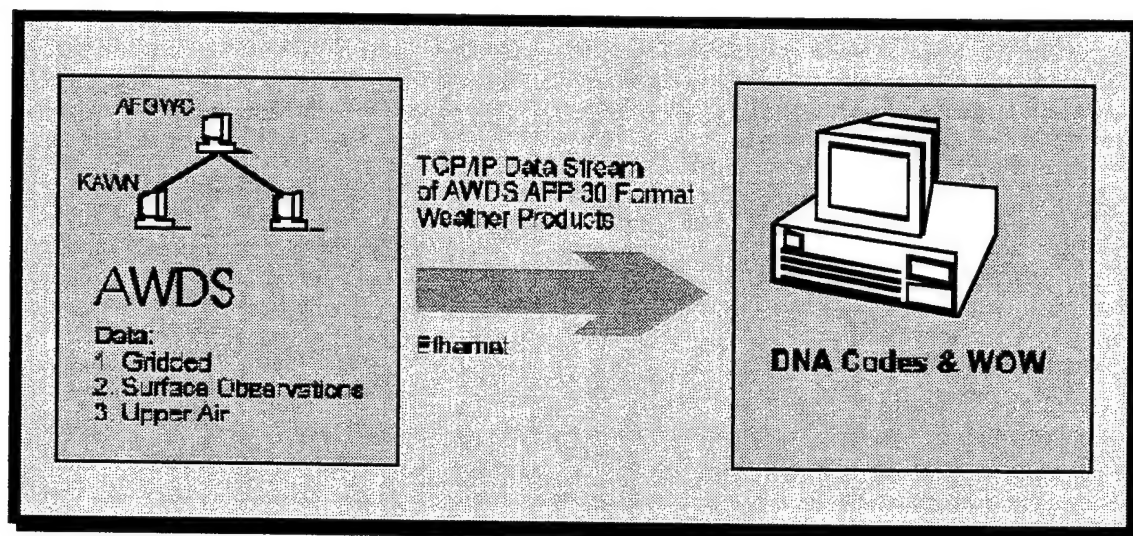


Figure 2: The Task 2 Weather On Windows Program (Completed August 1995). WOW is a suite of programs which interpret, display, and preprocess the AWDS weather products. Preprocessing is performed on Gridded, Surface Data, and Upper Air data and converted to DNA Model Formats or text display files. Files may be sorted by product type into a hierarchical directory structure.

1.2 What is AWDS?

The Automated Weather Distribution System (AWDS) is part of a global environmental support system which provides for the collection, processing, and dissemination of environment data and products to support the Department of Defense. This system also supports the collection and dissemination of Notice to Airmen (NOTAM) messages pertinent to hazards of flight.

The five basic types of AWDS products are:

Alphanumeric Products

These include MANOPED products (standardized messages concerning past, present and future environmental conditions, status of airfields, and hazards to flight); Addressed products (these are non-standard internal messages); Automated Response to Query (ARQ) Products; Individual Weather Report products (observed and forecast weather for locations having a valid location identifier); and NOTAM products.

<i>Formatted Binary Products</i>	These include surface observations, upper air observations, special weather reports, and others.
<i>Uniform Gridded Data Fields</i>	Sets of environmental data referenced at uniformly spaced geographical points. Generally, these are the output of environmental analysis and forecast models.
<i>Vector Graphic Products</i>	Vector graphic products are collections of data describing weather maps, charts and figures in machine-readable form.
<i>Raster Scan Products</i>	Visual images, e.g., satellite, graphic, or facsimile images.

The formats of these products are described in OCR-AWDS-01-130 dated July 15, 1991, "Appendix 30: Interface Control Drawing."

1.3 What are the DNA Hazard Prediction Models?

The Second-order Closure Integrated Puff model (SCIPUFF) is a Lagrangian transport and diffusion mode for atmospheric dispersion applications. SCIPUFF predicts the average concentration value, the statistical variance in the concentration field resulting from the random fluctuations in the wind velocity, and the uncertainty for the predicted concentration value. For meteorological data entry, the model uses surface and upper air observations or three-dimensional grid data. MS-Windows versions of the SCIPUFF programs have been developed by DNA.

2. WEATHER ON WINDOWS (WOW)

2.1 WOW Overview

WOW is a PC based software suite that provides an interface for receiving and interpreting weather products from the Automated Weather Distribution System (AWDS). The software can be compiled for either an MS-Windows system or a LINUX system. WOW provides:

- A UNIX TCP/IP network application for receiving weather products from an AWDS C2 port,

- An MS-Windows (Version 3.1 or higher) TCP/IP network application for receiving weather products from an AWDS C2 port,
- Utilities to sort weather products into a hierarchical directory reflecting weather product type,
- Utilities to create text files from binary AWDS products, and
- Utilities to extract weather data from AWDS products and reformat for DNA models, the Phillips Laboratory's Atmospheric Modeling suite, and others.

The primary goal of WOW is to provide access to real-time weather data for PC applications.

2.2 WOW System Requirements

The minimum hardware requirements for the system are:

- 386 or 486 PC.
- 8 Mbytes RAM.
- Any standard serial mouse.
- Ethernet Card.

2.3 WOW System Overview

The WOW software suite includes many utilities for weather data processing. PCWXXSYNC is the software that interacts with the AWDS C2 port and extracts data sets in real-time. VIEWAWDS is a program that will read the AWDS data sets, account for byte swapping of the data, and dumps it to the screen. AWDS view is essentially the first step in developing an AWDS reformatter to feed data to a PC or Work-Station model that requires real-time AWDS access.

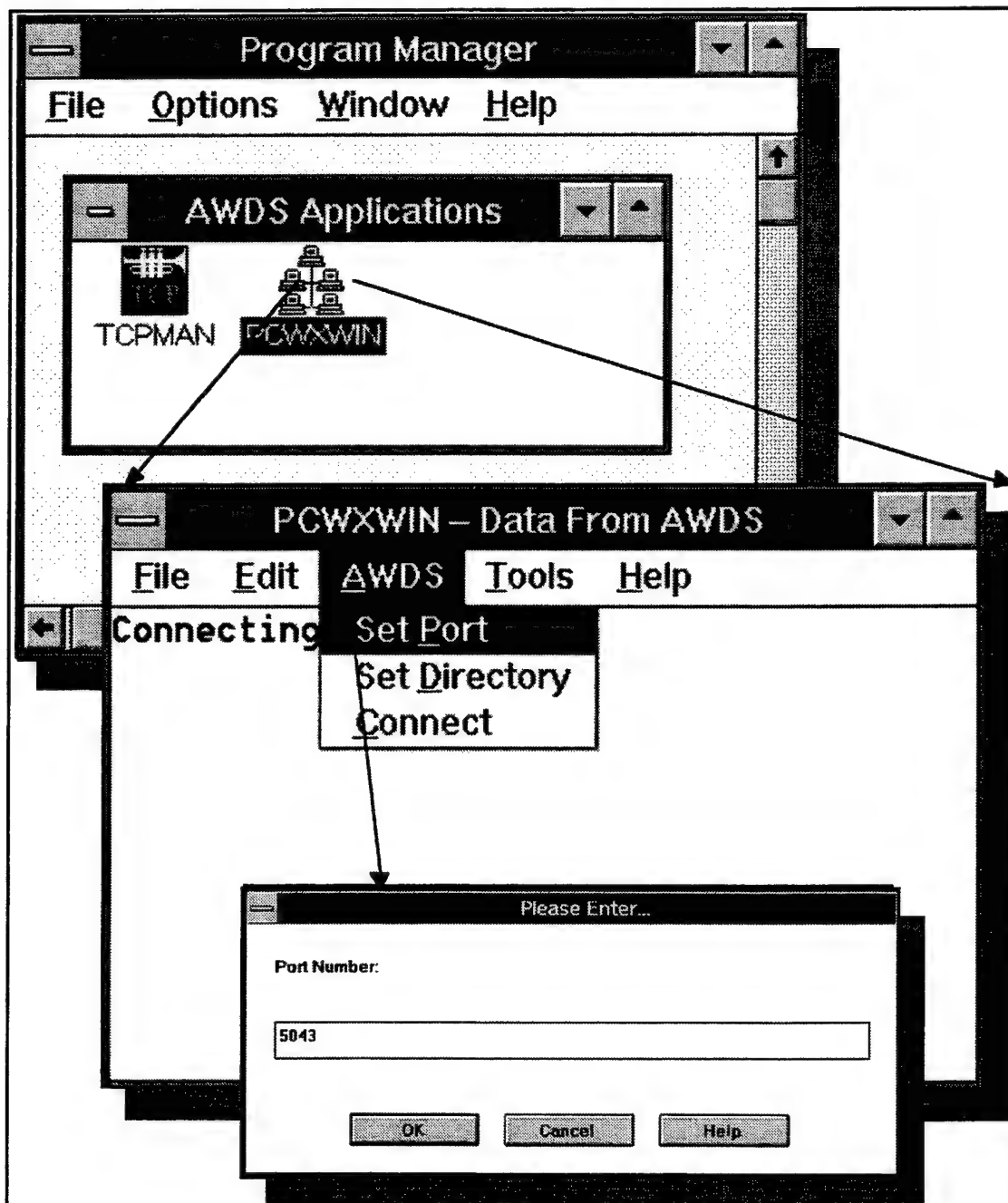


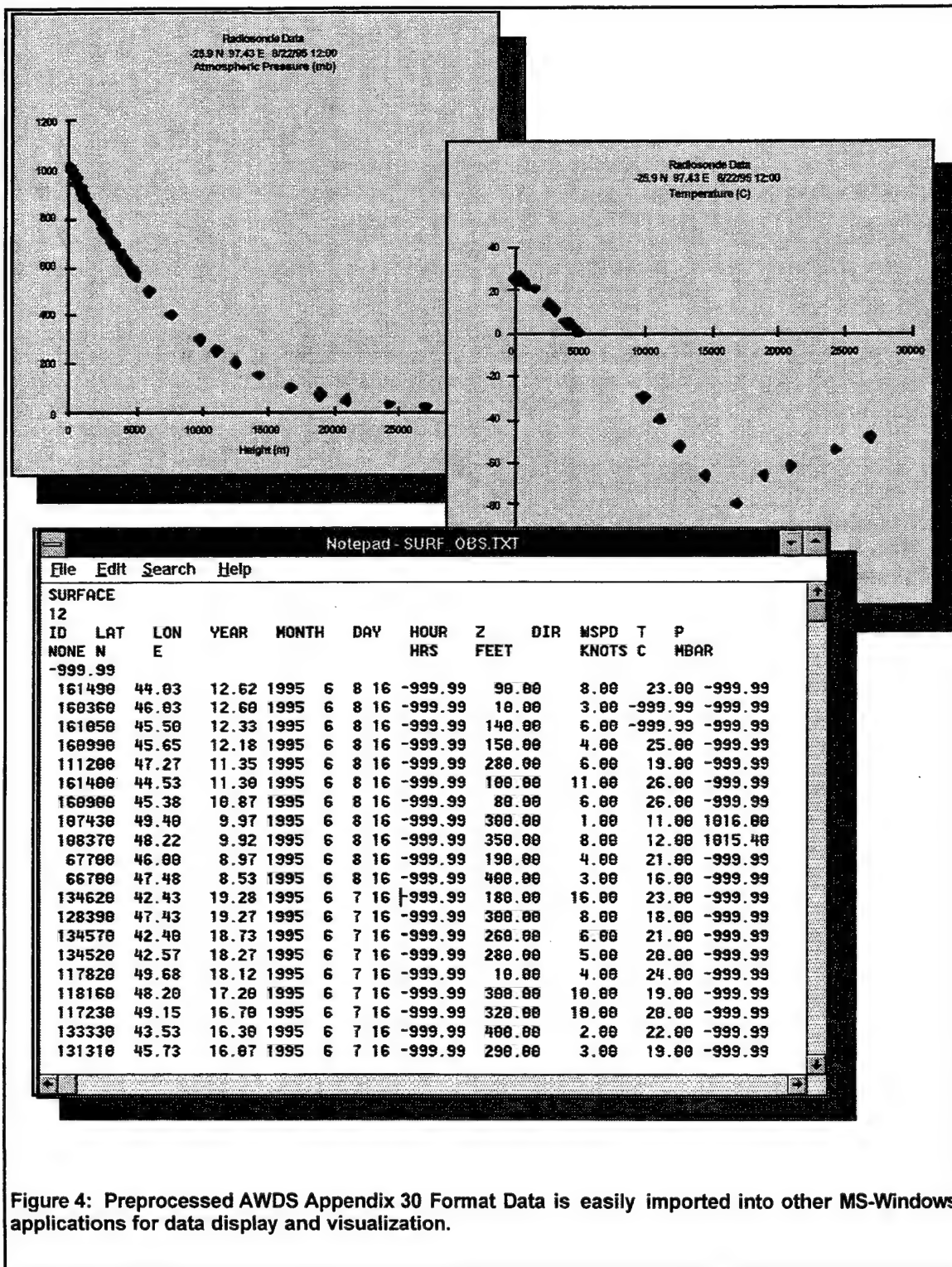
Figure 3: Receiving near real-time weather data on your MS-Windows system now requires only a few mouse clicks. The WOW software will support a wide variety of meteorological modeling applications.

2.4 WOW Distribution

The following programs compose the basic software suite:

Program	Description
pcwxwin	The pcwxwin program for MS-Windows, and The pcwxwin program establishes server communications with AWDS for receiving weather products.
pcwxsync	The pcwxsync program for Linux. The pcwxsync program establishes server communications with AWDS for receiving weather products.
sortawds	The sortawds program renames AWDS data products by their ID and copies them into a hierarchical directory structure reflecting their product type.
viewawds	The viewawds program creates ASCII text files from AWDS data products. These may be displayed with any word processor or text editor.
a2surf	Create SCIPUFF compatible surface observation files from AWDS Appendix 30 products.
a2air	Create SCIPUFF compatible upper air (profile) observation files from AWDS Appendix 30 products.
a2mrf	Create SCIPUFF gridded data files (mrf) from AWDS Appendix 30 products.

Figure 4 illustrates the ease with which WOW output can be imported, displayed and visualized in various MS-Windows applications.



3. FUTURE DEVELOPMENT OF WOW

The next phase in the development of the AWDS to PC interface will be to:

- Add a more user friendly, windows/menu interface to the VIEWAWDS program.
- Add options to sort the real-time AWDS data into a hierarchical directory structure reflecting product type or geographic location
- Add options to pre-process the AWDS data stream directly into input files for other applications. Allow the daemon and the application to run simultaneously.
- Develop a Daemon or Background process that will delete unwanted product files as a function of product type or geographic location. For example, NOTAMs could be deleted when only surface and upper air data are required.
- Develop a menu driven preprocessor that will take near-real-time surface and upper air data reports and massage them into the required format for ingest into various atmospheric models. The initial effort will be to interface to the RAMs Mesoscale Model.
- Along with PC versions of the software, Workstation based versions of the software will be developed in parallel for DNA applications.

Acknowledgement

This work was supported under contract number DNA001-94-C-0096 with the Defense Nuclear Agency. "The views expressed in this article are those of the author and do not reflect the official policy or position of the Department of Defense or the United States Government."

FURTHER ASSESSMENT OF THE METEOROLOGICAL OFFICE MESOSCALE MODEL FOR THE PREDICTION OF ARTILLERY BALLISTIC MESSAGES, AND THE DEVELOPMENT OF AN ARTILLERY METEOROLOGICAL PACKAGE FOR FORECASTERS

Peter F Davies
Services and Business Division, Defence Projects
Meteorological Office, Bracknell, Berkshire, RG12 2SZ, UK

ABSTRACT

During the Summer of 1994 an assessment of the potential of using data from the Met Office Mesoscale Unified Model (MM) to produce artillery ballistic messages was made in conjunction with the Royal Artillery. The original assessment was carried out using a limited set of data collected from Larkhill. This paper reports on the results of a further assessment using a significantly larger database.

Data obtained from radiosonde ascents flown at Larkhill was collected and used to validate the MM predictions. In particular wind speeds, directions and temperatures were compared through the zones used for artillery ballistics. The results are discussed in terms of the potential use of the MM, for making ballistic forecasts for training ranges, and the paper describes the 'artillery software package' subsequently developed for range forecasters.

1. INTRODUCTION

Larkhill Met Office is responsible for providing ballistic meteorological support to a number of artillery ranges throughout the British Isles. Most of these ranges are remote and radiosonde ascents are rarely made at these locations. Therefore to provide these ranges with ballistic meteorological data the Larkhill forecasters had to rely on choosing the most representative upwind ascent available even though this may have been flown some considerable distance away, and four to five hours previously. In addition the forecasters had access to forecast data such as wind speed, direction, pressure and temperatures at standard WMO levels for the UK upper air network stations. Clearly the reliability of the ballistic messages produced was very dependent on the forecaster's ability to interpret and process the available data. Since this was a manual process it was time consuming and its accuracy was questionable.

This led to the initial study by Turton et al, (1994) to assess the potential of using site-specific Mesoscale Model (MM) profiles for ballistic forecasting. The results from this study showed

that the MM profiles were sufficiently accurate to be useful for ballistic forecasting and suggested that these data should be made available for forecasters. However, this study was based on a limited dataset, covering just two months. This paper builds on that work and examines the accuracy of the MM profiles for a much larger dataset covering a period of 12 months, from July 94.

2. RADIOSONDE DATA

The ascent data collected for this assessment was obtained from the Vaisala PC-Cora system installed at Larkhill met office. This consists of an RS80 sonde that measures temperature and humidity. These are recorded by the sonde at two second intervals. Wind speed and direction are calculated by radar tracking a target which is suspended beneath the balloon. Using this archived data, temperatures and winds were calculated for the ballistic zones which are shown in Table 1.

Zone	Zone Height (m)	Mid point(m)
00	surface	0
01	0-200	100
02	200-500	350
03	500-1000	750
04	1000-1500	1250
05	1500-2000	1750
06	2000-2500	2250
07	2500-3000	2750
08	3000-3500	3250
09	3500-4000	3750
10	4000-4500	4250
11	4500-5000	4750
12	5000-6000	5500
13	6000-7000	6500
14	7000-8000	7500
15	8000-9000	8500
16	9000-10000	9500
17	10000-11000	10500
18	11000-12000	11500
19	12000-13000	12500
20	13000-14000	13500
21	14000-15000	14500
22	15000-16000	15500
23	16000-17000	16500
24	17000-18000	17500
25	18000-19000	18500
26	19000-20000	19500

Zone	Zone Height (m)	Mid point(m)
00	surface	0
01	0-200	100
02	200-500	350
03	500-1000	750
04	1000-1500	1250
05	1500-2000	1750
06	2000-3000	2500
07	3000-4000	3500
08	4000-5000	4500
09	5000-6000	5500
10	6000-8000	7000
11	8000-10000	9000
12	10000-12000	11000
13	12000-14000	13000
14	14000-16000	15000
15	16000-18000	17000

Table 1. Heights of the Standard Computer Meteorological Message (SCMM) zones (left) and Standard Ballistic Meteorological Message (SBMM) zones (right)

Typically the RS80 sensors have an accuracy of $\pm 2\%$ for humidity and $\pm 0.2\text{ }^{\circ}\text{C}$ for temperature. The rms vector wind errors are approximately $0.4 - 0.8\text{ ms}^{-1}$ from 9 km to 20 km height. The various parameters were calculated in different ways. The virtual temperature and pressure were given at specific heights that corresponded to the mid point of each zone, whilst the winds were means through the entire layer.

3. THE METEOROLOGICAL OFFICE MESOSCALE MODEL

The Met Office Mesoscale Model is part of the operational 'Unified Model' suite (Cullen, 1993) that is run routinely several times a day on the CRAY supercomputer at Bracknell. The suite consists of three versions of the Unified model, the largest being the Global model which has a horizontal resolution of 90 km and 19 vertical levels up to about 40 km. Nested within that is the Limited Area Model (LAM) which has a higher resolution of approximately 50 km with the same 19 vertical levels. This covers an area stretching from North America in the west to Russia in the east, and from Greenland in the north to North Africa in the south.

Finally there is the Mesoscale Model, the UK version of which takes its background fields from the LAM. The MM has a horizontal resolution of approximately 17 km and has 31 vertical levels. The heights of these levels (Table 2) vary slightly since they are defined using a hybrid sigma/pressure co-ordinate system which smoothes out the effect of topography higher up in the atmosphere. The MM domain is a grid of 92×92 points which covers the British Isles and part of north west France. This is shown in Figure 1. For any location in this area a forecast vertical profile of the atmosphere can be produced for hourly intervals. These are available out to a forecast time of 36 hours ahead.

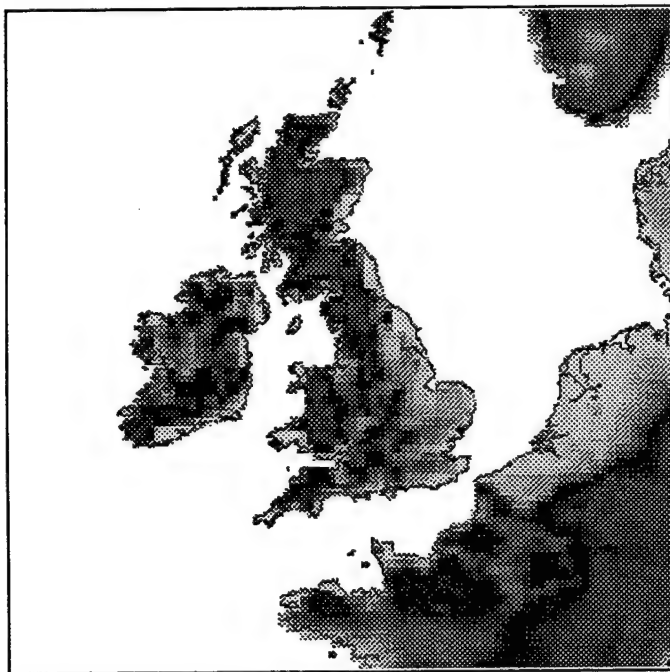


Figure 1. Area covered by the Mesoscale Model grid

Model Level	Height (m)	Model Level	Height (m)	Model Level	Height (m)
1	10	12	1600	22	7900
2	40	13	1870	23	9040
3	100	14	2200	24	10260
4	190	15	2600	25	11750
5	300	16	3080	26	13700
6	435	17	3640	27	16200
7	595	18	4300	28	19700
8	770	19	5050	29	23850
9	955	20	5870	30	29000
10	1155	21	6800	31	36000
11	1365				

Table 2. Approximate heights (above ground level) of the Mesoscale Model levels

4. COMPARISON AND ANALYSIS OF ACTUAL AND MODEL DATA

The model forecast data (out to T+18) for Larkhill (51.2°N, 1.8°W) was archived from the midnight (00Z) run of the model. Of particular interest was the MM data for T+6, T+8 and T+10 which coincided with the ascents made at Larkhill. On most occasions the 08Z flight at Larkhill was a 'pilot' ascent and so only wind data was recorded. However at all other times a full ascent was made. From the model data, temperature and winds were calculated for each zone. SCMM's and SBMM's were then created and these were compared to messages produced using the sonde data. As noted earlier the data was archived over a period of one year running from July 1994 through to July 1995. Over that time 483 ascents were available for analysis.

4.1 Wind Profiles

As far as artillery ballistics are concerned the dominant meteorological factor affecting the trajectory of a shell is the wind speed and wind direction, i.e. the wind vector. Figure 2 shows the magnitude of the MM vector wind errors for the SCMM zone midpoints. Up to approximately 5500 m the rms wind errors increase slightly with height with values of 3 to 4.5 ms^{-1} , with the T+6 forecast showing the smallest error. The errors increase noticeably in the region from 6000 to 12000 m (zones 13 to 19) up to a maximum of 5.7 to 6.4 ms^{-1} . These larger errors are associated with the jet stream, situated just below the tropopause (300 mb or approximately 10000 m), which has a core region of strong winds and significant wind shear. Because the winds are stronger and change more frequently it is clearly a region which is difficult to forecast accurately. Above this region the errors fall back to typically 3 to 4 ms^{-1} . Over all of the SCMM zones the average rms errors are 3.9 ms^{-1} for T+6, 4.2 ms^{-1} for T+8 and 4.6 ms^{-1} , for T+10.

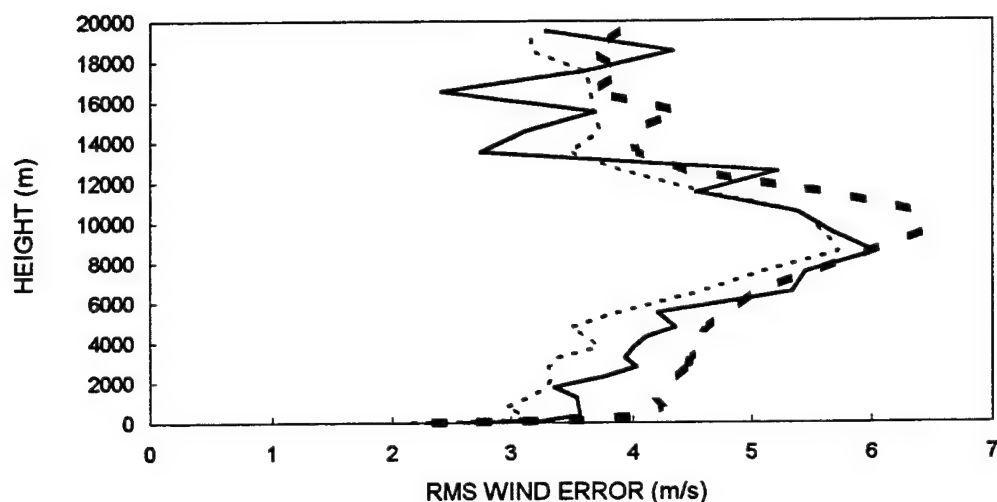


Figure 2. Magnitude of Mesoscale Model rms vector wind errors against height for T+6 (dotted), T+8 (solid) and T+10 (dashed).

Figure 2 shows that an increase in the forecast time generally leads to an increase in the mean errors. This is as expected since as the forecast time increases the less reliable the model data becomes. Overall, the wind errors are larger than those reported by Turton et al (1994). This is probably because the present data also covers the winter months during which the winds tend to be stronger and more changeable.

4.2 Temperature Profiles

For a given pressure, the temperature is inversely proportional to the air density which contributes to the range error in artillery fire. Figure 3 shows the rms temperature errors. Since the majority of 08Z flights were pilot ascents and no temperature data was recorded the results for T+8 are based on a much smaller dataset (17 cases). Even so they still give broadly consistent results.

The errors for those zones up to about 10000 m are between 0.8 °C for T+6 and 1.4 °C for T+10. As with the wind data, in the region of 10000 to 13000 m the errors increase markedly to 1.6 - 2°C. This again is associated with the tropopause. Fluctuations in the height of the tropopause can be difficult for the model to predict and thus give rise to increased temperature errors.

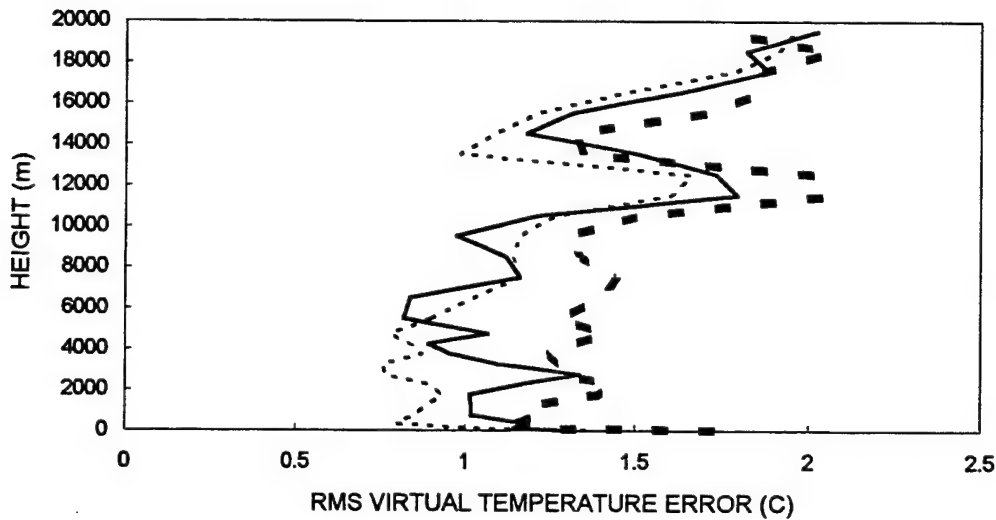


Figure 3. Mesoscale model rms virtual temperature errors against height for T+6 (dotted), T+8 (solid) and T+10 (dashed).

4.3 Ballistic Winds

The artillery ranges also make use of SBMMs which give the ballistic winds and temperatures. The ballistic wind up to a given line is calculated by applying various weighting factors to the wind data in the SBMM zones below that height. The higher zones have the greater weighting factors since a shell will spend a greater proportion of its flight time in this region than at lower levels. The effects of the individual zones are combined to give the overall ballistic wind and temperature. The ballistic wind is that wind, constant in speed and direction up to a given line, which would have the same effect on the shell as the actual wind conditions.

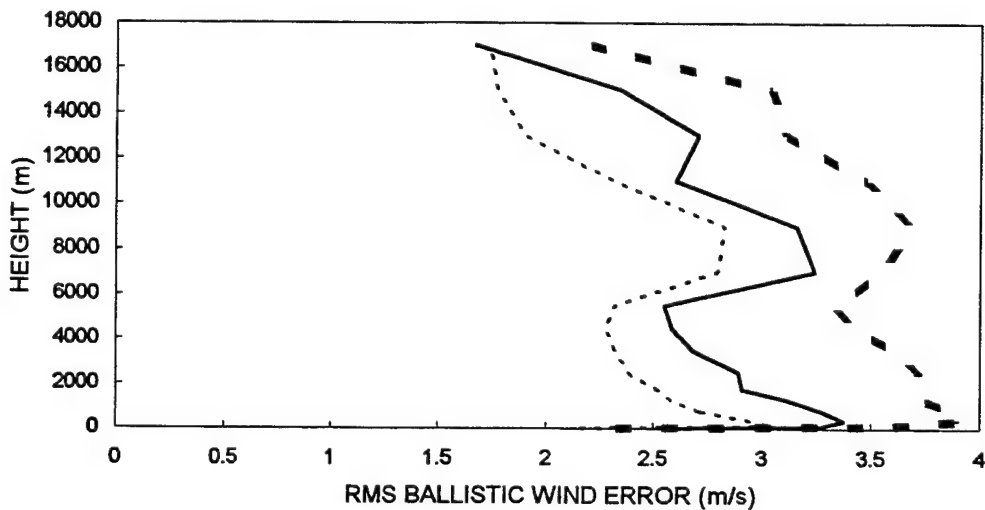


Figure 4. Mesoscale model rms ballistic wind errors against height for T+6 (dotted), T+8 (solid) and T+10 (dashed).

As noted by Turton et al (1994) the errors in the ballistic winds are less than those for the actual winds. However since the SBMMs are derived from the same data as the SCMMs, those regions that show up the largest errors should be roughly the same even though various weighting factors have been applied. From Figure 4, the area around the 'jet region' exhibits increased rms errors but these are significantly less than those associated with the actual winds. A jet region is a fast current of air (greater than 30 ms^{-1}), generally found near the tropopause, which is characterised by strong vertical and lateral wind shears. Throughout all of the SBMM zones (up to 18000 m) the average rms errors in the ballistic winds are 2.5 ms^{-1} for T+6, 2.8 ms^{-1} for T+8, and 3.4 ms^{-1} for T+10. This, again, is as expected with the errors increasing as the forecast time increases.

5. OUTCOME AND FURTHER DEVELOPMENT

The results from this further assessment of the MM reinforce the conclusion that the site-specific MM data is sufficiently reliable to be useful to the forecaster in providing ballistic meteorology for the artillery ranges. Consequently an 'Artillery Meteorology' software package has been developed for use by the forecaster. This system is briefly described below.

5.1. The Artillery Meteorology Package

The package consists of two distinct modules. The first is a communications module to allow the basic model data to be called-up by the forecaster. This is achieved by using 'dial-up' software and a link (via a modem) to a host system located at Bracknell that stores the appropriate model data. Having dialled in, forecast data out to T +18 hours, for several defined ranges, is automatically downloaded. The MM data held on the host system is updated four times a day from the 00,06,12 and 18Z model runs. To reduce the time required to download the data, the data is stored in BUFR (Binary Universal Form for Data Representation) code. As its name suggests, the code stores the data in binary form, thus significantly reducing the file size which permits a quick and efficient transfer of data.

The next module of the system, which is MS Windows based, decodes the MM data and displays it on the forecasters' PC monitor. This display screen is shown in Figure 5. The model data can then be subjected to 'forecaster intervention' such that any dubious or unreliable model data can be modified. For example, there may be occasions when the model clearly exhibits timing errors and the forecaster needs to take account of this. It is considered important that forecaster intervention is possible since value can still be added to the final product (SBMM, SCMM). The system is set-up such that any modifications to the profiles that need to be made can be easily done by editing the appropriate data. Where necessary, other parameters (e.g. the height) are automatically recomputed following any data editing.

Artillery Meteorology (Unified Model)							
File View Communications Options Help							
Larkhill							
51 20N 001 80W 27/03/95 06:00 UTC 1 x 07							
Model Level	Height (m)	Pressure (hPa)	Temperature (°C)	Dewpoint (°C)	Relative Humidity (%)	Wind Direction (deg. true)	Wind Speed (knots)
00	00	1000.5	6.4	-3.8	48	339	12
01	10	999.3	5.2	-5.5	46	339	12
02	38	995.8	4.9	-5.5	47	341	17
03	95	988.7	4.4	-5.6	48	343	21
04	180	978.3	3.5	-5.7	51	344	24
05	285	965.5	2.5	-5.8	54	345	25
06	418	949.5	1.2	-6.3	57	346	26
07	574	931.1	-0.3	-6.4	63	347	28
08	742	911.5	-2.0	-6.9	69	349	29
09	920	891.0	-3.7	-7.3	76	352	30
10	1110	869.6	-5.6	-7.8	84	354	31
11	1313	847.0	-7.4	-8.8	90	357	31
12	1533	823.1	-9.4	-12.9	76	359	31
13	1793	795.5	-11.1	-20.2	47	001	32
14	2109	763.0	-13.8	-23.9	42	002	33
15	2487	725.5	-16.9	-30.3	30	360	37
16	2934	682.9	-20.1	-37.3	20	357	36
17	3462	635.4	-22.5	-59.1	2	347	41
18	4091	582.8	-23.0	-49.2	7	335	58
19	4812	527.8	-22.8	-59.3	2	331	85
20	5610	472.6	-25.6	-45.9	13	332	104

Figure 5. Forecaster display of the Mesoscale Model data

The final step involves creating the SCMM and SBMM messages, printing them out and sending them on to the range customer. Various options are available that allow the messages to be tailored to the recipient's needs. The package was initially installed for trialling at Larkhill in April 1995 and has subsequently been installed at Brize Norton. A programme is in hand to install the system at all other UK met offices which have to provide ballistic meteorology.

5.2. Further Developments And Applications

An additional application of the system is in providing site-specific profiles (up to 3 km height) for making predictions of gun noise. This is particularly important at a number of ranges that have populated areas nearby where they have to balance training requirements against the need to minimise public nuisance and noise complaints.

An identical package has also been implemented during (October 1995) at Gütersloh Met Office to provide support for Royal Artillery units operating on German ranges. This operates in exactly the same way as for the UK except that the site-specific data has to be generated from

the Limited Area Model (which has a lower horizontal resolution). Nevertheless the LAM data is still of a sufficient quality to be useful to the forecasters.

There are also plans to supply the Mobile Meteorological Unit (MMU) with the Artillery Meteorology package. The MMUs primary role is to provide the allied forces with meteorological support, anywhere in the world, through teams of deployed forecasters. The provision of ballistic meteorology to artillery units is one of their jobs. There are currently MMU deployments in Italy, Turkey and the former Yugoslavia. These units are self sufficient and have all the equipment necessary to set up and receive met data from Bracknell or alternative sources.

6. CONCLUDING REMARKS

Although the accuracy of the model data is considered to be sufficiently good to support artillery units it must be recognised that model data will not be as accurate or as timely as on-site data. However for the UK the amount of actual upper air data is limited to that recorded at a number of fixed upper air stations throughout the country. Such is the spread of these fixed sites that in the past 'forecast upper air ascents' were being used to create messages for firing ranges that were many miles from the available fixed upper air stations. The results and analysis here suggests that site-specific model forecast data is sufficiently reliable to produce artillery met messages, which are likely to be as accurate if not more so than those based on manual 'forecast upper air ascents'. An important aspect of the system that has been developed is in the forecaster interaction which allows for manual quality control, and hence further improves the model data.

The analysis of the data clearly highlights two areas where the errors in the model forecast data are greatest, emphasising the need for forecaster intervention. Whilst it is difficult to add value to the model predictions for the 'jet stream' region (since actual data is not readily available), for the boundary layer the forecaster does have access to actual observations from which more accurate low level winds and temperatures can be determined.

The final outcome is that the Artillery Meteorology Package has been installed at several sites and is being used operationally to support artillery firing and to make gun noise predictions. Plans are in hand to install the package at all the range met stations throughout the UK.

REFERENCES

Cullen M J P, 1993: The Unified Forecast /Climate Model, Meteorol Mag, 122, 81-94.

Turton J D, Davies P F, and Wilson Maj. T G, 1994: An Assessment of the Potential of the Meteorological Office Mesoscale Model for Predicting Artillery Ballistic Messages. In Proceedings of the 1994 Battlefield Atmospherics Conference, White Sands Missile Range, NM, USA.

Session II

BATTLE WEATHER INTEGRATION

UAV DROPSONDES: A TARGET AREA SYSTEM

J. Cogan

Army Research Laboratory, Battlefield Environment Directorate
White Sands Missile Range, NM 88002

T. Greenling, S. A. Luces, and J. Thomas
New Mexico State University, Physical Science Laboratory
Las Cruces, NM 88003

1. INTRODUCTION

Detailed, quantitative, atmospheric data are essential for accurate analyses and forecasting of mesoscale phenomena for military and civilian applications. Environmental satellites provide qualitative and broad scale quantitative information (e.g., cloud amount and type) over remote areas and supply quantitative input more suitable for synoptic scale analyses (e.g., temperature and dewpoint soundings for standard atmospheric levels). However, satellite instruments for measuring atmospheric variables have relatively large footprints and vertical resolutions (Miers et al. 1992). For remote mesoscale areas (Orlanski 1975), especially those approximately 500 by 500 km or smaller, airborne systems remain the only reliable source of detailed, quantitative, accurate data. Within denied and target areas, use of manned aircraft for gathering atmospheric data, normally, does not occur because of the high risk to personnel and expensive equipment. Nevertheless, unmanned aerial vehicles (UAV) can carry small sensors and dropsondes into denied and target areas, without degrading other mission payloads, at no risk to personnel and at a very low cost. The small meteorological (met) sensor originally developed by the Battlefield Environment Directorate (BED) of the Army Research Laboratory (ARL) recently passed an operational test by the Navy using a Pioneer air vehicle and was certified as suitable for operational use on UAV.

The Joint Project Office for UAV has stated its support for the ongoing joint service program for development of a small dropsonde and dispenser system for UAV. The lead organizations on the project were the ARL/BED, the Tactical Oceanographic Warfare Support Program Office of the Naval Research Laboratory, and the Joint Technical Center/Systems Integration Laboratory. ARL/BED led the development of the dropsonde, assisted by the Physical Sciences Laboratory (PSL) of New Mexico State University. This paper briefly discusses the program and presents the results of the flight test at the conclusion of phase 1. For more details on the specific dropsondes and flight test, refer to Greenling et al. (1995). Phase 1 investigated current off-the-shelf capability (as of early FY95) with a modification to obtain wind profiles via Global Positioning System (GPS) techniques. Phase 2 will seek to produce proof-of-concept prototype dropsondes and a dispenser for an operational UAV. The third and final phase will produce a prototype system.

2. JOINT DROPSONDE PROGRAM

The joint program evolved out of an ARL/BED effort to test current dropsondes with a modification for GPS wind finding. The Army effort, now referred to as phase 1, successfully concluded in January 1995 following a test of two types of dropsondes manually ejected from a helicopter flying over White Sands Missile Range (WSMR), NM, in December 1994. The results

of this test provided input for specifications for a low-cost dropsonde capable of being carried in a dispenser on an actual UAV. An open solicitation led to the selection of Vaisala as the supplier of the proof-of-concept dropsonde for phase 2. The sonde was still under development when this paper was written and scheduled for delivery early in the first quarter of FY96. When funding becomes available to continue the program, it is planned to flight test the dropsonde system (dropsondes plus dispenser), following intensive ground and laboratory testing. For this test, the dropsondes will transmit data to a dedicated ground station for processing into met profiles. Most of the processing of the GPS information also will occur in the ground station. The dropsonde will receive, modify, and retransmit the signals from the GPS. The dropsonde profiles will be compared with rawinsondes launched by ARL/BED personnel and with atmospheric profiles generated by the Mobile Profiler System (MPS). Wolfe et al. (1995) and Cogan (1995) describe the MPS and the various types of output available. Software on the MPS will allow near real-time processing and comparisons of soundings generated by the MPS and the dropsonde, as well as comparisons of rawinsonde with dropsonde profiles.

Phase 3 will begin after the successful completion of phase 2 and the provision of sufficient resources. The final phase of the development program will concentrate on a prototype system that includes processing on-board the air vehicle. The UAV will transmit only the needed met information, thereby reducing the communications requirement to a bare minimum.

3. PHASE 1 TEST AND RESULTS

The flight test took place on 14 Dec 94 at WSMR, NM. Two types of sondes were tested, one built from commercial parts by PSL and another by Radian, Inc. Both sondes used GPS techniques to obtain wind speed and direction, and standard methods to obtain temperature, pressure, and humidity. The variables were recorded when the sondes were dropped from an altitude of approximately 12,000 ft (3,657 m) mean-sea-level (MSL).

Weather conditions at different altitudes for a given location can be measured by radar techniques, a rawinsonde (upsonde) carrying data collection equipment aloft, or a parachute suspended package (dropsonde) dropped from an aircraft. Wind speed and direction of a sonde are calculated by some form of direct tracking or with the aid of the OMEGA, LORAN, or GPS radio navigation systems by measuring time and location. The development of GPS has provided a means of increasing the accuracy of these measurements. GPS will be the replacement system for OMEGA and LORAN as they are phased out. There are several models of GPS receivers or engines that will acquire, track, and process the GPS coarse acquisition code and navigation information. The navigation accuracy of the GPS engine has a statistical distribution dependent on the error in the range signal caused by selective availability (SA) and the geometry or relative positions of the satellites and the receiver. A 3-D navigation solution can be computed when four satellites are being tracked by the GPS engine.

3.1 Radian Dropsonde

The Radian dropsonde prepared for this test is a small, tubular prototype that has a Trimble SVeeSix-CM2 GPS engine and antenna integrated with Radian's LORAN board. The board was modified to use GPS information coming from the Trimble engine instead of computing its location using the LORAN radio signals. Radian plans to redesign their dropsonde and build a board specifically for use with GPS. Several parameters in the sonde can be set, and commands can be

sent to the GPS engine via a connector on the module. The sonde transmits the GPS, pressure, temperature, and humidity (PTH) information to the ground station through a flexible wire antenna. The antenna is stowed with the dropsonde parachute in the top of the tubular structure. When the parachute deploys, the antenna is extended to its operational position by being attached to the parachute shroud line. GPS and PTH data are transmitted using direct digital modulation of the 403-MHz carrier with 1-kb/s encoded data. A ballute parachute is used to slow the descent of the sonde. A single shroud line connects the parachute to the top of the sonde. The vertical length of the parachute is approximately 84 cm (33 in.), and the horizontal section (measured diagonally) is 94 cm (37 in.).

A portable computer, battery, GPS antenna, GPS receiver/control box, and acquisition tube are used to prepare the dropsonde before it is dropped. This equipment is used so the Trimble GPS engine will acquire the GPS signals and go into a 3-D navigation mode quickly after the sonde is dropped from an aircraft. The antenna must be mounted outside the aircraft to receive the GPS signals. The acquisition tube is a hollow tube containing another antenna that retransmits the signals received by the external antenna. The GPS receiver/control box transfers up-to-date time, initial position, and almanac data to the dropsonde's GPS engine.

The Radian ground station consists of an antenna, receiver, and computer. The receiver/frame buffer decodes the telemetry data from the sonde and stores (buffers) the data in frames consisting of 16 data words. The frame rate from the sonde is 4 frames/s resulting in 64 words/s. Each word is 16-b quantity encoded as 4 ASCII hexadecimal digits. Sensor data are received in a raw, uncorrected format to reduce the processing load on the sonde. A 16-b time tag is also added by the frame buffer to each frame to provide unambiguous lost frame detection. The receiver sends each frame of data to the computer where it is stored for postprocessing. Commands can be sent to the receiver to control the receiver frequency and other parameters.

3.2 PSL Dropsonde

PSL constructed a dropsonde as proof of concept using a Rockwell Microtracker GPS engine, microcontroller board, Vaisala RS80-15 Radiosonde, and Aeroantenna Technology GPS antenna. The design concept in building the sonde was to buy off-the-shelf modules and minimize custom designs. The sonde was constructed using a 10-cm-(4-in.-)diameter by 51-cm-(20-in.-)length cardboard tube. Components were assembled in a tier structure and slid into the tube. The weight of the sonde with parachute is 1.45 kg (3.2 lbs).

An assembly language program was written to command the Microtracker, record navigation data, and transmit the desired information. The navigation information is stripped out and retransmitted to a ground station. The Microtracker sends frames of navigation and status information with a message ID over a serial receiver at 300 Bd using Vaisala's 403-MHz carrier. A total of 52, 8-b bytes are sent to the ground station from the dropsonde. The Microtracker provides navigation data once a second, but data are transmitted every 3 s because of the low baud rate. In addition, the PTH data are sent to the ground station on the 403-MHz carrier via a quarter-wave wire dipole antenna extending out of the bottom of the dropsonde during descent.

The sonde is built so the Microtracker can be switched to a standby (keep-alive) or normal operation mode. In normal operation mode, the Microtracker tracks the GPS satellites and transmits navigation telemetry data to the ground station. In the standby mode, satellites are no

longer tracked, which reduces current going to the Microtracker. Only the Microtracker's internal clock is incremented and the last sets of satellite parameters are maintained in static RAM. The stored satellite parameters allow a rapid navigation fix when the sonde is switched to operate mode if the age of the parameters is less than 4 h. The dropsonde's GPS antenna is mounted at the top of the tube, and the parachute is folded over the antenna. The parachute is a cross type configuration with eight shroud lines. Length across one section of the cross is approximately 152 cm (60 in.).

The dropsonde is operated by first acquiring and tracking GPS satellites while on the ground. The GPS engine is switched to standby mode and taken aloft in the aircraft. At the desired test altitude, the GPS engine is switched to normal operation mode and the sonde is dropped from the aircraft. Table 1 shows specifications for the Microtracker.

Table 1. Rockwell Microtracker specifications

	<u>Receiver Navigation Accuracies</u>				
	Horizontal		Position (m)	Vertical	Velocity (m/s)
	CEP	(2 dRMS)	3-D (2 sigma)	(2 sigma)	3-D (2 sigma)
Nav Accuracy, SA Off	25	50	93	78	0.5
Nav Accuracy, SA On	50	100	188	158	Not Specified
	<u>Maximum Vehicle Dynamics</u>				
			Navigation w/o Power		
	Acquisition		Management		
Velocity (m/s)	950		950		
Acceleration (m/s ²)	10		40		
Jerk (m/s ³)	20		40		

The ground station consists of a Vaisala Digicora MW11 Radiosonde receiver, two computers, a modem, and a Rockwell Microtracker. The Digicora receives and demodulates the PTH and GPS data. The PTH data are recorded on one of the computers via a serial communications port. A sample of the demodulated frequency module (FM) signal is sent into the modem, which decodes the 300-Bd GPS data and sends it to the second computer at COM port 2. The second computer also receives GPS information from the ground station Microtracker on COM port 1.

The PSL ground station uses a modified version of LABMON software to display and record the received GPS information. LABMON is the software supplied with the Rockwell Microtracker development kit. The modified software decodes the ground station GPS data and the dropsonde telemetry data and produces a real-time display as shown in figure 1. The dropsonde data are in the lower box in figure 1. The state and space vehicle identification (SVID) numbers for each channel (CHAN) of the two receivers are shown. The SVID number is the satellite the channel is currently tracking and a state 5 indicates the CHAN is processing the satellite ranging data. The asterisk next to a CHAN number indicates the channel is being used as a utility channel. The utility channel acquires and cycles through the satellites in view that are not being used to compute the 3-D navigation solution. Figure 1 shows that only space vehicles (SV) 14, 22, 29, 25, and 15 are in view of the antenna.

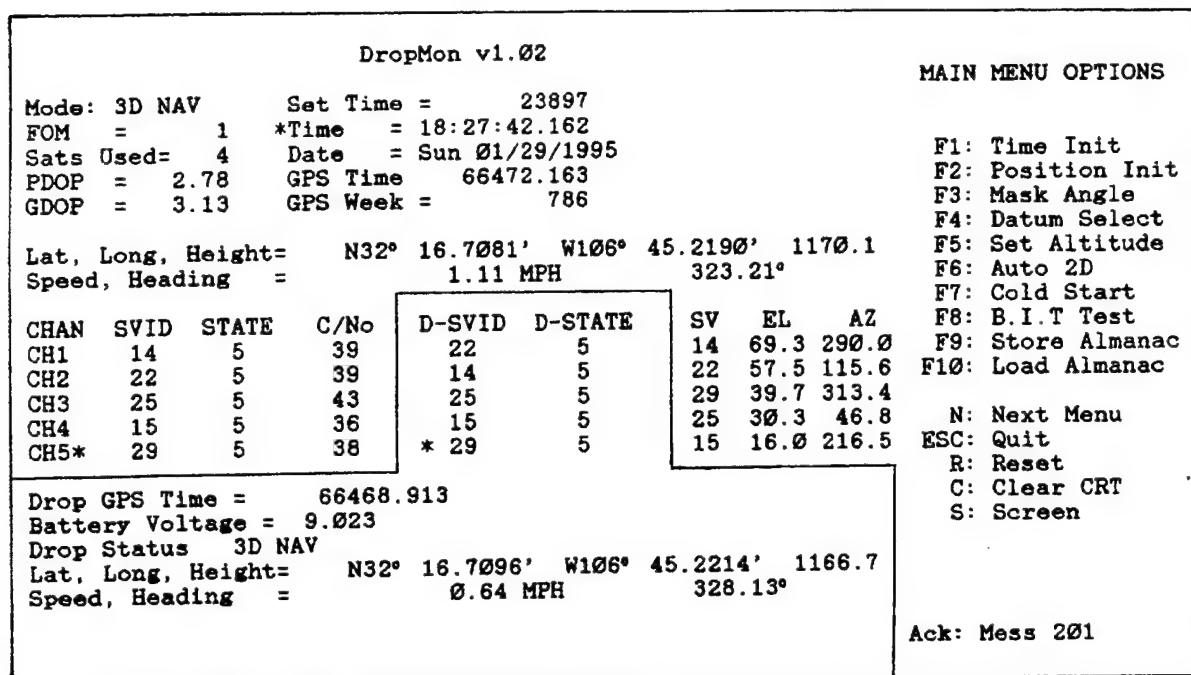


Figure 1. PSL ground station computer display.

Figure 1 also shows the antenna's latitude, longitude, height, speed, and heading. When figure 1 was made, the sonde and ground station antennas were positioned next to each other and stationary. The speed and heading values are caused by residual noise components in the navigation solution.

3.3 Dropsonde Test

The test of the dropsondes took place at the Dirt Site of WSMR on 14 Dec 94. A helicopter, rigged with a PVC tube and test computer, was used to take the sondes to an altitude of approximately 12,000 ft (3,658 m) MSL, 8,000 ft (2,438 m) MSL. Each sonde was inserted and dropped through the tube so its parachute would deploy below the helicopter. Two Vaisala upsondes were launched as part of the test. The first upsonde was launched at 1554 UTC before the helicopter arrived. The second upsonde was launched at 1820 UTC at the completion of the dropsonde tests. Data from each upsonde are used for comparison to the dropsonde information.

The first Radian sonde was programmed and dropped from the helicopter but did not transmit usable information to the ground station. We believe the parachute did not deploy based on the large number of telemetry check-sum errors received by the ground station receiver and because of the damage the sonde received when it hit the ground.

A PSL sonde was dropped next. The PSL sonde was dropped at approximately 1721 UTC or 1021 local and hit the ground 5 min 7 s later. The received telemetry shows the Microtracker acquired the GPS satellites and went to 3-D navigation mode approximately 45 s after leaving the helicopter. There are 4 min 22 s of usable GPS data from the sonde that start at the 3-D navigation mode and end when the sonde hit the ground. After hitting the ground, the sonde continued to transmit GPS and PTH data. The Microtracker stayed in a 3-D navigation mode for most of the time while on the ground. The sonde was found laying on its side when recovered after the test.

A second Radian sonde was dropped last. The Radian sonde was dropped without being updated with fresh GPS parameters because of a procedural oversight, which caused the sonde to take approximately 143 s to acquire the GPS satellites and go to a 3-D navigation mode. The sonde was dropped at 1730 UTC, acquired 3-D navigation at 1733 UTC, and stopped transmitting at 1736 UTC. The sonde transmitted good telemetry until it hit the ground. There are 2 min 48 s of usable GPS data from the sonde which started at the 3-D navigation mode and ended when the sonde hit the ground.

3.4 Test Results

Results of the test performed at WSMR 14 Dec 94 are presented in the following plots. Figures 2 through 5 contain raw wind data from the two dropsondes. In addition, wind profiler data measured by the WSMR Atmospheric Profiler Research Facility were taken but have not been included in this paper.

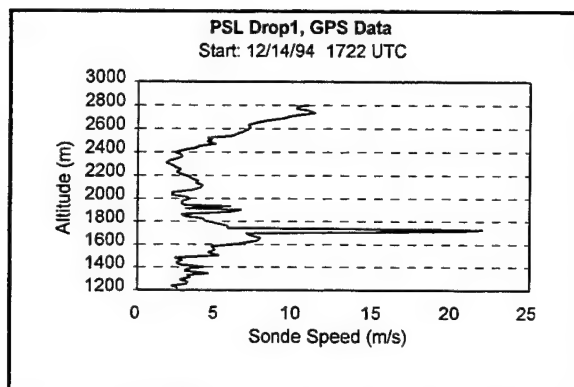


Figure 2. PSL dropsonde raw data, sonde speed versus altitude.

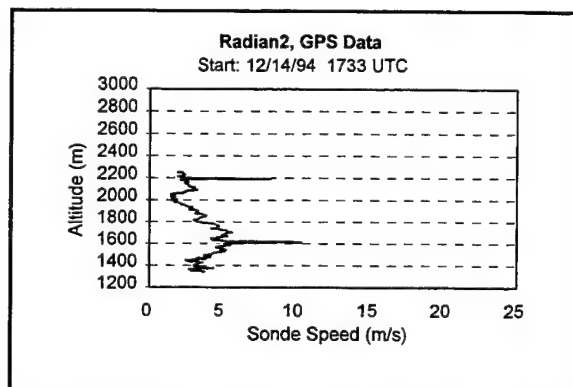


Figure 3. Radian dropsonde data, sonde speed versus altitude.

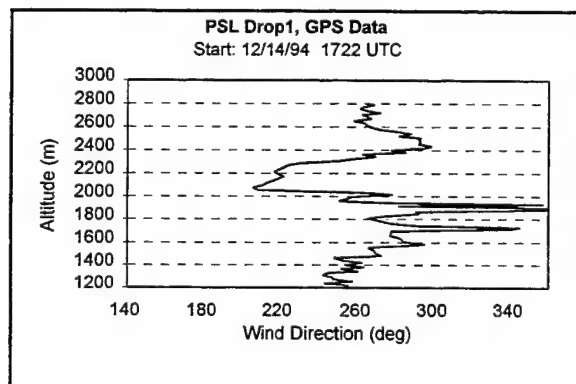


Figure 4. PSL dropsonde raw data, wind direction versus altitude.

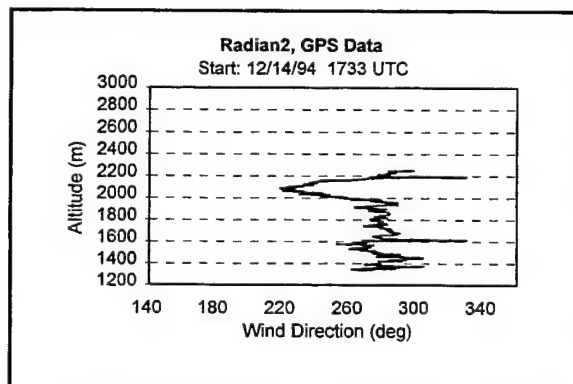


Figure 5. Radian dropsonde data, wind direction versus altitude.

All upper air sounding instruments appear to have some form of noise in their wind measurements. Rawinsondes or upsondes, for example, are influenced by small eddy motions in the atmosphere and swinging motions of the package under the balloon; real effects but not significant to synoptic

scale motion. Rawinsondes also have the problem of error caused by the method of measuring location (radio tracking, radar, or navigation aid). In addition, the balloon may not track the wind precisely as it rises because of the inertia of the system. Dropsondes suffer from all the problems of the rawinsondes. For example, Luces et al. (1995) discuss wind measurement corrections for dropsondes. In this experiment, the noise source of interest is the error introduced into the GPS location finding caused by the intentional SA errors. Wind profilers have their own set of noise sources (Wolfe et al. 1995; Cogan 1995).

To compare the results of the different wind measurements, the data had to be smoothed to reduce the effect of the noise. Figures 6 and 7 show PSL dropsonde data with only three point averages applied. This was done to slightly smooth the raw data for display only. The averaging is performed as follows: given data points A, B, and C, the new averaged data point is $B_{avg} = (A + B + C)/3$. One source, the rawinsonde truth, is already smoothed within the receiver when it receives and saves the data. The effect of this smoothing is to linearly fit the data in 600-m layers. Therefore, the PSL dropsonde data was also linearly fitted in 600-m layers for comparison to the rawinsonde. As the smoothing interval increased, the dropsonde profiles more closely matched those from the rawinsonde. At the 600-m smoothing, the wind speed and direction nearly fit between the earlier and later rawinsonde values.

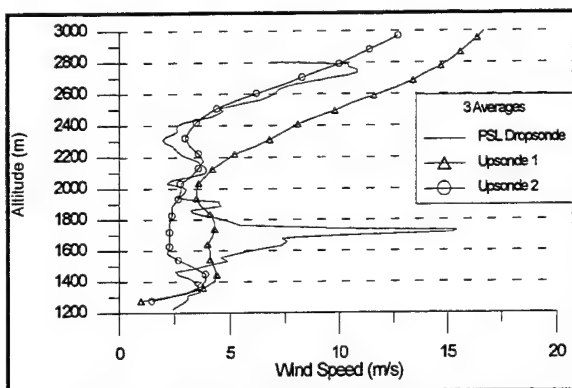


Figure 6. Comparison to PSL (speed, three point averages).

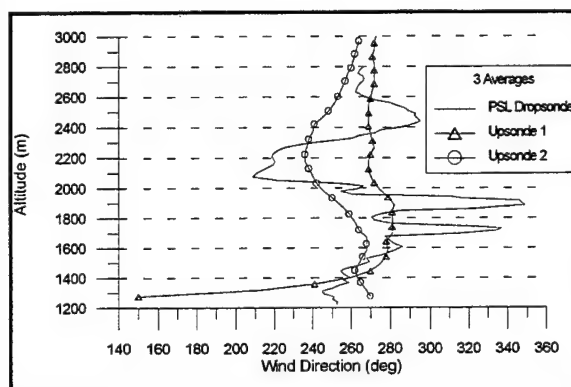


Figure 7. Comparison to PSL (direction, three point averages).

The method of smoothing is as close to the method reported by the maker of the rawinsonde instrument (Vaisala) as possible. This means that a linear fit is made to the data over the layer required. All data outside of the chosen confidence level (plus or minus one standard deviation in this case) are removed and replaced with the linear fit data. A linear fit is again produced and used in place of the original data. Figures 8 through 13 compare rawinsonde profiles with dropsonde profiles smoothed in 250- and 600-m (PSL only) layers. Figures 14 and 15 compare profiles from the PSL and Radian dropsondes, smoothed in 250-m layers.

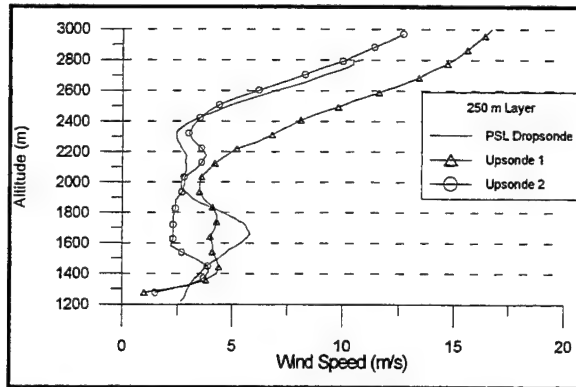


Figure 8. Comparison to PSL (speed, 250-m layer).

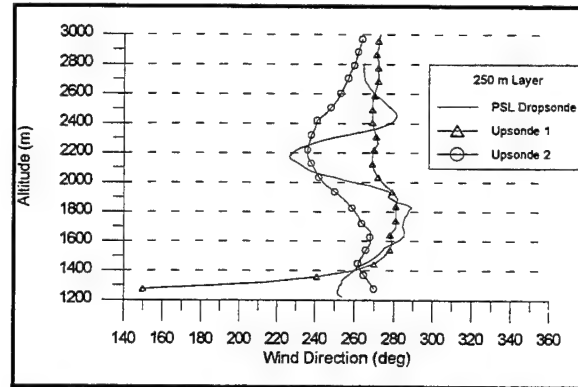


Figure 9. Comparison to PSL (direction, 250-m layer).

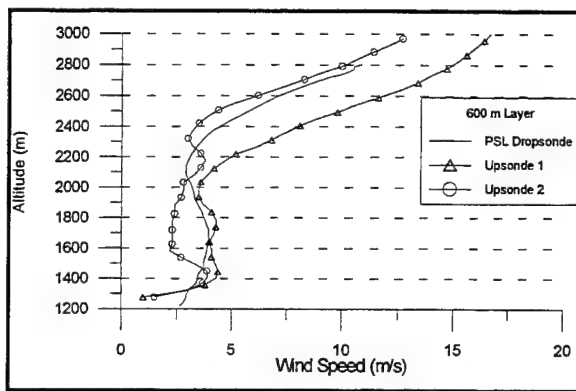


Figure 10. Comparison to PSL (speed, 600-m layer).

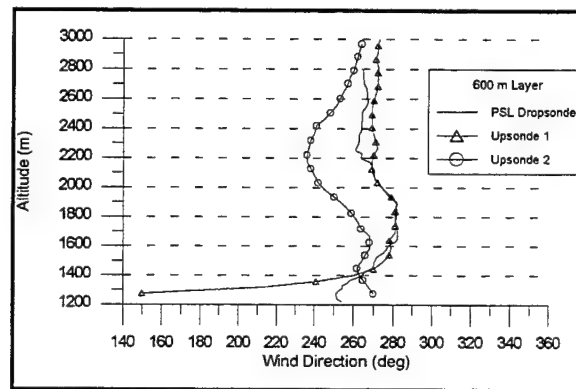


Figure 11. Comparison to PSL (direction, 600-m layer).

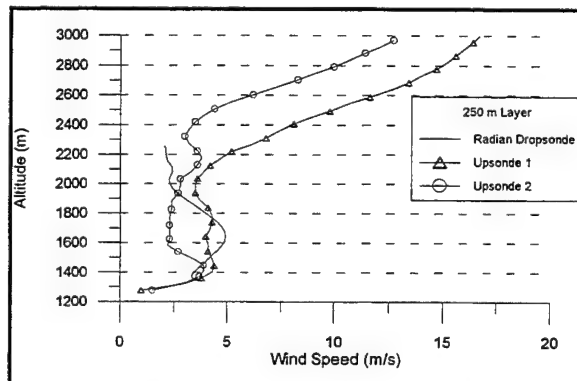


Figure 12. Comparison to Radian (speed, 250-m layer).

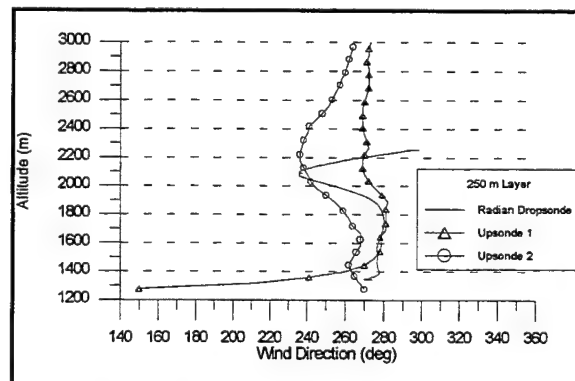


Figure 13. Comparison to Radian (direction, 250-m layer).

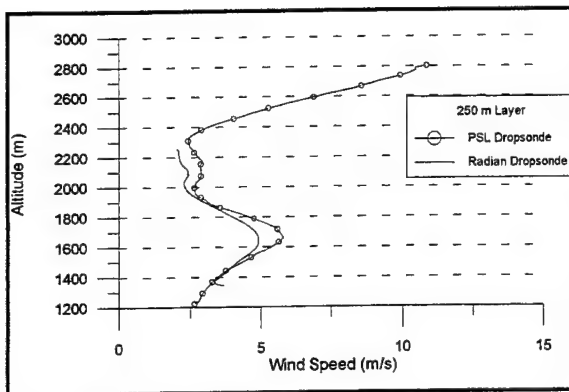


Figure 14. Comparison PSL to Radian (speed, 250-m layer).

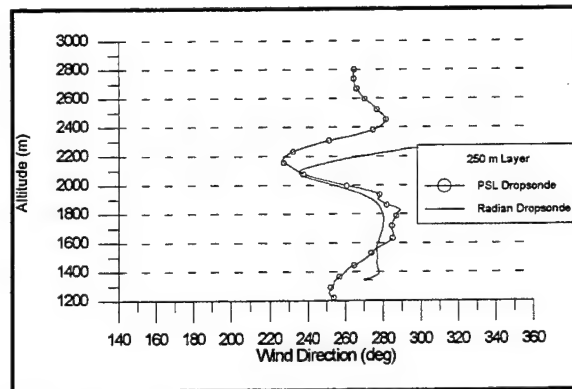


Figure 15. Comparison PSL to Radian (direction, 250-m layer).

4. PROBLEMS AND DISCUSSION

The PSL and Radian receivers had interference with the reception of the GPS satellite signals after the electronic sections were assembled and placed into the cardboard tubes. Shielding was required around the GPS engines to stop the transmission of interference signals. Radian soldered metal covers over the Trimble GPS engine and telemetry transmitter section of the LORAN board. The PSL sonde would not acquire any of the GPS satellites because of an interference signal coming from the GPS engine or Vaisala transmitter. The problem was corrected by wrapping the outer tube surface of the PSL prototype sonde with aluminum tape up to the GPS antenna.

The smoothed wind speed and direction data of the dropsondes are within the range of values given by the other accepted methods (upsondes and profiler). The majority of errors between the dropsondes and upsondes are caused by 1) differences between position accuracy of LORAN and GPS radio-navigation systems, 2) different flight characteristics of the parachute and balloon, and 3) time and location differences between measurements. Some of these types of errors are correctable by applying differential (position) correction techniques and by developing flight dynamic correction factors to account for the differences between the parachute and balloon. GPS position fixes are more accurate than the LORAN computed positions. Further, the GPS data requires data smoothing to be comparable to the currently accepted measurement results. The update rate of the GPS data in both dropsondes appears to provide an adequate representation of wind speed and direction. Radian's velocity is updated every 2 s and altitude is updated every 4 s. PSL's velocity and altitude data are updated every 3 s.

Of the two methods used to prepare for dropping the sondes, PSL's method is easier. Disadvantages of the PSL method are 1) the sonde must continually run on internal batteries or an external power supply until dropped from the aircraft, 2) the stored GPS information is time dependent, and 3) there is a time lag to reach the 3-D navigation mode after the sonde is dropped. The Radian preparation method benefits by allowing the dropsonde to be powered up shortly before the drop thus conserving its internal batteries. In addition, when uploaded with up-to-date GPS parameters, the dropsonde should acquire and reach the 3-D navigation mode quickly after clearing the aircraft launch tube. Disadvantages of the Radian method are the requirement of several pieces of auxiliary equipment with an externally mounted GPS antenna and the number of steps required to prepare the dropsonde.

5. CONCLUSION

The results from the phase 1 flight test indicated that current technology dropsondes updated with GPS wind finding technology are capable of producing atmospheric soundings with an accuracy close to that of rawinsondes. In fact, the 600-m smoothing (similar to that of the rawinsonde system) gave results that fell between the earlier and later rawinsonde flights. The flight tests planned for the phase 2 dropsonde system will check the quality of a system designed specifically for UAV that will require far less manual intervention. Coincident profiles from the MPS and nearly coincident rawinsonde launches will allow a thorough test and evaluation of the phase 2 system. The follow-on phase 3 will eliminate the need for a dedicated met ground station to process the data, because this function will occur on-board the air vehicle, probably within the dispenser container. With sufficient resources, the three-phase program could lead to a preproduction prototype before the end of FY97.

REFERENCES

- Cogan, J., 1995. "Test Results from a Mobile Profiler System." *Meteor. Appl.*, 2:97-107.
- Greenling, T., S. A. Luces, and J. Thomas, 1995. *Results of Dropsonde Tests Using the Global Positioning System (GPS)*. Final report under contract DAAD07-91-C-0139, Physical Science Laboratory, prepared for Battlefield Environment Directorate, Army Research Laboratory, White Sands Missile Range, NM, 39 pp.
- Luces, S. A., J. Spalding, G. Conrad, and J. Thomas, 1995. *Wind Measurement by Dropsonde: Comparison of Simulated Systems and a Wind Correction Method*. Final report under contract DAAD07-91-C-0139, Physical Science Laboratory, prepared for Battlefield Environment Directorate, Army Research Laboratory, White Sands Missile Range, NM, 29 pp.
- Miers, B., J. Cogan, and R. Szymler, 1992. *A Review of Selected Remote Sensor Measurements of Temperature, Wind and Moisture, and Comparison to Rawinsonde Measurements*. TR-0315, U.S. Army Atmospheric Sciences Laboratory, White Sands Missile Range, NM, 41 pp.
- Orlanski, I., 1975. "A Rational Subdivision of Scales for Atmospheric Processes." *Bull. Amer. Meteor. Soc.*, 56:527-530.
- Wolfe, D., B. Weber, D. Weurtz, D. Welsh, D. Merritt, S. King, R. Fritz, K. Moran, M. Simon, A. Simon, J. Cogan, D. Littell, and E. Measure, 1995. "An Overview of the Mobile Profiler System: Preliminary Results from Field Tests during the Los Angeles Free-Radical Study." *Bull. Amer. Meteor. Soc.*, 76:523-534.

**THE BATTLE WEATHER TEST BED:
A SYSTEM FOR PRODUCT DEVELOPMENT FOR
THE INTEGRATED METEOROLOGICAL SYSTEM**

J. R. Elrick
U.S. Army Research Laboratory
Battlefield Environment Directorate
White Sands Missile Range, New Mexico 88002-5501

ABSTRACT

The Integrated Meteorological System (IMETS) is a state-of-the-art soldier support system providing advanced meteorological technology and accurate weather-related information to Air Force Weather (AFW) personnel in worldwide Army operations. The IMETS is evolving through a block-improvement fielding approach implemented by the Project Director, IMETS through the Army's Program Executive Office Command, Control, and Communications Systems. The Battle Weather Division of the Battlefield Environment Directorate develops computer-based technology through the Battle Weather Test Bed (BWT). BWT research and development activities results are used by AFW forecasters to inform battlefield decision makers of weather conditions affecting operations and to facilitate prudent employment choices. BWT technology enables AFW personnel to provide more accurate weather support and allows the operational Army to use the knowledge of weather effects as a force multiplier.

1. INTRODUCTION

The technological superiority of the U.S. is essential to the future maintenance of battlefield dominance at all levels of conflict. The shrinking U.S. military force strength must be countered by smarter, more efficient war fighting capabilities. An accurate intelligence picture of the battlefield is required to plan operations and use battlefield conditions as a force multiplier to gain and keep dominance over the enemy. The Army's Intelligence and Electronic Warfare function of the Army Battle Command System (ABCS) combines knowledge of the enemy, the terrain, and the weather to paint a comprehensive battlefield picture. The Integrated Meteorological System (IMETS) provides state-of-the-art meteorological forecasting and analyses tools to the Staff Weather Officer so that decision makers will understand the weather and its effects on military systems. This knowledge, used properly, enables soldiers to prudently use existing or forecast weather conditions to gain advantage over the enemy. The Battlefield Environment Directorate (BED) is developing, refining, and testing weather-related software applications to make the IMETS an integral factor and part of intelligence preparation of the battlefield.

2. BATTLE WEATHER TEST BED

The Battle Weather Test Bed (BWT) is a research and development platform consisting of subsystems that are designed to have similar functionality to the operational IMETS. These functions include the following:

- Direct readout, processing, and display of Automated Weather Distribution System (AWDS) and Automated Weather Network (AWN) data using dedicated Air Force circuits from the Air Force Global Weather Central at Offutt Air Force Base (AFB), NE, and the weather data switch at Tinker AFB, OK, respectively.
- Assimilation of AWDS, AWN, and other weather data from various sources in and near the area of interest. Other data may consist of indigenous weather observations and forecasts, data from unmanned aerial vehicles, weather satellite transmissions (polar-orbiting and geosynchronous), artillery meteorological soundings, and ground-based observations from Army field personnel.
- Process and display the results of accurate battlescale (mesoscale) numerical forecast models providing four-dimensional fields of meteorological elements that affect operations to give a time-space battlefield weather forecast.
- Incorporate weather observations and analyses into tactical decision tools that allow soldiers, at any level, to make correct choices regarding weapons selection and employment tactics to gain the battlefield advantage. Armed with this information, the Army decision maker can use advance knowledge of weather and its effects to tactical advantage and "own-the-weather." This will save valuable resources and effectively use the weather as a force multiplier.

3. IMETS AND THE INTEGRATION SCHEME

The IMETS is a state-of-the-art weather system providing Air Force Weather (AFW) personnel with the advanced tools needed to support Army operations in peace-time exercises and at all levels of conflict. The IMETS concept of operations calls for it to be located at the echelons above corps level down to separate operating brigades and special operations units. The IMETS is fully self-contained in a standard integrated command post shelter mounted to a heavy High Mobility Multipurpose Wheeled Vehicle giving it the flexibility and mobility to deploy with its assigned combat unit. IMETS units are being fielded with BWT research and development technology as it evolves through a sequenced release process.

The integration scheme for BWT products is following a sequential, phased schedule coordinated between the IMETS Project Director and BED. The Block I BWT products were integrated in the first fielding of the IMETS hardware. A limited number of software applications were integrated to include the following:

- Data replication and data acquisition software to tailor AWDS and AWN data for BWT use
- Tactical decision aid products including; night vision goggle use, the weather effects matrix, and tactical weather effects messages

The products listed above were transitioned to Research and Development Associates (RDA) in Tacoma, WA, in November 1992. RDA served as the integration contractor for the initial production and fielding of the IMETS.

Since completion of the IMETS Block I release, BWT development has entered a three phase Block II research and development effort. Block II software releases are occurring on a regularly scheduled basis to the Communications and Electronics Command, Research, Development, and Engineering Center, Software Engineering Directorate (SED) at Fort Huachuca, AZ. Beta 1 was released to SED in February 1995 with an application suite that included the following:

- Improved data replication and data acquisition software
- Forecaster analyses and tactical decision aids for atmospheric sounding analyses; a Battlescale (mesoscale) Forecast Model (BFM); Gridded Meteorological Analysis products; nuclear, biological, and chemical downwind reports; and electro-optical system performance

Beta 2 was released in August 1995 and included improvements and technology refinements to the beta 1 applications.

The beta 3 effort is in development and will be the final BWT release to the IMETS and SED project directors. The beta 3 release is scheduled for early 1996. Before this release can take place, all of the previous software applications must be ported to the SUN computer system, which will be the platform for the new ABCS Common Hardware and Software (CHS II) system.

All beta releases, to date, have gone through rigorous local testing by a hand-picked test team comprised of meteorologists, including two with advanced academic degrees. All four test team members have operational weather support experience with detailed knowledge of weather support requirements and methods. The objective of the IMETS software testing, before its release to SED, is to ensure scientific reliability and user orientation. Testing is focused on making the software applications compatible with the operational support environment that IMETS will occupy both in peacetime and in time of actual or potential conflict. The philosophy is to go through a develop-test-fix-test cycle in which software discrepancies are identified early and corrected promptly, while the software applications are still in research and development. This approach provides IMETS with a useable software product before fielding. Follow-on activity will be required to correct problems discovered after fielding or when other user requirements are levied.

Documentation to include software test description documents, software users manuals, and software design documents are supplied with each release of BWT applications. The documents are revised to include the latest changes in software because of configuration management system problem reports or technology advances since the last release.

4. BATTLE WEATHER TEST BED TECHNOLOGY DEMONSTRATIONS

Since April 1994, the IMETS hardware platform and software applications with evolving technology efforts have been demonstrated at several locations in the continental U.S. and worldwide. The Army Research Laboratory (ARL) BED uses BWT to demonstrate the capabilities.

Communications capabilities and operational functionality were successfully demonstrated during Operation Desert Capture II (ODC II) at Fort Irwin, CA, in April 1994. The exercise involved sending data received at White Sands Missile Range (WSMR) from the Air Force

Global Weather Central (AWDS data) and the AWN data from Tinker AFB, OK, via satellite link to the remote IMETS at ODC II. Software applications, to include the BFM, were processed and used successfully by AFW personnel as the basis for operational support products in the field.

The BWT was an integral part of the Program Executive Office Command and Control Systems exhibit at the Association of the U.S. Army Convention held in San Jose, CA, in May 1994. In this exhibit, IMETS functionality was shown in its planned configuration as part of the Intelligence Electronic Warfare battlefield functional area feeding critical battlefield weather forecast information to nodes of the ABCS. Weather forecasts were fed automatically and upon demand to ABCS operators in a simulated tactical operations center.

Planned IMETS products, such as the Integrated Weather Effects Decision Aid and weather satellite connectivity capability, were demonstrated in Korea during August and September 1994. These capabilities were shown as part of the joint U.S./Korean Ulchi Focus Lens (UFL) exercise in support of the Louisiana Maneuvers Task Force technology demonstration in cooperation with the Battle Command Battle Laboratory at Fort Huachuca, AZ. At UFL, technology and advanced weather support capabilities were demonstrated in an extremely austere field environment. BWT technology and the associated products were actively used by weather personnel from the 607th Weather Squadron to give needed operational support to the joint exercise commander and his staff.

BWT and proposed IMETS capabilities were shown at a German field location in support of ATLANTIC RESOLVE (previously called REFORGER) during October and November 1994. Intercontinental satellite communications capabilities were shown as well as applications such as the ARL/BED BFM. The BFM demonstrated state-of-the-art techniques for predicting the terrain-induced mesoscale weather conditions over the area-of-interest out to 12-h in the future based on data received from WSMR as described in the ODC exercise.

In late January and early February 1995, BWT products were demonstrated as part of the Worldwide Intelligence Officer Conference held at Fort Huachuca, AZ. Advanced weather support techniques were shown to intelligence officers from around the world representing the full spectrum of military services. The ARL BED theme for the conference was "own-the-weather" through day-to-day operations by providing detailed information to weather personnel and the on-site battlefield decision maker in real time.

5. GENERAL FIELDING PHILOSOPHY/SCHEDULE

Currently, the BWT technology developed for IMETS is being fielded progressively. The philosophy is to field the system to users, according to need, in a three block approach with improvements and additions in each block. This is the objective for IMETS at the final fielding. In all likelihood, this will be modified to be a two block fielding to coincide with Army changes in the Common Hardware and Software (CHS). Block I used a Hewlett Packard computer hardware platform with a UNIX operating system, and Block II will use Sun Sparc computers operating with the Solaris operating system. The BWT transition to the new computer system began this year.

IMETS Block I has been fielded to units in the Republic of Korea, Fort Hood, TX, and Fort Bragg, NC. Weather personnel at Fort Bragg are using the IMETS for day-to-day operations

and in specialized exercise support to maintain proficiency. Their feedback is crucial to ongoing IMETS improvements, which will be made before future IMETS releases in the U.S. and overseas. This is consistent with the IMETS/BED test-fix-test used since the IMETS concept was conceived. The IMETS and BWT platforms were taken to various field locations in support of command post and field training exercises to determine system enhancements that could be made to make the system more useful to support the battlefield decision maker in using the weather as a force multiplier.

6. SUMMARY

The IMETS currently being fielded provides modern weather support capabilities to U.S. Army operations. The BWT efforts of BED will continue to be incorporated into IMETS so software and hardware advances keep pace with evolving technology. IMETS, when fully fielded, will provide weather personnel with the tools necessary to advise battlefield decision makers of the current and expected weather conditions in their area of operations. In this way, weather conditions may be exploited to the advantage of friendly forces to achieve battlefield dominance. Knowledge of the weather and its effects on military missions and associated systems will enable the battlefield commander to maintain the advantage over threats to truly "own-the-weather."

BATTLESCALE FORECAST MODEL APPLICATION TO ARTILLERY METEOROLOGY

T. Henmi and A. J. Blanco
U.S. Army Research Laboratory
White Sands Missile Range, NM 88002-5501, USA

J. Spalding
Physical Science Laboratory, New Mexico State University
Las Cruces, NM 88003, USA

ABSTRACT

The Battlescale Forecast Model (BFM) was adapted for artillery meteorology and was applied to the Twentynine Palms (29-Palms) Live Fire Exercise held in May 1995. BFM computed 6- and 12-h forecast fields. The model was initialized using input data such as the U.S. Air Force Global Spectral Model output and upper-air sounding available through Automated Weather Data System, as well as upper-air sounding data taken in the 29-Palms Marine Corps Air Ground Combat Center. Vertical profiles of pressure, windspeed, wind direction, temperature, and dew-point temperature forecast by the BFM were compared with observed sounding data. Different initialization methods were examined. Advantages of BFM to artillery meteorology are described.

1. INTRODUCTION

In previous applications of a mesoscale model to artillery trajectory calculations (Spalding et al. 1993; D'Arcy 1993), the Higher Order Turbulence Model for Atmospheric Circulation (HOTMAC), developed by Yamada (Yamada and Bunker 1989), was initialized by using only upper-air sounding data taken in the model domain. The Battlescale Forecast Model (BFM) (Henmi et al. 1995; Lee et al. 1994), developed at the U.S. Army Research Laboratory (ARL), employs HOTMAC for prognostic calculation and utilizes as input data the U.S. Air Force Global Spectral Model (GSM) forecast data, upper-air sounding data, and surface observation data, all of which are communicated through the Automated Weather Data System (AWDS) and Integrated Meteorological System (IMETS).

During the Twentynine Palms (29-Palms) Live Fire Exercise held in May 1995, the upper-air sounding data obtained at 29-Palms was transmitted to ARL at White Sands Missile Range (WSMR), and used, together with the data obtained through AWDS/IMETS, to generate the three-dimensional data file called *uvtq.file*. The data file, *uvtq.file*, was sent to 29-Palms to run BFM on a computer located at the exercise site.

ARL at WSMR and 29-Palms communicated through satellite communication.

The purposes of this paper are to describe data analyses methods for initializing forecast calculations in the exercise and to show how well the present method has improved forecast results.

2. MODEL DOMAIN AND OBSERVED DATA

Figure 1 shows the elevation distribution in the southern California area covering 1280 by 1280 km. The latitude and longitude of the center of the area are 35.066 N and 116.066 W, respectively. Objective analyses to create three-dimensional data fields were carried out over this area. The rectangle at the center covers the area of 112 by 272 km, and forecast computation was made for this area. The 29-Palms Live Fire Exercise was conducted in this area. Meteorological variables were calculated at 15 by 35 by 32 grid points with a horizontal grid spacing of 8 km. The top-of-model atmosphere was 10,000 m above the highest elevation in the domain.

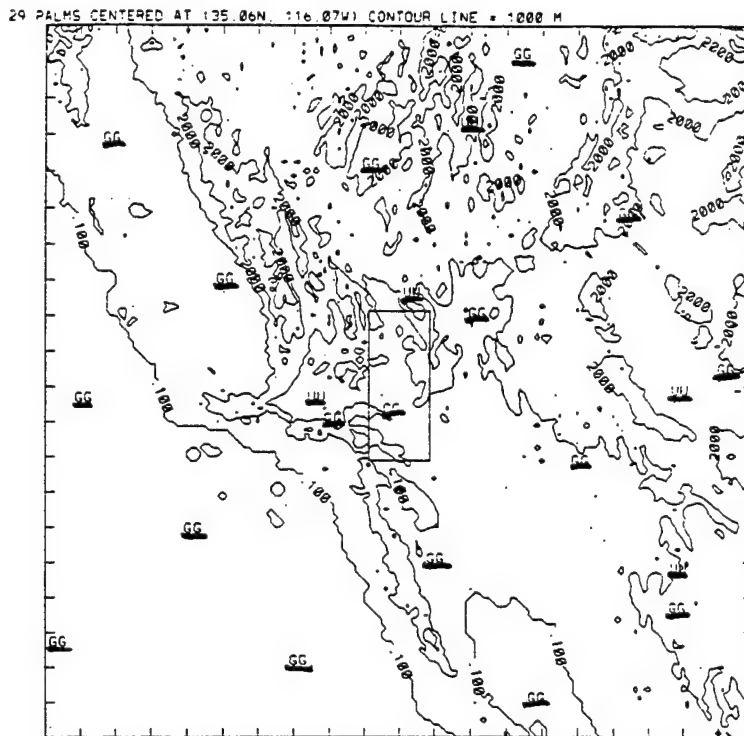


Figure 1. Elevation distribution map showing the locations of the 29-Palms Live Fire Exercise Area, GSM data (GG), upper-air data (UU), and special sounding data (CC). The latitude and longitude of the center are 35.066 N and 116.066 W, respectively.

GSM output is reported on grid points spaced 381 km apart on the mandatory pressure surfaces, as marked by GG in figure 1. Upper-air sounding data obtained through IMETS are marked by UU, and special sounding data taken during the exercise are marked by CC.

3. DATA ANALYSES METHOD

Using GSM (GG) and upper-air data (UU plus CC), three-dimensional data of horizontal wind vector components, temperature, and mixing ratio of water vapor are calculated by the following method (Hughes 1966):

1. From GSM data (geopotential height, temperature, dew-point depression, and west-east and south-north components of wind vectors, u and v , respectively), three-dimensional data fields of the above meteorological parameters, and surface pressure field are calculated for the entire area shown in figure 1. First, horizontal distributions of the parameters on standard pressure surfaces are calculated by using Barnes' objective analysis technique (Barnes 1973). Second, vertical profiles for the model grid are calculated by using a linear interpolation method.

If the elevation of a surface z is greater than the geopotential height ϕ_1 of the pressure surface P_1 and lower than ϕ_2 of P_2 , the surface pressure at the point n is calculated as,

$$P_n = P_1 + \frac{(P_2 - P_1)}{(\phi_2 - \phi_1)} (z - \phi_1). \quad (1)$$

Vertical distribution of the pressure in the model is calculated using P_n and the hypsometric relationship.

2. The three-dimensional data field created from the GSM output is used as a background field G , and composited with the upper-air observations (UU plus CC). The mean difference is defined as follows:

$$\bar{d} = \frac{\sum_{i=1}^N (O_i - M_i)}{N} \quad (2)$$

where

M = the values of G interpolated at station i
 O = the observed value at i .

By replacing G

$$G^* = G + \bar{d} \quad (3)$$

the mean error is removed, but the values of M_i^* interpolated in G^* for station i are not equal, in general, to O_i . Local difference

$$d_i^* = O_i - M_i^* \quad (4)$$

is not zero, but the mean d^* is

$$\bar{d}^* = \frac{\sum_{i=1}^N d_i^*}{N} = 0. \quad (5)$$

The next step is to distribute d^* to the entire field using a weighting function of $1/r^2$ as

$$G^{**} = G^* + \frac{\sum_i W_i d_i^*}{\sum_i W_i} \quad (6)$$

where

$$W_i = 1/r^2.$$

The above procedure is applied to all vertical levels of the model for all the parameters.

4. RESULTS

4.1 Result of Data Analyses

Figure 2 shows the result of compositing the GSM data with the upper-air data. Only the vertical profiles at the special sounding site (CC) in 29-Palms for 12 GMT 09 May 1995 are shown. Figure 2a is the vertical profile of GSM forecast data interpolated for CC. Windspeed, direction, temperature, and dew-point temperature are shown at the left, middle, and right portions of the figure. Figure 2b is the corresponding profile observed at the same site and same time, and figure 2c is the result of compositing GSM and sounding data. The method has produced reasonable profiles exhibiting the characteristics of figure 2a and b.

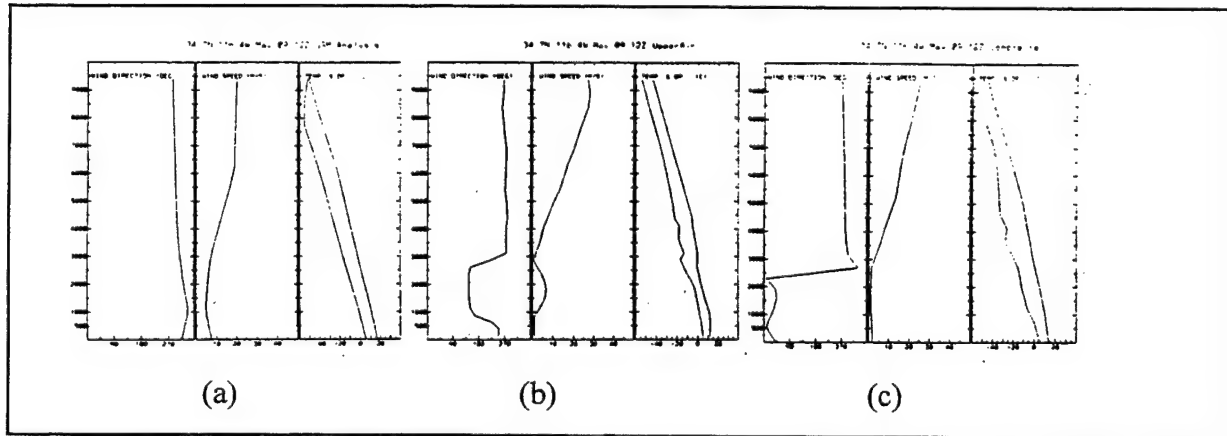


Figure 2. Vertical profiles of wind direction, windspeed, temperature, and dew-point temperature at the special sounding site in 29-Palms for 12 GMT 09 May 1995 (a) interpolation from GSM forecast data, (b) observation, and (c) composite.

4.2 Comparisons of Forecast Results with Observation

In the forecast calculations, the initial and 12-h forecast fields of GSM are used to produce hourly data by a linear interpolation between two time periods. At 2 h before the initiation of forecast computation, the initial field data are assimilated using the nudging method for 2 h. After that, the next hourly data are assimilated in at 1 h ahead of forecast time for 1 h. This process is repeated for the entire forecast period.

The difference between observed and forecast values of meteorological parameters is calculated as follows:

$$F_{dif} = F_{for} - F_{obs} \quad (7)$$

where

F_{dif} = meteorological parameter difference
 F_{for} = meteorological parameter forecast
 F_{obs} = meteorological parameter observation.

Figure 3 shows the vertical distributions of the difference between observation and 6-h forecast at the special sounding site (CC) at 18 GMT 11 May 1995. The model was initialized at 12 GMT using the composite fields of GSM and upper-air sounding data including UU and CC. The differences of pressure, temperature, dew-point temperature, windspeed, and direction are shown in the figure.

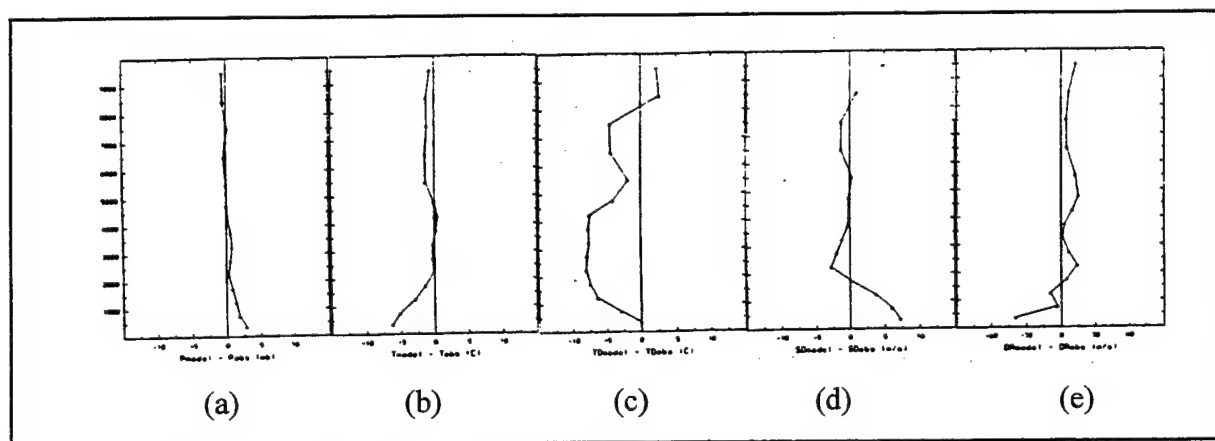


Figure 3. Differences of vertical profiles between forecast and observation for 6-h forecast, 18 GMT 11 May 1995. (a) pressure (mbar), (b) temperature (°C), dew-point temperature (°C), (d) windspeed (m/s), and (e) wind direction (degree). Forecast calculation was initialized using GSM and upper-air sounding data, including UU and CC.

For comparison purposes, forecast calculations using the three-dimensional data based on only upper-air sounding data (CC only) were also conducted, and the results are shown in figure 4. In this calculation, the assimilation of the data was done only for 2 h prior to initialization time.

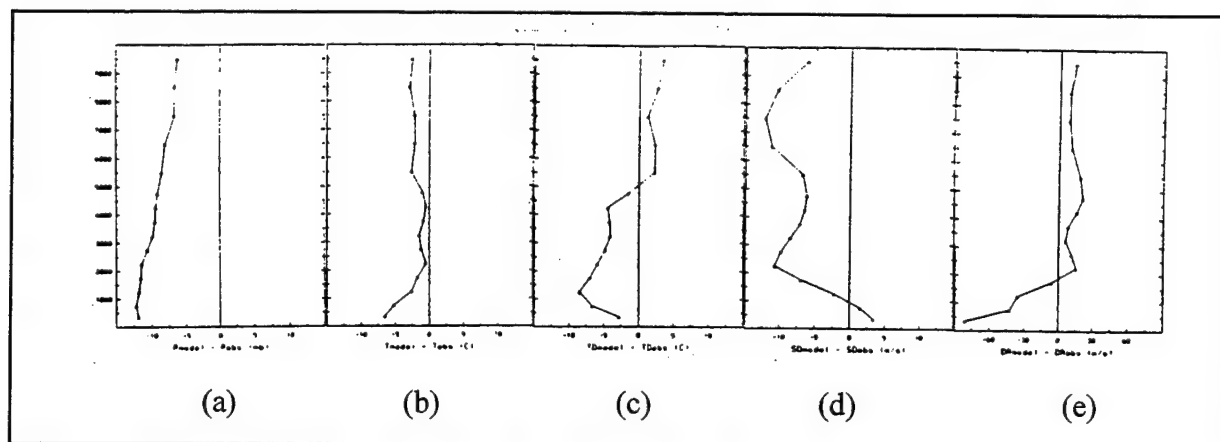


Figure 4. Differences of vertical profiles between forecast and observation for 6-h forecast, 18 GMT 11 May 1995. (a) pressure (mbar), (b) temperature ($^{\circ}\text{C}$), dew-point temperature ($^{\circ}\text{C}$), (d) windspeed (m/s), and (e) wind direction (degree). Forecast calculation was initialized using only upper-air sounding data, including UU and CC.

- (1) The model calculations based on the GSM and upper-air data produced better agreements of pressure, temperature, and wind field for the 6-h forecast.
- (2) The model, in figures 3 and 4, produced drier air than observed.
- (3) The pressure calculation based on only upper-air sounding data produced substantial errors.

Similar results were obtained for 9 and 10 May cases, but because of page limitations only the results of 11 May are shown.

5. SUMMARY

BFM was adapted for artillery meteorology and applied to the 29-Palms Live Fire Exercise held in May 1995. BFM was initialized using input data based on GSM and upper-air sounding data. The forecast calculation results produced considerably better results than those based on only single sounding data.

REFERENCES

- Barnes, S. L., 1973. *Mesoscale Objective Analysis Using Weighted Time-Series Observation*, NOAA Technical Memorandum, ERL NSSL-62.
- D'Arcy, E. M., 1993. "Effects of a Proposed CAMM Model on the Impact of the MLRS." In *Proceedings of the 1993 Battlefield Atmospherics Conference*, Army Research Laboratory, White Sands Missile Range, NM 88002-5501.
- Henmi, T., M. E. Lee, and T. J. Smith, 1995. *Battlescale Forecast Model and its Evaluation Using White Sands Missile Range Meteorological Data*, ARL-TR-569, Army Research Laboratory, White Sands Missile Range, NM 88002-5501.

- Hughes, R. E., 1966. *Computer Products Manual, FNWF Objective Analysis of Randomly Distributed Data*, Fleet Numerical Weather Facility, Technical Notes No. 21.
- Lee, M. E., J. E. Harris, R. W. Endlich, T. Henmi, R. E. Dumais, D. Knapp, and D. C. Weems, 1994. "U.S. Army Battlescale Forecast Model Concept of Operation." In *Proceedings of 1994 Battlefield Atmospherics Conference*, Army Research Laboratory, White Sands Missile Range, NM 88002-5501.
- Spalding, J. B., N. G. Kellner, and R. S. Bonner, 1993. "Computer-Assisted Artillery Meteorology." In *Proceedings of 1993 Battlefield Atmospherics Conference*, Army Research Laboratory, White Sands Missile Range, NM 88002-5501.
- Yamada, T., and S. Bunker, 1989. "A Numerical Study of Nocturnal Drainage Flows with Strong Wind and Temperature Gradients." *Journal of Applied Meteorology*, 28, 544-554.

VALIDATION OF A MASS CONSISTENCY WIND MODEL AT WHITE SANDS MISSILE RANGE*

JOHN SONTOWSKI¹, ROBERT M. COX²,
CATHERINE M. DOUGHERTY¹, AND RICHARD N. FRY, JR.³

ABSTRACT

A comprehensive set of weather data was collected and analyzed for the White Sands Missile Range during the month of April 1995. These included 11 to 15 surface stations, 1 to 3 upper air stations and 1 mobile profiler. A range of conditions were encountered, including inversion and post-inversion breakup; light, moderate, and strong winds; and a broad distribution of geostrophic wind directions. Highly complex wind fields were generated by interaction of winds with the locally complex terrain.

Complete, 3D, high resolution gridded wind fields were generated from observations using the MINERVE mass consistency wind field model. MINERVE fits observations (in a least squares sense) while satisfying a strong constraint for mass conservation. Statistical evaluations were performed comparing MINERVE generated winds with the observations at selected times using all available data. While MINERVE is a diagnostic model, its ability to provide realistic prognostic estimates over limited time periods (2 to 4 hours) was also tested for the WSMR environment during different diurnal periods (pre, transitional, and post inversion breakup).

Results show MINERVE to be an excellent diagnostic tool for high resolution diagnostic wind field generation. Further it was found to give reasonable prognostic estimates during certain diurnal periods (non-transitional) and under certain predictable conditions (e.g., non-frontal passage). Thus MINERVE appears well suited for its intended use in generating wind field inputs for material transport/diffusion models.

1. INTRODUCTION

Weather data, including winds, are regularly collected by an extensive network of surface stations at the White Sands Missile Range (WSMR). Upper air data are also collected, though less regularly, to supplement the surface data. However, because the WSMR terrain is highly complex, in many places involving very steep slopes and narrow mountain passes, winds at

* This paper was reviewed by the Defense Nuclear Agency. Review of this Material Does Not Imply Department of Defense Endorsement of Factual Accuracy or Opinion.

¹ Science Applications International Corporation, Wayne, PA 19087 USA

² Defense Nuclear Agency, Alexandria, VA 22310-3398 (Currently at National Defense University)

³ Defense Group Incorporated, Arlington, VA 22203

very short distances from weather stations can be forced to diverge significantly from the observations. Complete wind fields, including effects of the terrain, are therefore expected to be correspondingly complex. The intent of the work presented here is to demonstrate a methodology for modeling such wind fields in a computationally efficient yet realistic manner consistent with observations and including the effects of terrain.

The modeling of wind fields influenced by complex topography can be carried out in a variety of ways from complete first principles prognostic methodologies to relatively simple diagnostic techniques. The selection of a modeling methodology for WSMR applications was dictated by two primary considerations. First was the need to generate wind fields in a timely manner, i.e., minutes on a workstation level platform and, because of the topography, to do so with very high resolution. Second was the ultimate objective of providing wind fields for input to material transport/diffusion models. Given the current state of the art, the first objective required a computationally efficient diagnostic model. Considering the second objective, it was essential that the chosen model provided wind fields which were mass consistent, i.e., wind fields which did not lead to the artificial creation or destruction of material mass. Given these considerations, a mass consistent wind field reconstruction (diagnostic) model, in particular the MINERVE model, was selected.

MINERVE was originally developed by the French Electricity Board (Electricite De France - EDF) as part of an emergency response system for potential nuclear power plant accidents in mountainous regions of France (Geai, 1987). MINERVE was, and is, to be used to rapidly model wind fields in such regions for subsequent input to material transport/diffusion models which predict the potential impact from a hazardous nuclear release. More recently, as part of the Defense Nuclear Agency (DNA) Multiscale Environmental Dispersion Over Complex Terrain (MEDOC) program, MINERVE, along with other EDF codes has been modified specifically for DOD/battlefield type applications (Sontowski and Dougherty, 1994). The following is intended to show the utility of MINERVE for such applications.

2. MINERVE METHODOLOGY

The MINERVE mass consistency model is formulated to fit weather observation data in a complex terrain environment while also satisfying the principle of conservation of mass. The data are fit in a least squares sense, using a variational methodology. The data can include any number of surface stations greater than or equal to three, and upper air profiles of one or more. An initial gridded wind field is approximated by interpolation from the observation data. Various interpolation procedures are included as options which can be selected based on the nature/distribution of the observation points. Adjustments are then made to the interpolated wind field so as to satisfy conservation of mass in a way that also minimizes an integral function of the differences between observations and the adjusted field. To model the effects of atmospheric stability, the relative amount of adjustment to vertical and horizontal wind components is controlled by specification of an adjustment coefficient (Gauss precision modulus). The adjustment coefficient can be spatially uniform or a three-dimensional function of position; it can be user specified or internally calculated in terms of stability related factors such as the temperature field.

The solution procedure involves iteration, by successive overrelaxation, of a partial differential equation for the Lagrange Multiplier derived from the Euler-Lagrange equations corresponding to the integral function minimization. Substitution of the resulting Lagrange Multiplier into the Euler-Lagrange equations then yields the adjusted wind components. The equations are formulated in terms of a terrain following coordinate system which represents the terrain slopes in a natural continuous manner and is most conducive to accurate numerical solution. In addition, the vertical grid is nonuniformly distributed so as to provide enhanced resolution in lower boundary layer regions where profiles change most rapidly, and reduced resolution in upper regions where change is generally more moderate. Various functional forms are provided as options for the distribution.

The version of MINERVE used for the WSMR application was designed for operation on a workstation level platform (IBM RISC/6000). Execution of the calculations for a typical adjusted wind field (100x100x30 grid points) generally requires a few minutes on an IBM Model 590 workstation.

3. TEST DATA SETS

During April 1995, a comprehensive set of meteorological data was collected at WSMR. These data included observations from the WSMR Surface Automated Meteorological System (SAMS) sites. The SAMS are instrumented 10 meter towers that record requested meteorological data. Figure 1 outlines the test domain and where the SAMS were located during the test. Elevation contours are also shown in Figure 1, illustrating the complexity of the topography. All terrain data used for this study were obtained from the Defense Mapping Agency Digital Terrain Elevation Data (DTED). These data were coarsened to 1 km resolution. A coordinate transformation was then performed by MINERVE from latitude/longitude to Universal Transverse Mercator (UTM) coordinates as shown in Figure 1.

For the purpose of this study, surface observations were collected every hour for the weekdays (Monday through Friday). The test required, at a minimum, wind and temperature data, although other parameters were measured. The temperature data were required in order to allow automatic, rather than user, specification of atmospheric stability conditions. A sample of the SAMS output is shown in Table 1. The data are provided for each station indicated by the index ## for the stated Julian day and mountain standard time. In addition to surface observations, the MINERVE mass consistency model as noted above also requires at least one upper-air sounding. For the days of interest, between one and three rawinsondes were released. The primary points of release were the Jallen Site and Holloman Air Force Base. Periodically other balloons were released for other range activities. Table 2 lists the rawinsonde releases during the month, which were considered for this study. Unfortunately, the upper air soundings were not available on an hourly basis, i.e., coincidentally with the surface data as is ideally required in mass consistency modeling. Therefore, in most cases the calculations for any given hour were based on the surface observations from that hour together with upper air soundings from the nearest hour. Exceptions were made where the nearest hour was expected to be in a different atmospheric state than the hour of interest. For example, an 1100 GMT (5

Table 1. Typical SAMS Data Output

LATEST SAMS DATA													
7:08 AM THU., 24 AUG., 1995													
#	JUL	MST	TEMP			PRESSURES			WINDS			SOL	BV
			AIR	DEW	RH	Stat	ALT	SEA	DIR	SPD	PK		
##	DAY	hhmm	f	f	%	PRESS	SET	LVL	deg	kts	kts	RAD	PREC
						mb						ly	in TS
01	238	0700	71	61	72	880.5	30.11	1012.9	38	4.4	6.4	.3	0.00 13
02	238	0700	71	59	66	882.1	30.11	1012.9	336	5.1	7.2	.3	0.00 14
03	238	0700	78	58	50	873.0	30.15	1013.4	CCCC	.3	1.3	.1	0.00 13
04	238	0700	68	58	68	884.1	30.13	1014.0	344	4.9	5.9	.2	0.00 14
05	238	0700	70	52	53	824.2	30.25	1014.1	98	8.2	9.5	.3	0.00 13
06	238	0700	70	57	63	840.5	30.22	1014.9	359	1.6	2.8	.3	0.00 14
07	238	0645	68	59	75	879.3	30.13	1014.0	9	1.5	2.3	.2	0.00 14
08	238	0700	64	37	37	858.6	30.18	1015.2	207	1.6	2.5	.3	0.00 13
09	238	0700	58	46	64	740.0	30.47	1017.7	182	13.2	17.2	.3	0.00 13
12	238	0700	64	52	66	857.1	30.17	1015.2	38	4.5	5.7	.2	0.00 14
14	238	0645	68	57	72	865.5	30.18	1015.0	26	6.2	8.9	.2	0.00 13
15	238	0700	71	59	66	879.6	30.14	1013.8	4	1.9	2.8	.2	0.00 14
17	238	0700	58	47	66	731.7	30.40	1015.1	311	1.0	2.8	.3	0.00 14
18	238	0700	77	62	60	875.5	30.13	1013.0	293	.8	2.3	.3	0.00 13
21	238	0700	70	59	67	880.1	30.12	1013.5	360	3.4	4.7	.2	0.00 14

Table 2. Rawindsonde Release Times at WSMR Locations

DATE (April)	RAWINDSONDE RELEASE TIMES (GMT) AT:				
	HOLLOMAN	JALLEN	NM SHOT	STALLION	OASIS
3	1057, 1650				
4	1056, 1648	1842			
5	1054, 1824	1758			
6	1101, 1227	1800			
7	1055, 1555	1759			
10	1050	1759			
11	1050	1600, 1800			
12		1800			
13	1053, 1230	1515, 1800			
14	1054	1800			
17	1054	1800			
18	1829			0747	
19	1046	1636, 1837	1405, 1621, 1838		
20	1053	1800			
21		1800		0903	
24					0809, 1007, 1207, 1411
25	1100	1759			
26	1100	1759		1358	
27	1129	1800		1455	
28		1759			

AM local time) sounding was considered more appropriate for a 1400 GMT pre-inversion breakup-calculation than a 1600 GMT post inversion sounding. In addition to the surface and upper air observations, surface synoptic weather charts were collected. These provided a general overview of the weather pattern WSMR was experiencing for any given day.

As with any test, there were days when for one reason or another the data were incomplete or unusable. Three such days were the 18th, 24th, and 28th. Of the remaining days, some were much more turbulent than others. The primary reason for this turbulence was frontal passage or fronts in the vicinity of the range. For the purpose of reviewing how well the mass consistency model performed under these conditions, those days were left in the data set. However, when considering using those days for transport (see accompanying paper), they were generally ignored. The wind speed was also stratified for this study. Winds from 0 - 2.5 m/s were labeled light; winds from 2.5 - 7.5 m/s were labeled moderate; and winds greater than 7.5 m/s were labeled strong.

For the present study, the primary hours investigated were 1100, 1400, and 1800 GMT. These particular times were selected because they were considered representative of different atmospheric conditions, in particular periods of radiation inversion, inversion dissipation, and post inversion break-up respectively. Thus they provided a reasonably complete test of the modeling methodology. MINERVE wind fields were generated at each of these times and compared to the measured data at the same times. As a further objective, an attempt was made to evaluate the utility of the modeling methodology as a short term predictive tool for the WSMR by applying it in a persistence mode over two-hour and four-hour time periods. Thus the MINERVE results generated at the primary times of 1100, 1400, and 1600 were also compared with observation data at T+2 and T+4 hours.

4. RESULTS

Several different types of plots were generated to evaluate and exhibit the performance of MINERVE relative to observations at the calculated time. Most helpful were wind vector plots such as displayed in Figure 2. The header in Figure 2 includes the date and time of the plot with the date as day-month-year and the time in local standard time. On the left side of the plot is the field maximum and minimum values in meter per second and the terrain contour level. The plot includes all surface wind vectors calculated at the 1 km resolution. Superimposed on the plot are the stations used in that calculation with their associated wind vector. The results shown in Figure 2 were calculated for the 13th of April, at 18 GMT (12 noon local time), and show a basically southerly wind field. Effects of terrain, however, are quite noticeable in the northwestern region of the domain where the wind is locally channeled through mountain passes in more of a southeasterly direction, parallel to the direction of the passes. Southeasterly winds are also calculated in the open valley region near the "NORTHURUP" site where the observed winds are southeasterly and exceptionally light. Comparisons of the calculated and observed wind vectors can be made at the indicated surface stations in Figure 2; however, given the scale used, such comparisons are at best qualitative.

To more clearly illustrate the comparisons between calculations and the measured data, plots of the type shown in Figures 3 and 4 were generated for wind direction and wind speed respectively. These are for the same date and time considered for the vector field of Figure 2. The plots show bar comparisons with measured values represented by the bar on the right and computed values by that on the left. Looking first at the wind directions in Figure 3, the computed and measured values are seen to be in excellent agreement, with deviations of less than 5 degrees at most observation sites. Concerning the general wind pattern, directions are seen to be within 10 to 20 degrees of 180 degrees, i.e., southerly as seen in Figure 2. The most notable exception to this is in the northwest region at Mockingbird Gap (designated as "MOCKINGB" in Figure 3), where the calculated and observed values are 124.3 and 126.0 degrees, respectively. Turning to the wind speeds, Figure 4 shows similarly good agreement between calculated and observed values. The speeds are seen to range from approximately 1 m/s at the NORTHRUP site, discussed above, to approximately 8 m/s at "SALINAS" and "MOCKINGB". As these sites are located on a mountain peak and in a mountain gap respectively, such local accelerations in the wind field are as expected.

Plots were also generated for comparison of the calculated and measured upper-air profiles. Figure 5 is an example of one such plot, generated for the "JALLEN" upper air site. The left plot is the wind speed comparison and the right plot is the wind direction. The calculated and measured profiles are seen to be in excellent agreement for both direction and speed. In this particular example, some speed shear is observed at altitudes of about 750 to 2300 meters above ground, with little or no occurrence of directional shear. Seven hundred and fifty meters is found to coincide with the top of the planetary boundary layer, as examination of the upper air temperature profile shows the lapse rate changing from superadiabatic to subadiabatic at this altitude.

For evaluation of the overall performance of the modeling methodology, both as a diagnostic tool and in a predictive persistence mode, statistical evaluations were performed comparing MINERVE generated winds with the observations. These focused on daily averages, over all surface stations, of the deviations between the measured and observed winds. For calculations at any given time, the average deviations were evaluated relative to observations at that same time as well as to observations two hours later, and four hours later. The latter two evaluations/comparisons were intended to provide some measure of the performance of MINERVE in a short term persistence predictive mode. As noted above emphasis was on calculations performed at three basically different periods, 1100, 1400, and 1800 GMT times.

A sample of the statistical results is given in Figure 6 for the mean deviations in wind direction for the 1800 GMT calculations. Looking first at the deviations relative to observations at the same time, designated as $T + 0$ HR, MINERVE is seen to produce calculated wind directions which, with one exception on the 11th of April, are on the average well within 10 degrees of the observations. As expected, the deviations are increased relative to observations at later times. In most cases, but not all, the greater the time difference, the greater the deviation. It is also noted that the deviations, relative to later time observations, tend to be either larger or

smaller over relatively protracted periods. For example, the deviations are relatively small during the period from the 13th to the 21st of the month. While the data examined here are much too limited to draw any definitive conclusions, the days with low wind direction deviations appear to correlate roughly with days of relatively strong winds.

Turning to the wind speed deviations corresponding to those described above for direction, Figure 7 shows similar statistical comparisons. Again, comparison of calculations with observations from the calculated time shows relatively small deviations, all within 1 m/s. Increases in the deviations as comparisons are made to later time observations do not appear excessive, being within about 2 m/s for the majority of days. In assessing the significance of wind speed deviations, it is helpful to examine the deviations relative to the magnitude of the wind speed, e.g., the deviation as a percent of the observed speed. Is it thus indicated that large speed deviations are in part a result of strong winds, with the percent deviation not being unusually large? Similarly, could one expect light winds to result in deviations which are small on an absolute basis, yet very large from a percentage point of view? Attempting to address these questions, the average deviations as a percent of the observed values were calculated, with results for the 1800 GMT period shown in Figure 8. Thus the large absolute deviation occurring at T+4HR on the 20th (Figure 7) does not appear unusually large from a relative point of view (Figure 8). In fact, the relative (%) deviations are considered generally small for all of the days evaluated at the 1800 GMT period. This is believed to be true because of the relatively strong afternoon winds as well as constant atmospheric conditions (post inversion break-up period). For contrast, Figure 9 shows percent deviations for the 1100 GMT period. Values are seen to be substantially greater than those for 1800 GMT. This corresponds with much lighter morning winds as well as possible transition through inversion break-up. From the point of view of material transport, the implication of smaller percent deviations in the afternoon is that calculated errors in downwind transport distance should be a small fraction of the total transport distance.

To obtain more of an overall measure of the performance of MINERVE, the daily deviations were further averaged over the monthly period. Thus deviations averaged over all stations and all days were obtained for each of the three daily time periods of interest, and for the three time differences of 0, 2, and 4 hours between calculated and observed values. The resulting mean deviations are presented in Table 3 for direction, absolute, and relative speed. Also shown are standard deviations indicating the amount of spread relative to the mean value. Examining these results it is first noted that the deviations are almost negligibly small for the T+0 time period, only 0.4 m/s in wind speed, and less than 10 degrees in direction. Thus MINERVE is performing well in the mode for which it was designed. Further this performance appears consistent, as the standard deviation or spread around these mean values is also quite small. While the deviations are seen to increase for comparisons with observations at later times (T+2 and T+4), they do not appear excessive in view of the general uncertainty of current predictive models. Considering the various times of day, the agreement between calculated and observed wind direction is clearly best for the afternoon time period. On the other hand, it is somewhat surprising that absolute deviations in wind speed appear independent of the time of day. On a relative (%) basis, deviations are seen to be significantly less during the afternoon period.

Table 3. Summary Wind Statistics - Deviations For April 1995 (MINERVE vs WSMR Surface Observations)

TIME T =	DIRECTION (DEG)			SPEED (M/S)			SPEED (%)		
	1100 GMT	1400 GMT	1800 GMT	1100 GMT	1400 GMT	1800 GMT	1100 GMT	1400 GMT	1800 GMT
MEAN DEV (T+0)	8	9	6	0.4	0.4	0.4	12	15	10
MEAN DEV (T+2)	34	54	29	1.4	1.6	1.5	52	50	29
MEAN DEV (T+4)	59	69	39	2.1	2.0	1.8	74	47	34
STD DEV (T+0)	3	4	3	0.2	0.2	0.2	6	11	5
STD DEV (T+2)	12	22	11	0.8	0.6	0.7	19	19	13
STD DEV (T+4)	17	35	17	0.9	0.5	0.8	35	14	16

5. CONCLUSIONS

A careful examination of detailed wind observations over a one month period at the WSMR clearly demonstrates the pronounced localized effects of complex topography on winds, and thus the need for an efficient high resolution 3D wind reconstruction model. To fill this role, the MINERVE mass consistency model was extensively tested for the very challenging WSMR topography. Results show MINERVE to be an excellent diagnostic tool, able to construct wind fields which are consistent with wind observations as well as the terrain. Further, it was found to give reasonable prognostic estimates operating in a short term persistence mode during certain diurnal periods (non-transitional) and under certain predictable conditions (e.g., non-frontal passage). Thus MINERVE appears well suited for its intended use in generating wind field inputs for material transport/diffusion models and applications involving short range transport and emergency response. The coupling of MINERVE with a transport code, namely SCIPUFF, is described in a companion paper (Cox, et al., 1995).

REFERENCES

- Geai, P., 1987: Methode D'Interpolation et de Reconstitution Tridimensionnelle d'un Champ de Vent: Le code d'analyse objective MINERVE. Electricite De France, Report ARD-AID: E34-E11, 178 pp.
- Sontowski, J. and C.M. Dougherty, 1994: Multiscale Environmental Dispersion Over Complex Terrain - The MEDOC Models. U.S. Defense Nuclear Agency, Technical Report No. DNA-TR-94-180, 87 pp.
- Cox, R. M., J. Sontowski, R.N. Fry, and C.M. Dougherty, 1995: Atmospheric Transport over White Sands Missile Range, *Proc. 1995 Battlefield Atmospheric Conference*, White Sands Missile Range, New Mexico, In printing.

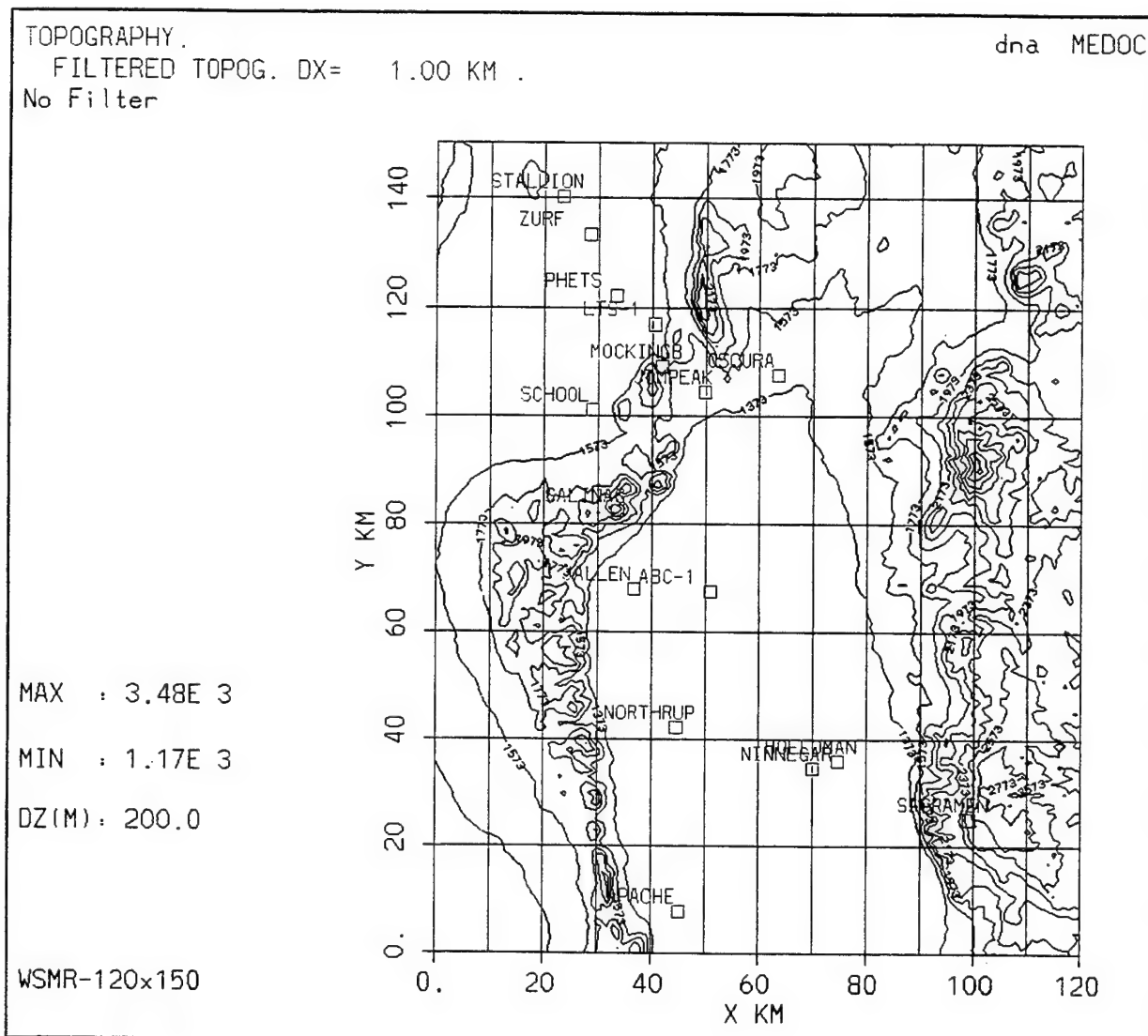


Figure 1. WSMR Topography With Meteorological Stations Indicated.

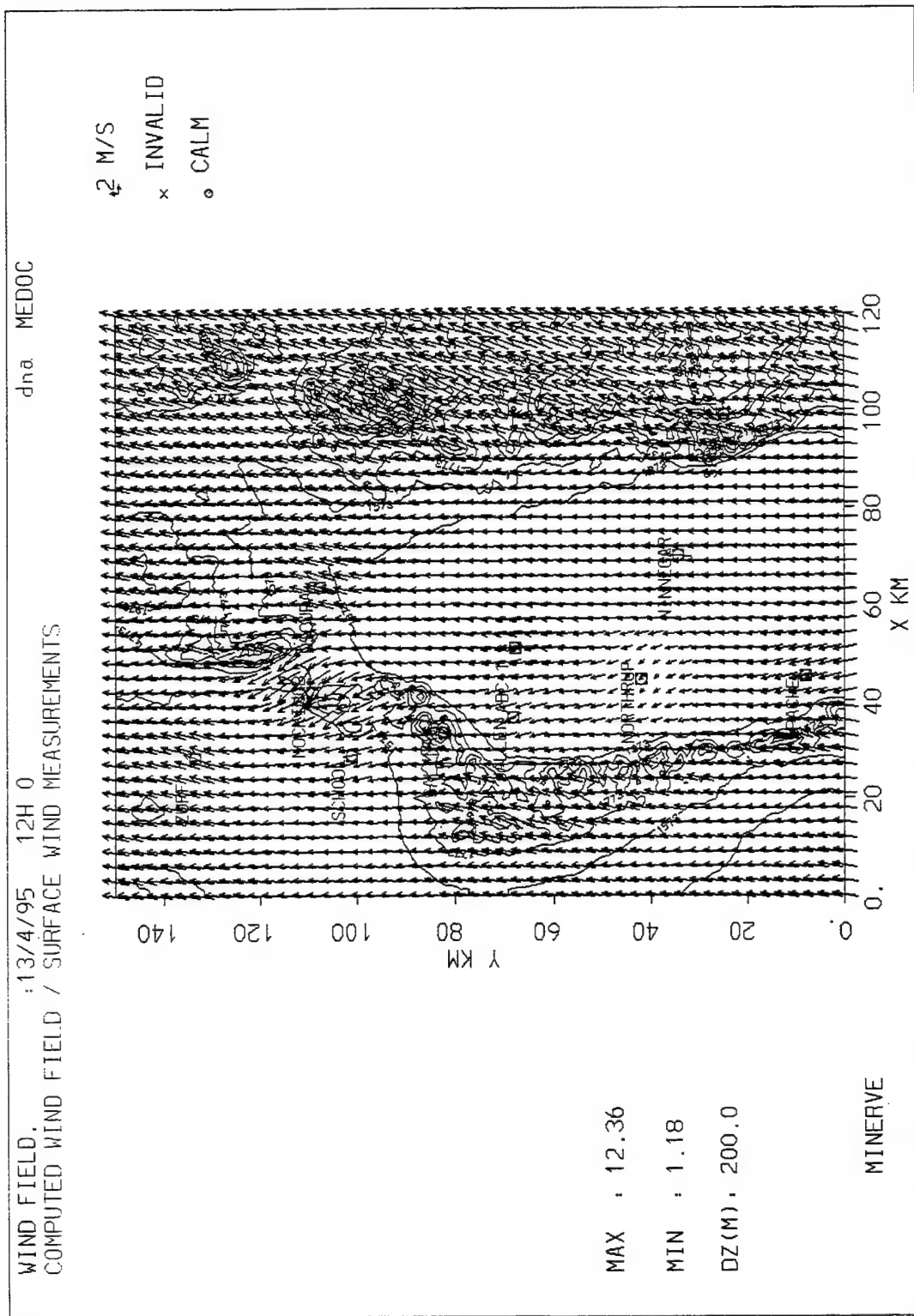


Figure 2. Observed and MINERVE calculated wind vectors near surface (~10 meters above ground).

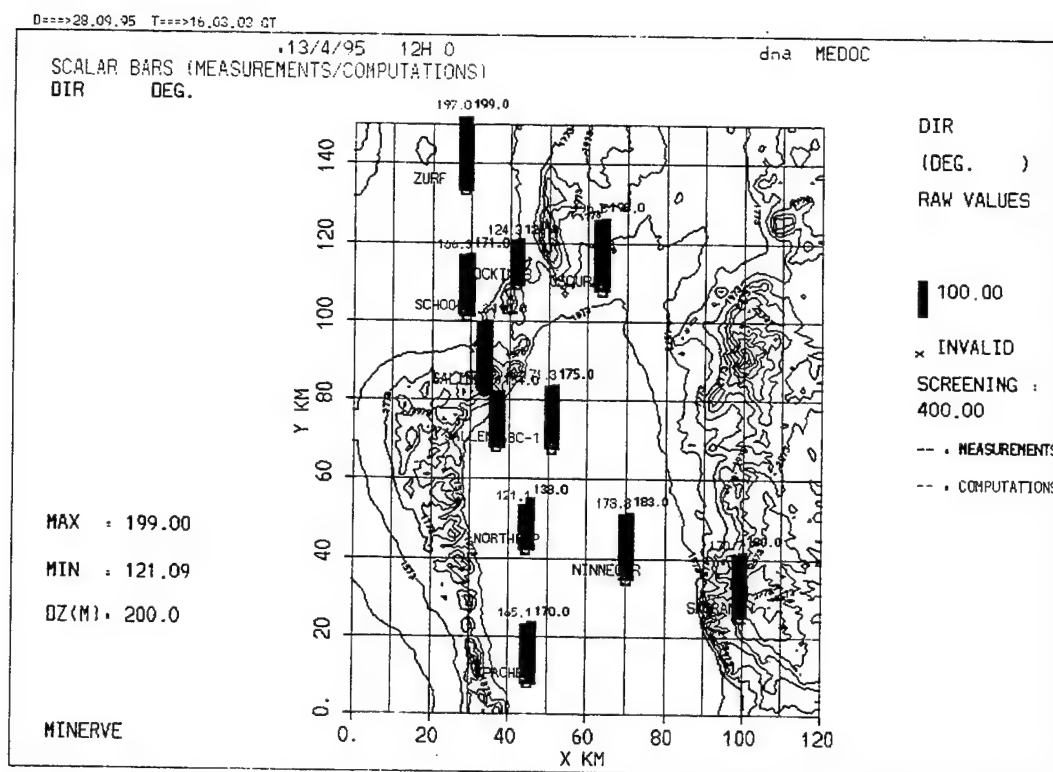


Figure 3. Bar indicator display of calculated vs observed wind directions.

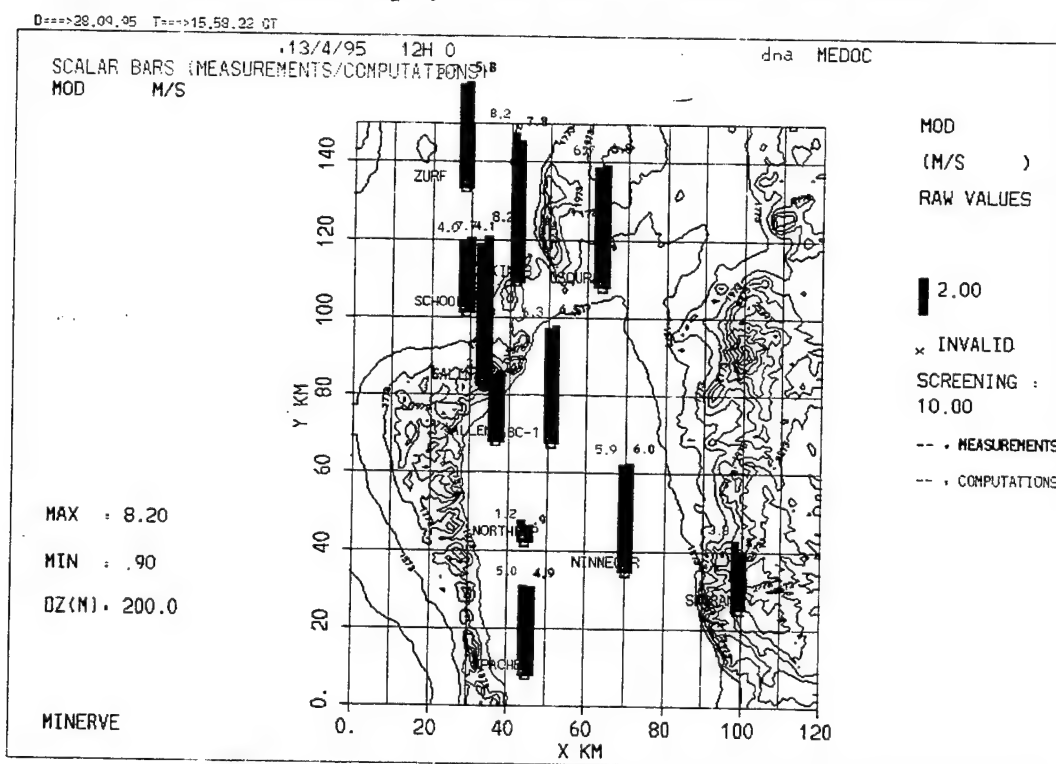


Figure 4. Bar indicator display of calculated vs observed wind speeds.

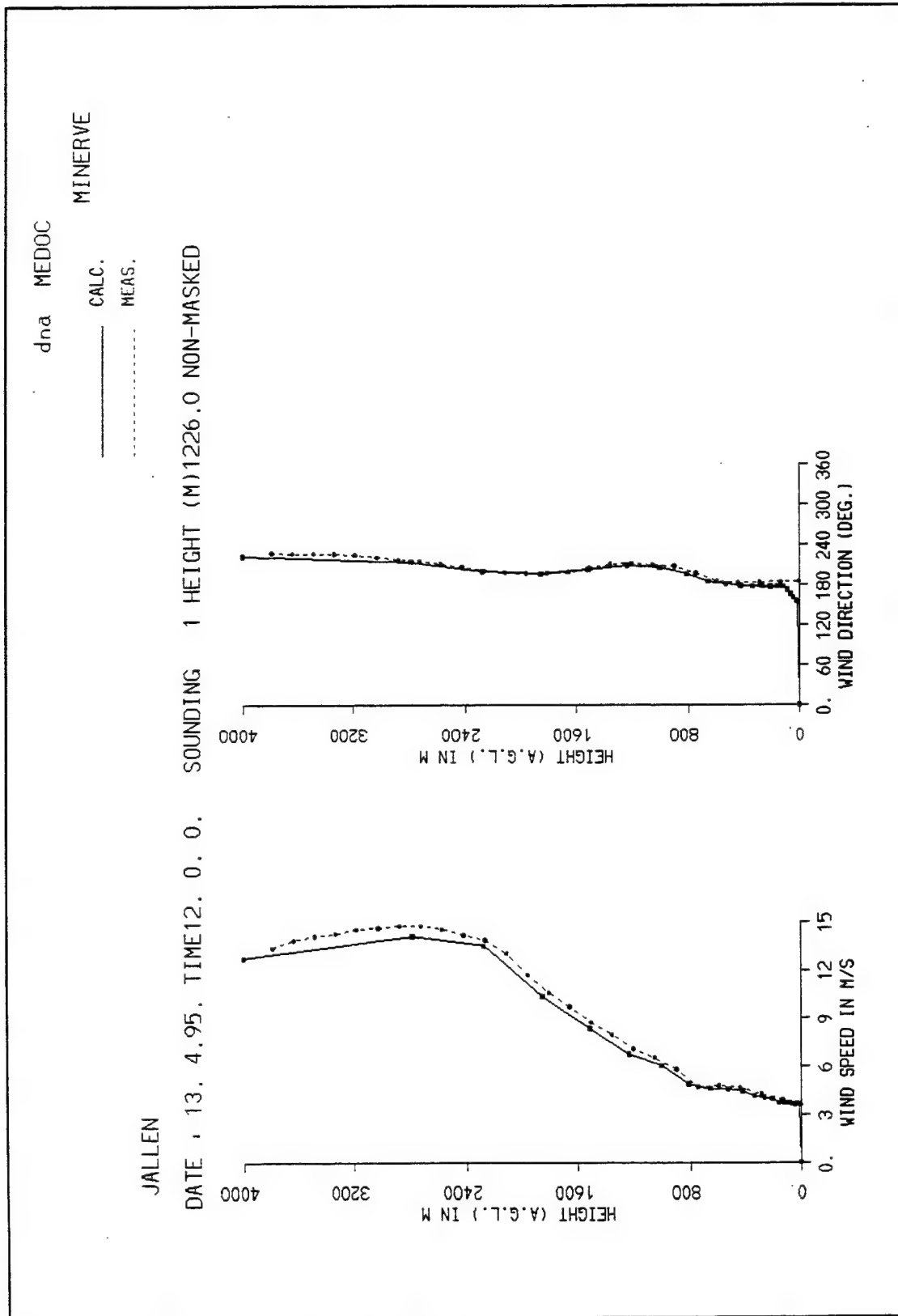


Figure 5. Calculated vs Observed Vertical Profiles For Wind Speed and Direction.

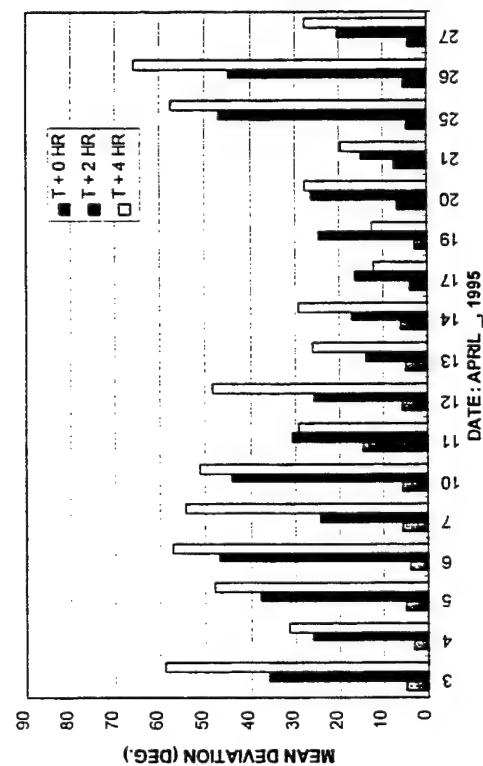


Figure 6. Daily Wind Direction Mean Deviations at T= 1200L.

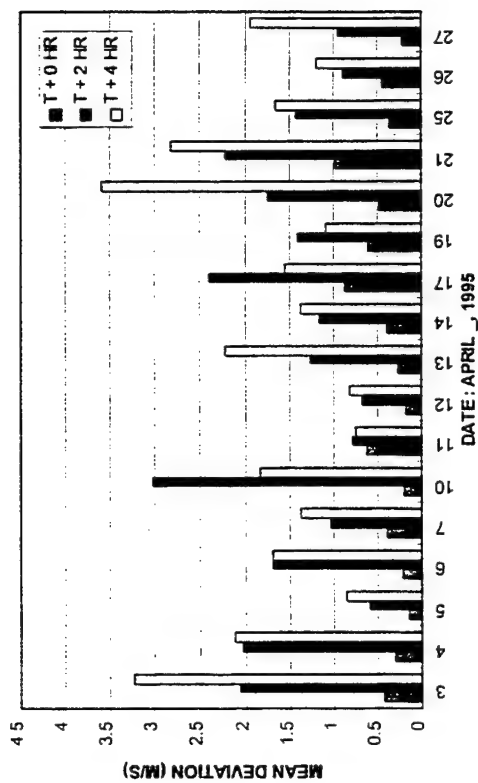


Figure 7. Daily Wind Speed Mean Deviations at T= 1200L.

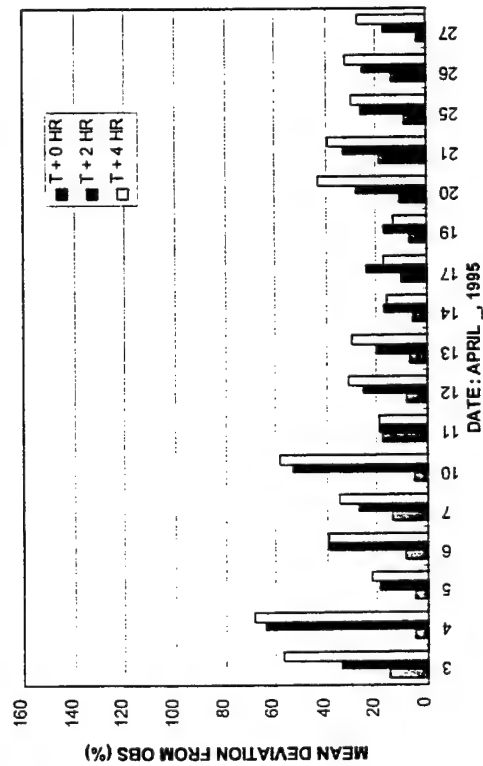


Figure 8. Daily Wind Speed Mean Percent Deviations at T= 1200L.

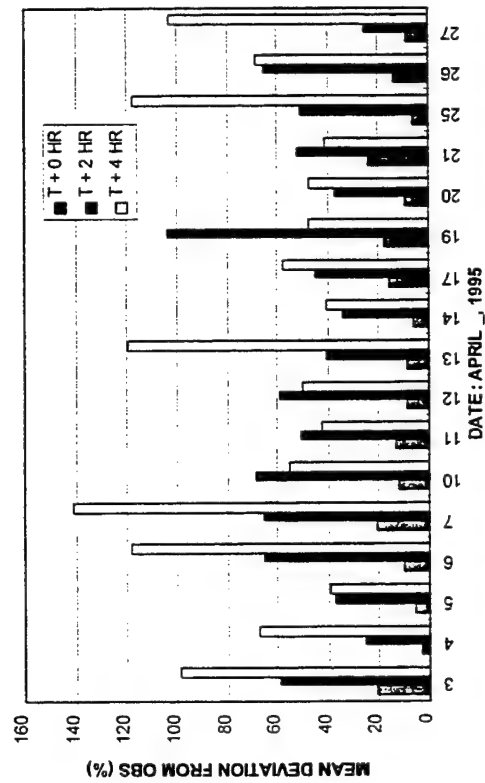


Figure 9. Daily Wind Speed Mean Percent Deviations at T= 0500L.

WEATHER IMPACT DECISION AIDS FOR ELECTRO-OPTICAL (E-O) WEAPONS SUPPORT

J. P. ALLECA

Phillips Laboratory, Geophysics Directorate
Hanscom Air Force Base, MA 01731, USA

ABSTRACT

Future E-O Weather Impact Decision Aids (WIDA) software will use improved, physics-based atmospheric models, high resolution targets, and digital geographical background data to predict the effects the atmosphere would have on the performance of electro-optical weapons sensors used in combat air operations. If integrated, WIDAs could provide these effects automatically during preparation of the Target Nomination List in the Rapid Application of Air Power (RAAP) system; the Air Tasking Order (ATO) in the Air Planning System (APS); modifications to the ATO in the Force-level Execution System (FLEX); and weapons to load at the Wing-level in the Wing Command and Control System (WCCS). At the Squadron-level, E-O sensor performance data could be integrated into The Air Force Mission Support System (AFMSS) providing E-O target detection range parameters and scene visualizations to aircrews.

1. INTRODUCTION

Existing procedures to provide mission planners and aircrews with E-O weapons sensor performance predictions have been mainly limited by manual mission planning processes and a lack of computer power and robust communications. Planned Command, Control, and Intelligence (C4I) programs attest to the military's efforts to use modern automation to make this planning process more efficient. Successful implementation of these programs promises a new era of faster and improved air campaign and operations planning.

Currently, Air Force planners and aircrews engaged in real-world air-to-ground operations receive atmospheric E-O sensor performance prediction information mainly in the form of paper printouts or briefing transparencies/copies from weather forecasters who use stand-alone Electro-optical Tactical Decision Aid (EOTDA) software on a PC. In the near future, weather forecasters will use work stations, with connectivity to C4I

systems, to run the existing EOTDA software, but still in a stand-alone mode. The WIDA program's ultimate goal is to improve on the underlying ideas, physics, and thermodynamics behind the manual EOTDA, and adapt it in steps to the needs of the modern air-to-ground operational mission planning community.

2. WIDA PROGRAM DESCRIPTION

The WIDA program currently includes three interacting efforts: Air Combat Targeting/Electro-optical Simulation (ACT/EOS), Weather Automated Mission Planning Software (WAMPS), and Night Vision Goggle Operations Weather Software (NOWS).

2.1. ACT/EOS

ACT/EOS provides the WIDA program with the core atmospheric physics, terrestrial, and thermodynamic models, and software to calculate performance predictions for laser, TV, and IR weapon sensors based on the atmospheric conditions. ACT/EOS includes rigorous data collection to support model verification and improvement. Software is also being developed to use the core models to build realistic target area scenes and fly-throughs suitable for use in operations and training by aircrews on automated planning systems like the AFMSS.

2.1.1. ACT/EOS Data Measurements and Model Verification

ACT/EOS includes a measurement site located on the northwest side of the Geophysics Directorate complex and a data collection facility, the WIDA Laboratory, located inside the complex. The data collection instrument suite currently includes standard meteorological sensors (i.e., temperature, air pressure, wind, relative humidity, present weather), geophysical sensors (i.e., soil temperatures, soil moisture, diffuse/direct visible and IR solar radiance, upwelling and downwelling IR radiance), experiment targets (camouflage painted aluminum and Styrofoam boxes with thermistors on each facet), calibration targets with thermistors, an 8-12 micron Forward Looking Infrared (FLIR) scanning camera, a 3-5 micron camera (when conducting joint experiments with Rome Lab), a 24 hour visible band sky camera for clouds (automatically switches to a night vision goggle filter at night), and a vertically-oriented cloud and precipitation detecting radar (AN/TPQ-11).

Data is transmitted to the WIDA Lab via cable or radio link, automatically processed and viewed in time sequences on work stations and monitors, and archived on video tape and CD-ROM (since July 1994). Instruments can be controlled and maintained from the WIDA Lab on the work stations either directly or remotely. Besides the simple box targets, data has also been collected on more complex targets and backgrounds on Hanscom Air Force Base to include the runway, buildings, towers, and forested areas.

The main ACT/EOS model suite consists of thermal target and high resolution background (including vegetation) modeling, atmospheric transmission, and weapons sensor performance. So far, analysis has focused on the thermal modeling, which is believed to have the potential for the most inaccuracies. Analysis of the data collected at Hanscom site suggests that modifications to the convection model used by the IR thermal contrast model may be needed. When the thermal model is run on the test targets for certain wind directions and speeds, the temperatures of some of the target facets do not appear to be properly modeled.

2.1.2. ACT/EOS Scene Visualizations

The ACT/EOS 4-D visualization effort incorporates the ACT/EOS atmospheric models with a Geographic Information System (GIS) to produce target area scenes at locations specified by the user. Initial efforts have focused on producing 8-12 micron IR images of target-to-background thermal contrast. Atmospheric transmission and sensor performance modeling as well as other wavelength bands will be integrated later. In addition, a target builder will be developed to allow users to easily modify the geometry and material types of baseline targets.

The scene visualization system resides on a portable Unix platform. Internal GIS software has the capability to ingest and overlay Defense Mapping Agency (DMA) terrain and vegetation, soil, and surface type products and also manmade features down to a resolution of 2.5 meters. Satellite imagery and aerial photography can also be included to aid in identifying visual cues for the user, and can be "stretched" over an underlying terrain overlay to produce a 3-D picture of a specified area.

Once the user defines a geographical area and positions and defines the targets in the area, the ACT/EOS models receive the target parameters and background surface material codes, then run with weather data to produce thermally rendered images. Images can also include "billboarded" vegetation (given sets of characteristic vegetation shapes, sizes, and thicknesses) where vegetation radiances are calculated from temperatures provided by the vegetation model. Future additions will include an automatic grid point weather forecast data ingest capability, multiple bounce radiation calculations, bidirectional reflectance, and more sophisticated target-background radiation interactions including shadowing by targets.

2.2. NOWS

NOWS provides the Air Force Special Operations Forces (AFSOF) with performance prediction software for their night vision goggles (near-infrared) based on lunar and celestial illumination, weather conditions, and the atmospheric

constituents present. The first operational versions will be run stand-alone on a PC by AFSOC weather forecasters to provide manual support according to present day requirements. For the future, the capability of NOWS could be integrated into data and visualization output software modules residing on the AFMSS.

2.2.1. NOWS Capabilities

The first developmental version of NOWS (NOWS 1.0) was released for feedback to the AFSOC weather forecasters on 30 Jun 95. A user-friendly Graphical User Interface (GUI) defines mission parameters (e.g., location and time, altitudes, target/obstacle types or drop zone, night vision goggle type, weather, background types, etc.) and controls operation of the physical models which produce predicted parameters supporting helicopter operations including refueling under low-light conditions and twilight.

Specific parameters that are predicted include target detection ranges in terms of azimuth to target or time period for user-defined probabilities. These probabilities are provided for the target or its shadow (whichever is best) in and out of cloud shadow. The probabilities are a function of target/background contrast and target size which both decrease with increasing range; the former because of atmospheric attenuation, which is accounted for in the models. NOWS also modifies the target and shadow detection ranges with scene clutter.

Other NOWS-computed parameters available in tabular or graphical formats include Cloud Free Light of Site (CFLOS) probabilities; lunar and celestial illumination; the probability that the target is in direct light; solar/lunar elevation, azimuth and angle; lunar phase (percentage of visible lunar disk); atmospheric transmissivity; and target and background radiance.

Future versions of NOWS will include, among other capabilities, a probability of seeing the horizon product, automatic ingest of grid point weather forecast data fields, and possibly a scene visualization for specific night vision goggles similar to the ACT/EOS IR scene visualization.

2.2.2. NOWS Data Measurements and Model Verification

Beginning later next year, the WIDA program will undertake an effort to verify and improve the NOWS near-IR models and output parameters. A van for mobile use is currently being equipped with a full suite of meteorological and geophysical sensors, a coupled night vision goggle/video camera system, and processing equipment to collect nighttime ground illumination measurements and video at sites within the various munitions test target ranges available at Camp Edwards Army Base in Falmouth, Massachusetts. This area is relatively free of cultural light contamination and offers a wide range of targets (e.g., small

buildings, towers, tanks, etc.) and backgrounds (e.g., trees, shrubs, grass, sand, water, etc.) from which to collect accurate ground truth data to support model verification analysis and to guide model physics improvements. The data would also provide an additional geophysical data set for the ACT/EOS model analysis efforts.

2.3. WAMPS

WAMPS includes a Requirements Study and follow-on C4I E-O weapons sensor performance prediction software. The Requirements Study involves interviews with air-to-ground mission planners and aviators to learn, update, and document the E-O products needed in terms of data (e.g., lock-on range, target/background thermal crossover, etc.) and format (e.g., alphanumeric, graphics, visual scenes). This Study is scheduled for completion by the end of January 1996. Based on the requirements, the WIDA team members will then work with the program managers and system developers of specific C4I systems to plan software tailored towards their specific needs. The software would be built around the core of improved atmospheric models from the ACT/EOS and NOWS efforts.

3. SUMMARY

WIDA is an advanced research and development program with a focus on the automated mission and flight planning functions of the near future. By working with users, the program has become structured to ease the transition to operations from research of the needed E-O weather information required by mission planners and aircrews to help conduct effective air operations.

ACKNOWLEDGMENTS

Special thanks to the Geophysics Directorate WIDA team for their valuable support: Paul Tattelman, Rene Cormier, Joe Eicher, Stan Heckman, Guy Seeley, Tim Hiett, Dana Madsen and Steve Luker.

REFERENCES

Touart, C.N. et al., 1994. *Electro-optical Tactical Decision Aid (EOTDA) User's Manual, Version 3.1, Appendix A: Technical Description*. PL-TR-94-2174(II), Phillips Laboratory, Geophysics Directorate, Hanscom Air Force Base, MA 01731

Gouveia M.J. et al., 1995. *Night Vision Goggles Operations Weather Software (NOWS) User's Manual, Version 1.1*. PL-TR-95-7611, Phillips Laboratory, Geophysics Directorate, Hanscom Air Force Base, MA 01731

Hiett T. and Eicher J., 1993. *ACT/EOS Calibration Sensor Suite*. PL-TR-93-2235, Phillips Laboratory, Geophysics Directorate, Hanscom Air Force Base, MA 01731

Heckman S. and Seeley G., 1995: "ACT/EOS Model Evaluation and Visualization - First Year Results." *Proceedings of the Sixth Annual 1995 Ground Target Modeling and Validation Conference*, Keeweenaw Research Center, Michigan Technological University, Houghton, MI

The Processing, Databasing, and Displaying of AVHRR and DMSP Data for the Integrated Meteorological System

by

Stephen F. Kirby
U.S. Army Research Laboratory
Battlefield Environment Directorate
White Sands Missile Range, NM 88002-5501

ABSTRACT

To satisfy the need for cloud information, (i.e. areal coverage, tops, and bases) in the Integrated Meteorological System (IMETS) database a methodology is being developed whereby software functions on the Sun will be employed to process raw AVHRR and DMSP data and place the data in an IMETS database. The functions are integrated with nephanalysis algorithms from the Air Force Tactical Nephanalysis (TACNEPH) cloud analysis software module. The data flow from reception to its processing and finally placement in the IMETS database will be described. 3-D display of this cloud data over a map background will be the last stage.

1. INTRODUCTION

To satisfy requirements for more detailed cloud information in the IMETS database an examination of the most current and available nephanalysis software program, "Support of Environmental Requirements for Cloud Analysis and Archive" (SERCAA) produced by Phillips Laboratory and their contractor, Atmospheric and Environmental Research, Inc. has begun. SERCAA algorithms synthesize satellite data information from three platforms, AVHRR, DMSP, and GOES into data products consisting of: 1) Total cloud cover fraction, 2) number of cloud layers, 3) cloud layer coverage fraction, 4) cloud type, 5) cloud height, and 6) analysis confidence level.

The hardware platform which provides AVHRR and DMSP data to the Battlefield Environment Directorate (BED) is a Sun Sparc 2 which runs proprietary data processing software written by SeaSpace Corporation. A GOES data source is now available to BED on a Pentium platform. As soon as the associated software for the this system is complete, GOES data will be available for processing via the SERCAA algorithms.

The purpose of this paper is to show that satellite data can be received on the Seaspace system, where initial processing of the raw telemetry takes place and where it can be displayed if desired, and then the data undergoes very preliminary nephanalysis producing cloud information which is placed in the IMETS database.

2. Data Processing

2.1 SERCAA Algorithms Tested

BED is not yet in possession of the SERCAA software from Phillips Laboratory. A subset of the SERCAA algorithms, extracted from a Phillips Laboratory Technical Report describing SERCAA (1994) have been implemented in C, specifically some of the algorithms for analyzing AVHRR data. The intent of this initial effort is not to verify how well SERCAA can analyze for cloud. Rather, the goal is to ingest raw satellite telemetry, perform some preliminary cloud analysis so real cloud information is produced, and to database this information.

Seven AVHRR cloud typing/detection tests, derived from the SERCAA technical report, have been implemented in C by the author. They test for the following:

1. Low Cloud and Fog
2. Precipitating Cloud
3. Daytime Thin Cirrus Cloud
4. Visible Brightness Ratio
5. Cirrus Cloud
6. Fog, Low Stratus
7. Nighttime Thin Cirrus Cloud

Two background determination tests were implemented as well:

1. snow, ice background
2. desert background

2.2 Seospace Data Processing

Three days of AVHRR data were archived onto tape over the period 1-3 August 1995 on the Seospace system. During this time 18 NOAA Polar Orbiter passes were captured. The Seospace software is used to convert the raw HRPT telemetry data into albedo values for channels one and two and temperature values for channels 3, 4, and 5. The functions 'avin' and 'avcal' perform this function. 'avcal' does the data calibration and references the AVHRR visible coefficients which must be periodically updated within the Terascan software due to 'instrument drift' aboard the NOAA Polar Orbiters. Next the data is registered via 'fastreg' which ensures that each data set is composed of the exact same number of pixels and registers each pixel to a particular latitude and longitude. 'angles' extracts the latitude, longitude, solar and satellite zenith angles at each pixel. Finally 'expbin' extracts a particular dataset such as A(1). In order to extract an ambient surface air temperature at each pixel, (information used in the desert background test) the Tiros Operational Vertical Sounder (TOVS) software available on the Seospace platform was used. Due to a faulty sensor on board the NOAA-14 satellite only NOAA-12 data could be processed via the TOVS software. A series of 5 TOVS processing functions are needed to eventually output such entities as vertical profile of temperature, geopotential height, total ozone, and stability parameters.

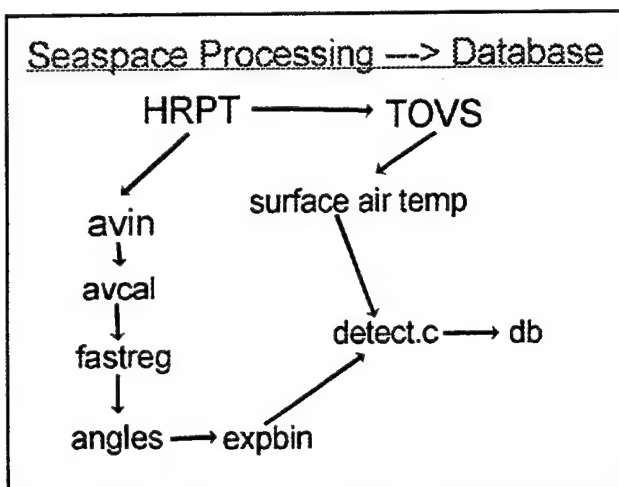


Figure 1. Seospace data processing flow.

detect.c is the author's C encoding of the particular SERCAA algorithms described above and are extracted from the SERCAA technical report. db represents the IMETS

database.

2.3 Databasing

Within the IMETS database cloud information (as well as a variety of other meteorological parameters) is held in four "sys_ids": SAWD, SINT, SMET, and SSAO. Cloud information decoded from binary data files from Offutt AFB, NE is placed in the SAWD sys_id. SAWD holds the following cloud information: sky cover, ceiling, and height, type, and coverage for low, mid-level, and high clouds. SINT, SMET, and SSAO are sys_ids for information decoded from alphanumeric data files sent from Tinker AFB, OK. SINT is data from intermediate reports and contains height and coverage for high, mid-level and low clouds plus sky cover and ceiling. SMET holds data derived from METAR reports and consists of sky cover and type, height, and coverage for high, mid-level, and high clouds. Lastly, a SSAO sys_id exists to store cloud data from surface airways reports and contains height, type, and coverage for high, mid-level, and low clouds. High clouds are considered to be anything above 20,000 feet. Mid-level clouds are between 6500 and 20,000 feet while low cloud is anything below 6500 feet.

It is clear that when the SERCAA software is implemented at BED a new sys_id to hold strictly cloud information will need to be created because much finer cloud information will then be available. SERCAA's "Analysis Integration Algorithm" synthesizes a multitude of cloud information from three platforms, NOAA Polar Orbiter, GOES, and DMSP, into the following parameters for a particular analysis region:

1. Number of Cloud Layers (up to 4)
2. Total Cloud Fraction
3. Layer Cloud Fraction
4. Layer Cloud Top IR Temperature
5. Analysis Confidence Flag Index
6. Layer Cloud Type
7. Estimated Error in Total Cloud Fraction
8. Estimated Error in Layer Cloud Fraction
9. Local Standard Deviation of Analyzed cloud Top IR Temperature
10. Precipitating Cloud Detection Index
11. Thin Cirrus Cloud Detection Index
12. Low Cloud Detection Index

Nine cloud types can be identified by SERCAA: cirrus, cirrostratus, altocumulus, altostratus, stratocumulus, stratus, cumulus, cumulonimbus, and nimbostratus.

The new sys_id should store the 12 parameters listed above.

To insert cloud information into the IMETS database, the function 'dbinter' is called. dbinter requires a number of parameters, among them the sys_id currently being dealt with, a latitude and longitude, an array of values to be inserted, and the number of values. So for example, using a current sys_id such as SMET, one would input the appropriate cloud type in position 12 of the data vector for high clouds, a value for areal coverage in position 15 and a value for height in position 18. This would be done for each pixel by giving the dbinter function the latitude and longitude of that pixel.

2.4 Test Results

2.4.1 AVHRR data analysis

2.4.1.1 Case 1

A subsection of a nighttime pass on 02 August 1995 at 0813Z in the Louisiana area was chosen to see if the nighttime cirrus cloud detection algorithm would identify those cloud types correctly. The scene coordinates are 30.74 N to 32.02 N and 93.59 W to 92.18 W. Note that the navigation of the overlay for the Red River is significantly off but illustrates vividly how clearly it is seen in channel 3 displayed in figure 2. The author had surface synoptic analyses to check the algorithm output against.

Two cloud types were identified by the SERCAA algorithms: cirrus and low stratus/fog. Cirrus clouds were identified by both the 'cirrus' test and the 'nighttime thin cirrus' test. At this particular time, Tropical Depression Dean was centered over West Central Texas. The SERCAA algorithm identified cirrus (from the cirrus test) in the northwest corner of the scene as seen in figure 3. Ahead of T.D. Dean, the surface synoptic analysis shows layered altocumulus in the lower left portion of the scene and overcast skies in the upper left with no mid-level or high clouds reported. It is apparent that the low cloud layer in the northwest section of the scene would cause problems for an observer looking for cirrus clouds. However, given Dean's location in Texas, finding cirrus bands out ahead of the system in Louisiana is very reasonable. The nighttime thin cirrus test also identified cirrus clouds but in this case, over much of the scene. The synoptic chart shows thin cirrus reported in the southwestern part of the scene. There are no reporting surface stations in the eastern part of the scene to reference. In this case the SERCAA algorithm has likely incorrectly found some of the cirrus in the eastern part of the scene due to the fact that this

is a high humidity area which would lead to decreased T(5) radiances. In this case, as is outlined in the SERCAA report, one should check whether the clear scene brightness temperature exceeds some empirically derived threshold. If so, use $T(3) - T(4)$ rather than $T(3) - T(5)$ because of the reduced sensitivity to water vapor attenuation in channel 4. In the northwest corner of the scene, fog and low stratus were identified by the fog, low stratus test. Given the very moist conditions reported there, 75F air temperature and 74F dew point this test result looks correct. Note in the analysis figures that the contouring algorithm is by Wyvill whereby each grid square is checked to see if the contour should pass through it. If so a line is drawn connecting the midpoints between the two appropriate points, i.e. no interpolation is done.

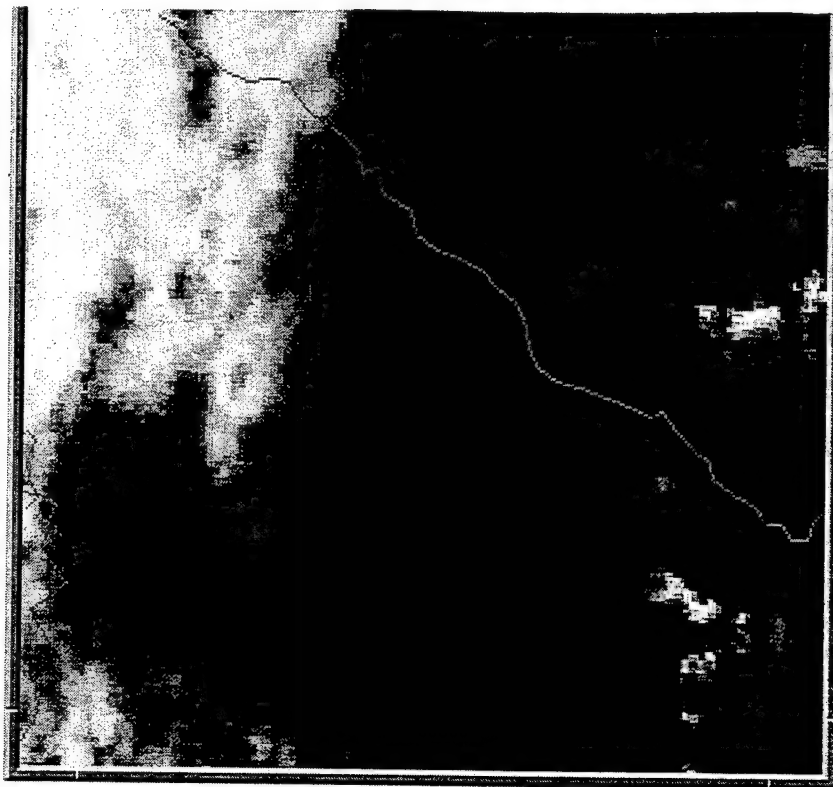


Figure 2. AVHRR channel 3 radiances at 0813Z, 02 August 1995 over E. Texas, Louisiana.

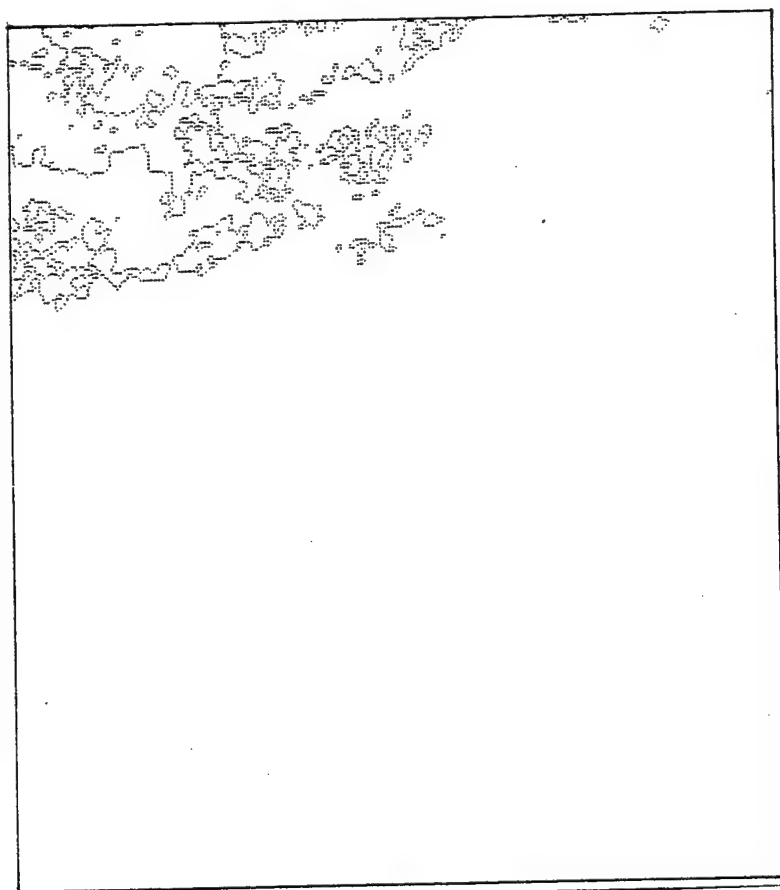


Figure 3. cirrus detected over E. Texas, Louisiana by the cirrus test.

2.4.1.2 Case 2

A subsection of a daytime pass in the Minnesota/North Dakota area, at 1449Z 03 August 1995, was also analyzed. The scene coordinates are 45.41 N to 47.32 N and 98.89 W to 94.26 W. This is an early morning scene and in channel 2 (figure 4) one can clearly see the shadows of 2 cumulus towers in southern Minnesota as well as a cumulonimbus (Cb) cloud in the upper right quadrant. Most assuredly the algorithm for detecting precipitating cloud would have located the Cb if a climatological database of clear scene brightness temperatures had been available. In that case the very large departure between cloud top temperature and clear scene temperature would have been noted. Only low cloud and fog were identified in this scene and this agrees well with the 02 August 1995 12Z surface analysis over the region which shows a low centered over southeast Minnesota and an associated stationary front. Fog is reported over nearly the entire southeast third of the state. Given the fact that a stationary front is present, fog recurring the next morning is reasonable. The

contours in figure 5 are algorithm output and distinctly show the clear, fog/low stratus boundary with clear skies in the northwestern half and mainly cloud in the southeastern half.

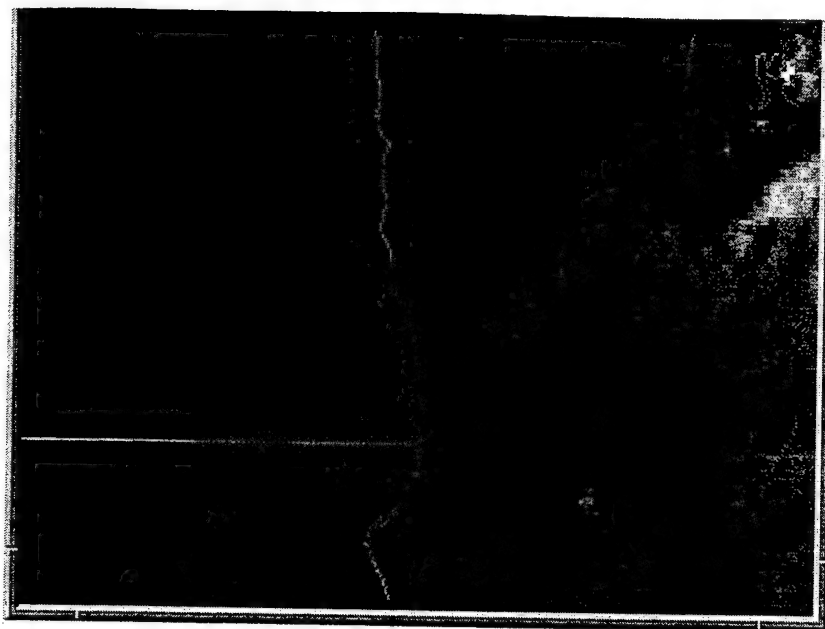


Figure 4. AVHRR channel 2 albedos at 1449Z, 03 August 1995 over sections of Minnesota, North Dakota, and South Dakota.

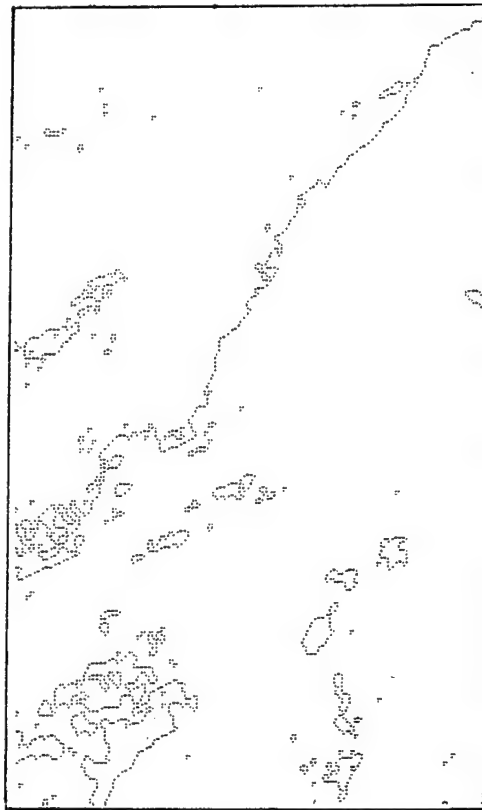


Figure 5. Low cloud and fog detected over Minnesota, N. Dakota, and S. Dakota.

3. Conclusions

These somewhat simplistic tests have verified a small portion of the SERCAA algorithms. What remains is implementation of the complete set of SERCAA software modules. This will involve porting the code from a VAX/VMS environment to a SUN/UNIX environment and thus a conversion of all system calls. Then a new sys_id as described will need to be created within the IMETS database to support the new cloud information that will be available via SERCAA.

Acknowledgements

The author would like to thank Mr. Jim Bunting of Phillips Laboratory for the multiple phone conversations on the various nephanalysis algorithms and Mr. Patrick Laybe of the Battlefield Environment Directorate for discussions on

how cloud information is currently stored in the IMETS database.

References

1. Support of Environmental Requirements for Cloud Analysis and Archive (SERCAA): Algorithm Descriptions, Technical Report, by Atmospheric and Environmental Research, Inc. under contract to Phillips Laboratory, Hanscom Air Force Base, MA, PL-TR-94-2114.

AUTOMATED THERMAL INJURY RISK ASSESSMENT FOR THE DISMOUNTED SOLDIER

G. B. McWilliams and E. S. Barnes
U.S. Army Research Laboratory
White Sands Missile Range, NM 88002

W. T. Matthew
U.S. Army Research Institute of Environmental Medicine
Natick, MA 01760

ABSTRACT

A computer modeling system for the real-time risk assessment of thermal injury over a battlescale region is described. The model assesses heat risk in terms of probability of casualty, maximum work time before injury occurs, and the water and rest requirements needed to prevent injury. Assessment of cold injury is made in terms of expected survival time. Input data to the model include information about the environment - weather and terrain data and information about the soldier - activity level, physical attributes, and clothing type (MOPP level). The model software is designed for a Unix operating system using a Motif windowing environment. It is being installed for use as a risk management tool for the 6th Ranger Training Battalion at Camp James E. Rudder on Eglin Air Force Base, Florida. Data collected at this site will be used to improve the model's capabilities.

1. INTRODUCTION

The performance of the dismounted soldier whether engaged in training activities or actual combat operations can be significantly impacted by the weather. Thermal injury is one of the greatest potential weather impacts the dismounted soldier will encounter. Thermal injuries can be caused from either heat (hyperthermia) or cold (hypothermia) exposure.

The capability to quickly assess the risk of thermal injury would be of great value to military planners and commanders. This information could be used to not only

minimize thermal injuries but also to better plan needed medical and logistic activities.

In order to provide the Army with this capability, the U.S. Army Research Laboratory's (ARL) Battlefield Environment Directorate (BED) and the U.S. Army Research Institute of Environmental Medicine (USARIEM) are jointly developing an automated thermal injury risk assessment system. This software system is designed to operate in real-time and to output information for an entire battlescale region in a overlay format that is readily interpreted.

2. SYSTEM DESIGN

The software has been designed with a modular architecture. This modularity facilitates evaluation and software modification, better enables the individual modules to interface with other models, and allows software engineers to work more independently.

Three primary modules comprise the system. The first module is called MERCURY. MERCURY provides all the user interface utilities and is responsible for ingesting and processing all the weather and terrain data. The second module is the heat strain model which uses the gridded weather data output from MERCURY to calculate four different heat related variables. The third module is a model that calculates cold survival time. It also uses as input the gridded weather data that MERCURY generates.

This software is designed to run with the Unix operating system and the X11/Motif windowing environment. All development work has been performed on a SunSparc workstation. Thermal strain prediction model software implementations have been accomplished by Science Applications International Corporation in Joppa, Maryland.

2.1. MERCURY

MERCURY grids met data over a battlescale region using data which are typically gathered from a low density observation network. This capability can be very valuable for military applications. First it provides a high resolution data grid throughout the region of interest. Second the data have high fidelity because they have been corrected for the localized weather effects attributable to terrain and land use

influences. Third the gridding procedure is automated and thus reduces the amount of manpower and time that would otherwise be necessary for the effort.

Required input data include weather, land use, and terrain elevation data. MERCURY needs the land use and elevation data for its rule-based gridding algorithms and for creating map backgrounds for various output overlays. MERCURY has been designed with the intention that in a tactical environment it will automatically ingest the weather data from the Army's Integrated Meteorological System (IMETS) or a system similar to IMETS. The Defense Mapping Agency's Digital Terrain Elevation Data Level 1 (DTED1) are the preferred source of the elevation data.

The land use data need to have a resolution compatible with the elevation data. Land use data derived from Landsat satellite imagery are ideal for this application. These data have the proper resolution (30m) and are usually the most current data. However these data are not readily available for most parts of the world and must be specially processed by organizations such as the U.S. Army Waterways Experiment Station.

All the source code for the MERCURY module has been written in the C programming language. This module has been developed by the ARL/BED. Further information about the MERCURY module is available in a report by McWilliams (1995).

2.2. HEAT STRAIN MODEL

The heat strain model consists of a series of predictive equations that relate equilibrium core body temperature responses to various work regimes, clothing ensembles, states of

acclimation, physical attributes, and environmental conditions. Equilibrium core body temperature is determined through a thermal balance calculation and represents that temperature where the body's heat gain and loss are equal. The major parameters in the thermal balance calculation are metabolic heat production and convective, radiant, and evaporative heat exchange (Pandolf et al. 1986).

The input data include the weather parameters - wind speed (m/sec), ambient temperature (°F), relative humidity (%), and solar radiation (watts/m²); and soldier specific information - dehydration level (%), work activity level (watts) clothing type (MOPP level), acclimatization time (days), height (cm), and weight (kg). Heat strain calculations are made for each weather grid point generated by MERCURY. The gridded weather data are accessible from a file created by MERCURY and the soldier specific data is entered by the user using a popup window that is part of the MERCURY user interface (Matthew et al. 1993).

The model measures heat strain not in terms of actual equilibrium core temperature but in the more tactically meaningful terms of probability of casualty, work-to-rest ratios, maximum work time, and water requirements. All four measures can be displayed as overlays selectable from the MERCURY interface. The overlays provide the following information:

- 1) casualty overlay - the probability of casualty in percentages for soldiers who observe no work-rest discipline.
- 2) work-rest overlay - the ratio of work-to-rest in minutes per hour for work-rest

disciplines required to sustain soldier performance.

- 3) maximum work time overlay - displays the predicted straight time period that a soldier could work before becoming a heat strain casualty if no work-rest or water disciplines are observed.

- 4) water requirements overlay - the predicted number of canteens of water needed per soldier per hour to sustain continuous operations when work-rest disciplines are observed.

The source code for the heat strain model is written in the Ada programming language. It will compile on a Sun Ada compiler without any modifications and will compile on any other Unix computer with few modifications (McNally et al. 1994).

The heat strain model has been developed by the USARIEM.

2.3. COLD SURVIVAL TIME MODEL

The cold survival time model is a mathematical model developed by the Canadian Defense and Civil Institute of Environmental Medicine (DCIEM) to predict survival time in the cold. Survival time in the model is defined as the point at which the body's core temperature reaches a value of 30°C. This is the temperature at which unconsciousness normally develops (Tikuisis and Frim, 1994).

The DCIEM model is based on the principles of steady state heat conduction in a single cylinder. This cylinder is comprised of a core and two annular concentric shells representing body fat and skin and clothing plus still air, respectively. The ambient

condition can be either air or water. The model distinguishes between the two conditions by assigning different values of insulation to the still boundary layer. However it cannot currently handle situations involving partial immersion or repeated immersions.

It assumes that protection against the cold is uniformly applied to the surface of the body. The model also excludes the body's initial transient response to cold which is characterized by vasoconstriction usually resulting in a delay in the fall of body temperature for up to one hour.

The model was developed for a sedentary person. Therefore the two sources of heat production are resting metabolism and shivering. Heat production from resting metabolism has been assigned a fixed rate of $50 \text{ W}\cdot\text{M}^{-2}$. Heat production from shivering assumes the individual is healthy and uninjured and is not allowed to exceed $200 \text{ W}\cdot\text{M}^{-2}$.

The environmental data required as input depends on whether the model is operating in the air or water mode. When the model is operating in the air mode, the required input data are the ambient air temperature and wind speed. Only water temperature data are needed when the model is operating in the water mode.

Like the heat strain model, the cold strain model calculates output for each weather data grid point. This information can then be displayed as an areal overlay.

All the source code for this model is written in the C programming language.

3. SYSTEM PERFORMANCE

The system software is generally demonstrated on a SunSparc workstation, the computer on which it was developed. However the code has been successfully and easily ported to other hardware platforms running the Unix operating system and the X11/Motif windowing environment. In order to achieve maximum performance, it is recommended that the computer have at least 48 MB of RAM and 100 MB of disk memory available. The software has been run with as little as 8 MB of RAM.

Figure 1 is a picture (not to scale) of the user interface which is generated using weather and terrain data files for the Los Angeles Basin region. The main screen display contains two windows. The upper window shows a 3-D rendering of the terrain elevation data. The lower window is where all the weather/terrain and thermal injury overlays are displayed. These overlays which total 13 can be displayed with either a map or a grayscale relief background. In Figure 1 a relief background is shown along with a legend defining the grayscale in terms of meters above sea level. The latitude and longitude coordinates at any point on the relief or map background can be obtained by putting the mouse cursor on that point and clicking on the middle button. Similarly clicking on the left mouse button displays a box showing the values for seven weather parameters along with the location coordinates, the date and time for which the values are valid, and the elevation at the cursor location. The location of the actual reporting weather stations are shown as icons with a three-letter station identifier.

At the top of the screen are buttons for activating the File, Terrain, Utilities, and Export menus.

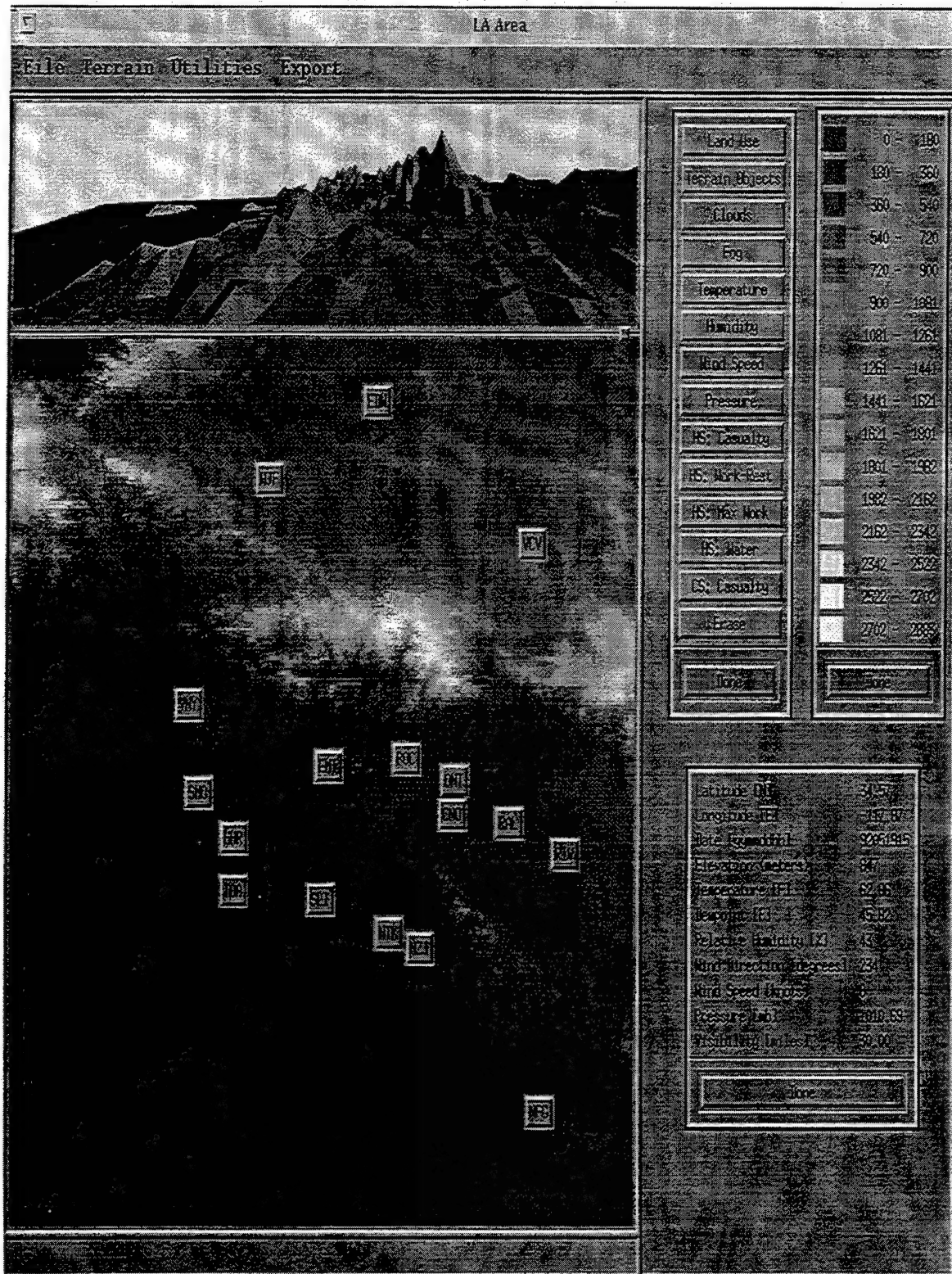


Figure 1. User interface with Los Angeles Basin weather and terrain data.

3.1 File

The file menu allows the user to select a new region of interest or to exit the program. Presently the program contains archived weather and terrain data for three regions - the Los Angeles Basin, Fulda Gap, Germany, and a section of South Korea.

3.2 Terrain

One option in the terrain menu allows the user to select the type of background - map or grayscale relief. Other options allow the user to "Zoom In", "Zoom Out", "Center View", "Set View", and "View Home". "Center View" centers the display according to latitude/longitude coordinates entered by the user. "Set View" defines the viewing area according to user-entered latitude/longitude coordinates. "View Home" redraws the originally displayed screen.

3.3 Utilities

The utilities menu contains three options. Option 1 toggles on and off the icons denoting the location of the reporting weather stations. Options 2 and 3 execute the heat strain and the cold survival time models. The heat strain option yields another popup menu in which the user can change the default values for the soldier's dehydration level, work activity, clothing type, acclimation time, height, and weight.

3.4 Export

The export option provides the user the ability to save to file the current map information. This information can include the meteorological, terrain, heat strain, and cold survival time data used in the display of

the 2-D screen and associated overlays. The saved files are formatted in a general interchange format (GIF) for direct use by ArcInfo and ER-Mapper and other geographic information systems that read tabular, ASCII text data (Fischer, 1995).

4. CAMP RUDDER INSTALLATION

At the request of the Dismounted Battle Space Battle Lab and the 4th Ranger Training Brigade at Fort Benning, Georgia, ARL/BED and USARIEM are planning to install the automated thermal injury risk assessment system at Camp James E. Rudder located on the Eglin Air Force Base, Florida. Camp Rudder is the home of the 6th Ranger Training Battalion.

At Camp Rudder the system will function as a training management tool. Features added to the Camp Rudder system include the capability to manually edit weather data, to automatically ingest data from the ten Handar weather stations located on Eglin AFB, to process water temperature and water level data, and to generate appropriate map backgrounds for the region. This software will reside on a Sun SparcStation V running the Solaris operating system and the X11/ Motif windowing environment.

5. FUTURE DEVELOPMENT

Future development plans call for the implementation of a cold survival time model applicable to partial immersion situations, for implementing solar radiation effects into the cold survival time models, for using forecasted weather data in order to make thermal predictions out to 12 hours, and for implementing any improvements identified during an on-site system performance evaluation to be conducted at Eglin AFB.

Development work on the cold models will be jointly performed by USARIEM and DCIEM. The forecasted data will be generated by a high resolution mesoscale prognostic model. The most likely candidate for the mesoscale model is the Battlescale Forecast Model (BFM) under development at ARL/BED.

6. CONCLUSION

The dismounted soldier must be prepared to perform in all types of natural environments. Tools available to minimize the soldier's medical risk when performing in these environments are of great benefit to the Army. One such tool is the automated thermal injury risk assessment system. This system is not only capable of helping to prevent thermal injury but can, for instance, be used as a planning aid for defining logistic (e.g. water requirements) and medical (e.g. treating heat exhaustion) support.

7. REFERENCES

- Fischer, B., 1995. Mercury/Heat Strain/Cold Survival Time Geographic Information System (GIS) Software - Software User's Manual, DAMD17-93-C-3141, Science Applications International Corporation, Joppa, MD 01760-5007, 22 pp.
- Matthew, W., R. McNally, G. McWilliams, S. Kirby, H. Pfeiffer, 1993. "Integration of a Heat Prediction Model with Army Weather Data Resources". In Proceedings of the 1993 Battlefield Atmospherics Conference, U.S. Army Research Laboratory, White Sands Missile range, NM 88002-5501, pp. 479-488.
- McNally, R., J. Berndt, J. Fisher, N. J. Simini, 1994. Mercury/Heat Strain Programmer's Manual. Final Report, DAAL-90-C-0071, Science Applications International Corporation, 626 Towne Center Drive, Joppa, MD 21085, 646 pp.
- McWilliams, G., 1995. Real-Time Thermal Risk Assessment for the Dismounted Soldier. U.S. Army Research Laboratory Technical Report, White Sands Missile Range, NM 88002-5501. In Publication.
- Pandolf, K., L. Stroschein, L. Drolet, R. Gonzalez, M. Sawka, 1986. "Prediction Modeling of Physiological Responses and Human Performance in the Heat," Computers, Biology, and Medicine, Vol. 16, No. 4, 319-329 pp.
- Tikuisis, P., and J. Frim, 1994. Prediction of Survival Time in Cold Air. Defense and Civil Institute of Environmental Medicine, Ontario, Canada, 31 pp.

SELECTION OF THE THEATER FORECAST MODEL

B. L. Bauer and C. Tremback
Mission Research Corporation
Huntsville, Alabama and Fort Collins, Colorado

R. M. Cox *
Defense Nuclear Agency
Alexandria, Virginia

ABSTRACT

Air Force Weather (AFW) identified a deficiency in producing timely and accurate theater forecasts. To overcome this deficiency, AFW and the Defense Nuclear Agency (DNA) sponsored the selection of the Theater Forecast Model (TFM). The objectives of the TFM effort were to identify a candidate numerical weather prediction model from currently available models that would be suitable for use in theater. This paper will describe the selection process, the results of the evaluation, and the model selected.

The actual model selection process began with the "Combat Weather System Technical Alternatives Study." This study reviewed over 100 different numerical weather prediction models and compared and ranked their capabilities. The ranking was based on an integrated set of customer requirements and relied on published and developer provided information on the models.

The selection process continued with detailed performance comparisons of three of the top ranked models. The baseline was the performance of the current model, the Relocatable Window Model (RWM), operating at Air Force Global Weather Central (AFGWC). The three candidates are the Pennsylvania State University/National Center for Atmospheric Research Mesoscale Model Version 5 (MM5), the Navy Operational Regional Atmospheric Prediction System Version 6 (NORAPS6) model, and the Colorado State University Regional Atmospheric Modeling System (RAMS) Version 3b. The performance comparisons were both objective and subjective. Comparisons were made for multiple seasons in five regions of the world. Candidate models were run on a supercomputer and a workstation to gauge their adaptability to the expected theater workstation environment.

The evaluation of this data was accomplished by the Air Force (AF) and DNA. This resulted in the selection of a single model to be the basis of the new TFM.

** Currently assigned to the National Defense University, Fort McNair, D.C.*

1. Introduction

Air Force Weather (AFW) identified a deficiency in producing timely and accurate theater forecasts. To overcome this deficiency, AFW and the Defense Nuclear Agency (DNA) sponsored a project to select of the Theater Forecast Model (TFM). There were two main objectives of the TFM effort. The first objective was to identify a candidate numerical weather prediction model, suitable for theater use, from currently available models. Once the best model was selected, it was to be implemented and adapted to meet the needs of deployed forces on the battlefield.

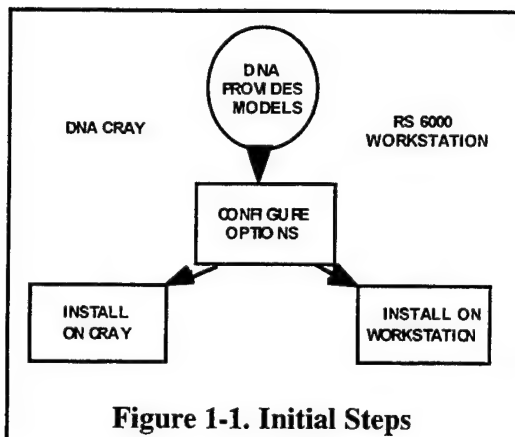
The actual model selection process began with the "Combat Weather System Technical Alternatives Study." This study reviewed over 100 different numerical weather prediction models and compared and ranked their capabilities. The ranking was based on an integrated set of customer requirements and relied on published and developer provided information on the models.

The second phase of the selection process was the detailed performance comparisons of three of the top ranked models. Performance in this phase of the evaluation was defined as how well the model could forecast the observed weather. The emphasis of the performance evaluation was on statistical measures of model performance rather than subjective measures. The ability of the models to operate on a workstation was also evaluated by actually making forecasts on a representative workstation.

The baseline was the performance of the current model, the Relocatable Window Model (RWM), operating at Air Force Global Weather Central (AFGWC). The three candidates are the Pennsylvania State University/National Center for Atmospheric Research Mesoscale Model Version 5 (MM5), the Navy Operational Regional Atmospheric Prediction System Version 6 (NORAPS6) model, and the Colorado State University Regional Atmospheric Modeling System (RAMS) Version 3b. To insure the model evaluation was not biased to a particular region or climate type, test forecasts were accomplished in five regions of the world. These regions were Alaska, Central America, the Continental United States (CONUS), Korea, and the Middle East.

2. Test Process

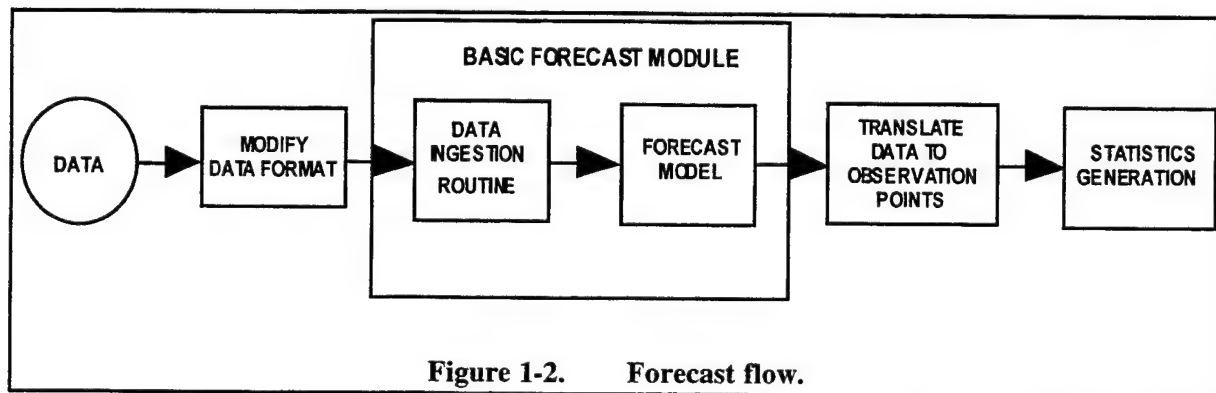
The models were configured to use the "best" physics available, to use identical sets of input data, and to generate forecasts that could be directly compared. The requirements provided a challenging set of criteria to evaluate in a single program.



Most of the models were developed on some version of a mainframe Cray computer and would operate on that platform with minimal changes. After obtaining the models, we attempted to install all but RWM on DNA's UNIX based Cray and an RS/6000 (Figure 1-1.). RWM normally operates on a Cray XMP with data input support from the mainframe computers and data bases at AFGWC. The model had been ported and validated on a workstation at AFGWC and this version was used.

It was run only on the workstation since no validated version for a Unix-based Cray exists. A convenient and available workstation, the IBM RS/6000-370, was used as the test workstation for all forecasts. The RS/6000 is a RISC-based machine made by IBM that is in the middle- to high-performance category today, but will probably represent the medium- to low-end capability when the Theater Forecast Model (TFM) is operational. The configuration of models and input data sets were the same on both the workstation and the Cray.

Each model's native data ingestion routine was used to construct the initial forecast fields from the observations and boundary conditions supplied by the global circulation models. Since data from both the National Center for Atmospheric Research (NCAR) and AFGWC were used to initialize the various forecast runs, we translated the data into a standard data format and modified each data ingestion routine to accept the standard format.



The basic forecast modules were used, to the extent possible, as received (Figure 1-2.). The only changes made were to read the standard data format and to remove any mathematical smoothing of the output. The elimination of smoothing was done to ensure that the forecast ability and not display capability was measured.

3. Software Models and Configuration

Each model was configured using the "best" physics available, with an apriori assumption being that this will produce the best forecast. Candidate models can be grouped by their current use. NORAPS and RWM are currently used in operational settings and have few switches to select different physical models. Their options are more related to types of data output available. The MM5 and RAMS models have more of a research background and have numerous physical model switches. In addition, they have many of the same types of options for data assimilation and output. The four candidate models have existed for some time, or are new upgrades of existing models. RAMS and its immediate predecessors have a history dating back to the mid-1970's. The MM5 and NORAPS6 have similar lineages that provide a track record of what they can and cannot do and how well they can do it.

The three candidate models, RAMS, MM5, and NORAPS6 have much in common: they are all 3-D, primitive equation, relocatable, regional mesoscale models; they can all use staggered gridding, terrain-following vertical coordinates, and four dimensional data assimilation using nudging; and they include many similar parameterizations for sub-grid mixing, cumulus, and radiation. There are some differences, however, particularly between NORAPS6 and the other two models.

The NORAPS series of codes has been developed by the Navy for their own operational use and are optimized for ocean area forecasts; MM5 and RAMS are not. This distinction is easily seen by noting that NORAPS6 models sea ice, but RAMS and MM5 do not. However, RAMS and MM5 both model numerous types of land use, which can significantly affect local weather, but NORAPS6 has no land use model.

Two of the models that were tested (NORAPS and RWM) do not have options for a non-hydrostatic equation set. A non-hydrostatic model is critical in the simulation of a variety of atmospheric features. One can do a scale analysis of the terms in the governing equations and derive an "aspect ratio", the ratio of the vertical scale of an atmospheric circulation divided by the horizontal scale. If the aspect ratio is much less than one, then the hydrostatic assumption is valid. However, there is a difference in the theoretical and numerical treatment of the equation set. Experience has shown the following re-definition of the aspect ratio argument: Define the aspect ratio as the distance in the vertical that a parcel can travel by buoyancy divided by the horizontal grid spacing. If this ratio is less than 1, then a hydrostatic model will give you basically the same results as a non-hydrostatic model. Using this definition, one can easily see that a buoyancy-driven circulation like a thunderstorm or a boundary layer thermal, if these are resolved by the model grid, require a non-hydrostatic model. However, there is another class of circulation that requires a non-hydrostatic model. This class can be loosely called "oscillatory circulations," where a parcel will overshoot its equilibrium buoyancy level and a wave train will be set up. A

trapped lee wave train set up by flow over a mountain barrier is an example of this type of circulation. While this circulation will show an aspect ratio of less than one, these waves cannot be formed by a hydrostatic model, since it will not allow parcels to be out of hydrostatic equilibrium.

For the grid scales that were used in the TFM Model Selection, neither the buoyancy-driven nor the oscillatory circulations were able to be resolved by the specified grid spacings. A large thunderstorm may only be 10-20 km in diameter, and since a numerical model needs to have a circulation defined by at least 4 grid spaces to be handled properly by the numerics, the test runs would not resolve these circulations. A lee wave train usually has a horizontal wavelength of about 20 km, so these will not be resolved well either.

However, as computers get faster, the spacing of the objective domain will be able to have a finer grid spacing or, even today, numerical forecasts for smaller domains at a much higher resolution can be made. Once the grid spacing is reduced below 10 km, a non-hydrostatic model will become necessary.

4. Grid Configuration

The objective of these tests was to compare predicted forecasts produced by the various models. To accomplish these comparisons the computational domains were made to be as similar as possible. There is no common map projection available for all the models, so projections were chosen that are appropriate for each theater and as similar as possible. The RAMS model uses a rotated polar-stereographic projection, which "rotates" the pole point of the projection to the center of the computational domain. This allows the use of the same projection with a minimum of distortion, but MM5, NORAPS, and RWM do not use a rotated projection. Therefore, two projections had to be used in an attempt to minimize distortion. The three models used a Mercator projection for the Central America domain and a Lambert-Conformal projection for the remaining areas. The Mercator projections differed slightly as MM5 and NORAPS are hardwired to use the equator as the standard latitude, and RWM uses 22.5° N. The same 71 x 71 computational domain or grid with a nominal 46.3 km spacing was used in all the tests. The gridded regions are displayed below (Figures 4-1. through 4-5.).

Vertical structures also differ. The RAMS model uses a terrain-following height coordinate and the others use a terrain-following pressure coordinate. However, even with these differences, the models "effective" resolutions were fairly close. Approximately twenty layers were used for each model. Some of the models may have been designed (or work better) with more levels than the target of twenty. The NORAPS model is run operationally with thirty six. The target number of levels, while adequate in some cases, should be greater to allow for increased resolution near the ground and additional levels in the stratosphere.

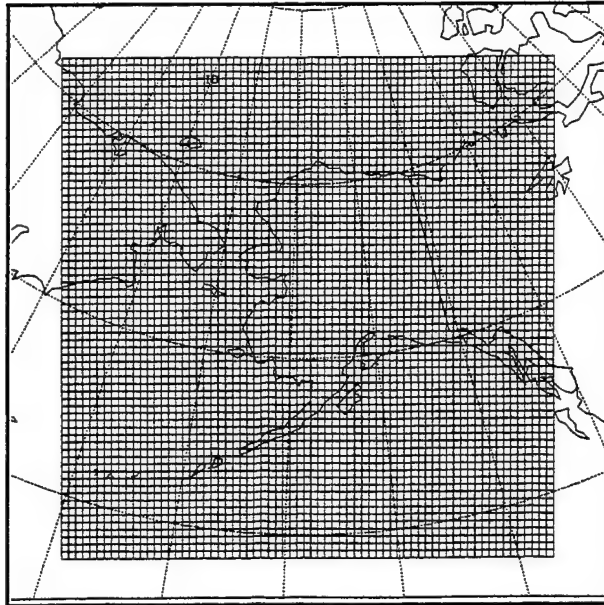


Figure 4-1. Alaskan grid centered at 63 N and 158 W.

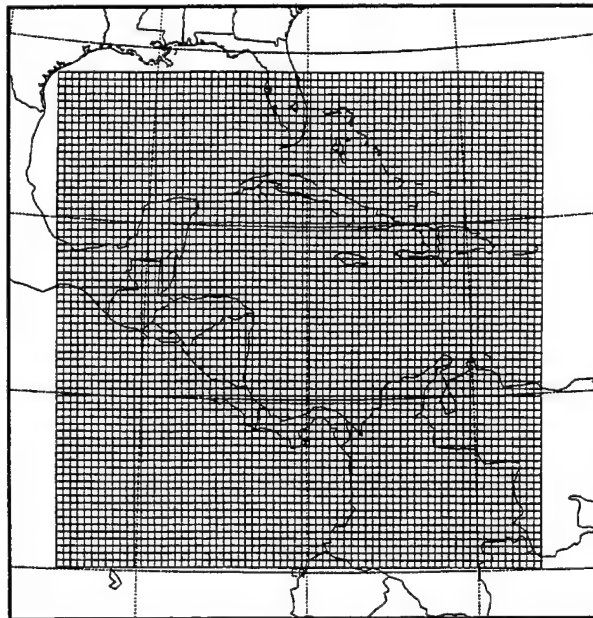


Figure 4-2. Central American grid centered at 14.6 N and 80.5 W.

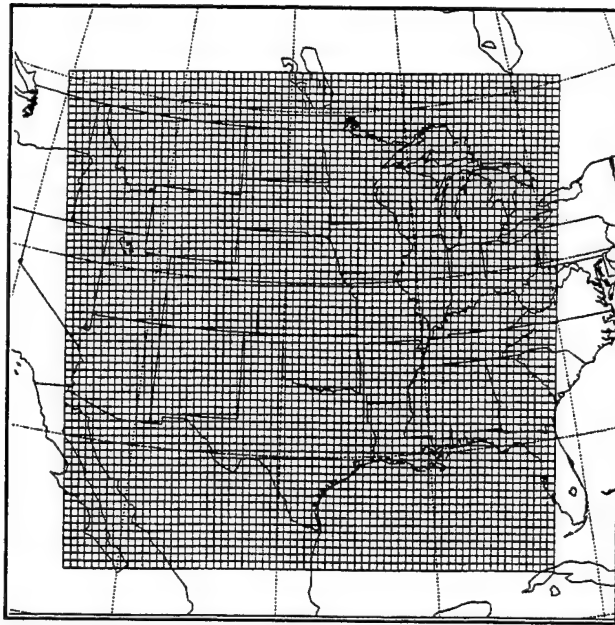


Figure 4-3. CONUS grid centered at 38 N and 98 W.

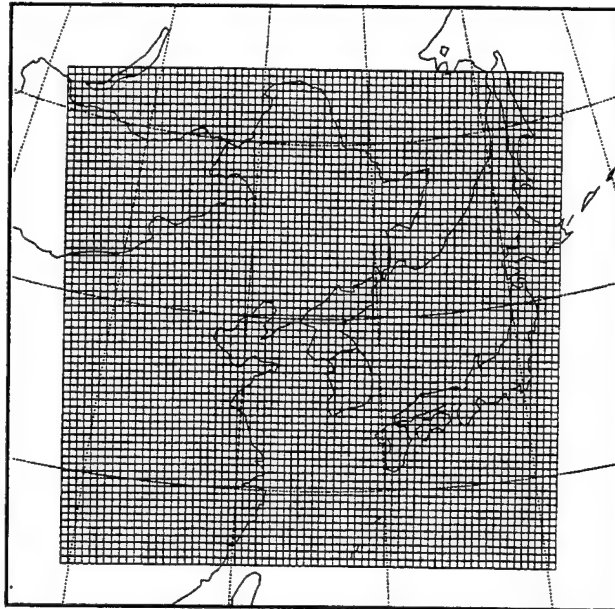


Figure 4-4. Korean grid centered at 40 N and 125 E.

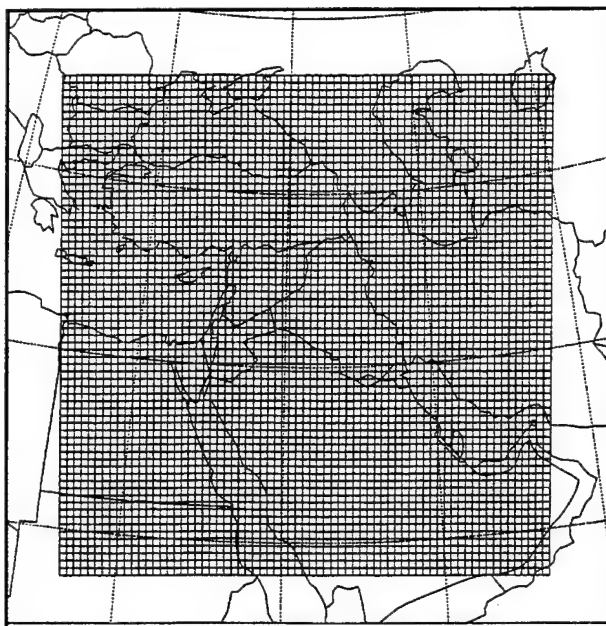
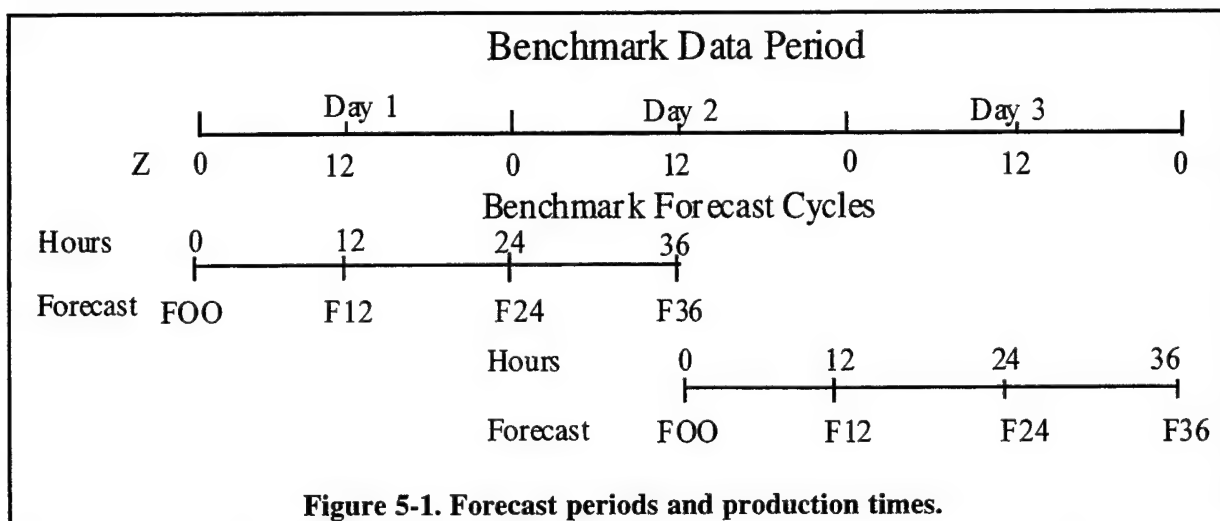


Figure 4-5. Middle Eastern grid centered at 32.5 N and 41.5 E.

5. Forecasts

Each test consisted of a thirty six hour forecast. This forecast period was selected to reduce the amount of run time required for testing while allowing the models adequate time to "spin-up."



Spin-up refers to the time required for the model to overcome "noise" resulting from the initial conditions. For these tests, data was obtained for a three day period.

Once a forecast was accomplished, the computed data were interpolated to the observation points. Forecast data were compared to observed data using a program called REVU, which was designed to produce the required statistical data. Figure 5-1. indicates that two independent forecasts were accomplished during each three day period. One forecast was initialized at the beginning of the three days and the second initialized midway through the data period. Forecasts were made at the times indicated to allow comparison with surface and upper air observations.

Table 5-1. summarizes the threshold tests. Initially, a well reported set of data were run. It was the Atmospheric Variability Experiment—Severe Environmental Storms and Mesoscale Experiment (SESAME) 1 Test, that took place in CONUS during April 10-11, 1979.

Test forecasts were based on and compared to data extracted from NCAR archives corresponding to the days April 9-11. With the RWM exception noted, forecasts were intended to be duplicated

Table 5-1. Threshold forecast cases.

Test	Benchmark	Benchmark	Benchmark
Data Source	NCAR April 79	NCAR August 94	AFGWC November 94
Theater			
CONUS	SESAME		
Alaska		Summer	Winter
Central America		Wet	Winter
Middle East		Summer	Winter
Korea		Monsoon	Winter

on the Cray and the workstation. This exercise was to provide specific information about code portability, any performance degradation on a workstation, and the integrity of each model—whether it

produces the same results on the workstation as on the supercomputer. This was accomplished for all the candidate models except MM5. Each of the models that was able to run on both platforms produced forecasts that were independent of the platform used. The version of MM5 used would not operate on the workstation. This was entirely due to problems encountered with the data ingestion routines. The version obtained was described as a workstation version, but it was found that workstation compatible data ingestion routines do not exist for MM5. The workstation version of MM5 exhibited a large number of changes from the standard Cray version. Rewriting the ingestion routines was started, but was quickly determined to be beyond the scope of this effort. A hybrid approach was considered, e.g. running the data ingestion routines on the Cray and transferring their output to the workstation. However, MM5 uses binary transfer files, and data conversion and validation would have significantly delayed testing. As a result of these problems, MM5 was restricted to the Cray. The workstation forecast module was tested on the Cray by comparing its forecast to that produced by the Cray version using identical input data created by the Cray ingestion routines. Even with the substantive rewrite evident in the workstation version, both versions gave the same results.

Once the SESAME comparisons were completed, the remaining benchmark tests were accomplished. The next tests used August 1994 data from NCAR and were accomplished for Alaska, Korea, Central America, and the Middle East. The final tests in this series looked at simulated operational data from AFGWC. This data was downloaded by AFGWC personnel in November 1994. The data corresponds to the operational time AFGWC would have initialized the TFM. The intent was to reproduce the environment in which the TFM would need to operate. Late reporting stations were not included. In all of these post-SESAME tests, NORAPS and MM5 were used on the Cray, and RWM and RAMS on the workstation.

6. Performance

The performance of each model using several different error measures was evaluated. With 4 models, 5 regions, 2 seasons, and forecasts every 12 hours out to 72 hours for each case, a wealth of forecast data was compared with actual observations. Models were ranked based on which had the smallest root mean square (RMS) error for each observation level. This approach rates each model's general performance without regard to the AF's accuracy requirements for the various quantities. Second, models were ranked based on the AF accuracy criteria for each observable.

RMS Performance

Table 6-1. RMS rank ordering.

		Number of Cases				Total Cases
		MM5	NORAPS	RAMS	RWM	
4/79	CONUS	74	19	117	22	232
8/94	Alaska	65	33	143	23	264
8/94	Korea	36	26	177	25	264
8/94	Mid East	22	34	168	40	264
8/94	Cent America	29	27	169	39	264
11/94	Alaska	55	44	145	20	264
11/94	Korea	73	49	122	20	264
11/94	Mid East	54	56	113	23	246
11/94	Cent America	72	34	95	32	233
9/93	Korea	21	12	89	10	132
Total		501	334	1338	254	2487

First we will describe the results of the rank scoring using RMS error as the measure of each model's performance. Three of the statistics, temperature RMSE, relative humidity RMSE, and wind RMSVE, were used to generate Table 6-1. by accumulating the scores by season and region.

AF Accuracy Requirement Performance

We also ranked the four models based on how frequently they satisfied the AWS accuracy criteria for predicting temperature (2 degrees), dew point depression (2 degrees), wind speed (2 knots<20 knots, 5 knots>20 knots), wind direction (30 degrees), and sea level pressure (1.7 millibars). For the first four quantities we ranked them separately for their agreement with surface

observations and with upper air observations. Again, we tabulated how often each model was best in satisfying AWS criteria. The summary of this data is provided in Table 6-2.

Table 6-2. Total predictions meeting criteria

	Number of Predictions That Meet AWS Criteria				Total Observations
	MM5	NORAPS	RAMS	RWM	
8/94 Alaska	2,312	2,027	2,651	1,634	4,855
11/94 Alaska	2,486	2,227	2,944	1,656	6,685
8/94 Cent America	2,142	2,004	2,877	2,274	6,231
11/94 Cent America	1,745	1,347	2,267	1,443	5,369
4/79 CONUS	12,715	9,969	12,888	9,145	24,971
8/94 Korea	10,936	10,887	14,462	11,177	31,427
11/94 Korea	3,260	3,381	4,151	3,367	8,401
8/94 Mid East	2,829	3,489	4,337	3,337	11,392
11/94 Mid East	2,474	2,435	2,985	2,206	8,519
Total	40,899	37,766	49,562	36,239	107,850
Percent	38	35	46	34	

7. Summary

A model comparison was accomplished in an attempt to determine which current mesoscale forecast model would be the best candidate to replace the RWM in operations at AFGWC. Tests were made comparing output to observations in five completely different regions of the world. Also, models were run during different seasons of the year to ensure the model selected not only produced the best results for one region/season, but produced the most reliable forecast to meet mission requirements for anywhere in the world.

When compared to stated requirements, the RAMS model met those requirements forty six percent (46%) of the time with the MM5 model satisfying the requirements thirty eight percent (38%) of the time. It was shown that the MM5 model had difficulty initially and by the twenty four hour point, produced similar accuracies as the RAMS models. This probably can be related to the analysis routine distributed with the model. The MM5 has a Cressman scheme (1950's technology), whereas RAMS uses a hybrid isentropic terrain following height initialization scheme. If the analysis routine with MM5 were replaced, with a modern scheme, such as being developed at the Forecast Systems Laboratory, then MM5's performance would be greatly enhanced. However, RAMS performance was better overseas, too. This could potentially be related to a more sophisticated soil and vegetation routine in RAMS. In areas with less observational data, the model with a more robust soil and vegetation routine would produce superior results.

with less observational data, the model with a more robust soil and vegetation routine would produce superior results.

Based on these observations the RAMS model was shown to meet AF requirements more often than the other models in this study.

REFERENCES:

1. *Combat Weather Systems Technical Alternative Study, "Interim Report"*, 30 June 93, ESC, Headquarters AFMC, Hanscom AFB, MA.
2. *Benchmark Report-Theater Forecast Model Selection*, 15 October 1995, Headquarters Defense Nuclear Agency, Washington, D.C. 20305, (to be published), MRC-HSV-R-95-001.

ACKNOWLEDGMENT

This work was supported under contract number DNA001-94-C-0096 with the Defense Nuclear Agency. "Review of this Material Does Not Imply Department of Defense Endorsement of Factual Accuracy or Opinion".

Session III

BOUNDARY LAYER RESEARCH

ATMOSPHERIC TRANSPORT OVER WHITE SANDS MISSILE RANGE

ROBERT M. COX¹, JOHN SONTOWSKI²,
RICHARD N. FRY, JR.³, and CATHERINE M. DOUGHERTY²

ABSTRACT

An extensive database of surface and upper-air data for April 1995 were collected and analyzed for White Sands Missile Range (WSMR). These data were used to create high resolution (1km) wind fields from the MINERVE model for the ingestion into a transport and diffusion model.

The atmospheric transport and dispersion were accomplished using the model SCIPUFF, Second-order Closure Integrated PUFF. This model is a Lagrangian transport and dispersion model. It numerically solves the model equations using a Gaussian puff methodology and couples this with a second order turbulent diffusion parameterization. By using a Lagrangian framework, one avoids artificial diffusion problems that are introduced by an Eulerian scheme. Also, a wide range of scales can be treated as the hazardous cloud grows from its source to potentially large atmospheric scales. Another important feature of SCIPUFF is its adaptive time step. For each puff, a time step is selected that most represents that which is required to accurately resolve the local evolution. This enables SCIPUFF a multiscale range without restricting the calculation to a single small time step for the entire domain. Coupled with the adaptive time step is an adaptive grid that the output spatial fields are computed over. Once again computational resources are applied where most needed.

The SCIPUFF model was used to simulate the transport of hazardous agents. For this paper, Sulfur Hexafluoride (SF₆) was used to simulate the hazardous agent. Several experiments were performed with the April meteorological data. During the weekdays, MINERVE wind fields were generated at 18 GMT. These wind fields were passed to SCIPUFF for material transport. As a basis of comparison, the raw observations were passed to SCIPUFF separately for the same period and once again SCIPUFF was used to transport SF₆. On selected days SCIPUFF was used to simulate the transport of agents during the transition period from a stable atmosphere with an inversion through its breakup to a more turbulent atmosphere.

¹ Defense Nuclear Agency, Alexandria, VA 22310 (currently at National Defense University)

² Science Applications International Corporation, Wayne, PA 19087

³ Defense Group Incorporated, Arlington, VA 22203

The validation of SCIPUFF will continue with several transport experiments at WSMR during the next year. These experiments will further show SCIPUFF's utility as an accurate atmospheric transport and dispersion model.

1. INTRODUCTION

The injection and transport of hazardous materials into the atmosphere are of great concern. With national policies being influenced by the potential of both small and large scale transport and dispersion of these agents, it is of the utmost importance to develop and validate operational forecasting models capable of predicting the dispersal of hazardous atmospheric releases in virtually any scenario. These predictions must be at higher resolutions than are available with existing models and be able to produce their results at a moment's notice since a scenario can occur without warning anywhere in the world.

To develop a transport prediction in real-time is very difficult. One must have the local wind measurements. These measurements often are not available, thus dependence on computer-based wind forecasts are required in lieu of these data. To produce the needed wind field at high resolution (a kilometer or less) is computer intensive. However, often the operator has to decide between a timely prediction and a higher resolution prediction. The result becomes an approximation for a few points over a broad region that may be less accurate in speed, direction, or shear characteristics.

During Operation DESERT STORM, quick-turn predictions were required for troop safety. These predictions of the dispersal of potential hazardous agents were made on a regular basis. Later evaluations produced the discovery that in some cases local effects due to topography were not adequately accounted for and the actual deposition patterns would have been significantly different from those predictions.

In order to address these deficiencies, high-resolution atmospheric simulation and transport models are needed. The Hazard Prediction and Assessment Capability (HPAC) program was initiated (Byers et. al., 1995). Within the HPAC program, the need was seen to produce a mass consistent wind field. The Multiscale Environmental Dispersion Over Complex Terrain (MEDOC) models were chartered to provide HPAC with the desired mass consistent wind field (Sontowski et. al., 1995). The MINERVE model, which is described in an accompanying paper, provides such a wind field. Once a wind field is generated, the Second-order Closure Integrated PUFF (SCIPUFF) model is used to show the transport of hazardous agents.

In this paper, we give a brief description of the SCIPUFF methodology. Next, the test data sets employed in this study will be described. Then we will outline how they are used and manipulated. This will be followed by a discussion of the results followed by concluding remarks.

2. SCIPUFF METHODOLOGY

The SCIPUFF model was conceived and developed over the last decade. It is our desire to provide a brief overview of the methodology. For a more complete description, the reader is referred to one of the several articles written by the developer of SCIPUFF (Sykes et. al 1984, 1986, and 1988).

SCIPUFF is a Lagrangian transport and dispersion model based on numerical techniques discussed by Bass (1980). These techniques employ the Gaussian puff method to solve the dispersion model equations. Essentially, SCIPUFF represents the time-dependant concentration field as a collection of three-dimensional puffs. It also contains buoyant rise dynamics and evaporation physics.

The uniqueness of the SCIPUFF methodology is found in how the model treats turbulent diffusion. In modeling the atmosphere, SCIPUFF, through the second order turbulence closure theories of Donaldson (1973) and Lewellen (1977), provide the user with a direct connection between measurable velocity statistics and the predicted dispersion rate. This methodology is discussed fully in Sykes et al. (1986, 1993). Briefly, SCIPUFF's diffusion is affected by the spectrum of motions which shear and stretch the field until scales are small enough for molecular effects. Knowing that the complete spectrum from global scales down to millimeters can never be known, an ensemble average is used. The conservation equations and Reynolds transport equations are integrated spatially and second order turbulence is applied. This gives a direct relationship between the measurable turbulence quantities and diffusion.

One of SCIPUFF's unique features is that it provides a probabilistic prediction of the atmospheric dispersion and surface deposition processes with a capability to model multidimensional, time-dependent wind fields. There are uncertainties in the wind field measurements and forecasts, in both the boundary layer and larger scales, which lead to a random variation in the concentration field. These uncertainties can lead to less accurate predictions of the concentration field. Therefore, SCIPUFF uses a truncated Gaussian or clipped normal distribution to describe the short-term concentration fluctuations. A complete description of the probability distribution is not provided by SCIPUFF. But, the mean value and standard deviation can be used to generate an empirical distribution function that has a specific shape. The SCIPUFF prediction can then be used to compute probabilistic doses and provide an assessment of the likelihood for health effects. Because there is so often an uncertainty in the lack of detailed knowledge in the wind field, the probabilistic description may be the only meaningful approach.

The SCIPUFF model is being integrated into the HPAC program. It will become the primary transport tool in what is call HASCAL, Hazard Assessment System for Consequence Analysis. HASCAL is based on the U.S. Nuclear Regulatory Commission Radiological Assessment System Consequence Analysis (RASCAL). However, HASCAL will not only be able to do radiological accidents, but it will be able to do nuclear, biological, and chemical

accidents. These include both storage facilities and weapons. HASCAL has been developed to operate in a WINDOWS environment and can read real-time, historical, and climatological weather data in either gridded format or raw observations.

3. TEST DATA SETS AND DATA HANDLING

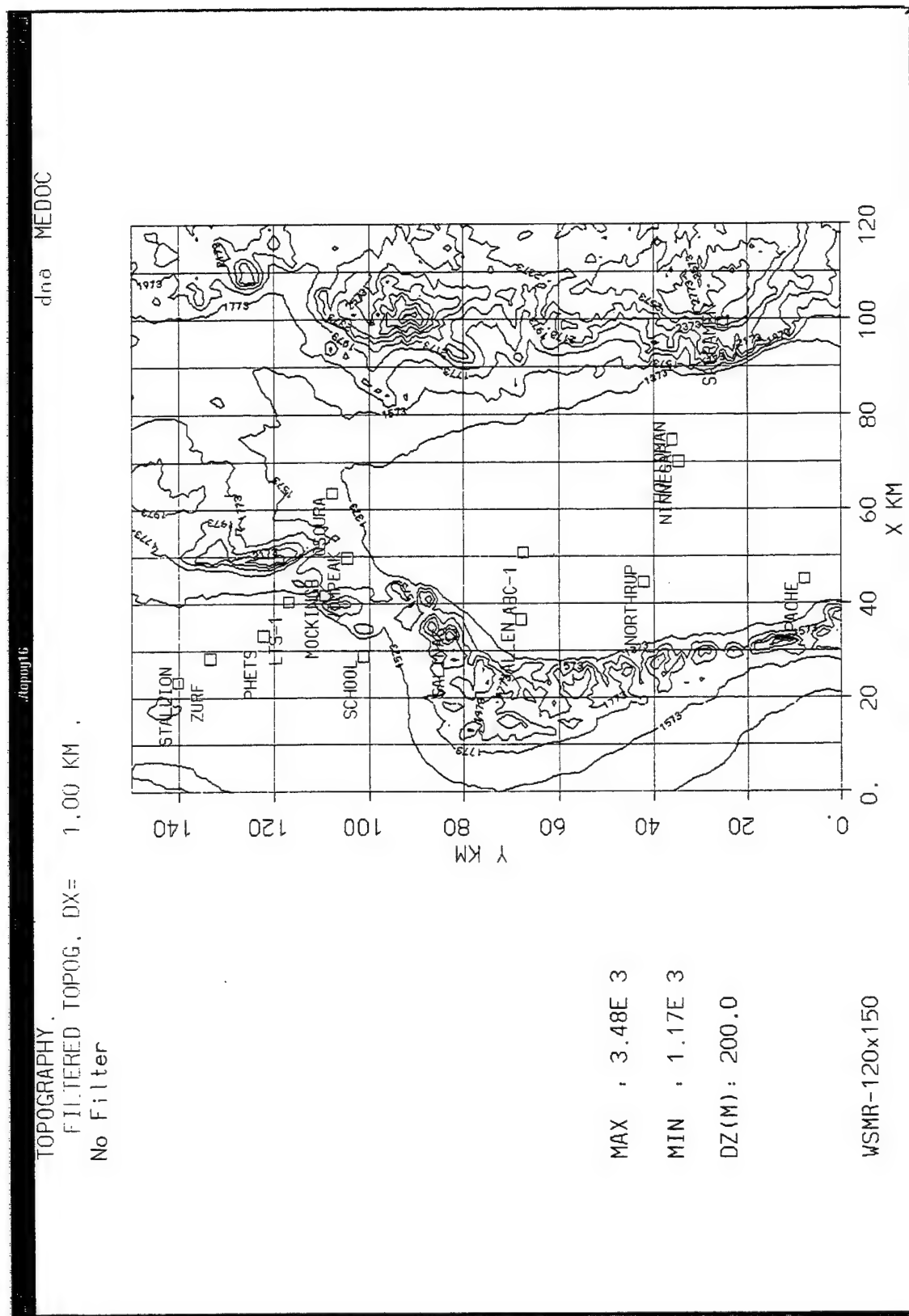
During April 1995, a comprehensive set of meteorological data was collected at WSMR. These data included both surface and upper-air observations. The surface data were measured by the WSMR Surface Automated Meteorological System (SAMS) sites. A SAMS site is an instrumented 10 meter tower that measures various meteorologically significant parameters. Figure 1 outlines the test domain and where the SAMS were located during the test. For the purpose of this study, observations were collected every hour for the weekdays (Monday through Friday). The test required at a minimum wind and temperature data even though other parameters were measured. A sample of the SAMS output is shown in the companion paper (Sontowski et al., 1995). The mass consistent model required upper-air soundings. These data were collected in two ways. During data collection days, between one and three rawinsondes were released. The primary points of release were the Jallen Site and Hollomon Air Force Base. Periodically other balloons were release for different range activities. The rawinsonde released during the month are listed in the companion paper. Second, the Mobile Profiling System (MPS) being developed at WSMR in cooperation with the Defense Nuclear Agency collected data during the first half of the month. The MPS measurements applicable to this study were the u- and v-wind components, height of measurement, and temperature. The surface synoptic weather charts were collected, too. These provided a general overview of the weather pattern WSMR was experiencing for a given day.

As with any test, there were some days which for some reason or another the data were incomplete or unusable. There were three days that qualified for these reasons. They were the 18th, 24th, and 28th.

There were days that the weather was more turbulent than others. The primary reason for this turbulence was frontal passage or fronts in the vicinity of the range. For the purpose of reviewing how well the mass consistent model performed under these conditions, those days were left in the data set. However, when considering using those days for transport validation, they were generally ignored. The wind speed was also stratified for this study. Winds from 0 - 2.5 m/s were labeled light; winds from 2.5 - 7.5 m/s were labeled moderate; and winds greater than 7.5 m/s were labeled strong. During live testing, SF₆ is released. In order to monitor the cloud as it disperses, strict meteorological conditions were set. The wind must be between 1.5 and 5 m/s and the skies must be clear to partly cloudy. Generally a wind direction was sought to ensure the SF₆ cloud did not initially blow into the mountains.

Several different types of plots were generated from these data. Wind field analyses were generated. The plot included all wind vectors generated at the 1 km resolution. All

Figure 1. WSMR Topography With Meteorological Stations Indicated.



terrain data used for this study was from the Defense Mapping Agency Digital Terrain Elevation Data (DTED). These data were coarsened to 1 km resolution.

The primary hours investigated were 11 GMT, 14 GMT, and 18 GMT. The wind fields were generated at these times and the +2 and +4 hour transport and diffusion plot were generated.

Data were ingested by the SCIPUFF model in two different formats. These two formats were gridded and raw observations. To produce the gridded format, the raw observations were passed to the MINERVE mass consistent model (Sontowski et al., 1995). The model then produced a 1km horizontal resolution three-dimensional gridded wind field. This wind field was post-processed to make it into a compatible format that SCIPUFF could readily ingest. Because the MINERVE wind field can be quite large (on the order of 100 megabytes), the post-processor not only put it into a format that SCIPUFF could read, but it only passed SCIPUFF every other grid point. There was no interpolation, only selective elimination of grid points that were passed to SCIPUFF. This ensured SCIPUFF received the MINERVE calculated wind field, but was not swamped with data. In general, the post-processor allows the user to select every n^{th} point as well as smaller sub-domains. The second format used for the ingestion of data into SCIPUFF were raw observations. This entailed reading the raw surface and upper-air observations, passing them through a formatter, and finally having SCIPUFF ingest it.

These two methods of passing data to SCIPUFF allow for some unique comparisons of the transport methodology. The gridded wind field, which was previously validated, (Sontowski et al., 1995) provides a high resolution input that will subsequently produce a high resolution output. However, this method has a price, which is computational time. From data receipt to output plume, it takes approximately 10 minutes to generate a plume forecast. This is accomplished in two steps. The first is computing the wind field with the MINERVE model using an International Business Machine (IBM) RS6000/590 workstation. Step 2 is generating the plume from the wind field. This is accomplished using a 486/100 megahertz (MHZ) Personal Computer (PC). To computer the plume forecast using just the raw observations, it takes approximately to 2 -3 minutes using the 486/100 MHZ PC. With MINERVE, numerical techniques are used to produce a uniform gridded field from non-uniform input data. The methodology SCIPUFF uses when raw observations are used is not as robust, thus, the less time and less capable machine to produce a result.

The resourceful operator will use both techniques. When a hazardous event occurs, the operator could run a SCIPUFF calculation with the observations available at the time of event. Simultaneously, a high resolution calculation should be made with MINERVE. Therefore, the authorities will know within minutes where the plume is generally going and approximately 10 minutes later have a detailed solution to include complex topography.

4. RESULTS

Data from April 1995 were analyzed for differences in transport. Initially, observations were inputted directly into SCIPUFF. All available data days were computed. Figure 2 is an example plot. For purposes of demonstration, this calculation was terminated after 2.6 hours. The SCIPUFF output allows for comprehensive summary tracking. This summary provides the researcher or operator a quick review of the project status to include domain size, meteorology used, material(s) transported, time, etc. The surface dose levels displayed on the right of the figure can be modified for the material being transported. Currently, scientific units are used. Studies are underway to translate these units into meaningful categories for the operator.

Once all SCIPUFF calculations were completed using just observational data, SCIPUFF calculations were made using the high resolution gridded wind fields provided by MINERVE. Figure 3 is an example of such a plot. The plot is created using the same output interface as with the observational data; therefore, an easy comparison can be accomplished between observational data and gridded data. In this case, the two are very consistent. Some variations are observed. The plume generated from observational data is smoother and is transported in a more northerly direction; whereas, the plume generated from the MINERVE wind field shows the effects of using high resolution terrain. The plume is transported in the direction of mountains to the east of the origin. These mountains have peaks in excess of 2000 meters above ground level. One would not expect a continuous surface deposition as the plume traverses these peaks. That is what is evidenced by the SCIPUFF plot using the MINERVE generated wind field. Approximately 10 km from the origin, the maximum concentration area stops, then about 5 km later a maximum is seen again. This coincides with the mountain range. As the plume begins to rise over the mountains, the surface dose increases as it is forced to deposit the agent on the mountain side; then on the lee side of the mountains there is an area of lesser concentration of the material as the plume begins its diffusion downward. Eventually, the surface dose is again high as the material begins to deposit in high concentrations. Also, the individual concentration isopleths generated by using the MINERVE wind field exhibit fluctuations as opposed to the smooth isopleths generated by using the observations. These plots were created using meteorology from 21 April. The same basic conclusions can be made looking at plumes generated using 14 April data (figure 4). Therefore, the SCIPUFF model is responding to the input data in a consistent manner.

There were times when the SCIPUFF plots generated from observational data and MINERVE data were not in as good of agreement. One such time can be seen in figure 5. After 4 hours, the plume generated from the observational data has been transported more than 75 km, is somewhat smooth in appearance, and is fairly unidirectional. The plume produced from MINERVE data shows a maximum extent of only about 40 km, is more circular in appearance, and shows a broader area of concentrations in excess of 10^{-6} . The difference is directly related to the mass consistency. MINERVE models the wind field in

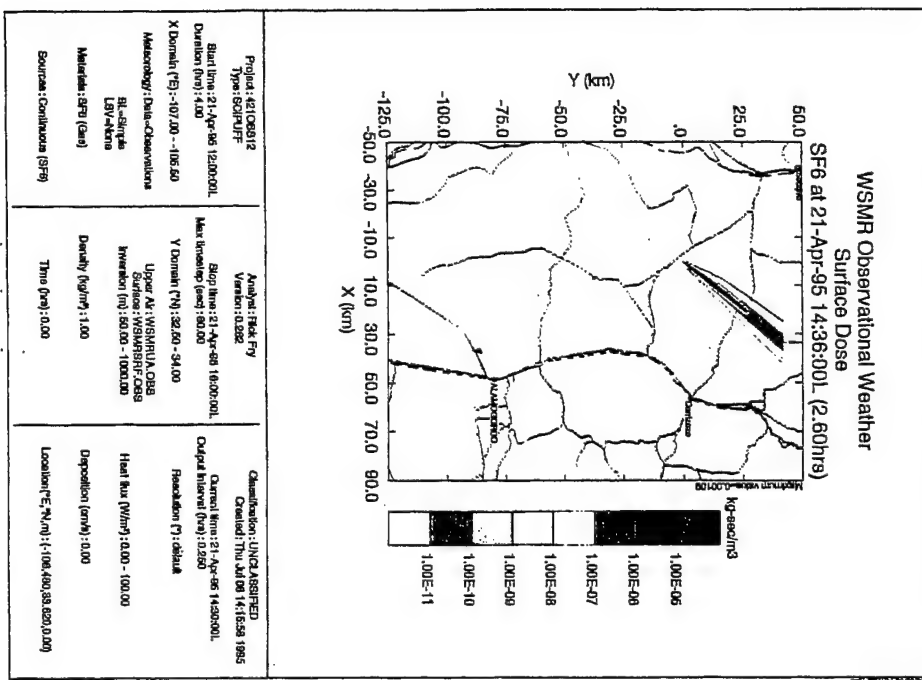


Figure 2. SCIPUFF plot using observations. 21 April 1995.

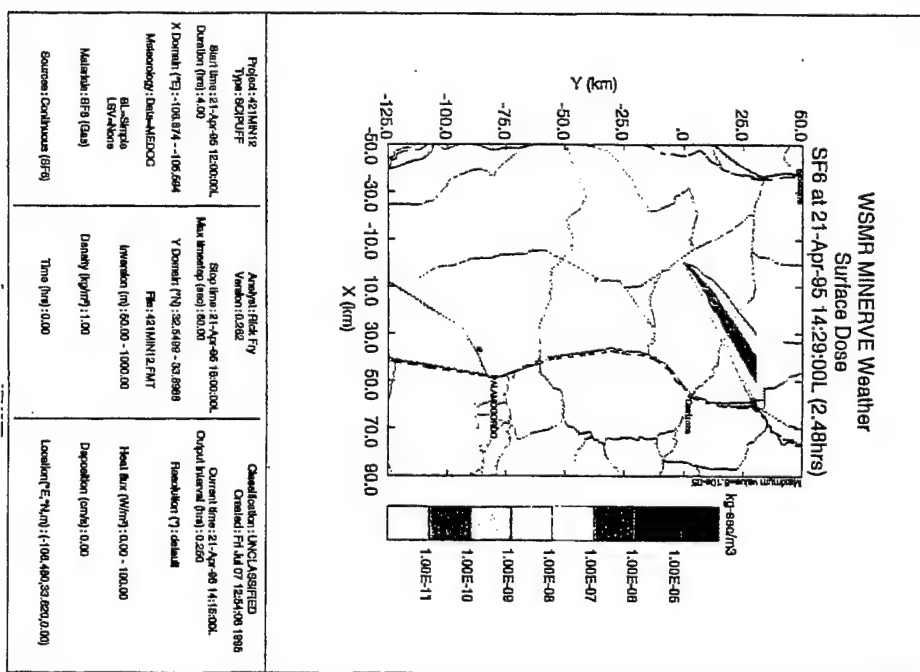


Figure 3. SCIPUFF plot using MINERVE data, 21 April 1995.

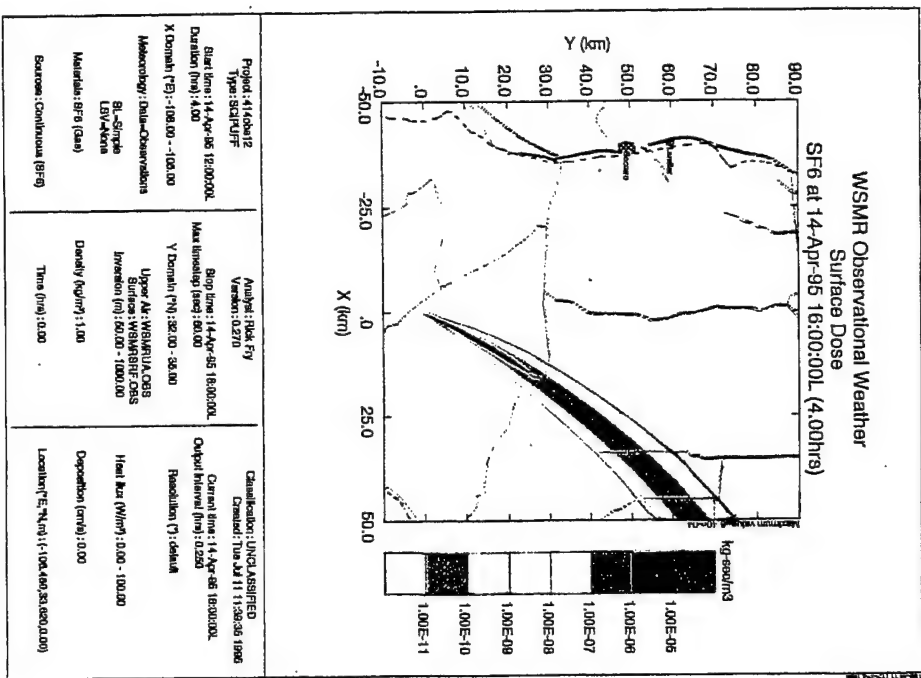


Figure 4a. SCIPUFF plot using observations, 14 April 1995.

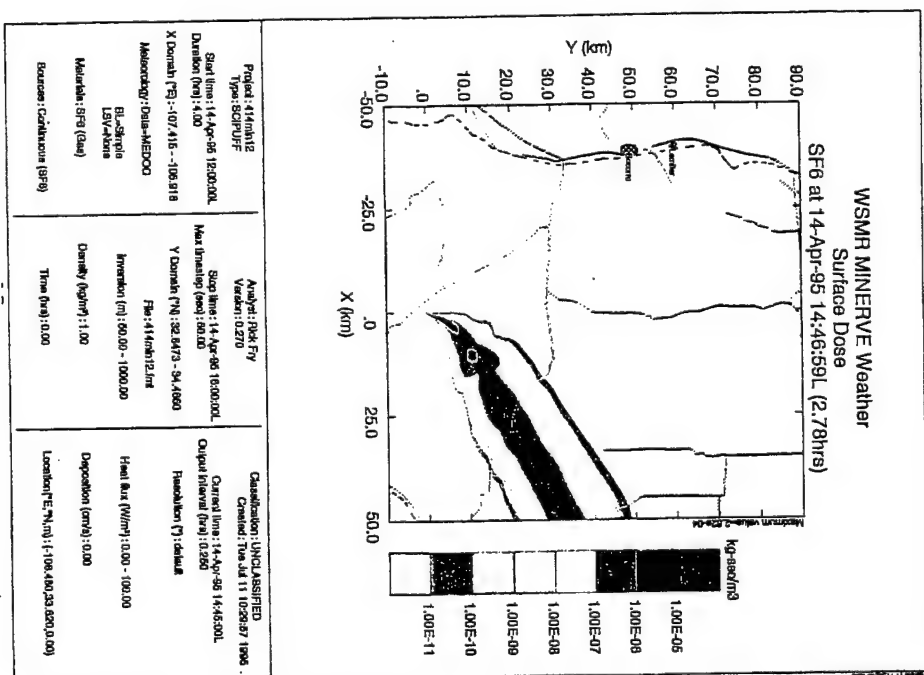


Figure 4b. SCIPUFF plot using MINERVE data, 14 April 1995.

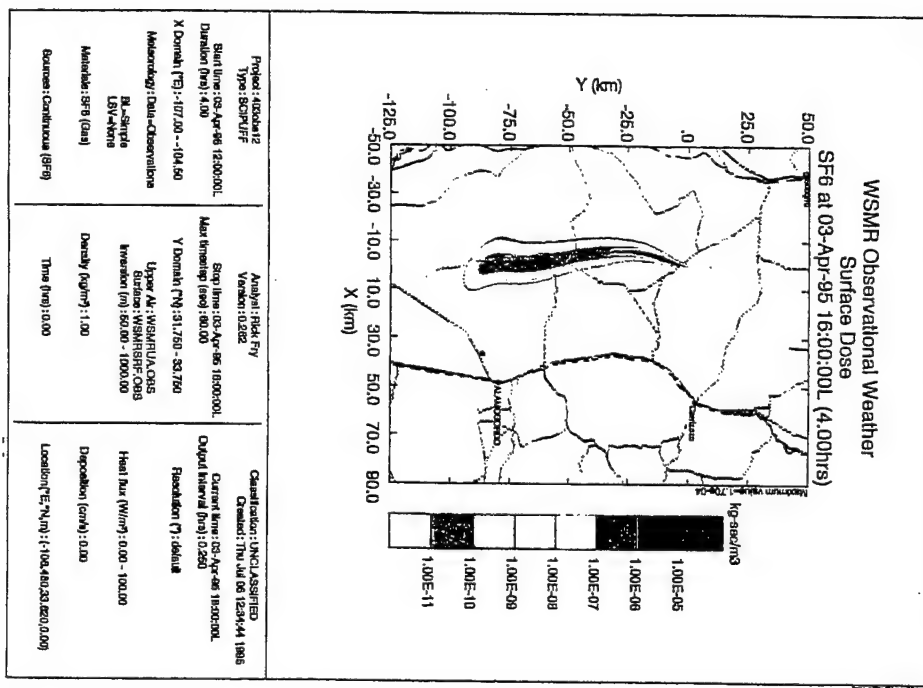


Figure 5a. SCIPUFF plot using observations, 3 April 1995.

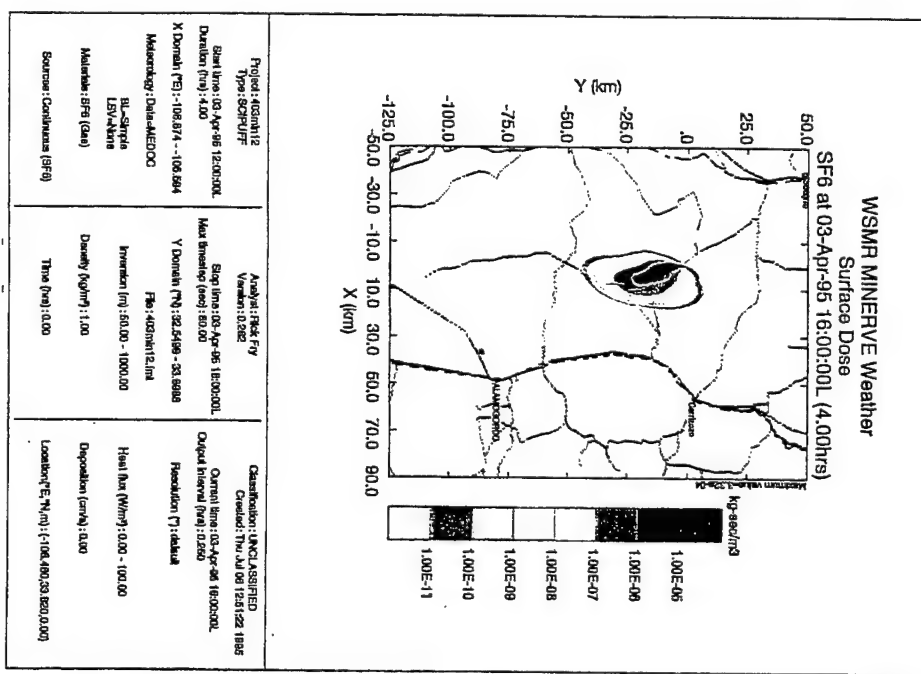


Figure 5b. SCIPUFF plot using MINERVE data, 3 April 1995.

such a fashion as to ensure the effects of atmospheric stability and adjustment of the horizontal and vertical wind components are correctly solved by successive over relaxation of the partial differential equations.

The 14 GMT time was also investigated. This time period proved challenging because the 4-hour time period used for transport spanned the time frame during which the morning radiation inversion dissipated. The results of the transport mirrored those found in the validation of MINERVE. As the winds began to increase in magnitude and the direction became more constant over the period, the plume settled into a uniform direction. The observations tended to cause the plume to be extended beyond the distance of the plume generated with the MINERVE winds.

5. CONCLUSION

A careful examination of the detailed atmospheric transport calculations over a one month period at WSMR was accomplished. It has been shown, plume generation using high resolution wind field data provided by the MINERVE model presents a more detailed result than using just observations. Further, it was shown that using only observational data can produce results which may overestimate the extent of plume transport. Also, the terrain effects were shown to be modeled using a system which includes it in calculations.

Upcoming studies and tests will be conducted. These will include releases of SF_6 and real-time monitoring of its transport and dispersion. The meteorological conditions will be monitored and MINERVE and SCIPUFF will be used to model the transport and dispersion, thus providing further validation.

6. REFERENCES

- Bass., 1980: Modeling long range transport and diffusion. *Proc. Second Joint Conf. On Application of Air Pollution Meteorology*, New Orleans, Amer. Meteor. Soc., 193-215.
- Byers, M. E., J. K. Hodge, and R. M. Cox, 1995: Hazard Prediction and Assessment Capability (HPAC), *Proc. Fifth Topical Meeting on Emergency Preparedness and Response*, Savannah, American Nuclear Society, 150-156.
- Donaldson, C. Du P., 1973: Atmospheric Turbulence and its Dispersal of Atmospheric Pollutants, *Proc. AMS Workshop on Micrometeorology*, ed. D. A. Haugen, Science Press, Boston, 313-390.
- Lewellen, W. S., 1977: Use of invariant modeling, *Handbook of Turbulence*, W. Frost and T. H. Moulden, Eds., Plenum Press, 237-280.

Sontowski, J., R. Cox, J. Hodge, J. Moussafir, and C. Dougherty, 1995: Multiscale Environmental Dispersion over Complex Terrain - the MEDOC Models, *Proc. Fifth Topical Meeting on Emergency Preparedness and Response*, Savannah, American Nuclear Society, 447-451.

----, ----, C. M. Dougherty, and R. N. Fry, Jr., 1995: *Proc. 1995 Battlefield Atmospheric Conference*, White Sands Missile Range, U. S. Army, In printing.

Sykes, R. I., W. S. Lewellen, and S. F. Parker, 1984: A turbulent-transport model for concentration fluctuations and fluxes. *J. Fluid Mech.*, **139**, 193-218.

-----, -----, and -----, 1986: A Gaussian plume model of atmospheric dispersion based on second-order closure. *J. Climate Appl. Meteor.*, **25**, 322-331.

----, ----, ----, and D. S. Henn, 1988: A hierarchy of dynamic plume models incorporating uncertainty. Vol. 4: Second-order closure integrated puff. EPRI Report EPRI EA-6095, Project 1616-28, 99 pp.

----, S. F. Parker, D. S. Henn, and W. S. Lewellen, 1993: Numerical simulation of ANATEX tracer data using a turbulence closure model for long-range dispersion. *J. Appl. Meteor.*, **32**, 929-947.

Analysis of condensation nuclei counter measurements in the Arabian Gulf and the Gulf of Oman.

Andreas K. Goroch, Marine Meteorology Division, Naval Research Laboratory, Monterey, CA and John W. Raby, Army Research Laboratory, White Sands Missile Range, NM

The total number concentration of surface atmosphere aerosol particles was measured in the Arabian Gulf and in the Gulf of Oman during February 1995. Particle concentrations were measured aboard ship with a condensation nuclei counter. Three regimes corresponding to different aerosol concentrations were identified: winter shamal and pre-shamal in the Arabian Gulf, and calm conditions in the Gulf of Oman. The total particle concentrations in each regime were approximately 80,000, 1,000, and 18,000 particles/ml respectively. Ship effects were found to be such as to mask out all differences between regimes, if not carefully controlled.

Introduction

The concentration of aerosol particles in the atmosphere has a strong effect on optical propagation in the visible and infrared frequencies. Aerosol particles cause most of the extinction and scattering of a signal in the visible wavelengths as well as being comparable in effect to water vapor absorption in the near infrared and mid infrared regions. The purpose of this report is to document measurements made aboard the USS Lake Erie (CG 70) during the US Navy SHAREM 110 exercise from 5 February to 18 February 1995. The measurements describe total aerosol concentrations and winds during pre-shamal and shamal conditions in the Arabian Gulf, and during calm, winter conditions in the Gulf of Oman. The data collection region is shown in Figure 1.

We observed three aerosol regimes, corresponding to pre-shamal and shamal conditions in

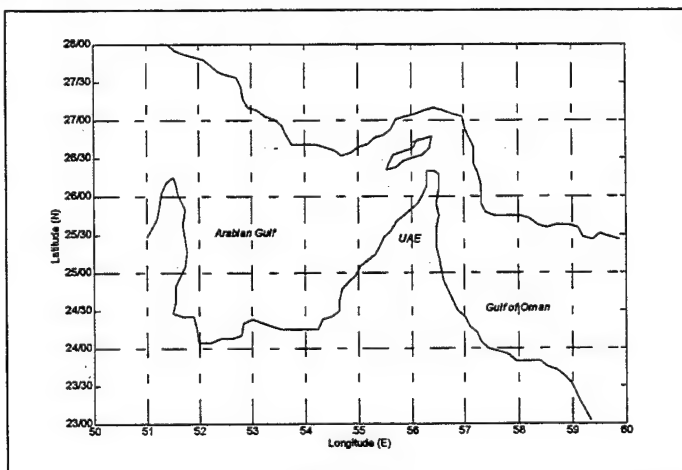


Figure 1. SHAREM 110 operating region

the Arabian Gulf, and calm conditions in the Gulf of Oman. Pre-shamal conditions in the Arabian Gulf exhibited lowest aerosol concentrations, with Gulf of Oman and shamal conditions having greater concentrations. The effect of ship emissions was found to be substantial, masking any local changes due to weather or topographic conditions.

Measurement Techniques

Total aerosol concentrations were measured aboard the US Navy guided missile cruiser USS Lake Erie, CG-70 (LKE). The total number concentration of aerosol particles was measured by an Environment One condensation nuclei (CN) counter (Environment One Corporation, 1988). The air intake was located aboard the bridge of LKE, approximately 25 m above the waterline, on an HF antenna, 2 m forward of the main bridge superstructure. The intake was connected to the counter by 16 m of ½ inch Tygon tubing. Data were recorded as one minute averages of signal voltage and scale voltage on a PC. The aerosol data were supplemented by wind, temperature, and humidity measurements taken aboard the jackstaff on the bow of the ship, approximately 12 m above the waterline using the Shipboard Surface Automated Weather System (SSAWS). The data were collected at a frequency of 1 Hz, and averaged to provide 10 minute average values. These data were stored at UTC (Zulu). All others were stored at Bahrain local (UTC-3 hours).

The CN voltages were converted to particle concentrations by multiplying with a scaling factor corresponding to ten ranges. It was found that when scale voltage of the system changed to a higher scale, the first following signal voltage was spuriously high. These anomalies were not included in the averaging. The counts were further averaged over a 10 minute interval to correspond to the 10 minute averaging of the meteorological data.

Although the CN counter was mounted on the ship bridge, well forward of the ship stacks, influence of the ship emissions was quite marked, and seemed to correspond exactly to when relative wind was from 150° to 210° relative to the ship course. These data were not studied in detail to identify sources or characteristics of the effluents. The aerosol data used for this analysis was that data which met the criteria that meteorological data were available, and there was no contamination by ship effluents.

The CN counter operates by saturating an air sample until all particles are condensed and grow to a measurable size. Since the marine atmospheric aerosol size distribution is approximately described by a power law with exponent -3, the dominant particles measured by the counter are the small particles, less than 1 µm in radius. There is relatively little information contributed by the larger particles.

Simultaneous land based measurements of aerosol concentration and size distributions were taken in Bahrain. The land based results are being reported separately (Gathman, et al., 1995).

Results

The measurements were separated into three groups corresponding to the three separate regimes observed. The Arabian Gulf measurements were taken before and during the occurrence of a winter shamal event. The shamal period was marked by a temperature drop, a shift in wind direction, and subsequent increase in wind speed. Frontal passage occurred at 0800

on 8 Feb 95, with wind speeds increasing to greater than 20 knots by 1100. For this work, the shamal time period is defined to be when the wind speed became greater 20 knots. Gulf of Oman measurements were taken following the shamal. The meteorological conditions from the USS Lake Erie ship weather log are shown in Figure 2, with the pre-shamal, shamal and Gulf of Oman conditions identified.

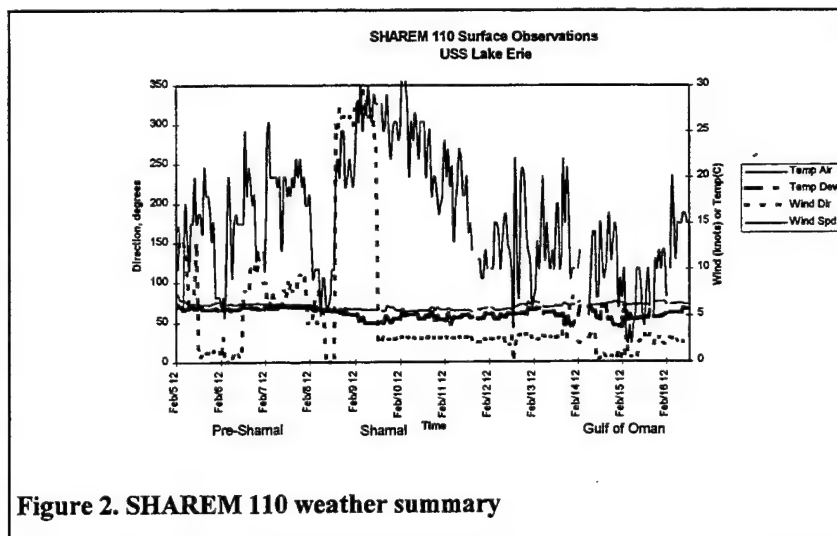


Figure 2. SHAREM 110 weather summary

Pre-shamal conditions in the Arabian Gulf

The first set of measurements were taken during the transit from Bahrain to the central Arabian Gulf on 5-7, February, 1995. Winds averaged 15 knots or less, seas were calm, and temperatures were moderate, in the range of 25° C. The particular segment of the data collection was taken because the ship was proceeding into the wind, with little evidence of ship induced contamination of the CN counts. The ship track is shown in Figure 3.

The CN counts during this period are consistently low, in the range of 10^3 particles per milliliter, characteristic of a clean marine environment. These concentrations are characterized by measurements from 1200 to 1600Z on 5 February shown in Figure 4.

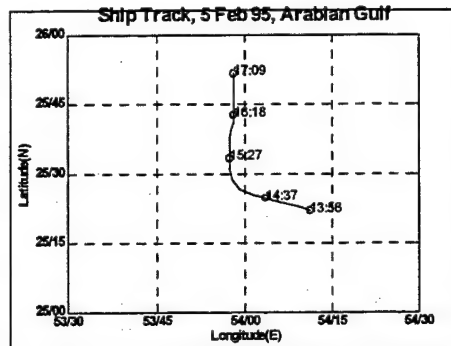


Figure 3. Ship track during pre-shamal conditions

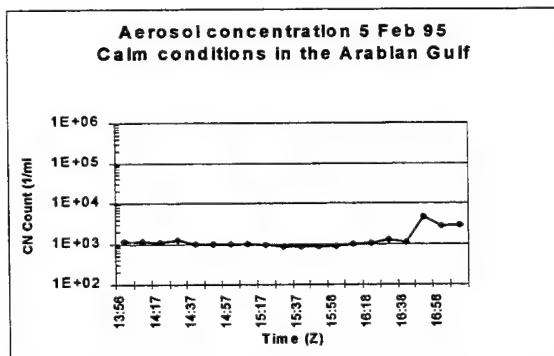


Figure 4 Aerosol Concentrations during calm conditions in Arabian Gulf

Ship Effects

On the evening of 5 February, at approximately 1600Z, ship course was changed from east to northwest. This course was varied, but generally in the direction with the generally prevailing wind, resulting in light relative winds coming from the stern of the ship. The ship contamination can be readily seen by plotting CN counts versus the difference between relative wind and true wind. When the difference between true wind and relative wind is large, the vessel is headed

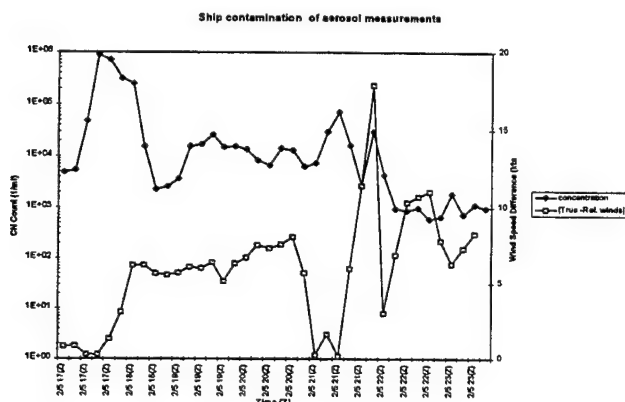


Figure 6. Aerosol contamination by ship environment.

aerosol concentrations accompanying these course changes are shown in Figure 6.

Shamal Conditions in the Arabian Gulf

Shamal conditions developed on 8 February with the appearance of a low to the Northeast over central Iran. A cold front passed at 0800, as evidenced by a sharp decrease in air temperature and dew point temperature. Winds were light, but veering, becoming 20-35 knots from the northwest by 1100. Seas increased with estimated wave height ranging from 4 to 10 ft. The shamal conditions (as defined by winds being greater than 20 knots) continued until 10 February, with winds slowly decreasing in speed. These

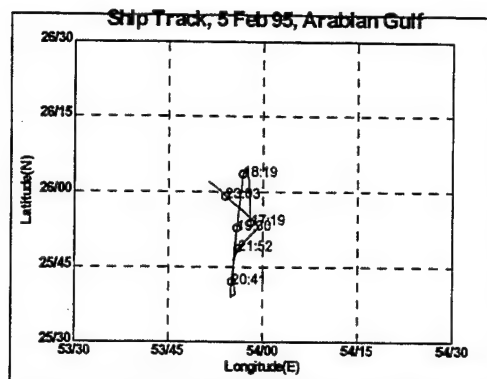


Figure 5. Ship track during aerosol contamination events

into the wind, and there is little contamination. When the wind difference is small, the vessel is headed downwind, and ship contamination is expected to occur.

As ship course changed to head away from the wind, the CN count immediately increased by a factor of 50-100. As the relative wind increased, the CN count also decreased. The increase is attributed to the aerosol emitted from the ship stack, as well as from normal ship activity. The change in

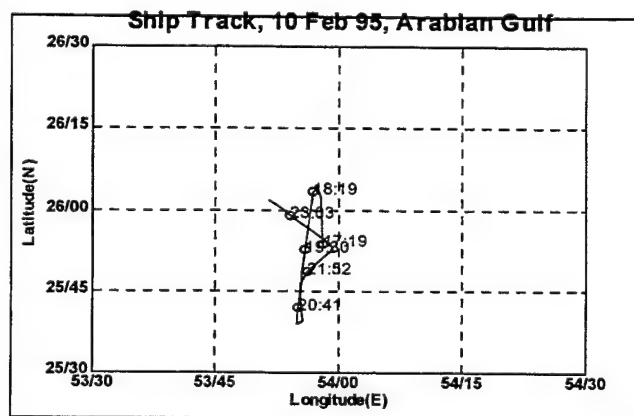


Figure 7. Ship Track during Arabian Gulf Shamal

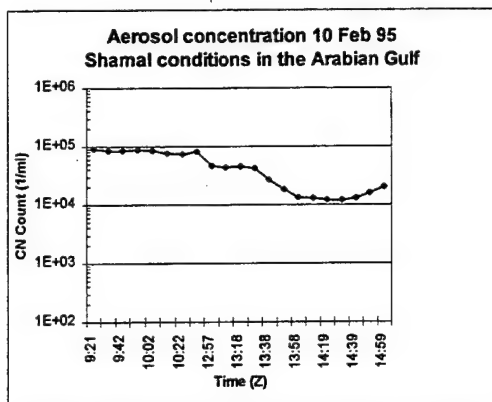


Figure 8. Aerosol concentrations during Arabian Gulf Shamal.

meteorological changes can be seen in Figure 2. The ship track was in the same general area and is shown in Figure 7.

The CN counts during the period are characterized by the data from 0900-1500Z on 10 February. The counts jumped by a factor of about 20-40 over those observed prior to the shamal, probably in response to local sea generation associated with the shamal winds. Ship course on 10 February, showed good ventilating relative winds either bow-on or off the starboard bow until late in the day, which

assured little or no contamination from the ship stack.. The CN counts are shown Figure 8.

Calm conditions in the Gulf of Oman

The USS Lake Erie transited the Straits of Hormuz on 13 February, 1995 and remained in the Gulf of Oman until the end of the exercise. Weather conditions were quite calm, with winds generally from the East at 10 knots. Seas were calm, with slight capillary waves about 5 to 10 cm in height. Humidity was noted to be abnormally low (less than 30% at a height of 6 m, see Rowland(1995) for further details). The ship track is shown in Figure 9.

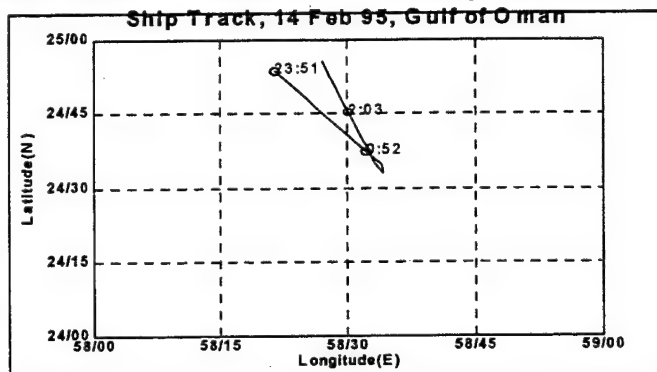


Figure 9. Ship track in Gulf of Oman

CN counts during the period are characterized by the data from 14 February and are shown in Figure 10. The CN counts dropped down to a level of about 10-15 times that observed prior to the shamal in the Arabian Gulf. Ships course was generally in a direction such that the relative wind was abeam, assuring good ventilation, with little contamination by ship sources.

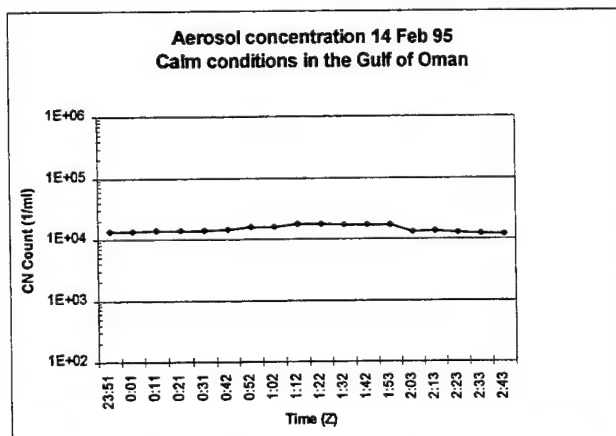


Figure 10. Aerosol concentration in Gulf of Oman

Conclusions

Aerosol measurements collected during the period 5-18 February, 1995 aboard the USS Lake Erie(CG-70), demonstrated the existence of at least three different aerosol regimes in the

Arabian Gulf and Gulf of Oman. The three regimes corresponded to local ambient wind conditions. The aerosol measurements consisted of total condensation nuclei concentrations, with no information on the size distribution. Since the number concentration is dominated by the small particles (smaller than 0.1 micrometers radius), the primary application is to extinction in the visible wavelengths, with little application to the middle infrared (3-5 μ m), and no application to the far infrared (8-12 μ m). These are the first known ship-borne aerosol measurements in the region.

Aerosol Distribution before and during winter shamal Conditions

In the Southern Arabian Gulf the pre-shamal regime is characterized by relatively light winds with CN counts on the order of 10^3 . The particle concentration is characteristic of clean maritime or Arctic (Murphy and Bodhaine, 1979; Shives and Robinson, 1980) conditions, with little influence from shore, although measurements were taken within 20 miles of the coast. The shamal regime is characterized by higher winds from the northwest. Locally generated waves produce aerosols, resulting in increased aerosol concentrations. CN counter measurements showed aerosol concentrations to be elevated by a factor of 20 - 40 greater than pre-shamal concentrations.

Geographical differences in aerosol distribution in the Arabian Gulf and the Gulf of Oman

In the Gulf of Oman, CN counts were observed to be on the order of 10-15 times those observed in the Arabian Gulf during the pre-shamal regime despite the relatively light winds and calm seas. It is not clear whether these aerosols are residual from the wind-generated aerosols in the Arabian Gulf, transported to the Gulf of Oman, or whether they are characteristic of the region.

Ship contamination of ambient marine aerosol measurements

The effect of contamination by the ship stack, was noted during the Pre-shamal regime when the relative wind was from 180 degrees. The contamination resulted in an increase of 50-100 times the pre-shamal counts. Comparing the ship effect to the shamal, it was found that the shamal counts were approximately 1/10 those observed during the period of contamination.

Recommendations

These measurements describe a limited sampling of the aerosol concentrations in the Arabian Gulf and the Gulf of Oman, and indicate the weather and regional dependence of the coastal maritime aerosol concentrations. These measurements are vital to development of optical propagation models for prediction of performance by electro-optical sensors. This baseline set of measurements should be improved by:

1. Size distribution measurements. The total aerosol concentration measurements provide no size distribution measurements, and as such no inference about the applicability to wavelengths beyond the visible. Size distribution measurements, such as by nephelometers or aerosol spectrometers should be taken to provide propagation information for other spectral bands.

2. Local seasonal measurements. These measurements were taken during one set of winter time conditions. The data base should be expanded with data from other seasons, as well as more data from the winter season, which can be variable due to importance of continental source aerosol, duration of shamal conditions, and large scale meteorological forcing.

3. Ship influence. The ship influence can mask the observed range of measurements. The measurements should be improved to characterize contaminating ship sources, and means of eliminating contamination for operational support measurements.

4. Extension to other regions. These measurements show the importance of local conditions, different from the commonly used US East coast and West Coast measurements. The data base should be extended to other operational regions to determine the applicability and extensibility of the current data base. Other potential regions, which are expected to differ substantially are the East Indian Ocean, the Yellow Sea, Sea of Japan, and the Southern Hemisphere.

Acknowledgments

This effort was supported by the Space and Naval Warfare Systems Command, Program element 0603207N Project Number X0514-01. The measurements were taken during the SHAREM 110 exercise, planned and executed by the Surface Warfare Development Group (SWDG), Little Creek, VA. Commander Raby was assigned to the Naval Research Laboratory for temporary duty in the US Navy Reserve. The authors thank Dr. Stu Gathman, Dr. Doug Jensen, and Ms Kathleen Lifkin of NRaD, San Diego, CA for use of their sensors, aid in measurement, and extended discussion. AG also thanks Mr Mike Pastore of IPS, Inc. and CDR Richard Callas of SWDG for help and support during the preparations and measurements at sea, as well as the Commanding Officer and crew of the USS Lake Erie (CG 70) for support and assistance during the cruise in the Middle East.

References

- Environment One Corporation, 1988. CN Monitor Model Rich 200, Instrument Instruction Manual, 1033A-123, September, 1988, Environment One Corporation, 2773 Balltown Rd, P.O. Box 773, Schenectady, NY 12309.
- Gathman, Stuart, Douglas Jensen, Kathleen Lifkin, and Andreas Goroch, 1995. Aerosol size and concentration measurements during SHAREM 110 in Bahrain. (in preparation)

Murphy, Mark E., and Barry A. Bodhaine, 1980: Barrow, Alaska, automatic condensation nuclei counter and four-wavelength nephelometer: instrument details and four years of observations, Environmental Research Labs., Silver Spring, MD., Technical Memorandum (NOAA TM ERL ARL-90)

Rowland, John, 1995: SHAREM 110 Phase 1 Data Report, Johns Hopkins University, Applied Physics Laboratory, (In preparation)

Shives, Fletcher G, and Elmer Robinson, 1979: Condensation nuclei concentrations at two Pacific Northwest coastal sites, Atmospheric Environment, 13(8): 1091-1098.

Measured Parameters of Puff Dispersion

Max P. Bleiweiss
U.S. Army Research Laboratory
Battlefield Environment Directorate
White Sands Missile Range, New Mexico

Kenneth C. Payne and Donald Stogden
Physical Science Laboratory
New Mexico State University
Las Cruces, New Mexico

Christopher D. Padilla
U.S. Army Research Laboratory
Battlefield Environment Directorate
White Sands Missile Range, New Mexico

ABSTRACT

A series of single smoke grenade (statically discharged) transport and dispersion trials have been analyzed to determine the various statistical features necessary to describe the dynamics of the puff. The use of the ATLAS (Bleiweiss 1995) processing technique allows the crosswind integrated concentration (CWIC) to be determined in a plane (nearly) perpendicular to the line of sight (LOS) of the observer. For the situation where the observer is looking perpendicular to the mean wind, the measured distribution of CWIC in the horizontal and vertical directions yield, after proper reduction, the measured values of the corresponding dispersion parameters (σ_x and σ_z , respectively). Furthermore, the effects of wind shear on the puff are also measured and discussed. The values for σ_x and σ_z for one trial are presented and discussed relative to the meteorological conditions measured during the trials.

1. INTRODUCTION

The unique coincidence of a particular U.S. Army smoke test and the presence of the ATLAS (Bleiweiss 1995) characterization capability has allowed the investigation of the dispersion of a puff of aerosol material as never before possible. The smoke test was important because of the static discharge of several "smoke grenades"; all in the same orientation. This occurred under a variety of meteorological conditions. The use of the ATLAS system to characterize these trials is

important because ATLAS is capable of measuring, in a plane which is perpendicular to the observer line of sight (LOS), the two-dimensional distribution, with high time resolution (10 Hz), crosswind integrated concentration (CWIC). ATLAS is an imaging transmissometer system which currently operates in the far infrared portion of the electromagnetic spectrum. The transmission measurements are made by using a thermal imaging system as a "receiver" and the natural background thermal radiation as the "source". A schematic of ATLAS is shown in Figure 1. The ATLAS system has been documented through an extensive "validation" effort as reported by Bleiweiss (1995). In that report, the limitations and other details of ATLAS are delineated -- they will not be discussed further here.

The smoke test was conducted on a "test grid" (Figure 2) such that the characterization instrumentation and discharge positions were fixed geographically and a variety of "trials" exercised under meteorological limitations so that the "smoke" traveled in the same directional fan for all trials. The single grenades were always discharged in the same orientation. This has led to considerable homogeneity for the data set. 30 trials have been studied. The particular grenades used are configured so that the screening material is contained in a "hollow" cylinder which surrounds, or is filled by the "burster" material. This results in an initial cloud which is toroidal in shape; this toroid quickly fills in to form a thick disc of material. The initial cloud is heated in the explosive process which causes the very initial portion of the trial to not be amenable to ATLAS processing; however, we do know that the initial cloud is about 6 m in diameter and the ring is about 2 m thick. For these trial studied here, the toroid was always positioned such that the "ring" was in a plane perpendicular to the viewing line of sight and parallel to the mean wind.

Another characterization system, MIDAS, was also present at that test. MIDAS is a system used to estimate smoke cloud growth dynamics through the use of two or more multispectral imaging stations -- the parameters yielded include cloud height, cloud length, cloud volume, cloud position, etc. with time. the MIDAS data were used to corroborate some of the information derived from the ATLAS measurements. Additional test support was provided by MMW and visible-far infrared transmissometers, MMW radar systems, and meteorological data collection.

A review of the literature indicates many instances of a desire to have measured dispersion coefficients for use in modelling efforts (Zannetti, 1990):

"...little information is available for the description of the diffusion of a single puff, i.e., for the evaluation of the relative diffusion sigmas, even though it is clear that the plume sigma equations ... cannot be applied (even though they often are) to relative diffusion calculations."

This is just what the ATLAS processing of these single grenade trials provides. Figure 3 is the first few frames from the data set for trial T43. The contours are in percent transmittance which can be converted to CWIC or a number proportional to CWIC by inversion of Beer's Law:

$$CWIC \propto \alpha CL = -\ln T$$

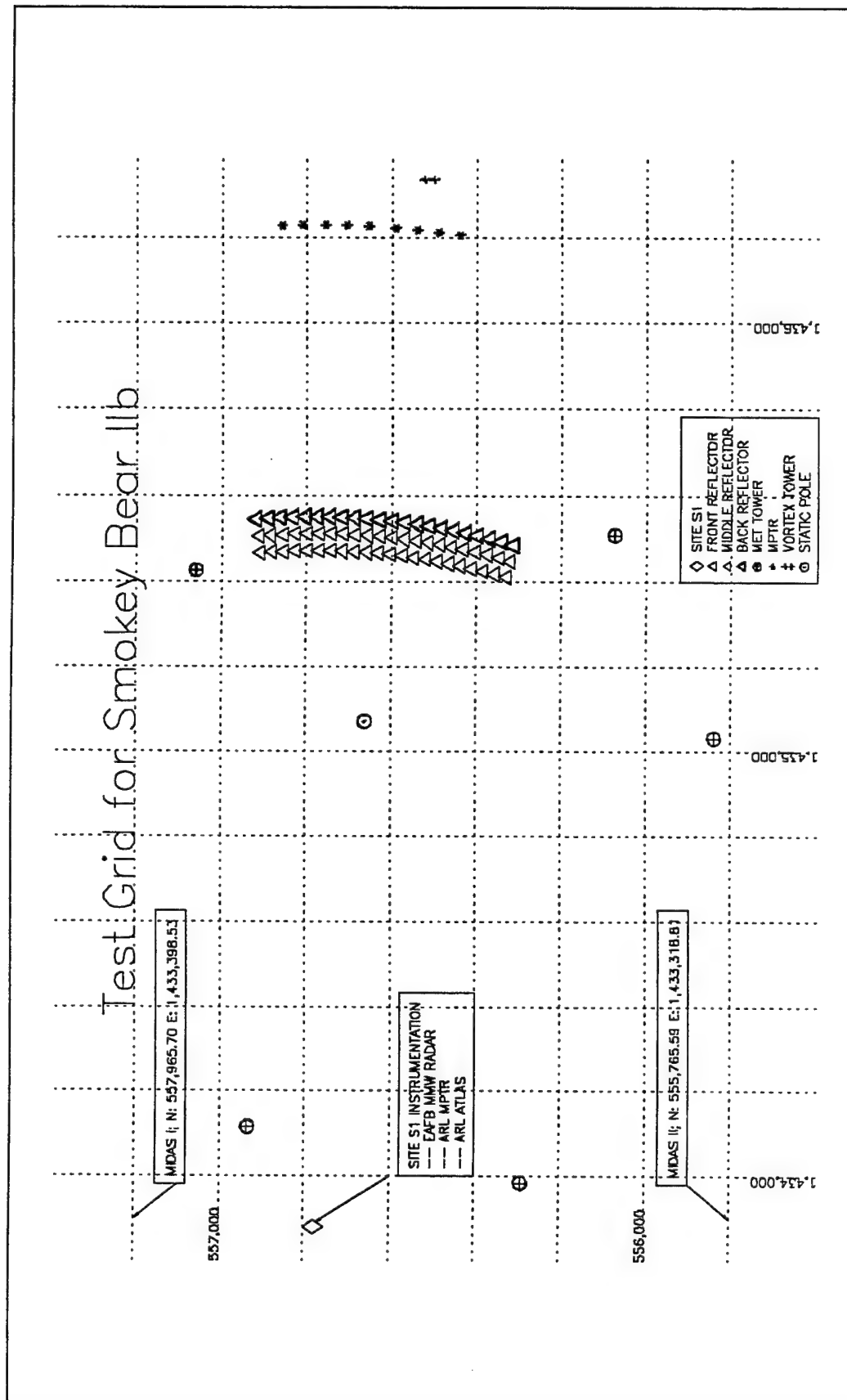
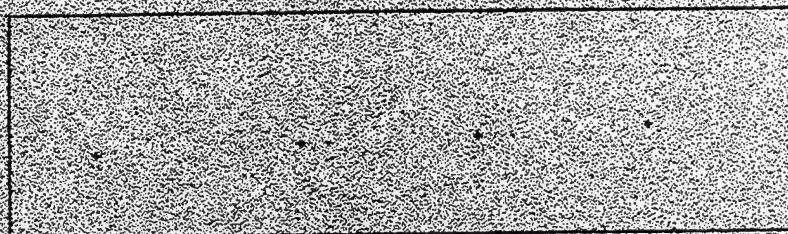
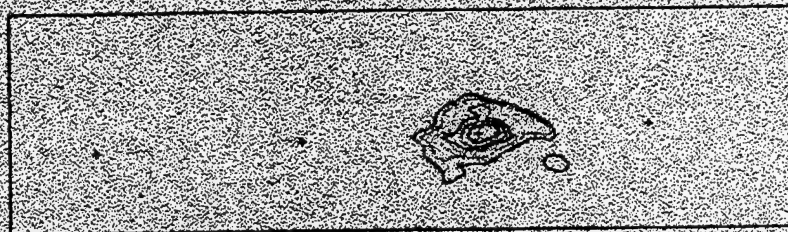


Figure 2. The test grid utilized during the smoke test from which the data in this paper were acquired. The grenades were detonated at the position labeled as "static pole". The mean wind was in a direction perpendicular to this line. Other measurement capabilities are indicated but not discussed in this paper, with the exception of the meteorological towers.

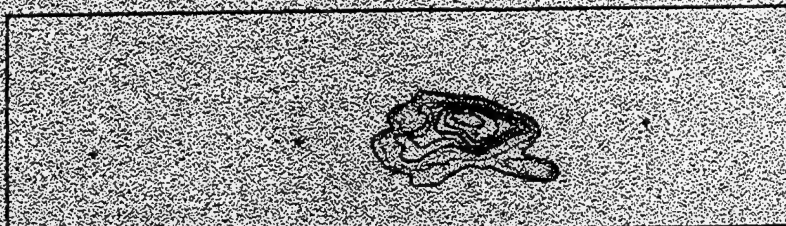
ATLAS TRANSMITTANCE CONTOUR MAPS
 TRIAL T-43 ATLAS SITE 05-13-92 TO = 17:46:01.9



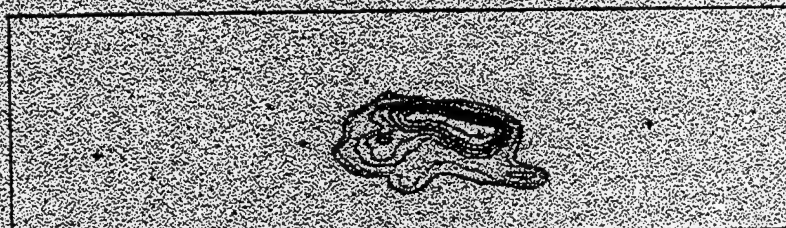
TIME = TO + 0.0 SECS



TIME = TO + 0.5 SECS



TIME = TO + 1.0 SECS



TIME = TO + 1.5 SECS

Figure 3. Sample frames from a series of ATLAS transmission maps for Trial T43. These particular panels encompass the first 1.5 seconds of the trial. The colors in the contour plot represent, from black to red, 10% to 80% transmission levels. The spatial scale is, within the black border of each panel, 5.4 degrees by 1.1 degrees (approx. 34 m by 11m).

where α is the mass extinction coefficient, CL is the path-integrated concentration length (CWIC), and T is the observed transmission. These 2-D distributions of transmittance have been converted to $-\ln T$ and the results used in the calculation of a large number of statistics for each "frame". This has been done for each of the samples which were acquired at the 10-Hz rate. The results of this processing for one trial will be detailed and then discussed.

2. ANALYSIS

For the purposes of this paper, the basic test setup and data reduction procedures are being emphasized as the results from all of the trials have not, as yet, been assimilated. An example of some of the parameters deemed more important are shown and discussed. An important aspect of this investigation is not so much the actual results but, instead, the methodology demonstrated -- the ability to directly measure the distribution of concentration in an aerosol cloud is of utmost importance to the study of the transport and dispersion of aerosols. We have not found any results in the literature which contain the same level of detail possible with the techniques demonstrated here. Another reason for this emphasis is that some of the measurements made for this test were not of the caliber necessary for a full discourse; for example, the meteorological measurements at the time were not of the type for proper transport and dispersion studies and, in the interim, the detailed records that were made have been lost, leaving only trial summary sheets. Another limitation of these particular measurements is that only the first 5 or so seconds following release were monitored -- though this early time in the formation of the puffs is important, it is at greater downwind distances that most of the interest lies. This will have to await further trials which it is hoped can be justified based on the results of this effort.

A large number of statistics were compiled for each trial. This was accomplished in an attempt to fully describe the distribution of the concentration of the puff in a two-dimensional plane (x-z). The following statistical features were determined for each CWIC map (most of these equations are from Murphy and Heyler (1994):

$$\text{Size} \equiv \sum_{i=1}^{512} \sum_{j=1}^{512} I(i, j) \quad (1)$$

$$\text{Centroid column} \equiv \text{column} = \sum_{i=1}^{512} \sum_{j=1}^{512} \left(i + \frac{1}{2}\right) p(i, j) \quad (2)$$

$$\text{Centroid row} \equiv \text{row} = \sum_{i=1}^{512} \sum_{j=1}^{512} \left(j + \frac{1}{2}\right) p(i, j) \quad (3)$$

$$\text{Orientation } \theta \equiv \frac{1}{2} \tan^{-1} \left(\frac{2\mu_{11}}{\mu_{20} - \mu_{02}} \right) \quad (4)$$

$$\text{Eccentricity} \equiv \frac{(\mu_{20} - \mu_{02})^2 + 4\mu_{11}^2}{(\text{Size})^2} \quad (5)$$

$$\text{Semimajor axis length} \approx \left\{ 12[\mu_{20}\cos^2(\theta) + 2\mu_{11}\cos(\theta)\sin(\theta) + \mu_{02}\sin^2(\theta)] + 1 \right\}^{\frac{1}{2}} \quad (6)$$

$$\text{Semiminor axis length} \approx \left\{ 12[\mu_{20}\sin^2(\theta) - 2\mu_{11}\cos(\theta)\sin(\theta) + \mu_{02}\cos^2(\theta)] + 1 \right\}^{\frac{1}{2}} \quad (7)$$

$$\text{Sigma ratio} \equiv \frac{\text{Semiminor axis length}}{\text{Semimajor axis length}} \quad (8)$$

$$\text{Total Concentration} \equiv \sum_{i=1}^{512} \sum_{j=1}^{512} \text{CWIC}(i,j)I(i,j) \quad (9)$$

$$\text{Average CWIC} \equiv \frac{\text{Total Concentration}}{\text{Size}} \quad (10)$$

$$\text{Maximum CWIC} \equiv \max[\text{CWIC}(i,j)I(i,j); \forall(i,j)] \quad (11)$$

$$\text{CWIC ratio} \equiv \frac{\text{Average CWIC}}{\text{Maximum CWIC}} \quad (12)$$

where the following definitions hold:

$$\text{Indicator } I(i,j) \equiv \begin{cases} 1; & \text{for } (i,j) \in \text{puff} \\ 0; & \text{else} \end{cases}$$

$$\text{Normalized intensity } p(i,j) \equiv \frac{\text{CWIC}(i,j)I(i,j)}{\sum_{k=1}^{512} \sum_{m=1}^{512} \text{CWIC}(k,m)I(k,m)}$$

$$\text{Central moment } \mu_{pq} \equiv \sum_{i=1}^{512} \sum_{j=1}^{512} \left(i + \frac{1}{2} - \text{column} \right)^p \left(j + \frac{1}{2} - \text{row} \right)^q p(i,j)$$

where p and q are integers. The second order moments (the sum of p and q defines the order) of the central moments are the variance about the vertical and horizontal, for $(p,q) = (0,2); (2,0)$, respectively. Therefore, the standard deviations (σ_x and σ_y) are just the square roots of these variances:

$$\sigma_x = \sqrt{\mu_{20}} \quad (13)$$

$$\sigma_z = \sqrt{\mu_{02}} \quad (14)$$

Obviously, these are a large number of statistics; however, in an attempt to better understand the true dynamics of the puff, it was felt necessary to explore as many avenues as possible. Simply calculating the standard deviations in the horizontal and vertical as a function of time (Figure 4) does not completely describe what is happening to the puff; especially regards the effects of wind shear. And, in fact, Sheih (1978) uses the parameters of an ellipsoid to describe the effects of wind shear in his model. One point of departure from his description; however, is his use of the semi-major and minor axes to describe the dispersion coefficients (standard deviations of concentration). In this paper, the two are treated quite differently: the ellipse axes presented describe the best fit ellipse in a least square sense and, consequently, would describe the boundary of the ellipse at, perhaps, the 90% transmission level or some equivalent concentration level. This is approximately the 3σ level for a normal distribution; this is just what our numbers show: the semi-major axes is about 3X the σ_z . In any case, the growth of the ratio of the two axes (Figure 5) and the growth of the angle of inclination (Figure 6) attest to the presence of wind shear. In fact, it is anticipated that the growth of the standard deviation of the aerosol at a constant height will show little increase in the alongwind direction and it is the shear which is causing the overall increase in the alongwind direction (this will be investigated in more detail in future efforts). The meteorological measurements which pertain to this trial are presented in Table 1.

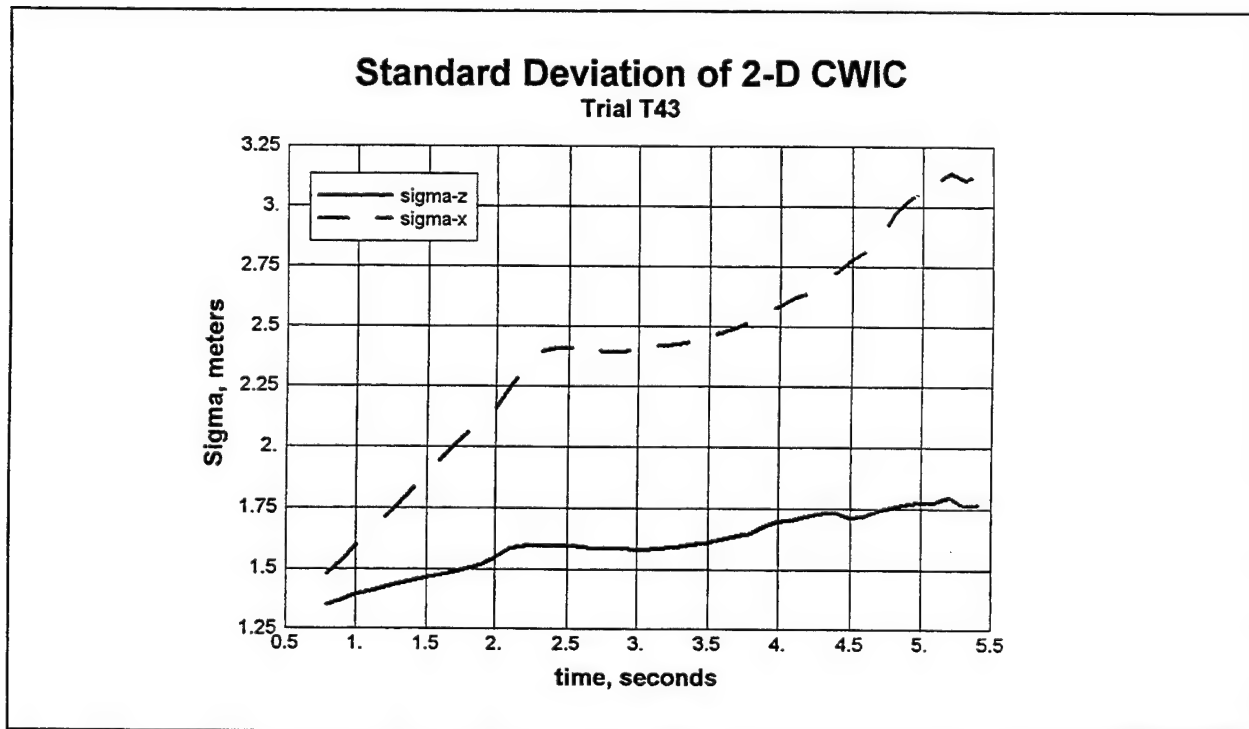


Figure 4. Plots of the vertical (z) and along wind (x) standard deviations for Trial T43.

Table 1. The meteorological conditions during trial T43.

Tower:						Miscellaneous:
level (m)	wind speed (m/s)	wind dir. (deg.)	vert. winds (m/s, (+ = ↑)	temperature (C)	rel hum (%)	local time: 12:46 air density: 1.167 g/m ³ soil temp: 31.6 C pressure: 1008.3 mbar solar rad: 1129 W/m ² Pasquill category: B visibility: 50 km
30	5.9	218	0.2	26.4	76	
16	5.7	218	0.1			
10*						
8	5.5	219	0.3			
4	4.9	222	0.1	27.9	69	
2	4.4	223	0.2			

* Other towers on the grid measured at 10-m level with indications that the winds at that level were slightly higher than would be expected from these 30-m tower measurements.

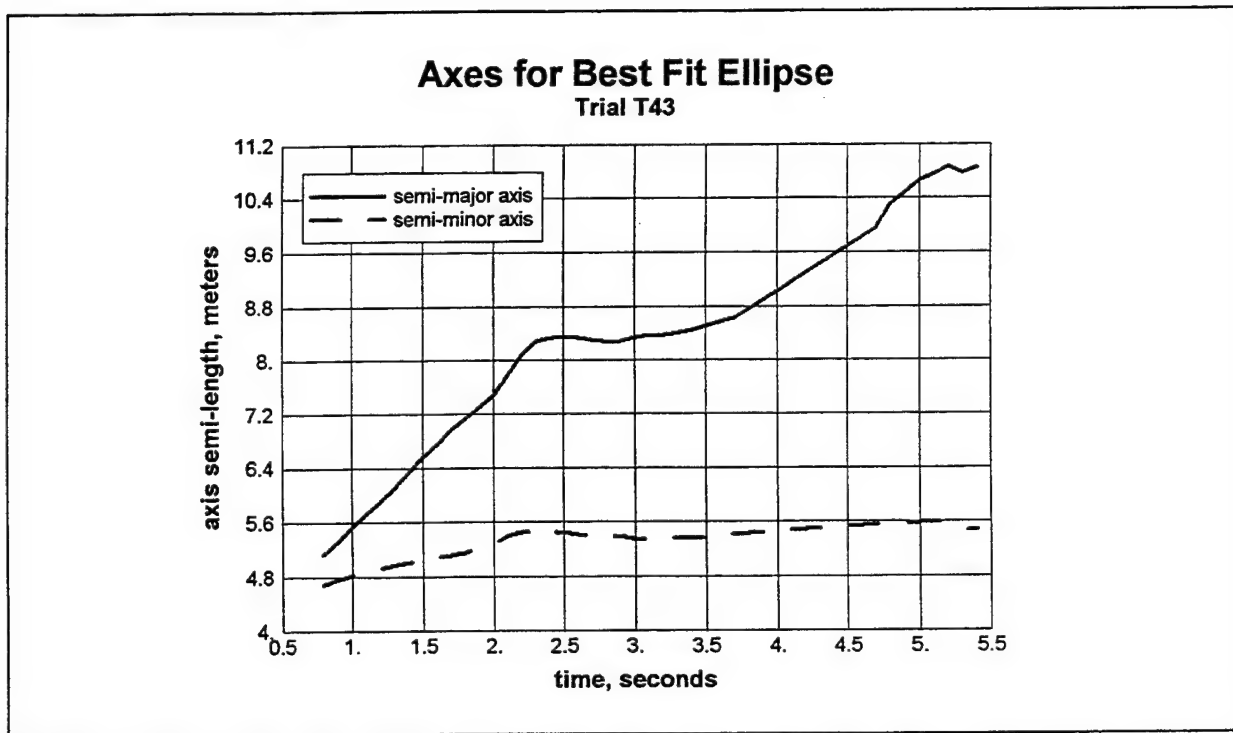


Figure 5. The development of the semi- major and minor axes of the best fit ellipse for Trial T43.

3. Summary

The acquisition and processing of the data necessary to provide a two-dimensional distribution of the crosswind integrated concentration in a puff has been demonstrated. A variety of statistics have been derived from that distribution. Among these are the standard dispersion parameters σ_x and σ_z . In addition, the fitting of those distributions to an ellipse enables the discussion of the effects of wind shear (Sheih 1978) which have been shown to exist. Future work will concentrate on the complete reduction of the data at hand and its comparison with a variety of models.

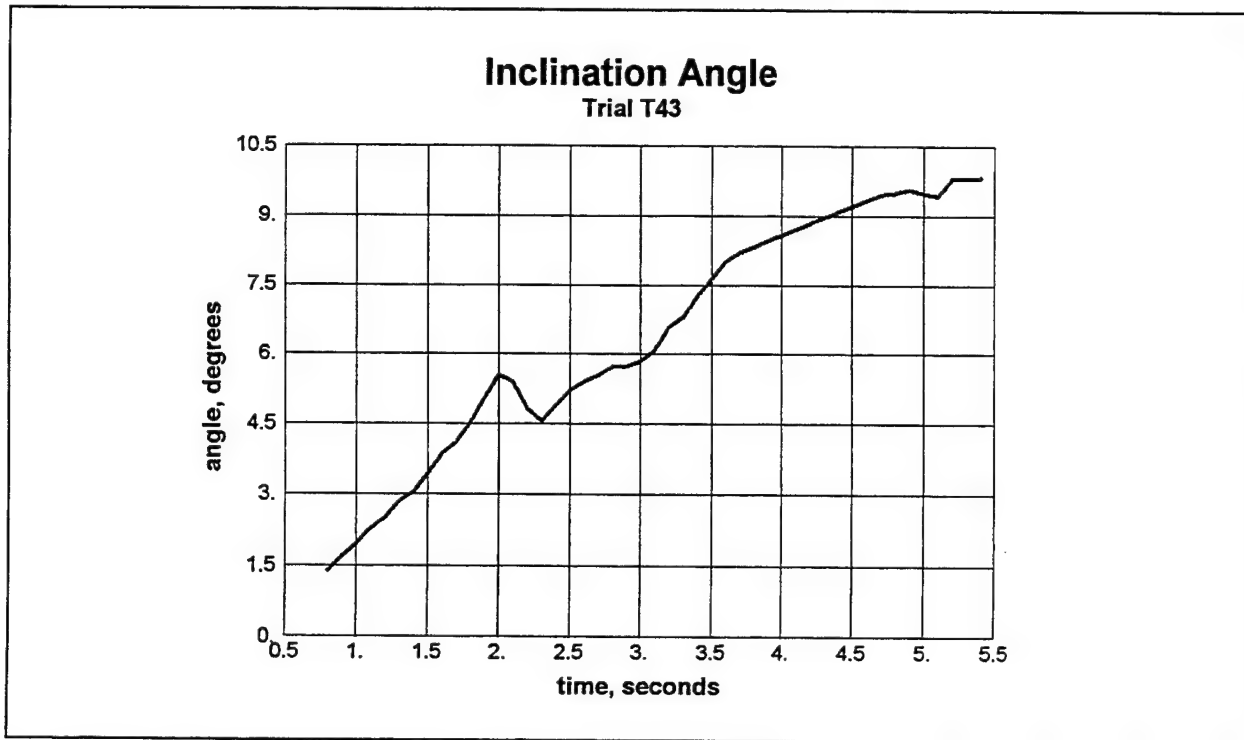


Figure 6. Plot of the inclination angle with time for trial T43.

ACKNOWLEDGMENT

Ms. Connie Kilgore Wolf and Mr. Jeffrey Moore (both of the U.S. Army Edgewood Research and Engineering Center) for permission to use their smoke test data.

REFERENCES

- Bleiweiss, M.P., 1995: "Validation of the Atmospheric Transmission Large-Area Analysis System (ATLAS)", ARL-TR-544, U.S. Army Research Laboratory, Battlefield Environment Directorate, White Sands Missile Range, NM 88002.
- Murphy, P.K. and G.A. Heyler, 1994: "Image Processing Aboard the Midcourse Space Experiment Using the Ultraviolet and Visible Imagers and Spectrographic Imagers Instrument", *Johns Hopkins APL Technical Digest*, Volume 15, Number 3, p. 195+.
- Sheih, C.M., 1978: "A Puff Pollutant Dispersion Model With Wind Shear and Dynamic Plume Rise", *Atmospheric Environment*, Vol. 12, pp. 1933-1938.
- Zannetti, P., 1990: Air Pollution Modeling, Theories, Computational Methods, and Available Software, Van Nostrand Reinhold, New York.

HIGH RESOLUTION WIND FIELD SIMULATIONS RUN REAL-TIME AND WITH OTHER INPUTS TO OPTIMIZE MODEL OUTPUT

J. H. Byers and R. M. Cionco
U.S. Army Research Laboratory
Battlefield Environment Directorate
White Sands Missile Range, NM 88002, USA

ABSTRACT

An integral part of planning and conducting the MADONA Field Study was the simulation of high resolution microscale wind fields over the test domain of complex terrain. ARL's microscale wind code was run on-site and real-time during the ten days of smoke and SF₆ diffusion and concentration fluctuation experiments four times daily. On-site, real-time data (from a fixed site) were input directly to initialize model runs during MADONA. Meteorological fields were simulated during unstable, neutral, and stable atmospheric conditions for a 5 km by 5 km area with a 100 meter computational grid. Later in the laboratory, we further tested the premise that another data set could produce better results than the on-site, real-time input data. An effort was made to compare the simulations using data from the real-time data input with additional solutions run using meteorological observations from several other sites to initialize the model. The other sites were selected to be in the experimental area near the tracer release points as well as upwind of notable terrain features. These solutions were used for evaluation and inter-comparison with each other and with the real-time solutions to determine which site, if any, provided the optimum initializing data for the HRW model. In addition to providing surface layer meteorological fields of wind vectors and streamlines, temperature, friction velocity, stability etc, the effects of terrain upon the these fields and thus upon the diffusion experiments were also analyzed. In general the real-time simulations did quite well, but simulations initialized with data from a site in the middle of the diffusion test area produced even better agreement. Simulations initialized by the other sites showed better agreement in some, but not all, cases in regard to the observed fields than did the real-time data simulations.

1. INTRODUCTION

The high resolution wind model/code, HRW (Cionco, 1985), was used on-site with real-time data as inputs to simulate high resolution meteorological fields over variable terrain of rolling hills during the MADONA Field Study (Cionco and Byers, 1995). Even though satisfactory results were obtained from this real-time initialization, it was also felt that initializing with data

for certain fetches may produce simulated fields of equal or better values versus the observed data fields. Post study analyses have permitted a second look at model simulations that are initialized with data from other sites located within the MADONA domain at either the diffusion experimental area or upwind of or at the aerosol release sites.

2. MODEL AND DATA SETS

2.1 The HRW Model

HRW is a two dimensional, diagnostic, time independent model that simulates wind flow over a grided area of 5 km by 5 km with a preferred spacial resolution of 100 m. The computational domain can range from 2 km by 2 km to 20 km by 20 km with grid resolutions of 40 m to 400 m respectively. The thickness of the computation layer is defined to be 1/10th the magnitude of the grid size, i.e. the 100 meter grid spacing imposes a layer thickness of 10 meters.

The simulation results are obtained by a direct variational relaxation of the initial wind and temperature fields in the surface layer. The solution is reached when the internal constraint forces imposed by the warped terrain surface, thermal structure and the requirement for flow continuity are minimized. The procedure makes use of Gauss' Principle of Least Constraints (Lanczos, 1962) which requires these forces to be minimized in order to satisfy the equations of motion. When applied to the surface layer, this procedure also requires the use of empirical wind and temperature profiles.

Input parameters consist of wind speed, wind direction and temperature at one site preferably at the 10 m level and an estimate of atmospheric buoyancy derived from an upper air sounding using the temperature-pressure-height profile values at 850, 700, and 500 mb levels. The code is initialized with a uniform field of wind speed and wind direction. A non-uniform initial temperature field is used, with the temperature adjusted according to the variations in the terrain elevation at each grid point within the computational domain.

Output from the code includes simulated values at each grid point within the 5km by 5km area for: wind speed, wind direction, potential temperature, Richardson's Number, friction velocity, vertical impaction motion, and the Wind Power Law exponent.

2.2 The Test Scenario

The model is initialized with data from a single upper sounding and meteorological data at the surface, near the area of interest. For the simulations produced for this analysis, these data were collected at (a) the real-time (R-T) site, (b) the middle of the diffusion study area, (M-10), and (c) upwind, (M-13), or at the aerosol release point, (M-12). Figure 1 shows a 5km by 5km elevation contour map of the Porton Down area in the United Kingdom, where the MADONA tests were conducted. Figure 2 is an enlarged view of a portion of the same area, known as the Bowl, showing terrain contours, vegetation, and the location of the specific sites that collected the surface meteorological data used in this analysis. The enlarged area shown in Figure 2 was the primary area used for conducting most of the tests.

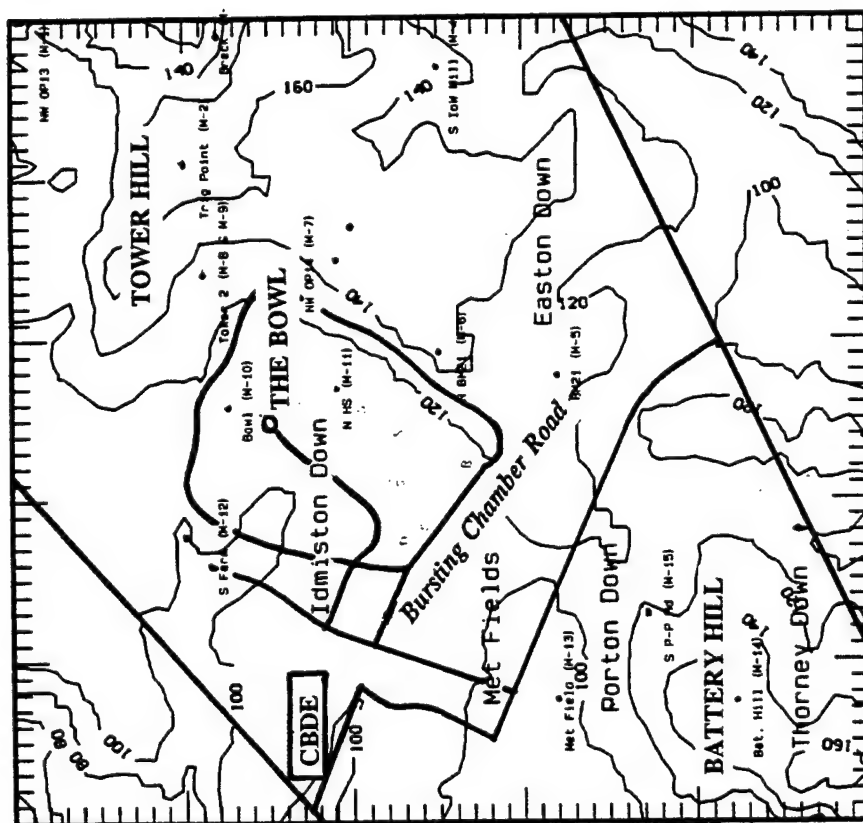


Figure 1. MADONA Test Site at Porton Down, U.K. showing elevation contours and meteorological tower locations.

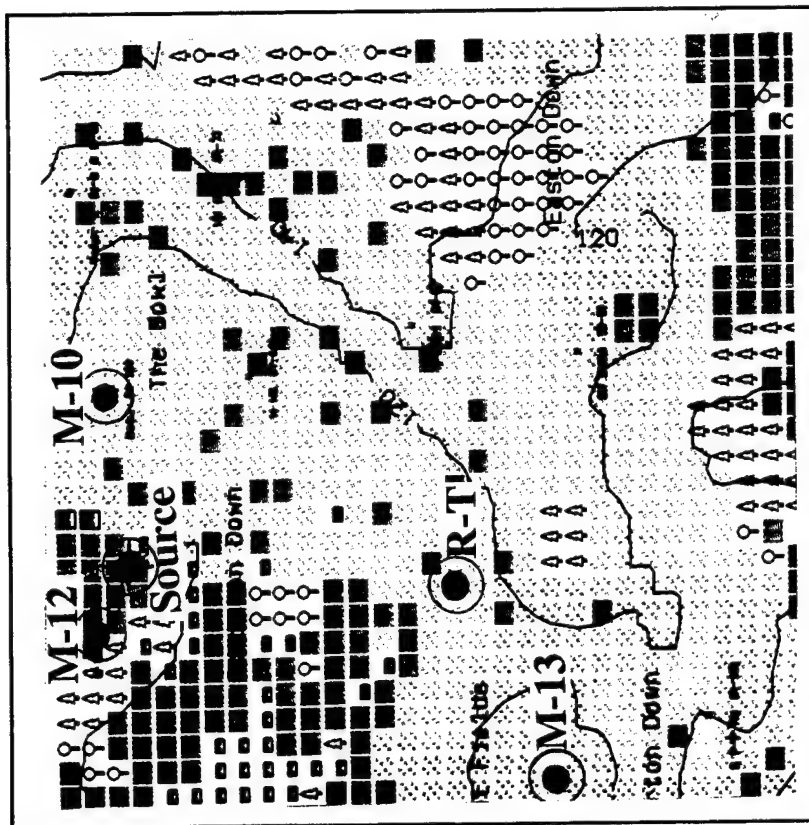


Figure 2. Exploded view of the Bowl in the MADONA test area, showing the R-T, M-10, M-12, and M-13 met sites.

3. ANALYSIS AND RESULTS

Forty cases were run to produce simulations for input data defined in (a) and (b) above. A third set of select runs were also made for (c) inputs, but not for each of the forty cases. If neither (a) nor (b) input data runs produce reasonable fields versus the observed fields then a select set of (c) data cases were run for further comparison. The premise is that we then would be initializing with the same wind and temperature of the air parcel that the smoke and SF₆ experienced at or somewhat upwind of the aerosol release point.

Plots of simulated wind streamlines for 1200 GMT on Julian day 267 are shown in Figures 3 through 6. These four simulations were all initialized with the same upper air data, but used surface meteorological data from R-T, M-10, M-12 and M-13. For comparison purposes, the wind vectors at 1200 GMT, obtained from data collected from each of the 15 met stations, are also overlaid on these plots. Although a comparison of the magnitude of the wind speeds cannot be obtained from these plots, the plots do show generally good agreement in wind direction at most of the various sites.

Plots of the simulated data versus the observed data are shown in scatter diagram form in Figures 7 through 10, for simple comparison against the line of perfect prediction. Note that data for sites M-1, M-3, and M-9 are excluded from the analyses in that M-1 and M-3 are technically outside of the computational domain and M-9 is located at 30 m height rather than 10 m as these other measurements are. Correlation coefficients were also calculated as a more stringent test of agreement.

For the real-time input, case (a), Figures 7 and 8 present the wind direction and wind speed comparison plots respectively. Figures 9 and 10 show these plots for the simulations initialized with the M-10 data, case (b). Qualitatively, for both cases, the model simulated wind directions quite good whereas wind speed did not have the same high agreement. For those individual cases that did not agree well with the observed fields (speed and direction), select cases (c) were run for further test and comparison. Space limitations do not permit including these other plots.

Correlation coefficients were calculated for the above cases of (a) and (b). These values are shown in Table 1.

Table 1. Correlation Coefficients for Case A (R-T) and Case B (M-10)

	(R-T)	(M-10)
Speed	0.7997	0.8567
Direction	0.9457	0.9701
Data Pairs	383	425

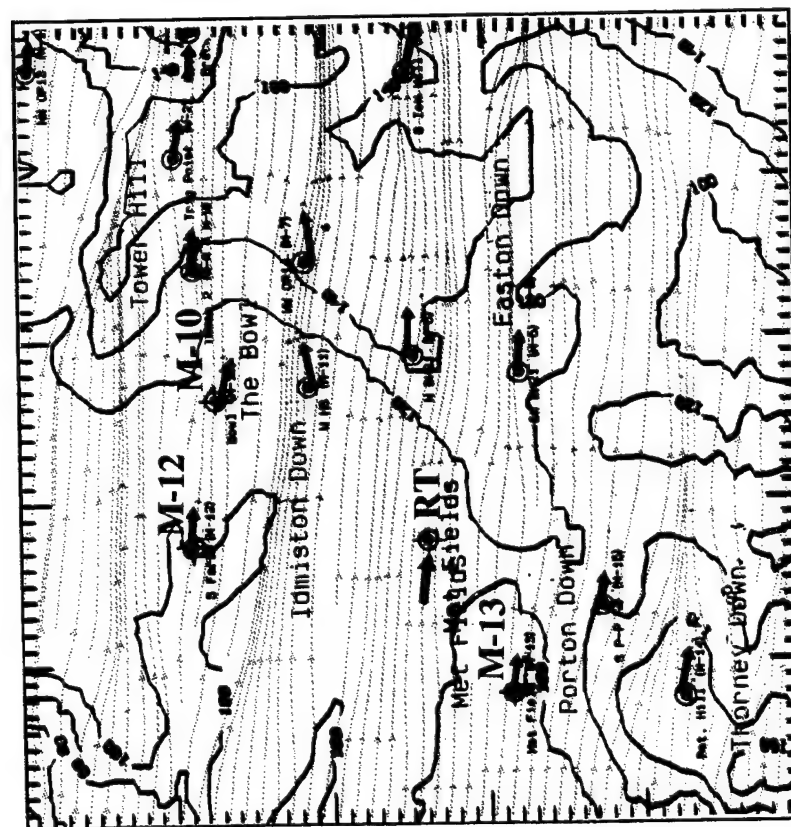


Figure 3. Simulated streamlines overlaid with observed wind vectors. Simulation is initialized with R_T data.

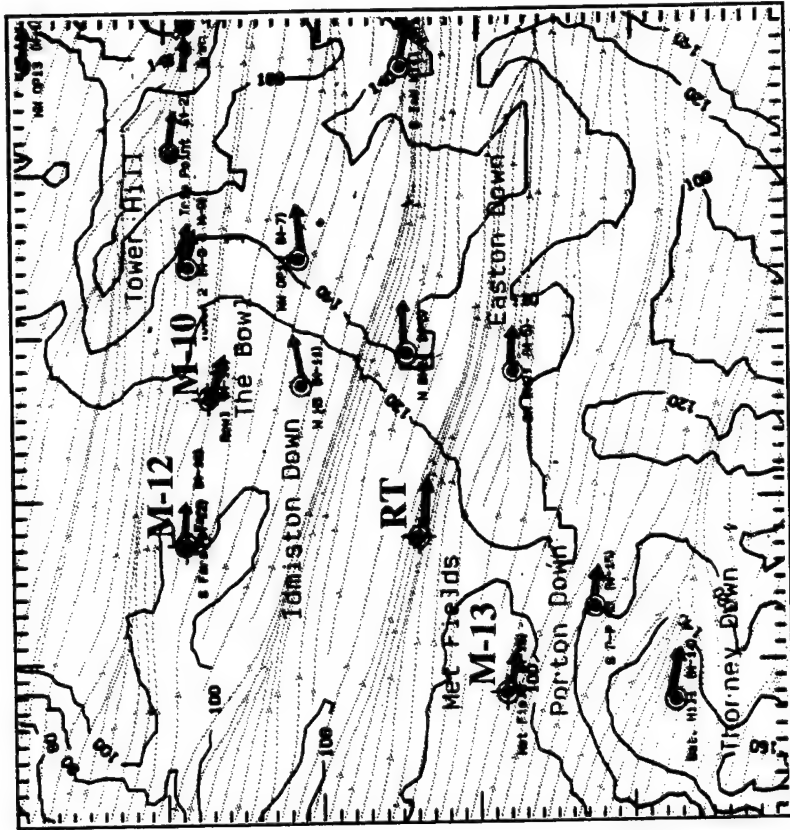


Figure 4. Simulated streamlines overlaid with observed wind vectors. Simulation is initialized with M-10 data.

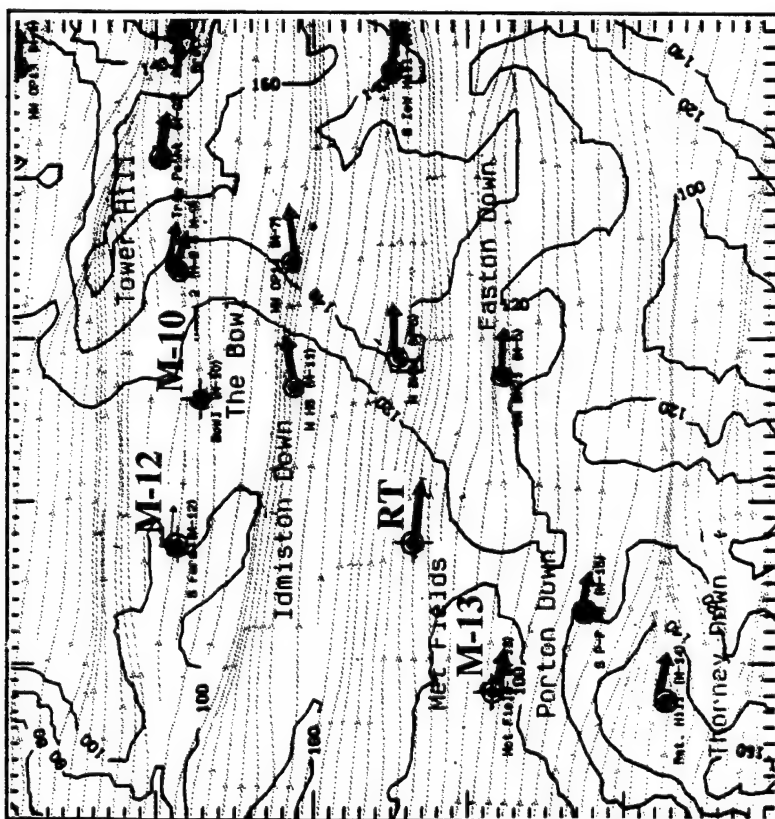


Figure 5. Simulated streamlines overlaid with observed wind vectors. Simulation is initialized with M-12 data.

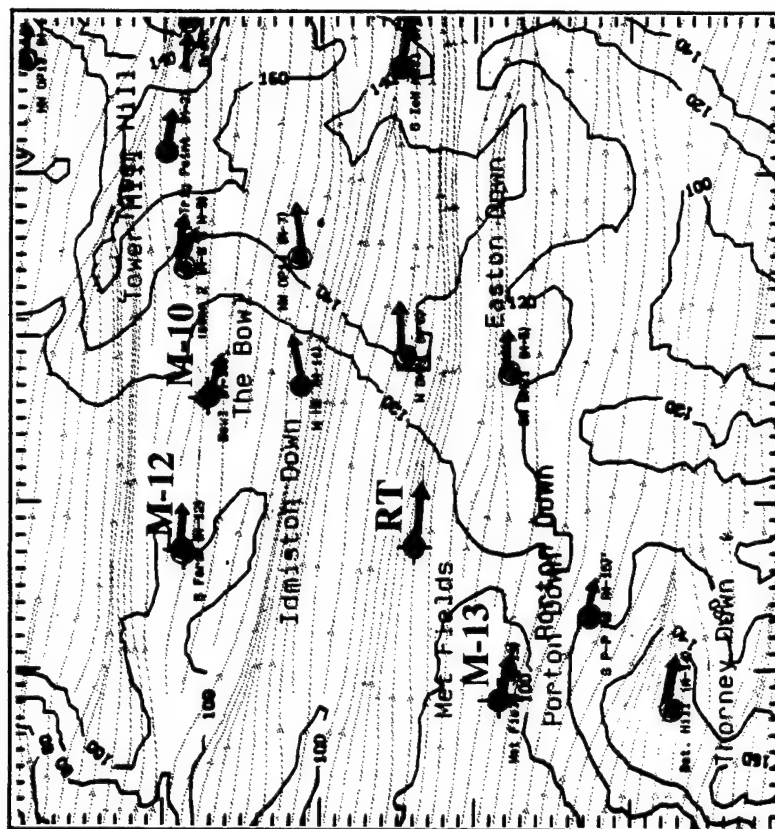


Figure 6. Simulated streamlines overlaid with observed wind vectors. Simulation is initialized with M-13 data.

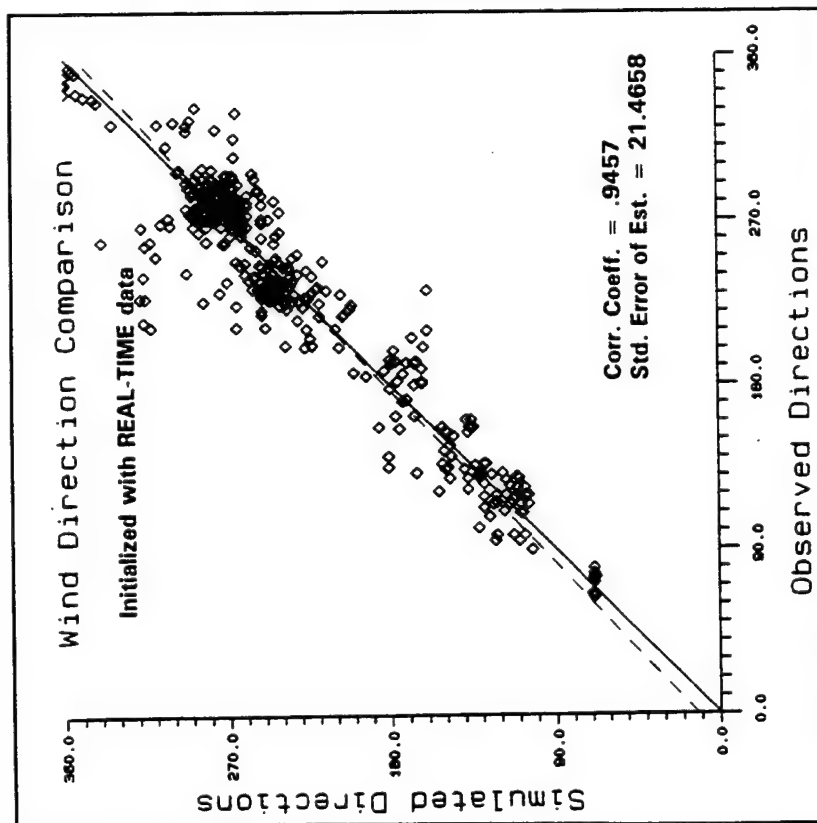


Figure 7. Scatter diagram of Case A (R-T) for simulated wind direction versus observed values for all simulations.

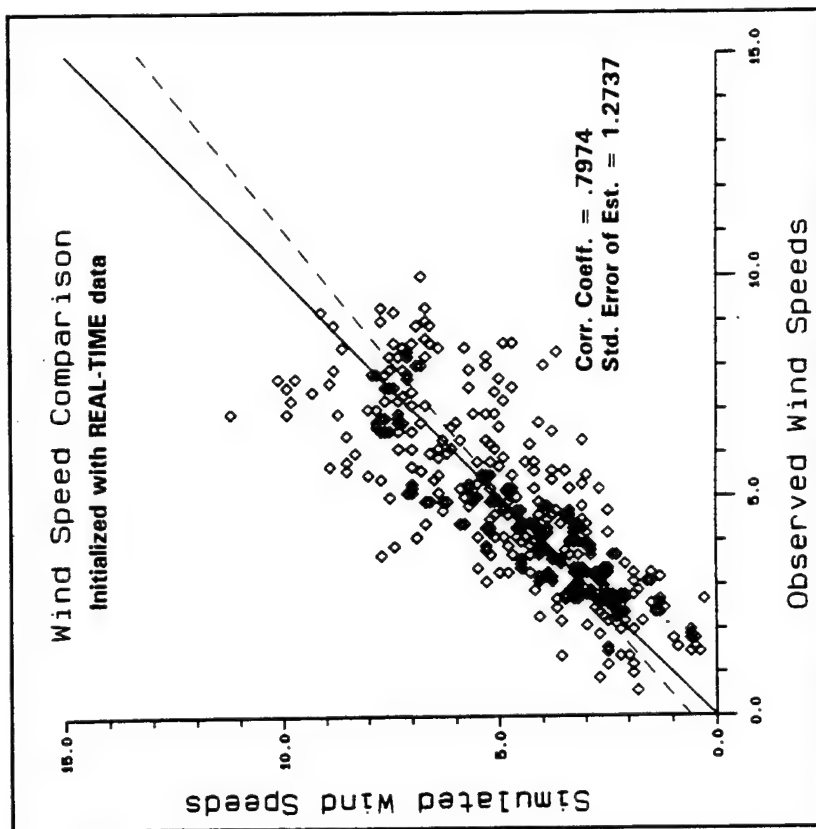


Figure 8. Scatter diagram of Case A (R-T) for simulated wind speed versus observed values for all simulations.

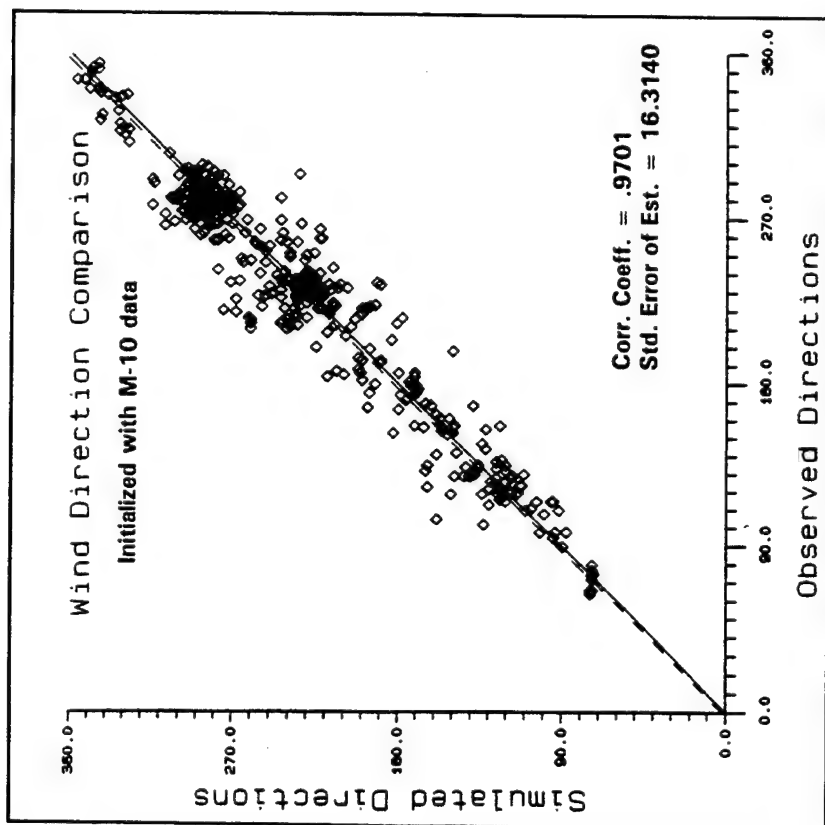


Figure 9. Scatter diagram of Case B (M-10) for simulated wind direction versus observed values for all simulations.

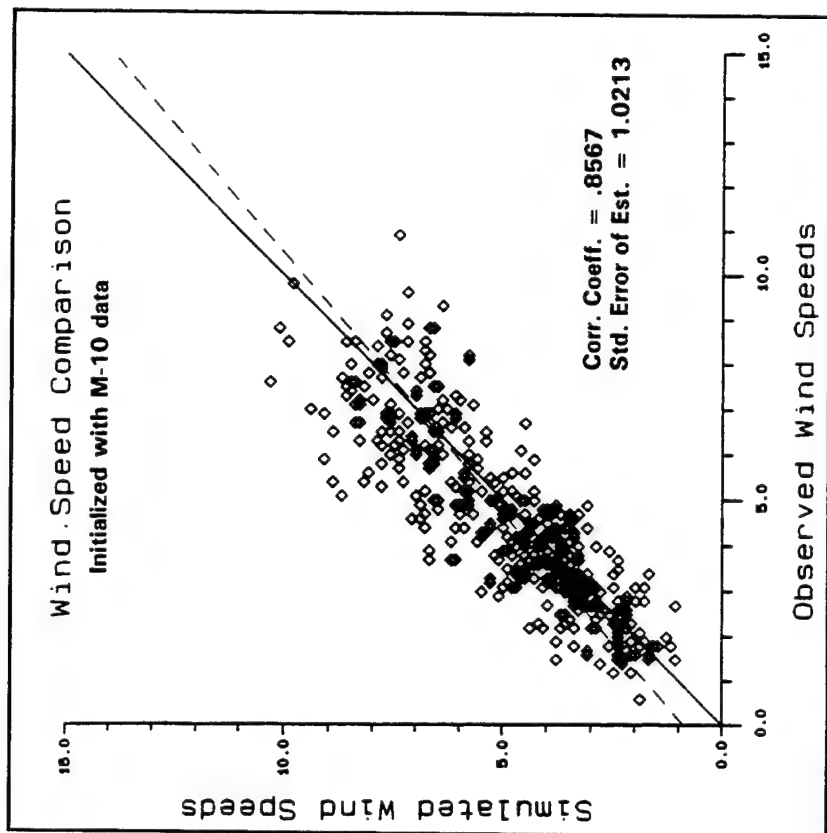


Figure 10. Scatter diagram of Case B (M-10) for simulated wind speed versus observed values for all simulations.

4. SUMMARY

As is shown in Figures 7 through 10 and Table 1 for all simulation runs, Case (a) with Real-Time data inputs produced a high positive correlation of simulated values versus the observed values. The wind direction correlation coefficient is 0.9457 with a regression line off set of 12 degrees. The wind speed correlation coefficient is 0.7997. For Case (b) with inputs from Station M-10, the model produced even better agreement and higher correlations indicating that M-10 had a better field exposure than the Real-Time site and is therefore more representative of the local wind fields in general. The wind direction correlation coefficient for the M-10 case is 0.9701 and 0.8567 for wind speed.

A series of simulations were also made for other input cases. Better agreement and higher correlation were always found to exist for wind directions more so than for wind speeds. Analyses will continue further dissecting the details of this level of agreement. The data sets will be conditionally sampled in regard to wind direction, range of speeds, and stability.

5. REFERENCES

Cionco, R. M., 1985: Modeling Wind fields and Surface Layer Profiles Over Complex Terrain and Within Vegetative Canopies. Forest-Atmosphere Interactions, Editors: B. A. Hutchison and B. B. Hicks, D. Reidel Publishing Co., Holland.

Cionco, R. M. and J. H. Byers, 1995: High Resolution Wind Field Simulations Run Real-Time During The MADONA Field Study (Paper 10.5). Proceedings of the 11th Symposium on Boundary Layers and Turbulence, AMS, Boston, Mass.

Lanczos, C., 1962: The Variational Principles of Mechanics. (2nd Edition), The University of Toronto Press, Toronto, Canada.

Forecasting Atmospheric Optical Turbulence Neutral Events-Part II

Gail Tirrell Vaucher
U.S. Army Research Laboratory
White Sands Missile Range, New Mexico 88002, U.S.A.

Robert W. Endlich
U.S. Army Research Laboratory
White Sands Missile Range, New Mexico 88002, U.S.A.

ABSTRACT

Boundary layer atmospheric optical turbulence (AOT) and meteorological data were collected from March 1994 through June 1995 over a 1 km horizontal path in the Tularosa Basin, New Mexico. The purpose of the measurement set was to determine if the diurnal AOT minima, or Neutral Events (NE), could be forecast. We previously examined the time difference between the astronomically calculated sunrise (sunset) and the NE. These differences were found to increase as the months progressed from March to June. Here, we extend the study to include the entire annual cycle. We describe the AOT and meteorological dataset, present the data analysis and observations, and finally, provide explanations useful in forecasting the morning (evening) NEs for a desert basin.

1. INTRODUCTION

Atmospheric optical turbulence (AOT) occurs when there are random, dynamic density variations in the atmosphere. To quantify AOT, one employs a statistical parameter called the index of refraction structure function, C_n^2 . In its most basic form, C_n^2 is defined as:

$$C_n^2 = \frac{\langle (n_1 - n_2)^2 \rangle}{r^{2/3}} \quad (1)$$

where $\langle (n_1 - n_2)^2 \rangle$ is an ensemble average of the atmospheric index of refraction differences (index of refraction variance), and r is the separation or distance between n_1 and n_2 . Typically, C_n^2 is sampled along a fixed path, with the assumptions that the path is homogeneous and isotropic, and the distance separating the two endpoints is within the turbulence inner and outer scales. A detailed review of the AOT equations is found in Tatarski (1961).

Experimentally, AOT can be quantified by measuring the index of refraction fluctuations. The interpretation of AOT measurements correlates directly with the C_n^2 magnitude fluctuations. In general, the high and low AOT values for C_n^2 at 1 m above ground level (AGL) are about $10^{-11} \text{ m}^{-2/3}$ and $10^{-18} \text{ m}^{-2/3}$, respectively. Figure 1 demonstrates a typical C_n^2 diurnal time-series over a desert terrain, and will be elaborated upon in the next section.

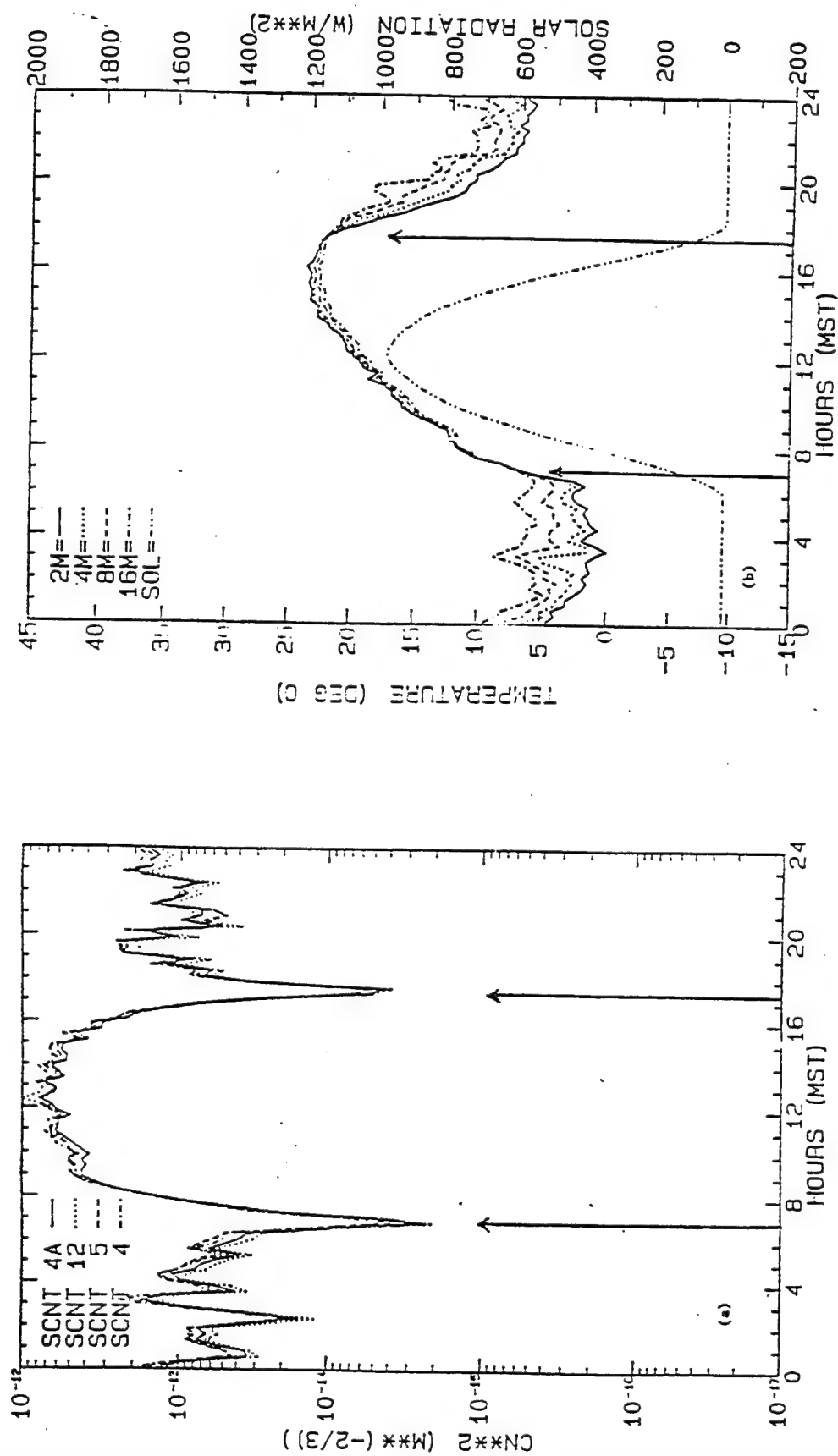


Figure 1. Day plots of scintillometer data, vertical temperatures, and solar radiation for March 25, 1992. a: scintillometer data at 1 m AGL; b: 2-, 4-, 8-, and 16-m temperatures and solar radiation.

1.1 The AOT Diurnal Cycle

Before a Neutral Event (NE) can be forecasted, an understanding of the "normal" diurnal AOT dynamics and "typical" measurement signatures is required. The following briefly reviews these NE dynamics, as observed in the various measurable variables.

Figure 1 displays a typical C_n^2 diurnal cycle sampled at 1 m AGL, over a desert floor under clear skies and light winds (Vaucher & Endlich, 1993). The coincident insolation, and temperature time-series sampled at 2, 4, 8, 16 m AGL, are also shown. Overlaying these plots, one quickly observes the strong correlation between the timing of the sunrise/sunset transitions (insolation rises from/lowers to, zero) and the two C_n^2 minima. In fact, four unique AOT scenarios can be extracted from this diurnal cycle. For simplicity, we'll reduce the four temperature time-series by focusing on just the 16 minus 2 m temperature differences, hereafter labelled "Delta-T". The first of four scenarios occurs prior to sunrise (no insolation), where the Delta-T indicates that the atmosphere is stable (positive Delta-T) and AOT is moderately high. In contrast, a second case is observed around mid-day. Here, the atmosphere is unstable (Delta-T is strongly negative) and AOT reaches the daytime maximum. The final two scenarios occur during the transitions between these two extrema. Shortly after sunrise (insolation begins to increase), the stable atmosphere of the night (positive Delta-T) evolves into an unstable (negative Delta-T) daytime environment. Mirroring the morning's event, another transition occurs just prior to sunset (as insolation goes to zero). In this case, the unstable daytime (negative Delta-T) scenario changes into a stable (positive Delta-T) nighttime atmosphere. In both of these latter cases, the C_n^2 minimum occurs when the atmosphere is dry adiabatic. Assimilating these dynamics, an empirical forecasting algorithm begins to form.

1.2 What are Neutral Events and Why Study Them?

There are two periods during a typical 24 hour cycle when low level AOT drops to a minima (figure 1). These phenomena, called Neutral Events (NE), are primarily a function of the local heat flux. During these two periods, optical propagation encounters a minimal amount of degrading atmospheric effects. As a result, knowledge of these natural turbulence minima are especially useful to those in astronomy, laser propagation, and visual imaging fields.

1.3 Previous NE Study at the White Sands Missile Range

In a previous study, we examined AOT and meteorological data from April and May of 1994. The objective was to identify and investigate any atmospheric patterns relevant to forecasting a NE.

The principle AOT measurements were collected by Lockheed Model IV scintillometers, mounted 8 and 32 m AGL, over a 1 km horizontal desert path in the Tularosa Basin, New Mexico. Three fixed and

fully instrumented 32 m (100 ft) meteorological towers marked the 0, 0.5 and 1 km points along this AOT path. Specific tower measurements included 3-component winds, ambient and dewpoint temperatures, and insolation. Meteorological observations supplemented the instrument measurements, providing empirical definitions for the "ideal" and "less than ideal" forecasting scenarios. These conditions will be discussed later.

The previous study's data analysis focused on the 8 m AOT measurements, the Delta-T, and onsite meteorological observations. Tabulated sunrise (sunset) times were used as reference points for determining the occurrence of the morning (evening) NEs.

Based strictly on the limited dataset, the results were: (1) The average morning NE occurred about 70 minutes after sunrise, with tabulated values ranging from 40 to 133 minutes after sunrise; (2) The average evening NE occurred about 60 minutes before sunset, with the individual values spanning from 12 to 98 minutes prior to sunset; (3) A month-by-month analysis showed the sunrise-NE time difference increased about 12 minutes per month during the spring; and (4) When the results were applied in an operational environment, two types of cases were discovered. The first case, called the "Ideal" NE forecasting scenario, consisted of those conditions under which the statistically derived NE forecast provided the best precision. These Ideal cases were characterized by clear skies, low winds, and no significant ground moisture within the previous 24 hours. The second case was labelled the "Less Than Ideal" scenarios, and included the majority of days studied. In an attempt to understand what made each case "Less Than Ideal", these scenarios were subdivided into three groups based on the local forcing effects of cloud cover, soil moisture, and mountain shadowing. In short, any anomaly in the insolation affected the NE timing. Specific local forcing effects resulted in (1) a delayed or early NE timing, (2) an elongated and shallower AOT minimum, or (3) creating a NE too ill-defined to quantify.

1.4 Current AOT and Meteorological Data Collection

In the current study, we have extended the original two months of data to fifteen months, more than a full annual cycle. As in the previous study, the AOT data were collected from scintillometers sampling at 8 and 32 m AGL, along a 1-km horizontal desert path in the Tularosa Basin, NM. The coincident meteorological data were taken from three fixed and fully instrumented 32 m meteorological towers (See Section 1.3). Daily meteorological observations supplemented the study's database.

2. DATA ANALYSIS AND OBSERVATIONS

NE times were defined by the 8 m C_n^2 minimum. When multiple equivalent minima were observed, an average of the extended event was calculated. Unclear or ill-defined NE were noted and excluded from the statistics. The meteorological data analysis focused on

the two most informative variables, the Delta-T and insolation. Data processing included a calculation of sunrise (sunset) and morning (evening) NE time differences. All tabulated sunrise (sunset) times were taken from the same listing used in the previous study. The Delta-T and insolation values, occurring simultaneously with the NE, were retrieved from their respective time-series and analyzed. The following results were observed.

2.1 A Seasonal NE Pattern

Figure 2 displays one of the most useful tools for NE forecasting. Here, the sunrise (sunset) times, the original NE forecasting equation, and the actual NEs are shown on a single plot. At first, the original equation and NE data appear to fit well. However, a closer examination reveals a seasonal oscillation. Figure 3 clarifies this seasonal pattern, by displaying the monthly sunrise (sunset) minus NE time difference averages. Notice that the greatest time differences correspond with those months in which the solstices occur (June, Dec). The two minima occur in the equinox months (Mar, Sep). Previously, we had reasoned that the sunrise-NE time differences were a function of the local temperature inversion strength (Vaucher & Endlich, in press). This reasoning is still valid, with the caveat that the skewed day-night heating-cooling, characteristic of the solstices, evidently generate equivalently strong surface temperature inversions. Thus, the time required for the atmosphere to evolve into the NE's required adiabatic environment, is appropriately lengthened. In contrast, when the diurnal heating-cooling is equal, such as during the equinox, the surface inversions are the weakest. The time needed to generate the near-surface adiabatic atmosphere for these cases is reduced.

2.2 Correlation of Meteorological Measurements

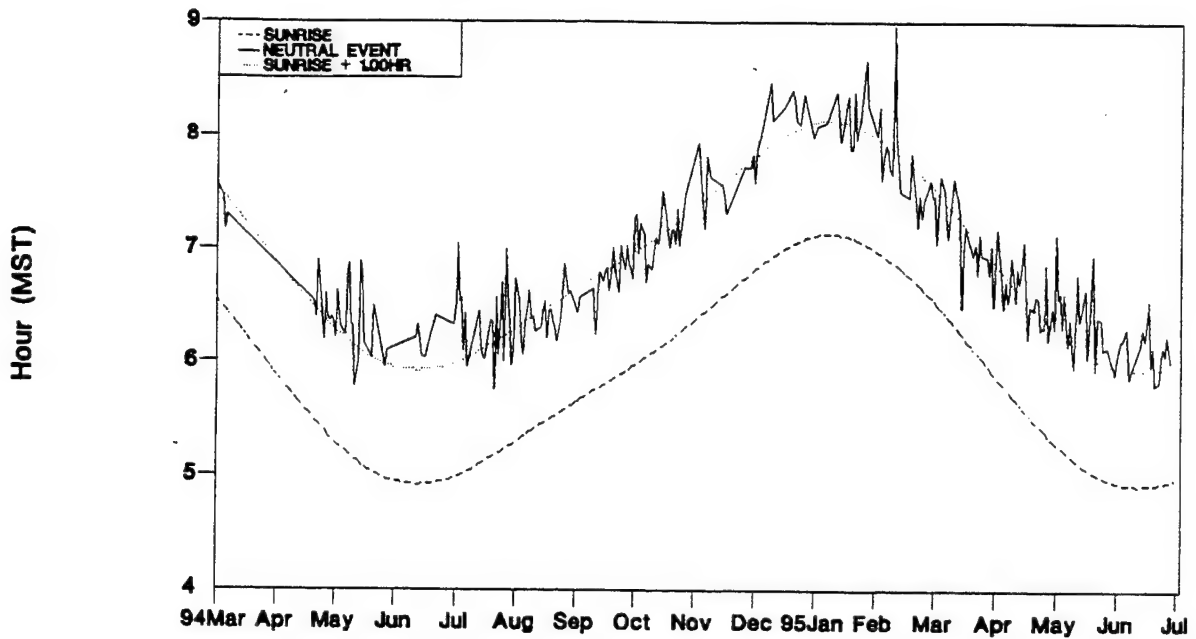
The purpose of the Delta-T data was to verify the onset of an adiabatic environment during the NE. In fact, as C_n^2 dropped to a minimum, Delta-T values exhibited an adiabatic lapse rate.

The annual cycle of coincident NE-insolation measurements revealed average values for the sunrise-NE insolation were between 80 and 142 W/m². The average sunset-NE values ranged from 19 to 78 W/m². The monthly standard deviations were less for the sunset-NE cases than in the sunrise-NE cases; sample-sizes were comparable. These contrasting insolation magnitudes can be explained with the fact that the sun's elevation angle at the sunset-NE is lower than during the sunrise-NE. In other words, the sun is approximately 20 minutes closer to the horizon at the sunset-NE than at the sunrise-NE. The reduced standard deviations may be explained by the generally greater complexity in the morning heating.

3. REVISED NE FORECASTING EQUATIONS

In Section 2.1, we discussed a seasonal variation oscillating around the original NE forecasting equations. In figure 4, we

Sunrise and Neutral Event Times



Sunset and Neutral Event Times

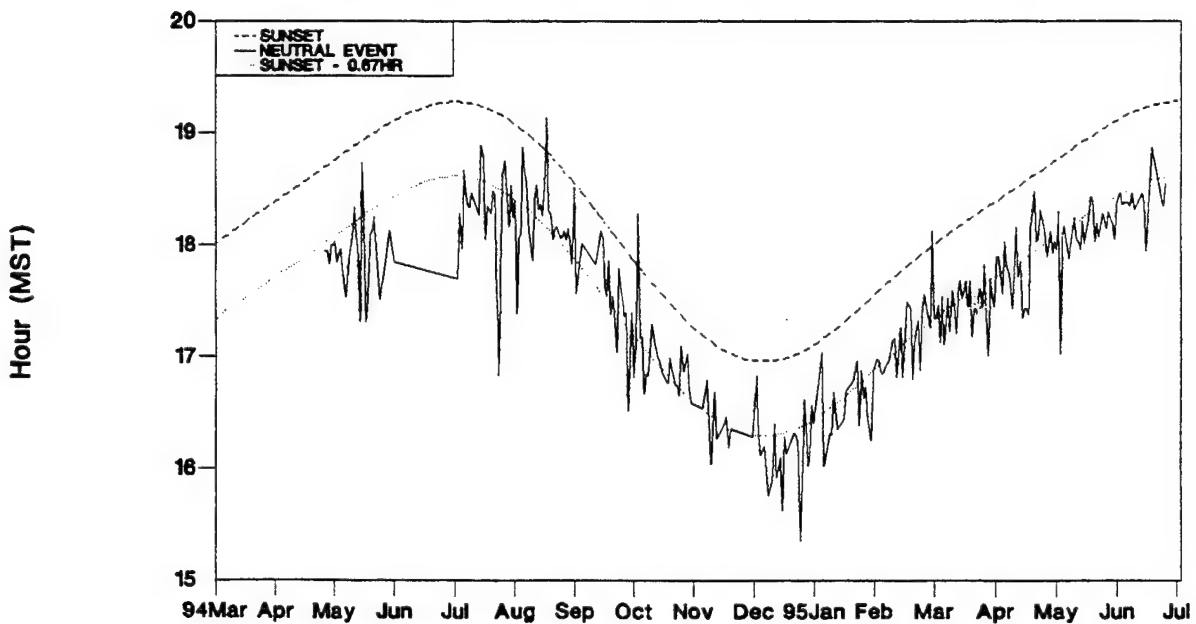
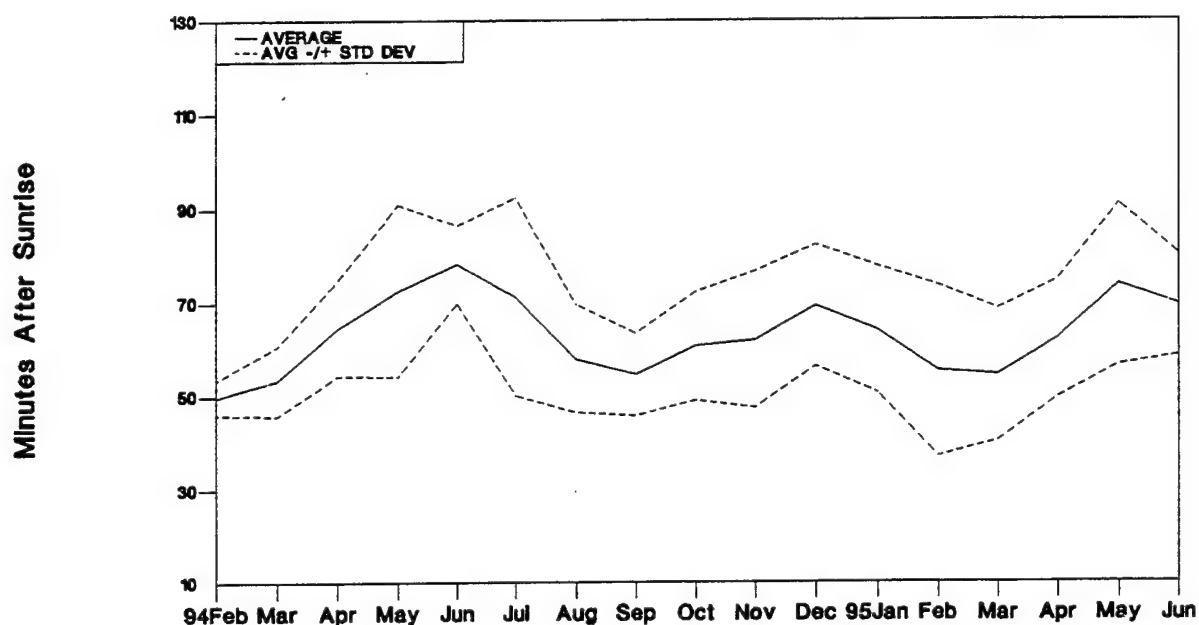


Figure 2. NEUTRAL EVENT(NE) TIMES: (a) Time of sunrise (dashed-line), actual NEs (solid-line), and original NE Forecasting Model (dotted-line). (b) Time of sunset (dashed-line), actual NE (solid-line), and original NE Forecasting Model (dotted-line).

Time of Neutral Event After Sunrise

Monthly Averages & Standard Deviations



Time of Neutral Event Before Sunset

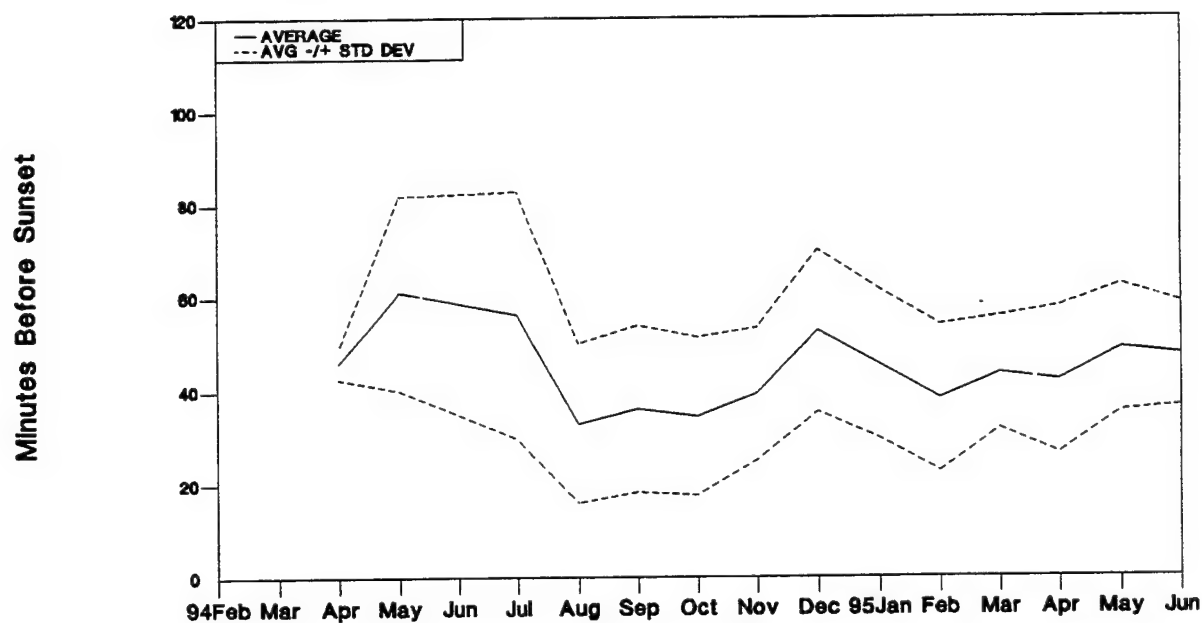
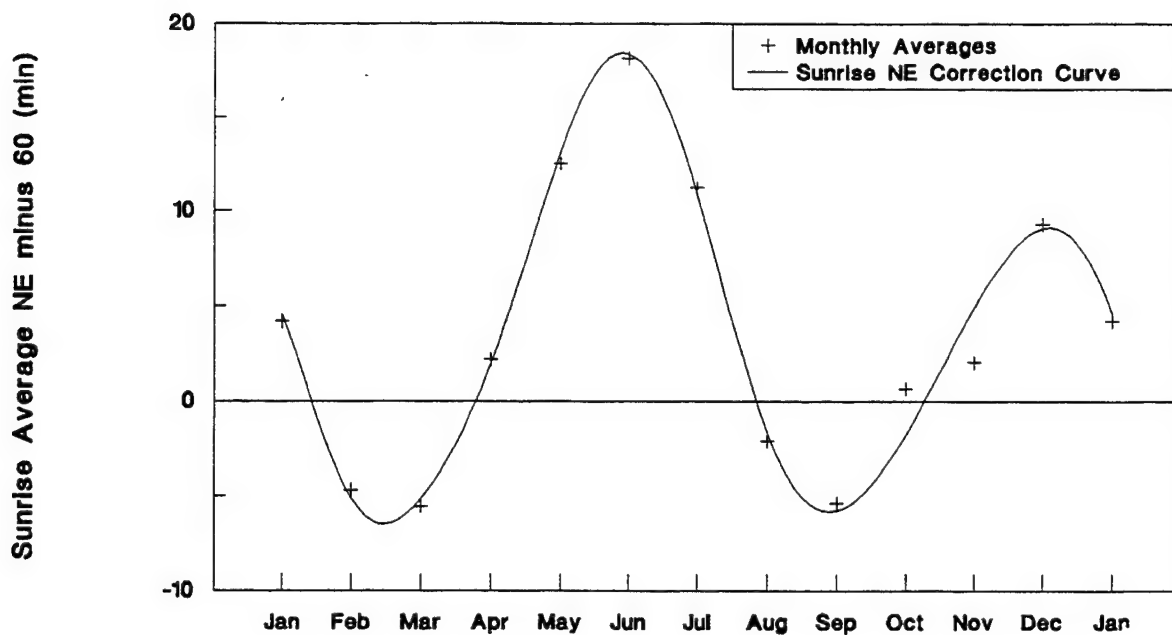


Figure 3. Monthly average and standard deviation of the NE time, in minutes, (a) after sunrise and (b) before sunset.

Sunrise NE Correction Fourier Series Curve Fit



Sunset NE Correction

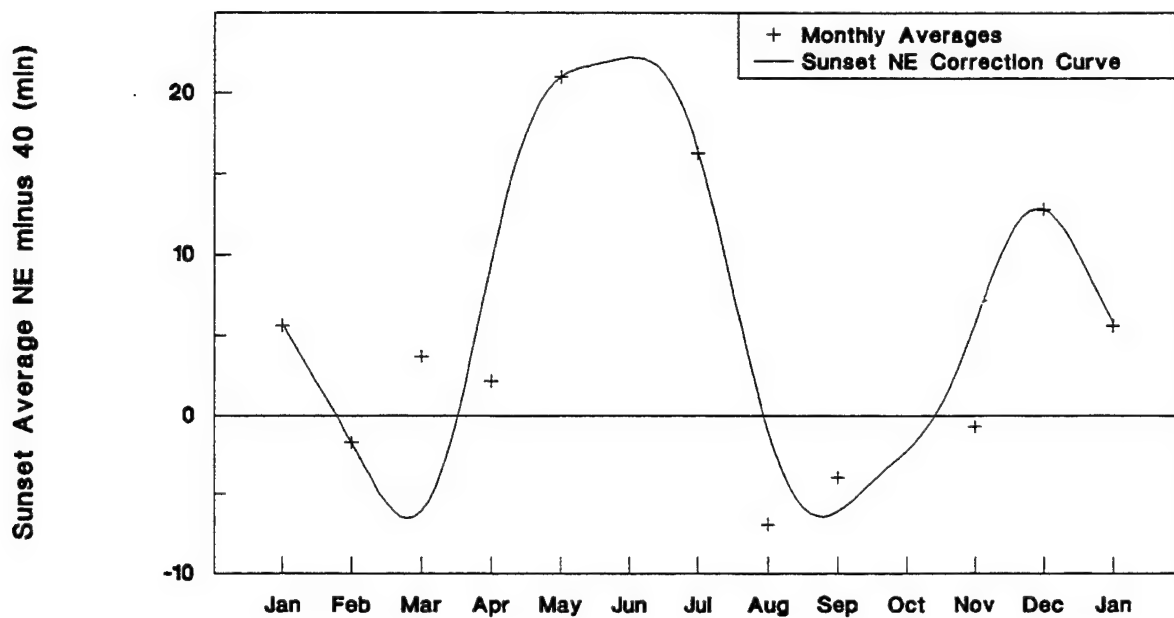


Figure 4. Correction curves for the original (a) sunrise-NE and (b) sunset-NE equations. Monthly averages shown as pluses.

defined a perfect data fit with these original equations to be equal to 0 minutes. Each "plus" represents the monthly-NE-average minus the original equation. For both the sunrise and sunset NE cases, the greatest excursions were about 20 minutes (33% of an hour) and, a definite cyclical pattern was evident. Keying on this 12 month periodicity, we utilized a Fourier Waveform Analysis to create correction curves (solid lines) for the original NE equations. These correction curves were defined as:

$$\text{Correction (in min)} = a_0 + \sum_{n=1} (a_n \cos n\theta + b_n \sin n\theta), \quad (2)$$

where θ (in radians) = (month number - 5)*PI/L. Since the wave period is 12 months, L is 6; PI is 3.1415. The dataset defined May as the wave's zero point in the annual cycle; therefore, a 5 month offset was used. The coefficients for these curves are listed in Table 1. Assimilating this correction with the original formulas, the final NE Forecasting Equations are:

$$\text{SUNRISE-NE} = \text{Time of Sunrise} + 60 \text{ minutes} + \text{Correction}, \quad (3)$$

$$\text{SUNSET-NE} = \text{Time of Sunset} - 40 \text{ minutes} - \text{Correction}, \quad (4)$$

where all units are defined in minutes. Note: a positive Correction term brings the time further from sunrise (sunset); a negative Correction value shortens the time from sunrise (sunset).

TABLE 1. SUNRISE-NE AND SUNSET-NE CORRECTION CURVE COEFFICIENTS.

<u>SUNRISE-NE Coefficients</u>		<u>SUNSET-NE Coefficients</u>	
$a_0 = 3.60$		$a_0 = 6.36$	
$a_1 = 3.83$	$b_1 = 1.86$	$a_1 = 6.48$	$b_1 = 1.46$
$a_2 = 6.04$	$b_2 = 7.72$	$a_2 = 7.60$	$b_2 = 8.96$
$a_3 = 0.217$	$b_3 = 0.358$	$a_3 = 0.768$	$b_3 = -0.512$
$a_4 = -0.798$	$b_4 = 0.150$	$a_4 = -0.348$	$b_4 = -0.950$
$a_5 = 0.0714$	$b_5 = -0.221$	$a_5 = 0.377$	$b_5 = -1.61$
$a_6 = 0.138$		$a_6 = -0.234$	

4. SUMMARY OF NE FORECASTING TOOLS

Much of forecasting involves recognizing and interpreting repeatable atmospheric patterns. AOT is primarily a function of heat flux. We have isolated three variables relating to the heat flux (sunrise/sunset, Delta-T, and insolation) and observed their relationship to the NE for a 15 month cycle, over a 1-km desert path. The Delta-T measurements verified the near-surface adiabatic conditions present during a NE. The NE-insolation values showed that the range of insolation magnitudes at the sunrise-NE were about twice those sampled at the sunset-NE. This observation was explained as a function of the sun's elevation.

One of the most useful forecasting tools gained from our NE study came from overlaying the sunrise (sunset) times, the NE times forecasted from the original NE equation, and the actual NE data. The maximum time differences separating the sunrise and NE were reported during the solstice months. Minimal time differences occurred during the months of the equinox. We theorize that the skewed diurnal heating-cooling of the solstice periods generate strong near-surface temperature inversions that delay the transition into the adiabatic atmosphere required for a NE. During the equinox, the heating-cooling cycle is nearly equal. Therefore, minimal time is needed for the day or night-time atmosphere to transition into an adiabatic environment.

While the original NE forecasting equation's fit to the actual NE was adequate, the NE data showed a definite oscillation about the original equation. The greatest excursion was about 20 minutes, or one-third of an hour. A correction curve was calculated based on a Fourier Waveform Analysis. Table 1 listed the coefficients for this curve. Assimilating this correction with the original formulas, the refined NE forecasting equations were defined.

5. RECOMMENDATIONS AND COMMENTS

Implementing the corrected-NE forecasting equations did significantly improve our NE forecasts. However, there is still a need to isolate and quantify the local forcing effects, such as changing cloud cover, soil moisture and irregular shadowing.

Finally, insolation over a desert terrain is considerably different from a forested region. A study examining the diurnal AOT patterns for a wooded mountainside would be most useful, especially for the stellar observatories.

ACKNOWLEDGEMENTS

A special thanks to J.Niehans for her persistent work as the data manager; R.Douglas for tenaciously pursuing the data processing, and special plots; C.Vaucher for his volunteered article critique.

REFERENCES

Tatarski, V.I., 1961. Wave Propagation in a Turbulent Medium. Dover Publications, Inc., New York, NY, 285 pp.

Vaucher, G. Tirrell, and R.W. Endlich, 1993. "Intercomparison of Simultaneous scintillometer Measurements over Four Unique Desert Terrain Paths." Eighth Symposium on Meteorological observations and Instrumentation, American Meteorological Society, Boston, MA.

Vaucher, G. T., and R.W. Endlich, in press. "Forecasting/Modeling the Atmospheric Optical Neutral Events over a Desert Environment." 1994 Battlefield Atmospheric Conference Proceedings, WSMR, NM.

THE NOAA BOULDER ATMOSPHERIC OBSERVATORY BOUNDARY LAYER STUDY - CLEAR AIR OR NOT?

J. Hines*, C. Riese**, F. Eaton*, W. Hatch*, S. McLaughlin**

* Army Research Laboratory
Battlefield Environment Directorate
White Sands Missile Range, NM 88002

** Radian Corporation
Electronics Division
Austin, TX 78728

ABSTRACT

The Army Research Laboratory (ARL) participated in a joint study at the Boulder Atmospheric Observatory (BAO) to study the stable and unstable boundary layer evolution. The primary participants included the NOAA Environmental Technology Laboratory, the Environmental Protection Agency, the ARL and Radian Corporation. The ARL FM-CW radar joined a variety of sodars, 915-MHz boundary layer profilers and in situ sensors mounted on the BAO 300 m tower. The study included the period from late March 1995 to early May 1995, but primarily focused on April 1995. Many different weather conditions were noted including snow, rain, and low and high winds. This paper discusses the general goals of the study, describes the FM-CW radar characteristics and operational settings, and presents a variety of unusual backscatter images depicting atmospheric clear air return (nocturnal layers / convective plumes / sheer zones under various wind conditions / etc). One example of the morning boundary layer evolution is presented -- concurrently measured by the tower sensors. These data will be used to interpret wind data sensed by the 915-MHz profiler and sodars, each with considerably larger sampling volumes than the high resolution of the FM-CW radar.

1. INTRODUCTION

The U.S. Environmental Protection Agency (EPA), in cooperation with the National Oceanic and Atmospheric Administration (NOAA), sponsored a Ground-Based Remote Sensor Characterization Study at the Boulder Atmospheric Observatory (BAO) near Erie, Colorado, during April 1995. The BAO is a 300-meter instrumented tower used as a ground-truth profile device for calibrating tower mounted in situ or ground-based remote sensors. During the test period, Radian Corporation provided the following remote sensors as part of the study:

- 915 MHZ Boundary Layer Radar Profiler,
- Phased Array Sodar,

- Fixed-Beam Sodar.

The Army Research Laboratory (ARL) Battlefield Environment Directorate located at White Sands Missile Range (WSMR), New Mexico, supported through an existing Cooperative Research and Development Agreement with Radian Corporation, provided the following unique instrument:

- 2.9-GHz FM-CW Boundary Layer Radar.

These instruments typically operate in a variety of temporal and spatial sampling modes. Their sampling geometries were configured to overlap the BAO tower instrumental heights during the study. All of the remote sensing instruments acquired both Doppler wind profile data and vertical temperature structure or virtual temperature profiles with the exception of the FM-CW radar which was operated continuously in a non-Doppler high-resolution backscatter mode.

This paper discusses the general goals of the study, describes the excellent agreement among these various instruments and the BAO tower using traditional comparative graphic plots and tables, summarizes the FM-CW radar characteristics and operational settings, and presents a variety of unusual backscatter images depicting atmospheric clear air return (nocturnal layers / convective plumes / sheer zones under various wind conditions / etc). Data were collected at the BAO site continuously over the study period. The variety of synoptic weather features and diurnal inversion cycles during the study period made the comparisons particularly useful for objective data comparison analyses.

2. STUDY GOALS

Ever since the idea of remote sensing came to the attention of atmospheric scientists and modelers, the potential for more frequent observations in time sparked interest in making this capability a legitimate extension to traditional in situ systems. Remote sensing technology has matured significantly from its earlier experimental days to current off-the-shelf availability. This maturity and ready availability has spawned many new applications and demands for extended capabilities.

For several years now, the atmospheric modeling and regulatory community has been at a point where serious consideration is being placed on applying remote sensing for use in EPA field programs. A key objective of this study is to define the rules by which such data is collected for use in composing effective field implementation plans and in the formulation of upper air data requirements. The results presented herein will not affect the EPA guidance and regulations in the immediate future but do offer encouraging comparative data results for the interested community.

The ARL FM-CW Radar was deployed at the NOAA BAO facility to monitor 1) mixing/boundary layer development and 2) insect/bird presence in the test volume. The FM-CW radar, used as the reference backscatter instrument, helped define the high spatial resolution structure of the atmosphere above the BAO.

The upper-air remote-sensing data, of the type acquired by the instruments described in this paper,

are directly applicable to national and international strategies to understand and influence ambient air quality. The twice-per-day NWS upper air soundings lack both the temporal and spatial resolution required for contemporary pollution transport models such as the widely-used Urban Airshed Model. Air diagnostic models, and analysts, now require hourly inversion height data as well as wind and temperature profiles within the atmosphere's boundary layer.

3. WIND DATA COMPARISONS

Pulsed Doppler remote sensing instruments, such as sodars and radar wind profilers, measure the wind flow above the instrument in discrete layers, or volumes of air. These type of instruments transmit a fixed frequency acoustic or radio frequency signals, respectively, vertically into the atmosphere, then listen for the faint reflections back to the antenna. The Doppler shift is computed along each beam and converted to equivalent radial speeds. By using a mix of vertical and three-or-more oblique beams' speeds, wind profiles are computed by simple trigonometry. During this process, weak returns, noise, and interference can either confuse the Doppler computations or make them erroneous. To overcome these problems, many samples are taken during the measurement period, and a final average is computed using only accepted individual samples.

Typical parameters for a boundary layer wind profiler, a mid-range sodar, and the FM-CW radar are shown in Table 1. The sodar which provides higher resolution sampling below

TABLE 1. Typical Sodar, Boundary Layer Wind Profiler (BLWP), and FM-CW Parameters

Parameter	Sodar	BLWP	FM-CW
Operating Frequency	2 kHz	915 MHz	2.9 MHz
Wavelength	0.17 m	0.33 m	0.01 m
Minimum Sampling Height	20-50 m	80-150 m	50-100 m
Maximum Sampling Height	400-800 m ¹	2-6 km ¹	1-10 km ²
Range Resolution	10-40 m	60-400 m	1-10 m ³
Temporal Resolution	5-15 min	15-60 min	10-12 s ⁴

¹ - Depends on atmospheric conditions

² - Hardware adjustable

³ - Dependant on maximum range selected

⁴ - Per cycle including processing / presentation

600 m covers the lower boundary layer. To get a complete picture of the boundary layer, particularly during convective afternoons where its reach goes beyond the reach of sodars, the higher range

boundary layer radar profiler is a more suitable tool.

Simultaneous wind measurements at 200 meters by two sodars, a wind profiler, and tower-mounted sensors are shown in Figure 1. The sodars and the tower are sampled at 15-min intervals, while the wind profiler was sampled at 30-min intervals. The conditions were light and variable during the morning, with strong steady winds in the afternoon. Just before noon, when the mean wind speed was below 2 m/s, the wind direction measurements fluctuated considerably as would be expected. The stronger winds measured in the middle afternoon period showed less direction scatter and the different remote sensors agreed closely with each other and with the tower.

Riese, et al., (1996) presents the individual correlation comparisons between each of the three remote wind sensing instruments and the BAO tower sensors at the 200 m level. The noted off-line variations are attributed to the different measurement techniques used by the instruments, i.e., the remote sensors measure the average winds within a *large scattering volume*, while the in situ sensors on the BAO tower measure the average winds at a *point*.

4. TURBULENCE DATA

The ARL FM-CW Radar was deployed at the NOAA BAO facility to support the EPA-sponsored program specifically to monitor 1) mixing/boundary layer development and 2) insect/bird presence in the test volume. The FM-CW radar, used as the reference backscatter instrument, defined the high spatial resolution structure of the atmosphere above the BAO.

The FM-CW radar is unique in its ability to generate high resolution backscatter profiles in a very short period of time. A typical backscatter profile is produced with a range resolution of less than 4 m from near ground to 4 km approximately every 10 s. Other range resolutions were evaluated during the study including 1, 2, and 8 m. Unlike conventional pulsed-type clear-air weather radars/profilers that transmit pulses of radio frequency energy and use time modulation, the FM-CW radar uses the frequency-modulated, continuous-wave (FM-CW) transmission technique. Three important characteristics of the FM-CW technique are thus realized: 1) close-in range; 2) very high range resolution; and 3) high levels of transmitted power due to nearly 100% duty cycle.

The FM-CW radar uses two large diameter antennas simultaneously, one for transmitting and one for receiving. The transmitted signal, centered at 2.9-GHz, is frequency-modulated ± 100 -MHz over 50 ms in a sawtooth waveform. After being scattered by the atmospheric turbulence (weighted heavily by humidity flux) and gathered by the receiving antenna, the returned signal is mixed with a slightly delayed sample of the transmitted signal. At this point in the returned signal, the range data is now proportional to frequency. After further filtering and digitizing, a Fast-Fourier-Transform (FFT) is performed to "decode" the modulation and calculate the amplitude of returned atmospheric backscatter per FFT point (or range cell). This technique, with its high temporal and spatial resolution, yields almost picture-like images of the lower atmosphere turbulence structure. Eaton, et al., (1995) provides FM-CW specifications and examples of sensed meteorological phenomena. The FM-CW radar is shown in Figure 2 in its normal operational configuration at WSMR, NM.

The high resolution FM-CW radar results provide excellent insight into the volume filling problem when using lower resolution pulsed radars. Without concurrent FM-CW radar results, it cannot be determined which part of the sensed volume (of pulsed radar results) is contributing to the backscatter and associated derived wind information. Particularly if a strong contribution is found near the bottom or top of the sensed volume, significant errors in wind measurements are possible.

A zoomed view of FM-CW radar atmospheric turbulence data on April 27, 1995, is shown in Figure 3. This period shows a clear-air return void of insects, birds, and rainfall and shows the nighttime boundary layer beginning to lift in the early morning as the ground begins to heat the lower boundary layer. As a point of interest, same-time sodar wind profiles are shown in Figure 4 with a line representing the top edge of the turbulence boundary of Figure 4. Note the wind direction change from the nighttime synoptic flow above the boundary to drainage flow from the Rockies under the rising boundary.

Figures 5-10 provide additional examples of boundary layer phenomena as detected by the FM-CW radar.

5. SUMMARY

Preliminary study results show good agreement between the remote wind sensors and the BAO tower instrumentation. Several examples of clear-air radar backscatter, some showing multiple low level structures and the presence of insects and birds, suggest that the local atmosphere was certainly not clear at radar wavelengths as opposed to visible wavelengths.

LITERATURE CITED

Eaton, F. D., S. A. McLaughlin, J. R. Hines, 1995. "A New Frequency-modulated Continuous-Wave Radar for Studying Planetary Boundary Layer Morphology", *Radio Science*, Vol 30, No. 1, pp 75-88.

Riese, C., F. Eaton, L. Best, J. Hines, R. Peterman, S. McLaughlin, 1996. "Multi-Instrument Remote Sensor Characterization Study", Submitted to the Ninth Joint Conference on the Applications of Air Pollution Meteorology with the Air and Waste Management Association, AMS Committee on Meteorological Aspects of Air Pollution, 28 January-2 February 1996, Atlanta, Georgia.

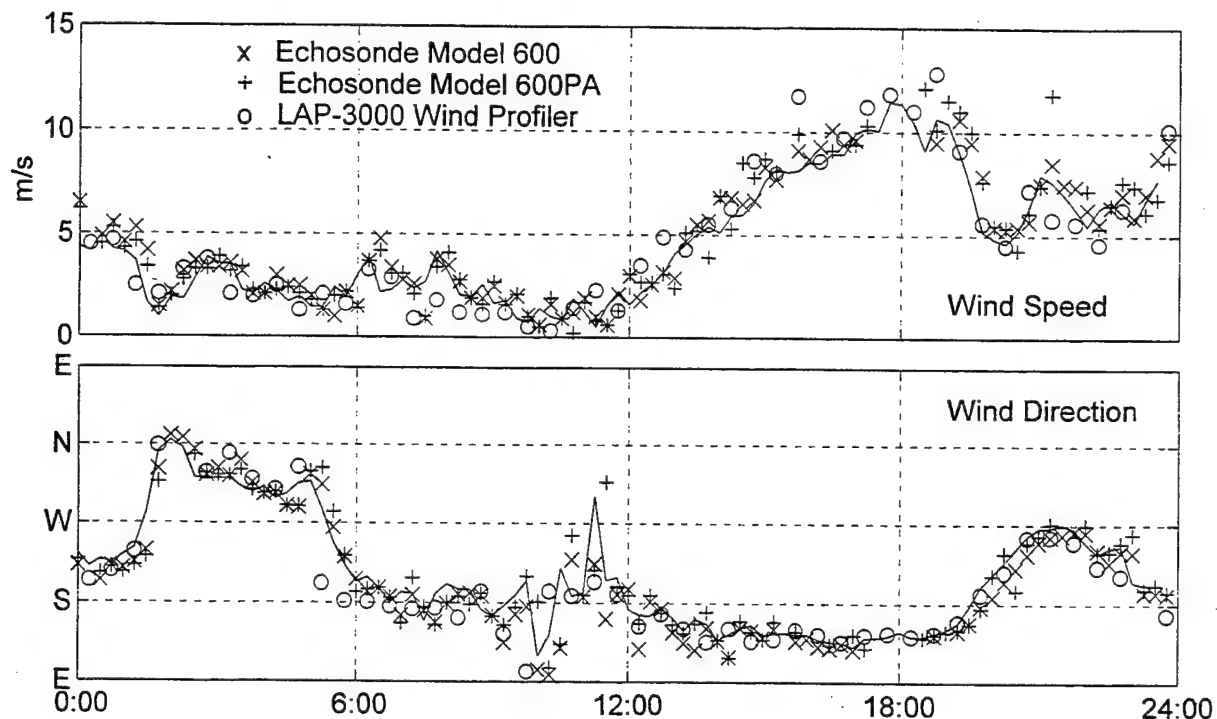


Figure 1. Overlay of remotely sensed data points on BAO tower in situ sensors (solid line) for 17 April 1995. Time is MST.

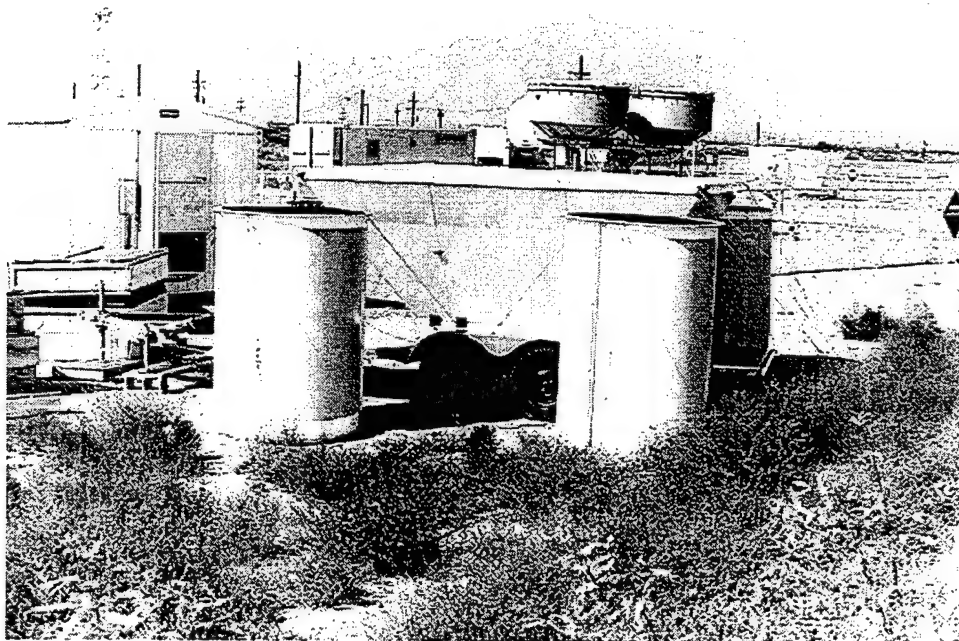


Figure 2. FM-CW Radar, WSMR (view toward the west with the 924-MHz wind profiler in the foreground and the Organ Mountains in the background).

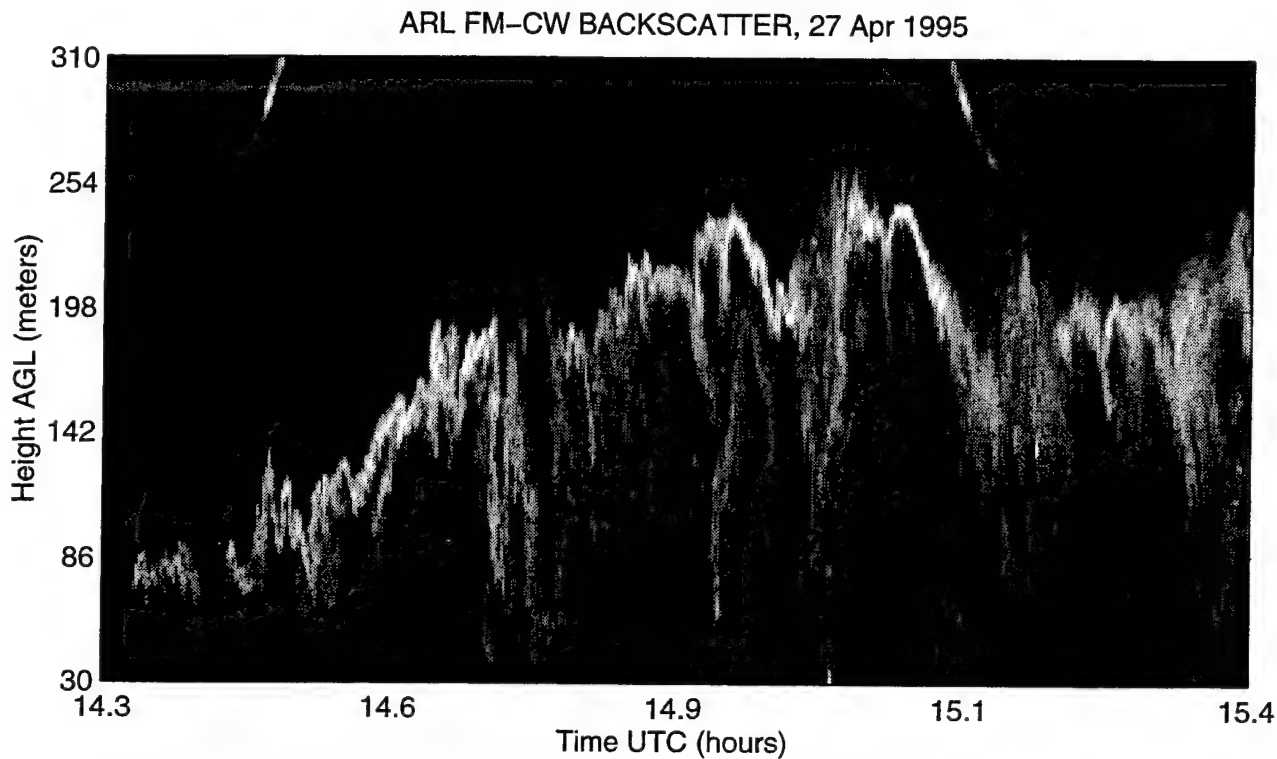


Figure 3. FM-CW radar backscatter data showing morning boundary layer on 27 April 1995.

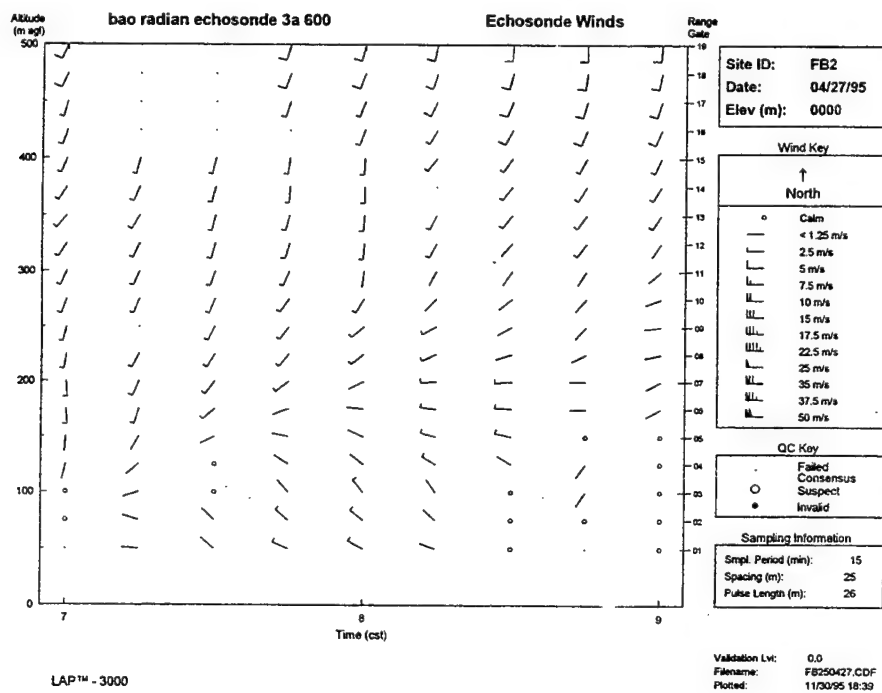


Figure 4. Sodar wind profile for same period as shown in figure 3.

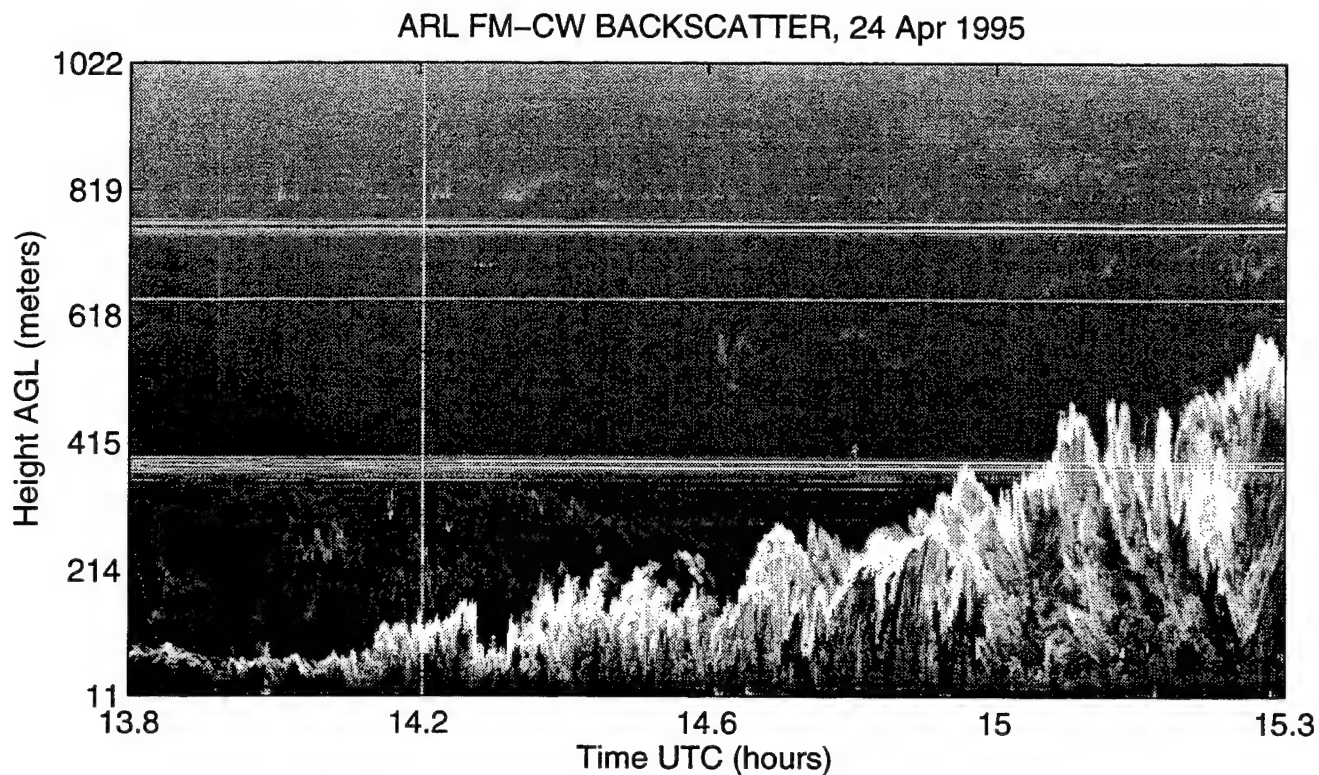


Figure 5. Example of early morning transition on 24 April 1995.

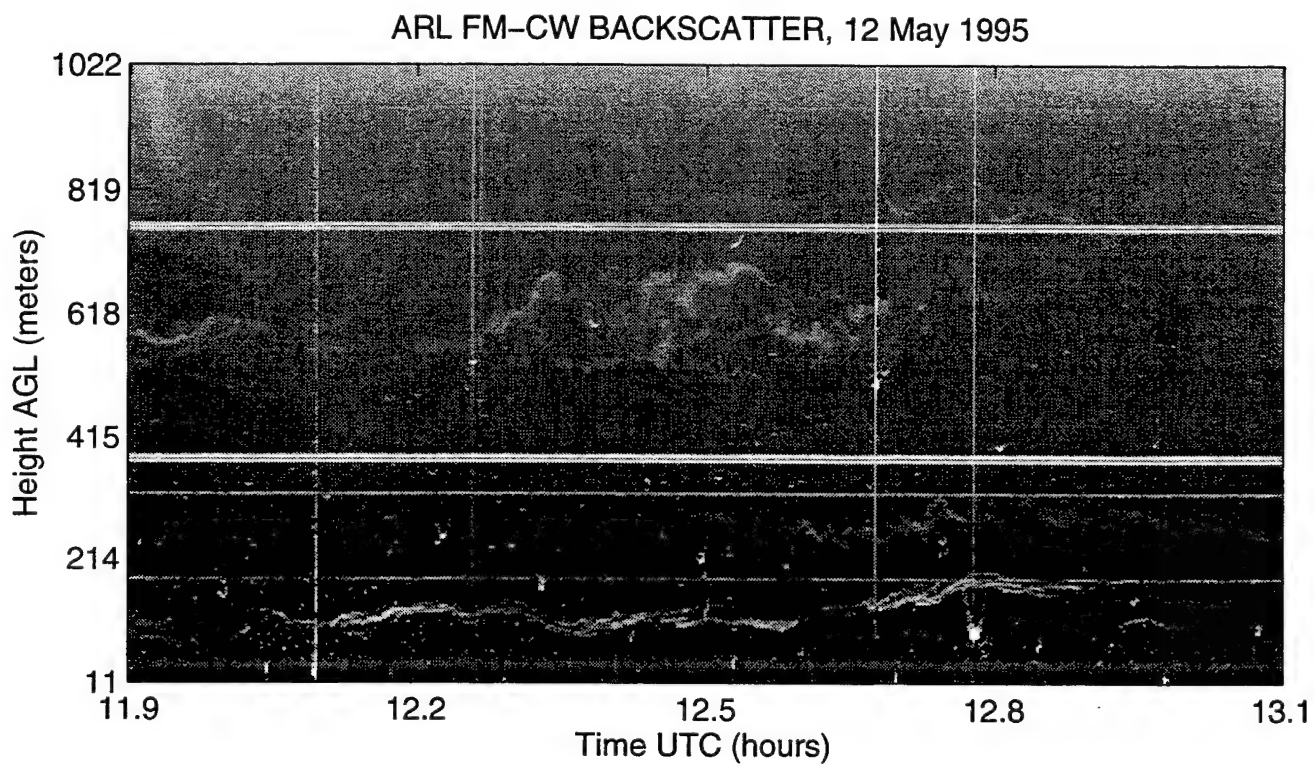


Figure 6. Example of stable layer during nocturnal boundary layer on 12 May 1995.

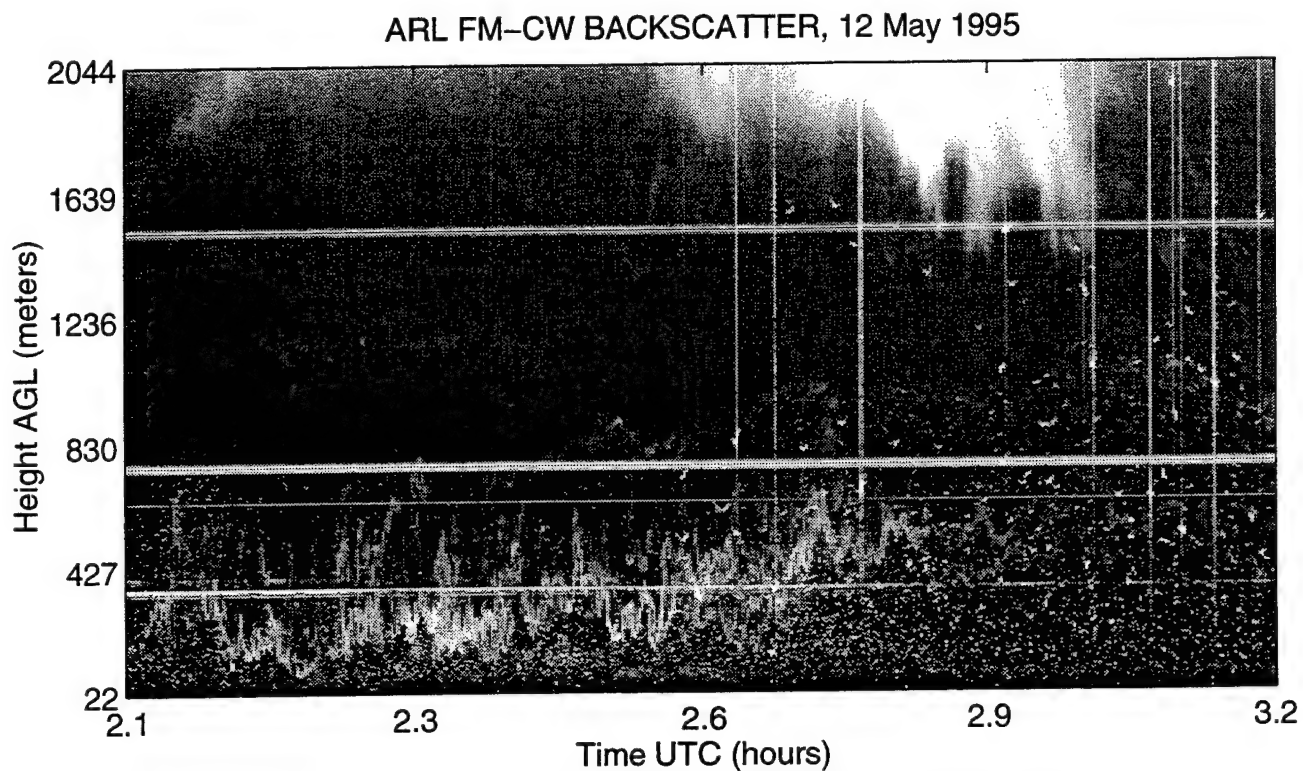


Figure 7. Example of onset of nocturnal insect flight with virga on 12 May 1995.

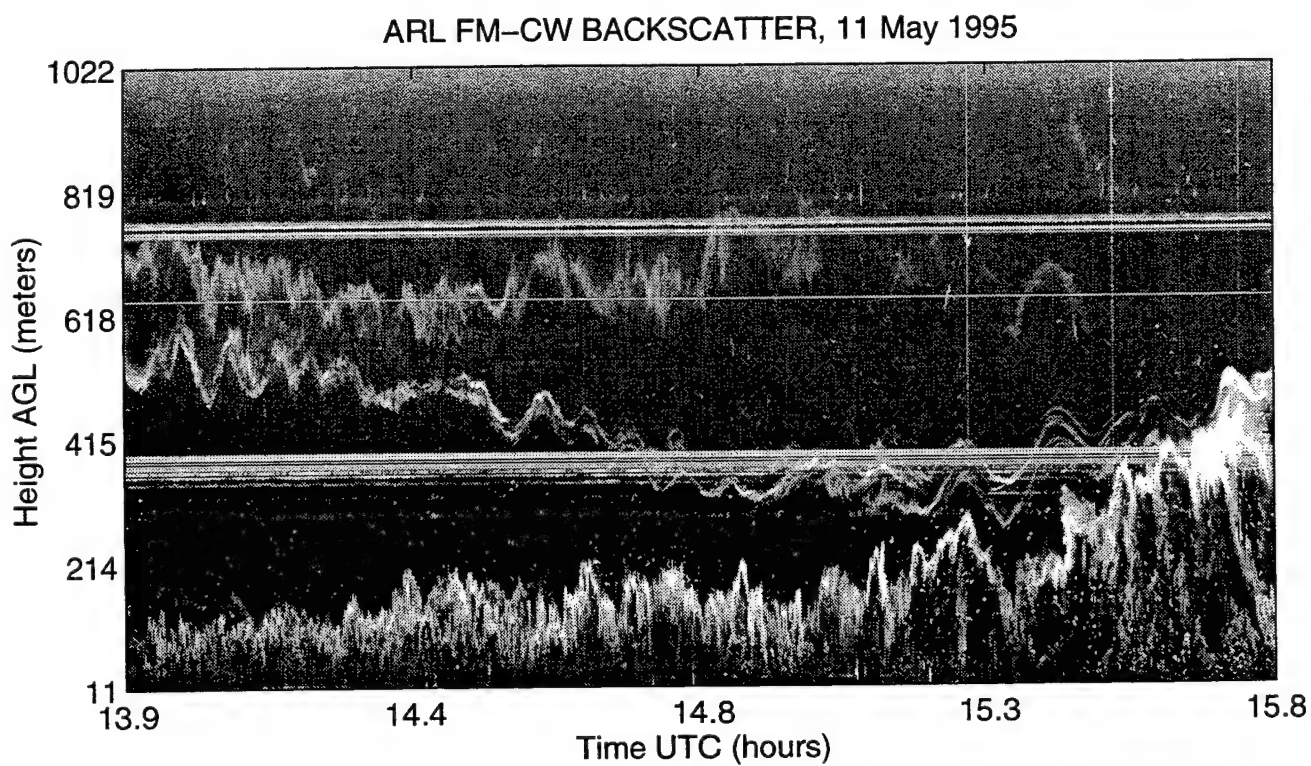


Figure 8. Example of early morning transition zone with upper level laminated structures on 11 May 1995.

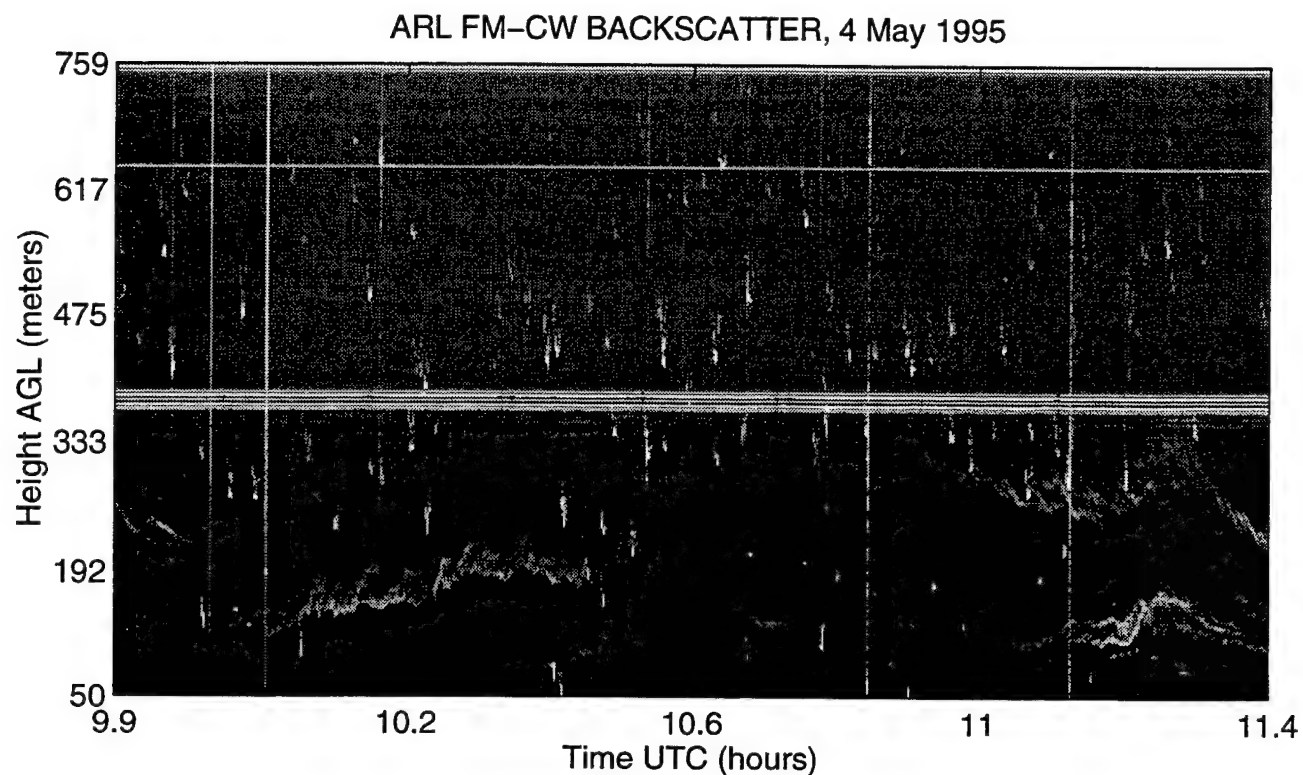


Figure 9. Example of nocturnal wave activity with bats or nocturnal birds on 4 May 1995.

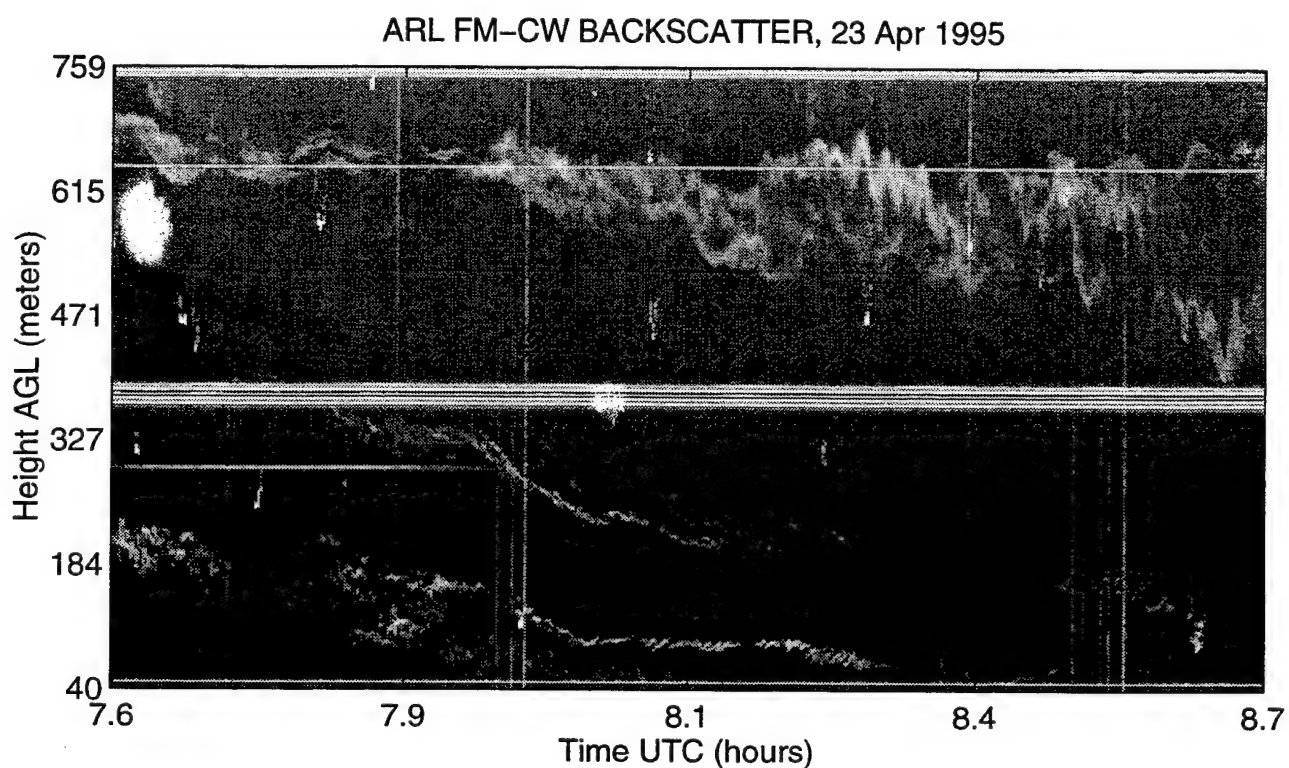


Figure 10. Example of nocturnal waves at several heights on 23 April 1995.

MODELLING AND MEASUREMENTS OF ATMOSPHERIC TURBULENCE OVER LAND

D. L. Hutt

Defence Research Establishment Valcartier
P.O. Box 8800 Courcellette, Québec, Canada, G0A 1R0

D. Stryckman

Dep. Physique, Université Laval
Ste. Foy, Québec, Canada, G1K 7P4

ABSTRACT

We present a simple model for the structure constant of atmospheric refractive index fluctuations (C_n^2) and inner scale (ℓ_0) valid in the lowest few hundred meters above land. The inputs to the model are standard meteorological parameters plus solar irradiance and parameters characteristic of the local terrain. Results are compared with measurements of C_n^2 and ℓ_0 made with a displaced-beam scintillometer.

1. INTRODUCTION

Electro-optical (EO) systems depend on the propagation of light over large distances and are thus susceptible to the influence of optical turbulence. The turbulent atmosphere causes the intensity of a light beam to fluctuate or scintillate, causes beam wander and causes the distortion and random displacement of images. Predictions of the refractive index structure parameter C_n^2 and the inner scale ℓ_0 , the most important parameters which characterize the optical effects of atmospheric turbulence, can be used to predict and optimize the performance of EO systems.

We present a simple model of atmospheric turbulence based on the Monin-Obukhov similarity theory (Monin, Obukhov 1954, Wyngaard, 1973) as interpreted by Thiermann and Kohnle (1988, 1989) and Thiermann and Grassl (1992). The model provides profiles of C_n^2 and ℓ_0 using standard meteorological parameters as inputs. Model results are compared with measurements of C_n^2 and ℓ_0 made with a displaced-beam scintillometer installed in a field. The scintillometer provided the path averaged values of C_n^2 and ℓ_0 over a 185 m path at a height of 1.8 m.

2. OPTICAL TURBULENCE

When light propagates through turbulent air, it encounters inhomogeneities in the refractive index that transform its phase front. The inhomogeneities are caused by the mixing of air of different temperature by wind and convection. Near the ground, the intensity of temperature fluctuations depends on the type of ground cover, ambient temperature, solar irradiation and wind speed. The optical effects of atmospheric turbulence may be characterized in terms of the refractive index structure parameter C_n^2 and the inner scale ℓ_0 .

C_n^2 is a measure of the intensity of the refractive index fluctuations. For homogeneous and isotropic turbulence it is defined as (Smith 1993)

$$C_n^2 = \frac{\langle [n(\tilde{r}_1) - n(\tilde{r}_2)]^2 \rangle}{|\tilde{r}_1 - \tilde{r}_2|^{2/3}}, \quad (1)$$

where n is the index of refraction at points \tilde{r}_1 and \tilde{r}_2 . In SI units (used through this paper), C_n^2 has the dimensions of $m^{-2/3}$ and varies from about $10^{-16} m^{-2/3}$ to $10^{-12} m^{-2/3}$ in the boundary layer. Equation 1 is valid for distances $|\tilde{r}_1 - \tilde{r}_2|$ within the bounds of the inertial subrange. C_n^2 is expressed in terms of the fluctuations in air temperature by (Smith 1993)

$$C_n^2 = \left(\frac{79P}{T^2} \times 10^{-6} \right)^2 C_T^2, \quad (2)$$

where C_T^2 ($K^2 m^{-2/3}$) is the temperature structure parameter, P is the air pressure in hPa (or millibars) and T is the ambient temperature in degrees K.

The inner scale ℓ_0 (m) marks the lower limit of the inertial subrange. In the boundary layer ℓ_0 is of the order of millimeters. ℓ_0 is given by (Thiermann, Grassl 1992)

$$\ell_0 = 7.4 \nu^{3/4} \epsilon^{-1/4}, \quad (3)$$

where ν is the kinematic viscosity of air ($1.46 \times 10^{-5} m^2/s$ at STP) and ϵ (m^2/s^3) is the dissipation rate of turbulent kinetic energy. C_T^2 and ϵ are provided by the model and Eqs. 2 and 3 are then used to calculate C_n^2 and ℓ_0 .

3. TURBULENCE MODEL

The solutions for C_T^2 and ϵ are expressed in terms of the friction velocity u_* (m/s), the turbulent temperature scale T_* (K) and the Monin-Obuhkov length L (m). u_* , T_* and L are scaling parameters defined as (Thiermann, Kohnle 1988, 1989)

$$u_* = uk \left[\ln \left(\frac{z_u}{z_o} \right) - \psi(L) \right]^{-1} \quad (4)$$

$$T_* = -\frac{Q_o}{u_*} \quad (5)$$

$$L = -\frac{u_*^2 T}{kgT_*} \quad (6)$$

In Eqs. 4 to 6, u (m/s) is the wind velocity measured at height z_u (m) above the ground, z_o (m) is the roughness length of the ground surface, Q_o (Km/s) is the vertical turbulent kinematic heat flux, T is the air temperature measured at height z_u , k (dimensionless) is the Von Karman constant taken to be equal to 0.35 and g is the acceleration of gravity ($9.81 m/s^2$).

Derivation of the scaling parameters depends upon the form of $\psi(L)$ which is chosen according to whether the conditions are stable (air warmer than the ground) or unstable (air colder than the ground). The $\psi(L)$ are given by (Thiermann, Kohnle 1989; Businger et al. 1973)

$$\psi(L) = -4.7z_u/L \quad z_u/L > 0, \text{ stable} \quad (7)$$

$$\psi(L) = 2\ln\left(\frac{1+y}{2}\right) + \ln\left(\frac{1+y^2}{2}\right) - 2\tan^{-1}y + \frac{\pi}{2} \quad z_u/L < 0, \text{ unstable} \quad (8)$$

where $y = (1 - 15z_u/L)^{1/4}$.

During the day Q_o is estimated by (Thiermann, Kohnle 1989; Holtslag, Van Ulden 1983)

$$Q_o = \frac{\eta}{c_p \rho} \left\{ \left(1 - \frac{\alpha}{1 + \gamma/s} \right) (1 - A) R - \beta \right\} \quad (9)$$

where η (dimensionless) is an empirical constant equal to 0.9, c_p (J/kg/K) is the specific heat of air, ρ (kg/m³) is the density of air, α (dimensionless) is a parameter between 0 and 1 that represents the humidity of the ground, γ is the ratio of the specific heat of air at constant pressure to the latent heat of water vapor, s is the temperature derivative of saturation specific humidity. The dimensionless ratio γ/s is a function of temperature only and is tabulated in Holtslag and Van Ulden (1983). A (dimensionless) is the surface albedo, R (W/m²) is the solar irradiance and β is an empirical constant which we have set equal to 35 W/m².

Equation 9 describes how the solar irradiance is partitioned at the ground leaving a component that contributes to the sensible heat flux. The factor $(1-A)R$ is the fraction of solar irradiance absorbed by the ground. Part of this power is dissipated by infrared radiation and ground conduction. This loss is accounted for by the factor η and offset β . The remaining power gives rise to both sensible and latent heat fluxes. The latent heat flux is due to both evaporation at the ground surface and transpiration by vegetation. The fraction of power available for sensible heat flux is determined by the factor $1 - \alpha/(1 + \gamma/s)$. According to Holtslag and Van Ulden (1983) $\alpha \approx 1$ is an appropriate value for grass covered land as is the case at our location. For dry areas without vegetation (desert), $\alpha \approx 0$. For $\alpha = 1$ at a temperature of 25 C, $1 - \alpha/(1 + \gamma/s) = 0.26$ which means that only just over one quarter of the available solar irradiance is transformed into heat flux.

The night time kinematic heat flux is difficult to estimate because it does not depend on one dominant factor as is the case with solar irradiance for the daytime heat flux. The phenomena on which the night time heat flux depends; radiative cooling of the ground, thermal conduction losses and latent cooling or heating due to evaporation or formation of dew, may all have similar importance. Not only is the interaction of these parameters complex but information regarding them would be too specialized for a practical model. To estimate the night time heat flux (Thiermann, Kohnle 1989), developed an expression which depends on the one parameter that is both important and readily available, the wind speed u :

$$Q_o = \frac{cu^3}{1 + \frac{c}{Q_{o\max}}u^3} \quad (10)$$

where $c = \frac{-4}{27} \cdot \frac{k^2 T}{5gz_u (\ln(z_u/z_o))^2}$.

The structure of Eq. 10 ensures that Q_0 does not diverge at high wind speed but increases asymptotically to a saturation value Q_{0max} . This saturation value is given by $Q_{0max} = H_{max}/c_p \rho$ where the sensible heat flux H_{max} is chosen to be between -5 to -100 W/m². The most appropriate value of H_{max} depends on local vegetation, ground characteristics, air humidity and cloud cover. For our location we set $H_{max} = -12$ W/m².

Since L cannot be written as an explicit function of ψ , an iterative procedure must be used to find mutually consistent solutions u_* and L to Eqs. 4 to 6. Following Holstag and Van Ulden (1983), an initial guess for u_* is found by evaluating Eq. 4 with $\psi(L)=0$. L is then estimated by using the initial u_* in Eq. 6. u_* is then reevaluated using L with $\psi(L)$ given by Eqs. 7 or 8, thus beginning a cycle where subsequent values of u_* are compared to the previous one until they are within 0.5% of each other. Typically three to ten iterations are required to determine u_* and L .

The decision as to whether conditions are stable or unstable is based on the value of the daytime heat flux Q_0 given by Eq. 9. If the daytime Q_0 is positive then conditions are assumed to be unstable and Eq. 8 is used to derive L . If the daytime Q_0 is negative then conditions are assumed to be unstable, the night time heat flux is calculated using Eq. 10, and Eq. 7 is used to calculate L .

Once the scaling parameters are determined, the vertical profiles of C_T^2 and ϵ are given by (Thiermann, Grassl 1992)

$$C_T^2 = 4\beta \frac{T_*^2}{(kz)^{2/3}} \left[1 + 7\frac{z}{L} + 20\left(\frac{z}{L}\right)^2 \right]^{1/3} \quad (11)$$

$$\epsilon = \frac{u_*^3}{kz} \left[1 + 4\frac{z}{L} + 16\left(\frac{z}{L}\right)^2 \right]^{1/2} \quad (12)$$

for the stable case ($z/L > 0$) and by

$$C_T^2 = 4\beta \frac{T_*^2}{(kz)^{2/3}} \left[1 - 7\frac{z}{L} + 75\left(\frac{z}{L}\right)^2 \right]^{-1/3} \quad (13)$$

$$\epsilon = \frac{u_*^3}{kz} \left[\left(1 - 3\frac{z}{L} \right)^{-1} - \frac{z}{L} \right] \quad (14)$$

for the unstable case ($z/L < 0$). the parameters C_n^2 and ℓ_0 of interest here are then found substituting C_T^2 and ϵ into Eqs. 2 and 3.

A multitude of physical quantities are required in the calculations. The specific heat of air c_p is taken to be a constant equal to 1004.6 J/kg/K (Stull, 1988). The density of dry air ρ , the ratio γ/s and the kinematic viscosity of air ν are given in following formulae where temperature T is in degrees C:

$$\rho \text{ (kg/m}^3\text{)} = 1.286 - 0.00405T \quad (15)$$

$$\gamma/s = 1.4631 - 0.0923T + 0.0027T^2 - 3.18 \times 10^{-5}T^3 \quad (16)$$

$$\nu \text{ (m}^2\text{/s)} = \left(\frac{1.718 + 0.0049T}{\rho} \right) \times 10^{-5} \quad (17)$$

Equation 15 is derived from Annex C of Stull (1988), Eq. 16 is a least squares fit to data tabulated in Holtslag and Van Ulden (1983) and Eq. 17 is from Annex C of Stull (1988). The roughness length z_0 chosen to represent our location was 0.02 m based on estimated values listed in Holtslag and Van Ulden (1983). The ground humidity parameter α was set at 1. The value of ground albedo A used is 0.2 based on measurements made with a commercial albedometer and is a typical value for grass covered land according to Holtslag and Van Ulden (1983). For the purposes of comparing the model to measured turbulence, we have measured the solar irradiance R . However R may be easily estimated on the basis of geographic location, time of day and cloud cover. An algorithm is given in Chap. 7 of Stull (1988).

4. TURBULENCE MEASUREMENTS

The experiments were performed at the Defence Research Establishment Valcartier (DREV) in July and August, 1995. The site was a level grass covered field with sandy soil. The site was about 300 m across, surrounded by pine trees on the West side and by low buildings on the East. The scintillometer transmitters and receiver were housed in small instrument sheds with a propagation path of 185 m. The path was 1.8 m above the ground and oriented North-South with prevailing winds coming from the West.

The Scintec SLS-20 scintillometer, used to measure C_n^2 and ℓ_0 , is described in detail in Thiermann (1992). The SLS-20 uses the independently measured scintillation of two displaced but parallel laser beams to derive the turbulence parameters. The source is a 1 mW laser diode with a wavelength of 670 nm and divergence of approximately 5 mrad. The beam displacement of 2.7 mm is achieved by passing the beam through a birefringent calcite crystal which splits the beam into displaced but parallel components with crossed polarizations. At the receiver the two overlapping beams are resolved by a polarizing beam splitter allowing the scintillation of each beam to be measured independently by two 2.5 mm diameter detectors. The transmitted laser beams are modulated at 20 kHz to allow AC coupling at the detectors which eliminates the background. The calculations to derive C_n^2 and ℓ_0 are carried out in real time by the instruments laptop computer which also derives C_T^2 , the kinetic energy dissipation rate, the turbulent fluxes of sensible heat and momentum, and the Monin-Obukhov length using the expressions of Sec. 2. A calibration was carried out for the 185 m path length according to the manufacturer's instructions.

Meteorological conditions were monitored simultaneously near the receiver station using standard sensors for wind speed, wind direction, barometric pressure, solar irradiation air temperature and dew point temperature. The ground albedo was also measured with an albedometer. The wind measurements were made at a height of 3.0 m. The meteorological data was recorded using the SLS-20 analog input channels.

5. COMPARISON OF MODEL AND MEASUREMENTS

Figure 1 shows measurements during a four day period from midnight local time Aug. 23 to midnight Aug. 27, 1995. The first day was overcast with subsequent days mostly clear as indicated by the solar irradiance curve (a). Wind speed (b) and relative humidity (c) exhibit diurnal cycles with wind usually less than 3 m/s at night and between 3 and 8 m/s during the day. Humidity was often 100% at night and always less than 75% during the day. No record was kept of the cloud conditions at night.

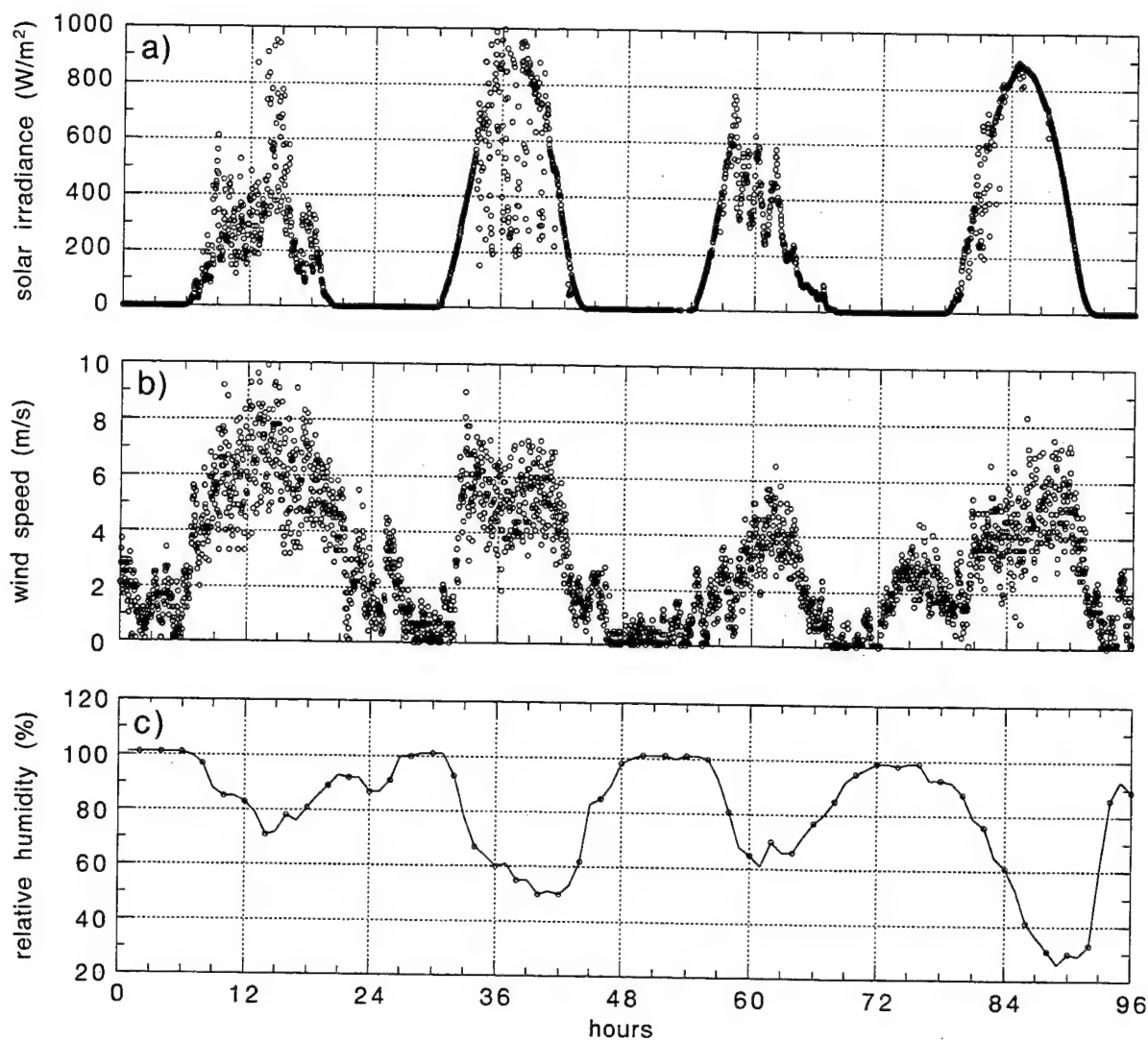


Figure 1. Measurements from midnight Aug. 23 to midnight Aug. 27, 1995: solar irradiance (a), wind speed at 3 m height (b) and one hour averages of relative humidity (c).

Measurements of C_n^2 and model calculations are shown in Figs. 2 (a) and (b). The calculated C_n^2 follows closely the measured data for daytime periods. At night the agreement between measured and modelled C_n^2 , although reasonably good, is poorer than during the day due to the approximate method of determining the night time heat flux based on the wind speed (Eq. 10). Gaps in the night time model results occur when the wind speed is less than 0.5 m/s. Below this value, calculations were not performed to avoid inherent instabilities for near neutral conditions.

Measurements and model calculations of ℓ_0 are shown in Figs. 3 (a) and (b). The relatively large values of ℓ_0 during calm night periods and small values during windy day conditions is typical. Agreement between the measurements and model is generally good, being somewhat better during the day. That the model is better able to represent night time ℓ_0 than C_n^2 is consistent with an analysis by Thiermann and Kohnle (1989) of the sensitivity of the similarity equations to input errors. They showed that C_T^2 , and hence C_n^2 , is ten times more sensitive to errors in input Q_0 than ℓ_0 is.

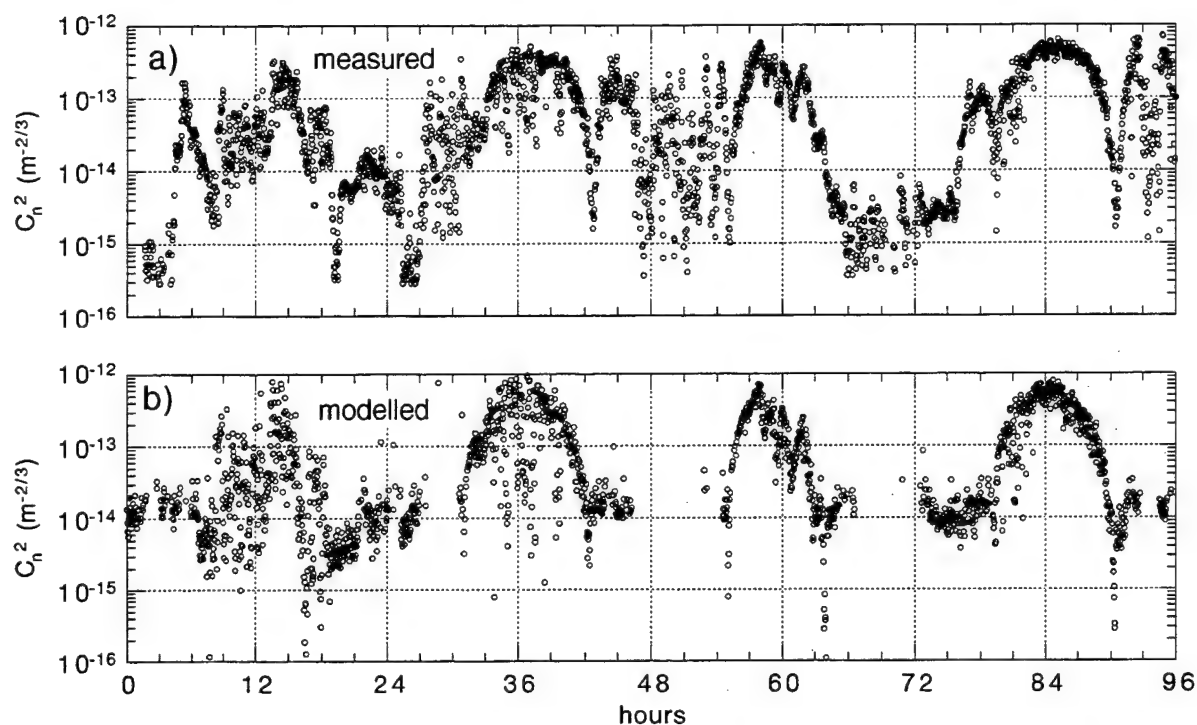


Figure 2. C_n^2 measured with SLS-20 scintillometer at 1.8 m height (a) and modelled C_n^2 (b).

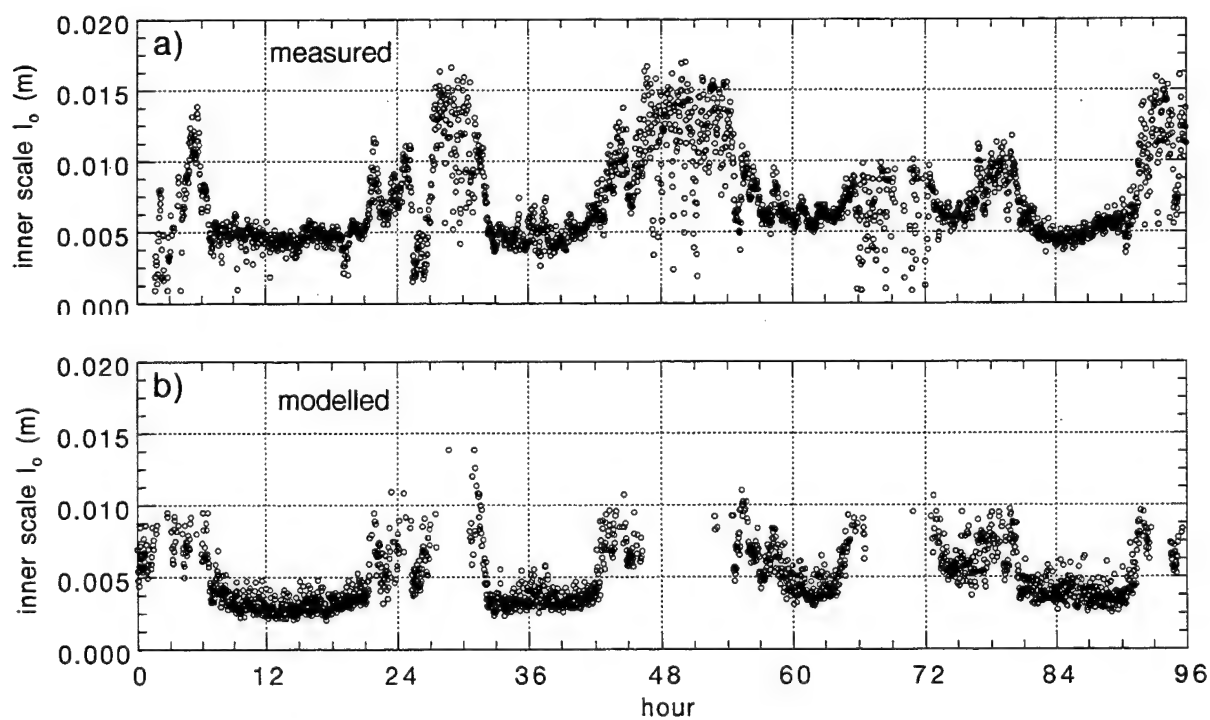


Figure 3. Measured and modelled inner scale l_0 .

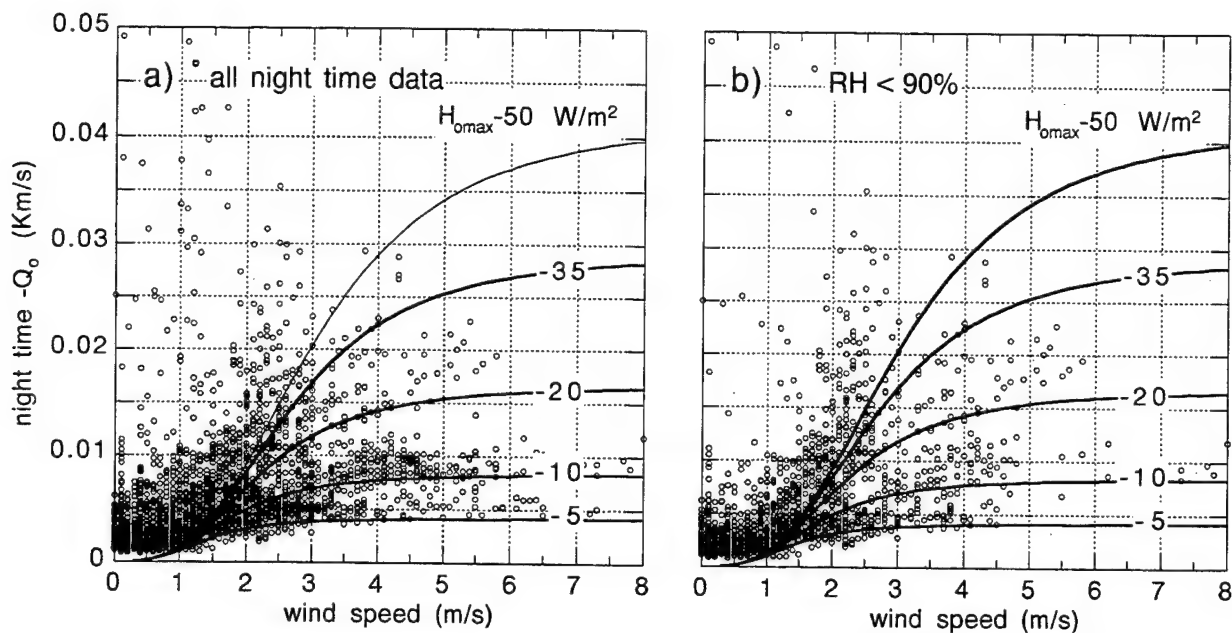


Figure 4. Nocturnal kinematic heat flux measured with the SLS-20 scintillometer as a function of wind speed. Equation 10 is plotted for several values of saturation heat flux H_{omax} .

The main reason that the modelled turbulence parameters are in poorer agreement with the measurements at night is because the night time heat flux estimated with Eq. 10 is not as accurate as the daytime estimates made with Eq. 9. Figure 4 (a) shows the kinematic heat flux measured with the scintillometer as a function of wind speed. The curves are Eq. 10 plotted for various values of saturation heat flux H_{omax} . For our calculations we set $H_{omax} = -12 \text{ W/m}^2$. The scatter of the data points shows that the nocturnal Q_0 has only a vague wind speed dependence under the conditions of our measurements. It is likely that humidity effects play a role in generating heat flux which was not taken into account. The data indicates that periods of high C_n^2 at night coincided with 100% relative humidity, for example hours 48 to 54. Dew was usually observed in the mornings, evidence that latent heat was released during the night. Figure 4 (b) also shows the nocturnal Q_0 as a function of wind speed, but with data occurring with relative humidity greater than 90% removed. If formation of dew contributed to the measured Q_0 then we would expect that the wind speed dependence be more pronounced for data restricted to relatively dry air. However the Q_0 data of Fig. 4 (b) appears only slightly better correlated with wind speed compared to Fig. 4 (a).

CONCLUSIONS

We presented results from a simple model for the structure constant of atmospheric refractive index fluctuations (C_n^2) and inner scale (ℓ_0) valid in the lowest few hundred meters above land. The model is based on the Monin-Obukhov similarity theory (Monin, Obukhov 1954, Wyngaard, 1973). The model equations are from Thiermann and Kohnle (1988, 1989) and Thiermann and Grassl (1992). The required input parameters are solar irradiance, air temperature, wind speed, barometric pressure and terrain characteristics albedo, roughness length and humidity. Values of C_n^2 and ℓ_0 calculated with the model were in good agreement with measurements made with a

displaced-beam scintillometer installed in a field. The scintillometer provided the path averaged values of C_n^2 and ℓ_o over a 185 m path at a height of 1.8 m. The poorest agreement was observed during calm night periods of high humidity where the model failed to predict the high levels of C_n^2 measured by the scintillometer. It is believed that the release of latent heat at night during formation of dew contributes to the nocturnal heat flux, an effect that was not taken into account.

Predictions of C_n^2 and ℓ_o made with this model could be used to predict and optimize the performance of electro-optical systems which are susceptible to the scintillation, beam wander and image distortion caused by optical turbulence. Our next effort will be to apply the model to winter conditions with snow covered terrain.

REFERENCES

1. Monin, A. S. and A. M. Obukhov, 1954. "Basic laws of turbulent mixing near the ground." Tr. Akad. Nauk., SSSR Geophys. Inst., No. 24 (151), 1963-1987.
2. Wyngaard, J. C., 1973. "On surface layer turbulence." *Workshop on micrometeorology*, (Ed. D. A. Haugen). Am. Meteor. Soc. 101-148.
3. Thiermann, V. and A. Kohnle, 1988. "A simple model for the structure constant of temperature fluctuations in the lower atmosphere." J. Phys. 21, S37-S40.
4. Thiermann, V. and A. Kohnle, 1989. "Modelling of optically and IR effective atmospheric turbulence." AGARD CP-454, paper 19.
5. Thiermann, V. and H. Grassl, 1992. "The measurement of turbulent surface layer fluxes by use of bichromatic scintillation." *Boundary-Layer Meteor.* 58, 367-389.
6. F. G. Smith, Ed. 1993. *The infrared & electro-optical systems handbook*. Vol. 2, Section 2.2.6, SPIE Optical Engineering Press, Bellingham.
7. Businger, J. A., J. C. Wyngaard, Y. Izumi and E. F. Bradley, 1973. "Flux-profile relationships in the atmospheric surface layer." J. Atm. Sci. 28, 181-189.
8. Holtslag, A. A. M. and A. P. Van Ulden, 1983. "A simple scheme for daytime estimates of the surface fluxes from routine weather data." J. Clim. Appl. Meteor. 22, 517-529.
9. Stull, R. B., 1988. *An introduction to boundary layer meteorology*. Kluwer Academic Publishers, Boston.
10. Thiermann, V., 1992: A displaced-beam scintillometer for line-averaged measurements of surface layer turbulence, 10th Symposium on Turbulence and Diffusion, Portland, Or.

Session IV

ATMOSPHERIC PHYSICS

Center for Geoscience Overview of DoD-Sponsored Research
at the Cooperative Institute for Research in the Atmosphere (CIRA)

Kenneth E. Eis, Thomas H. Vonder Haar, and Donald L. Reinke
Colorado State University
Cooperative Institute for Research in the Atmosphere
Fort Collins, Colorado U.S.A.

ABSTRACT

CIRA has just completed the first year of research sponsored by the DoD under the Center for Geosciences¹ Phase II activity. This multidisciplinary research effort is summarized in this paper with examples of the first year results. The research is divided into 12 distinct activities, bound together with an over-arching theme of probing regional-scale moisture. All of the research activities were scientifically peer-reviewed and screened for military relevance prior to funding.

Note to readers: Many of the figures in this paper lose their informational content when not viewed as color plates. This paper with original color information is available for your review on CIRA's World Wide Web home page (<http://www.cira.colostate.edu/geosci/overview.htm>). You are welcome to down-load the figures for your own use.

1. Introduction

Military operations, in the age of precision guided weapons, virtual reality simulations, and satellite coverage of the battlefield are still sensitive to weather. Much of the impacts range from atmospheric moisture obscuring target-to-sensor views; to bogged down tanks and trucks after the moisture rains out of the atmosphere. A tri-service three year research effort titled Phase II of the Center for Geosciences, now underway at CIRA is designed to address the understanding of basic weather-related issues. 12 research activities are summarized as follows:

1.1 Fog and Haze Observations. Visual and infrared GOES-8 and 9 imagery are being analyzed using structure functions, textural analysis, spectral analysis, time series analysis and other methods to remotely detect (sense) fog and limiting visibility from geostationary satellites. This research has a clear operational goal - to develop an overland visibility-from-orbit application.

1.2 Fog Forecasting. The CSU Regional Atmospheric Modeling System (RAMS) will be used to simulate and predict fog events over irregular terrain. A better forecast of fog has significant military application. It can be used as a natural screen for covert operations, and can be used to avoid low visibility when visibility-sensitive operations are being planned.

¹ DoD Grant DAAH04-94-G-0420

1.3 Cloud Drift Winds: New Development and Demonstration. New methods for producing wind vectors derived from cloud motions will be demonstrated and refined, which combine advanced cloud motion computation techniques with a new cloud height from shadows algorithm. It has demonstrated dramatic improvements in accuracy (plus or minus 1 m/sec). Remote sensing of winds over data-denied areas is at hand. Applications relate to air operations, theater missile defense, reconnaissance planning, and toxic dispersion.

1.4 Detection of Total Cloud Liquid Water (CLW) over Land from a Combination of Microwave and Infrared Satellite Measurements. This effort will extend satellite-based liquid water detection from ocean regions to over continental land masses. Calibrated, objective CLW values would be invaluable to engineering sensor studies and simulations in the IR and microwave regions where objective values are now crudely inferred from cloud statistics and cloud typing studies.

1.5 Coupling of Satellite Remote Sensing of Land Surface Properties with a Hydrological Soil Model and Mesoscale Atmospheric Model. The outcome of this research could lead to a remotely sensed trafficability parameter for the DoD and other dual-use applications including fog forecasting mesoscale agricultural indices, surface-to-boundary layer moisture flux parameterizations, and vastly improved Electro-Optical Tactical Decision Aid background specifications.

1.6 2-D Hydrological Modeling of Mesoscale Convective Systems. A larger set of remotely sensed data will be used to run the model. One of the major technical issues is the optimum grid size determination given the spatial variability of the terrain and spatio-temporal characteristics of thunderstorms.

1.7 A Multisensor Approach to the Remote Sensing of Water Vapor. This effort is developing water vapor profiles by applying the Bayes Theorem to the inversion problem. This methodology will be used to create a multispectral (microwave and infrared DMSP data) approach to the extraction of water vapor variation with height. This task has the potential for improved accuracy's of satellite sounder-derived moisture profiles with resulting applications in several tactical DoD and civilian areas.

1.8 High Spectral Resolution Lidar (HSRL) Technique for Assessing Aerosol, Wind, and Temperature Variability. This effort will complete the Phase I effort to use a 0.589 micron and build a 0.532 micron vertically pointing lidar that uses an Iodine filter to measure vertical profiles of temperature, wind (w component), extinction, and to characterize aerosols and cirrus clouds by phase function and depolarization ratios. Ranges of 5-10 km will provide near-continuous base-area environmental information and changes.

1.9 Measurement and Analysis of Complex Layered-Cloud Systems (94 GHz Radar and Micro Pulsed Lidar). This effort will use 94 GHz radar and visible (or near IR) lidar data to analyze cloud liquid water and ice in complex layer cloud situations. One of the goals of this analysis

will be to parameterize cloud bases with cloud type/textural information that can be sensed with a satellite-only algorithm. A longer range goal will be the detection and incorporation of existing cloud situations into state-of-the-art atmospheric models. This activity represents one of the few middle cloud studies and field experiments of the last decade. It is closely related to supporting air operations.

1.10 NEXRAD/CSU-CHILL Algorithm Studies. This effort uses the CSU-CHILL polarimetric radar as a "bench mark" for testing NEXRAD algorithms based on reflectivity and storm structure. Currently NEXRAD algorithms are being developed for the Midwest (Oklahoma) and are frequently inaccurate for other climatological regimes. Using the CSU-CHILL facility and the 94 GHz cloud radar data in combination, we will investigate hail and precipitation algorithm accuracy and related scientific questions.

1.11 Neural Network Approach to Cloud Data Analysis. Our new approach to cloud type-detection promises to extend existing satellite imagery analysis from simple multispectral threshold techniques into textural analysis. This analysis methodology can also be "trained" against cloud base, haze, and other parameters being investigated by the other Center efforts.

1.12 Atmospheric Compression Waves. This task uses acoustic arrays to sense very low frequency sound waves (pressure changes) that result from volume displacements in the atmosphere. The lowest frequency components in these signals will be used to remotely measure heating due to convective development. This approach has the potential of providing the military a passive sensor for locating thunder storm development areas.

1.13 These research tasks are all at temporal and spatial scales applicable to battlefield support (i.e. minutes to days and from 1000 km to less than 1 km).

2. Selected Highlights of the 1st Year's Research

Although only a third of the Center's three year research funding effort has funded, many exciting discoveries have been encountered. A few of the first year's highlights are presented below.

2.1 Cloud drift winds - This method has been used by AFGWC and NWC for years. The Center's research is extending this methodology to include four new ideas: the use of cloud shadow geometry, the use of high temporal resolution (1 minute to 30 minute image refresh), stereo paired images, and time corrected stereo pairs. This work is well underway with wind field extractions in regions of complex meso-scale developments. Figure 1 shows one of these extractions from a 5-minute refreshed GOES-8 data set taken on 31 May 1995 of a thunderstorm near Abilene, TX. The time-corrected component is necessary since each pixel from a satellite image is taken at a different time. For instance, if we were to use a paired GOES-8 and GOES-9 set of images, the pixels that correspond to the Figure 1 could be displaced by several minutes. If we did not correct for the cloud motion in these intervening

minutes we would get drift errors larger than the winds extracted from the images. The outcome of this research is not only to produce cloud drift winds over much of the world, but cloud heights determined from geometry, not by the infrared radiometric assumption. Given that we can determine cloud heights from both methods, the radiometric values can be used to determine optical depth of the clouds and the actual cloud top temperature with the classic contamination issues resolved. This line of research has obvious military value. It promises to provide a high resolution boundary layer wind field to planners of paradrop operations without alerting the enemy with a predrop reconnaissance flight. High drag weapons (like the sensor fused weapon) can also use this data for detailed mission planning. Clearly this information can be used by numerical weather models to improve their initialization.

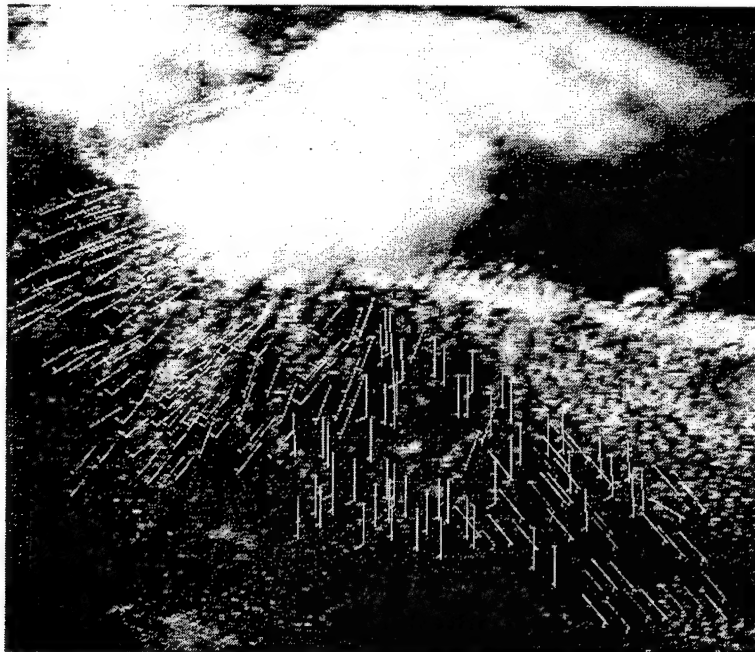


Figure 1. Cloud drift winds from low level thunderstorm inflow 31 May 1995 Abilene, TX.

2.2 Fog and Haze Observations - Researchers have explored two methods of visible optical depth, τ , extraction using GOES-8 satellite imagery. Figure 2 (bottom) shows an optical depth map at the 1 km resolution using the two stream doubling and adding technique. Another method explored and rejected is the 2D FFT. technique which was unable to distinguish between background clutter and atmospheric signal. The research team will continue to explore both radiative extraction methods to determine τ . The reason for this two pronged approach is that the radiative processes become insensitive to aerosol loading at the critical albedo value. Critical albedo is a point where the surface radiance matches the backscatter from an aerosol. As the aerosol increases in optical depth and contributes more backscatter to the satellite sensor, the surface backscatter decreases in the same proportion. When this occurs there is no unique

solution to the radiation transfer calculations (regardless of method). The next step in the research is to determine whether the aerosol is thin cirrus or in the boundary layer. Boundary layer τ contributions will be converted to horizontal visibility in the follow on research. Optical depth and visibility values will be validated and compared against a network of aerosol sensors (IMPROVE) in the next year.

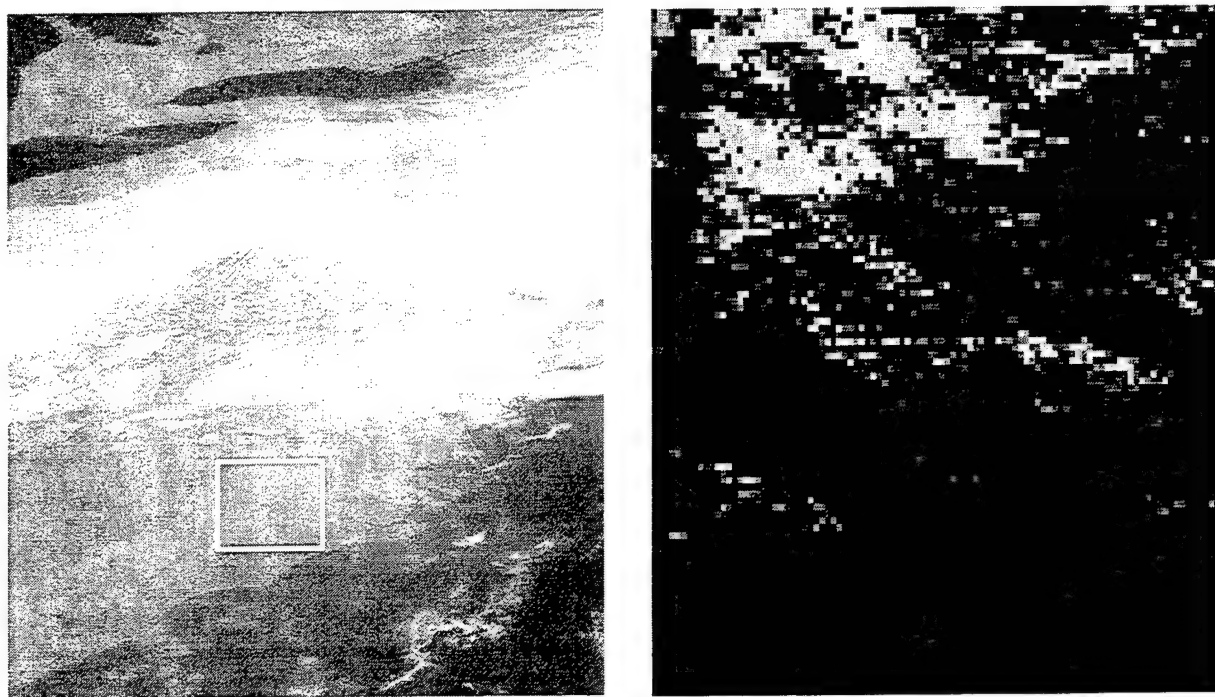


Figure 2. Region containing τ extraction (left) and optical depth (1-7 range) (right).

2.3 Atmospheric Compression Waves - What every battlefield commander has always wanted is a NEXRAD radar interrogating the weather over the battlefield including enemy and friendly air space. The problem with this "wish" has been two fold. First a tactical radar is a big piece of equipment that doesn't penetrate deep into enemy air space and it is difficult to transport. Secondly, anti-radiation missiles make a continuous active, statically placed radar system a exceedingly vulnerable target. This task will couple passive acoustic sensors to a mesoscale model. The output is a map showing regions of thermal heating (thunderstorms and convective development). The Center is working a two pronged effort, one theoretical, the other collecting real data in the Colorado area. Both are well under way. Figure 3 shows a theoretical calculation of the pressure perturbations 40 minutes after convective initiation.

Two acoustic sampling networks have been designed and deployed to detect two domains of low frequency pressure waves. One system is permanently deployed in conjunction with the CSU CHILL radar facility in Greeley and the other is a mobile system. Both are GPS positioned systems that should be able to detect adiabatic heating events far beyond weather radar ranges, possibly to a thousand kilometers!

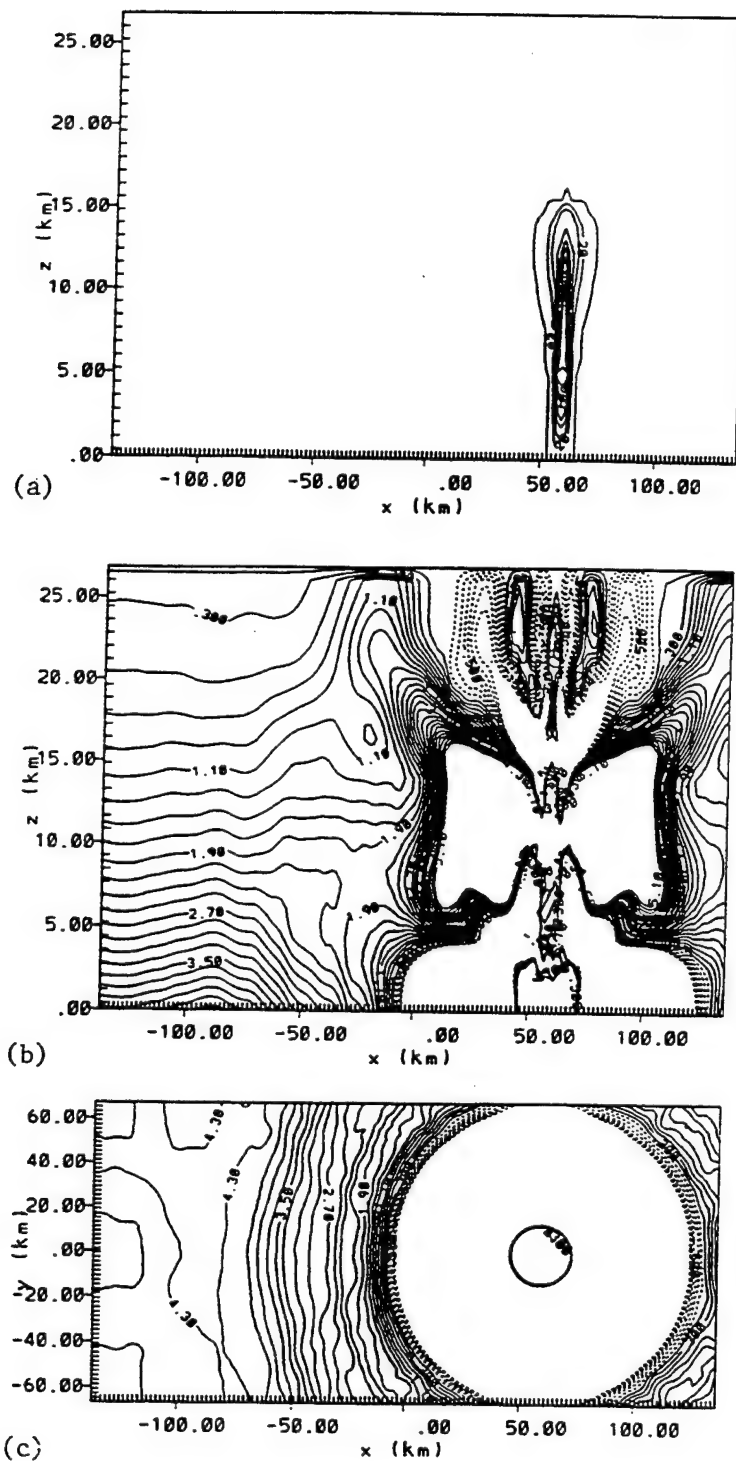


Figure 3. Results of the numerical simulation of a thunderstorm at $t=40$ mins. (a) Vertical cross-section of the total condensate through the center of the thunderstorm. The contour interval is 2g/kg ; (b) Vertical cross-section of the pressure perturbation. The contour interval is 0.2 Pa . Positive values are indicated by solid line and negative values by dashed line. (c) Horizontal cross-section of the pressure perturbation near the surface. The contour interval is 0.2 Pa .

2.4 Coupling of Satellite Remote Sensing of Land Surface Properties with Hydrological Soil Model and Mesoscale Atmospheric Model -

This Center effort represents one of first attempts to fuse remote sensing data and models. The classic problem has been to convert the radiances obtained from satellite imagery, at any wavelength, to standard meteorological parameters. This task uses a soil moisture index derived from fusing of GOES infrared imagery and DMSP SSM/I data. (See Figure 4). After this index is produced, the data will be compared to existing indices such as the NOAA NVDI, API and soil type databases. This research has the potential of providing the highest resolution soil moisture values yet possible to drive trafficability analysis and give mission planners a clear idea of how moisture effects the IR backgrounds in target acquisition, within the EOTDA algorithms. The next step will go even further coupling the data to the moisture and heat flux parameters in diagnostic meso models.



Figure 4. 85 GHz SSM/I and GOES IR surface emissivity calculation.

2.5 Neural Network Approach to Cloud Data Analysis - This neural network analysis of weather related data is one of the most technically exacting attempts to date. CSU neural network experts first analyzed cloud imagery (GOES-7) and developed a cloud/no cloud feature detection network based on IR imagery. This method analyzed cloud/no cloud to better than 85 percent reliability (visual inspection). Neural analysis has typically been a single channel textured analysis. More powerful multispectral and temporal networks have not been available until recently. In the last year a true multi-spectral neural network method has been developed that offers even more insight into satellite-based cloud analysis. First, a variety of neural network image transform methods such as Wavelet, Singular Value Decomposition, and Gabor Transforms were applied to GOES-8 imagery. Wavelet transforms were determined to be the most appropriate for satellite imagery. Subsequently, an unsupervised network (Kohonen) was selected to build the classification. Meteorologists should understand that cloud classification can be thought of as four separate and semi-independent schemes. First, there is the surface observer classification that all meteorologists are familiar with that includes the classical Cirrus, Stratus, Alto-stratus...descriptors. Next, is the satellite interpretation method that includes open cell cumulus, closed cell cumulus etc. This methodology is based on single channel (visible or infrared) human analysis. Third, is the physical classification of clouds based on ice/water phase, optical depth, and cloud top height. Lastly, an entire set of classifications can be produced by neural network engines. These classifications are dependent

on the images used to train the network. Since each class is determined by the network during training, the classes are determined by the energy across the channels being interrogated. Figures 5 and 6 show the visible and 20-class neural network output using the multi-spectral approach. The Center will be spending the next two years correlating the classes with physical cloud analysis and exploring temporal analysis within the neural network arena.



Figure 5. Visible cloud image.

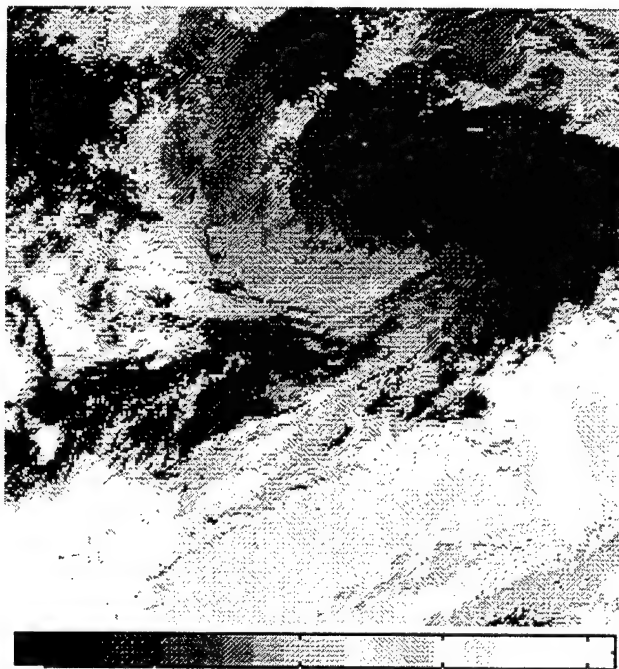


Figure 6. 20-class neural network analysis of Fig. 5.

2.6 Measurement and Analysis of Complex Layered-Cloud Systems. This research task addresses one of the largest military meteorological problems of today. Desert Storm and the current operations in the Balkins both require knowledge of cloud bases near 10,000 feet. Unfortunately, more cloud research has been on boundary layer clouds such as marine stratus or cirrus clouds. This research addresses this void directly. An extensive field program over the central U.S. next summer using an airborne 94 GHz micropulsed radar, satellite data, and a variety of ground-based instruments is planned.

Figure 7 shows preliminary work done on this problem using currently available data sources. The top left panel shows the normal relative humidity 3 layer analysis. The top right panel shows the cloud top temperature analysis from a GOES-8 IR image. The bottom left image shows a merged product using the layer information from the top panels and masked by the satellite cloud/no cloud analysis. Finally, the bottom right panel shows the cloud base information from surface observations but masked by the satellite cloud analysis (top right panel). This approach gives surface cloud bases, but partially solves the limited-domain (representitiveness) problem associated with the surface observers limited view of the atmosphere.

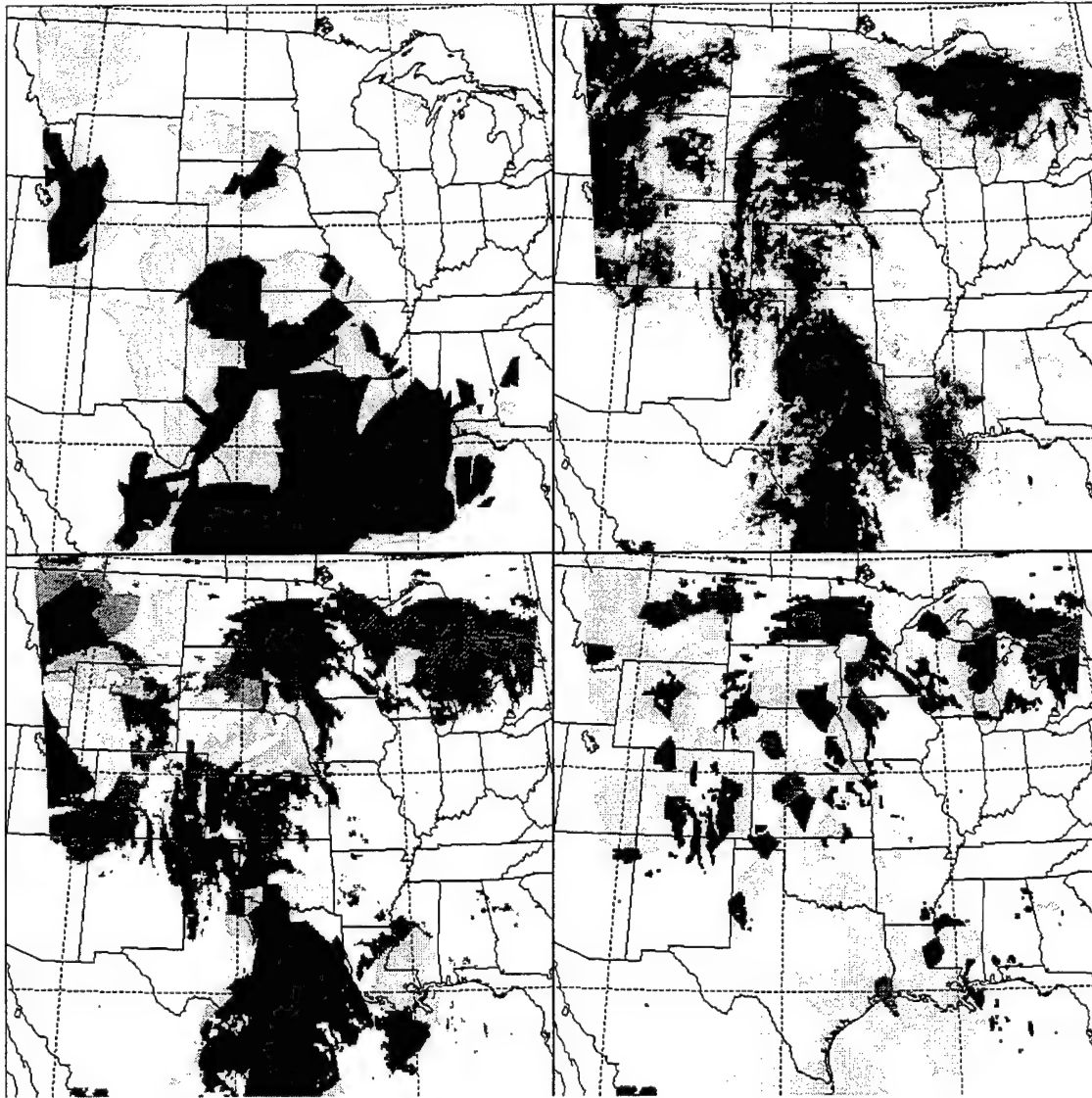


Figure 7. Number of layers from RH analysis (UL), cloud top heights based on GOES infrared imagery (UR), 8-level binary cloud-layer image from combined satellite and relative humidity analysis (LL), and cloud base analysis from surface observation grid (LR).

BI-FRACTAL ANALYSIS OF ATMOSPHERIC SIGNALS

ILLUSTRATED WITH CLOUD DATA[†]

A. Davis and A. Marshak

NASA – Goddard Space Flight Center, Climate and Radiation Branch,
Greenbelt, MD 20771, USA.

ABSTRACT

Fractal analysis of atmospheric data has gained considerable momentum since Lovejoy's seminal (1982) paper on the area-perimeter relation for clouds and rain [*Science*, 216:185–187]. During the late 1980's, multifractal approaches were gradually imported into meteorology from statistical fluid dynamics and deterministic chaos. In this brief survey, we describe in algorithmically explicit terms both types of multifractal analysis: higher-order structure functions and singularity analysis. Both procedures can be applied to any atmospheric signal, observed or simulated, that represents a field or a time-series. These multifractal analyses are illustrated with *in situ* measurements of liquid water content along a 1D transect through a marine stratocumulus cloud deck. In a deliberate effort towards simplicity and robustness, bi-fractal analysis uses only two independent exponents, one from each multifractal approach. This enables us to quantify two key features of the data, physically and statistically speaking: “nonstationarity” with $H_1 \in [0,1]$ and “intermittency” with $C_1 \in [0,1]$. From this vantage point, the other exponents are needed to only qualify these two characteristics, and are probably not independent anyway.

1. ILLUSTRATIVE DATA USED IN THIS CASE-STUDY

1.1 Visualization and Description

Figure 1a shows spatial fluctuations of cloud liquid water content (LWC) as observed with an airborne PVM-100A probe (Gerber *et al.* 1994) along a horizontal flight leg. These data were collected inside a marine stratocumulus with some embedded towering cumulus during the Southern Ocean Coupled EXperiment (SOCEX) in the southern summer of 1994. In the following, we will denote these data and their associated spatial coordinates

$$\left. \begin{array}{l} f_i = f(x_i) \\ x_i = i\ell \end{array} \right\}, i = 1(1)N_{\text{pts}} \quad (1a)$$

where ℓ is the sampling length scale (or grid constant) and $L = \ell N_{\text{pts}}$ is the overall length of the dataset (or grid size). In our case, we have $\ell \approx 5$ m, $N_{\text{pts}} \approx 5000$, hence $L \approx 25$ km.

[†]This work was supported by the Environmental Sciences Division of U.S. Department of Energy (under grant DE-A105-90ER61069 to NASA's Goddard Space Flight Center) as part of the Atmospheric Radiation Measurement (ARM) program.

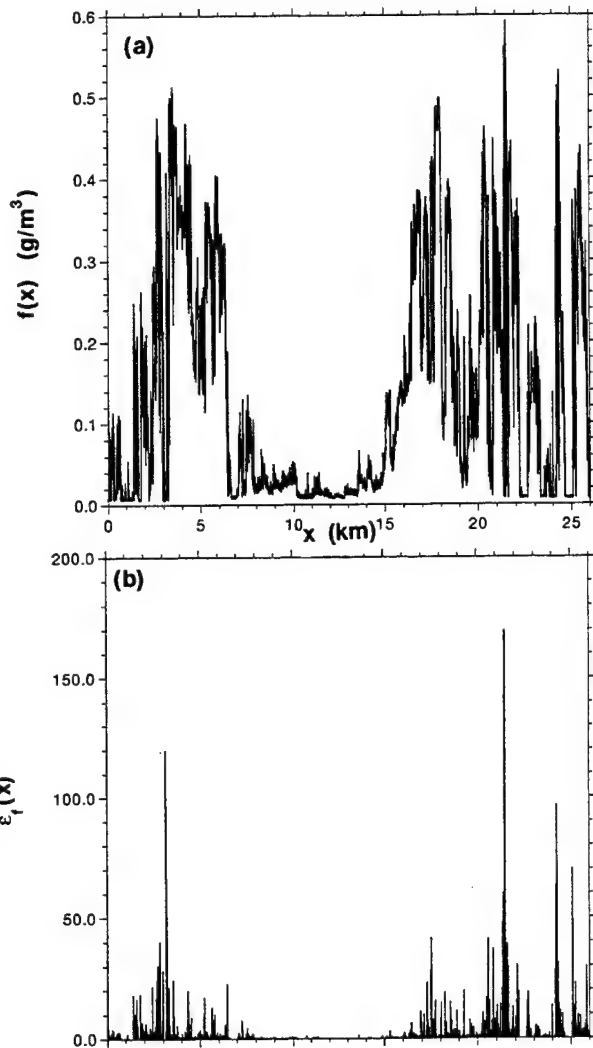
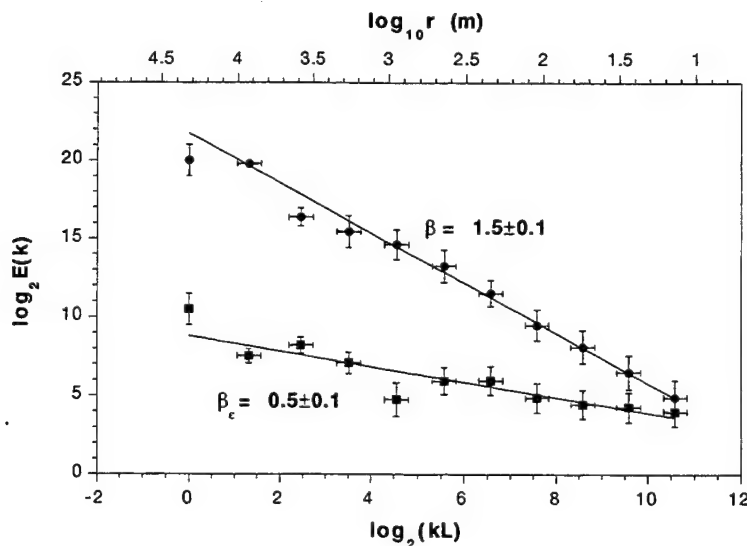


Figure 1: *Atmospheric Test-Data.*

(a) A 1D transect of LWC through a marine stratocumulus field captured during SOCEX (courtesy Dr. H. Gerber). The PVM-100A probe was actually sampling at 2 kHz (i.e., 4 cm resolution, for an aircraft speed of 80 m/s); here we degraded the resolution to 5 m. For a justification of this choice, see Marshak *et al.* (1996b).

(b) The squared small-scale gradients of the data in panel (a).

Figure 2: *Examples of Power-Law Wavenumber Spectra.* The LWC data in fig. 1a and corresponding ε field in fig. 1b were used in log-log axes. The horizontal "error" bars correspond to octave-wide wavenumber bins where we averaged the energy, as described by Davis *et al.* (1996a).



Clearly the variability of this datastream is such that its standard deviation is of the same order as its mean. Moreover the jumps from one value to the next are sometimes small and sometimes very large; these quasi-discontinuities tend to cluster in space. This “intermittency” is better visualized in fig. 1b where we have plotted

$$\varepsilon f(x_i + \ell/2) = \frac{|f(x_i + \ell) - f(x_i)|^m}{\langle |f(x_i + \ell) - f(x_i)|^m \rangle} = \varepsilon_i = \frac{|f_{i+1} - f_i|^m}{\langle |f_{i+1} - f_i|^m \rangle}, \quad i = 1(1)N_{\text{pts}} - 1, \quad (1b)$$

with $m = 2$. Angular brackets $\langle \cdot \rangle$ are used to designate “ensemble” averages. In principle (i.e., theory or model data), this means we leave x (or i) constant and average only over realizations of the field $\varepsilon(\cdot)$, or its progenitor $f(\cdot)$; in practice (i.e., with data), we necessarily use some form of spatial averaging and, if available, we also average over the various datasets.

If $f(x)$ in eq. (1b) were some component of velocity in a highly turbulent flow and ℓ were Kolmogorov’s scale, then $\varepsilon(x)$ would be a normalized estimate of the local rate of dissipation of kinetic energy. This type of secondary datastream was used by *Meneveau and Sreenivasan* (1987) and others to determine the multifractal nature of fully developed turbulence. Outside of this field, the choice of m is quite arbitrary; statistics obtained with different m ’s can be related anyhow (cf. Section 4).

1.2. Spectral Properties and “Scale-Invariance”

Consider the wavenumber spectrum $E(k)$ for $1 \leq kL_2 \leq k_{\text{Nyq}}L_2 = L_2/(2\ell)$ where $k_{\text{Nyq}} = 1/(2\ell)$ is the Nyquist wavenumber, and $L_2 = N_2\ell = 2^{\lfloor \log_2 N_{\text{pts}} \rfloor} \ell$ where $\lfloor \cdot \rfloor$ denotes integer part. (We assume that one of the more popular Fast Fourier Transform packages, such as *Press et al.’s* (1993), is used where the number of points is an integer power of 2.) In our case, we have $\lfloor \log_2 N_{\text{pts}} \rfloor = 12$ hence $N_2 = 4096$. A length scale r (expressed in units of ℓ) can be associated with wavenumber k : $r = 1/k\ell = N_2/(kL_2)$. In the remainder of this paper, we will be dealing with “scale-invariant” or simply “scaling” data, meaning that there is a substantial range of wavenumbers—hence scales—where $E(k)$ follows a power-law:

$$E(k) \propto k^{-\beta}, \quad (2)$$

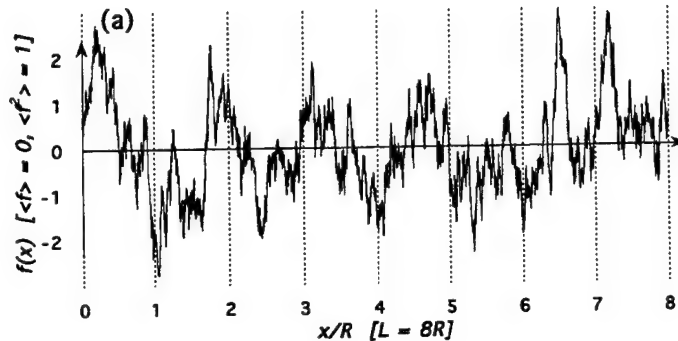
where β is the spectral exponent.

Figure 2 shows $E(k)$ vs. k in log-log axes for the data in figs. 1a,b; r (converted into km) is also indicated on the plot. In this case, we observe power-law behavior over the entire range of scales, as shown by the linear regression. (In the remainder of this paper, we will simplify our notation by assuming that the sampling scale ℓ is not an arbitrary instrumental feature but it in fact defines the lower end of the scaling range.) We find $\beta \approx 1.5$ for $f(x)$, not far from *King et al.’s* (1978) early finding that the fluctuations of LWC have a Kolmogorov-type “ $-5/3$ ” spectrum; similarly, we obtain $\beta_\varepsilon \approx 0.5$ for $\varepsilon f(x)$.

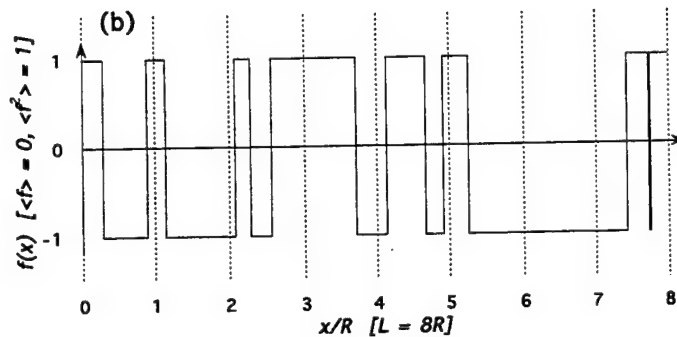
Spectral analysis is a natural first attempt at characterizing variance on a scale-by-scale basis as well as spatial correlations in the dataset. Indeed, the Wiener-Khinchin theorem states that $E(k)$ and the autocorrelation function $\langle f(x+r)f(x) \rangle - \langle f \rangle^2$ are (cosine) Fourier transforms of each other. For example, if the spectrum is flat ($\beta = 0$), the data are completely uncorrelated, or rather δ -correlated: $\langle f(x+r)f(x) \rangle - \langle f \rangle^2 \propto \delta(r)$, independently of its 1-point Probability Distribution Function (PDF). As β in eq. (2) increases so does the range of the correlations while (and because) the amount of small-scale (large k) variance decreases. However, it is well-known that stochastic processes that look radically different can have identical spectra, cf. fig. 3.

Figure 3: An Example of Spectral "Ambiguity" and an Illustration of the "Integral" Correlation Scale.

(a) A sample of zero-mean, unit-variance Gaussian "Ornstein-Uhlenbeck" process (O-Up) (e.g. Arnold 1974).



(b) A "Poisson point-process" (Pp-p) with zero-mean, unit-variance Bernoulli statistics (e.g. Papoulis 1965).



Spectral confusion: We have the same non-scaling spectrum $E(k) = (2/\pi)R/[1+(Rk)^2]$ in both cases. By Fourier duality, we also have identical autocorrelation functions: $G(r) = \langle f(x+r)f(x) \rangle = \exp(-r/R)$; being dependent only on r , we have broad-sense stationarity. [This is because we have made no special assumption about the value at the origin $x = 0$.]

Range of correlations: Parameter R in the above is the "integral correlation scale," in general, defined as

$$R = \int G(r)dr / G(0) = (\pi/2)E(0) / \int E(k)dk.$$

We indicate 8 of these along the x -axis in panels (a) and (b). So each case gives us the equivalent of 8 independent realizations of a scaling process that is "nonstationary" in the sense defined in §2.2 ($\beta > 1$). Indeed, for $0 \leq r \ll R$, the common spectrum $E(k)$ is $\propto k^{-2}$, hence $\beta = 2$ from eq. (2) and $\zeta(2) = 1$ from eq. (6).

Resolution of spectral ambiguity: However similar their spectral/autocorrelation (i.e., $q = 2$) properties, the multifractal properties defined in §§2-4 are radically different:

- (a) $\zeta(q) = q/2$, $q \geq -1$, for O-Up's which are Brownian motion-like at small scales;
- (b) $\zeta(q) \equiv 1$, $q > 0$, for Pp-p's which look like (a small number of) Heaviside steps at small scales.

Even in the (H_1, C_1) plane introduced in §4.3 and illustrated in fig. 7, the two cases are widely separated:

- (a) Brownian motion is non-intermittent ($C_1 = 0$) and has intermediate nonstationarity ($H_1 = 1/2$);
- (b) Heaviside steps are highly intermittent with $C_1 = 1$ (δ -function gradients) and highly nonstationarity with $H_1 = 1$ (differentiability almost everywhere).

2. WHAT ARE q th-ORDER STRUCTURE FUNCTIONS?

2.1. Computation and Scaling Parameterization

A possible way of removing spectral ambiguity is to form increments,¹

$$\Delta f(r; x_i) = |f(x_{i+r\ell}) - f(x_i)| = |f_{i+r} - f_i|, \quad i = 1(1)N_{\text{pts}} - r \quad (r \geq 0), \quad (3)$$

and compute their q th-order statistical moment $\langle \Delta f(r; x)^q \rangle$ for $q \geq 0$; these quantities called “structure functions” have been extensively used in turbulence studies (*Monin and Yaglom* 1975; *Anselmet et al.* 1984; *Antonia et al.* 1984; and others). For their scaling, we posit²

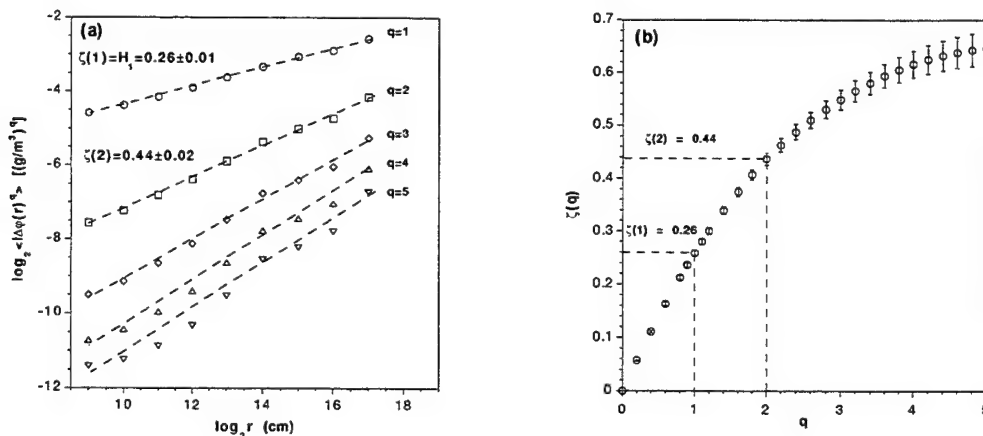
$$\langle \Delta f(r; x)^q \rangle \approx A(q)(r/R)^{\zeta(q)} \quad (1 \leq r \leq R), \quad q \geq 0, \quad (4)$$

where $\zeta(q) \geq 0$ is the scaling exponent and $A(q) \geq 0$, the associated prefactor.

The outer scale R in eq. (4) is taken to be the “integral correlation scale” of the data, as illustrated with models in fig. 3. For $r \leq R$, eq. (4) indicates that $f(x+r)$ and $f(x)$ are correlated; for $r > R$, they are not: $\langle \Delta f(r; x)^q \rangle \approx \text{constant}$, hence $\zeta(q) \equiv 0$, in this “stationary” regime, i.e., where statistical properties are translationally invariant. Many long datasets are needed to determine R accurately (e.g. *Davis et al.* 1996a); by default, we can take $R = N_2$ in eq. (4) and in the remainder of this paper for our illustrative dataset.

Figure 4a shows $\log \langle \Delta f(r; x)^q \rangle$ vs. $\log r$ for $1 \leq r \leq N_2$ by factors of 2 and $q = 1(1)5$; the linear portions indicate good scaling and the slopes define the corresponding exponents in eq. (4). Figure 4b shows the $\zeta(q)$ function; its curvature tells us that our data is “multiscaling” or “multifractal”—in the sense of *Parisi and Frisch* (1985)—or exhibits “anomalous” scaling, as opposed to what one would expect from the simplest form of dimensional analysis (see below).

Figure 4: Multifractal Analysis with Structure Functions. (a) Scaling of q th-order structure functions for the whole SOCEX LWC database (part of which is illustrated in fig. 1a). (b) Associated structure function exponents $\zeta(q)$ versus q . The discrepancy between $\zeta(2)+1$ and β from fig. 2, cf. eq. (6), comes from the comparison of ensemble-averaged structure functions and a single-realization energy spectrum.



¹Muzy et al. (1993) define a wavelet-based surrogate for $\Delta f(r; x)$ that they generalize to higher-order increments by invoking wavelets with more-and-more oscillations.

²Muzy et al. (1993) discuss the absolute lower bound for q in eq. (4) which is -1 .

2.2. Remarks

- a. Stationarity concerns: Implicitly, we have just made a non-trivial operational assumption of “ergodic” increments here, i.e., that *spatial* averages will lead to their *ensemble* counterparts for large enough samples. This means that the theoretically weaker assumption of “stationary” increments is certainly in order if we hope to obtain meaningful results from spatial averages (Davis *et al.* 1994b; 1996a). Relaxing stationarity from its narrow (any q) to its broad ($q = 2$) sense, this in turn implies $\beta < 3$ in scaling regimes, as shown below. This sufficient, hence somewhat conservative, condition for stationarity in the increments expressed in Fourier space is welcome. Indeed, methods for checking stationarity assumptions in physical space are always *ad hoc* since the spatial information required to assess translational invariance of average quantities is already used to produce the averages.
- b. Pre-determined exponent: We have $\zeta(0) = 0$ and even $A(0) = 1$ in eq. (4) as soon as all PDF's are properly normalized.
- c. Prefactors: If we choose f -units such that, for instance, $\langle \Delta f(r; x)^q \rangle_{r=R, q=2} = 1$, then we will have $A(q) = \langle \Delta f(R; x)^q \rangle \approx \langle \Delta f(R; x)^2 \rangle^{q/2} = 1$. Although it satisfies the usual dimensional requirements, using this “ \approx ” symbol is not a trivial one on statistical grounds. More precisely, it implies that increments over integral scales are distributed quite narrowly, like Gaussian deviates, and needs to be checked for each specific study. In our cloud LWC case-studies, this follows quite naturally from the simple fact that LWC is non-negative: the amplitude of large-scale fluctuations therefore cannot exceed much the mean LWC for that particular cloud, as determined from the available transect(s).
- d. Concavity and exponent “hierarchy:” If there exists a choice of f -units that removes most of the q -dependence in $A(q)$ as explained above, then $\zeta(q)$ is concave (namely, $\zeta''(q) \leq 0$); see Davis *et al.* (1994a) for a simple proof. Equivalently, the related exponent function

$$H(q) = \zeta(q)/q \quad (5)$$

is non-increasing, thus defining a hierarchy.

- e. “Monoscaling:” The special case $\zeta''(q) = 0$ with $\zeta(0) = 0$, leads trivially to $\zeta(q) \propto q$. This situation maps to weakly variable increments at all scales, not just $r \approx R$, in the sense that $\langle \Delta f(R; x)^q \rangle \approx \langle \Delta f(R; x)^2 \rangle^{q/2}$, as expected from straightforward dimensional analysis; indeed, this yields $\zeta(q) = (\zeta(2)/2)q$ hence $H(q) \equiv H(2)$. A process with constant (non-vanishing) $H(q)$ is called monoscaling, meaning that a single exponent determines all the others, or has “normal” scaling, meaning that dimensional arguments work well enough quantitatively.
- f. One extreme case: In particular, this implies that the whole class of stationary stochastic processes can be mapped *in principle* to $H(q) \equiv 0$ in eq. (5), the minimum value; *in practice*, we can only anticipate numerically small values.
- g. The other extreme case: The class of smooth (i.e., once differentiable almost everywhere) functions will have: $\langle \Delta f(r; x)^q \rangle \propto r^q$ hence $\zeta(q) = q$ and $H(q) \equiv 1$ in eq. (5), the maximum.
- h. Spectral (Wiener–Khinchin) connection: The $q = 2$ case can be related back to the autocorrelation function $\langle f(x+r)f(x) \rangle - \langle f \rangle^2$ since $\langle [f(x+r) - f(x)]^2 \rangle \equiv 2[\langle f^2 \rangle - \langle f(x+r)f(x) \rangle]$, thus to $E(k)$, leading to (e.g. Monin and Yaglom 1975)

$$\beta = \zeta(2) + 1 = 2H(2) + 1, \quad (6)$$

with $\zeta(2) > 0$ but also $\zeta(2) < 2$, hence our up-front requirement of stationary increments: $\beta < 3$ in eq. (2). Equation (6) also tells us that the whole structure function approach is of interest primarily for regimes where the data are nonstationary, i.e., when $\beta > 1$ in eq. (2).

3. WHAT IS SINGULARITY ANALYSIS?

3.1. Computation and Scaling Parameterization of “Singular Measures”

We now turn to the spiky $\varepsilon_f(x)$ field in fig. 1b derived from the data $f(x)$ to highlight its intermittency, described in the early turbulence literature as ‘*sudden bursts of high frequency activity*.’ For over a decade, many forms of singularity analysis have been described that apply to spiky non-negative fields such as $\varepsilon_f(x)$ that occur both in turbulence and in deterministic chaos. We opt to characterize its singularity in the simplest possible way, with the q th-order moments of “singular measures.”

First define a sequence of “coarse-grained” versions of $\varepsilon_i = \varepsilon(x_i) = \varepsilon(1/x_i)$, i.e., local averages:¹

$$\varepsilon_f(r; x_i) = \frac{1}{r} \sum_{i'=i}^{i+r-1} \varepsilon_{i'}, \quad i = 1(r)N_{\text{pts}} - r \quad (r \geq 0); \quad (7)$$

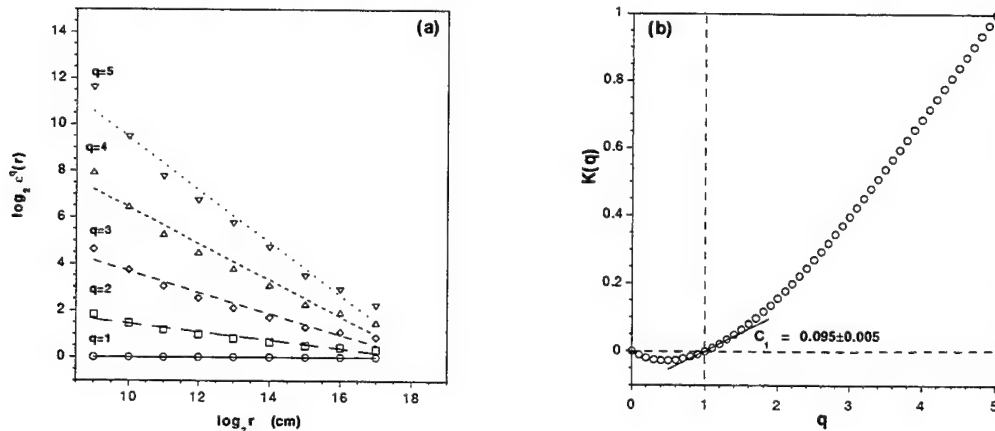
note that we consider averages over non-overlapping segments. We then compute the r -dependent (1-point) q th-order moments $\langle \varepsilon_f(r; x)^q \rangle$ of these fields for $q \geq 0$, averaging over the disjoint boxes. Adopting the notation of *Schertzer and Lovejoy (1987)*, we posit²

$$\langle \varepsilon_f(r; x)^q \rangle \approx (r/R)^{-K(q)} \quad (1 \leq r \leq R), \quad q \geq 0. \quad (8)$$

What if we had used $m \neq 2$ in eq. (1b)? Then certainly $K_m(q) \neq K_2(q)$; however, it can be shown (e.g. *Tessier et al. 1993*) that $K_m(q) = K_2(qm/2) - qK_2(m/2)$.

Figure 5a shows $\log \langle \varepsilon_f(r; x)^q \rangle$ vs. $\log r$ for $1 \leq r \leq N_2$ by factors of 2 and $q = 1(1)5$; the linear portions indicate the good scaling. Figure 5b shows the corresponding $K(q)$ function. Its curvature tells us that, in the sense of singular measures, our data is again “multiscaling” or “multifractal” —in the sense of *Halsey et al. (1986)*, *Meneveau and Sreenivasan (1987)*, *Schertzer and Lovejoy (1987)*, and others.

Figure 5: Multifractal Analysis with Singular Measures. (a) Scaling of q th-order moments of the coarse-grained measures based on the whole SOCEX LWC database at 5 m resolution (part of which is illustrated in fig. 1b, using squared rather than absolute gradients however). (b) Associated $K(q)$ exponents versus q .



¹For a wavelet-based counterpart of $\varepsilon_f(r, x)$ and singularity analysis, we refer to the study of multifractal measures by *Arnéodo et al. (1988)*.

²For a detailed discussion of the lower and upper bounds on q in eq. (8), including the interesting statistical phenomenon of diverging higher-order moments, we refer to *Schertzer and Lovejoy (1987; 1992)*.

3.2. Remarks

We cover here the *same subject matter in the same order* as in our Remarks *a–e* of §2.2.

- a. Stationarity concerns: The $\varepsilon(x)$ field we use here has not only stationary increments ($\beta_\varepsilon < 3$) but stationarity *per se* ($\beta_\varepsilon < 1$). This is why the r -scaled running spatial averages of the ε -data, but not of the f -data (with $1 < \beta < 3$), can be considered.
- b. Pre-determined exponents: Again, we will have $K(0) = 0$ as soon as the r -dependent PDFs are all normalized. However, we have another predetermined value in this approach; indeed, our definitions lead to $\langle \varepsilon_f(r;x) \rangle \equiv \langle \varepsilon_f(R;x) \rangle = 1$ for $1 \leq r \leq R$, hence $K(1) = 0$, because at $q = 1$ the r -scale spatial averages in eq. (7) and the overall spatial/ensemble average in eq. (8) commute (and yield unity due to the adopted normalization).
- c. Prefactors: We do not need to define prefactors here [as for for structure functions in eq. (4)], nor discuss their q -dependence, because the normalization adopted in eq. (1b) leads directly to $\langle \varepsilon_f(R;x)^q \rangle \equiv 1$, $q \in \mathbb{R}$.
- d. Convexity and exponent “hierarchy:” In this approach, $K(q)$ is a convex function (i.e., $K''(q) \geq 0$) implying that $K(q) \leq 0$ for $0 \leq q \leq 1$, and $K(q) \geq 0$ otherwise. Equivalently,

$$D(q) = d - K(q)/(q-1) \quad (9)$$

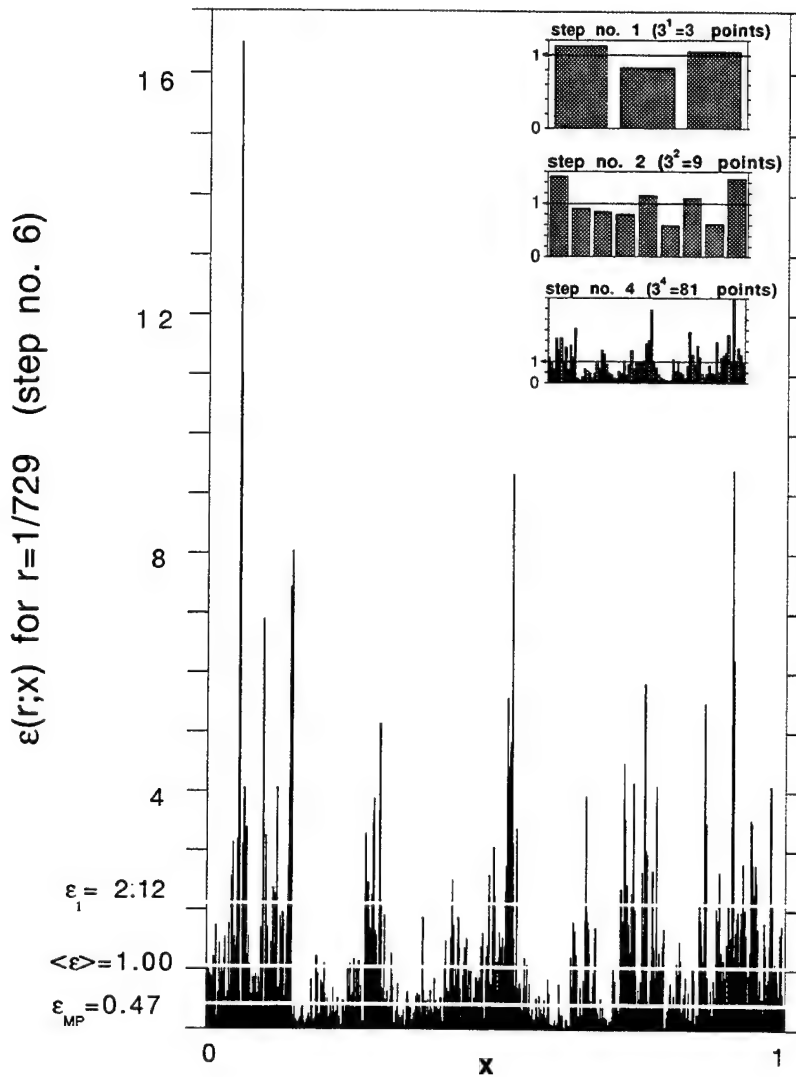
where d designates the number of dimensions, is a non-increasing function. This “hierarchy” of exponents was first used in chaos theory (where d = dimensionality of the “embedding” space) by *Hentschel and Procaccia* (1983) and *Grassberger* (1983) who related each value to a different fractal dimension describing the strange attractor. At any rate, $D(q)$ is bounded by 0 and d ($= 1$ here).

- e. “Monoscaling:” In the special case where $D(q) \equiv \text{constant}$ in eq. (9), hence $K(q) \propto q-1$ in eq. (8), we talk about monoscaling or monofractal measures, otherwise they are multiscaling or multifractal.
- f. One extreme case: Suppose the $\varepsilon_f(r;x)$ fields are Gaussian-like; because sums of Gaussian (-like) random variables will also be Gaussian(-like), this will be true as soon as the nonstationary random function $f(x)$ has narrowly distributed (absolute) increments at the smallest scales. In this case, their necessarily non-vanishing mean determines all their other moments: $\langle \varepsilon_f(r;x)^q \rangle \approx \langle \varepsilon_f(r;x) \rangle^q \equiv 1$, $0 < r \leq R$, hence $K(q) = K(1)q \equiv 0$ and consequently $D(q) \equiv d$. This characterizes a process with absolutely no intermittency (the measure is distributed everywhere in space).
- g. The other extreme case: It corresponds to $\varepsilon_f(x) = \delta(x-x^*)$, i.e., Dirac δ -functions randomly positioned on the unit segment ($0 \leq x^* \leq R = 1$), in the small-scale limit; equivalently, the nonstationary random functions $f(x)$ are Heaviside steps. Indeed, in this hypothetical situation, our definitions yield $\langle \varepsilon_f(r;x)^q \rangle = r(1/r)^q$ hence $K(q) = q-1$ and therefore $D(q) \equiv 0$. This is the smallest value that still has geometrical meaning: all the measure is concentrated onto a single point. For a discussion of the probabilistic interpretation of negative dimensions, see *Schertzer and Lovejoy* (1992).
- h. Spectral (Wiener–Khinchin) connection: When $\varepsilon(x)$ is a multiplicative cascade (cf. fig. 6) the 2nd moment in eq. (8) can be connected to $\langle \varepsilon(x+r)\varepsilon(x) \rangle \sim r^{-K(2)}$ (e.g. *Monin and Yaglom* 1975), thus to $E(k)$. In this case at least,

$$\beta_\varepsilon = 1 - K(2) = D(2) + (1-d). \quad (10)$$

where $0 \leq D(2) \leq d$, hence $1-d \leq 0 < \beta_\varepsilon < 1$. In particular, this means that cascade processes are (broad-sense) stationary.

Figure 6: Multiplicative Cascade Model for $\varepsilon(r;x)$ with Log-Normal Statistics. We start with a uniform measure on the unit segment. This segment is divided into $\lambda = 3$ equal portions where the measure is randomly boosted or decreased by multiplying it with λ independently and identically distributed multiplicative weights: $W_j, j = 1, \dots, \lambda$. We took $\ln W$ as Gaussian deviates with variance $\sigma^2 = 0.5$ and mean $\mu = -\sigma^2/2$; this makes the W 's log-normal and enforces $\langle W \rangle = 1$. The procedure is repeated in principle *ad infinitum* but, in practice, we stopped after the 6th step ($\lambda^6 = 729$ values); along with the 1st, 2nd and 4th steps (inset), this enough to see how singularities with variable "strengths" develop. Kolmogorov (1962) originally proposed this model for simulating the extreme spatial variability the rate of kinetic energy dissipation in highly turbulent flows. For log-normal cascade models of $\varepsilon(r;x)$, the q th-order moments yield $K(q) = C_1 q(q-1)$, as long as they do not diverge, i.e., $q < q_D = d/C_1$ in this log-normal case (Schertzer and Lovejoy 1992; Gupta and Waymire 1993; and references therein); in this case, $C_1 = \sigma^2/(2\ln\lambda) \approx 0.1$, hence $q_D \approx 10$. To emphasize the highly non-Gaussian nature of the 1-point PDF of $\varepsilon(r=1/\lambda^6;x)$, three remarkable ε -values are highlighted: the mean value $\langle \varepsilon \rangle$ which is unit by construction; $\varepsilon_1 = \lambda^{C_1} \approx 2.1$, that dominates estimates of $\langle \varepsilon \rangle$ (the fractal dimension of the set where $\varepsilon(r;x)$ exceeds this value is $d-C_1 \approx 0.9$); and the mode (most probable value) $\varepsilon_{MP} = \lambda^{-C_1} \approx 0.47$.



4. TOO MANY EXPONENTS?

4.1. Quest for the Minimal Number of Exponents to Describe Data

Are the two multifractal approaches to data analysis really independent? In other words: What is the degree of redundancy in the double multifractal analysis we have described in the above? It is widely believed that the two techniques are targeting a unique “multifractality” generated by the dynamics of the geophysical system under scrutiny. However, it is not clear how $\zeta(q)$ and $K(q)$ are related. Simple connections of the type

$$\zeta(q) = q/a - K(q/b) \quad (11)$$

have been proposed where a and b are two constants. For instance, the phenomenology of fully-developed turbulence suggests from dimensional analysis that $a = b = 3$. From there, eqs. (6) and (11) at $q = 2$ were used by *Kolmogorov* (1962), and others thereafter, to compute “intermittency” corrections to *Kolmogorov’s* (1941) “ $-5/3$ ” law, which is in fact a monoscaling extrapolation (from $q = 3$ to $q = 2$) of his rigorous result that $\zeta(3) = 1$. However, the generality of eq. (11)—even for turbulence at $q \neq 3$ —remains an open question (cf. *Davis et al.* 1993).

At any rate, there is a consensus that one more exponent at least is required to go from $K(q)$ to $\zeta(q)$. Let it be

$$H_1 = H(1) = \zeta(1) \quad (12)$$

which is the mean Hölder exponent of the signal $f(x)$, and indeed a straightforward index of nonstationarity going from 0 (stationary processes) to 1 (smooth functions). For the data in fig. 1a, we have $H_1 \approx 0.26$. Related quantities are:

- the fractal dimension of the (self-affine) graph of $f(x)$ $D_f = (d+1) - H_1$ (*Mandelbrot* 1977) which describes the “roughness” of the graph embedded in $d+1$ dimensions. Stationary $H_1 = 0$ data fills a finite area of this space ($D_f = d+1$) whereas differentiable $H_1 = 1$ data is as smooth as the d -dimensional Euclidian plane ($D_f = d$).
- *Ott et al.’s* (1992) recently introduced “cancellation” exponent κ , which measures the rate at which the data changes direction, from going up to going down or vice-versa; since we have $\kappa = 1 - H_1$ (*Vainshtein et al.* 1994), smooth $H_1 = 1$ data hardly ever changes direction ($\kappa = 0$) whereas stationary $H_1 = 0$ data is changing all the time ($\kappa = 1$).

The aim of performing statistics is often to extract from the data a very small number of meaningful quantities. So two (or even one) infinite hierarchy of exponents can be too much to characterize data, parameterize a stochastic model, and other applications. If the data appears to be nonstationary with stationary increments (i.e., $1 < \beta < 3$, a common occurrence in geophysics), then we must consider H_1 —or one of its counterparts, or else β itself—as indispensable. It can be complemented naturally (still using $q = 1$) with

$$C_1 = d - D(1) = K'(1), \quad (13a)$$

a straightforward index of intermittency going from 0 (for Gaussian-type processes) to d (for Dirac δ -functions). For the data in fig. 1b, we have $C_1 \approx 0.095$. Another option would be to retain $K(2)$, known as the “intermittency parameter” in turbulence studies, as a natural ($q = 2$) complement β or, better still, $\zeta(2) = \beta - 1$ which vanishes as stationarity sets in.

Technically, C_1 is called the “information” codimension. The sparse subset of x -space that C_1 describes is essentially where the ε -field associated with the signal f takes values that dominate its mean $\langle \varepsilon_f(r; x) \rangle$. As seen in fig. 5, when $\varepsilon_f(r; x)$ is very large, it contributes little to the mean

because it occurs too rarely; when $\varepsilon_f(r;x)$ is very small (including $\varepsilon_f(r;x) \approx 1$), it contributes little to the same mean in spite of the relatively frequent occurrence.

4.2. Alternative Recipes and Other Reduced Parameterizations of Multifractal Data

In practice, obtaining C_1 from eq. (13a) implies a numerical differentiation of $K(q)$ by computations at 1^+ and 1^- . Parameter C_1 can also be obtained by computing a single statistic:

$$C_1 = \lim_{r/R \rightarrow 0} \langle \varepsilon_f(r;x) \log_{R/r} \varepsilon_f(r;x) \rangle, \quad (13b)$$

as follows when (8) is substituted into (13a). If only q th-order structure functions are known, then $K(q)$ can be defined through eq. (11); using $b = 1$ for simplicity, eq. (13a) then leads to

$$C_1 = K'(1) = \zeta(1) - \zeta'(1). \quad (13c)$$

We must bear in mind that, when analyzing real data (which always comes in limited quantities), the three recipes for obtaining C_1 in eqs. (13a–c) may lead to results that differ numerically. Our test data yields respectively 0.10 ± 0.02 and 0.05 ± 0.03 from eqs. (13b,c) in comparison with 0.095 ± 0.005 obtained above from (13a). This discrepancy is not an issue in an intercomparison study (cf. the one below, for cloud LW) as long as the choice of methodology is held constant for all the datasets involved.

Other ways of statistically reducing large amounts of multifractal data to a small number of parameters have been proposed:

- *Schertzer and Lovejoy* (1987) describe family of cascade models that obey log-Lévy statistics, and are parameterized in closed form by $\{\alpha, C_1\}$ where $0 < \alpha < 2$ (the log-normal case is retrieved in the limit $\alpha \rightarrow 2$). To access the $H_1 > 0$ domain of the (H_1, C_1) plane, they suggest “fractionally” integrating to order $H^* \in (0,1)$ the log-Lévy cascade. (This is simply a low-pass power-law filtering in $1/k^{H^*}$ in Fourier space.) As it turns out, H^* is related, but not equal, to $H(2) = (\beta-1)/2$ (*Davis et al.* 1996b). The authors refer to the resulting 3-parameter $\{\alpha, C_1, H^*\}$ class of models as “universal” multifractals. *Lavallée et al.* (1993) and *Tessier et al.* (1993) have developed techniques to estimate from data α , C_1 , and H^* , in that order and with cumulative contingencies. This means that their operational procedure for obtaining C_1 is different from all three described in connection with eqs. (13a–c) and that their “universal multifractal parameters” do not have the independence of H_1 and C_1 , as obtained from eqs. (12) and either (13a) or (13b).
- *Pierrehumbert* (1996) recently proposed a 2-parameter characterization of multifractal data using structure functions alone, as when eqs. (12) and (13c) are used; he adopts $\zeta'_0 = \zeta'(0) \in [0,1]$ and $\zeta_\infty = \zeta(\infty) > 0$. These quantities are obtained by fitting the empirical $\zeta(q)$ curve with a hyperbola branch: $\zeta(q) = q/(q/\zeta_\infty + 1/\zeta'_0)$. This functional relation enables us to connect his and our parameterizations: $1/H_1 = 1/\zeta'_0 + 1/\zeta_\infty$ and $C_1 = \zeta_\infty/[\zeta_\infty/\zeta'_0 + 1]^2$ (yet another algorithm, using indirectly all available q 's); conversely, $\zeta'_0 = H_1/[1 - (C_1/H_1)]$ and $\zeta_\infty = H_1^2/C_1$. The latter controls explicitly the multiscaling since $\zeta_\infty \rightarrow \infty$ ($C_1 \rightarrow 0$) leads to $\zeta(q) = \zeta'_0 q$ (i.e., monoscaling). Viewed as another intermittency parameter (as opposed to a means of qualifying large- q behavior), ζ_∞ is probably best obtained from our $q = 1$ values. Indeed, it will be highly sensitive to higher-order moments, the most prone to sampling problems (*Davis et al.* 1994a; 1996b), in the proposed fitting procedure; in contrast, H_1 and C_1 are based on robust statistics.

4.3. Bi-Fractal Analysis and LWC in the (H_1, C_1) Plane

Relying only on H_1 and C_1 , or $K(2)$ and $\zeta(2)$, to characterize data defines “bi-fractal analysis.” Table 1 shows the bi-fractal parameters and scaling ranges for a number of LWC or LWC-related datasets, using $m = 1$ in all instances. A striking feature is the tight clustering of the (H_1, C_1) ’s for the ensemble averages for LWC from three different field programs in widely different areas of the globe, with vastly different climatological regimes. FIRE’87 occurred in the Pacific near southern California, ASTEX in the mid-Atlantic, and SOCEX off the coast of Tasmania. This implies that there seems to be a certain degree of universality in the mechanisms that generate and maintain marine stratocumulus; in contrast, Table 1 shows that the influence of local conditions appears in the range of scales involved, as well as the prefactors (Davis *et al.* 1996a; Marshak *et al.* 1996a; 1996b).

The quasi-coincidence of ensemble (H_1, C_1) ’s in Table 1 is all the more remarkable that the five datasets from FIRE show considerable variability; this argues for non-ergodic cloud models (different realizations yield different statistics). As expected, the H_1 for LW path (total LWC in the atmospheric column) is somewhat larger than that of LWC, i.e., the signal is smoother due to the vertical integration; however, the level of intermittency (as measured by C_1) is the same. Note that the LWC data is invariably from marine stratocumulus whereas the LW path data is collected over a mid-continental site, all cloud-types combined.

Table 1: (H_1, C_1) values for FIRE ASTEX and SOCEX LWC’s, and LW path data from ARM.

Database (dataset)	H_1	C_1	$r_{\min} - r_{\max}$	Reference
FIRE LWC (6/30, 22:41Z)	0.29	0.14	20 m – 20 km	Marshak <i>et al.</i> (1996a)
FIRE LWC (7/02, 02:23Z)	0.22	0.15	” ”	” ” ”
FIRE LWC (7/14, 23:09Z)	0.34	0.03	” ”	” ” ”
FIRE LWC (7/16, 17:17Z)	0.31	0.08	” ”	” ” ”
FIRE LWC (7/16, 18:19Z)	0.34	0.07	” ”	” ” ”
FIRE’87 LWC (ensemble)	0.28	0.10	” ”	” ” ”
ASTEX LWC (ensemble)	0.29	0.08	60 m – 60 km	Davis <i>et al.</i> (1994a)
SOCEX LWC (ensemble)	0.26	0.09	5 m – 5 km	Marshak <i>et al.</i> (1996b)
ARM LW path (ensemble)	0.37	0.08	1 min – 8 hrs	Wiscombe <i>et al.</i> (1994)

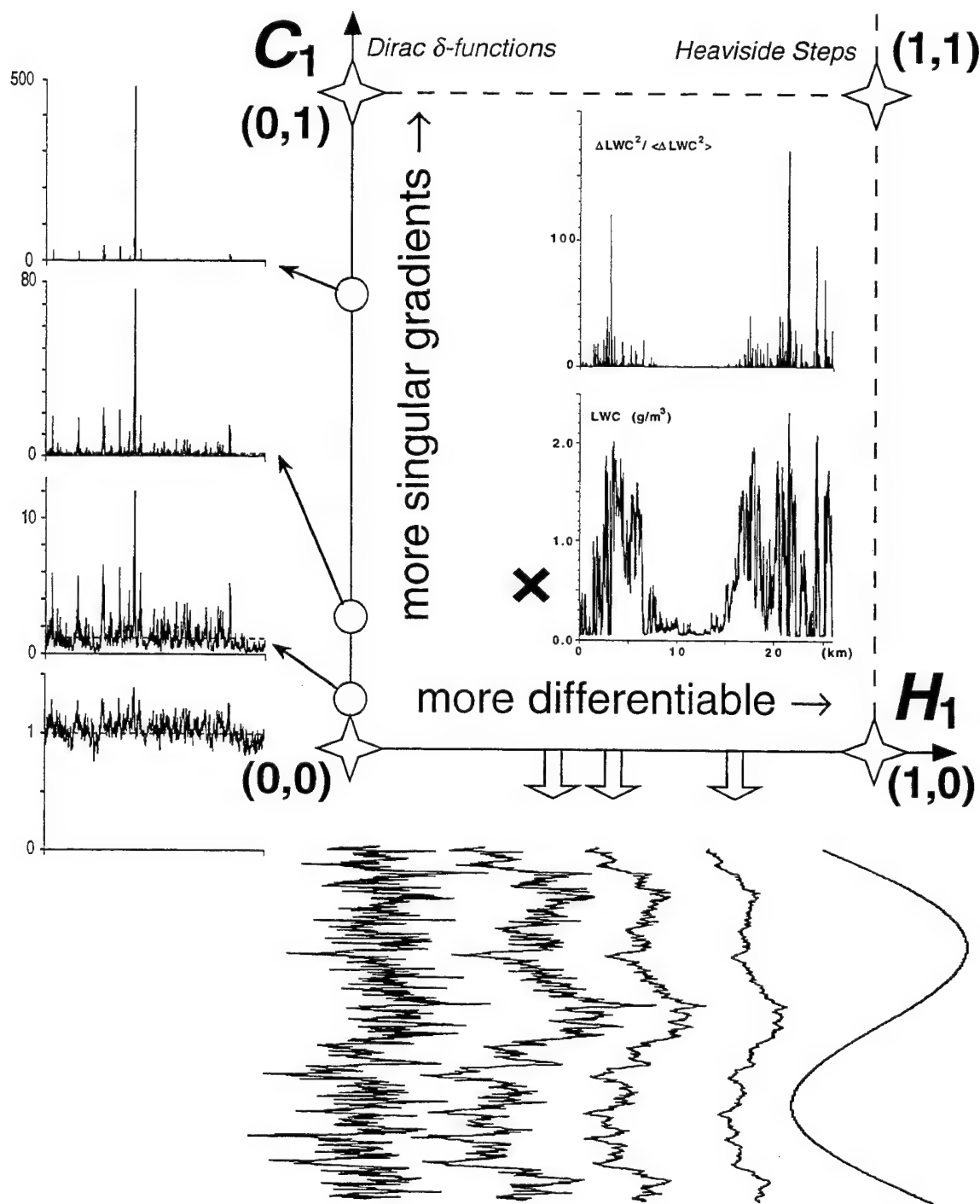
Figure 6 shows the relevant part of the (H_1, C_1) plane for $d = 1$ with the position of our illustrative LWC data and standard models living on the boundaries of the domain: (stationary but intermittent) multiplicative cascades along the vertical axis, (non-intermittent but nonstationary) fractional Brownian motions along the horizontal axis. There are still very few models in the literature that can reach into the domain where the data tends to live, at least atmospheric LWC; see Davis *et al.* (1996b) for a recent survey.

5. SUMMARY

We have explained how to perform and illustrated with cloud-related data the two main types of multifractal analysis on data that represents an atmospheric signal in time or space: “structure functions,” and “singular measures.” Together, these analyses constitute (in all likelihood) a redundant characterization of scale-invariant data that leaves us with two complete families of exponents. It is consequently reduced to only two numbers, one exponent from each approach, that are truly independent: H_1 and C_1 . These quantities are shown to be indices of nonstationarity and intermittency respectively. Having *quantified* these two important

Figure 7: *The Bi-Fractal (H_1, C_1) Plane.* We illustrate the statistical, geometrical and analytical meanings of the two axes with sequences of:

- i) fractional Brownian motion (Mandelbrot 1977) with an increasing degree of nonstationarity, roughness, and differentiability as H_1 increases horizontally; and
- ii) log-normal cascade models (cf. fig. 6) with an increasing degree of intermittency, sparseness, and singularity as C_1 increases vertically.



characteristics of the data, all the other exponents are required only to *qualify* them and, eventually, to describe how they interact.

Positioning atmospheric data on the (H_1, C_1) plane defines “bi-fractal” data analysis. After surveying how it has helped us uncover interesting similarities and differences of internal cloud structure as observed in three widely separated field programs, we conclude that bi-fractal analysis is a welcome complement to spectral analysis.

6. SUGGESTIONS FOR FURTHER READING

- *Seminal papers:* The first direct application of fractal concepts to atmospheric data analysis was in *Lovejoy's* (1982) investigation of the area-perimeter relation for clouds and rain. *Parisi and Frisch* (1985) coined the term “multifractal” in connection with structure function analysis of turbulent signals. Furthermore, they established the Legendre transform relation between $\zeta(q)$ and $D(h)$; this is the fractal dimension of the set where the local Hölder exponent of the signal is h , as defined in $|f(x+r)-f(x)| \sim r^{h(x)}$. *Halsey et al.* (1986) do the same in the framework of singularity analysis (primarily with the invariant measures of dynamical systems supported by their strange attractors in mind); in this case, the Legendre conjugate of $\tau(q) = (q-1)D(q)$ is $f(\alpha)$, the fractal dimension of the set where the (non-averaged) measure $p(r;x) = r^d \varepsilon(r;x) \sim r^{\alpha(x)}$.
- *A tutorial in multifractal analysis:* *Davis et al.* (1994a) use an artificial 16-point dataset to show graphically how both types of multifractal analysis proceed recursively from small to large scales, using the same method of moments as here; they then illustrate them with real LWC data.
- *Multifractal analyses using wavelets:* Multi-resolution analysis (*Mallat* 1989) consists in low- and high-pass filtering a signal on a point-by-point and scale-by-scale basis without loss of information. The localized filters are either “wavelets” (high-pass) or “scaling functions” (low-pass). Now, $\varepsilon_f(r;x)$ in eq. (7) can be viewed as the result of passing a portion of the stationary random measure $\varepsilon_f(x)$ —which already is rich in high frequencies—through a low-pass spatial filter (cut-off at wavenumber $k \approx 1/r$) centered at $x+r/2$. In the same way, the absolute increment $\Delta f(r;x)$ in eq. (3) is essentially the amplitude of the output of $f(x)$ —which, being dominated by low frequencies, is nonstationary *per se*—through a high-pass filter (eliminating wavenumbers $< 1/r$) centered at $x+r/2$. Elaborating on these ideas, Dr. Alain Arnéodo and his co-workers have developed a unified approach to multifractal analysis in general with an elegant thermodynamical formalism reviewed recently by *Muzy et al.* (1994); for an elementary survey focusing on geophysical applications, see *Davis et al.* (1994b).
- *Nonstationary scale-invariant signals:* “Stationarity”—and often the even stronger property of “ergodicity”—is implicit in all exercises in data analysis, in order to obtain meaningful estimates of statistical quantities by spatial averaging. Following ideas sketched out by *Mandelbrot* (1977), *Davis et al.* (1994b, 1996a) show that scale-invariance can be used to separate stationary and nonstationary cases, stationary increments, etc. These semi-empirical criteria provide guidelines for obtaining the most robust results from the data.
- *Sampling issues:* Increasing q in eqs. (4) and (8) amounts to emphasizing ever larger values of $\Delta f(r;x)$ or $\varepsilon_f(r;x)$; so sooner-or-later a single event will dominate the (large q) statistic. In some “microcanonical” (*Schertzer and Lovejoy* 1992) or “ergodic” (*Gupta and Waymire* 1993) cascade models this happens by design. In data analysis, the same phenomenon is the signature of under-sampling problems. It is well-known that a limited amount of monoscaling data can

look weakly multifractal; *Davis et al.* (1996b) propose a simple criterion for separating spurious from *bone fide* multiscaling.

- *A merger of both types of multifractal analysis:* The general validity of the linear connection between $\zeta(q)$ and $K(q)$ in eq. (11) is an important question that remains open. Partially to address the issue, *Davis et al.* (1993; 1994b) defined a form of joint multifractal analysis: $\langle \Delta f(r;x) \mathcal{P}_{\mathcal{E}f(r;x)} \rangle \sim r^{X(p,q)}$. If $X(p,q)$ takes on a particular functional form, then eq. (11) will be true for all q .
- *Other case-studies with LWC:* We have analyzed and will analyze elsewhere LWC data. King-, Knollenberg-, and Johnson-Williams probe data (respectively 5 m, 20 m and 16 m resolutions) from the First ISCCP Regional Experiment (FIRE) in 1987 (*Davis et al.* 1996a; *Marshak et al.* 1996a). PVM-100 data at 8 m resolution from the Atlantic Stratocumulus Transition EXperiment (ASTEX) (*Davis et al.* 1994a). For our present tutorial purposes, we used data from the Southern Ocean Coupled EXperiment (SOCEX) degraded to 5 m resolution; we are currently preparing a comprehensive study of this remarkable database using the full 4 cm resolution of the PVM-100A probe (*Marshak et al.* 1996b).
- *Multifractal analyses in 2D:* For the singular measures approach, this is a straightforward and well-documented (e.g., *Tessier et al.* 1993) generalization, even in anisotropic situations (*Lovejoy et al.* 1987). On the other hand, several conceptual and computational difficulties arise when it comes to structure functions, most easily overcome by invoking wavelets (*Arrault et al.* 1996); for an interesting monoscaling approach (at $q = 2$) in Fourier space that allows for anisotropy, see *Pflug et al.* (1993).
- *Fractal and multifractal models:* The converse operation of data analysis is the generation of (generally large amounts of) artificial data with given statistical properties (generally determined by a few parameters). *Mandelbrot* (1977) describes several random fractal (i.e., monoscaling) models, both stationary measures and nonstationary functions. *Schertzer and Lovejoy* (1987) present a new class of multiplicative cascade models with multiscaling log-Lévy statistics that incorporate previously published models as limiting cases: *Kolmogorov's* (1962) "log-normal model" and *Frisch et al.'s* (1978) "beta-model." *Meneveau and Sreenivasan* (1987) describe a simple algorithm in 1D for generating stationary singular measures from a 1-parameter class that obey multiscaling log-binomial statistics. *Cahalan et al.* (1994) generalize this so-called "*p*-model" to a 2-parameter class of bounded random functions that *Marshak et al.* (1993; 1994) show are nonstationary and multifractal. Both the singular stationary *p*-model and its nonstationary bounded counterpart are generalized from 1D to 2D by *Davis et al.* (1996b), incrementing the number of parameters by 2 in the process. These last authors also survey scale-invariant stochastic modeling at large, mentioning several applications to the theory of cloud-radiation interaction. Among the still relatively small number of studies that focus on multiscaling nonstationary random functions, *Benzi et al.'s* (1993) approach is noteworthy: they describe how to use an inverse wavelet transform to generate data with quite arbitrary scale-dependent statistics.

ACKNOWLEDGMENTS

We thank Dr. M. Bleiwiess for inviting us to the 1995 Battlefield Atmospheric Conference and acknowledge stimulating discussions with Drs. A. Arnéodo, R. Cahalan, H. Gerber, S. Lovejoy, Ch. Meneveau, D. Schertzer, and W. Wiscombe.

REFERENCES

- Anselmet, F., Y. Gagne, E. J. Hopfinger, and R. A. Antonia, 1984. "High-order velocity structure functions in turbulent shear flows." *J. Fluid Mech.*, 140:63-80.
- Antonia, R. A., E. J. Hopfinger, Y. Gagne, and F. Anselmet, 1984. "Temperature structure functions in turbulent shear flows." *Phys. Rev. A*, 30:2704-2707.
- Arrault, J., A. Arnéodo, A. Davis, and A. Marshak, 1996. "The wavelet transform maxima modulus approach to multifractal analysis in two dimensions." (in preparation).
- Arnéodo, A., G. Grasseau, and M. Holschneider, 1988. "Wavelet transform of multifractals." *Phys. Rev. Lett.*, 61:2281-2284.
- Arnold, L., 1974. *Stochastic Differential Equations, Theory and Application*, John Wiley & Sons, New York (NY), pp. x+228.
- Benzi, R., L. Biferale, A. Crisanti, G. Paladin, M. Vergassola, and A. Vulpani, 1993. "A random process for the construction of multi-affine fields." *Physica D*, 65:352-358.
- Cahalan, R. F., W. Ridgway, W. J. Wiscombe, T. L. Bell, and J. B. Snider, 1994. "The albedo of fractal stratocumulus clouds." *J. Atmos. Sci.*, 51:2434-2455.
- Davis, A., A. Marshak, and W. J. Wiscombe, 1993. "Bi-multifractal analysis and multi-affine modeling of non-stationary geophysical processes, application to turbulence and clouds." *Fractals*, 1:560-567.
- Davis, A., A. Marshak, W. J. Wiscombe, and R. F. Cahalan, 1994a. "Multifractal characterizations of non-stationarity and intermittency in geophysical fields, observed, retrieved or simulated." *J. Geophys. Res.*, 99:8055-8072.
- Davis, A., A. Marshak, and W. Wiscombe, 1994b. "Wavelet-based multifractal analysis of non-stationary and/or intermittent geophysical signals." In *Wavelets in Geophysics*, E. Foufoula-Georgiou and P. Kumar (Eds.), Academic Press, San Diego (Ca), pp. 249-298.
- Davis, A., A. Marshak, W. J. Wiscombe, and R. F. Cahalan, 1996a. "Scale-invariance in liquid water distributions in marine stratocumulus, Part I, Spectral properties and stationarity issues." *J. Atmos. Sci.* (accepted).
- Davis, A., A. Marshak, W. J. Wiscombe, and R. F. Cahalan, 1996b. "Multifractal characterizations of intermittent and nonstationary geophysical signals - A model-based perspective on ergodicity issues illustrated with cloud data." In *Proceedings of the 2nd International Workshop on Nonstationary Processes and their Applications*, G. Treviño (Ed.), World Scientific, Singapore (in press).
- Frisch, U., P. L. Sulem, and M. Nelkin, 1978. "A simple dynamical model of intermittent fully developed turbulence." *J. Fluid Mech.*, 87:719-724.
- Gerber, H., B.G. Arends, and A. S. Ackerman, 1994. "New microphysics sensor for aircraft use." *Atmos. Res.*, 31:235-252.
- Grassberger, P., 1983. "Generalized dimensions of strange attractors." *Phys. Rev. Lett.*, 97:227-330.
- Gupta, V. K., and E. C. Waymire, 1993. "A statistical analysis of mesoscale rainfall as a random cascade." *J. Appl. Meteor.*, 32:251-267.
- Halsey, T. C., M. H. Jensen, L. P. Kadanoff, I. Procaccia, and B. I. Shraiman, 1986. "Fractal measures and their singularities: The characterization of strange sets." *Phys. Rev. A*, 33:1141-1151.
- Hentschel, H. G. E., and I. Procaccia, 1983. "The infinite number of generalized dimensions of fractals and strange attractors." *Physica D*, 8:435-444.
- King, W. D., D. A. Parkin, and R. J. Handsworth, 1978. "A hot-wire liquid water device having fully calculable response characteristics." *J. Appl. Meteor.*, 17:1809-1813.
- Kolmogorov, A. N., 1941. "Local structure of turbulence in an incompressible liquid for very large Reynolds numbers." *Dokl. Akad. Nauk SSSR*, 30(4):299-303 (in Russian).
- Kolmogorov, A. N., 1962. "A refinement of previous hypothesis concerning the local structure of turbulence in viscous incompressible fluid at high Reynolds number." *J. Fluid Mech.*, 13:82-85.

- Lavallée, D., S. Lovejoy, D. Schertzer, and P. Ladoy, 1993. "Nonlinear variability and simulation of landscape topography." In *Fractals in Geography*, L. De Cola and M. Lam (Eds.), Kluwer, Boston (Mass), pp. 158–192.
- Lovejoy, S., 1982. "Area-perimeter relation for rain and cloud areas." *Science*, 216:185–187.
- Lovejoy, S., D. Schertzer, and A. A. Tsonis, 1987. "Functional box-counting and multiple elliptical dimensions of rain." *Science*, 235:1036–1038.
- Mallat, S. G., 1989. "A theory for multiresolution signal decomposition: the wavelet transformation." *IEEE Trans. Pattern Anal. Mach. Intel.*, 11:674–693.
- Mandelbrot, B. B., 1977. *Fractals: Form, Chance, and Dimension*. W. H. Freeman and Co., San Francisco (Ca), 365 pp.
- Marshak, A., A. Davis, R. Cahalan, and W. Wiscombe, 1993. "Multi-singular and multi-affine properties of bounded cascade models." *Fractals*, 1:702–710.
- Marshak, A., A. Davis, R. Cahalan, and W. Wiscombe, 1994. "Bounded cascade models as nonstationary multifractals." *Phys. Rev. E*, 49:55–69.
- Marshak, A., A. Davis, W. J. Wiscombe, and R. F. Cahalan, 1996a. "Scale-invariance in liquid water distributions in marine stratocumulus, Part II, Multifractal properties and intermittency issues." *J. Atmos. Sci.* (submitted).
- Marshak, A., A. Davis, W. Wiscombe, and H. Gerber, 1996b. "Cloud liquid water variability at 4 cm resolution: Two distinct multifractal regimes." *J. Geophys. Res.* (in preparation).
- Meneveau, C., and K. R. Sreenivasan, 1987. "Simple multifractal cascade model for fully developed turbulence." *Phys. Rev. Lett.*, 59:1424–1427.
- Monin, A. S., and A. M. Yaglom, 1975. *Statistical Fluid Mechanics*, vol. 2, MIT Press, Boston (Mass), 683 pp.
- Muzy, J.-F., E. Bacry, and A. Arnéodo, 1993. "Multifractal formalism for fractal signals: The structure-function approach versus the wavelet-transform modulus-maxima method." *Phys. Rev. E*, 47:875–884.
- Muzy, J.-F., E. Bacry, and A. Arnéodo, 1994. "The multifractal formalism revisited with wavelets." *Int. J. of Bifurcation and Chaos*, 4:245–.
- Ott, E., Y. Du, K. R. Sreenivasan, A. Juneja, and A. K. Suri, 1992. "Sign-singular measures: Fast magnetic dynamos, and high Reynolds-number fluid turbulence." *Phys. Rev. Lett.*, 69:2654–2657.
- Papoulis, A., 1965. *Probability, Random Variables, and Stochastic Processes*, McGraw-Hill, New York (NY).
- Parisi, G., and U. Frisch, 1985. "A multifractal model of intermittency." In *Turbulence and Predictability in Geophysical Fluid Dynamics*, M. Ghil, R. Benzi, and G. Parisi (Eds.), North Holland, Amsterdam, pp. 84–88.
- Pflug, K., S. Lovejoy, and D. Schertzer, 1993. "Generalized scale-invariance, differential rotation and cloud texture: Analysis and Simulation." *J. Atmos. Sci.*, 50:538–553.
- Pierrehumbert, R. T., 1996. "Anomalous scaling of high cloud variability in the tropical Pacific." *Geophys. Res. Lett.* (accepted).
- Press, W. H., S. A. Teukolsky, W. T. Vetterling, and B. P. Flannery, 1993. *Numerical Recipes in FORTRAN*, 2nd ed., Cambridge University Press, New York (NY).
- Schertzer, D., and S. Lovejoy, 1987. "Physical modeling and analysis of rain clouds by anisotropic scaling multiplicative processes." *J. Geophys. Res.*, 92:9693–9714.
- Schertzer D., and S. Lovejoy, 1992. "Hard and soft multifractal processes." *Physica A*, 185:187–194.
- Tessier, Y., S. Lovejoy, and D. Schertzer, 1993. "Universal multifractals: Theory and observations for rain and clouds." *J. Appl. Meteor.*, 32:223–250.
- Vainshtein, S. I., K. R. Sreenivasan, R. T. Pierrehumbert, V. Kashyap, and A. Juneja, 1994. "Scaling exponents for turbulence and other random processes and their relationships with multifractal structure." *Phys. Rev. E*, 50:1823–1835.
- Wiscombe, W., A. Davis, and A. Marshak, 1994. "Scale-invariance, nonstationarity and intermittency in the structure of cloud cover." In *Proceedings of the 4th Atmospheric Radiation Measurement (ARM) Science Team Meeting*, U.S. Dept. of. Energy, pp. 11–14.

OBSCURANT MASS EXTINCTION COEFFICIENT DETERMINATION BY LEAST ABSOLUTE DEVIATION

Brian R. Bullard and Roger E. Davis
Science and Technology Corporation
Las Cruces, New Mexico 88011

Walter Klimek
U.S. Army Research Laboratory
Aberdeen Proving Ground, Maryland 21010

ABSTRACT

The spectrally dependent mass extinction coefficient is a key parameter in obscurant cloud characterization. Calculating mass extinction coefficients for obscurant clouds from field data is difficult because the data required are typically collected from three different instrument types: transmissometers, nephelometers, and dosimeters. Historically, the Beer-Lambert law has been assumed valid in determining mass extinction coefficients for obscurant clouds of a single obscurant type. Although the Beer-Lambert law is straightforward, experience has shown that prudent mass extinction coefficient determination from field data requires extensive data processing and filtering. To that end, a variety of data reduction and analysis techniques have been applied in computing the coefficients. One largely successful technique has been to apply a constrained least-squares fit to filtered data sets of path-integrated concentration, derived from nephelometer and dosimeter data, and optical depth, determined from the transmissometer data. This paper reports on the analysis of an alternate method, least absolute deviation, which does not require filtering data or constraining the fit through the origin. Use of the least absolute deviation saves considerable data processing time and is recommended for determination of mass extinction coefficients. Validation of physical assumptions and comparison to the constrained least-squares approach are discussed. Data from the Large-Area Smoke Screen Experiment and the Mortar Non-Developmental Item Experiment were used for this analysis.

1. INTRODUCTION

The term "robust" was first used in statistics by G.E.P Box in 1953. It describes a statistical estimator that is not sensitive to fractionally large differences from the optimal model for a small number of data points in a data set. Such data points are called "outliers." Classical methods, such as least squares, can be unreliable estimators since they are sensitive to outliers (Launer, 1979; Tukey, 1979; Hogg, 1979). Eliminating outliers by data censoring can be time consuming and introduces a new possible error as well as the need to justify the censorship physically (Agee and Turner, 1979). Mass extinction coefficients are computed from data sets that include outliers, and an analyst must eliminate them before applying a least-squares fit to the data. A method for estimating mass extinction coefficients without censoring data was sought.

The group of robust estimators that use maximum likelihood are not sensitive to outliers and are applicable to estimating parameters or model-fitting. This group of estimators is applicable to the data reduction problem of estimating mass extinction coefficients. More specifically, the least absolute deviation method as an estimator calculates the slope of the best-fit straight line to a distribution in two dimensions. This

method is based on finding the second quartile, or median, of a set of numbers, which is also the value that minimizes the sum of the absolute deviations from the median (Press et al., 1986). The underlying proofs and derivations of the methods used are not discussed in detail; however, a brief description is provided to allow further discussion. This paper only attempts to describe the application of these techniques to a specific data set.

Before a linear fit is applied, the linear correlation should be confirmed. If a linear correlation does not exist between optical depth (OD) and path-integrated concentration (CL), then an argument can be made that none of the linear fitting techniques are applicable. Only trials with a correlation above 0.90 were used for this study and a discussion of trials with "poor" correlations is left for another paper. This paper does not discuss the correlation analysis in depth, but only states that all trials used have a linear correlation. This rationale for discarding trials only applies to the purpose of this paper. There are various other rationales for discarding trials from mass extinction coefficient analysis, which are discussed in detail in Davis and Catherson (1994) and Davis and Bullard (1995).

The first 11 trials from the Mortar Non-Developmental Item Experiment (MNDI) and the single obscurant XM56 and AE32U trials from the Large-Area Smoke Screen Experiment (LASSEX) were used for this study because they were readily available due to other analyses. Table 1 lists the linear correlation coefficients for the trials used in this analysis. The status of each trial is also given. Based solely on the 0.90 correlation acceptance criterion, 29% of the trials were discarded.

2. MASS EXTINCTION COEFFICIENT SIMPLE MODEL

The simple straight-line model for estimating mass extinction coefficients comes from the Beer-Lambert law:

$$T(\Delta\lambda) = e^{-\tau(\Delta\lambda)} \quad (1)$$

where

- $\Delta\lambda$ = spectral band bounded by λ_1 and λ_2
- $T(\Delta\lambda)$ = transmittance in spectral band $\Delta\lambda$
- $\tau(\Delta\lambda)$ = OD of obscurant in spectral band $\Delta\lambda$

The OD is the product of the mass extinction coefficient and the path-integrated concentration along the line of sight (LOS), referred to as the concentration length. The CL does not have wavelength dependence. Substituting this product for $\tau(\Delta\lambda)$ in eq. (1), taking the negative natural log of both sides, and solving for the mass extinction coefficient gives the following equation for the mass extinction coefficient:

$$\alpha_t(\Delta\lambda) = \frac{-\ln(T_t(\Delta\lambda))}{CL_t} \quad (2)$$

where

- $\alpha_t(\Delta\lambda)$ = mass extinction coefficient in the spectral band $\Delta\lambda$, at t , the moment in time the transmittance is observed and for which CL is calculated

Figure 1 is a scatter plot for trial 065 from LASSEX with OD as the dependent variable and CL as the independent variable. From eq. (2) it is apparent that the slope of the best-fit line is an estimate of the mass extinction coefficient.

Table 1. Linear correlation coefficients

Experiment	Trial	OD (vis) vs CL	OD (1.06) vs CL	OD (1.54) vs CL	Status
MNDI	001	0.92	0.92		A
MNDI	002	0.90	0.93		A
MNDI	003	0.74	0.75		D
MNDI	004	0.88	0.60		D
MNDI	005	0.76	0.81		D
MNDI	006	0.82	0.80		D
MNDI	007	0.92	0.91		A
MNDI	008	0.82	0.83		D
MNDI	009	0.89	0.89		D
MNDI	010	0.89	0.90		A
MNDI	011	0.86	0.91		A
LASSEX	001		0.99	0.98	X
LASSEX	002		0.94	0.91	X
LASSEX	003		0.94	0.96	A
LASSEX	004		0.81	0.81	D
LASSEX	005		0.14	0.13	X
LASSEX	011		0.91	0.91	X
LASSEX	015		0.80	0.80	X
LASSEX	017		0.90	0.91	A
LASSEX	018		0.93	0.94	A
LASSEX	022		0.97	0.97	X
LASSEX	023		0.83	0.82	D
LASSEX	026		0.96	0.96	A
LASSEX	065		0.90	0.80	A
LASSEX	066		0.91	0.90	A
LASSEX	071		0.97	0.97	A
LASSEX	078		0.97	0.98	A
LASSEX	079		0.97	0.97	A
LASSEX	080		0.97	0.97	A
LASSEX	081		0.95	0.94	A
LASSEX	082		0.99	0.98	A
LASSEX	084		0.90	0.90	A
LASSEX	085		0.93	0.93	A
LASSEX	086		0.99	0.97	A

Status: A = accepted trial

D = discarded trial

X = previously discarded trial (see Davis and Bullard, 1995)

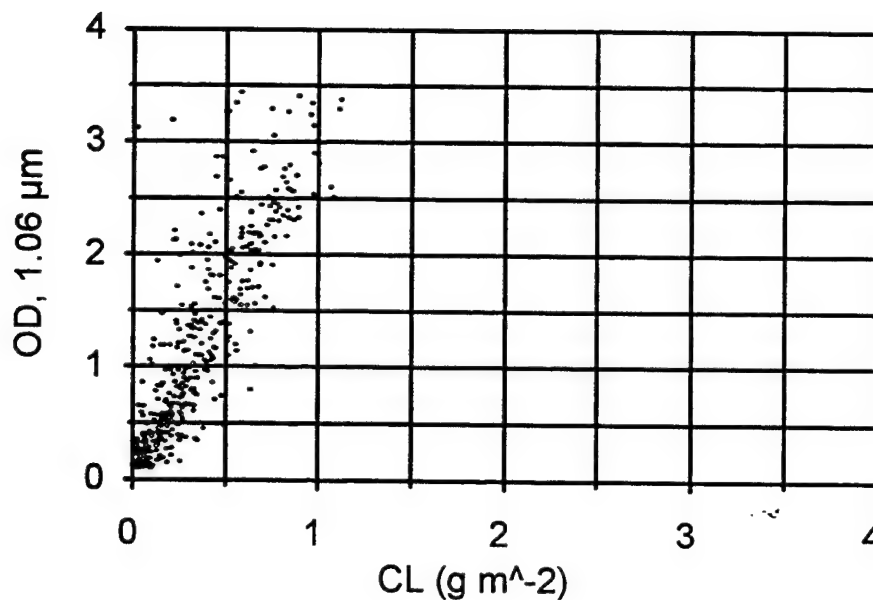


Figure 1. Scatter plot for trial 065.

3. LEAST-SQUARES ESTIMATE

Assume that the measurement error for each data point is random and distributed normally around the model. Further assume that the standard deviations of these distributions (σ_i) for all data points are equal. The simple straight-line model for estimating mass extinction coefficient is then the best-fit line given by

$$y = mx + c \quad (3)$$

where m is the slope and c is the y -intercept. Before the least-squares method is used, the data are screened to eliminate outliers. This process eliminates data points occurring primarily under conditions of high transmittance (clear air) and data points occurring when the transmissometer detector threshold was reached. Only data between 3% and 90% transmittance were used. Table 2 lists the percentage of data that are eliminated by this filter. Figures 2 and 3 show the scatter plots of unscreened and screened data, respectively.

In previous work by Davis and Bullard (1995) and Davis and Catherson (1994), a least-squares fit constrained to pass through the origin has been used. This constraint reduces the influence that clear-air or near-clear-air values have on the fit. Constraining the fit through the origin is justified physically, because if there is no concentration, then there should be 100% transmittance and the value of the function will be 0. Constraining the fit eliminates c from eq. (3). See Davis and Bullard (1995) and Davis and Catherson (1994) for additional discussion on using the least-squares method.

As described here, the least-squares approach to estimating the mass extinction coefficient is somewhat unsatisfying. Data screening to discard outliers is time consuming and the thresholds for screening are arguably subjective. Additionally, the constraint of the fit through the origin, although reasonable physically, has the effect of giving low weight to measurements made when the obscurant cloud is optically thin.

Table 2. Percentage of data eliminated with filter

Experiment	Trial	Total points	Screened data	% eliminated
MNDI	001	269	148	45
MNDI	002	267	136	49
MNDI	007	187	30	84
MNDI	010	230	22	90
MNDI	011	160	43	73
LASSEX	003	657	458	30
LASSEX	017	616	530	14
LASSEX	018	597	515	14
LASSEX	026	631	576	9
LASSEX	065	645	406	37
LASSEX	066	603	272	55
LASSEX	071	1021	966	5
LASSEX	078	850	680	20
LASSEX	079	951	798	16
LASSEX	080	1480	1459	1
LASSEX	081	941	575	39
LASSEX	082	839	742	12
LASSEX	084	969	821	15
LASSEX	085	848	714	16
LASSEX	086	1622	1089	33
Total:		14383	10980	24

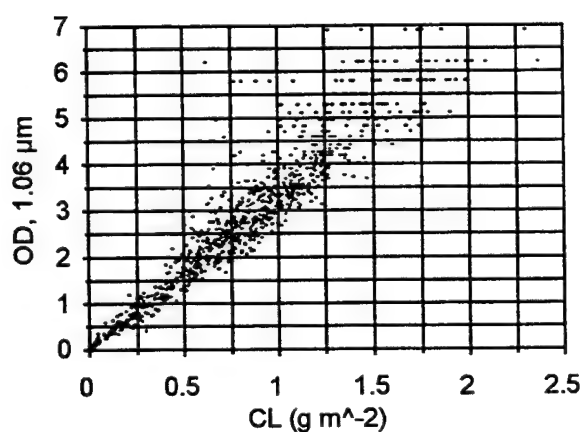


Figure 2. Unscreened data.

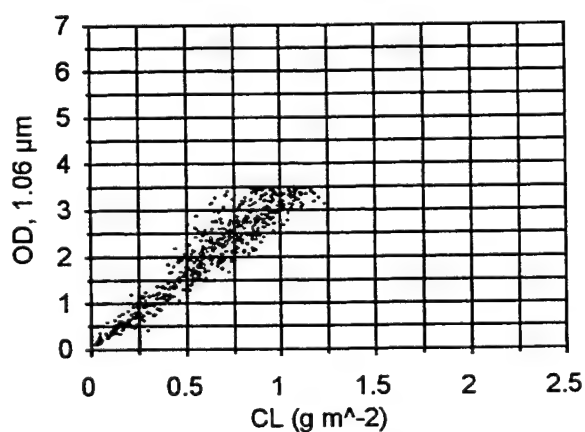


Figure 3. Screened data.

4. ROBUST ESTIMATES

Robust statistical techniques strive to reduce the influence of outliers on best-fit estimators, such as least squares. The outliers present in the optical depth and CL data sets are believed to be due primarily to errors in collecting caused by instrument limitations. Reducing the influence of these error-produced data points is desirable. This study focussed on two robust methods: the least absolute deviation method and the robust least-squares method. The least absolute deviation method requires code to be written independent of existing least-squares code, whereas the robust least-squares method only requires an additional subroutine be added to existing least-squares code (Huber, 1981).

4.1 Least Absolute Deviation Estimate

The least absolute deviation is a robust statistical method for computing a linear fit. Because the simple model described in Section 2 is a distribution in two dimensions represented by a straight line, least absolute deviation will give an estimation of the mass extinction coefficient less sensitive to outliers than least squares.

The merit function that we need to minimize is given by

$$\sum_{i=1}^N |y_i - mx_i - c| \quad (4)$$

If we take the derivative of this expression with respect to the parameter m , we get the equation that must hold at the chi-square minimum:

$$0 = \sum_{i=1}^N x_i \text{sign}(y_i - mx_i - c) \quad (5)$$

Here the sign function multiplies x_i by +1 if $y_i + mx_i - c \geq 0$ and by -1 if $y_i + mx_i - c < 0$. This merit function is used instead of the standard chi-square merit function since we assume the σ_i values are all equal. This merit function comes from the estimate of model parameters obtained by minimizing the chi-squared function [similar to eq. (4)] with the σ_i as a denominator given by the general maximum likelihood argument.

The problem, then, is to minimize the absolute deviation from an initial guess for the best-fit line. A nonconstrained least-squares fit is used as the initial guess. The median of a set of numbers is also the value that minimizes the sum of the absolute deviations from the median, so the value that will minimize eq. (5) with a fixed m is

$$c = \text{median}(y_i - mx_i) \quad (6)$$

If we replace c in eq. (5) with eq. (6), we get an equation with one unknown that can be easily solved with bracketing and bisection. For a complete discussion on bracketing and bisection, see Chapter 9.1 of Press et al. (1986).

4.2 Robust Version of Least-Squares Estimate

The robust least-squares method attempts to add a robust aspect to the existing least-squares fit method by replacing the y measurements with pseudo-measurements that have been adapted to "pull" the outliers in towards their estimated values. The fit is recomputed with these pseudo-values, thus decreasing the influence that outliers have on the fit. This process is repeated until the estimated variance converges. The criteria for adapting the dependent values is given by (Huber, 1981):

$$y_i^p = y_i, \quad \text{if } |\hat{e}_i| \leq cs, \quad (7)$$

$$= \hat{y}_i - cs, \quad \text{if } \hat{e}_i < -cs, \quad (8)$$

$$= \hat{y}_i + cs, \quad \text{if } \hat{e}_i > cs. \quad (9)$$

where

y_i^p	=	pseudo-measurements
y_i	=	actual measurements
\hat{y}_i	=	estimated y
\hat{e}_i	=	estimated error (residual)
s	=	estimated variance
c	=	constant (determines measure of robustness, usually $1 < c < 2$; 1.5 for this analysis)

As is evident from eqs (7), (8), and (9), only the outliers will be adjusted by this method. For a complete discussion of this method and a more technical description see Huber (1981).

5. RESULTS

Comparing the methods quantitatively is a substantial statistical task itself. Referring to one or another method as "better" should be avoided, since this term is difficult to define within the realm of statistics. The term does have application within the realm of data processing, however. A method that does not require *a priori* knowledge of the data set and does not require manual data screening can be accepted as a "better" data processing method. In this sense, the robust methods are better than the least squares method, since they require no subjective screening and less data processing.

Mass extinction coefficients determined from each method are presented for quick-look assessment of the methods. The estimated errors from each method were computed, as were the number of estimated errors outside of $\pm 2\sigma$. The estimated errors give an initial quantitative comparison of the methods. The estimated errors can be misleading, however, particularly with small sample sizes. The correlations mentioned in the introduction are also sensitive to the sample size, a topic left for future analysis and discussion.

5.1 Estimated Mass Extinction Coefficients

Table 3 lists the mass extinction coefficients computed by all three estimation methods. Based on the physical properties of the data, when the y -intercepts are computed, they should be close to zero. The table lists the y -intercepts for the two robust methods, and their values are close to zero. The α_1 , α_2 , and α_3 are

the estimates from the least squares, least absolute deviation, and robust least-squares methods respectively. The $y\text{-int}_2$ and $y\text{-int}_3$ values are from the least absolute deviation and the robust least-squares methods respectively.

The maximum difference in α estimation between the methods is 16.7% and the average difference is 7.2%. This result indicates that all methods provide a similar estimate. The maximum distance from the origin for the y -intercepts is 0.31 and the average distance is 0.05. The maximum α estimate difference is from the MNDI trial 010. The maximum distance from the origin is from the LASSEX trial 066. This result indicates that closer examination of the data from these trials would be necessary if the purpose of the study were to characterize the trials rather than to study the statistical estimators.

Table 3. Mass extinction coefficients from the three methods

Experiment	Trial	Visible					1.06 μm				
		α_1	α_2	α_3	$y\text{-int}_2$	$y\text{-int}_3$	α_1	α_2	α_3	$y\text{-int}_2$	$y\text{-int}_3$
MNDI	001	0.18	0.18	0.18	-0.01	-0.01	0.06	0.05	0.06	0.00	0.00
MNDI	002	0.21	0.20	0.21	-0.01	-0.01	0.08	0.06	0.06	0.00	0.00
MNDI	007	0.59	0.61	0.67	-0.04	-0.04	0.11	0.10	0.11	-0.01	-0.01
MNDI	010	0.28	0.24	0.24	-0.02	-0.01	0.35	0.32	0.33	0.00	0.00
MNDI	011	0.47	0.45	0.52	-0.07	-0.06	0.54	0.54	0.59	-0.05	-0.04
		1.06 μm					1.54 μm				
		α_1	α_2	α_3	$y\text{-int}_2$	$y\text{-int}_3$	α_1	α_2	α_3	$y\text{-int}_2$	$y\text{-int}_3$
LASSEX	003	2.71	2.53	2.53	0.09	0.06	1.11	1.15	1.15	-0.01	-0.02
LASSEX	017	1.28	1.21	1.25	0.03	0.02	1.29	1.23	1.26	0.04	0.03
LASSEX	018	1.31	1.24	1.24	0.08	0.07	1.33	1.25	1.25	0.09	0.08
LASSEX	026	1.24	1.17	1.18	0.06	0.06	1.28	1.19	1.20	0.07	0.07
LASSEX	065	3.26	3.22	3.53	0.11	0.05	1.68	1.64	1.87	0.02	-0.01
LASSEX	066	3.77	3.24	3.38	0.31	0.23	1.81	1.81	1.99	0.02	0.02
LASSEX	071	1.25	1.18	1.19	0.11	0.11	1.25	1.18	1.19	0.09	0.09
LASSEX	078	1.50	1.41	1.43	0.04	0.03	1.49	1.44	1.46	0.02	0.02
LASSEX	079	1.31	1.26	1.24	0.03	0.03	1.33	1.31	1.28	0.02	0.03
LASSEX	080	1.47	1.25	1.26	0.12	0.12	1.46	1.28	1.29	0.10	0.10
LASSEX	081	3.27	3.26	3.35	0.09	0.06	1.37	1.32	1.36	0.00	0.00
LASSEX	082	3.25	3.03	3.04	0.13	0.13	1.43	1.30	1.31	0.08	0.08
LASSEX	084	1.52	1.44	1.43	0.05	0.05	1.50	1.46	1.44	0.02	0.02
LASSEX	085	1.09	1.08	1.10	0.00	0.00	1.10	1.13	1.15	-0.04	-0.05
LASSEX	086	2.53	2.46	2.52	0.02	0.01	1.01	1.02	1.04	-0.04	-0.04

5.2 Comparison of Estimated Errors

Table 4 lists the standard deviations for the estimated y values and the estimated errors (residuals). The σ values for each method are close, indicating that the methods of estimation are in agreement. The low values of the percent of the absolute values of estimated errors greater than 2σ show that all three methods are adequate for these calculations.

Figure 4 displays the estimated errors plotted versus estimated y values for LASSEX trial 003. Top to bottom, the plots are the estimated errors for the least-squares method, the least absolute deviation method, and the robust least-squares method. These plots should have no trends if the data sets and the estimated errors are normal, and thus linear fits are applicable. This figure is representative of the data sets studied here. Such plots should be produced for each trial to check for major deviations from the linear fit model.

6. CONCLUSIONS AND SUGGESTIONS

The three estimation methods provided similar estimates for mass extinction coefficients for these data sets, and the study of the estimated errors indicates that all three are acceptable estimators. The significance of this observation is twofold. First, using one of the robust methods would eliminate data processing steps and some human intervention and would allow the acceptance of the entire data set. Second, the result adds some statistical validity to the physical assumptions made in screening the data and constraining the fit through the origin, since the robust methods do not rely on physical assumptions and still provide comparable estimates.

This is an ongoing study and is not presented as definitive. Continued work in the area of robust statistical applications for obscurant field experiment data is strongly suggested. Several avenues of interest are: (1) continued study of the linear correlation between optical depth and CL, (2) determination of levels of relative transmittance and concentration for optimal linear correlation, (3) study of the statistical processing applied to raw sensor readings, (4) application of robust methods to previous experiment data sets in an attempt to reevaluate the calculated estimates, and (5) investigation of robust methods of identifying outliers with strong influences on the fit.

ACKNOWLEDGMENT

The authors express appreciation to Dr. Clem Ota, Science and Technology Corporation, for reviewing the manuscript.

Table 4. Standard deviations of estimated y values and estimated errors

Trial	Band	Estimated y			Estimated error			Percent of error > 2 σ		
		σ_1	σ_2	σ_3	σ_1	σ_2	σ_3	1	2	3
00156 (MNDI)	vis	0.10	0.10	0.10	0.05	0.05	0.05	5.2	7.1	5.9
00156	1.06 μm	0.03	0.03	0.03	0.01	0.01	0.01	6.3	7.4	6.3
00256	vis	0.12	0.12	0.12	0.06	0.06	0.06	4.9	4.5	4.5
00256	1.06 μm	0.04	0.04	0.04	0.02	0.02	0.02	6.7	3.7	4.5
00755	vis	0.83	0.87	0.94	0.45	0.44	0.43	5.3	5.3	5.9
00755	1.06 μm	0.15	0.14	0.15	0.07	0.07	0.07	7.0	4.3	5.9
01060	vis	0.05	0.04	0.05	0.03	0.03	0.02	11.7	4.3	3.9
01060	1.06 μm	0.07	0.06	0.06	0.03	0.03	0.03	3.5	4.8	4.3
01160	vis	0.15	0.14	0.17	0.10	0.10	0.10	2.5	1.9	2.5
01160	1.06 μm	0.17	0.17	0.19	0.09	0.09	0.09	3.8	3.8	3.8
00381 (LASSEX)	1.06 μm	1.39	1.30	1.30	0.48	0.47	0.47	4.0	4.0	4.4
00381	1.54 μm	0.57	0.59	0.59	0.18	0.18	0.18	4.4	4.0	4.0
01782	1.06 μm	0.78	0.74	0.77	0.36	0.37	0.36	5.5	5.5	5.7
01782	1.54 μm	0.79	0.75	0.77	0.36	0.36	0.36	5.8	5.5	5.5
01882	1.06 μm	0.74	0.70	0.71	0.27	0.27	0.27	6.2	6.4	6.4
01882	1.54 μm	0.75	0.71	0.71	0.27	0.26	0.27	6.7	6.2	6.2
02679	1.06 μm	0.54	0.51	0.52	0.16	0.15	0.15	5.7	5.7	6.0
02679	1.54 μm	0.56	0.52	0.53	0.16	0.16	0.15	4.9	6.0	6.0
06578	1.06 μm	1.45	1.44	1.57	0.80	0.80	0.79	5.9	5.6	4.7
06578	1.54 μm	0.75	0.73	0.83	0.65	0.66	0.64	4.2	4.2	3.9
06681	1.06 μm	2.07	1.78	1.86	0.89	0.85	0.86	7.8	7.1	7.3
06681	1.54 μm	0.99	1.00	1.09	0.57	0.56	0.55	4.8	4.8	5.3
07179	1.06 μm	0.89	0.84	0.85	0.22	0.22	0.22	5.8	5.5	5.5
07179	1.54 μm	0.89	0.84	0.85	0.22	0.21	0.21	5.7	5.1	5.1
07879	1.06 μm	0.34	0.32	0.33	0.08	0.08	0.08	5.2	4.8	4.8
07879	1.54 μm	0.34	0.33	0.34	0.08	0.08	0.08	4.6	4.0	4.1
07982	1.06 μm	0.35	0.34	0.34	0.08	0.08	0.08	4.7	4.1	4.1
07982	1.54 μm	0.36	0.35	0.35	0.08	0.08	0.08	4.0	4.6	4.2
08082	1.06 μm	0.37	0.32	0.32	0.10	0.08	0.08	5.0	5.2	5.3
08082	1.54 μm	0.37	0.33	0.33	0.09	0.08	0.08	5.5	5.7	5.5
08181	1.06 μm	1.54	1.53	1.58	0.54	0.54	0.54	6.2	5.3	4.6
08181	1.54 μm	0.64	0.62	0.64	0.24	0.24	0.24	4.4	4.8	4.4
08278	1.06 μm	1.16	1.08	1.09	0.18	0.16	0.16	4.3	5.7	5.6
08278	1.54 μm	0.51	0.46	0.47	0.10	0.09	0.09	9.1	4.3	4.2
08479	1.06 μm	0.47	0.44	0.44	0.21	0.21	0.21	5.3	5.5	5.3
08479	1.54 μm	0.46	0.45	0.44	0.21	0.21	0.21	5.3	5.7	5.4
08579	1.06 μm	0.64	0.63	0.64	0.25	0.25	0.25	5.7	5.5	5.7
08579	1.54 μm	0.65	0.66	0.67	0.26	0.26	0.26	6.0	6.0	5.9
08678	1.06 μm	1.02	0.99	1.02	0.24	0.24	0.24	6.3	6.5	6.3
08678	1.54 μm	0.41	0.41	0.42	0.12	0.12	0.12	4.9	5.4	5.4

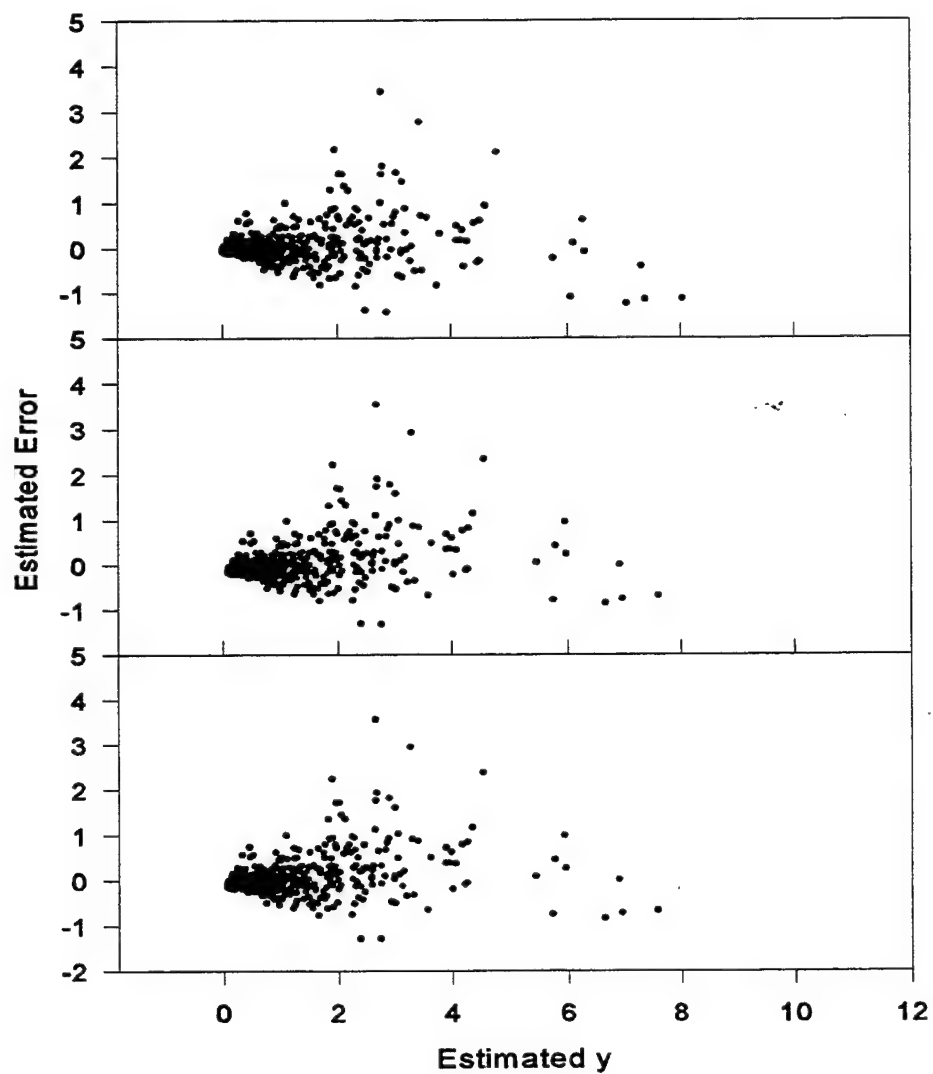


Figure 4. Estimated error plots for least-squares, least absolute deviation, and robust least-squares (top to bottom).

REFERENCES

- Agee, W.S., and R.H. Turner, 1979. "Application of Robust Regression to Trajectory Data Reduction." In *Robustness in Statistics, Proceedings of Robustness in Statistics Workshop*, R.L. Launer and G.N. Wilkinson, eds., Academic Press, New York, pp 107-126.
- Davis, R.E., and B.R. Bullard, 1995. *Characterization of Obscurant Clouds Produced by the XM56 and AE32U*. STC Technical Report 6254, Science and Technology Corporation, 101 Research Drive, Hampton, VA.
- Davis, R.E., and R.L. Catherson, 1994. *Analysis of Obscurant Clouds Produced by the XM-56 and SG-18 Bispectral Generators at Smoke Week XV*. STC Technical Report 6245, Science and Technology Corporation, 101 Research Drive, Hampton, VA.
- Hogg, R.V., 1979. "An Introduction to Robust Estimation." In *Robustness in Statistics, Proceedings of Robustness in Statistics Workshop*, R.L. Launer and G.N. Wilkinson, eds., Academic Press, New York, pp 1-18.
- Huber, P.J., 1981. *Robust Statistics*, John Wiley & Sons, Inc., New York.
- Launer, R.L. 1979. Preface to *Robustness in Statistics, Proceedings of Robustness in Statistics Workshop*, R.L. Launer and G.N. Wilkinson, eds., Academic Press, New York, pp ix-x.
- Miller, I., J.E. Freund, and R.A. Johnson, 1990. *Probability and Statistics for Engineers*. Prentice Hall, Englewood Cliffs, New Jersey.
- Press, W.H., B.P. Flannery, S.A. Teukolsky, and W.T. Vetterling, 1986. *Numerical Recipes, The Art of Scientific Computing*. Cambridge University Press, New York.
- Tukey, J.W. 1979. "Robust Techniques for the User." In *Robustness in Statistics, Proceedings of Robustness in Statistics Workshop*, R.L. Launer and G.N. Wilkinson, eds., Academic Press, New York, pp 103-106.

The Number of Laser Wavelengths Limit Biodetection in Fluorescence Lidar

David L. Rosen and James B. Gillespie

U.S. Army Research Laboratory

Battlefield Environment Directorate

White Sands Missile Range, NM 88002-5501

Abstract

Fluorescence lidar using a tunable laser source is theoretically analyzed. Factor analysis--rank annihilation is used as an algorithm for analyzing hypothetical lidar returns in the program, for bacteria alone, growth medium alone, and a mixture of growth medium and bacteria. For the sample studied, we found that six laser wavelengths were sufficient to determine the presence of a compound. If only four of those six laser wavelengths were used, the choice of which four was critical in determining the presence of the bacteria.

1. Introduction

Fluorescence lidar has been studied for remote detection of microorganisms. However, background fluorescence and sky radiance severely limit its performance. This

is because fluorescence emission spectra are broad and devoid of line structure. Because the spectra are so broad, the fluorescence spectrum of a microorganism often overlaps the fluorescence spectrum of other substances in the environment. Therefore, the emission spectrum, by itself, may be insufficient to discriminate between a microorganism and its background.

Fluorescence intensity can be measured as a function of both emission wavelength and excitation wavelength. The functional dependence of fluorescence on both excitation and emission wavelength, a 2-dimensional spectrum, is much more specific than an emission spectrum alone. We have studied factor analysis - rank annihilation (FARA) as a set of algorithms for analyzing 2-dimensional spectra.^{1,2} Our studies show that although FARA is a promising technique, it has certain requirements.

The number of wavelengths required by FARA limit potential lidar performance. FARA calculations require that both the number of excitation wavelengths and the number of emission wavelengths exceed the number of components in the unknown sample. A component is a fluorescent species, which is often a pure compound, in the unknown sample.

The number of excitation wavelengths are severely limited by the absence of wavelength tunable lasers. Lasers are currently the only plausible excitation source for remote sensing because of their wavelength purity and small angular divergence. Spectrometers with charge couple devices can rapidly measure emission spectra, but excitation spectra are not easily measured. In actual practice, one needs more excitation wavelengths than components to identify an unknown sample.

The effect of wavelength number on sample identification was analytically studied. We analyzed the identification of bacteria in a hypothetical mixture of bacteria and growth media for different numbers of wavelengths. This paper first describes the theory of the factor analysis - rank annihilation, the hypothetical data, and the calculations.

2. Theory

The theory of factor analysis - rank annihilation (i.e., FARA), as applied to detection algorithms, will be described in this section. We will describe excitation-emission matrices, laboratory measurements, lidar measurements, and the overlap index.

The excitation - emission matrix (i.e., EEM) is a way of storing two dimensional data.³ The EEM has rows that are emission spectra and columns that are excitation spectra. Consider a laboratory measurement of an EEM from an unknown sample. Let M be the number of excitation wavelengths, N the number of emission wavelengths, and D be the EEM from this ideal measurement, Λ_i be the measured excitation wavelengths and λ_j the measured emission wavelengths where $i=1,\dots,M$ and $j=1,\dots,N$. The sample EEM, D is an M by N matrix where an elements of the matrix, D_{ij} , are values of the fluorescence intensity at excitation wavelength Λ_i and emission wavelength λ_j . We call this laboratory EEM, D , the complete EEM of the sample.

The EEM from a lidar measurement would not contain as much information as an EEM from a laboratory measurement. Lidar would require powerful, robust lasers that may not have the same amount of wavelength tunability as laboratory excitation sources. Furthermore, sky radiance would limit the useful region of the emission spectra. In order

to reduce the noise from sky radiance, the user will restrict the measured emission spectra to the solar blind region. Consider a lidar measurement of an EEM from an unknown sample. Let m be the number of excitation wavelengths, n the number of emission wavelengths, and \mathbf{d} be the EEM from this ideal measurement, $\Lambda_{i'}$ be the measured excitation wavelengths and $\lambda_{j'}$ the measured emission wavelengths where $\Lambda_{i'}$ and $\lambda_{j'}$ are selected from the set of wavelengths in the laboratory measurements. The sample EEM, \mathbf{d} is an m by n matrix where an elements of the matrix, $d_{ij'}$, are values of the fluorescence intensity at excitation wavelength $\Lambda_{i'}$ and emission wavelength $\lambda_{j'}$. The indices i' and j' are different from the indices i and j . The index $i'=1,\dots,m$ and $j'=1,\dots,n$. We call the resulting EEM, \mathbf{d} , a truncated EEM of the sample. The complete EEM, \mathbf{D} , is identical to the truncated EEM, \mathbf{d} , where $m=M$ and $n=N$.

The overlap index provides a method for determining the presence of a compound in a sample by comparing an EEM from the sample with spectra from an analyte.⁴ We call a compound an analyte if the researcher is looking for it in the sample. We designate the analyte compound, s . The researcher takes an excitation spectrum, \mathbf{X} , and an emission spectrum, \mathbf{Y} , from the pure analyte under laboratory conditions. \mathbf{X} is a row vector with M elements and \mathbf{Y} is a row vector with N elements. The components of \mathbf{X} and \mathbf{Y} are the values of the intensity of the analyte spectra at the same wavelengths as were used to find \mathbf{D} .

The overlap index, $p(\mathbf{D},r,s)$, is now defined. Decompose the EEM, \mathbf{D} , by single value decomposition. Then, one has two sets of eigenvectors. Eigenvectors \mathbf{U}_k are all M elements long and eigenvectors \mathbf{V}_k are all N elements long. Order the eigenvectors so that as k increases, the corresponding singular value decreases. Assume there are r

fluorescing compounds in the sample. Then the overlap index, $p(D,r,s)$, for the complete EEM is:

$$p(D,r,s) = \frac{\sum_{k=1}^r |U_k \cdot X|^2 |V_k \cdot Y|^2}{\sum_{k=1}^r |U_k|^2 |V_k|^2} \quad (1)$$

The overlap index provides a method of detection in an ideal laboratory measurement. In an ideal laboratory measurement, the fluorescence spectra of all components are linearly independent. If the spectra are linearly independent, one can show the following. If $p=1$, then the analyte s is in the unknown sample. If $p<1$, the analyte s is not in the sample. Therefore, the value of p determines the presence or absence of s in an ideal measurement. In an actual laboratory experiment, often due to a multicomponent reference, $p(D,r,s)<1$ for an unknown containing analyte and background.

Ideal conditions are difficult to attain, although one can achieve them under laboratory conditions. The signal must be much larger than the random noise. The analyte must be a pure compound with only one fluorescent center in its molecule. Algorithms for calculating r exist but are sensitive to error. The choice of wavelengths determines linear independence. For example, if the chosen wavelengths λ_i or λ_j are too close together, so that the spectra are flat, the spectra will not be linearly independent. Linear independence implies that both the number of excitation wavelengths and the number of emission wavelengths are larger than the number of components, r .

A restricted choice of wavelengths in a lidar measurement results in a truncated EEM, d , which was defined previously. Only part of the complete analyte spectra are useful. We take the part of the analyte spectra, X and Y , that lie within the restricted choice

of wavelengths and define these spectra as a truncated excitation spectrum, \mathbf{x} , and a truncated emission spectrum, \mathbf{y} . The components of \mathbf{x} and \mathbf{y} are those components of \mathbf{X} and \mathbf{Y} at the same set of wavelengths used to define \mathbf{d} . The overlap index, $p(\mathbf{d},r,s)$, is:

$$p(\mathbf{d},r,s) = \frac{\sum_{k=1}^r |u_k \mathbf{x}|^2 |v_k \mathbf{y}|^2}{\sum_{k=1}^r |u_k \mathbf{x}|^2 + \sum_{k=1}^r |v_k \mathbf{y}|^2} \quad (2)$$

Although the laboratory measurement resulting in $p(\mathbf{D},r,s)$ is ideal, the lidar measurement resulting $p(\mathbf{d},r,s)$ may not be ideal. Even if $p(\mathbf{D},r,s)$ is 1, showing the presence of the compound s , $p(\mathbf{d},r,s)$ may not be 1. Similarly, even if $p(\mathbf{D},r,s)$ is less than 1, showing the absence of the compound s , $p(\mathbf{d},r,s)$ may be 1. We wish to show how truncating an EEM could bias interpretation of a lidar return.

Codes have been developed to apply FARA to lidar returns.⁵ The Fortran code, OVERLAPD, calculates the overlap index as a function of distance with shot noise. We will describe the feasibility of detecting bacteria against a fluorescence background of growth media.

3. Lidar Data

Emission spectra at 6 different wavelengths were measured, separately, for both bacteria (*B. cereus*) and the growth medium for bacteria by previous investigators.⁶ We assumed that the bacteria was the analyte and that the growth medium is the interfering background. The hypothetical lidar is trying to detect the analyte, bacteria, against a

background of growth medium. Using this data, we calculated EEM for 3 unknown samples: one containing bacteria alone, one containing growth medium alone, and one containing a mixture of bacteria and growth medium. We assumed that the peak fluorescence of growth media equaled the peak fluorescence of bacteria. We spaced the wavelengths so that for the complete EEM, D , there were 32 emission wavelengths equally spaced from 309 nm to 399 nm and 6 excitation wavelengths (228 nm, 244 nm, 252 nm, 272 nm, 283 nm, and 303 nm).

Effective ranks were calculated. We calculated the rank of bacterial EEM as 1. The ratio of second to first eigenvalue was very small for the bacteria EEM. The rank of 1 allowed us to use the following technique described by Malinowski.⁷ To remove some noise from the reference, we used the first eigenvectors of the bacterial EEM as excitation and emission spectra for the bacteria. The rank of the mixture EEM was estimated as 4, although the ratio of second to first eigenvalue for the mixture EEM was larger than the ratio for the bacteria EEM.

Different truncated EEM, d , were constructed from D by deleting rows. We constructed corresponding truncated spectra, x and y , from the first eigenvectors of the truncated EEM of the analyte. Using the first eigenvectors is a way of both truncating the spectrum and removing noise from the analyte spectra. Then, OVERLAPD calculated overlap index as a function of distance for each curve. We assumed a value of $r=4$ for all calculations. We compare p in the case of D and various d for the three hypothetical samples: pure analyte (bacteria), pure background (growth medium), and a mixture (bacteria and growth medium). We will show that the choice of wavelengths is critical for a determination of analyte against background.

4. Results

The overlap index, $p(\mathbf{D}, 4, \text{bacteria})$, as a function of distance is shown in Figure 1. We used 6 excitation wavelengths (228, 244, 252, 272, 283, and 303 nm) and 32 emission wavelengths (303-399 nm). No sky radiance was used in the calculation. For distances less than 1 km, the overlap index for both bacteria alone and the mixture are close to 1 and the overlap index for growth medium alone is about 0.8. For distances greater than 1 km, the shot noise overwhelms the signal for all cases that we will show. All overlap indices fall below 1 and the noise fluctuations are larger than the differences between the samples for distances greater than 1 km.

A truncated overlap index, $p(\mathbf{d}_1, 4, \text{bacteria})$, as a function of distance is shown in Figure 2. No sky radiance was included. We used 4 excitation wavelengths (244, 252, 283, and 303 nm) and 32 emission wavelengths (306-399 nm) to define \mathbf{d}_1 . For distances less than 1 km, the overlap index for both bacteria alone is close to 1 and the overlap index for both growth medium alone and mixture is about 0.8. Because the mixture and the background have nearly the same overlap index, 0.8, determining the presence of bacteria would be difficult against this type of background. However, the overlap index of the pure analyte was 1. This is clearly different from the overlap index of the background alone. Therefore, for this choice of excitation wavelengths, one could determine the presence of bacteria if the background of growth medium was sufficiently small.

A truncated overlap index, $p(\mathbf{d}_2, 4, \text{bacteria})$, as a function of distance is shown in Figure 3. No sky radiance was included. We used 4 excitation wavelengths (252, 272, 283, and 303 nm) and 32 emission wavelengths (303-399 nm) to define \mathbf{d}_2 . For distances

less than 1 km, the overlap index for both bacteria alone is close to 1 and the overlap index for both growth medium alone and mixture is about 0.95. Because the mixture and the background have nearly the same overlap index, 0.8, determining the presence of bacteria would be difficult against this type of background. However, the overlap index, 0.95, of the background is very close to that of the pure analyte, 1. Therefore, this choice of 4 excitation wavelengths is insufficient for any type of determination. Although d_1 and d_2 have the same dimensions, d_1 is clearly better than d_2 for determination of bacteria in growth media. The choice of excitation wavelengths made a difference.

5. Conclusions

Fluorescence lidar has a potential for detection of bacteria. This study demonstrated the analysis of bacteria against a background of growth medium. The more excitation wavelengths one has, the easier the determination of the bacteria. However, the choice of excitation wavelengths is critical for the determination of bacteria against background.

References

1. Rosen, David L. and James B. Gillespie, Appl. Opt. 31, 4214 (1992).
2. Rosen, David L. and J. B. Gillespie, Appl. Opt. 28, 4280 (1989).
3. Ho, C.-N., G. D. Christian, and E. R. Davidson, "Application of the Method of Rank Annihilation to Quantitative Analyses of Multicomponent Fluorescence Data from Video Fluorometer," Anal. Chem. 50, 1108 (1978).
4. Ho, C.-N., G. D. Christian, and E. R. Davidson, "Application of the Method of Rank Annihilation to Fluorescent Multicomponent Mixtures of Polynuclear Aromatic Hydrocarbons," Anal. Chem. 52, 1071 (1980).

5. Rosen, David L. and James B. Gillespie, "Atmospheric extinction effect on analysis of UV fluorescence signatures," *Appl. Opt.*, pp.4214-4223, 1992.
6. Faris, Gregory W., Andy Williams, Clinton Carlisle, and Burt Bronk, Spectrally Resolved Absolute Fluorescence of *B. Globigii* and *B. Cereus*," Report prepared by SRI International, Report Number 2913, for U. S. Army Chemical Research Development and Engineering Center, pp. 29-31 (1992).
7. Malinowski, Edmund R., *Factor Analysis in Chemistry* - 2nd ed., pp. 83-97 (Wiley, NY,1991)

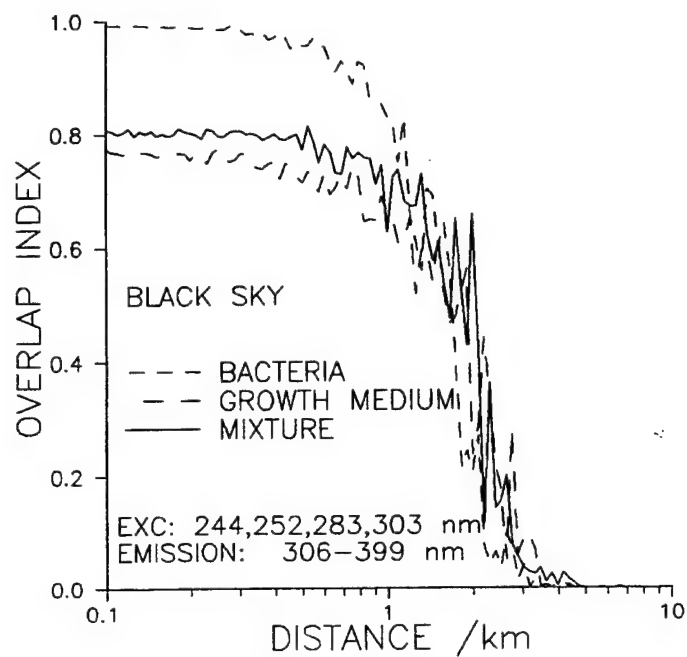


Figure 1. Four Compounds, six excitation wavelengths

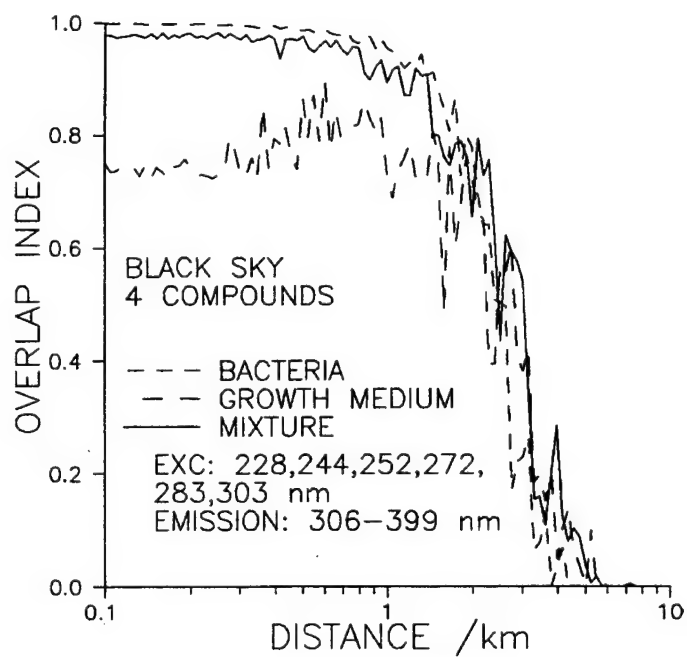


Figure 2. Four excitation wavelengths

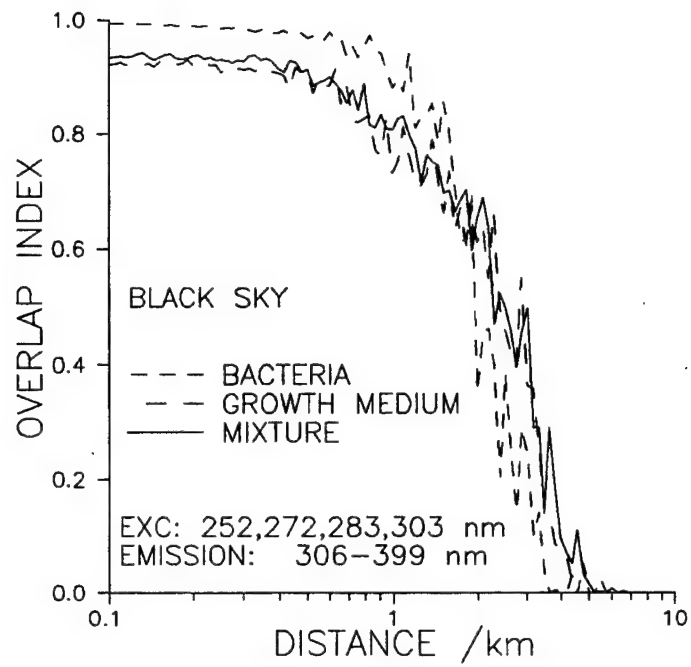


Figure 3. Four excitation wavelengths

Session V

**ATMOSPHERIC SIMULATION AND
ANALYSIS**

Multifractal Characterization As An Analytical Tool

For

Atmospheric Research

Thelma Chenault, Max P. Bleiweiss, Rene' Smith, and Martin Bayang
U.S. Army Research Laboratory
White Sands Missile Range, New Mexico USA

ABSTRACT

A recent paper by Davis et al. (JGR, Vol. 99, No. D4, pages 8055-8072, April 1994) described the tools necessary for the characterization of a process through the determination of the degree of intermittency and the degree of stationarity of that process. Both of these parameters are necessary for the understanding of atmospheric processes. Consequently, these tools were applied to three different data sets: temperature time series, wind speed time series, and concentration path length (CL) time series. In the first two instances, the attempt was to determine the degree of homogeneity of the data and in the last, to better characterize the underlying process. The results of this multifractal characterization are presented and discussed.

1. INTRODUCTION

This effort began as an attempt to discover appropriate procedures for the analysis of data (in particular, time series) obtained during the Smart Weapons Operability Enhancement (SWOE) Joint Test and Evaluation (JT&E) exercise (Welsh et al. 1995). For example, there is a large body of literature available which defines analysis procedures for time series (e.g., Bendat and Piersol 1986); however, most data sets encountered in the real world do not meet the assumptions of stationarity required by these tools (though, in many instances, analysis proceeds, regardless). One of the reasons for this quandary is that we are almost never dealing with an ensemble of observations but, instead, have only one realization -- a problem which makes it difficult, if not impossible, to make a proper determination of stationarity. In these instances, it is common, for example, to resort to invocation of "local stationarity" by breaking the data set into "stationary" segments (or segments with no trend). It seems as though these procedures merely ignore the "rules" and accomplish little. The paper by Davis, et al (1994) discusses some alternative tools and presents specific procedures along with a sample data set

Mean Multifractal Plane

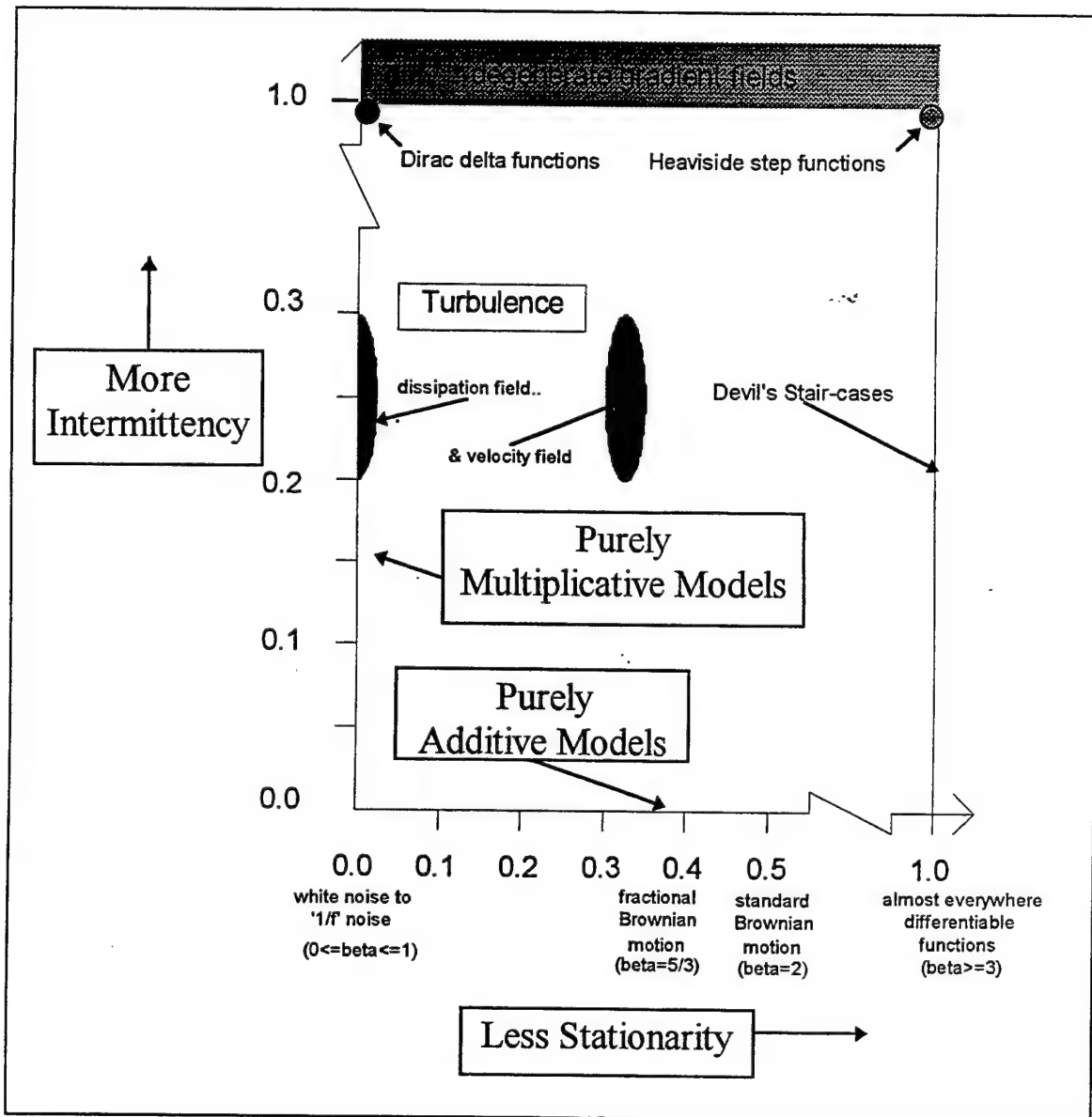


Figure 1. The "Mean Multifractal Plane", developed by Davis et al. 1994, and used extensively in their paper and in this paper, as well.

which may be used for verification of the application of their method. An important part of their procedures is the development of the "multifractal plane": the multifractal plane (Figure 1) allows the summarization of the analysis such that the characteristics of the data are succinctly stated and the relationship of the underlying process, relative to known processes, is understood. These parameters are the degree of stationarity, derived from "structure function" analysis and the degree of intermittency, derived from "singular measures" analysis. Both of these concepts are elaborated on below.

The basis for the development of these tools was the need, according to Davis et al. (1994), to "...find the simplest, most robust measures of the inherent variability in complex geophysical data or dynamical model output". And, because, geophysical systems "have a large range of scales and are governed by strongly nonlinear processes", the appropriate models to choose for this characterization are scaling or scale-invariant models. Additionally, the work of others has shown that these multifractal tools do have a place in understanding the underlying processes (e.g., Borgas 1993). The importance of these ideas is that we can begin to model these processes, which we are studying, in a realistic manner. For example, if we were able to model the atmospheric and meteorological processes which impact on the heat balance equation necessary for synthetic scene generation, we could then create synthetic scenes, "on-the-fly", without resort to the storage (and, costly acquisition of) huge data sets. Such models which make use of the concepts presented here are the class called "bounded cascade models" (Marshak et al. 1994).

The remainder of the paper will describe the analysis procedures (in a cookbook-type fashion which is a paraphrase from Davis et al. (1994)), a description of the three data sets processed, and a presentation of some of the results. This will be followed by a summary and conclusion.

2. ANALYSIS PROCEDURE

Davis et al. (1994), define four steps which need to be carried out to complete the analysis. These are given below (paraphrasing from their paper):

- 1) Determine the range of scales over which the scaling regime may be characterized. This is accomplished in two ways. The first is through use of the energy spectrum in Fourier space and is that region characterized by a single power law with exponent $\beta > 1$. In physical space, this is done by inspection of the second order structure function ($q = 2$) where the sample points fall along a straight line. We choose to use the structure functions for this determination and to use the energy spectrum for confirmation.
- 2) Compute the structure functions for a range of q .
- 3) Define an ensemble of stationary measures, beginning at the smallest scale of interest, and degrade this, through spatial averaging, to the largest scale.
- 4) Compute singular measures for a range of q .

These "generic" steps may be recast into a "cookbook" providing that this cookbook is not used blindly. These steps are described next.

The calculation of the energy spectrum is one of the requirements for this type of analysis to proceed as the "scaling as exhibited by the energy spectrum following a power law" must be verified. Also, that portion of the spectrum which does exhibit the power law scaling is used for confirmation for the structure function analysis which is described next. Of critical importance here is the proper "estimate" of the energy spectrum -- the square of the Fourier transform does not accomplish this! For single realizations of the ensemble, there are a variety of "smoothing" techniques available and one can arrive at almost any slope depending on what is actually used. We have chosen to bin by octaves and average the result and to then fit a line to that portion of the spectrum which does exhibit the power-law scaling -- all very subjective. This slope is used for comparison to the results of the structure function analysis.

For the following description, the definitions of the various symbols used are:

- $\Lambda = L / l$
- = overall scale ratio (assumed to be power of 2)
- L = length of the data set; i.e., the number of data points
- l = spacing between data points
- r = "scale"; i.e., the spacing between the differences
- x = the index for the data set
- $\varphi(x)$ = set of data points.

The determination of the degree of stationarity is the second step. This requires the determination of the set of exponents, $\zeta(q)$, as defined in the following equation:

$$\langle |\Delta\varphi(r; x)|^q \rangle \propto \left(\frac{r}{L} \right)^{\zeta(q)} \quad (1)$$

where

$$\Delta\varphi(r; x) = \varphi(x + r) - \varphi(x) = \varphi_{i+r} - \varphi_i, \quad (2)$$

and $i = 0, \dots, \Lambda - r$. An example of a plot for these functions is shown in Figure 2b (discussed later). These functions are known as structure functions of order q . For $q = 2$, we have the "structure function" of the turbulence literature. This is the type of plot (Figure 2b) which needs examination for the determination of the range of scales over which the nonstationary scaling regime holds (i.e., the data points fall on a straight line).

The value of H_1 , the abscissa of the multifractal plane, is determined to be the value of $\zeta(q)$ for $q = 1$. For the other values of q , we have:

$$H(q) = \frac{\zeta(q)}{q} \quad (3)$$

These exponents should be concave when plotted versus q ("...the hallmark of multifractality" according to Muzy et al. (1993), and, for more discussion, see Davis et al. (1994), and for an example of such a plot, see Figure 2d). This parameter, H , is known as the Hölder exponent (Barabási and Vicsek 1991). H_1 is also known as the Hurst exponent and is related to the "fractal dimension", D (also known as the Hausdorff or box dimension) by:

$$D = 2 - H_1. \quad (4)$$

The last step is to study the singular measures for the determination of the degree of intermittency of the process. The singular measures are formed by taking the next neighbor differences to "derive a stationary nonnegative field":

$$\Delta\varphi(1; x) = \varphi(x+1) - \varphi(x) = \varphi(x_i + 1) - \varphi(x_i) = \varphi_{i+1} - \varphi_i, \quad (5)$$

where $i = 0, \dots, \Lambda - 1$ and $\varphi_0 = 0$. These values are then normalized to make their average unity:

$$\varepsilon(1; x) = \frac{|\Delta\varphi(1; x)|}{\langle |\Delta\varphi(1; x)| \rangle}, \quad x = 0, \dots, \Lambda - 1, \quad (6)$$

with

$$\langle |\Delta\varphi(1; x)| \rangle = \frac{1}{\Lambda} \sum_{x=0}^{\Lambda-1} |\Delta\varphi(1; x)|. \quad (7)$$

This procedure is carried out for $r = 1, 2, 4, \dots, \Lambda$:

$$\varepsilon(r; x) = \frac{1}{r} \sum_{x'=x}^{x+r-1} \varepsilon(r; x'), \quad x = 0, \dots, \Lambda - r. \quad (8)$$

The q th order moment of these $\varepsilon(r; x)$ fields is next determined and the logarithm of the average value plotted versus the logarithm of the scale, r . An example, of such a plot for measured air temperature, is shown in Figure 2c (discussed later).

The parameter of interest, which is derived from this type of plot is $K(q)$. This is defined in the following way:

$$\langle \varepsilon(r; x)^q \rangle \propto \left(\frac{r}{L} \right)^{-K(q)}, \quad q \geq 0. \quad (9)$$

The values of $K(q)$ are plotted versus q -- this plot should be convex as required for the function $K(q)$ to have the required properties (i.e., see Davis et al. (1994) for discussion). From this plot, the derivative at $q = 1$ becomes the C_1 (or ordinate) value in the "mean multifractal plane".

3. DESCRIPTION OF THE DATA

3.1 SWOE JT&E Environmental Data

These data, consisted of the environmental data set acquired during the SWOE JT&E (Welsh et al. 1995); specifically, the standard set of meteorological parameters (i.e., wind speed, air temperature, etc.). The goal of the analysis was to determine the degree of homogeneity over the various test sites for the many parameters. The two test sites consisted of approximately a 1 km X 1 km (one at Grayling, Michigan and the other at Yuma, Arizona) which were instrumented with several meteorological towers. Of particular interest was whether it would have been sufficient to use only one tower vice the seven or eight which were used -- this would be of importance to other, future, tests. Of those tools contemplated, it seemed as though the use of the multifractal characterization was best suited for the task. By measuring the degree of stationarity and the degree of intermittency, the various sites could be compared and a judgment made. For example, if the analysis of two different sites showed that the wind speed for each were located at the same place on the mean multifractal plane (i.e., exhibited the same degree of intermittency and stationarity), then one could conclude that the underlying process was the same at both locations and that the wind speed were homogeneous relative to the two locations. These data were acquired at 1-sec intervals and averaged over a minute for archiving. The tests lasted of the order of 40 days so the data sets are about 57 ksamples long.

3.2 Smoke Week XII ATLAS Transmission Data

During the U.S. Army smoke test known as Smoke Week XII, data were acquired and processed utilizing the ATLAS technique (Bleiweiss 1995). The ATLAS system is essentially an imaging transmissometer system which forms a transmission map for that portion of the smoke cloud in the field of view of the data acquisition system. These data are then transformed, using the Beer-Bougher-Lambert Law:

$$T = e^{-\alpha c l}, \quad (10)$$

to path-integrated concentration (CL), or a number proportional to CL, by taking the negative natural logarithm of both sides of equation (13):

$$CL = -\frac{1}{\alpha} \ln(T) . \quad (11)$$

In our case, the observation point was such that these data are also known as crosswind integrated concentration (CWIC). These data, for one particular trial, have been processed to determine the CL versus time for several locations in the cloud in an attempt to determine whether the characteristics of the cloud vary with upwind/downwind distance and at various heights in the cloud. If, for example, the degree of stationarity and degree of intermittency are the same everywhere in the cloud, then it could be concluded that the underlying processes are the same everywhere in the cloud -- obviously, the situation is not this simple; however, it is a first step towards understanding the transport and diffusion process beyond the Gaussian Plume Model. This data set consists of transmittance images, 10 per second, for approximately 12 minutes. From these images, 50 pixels have been selected to sample the field of view through which the smoke flows, so that transmittance with time and as function of downwind position and elevation above ground can be studied. Each transmittance time series is then about 7200 values in length. Only one of these time series is studied in this paper.

4. RESULTS

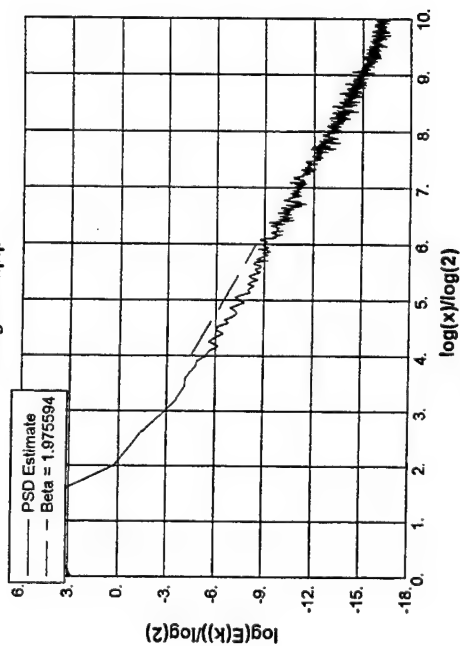
Though there remains much to be accomplished and the page limits imposed by this conference restrict the number of examples to be presented here, some of the results of our analysis can be shown here. Only the wind speed and air temperature from the Grayling II field exercise and one position in the Smoke Week XII cloud have been processed to date using the details described in this paper, though earlier work with the SWOE JT&E data set were presented elsewhere (Welsh et al. 1995). Table 1 summarizes these results. Figure 2a is the energy spectrum for the Grayling II air temperature data set, Figure 2b is the structure function plot and Figure 2c is the singular measures plot. The plots of the $\zeta(q)$ and $K(q)$ are shown in Figure 2d.

Table 1. Summary of the results of the Multifractal Characterization.

Data Set Type	Beta (Energy Spectrum)	Beta (2nd Order Structure Function)	H_1 (Stationarity)	C_1 (Intermittency)
Smoke (CWIC)	2.12	1.96	.552	.066
Wind Speed	1.46	1.59	.294	.050
Air Temperature	1.98	2.22	.761	.097

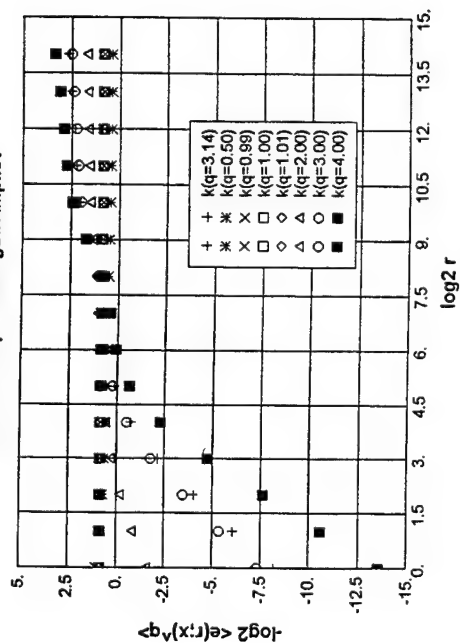
Power Spectral Density Estimate

File g2a1tmp.p



(a) Energy Spectrum Singular Measures

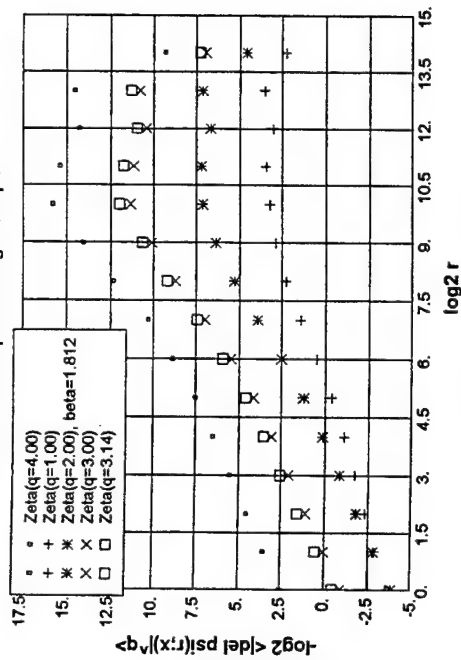
Data From Input File: g2a1tmp.lst



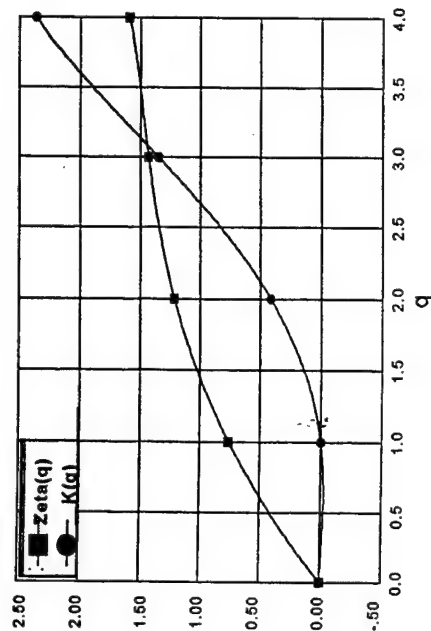
(c) Singular Measures

Structure Functions

Data From Input File: g2a1tmp.lst



(b) Structure Functions



(d) The $\zeta(q)$ and $K(q)$ Functions

Figure 2. For the Grayling II air temperature data series, the set of plots expressing the various factors involved in the multifractal characterization of the data.

It is seen, that for the air temperature data, that all of the requirements for this analysis tool to be valid are met:

- 1) the power-law scaling of the energy spectrum is mimicked by the second order structure function,
- 2) the plots of the exponents, $\zeta(q)$ and $K(q)$ are convex and concave, respectively, and
- 3) the value of β as determined by both the energy spectrum and the second order structure function are nearly the same. The results in Table 1 confirm that the other two data sets are also amenable to this analysis tool.

From the results in Table 1 and reference to Figure 1, it can be seen that we are dealing with three very different processes -- at least, as far as the mean multifractal plane delineates. And, it must be cautioned also, that some aspects of this analysis may change as the authors become more familiar with the technique and the finer points of the interpretation. Even though the three data sets show similar amounts of intermittency, the degree of stationarity is markedly different with the aerosol concentration data behaving very much like standard Brownian motion while the wind speed seems closer to what is expected from "fractional" Brownian motion and the air temperature data approaches the class of very smooth, everywhere differentiable, functions. These results may contain artifacts due to the signal processing techniques used in the data acquisition process and the effects of sample size. One aspect of this analysis which raises questions is the fact that all three data sets presumably are measuring some aspect of atmospheric turbulence (albeit, different levels or categories of turbulence) and should, then, fall in the same location on the mean multifractal plane but don't. Also, the slope of the energy spectrum for none of the cases is the "classical $-5/3$ reported by nearly everyone. It has been our experience, so far, that we can obtain about any slope that we want -- what has been reported here has been an honest attempt to be very objective in the matter. There is still more work to be done regards spectral estimation as alluded to earlier.

5. SUMMARY AND CONCLUSIONS

The applicability of the multifractal characterization as an analysis tool for three different data sets has been demonstrated -- the aerosol plume data (CWIC), wind speed, and air temperature. This has allowed at least some of the objectives for this type of analysis to be met (i.e., the utility for determining the degree of homogeneity of the wind speed and air temperature over the test site was made for Grayling I, Grayling II, and Yuma I, both individually and together (Welsh et al. 1995). Before a more detailed analysis of the smoke data can be completed, all of the data set must be processed in a similar manner and the results studied -- if the results for the rest of the plume are similar, then it may be concluded that the processes are everywhere the same, or different, depending on the specifics of the results. Two more efforts are desired; first, the processing of additional data sets to determine the viability of this tool for further analysis, the attempt to use these results to model these processes and apply these models to transport and diffusion processes as well as for the creation of synthetic data sets for use in simulation efforts.

ACKNOWLEDGMENT

The SWOE JT&E effort, Dr. J.P. Welsh, Director, provided partial funding for this effort. The authors thank Drs. A. Davis and A. Marshak for providing additional insight to this effort; though, much still remains to be learned.

REFERENCES

- Bendat, J.S. and A.G. Piersol, 1986: **Random Data (Analysis and Measurement Procedures)**, Second Edition, John Wiley and Sons, New York.
- Barabási, A.-L. and T. Vicsek, 1991: "Multifractality of self-affine fractals", *Physical Review A*, Vol. 44, No. 4, pp. 2730-2733.
- Bleiweiss, M.P., 1995: *Validation of the Atmospheric Transmission Large-Area Analysis System (ATLAS)*, ARL-TR-544, U.S. Army Research Laboratory, White Sands Missile Range, New Mexico.
- Borgas, M.S., 1993: "The multifractal lagrangian nature of turbulence", *Philosophical Transactions of the Royal Society, London, Series A*, Vol. 342, pp. 379-411.
- Davis, A., A. Marshak, W. Wiscombe, and R. Cahalan, 1994: "Multifractal characterizations of nonstationarity and intermittency in geophysical fields: Observed, retrieved, or simulated", *Journal of Geophysical Research*, Vol. 99, No. D4, pp. 8055-8072.
- Davis, A., A. Marshak, W. Wiscombe, and R. Cahalan, 1995: "Scale-Invariance of Liquid Water Distributions in Marine Stratocumulus; I - Spectral Properties and Stationarity Issues", Submitted to the *Journal of the Atmospheric Sciences*, preprint.
- Marshak, A., A. Davis, R. Cahalan, and W. Wiscombe, 1994: "Bounded Cascade Models as Nonstationary Multifractals", *Physical Review E*, Vol. 49, pp.55-69.
- Muzy, J.F., E. Bacry, and A. Arneodo, 1993: "Multifractal formalism for fractal signals: The structure-function approach versus the wavelet-transform modulus-maxima method", *Physical Review E*, Vol. 47, No. 2, pp. 875-884.
- Welsh, J.P., et al., 1995: "*SWOE JT&E Final Report*", U.S. Army Cold Regions Research and Engineering Laboratory, Hanover, New Hampshire.

CLIMATOLOGICAL AND HISTORICAL ANALYSIS OF CLOUD
FOR ENVIRONMENTAL SIMULATIONS - APPLICATIONS TO BATTLEFIELD ATMOSPHERICS

Donald L. Reinke, Thomas H. Vonder Haar, and **Kenneth E. Eis**
STC-METSAT
515 South Howes Street
Fort Collins, Colorado 80521

ABSTRACT

The Science and Technology Corp. (STC)-METSAT Climatological and Historical Analysis of Clouds for Environmental Simulations (CHANCES) project is an SBIR Phase II effort for the United States Air Force (USAF) that produced a global, 1-yr, 1-hr, 5-km resolution, satellite-derived cloud product. The global cloud database has been built at a higher spatial and temporal resolution than any previous DoD cloud product, using almost two orders of magnitude more data than the USAF Real-Time NEPHanalysis (RTNEPH) cloud product. Input for the database includes visible and infrared satellite imagery from four geostationary and four polar orbiting vehicles with ancillary input from the USAF Surface Temperature database and the Navy Snow/Ice database. The input geostationary satellites include GOES, GMS, and two Meteosat vehicles. The polar satellite input is from two DMSP and two NOAA vehicles. The CHANCES output products include a cloud/no cloud image, a quality assessment (QA) image, and merged, global, visible and infrared images. Data from the eight input satellite platforms are processed independently to produce cloud/no cloud products, then merged to build the global output images. The QA image contains a separate visible and infrared cloud/no cloud flag, vehicle identification, and a quality index for each 5-km grid point in the global dataset. All missing points are filled to provide a seamless global cloud field. An overview of the data, processing algorithms, and disposition of the database is presented, along with examples of a number of new prototype products that are being generated from the database.

1. INTRODUCTION

The Department of Defense (DoD) is required to assess, via simulation, the impact of the environment on new systems before they enter the acquisition process. This requirement has now placed a renewed emphasis on building an accurate, high resolution, global cloud database to test and simulate system performance. In short, clouds are an obstacle for systems requiring visual or infrared target acquisition and also affect other aspects of operation and training. Since these requirements have been identified, much has been learned about the analysis of clouds from satellite imagery. Unfortunately, the community is still operating with a very limited satellite-derived cloud database that does not even approach full exploitation of today's meteorological satellite imagery's resolutions, frequency of observation, or rapid update capabilities.

Unfortunately, the current DoD cloud database does not meet the increasing demands of environmental simulations. The Real-Time NEPHanalysis

(RTNEPH), is limited because it is based primarily on surface observations over land areas, has a spatial resolution of 46-km, and has a temporal resolution of 3 hours. In an STC-METSAT Small Business Innovative Research (SBIR) Phase I project, it was shown that the RTNEPH cloud database can be improved significantly. Also, the Probability-of-Cloud-Free-Line-Of-Sight (PCFLOS) models that are often used as input to simulations are surface-observation based and are derived on a spatial resolution of approximately 200 km. The Phase I results show that approximately 90 percent of cloud-free intervals are less than 10 km. Thus, both the RTNEPH and, even more so, the PCFLOS models based on surface data (200 km) will not provide a representative measure of the impact of clouds in specific geographic locations.

There are clearly two technical challenges to building an improved cloud database. The first is to develop and refine techniques that are required to perform a reliable cloud analysis from today's high-resolution meteorological satellite imagery. This work is being done by a number of research groups around the country. Most notably, the International Satellite Cloud Climatology Project (ISCCP) group (Rossow et al., 1991) and by the DoD sponsored Support of Environmental Requirements for Cloud Analysis and Archive (SERCAA) project at the United States Air Force (USAF) Phillips Laboratory (PL) in Hanscom, Massachusetts (Gustafson et al., 1994). The second challenge is a systems engineering issue; to implement such cloud analysis algorithms in a working system that is designed to ingest and process the massive amounts of satellite imagery that are required to produce a global product every hour. Providing a solution to the second challenge is the objective of the Climatological and Historical ANALysis of Clouds for Environmental Simulations (CHANCES) project.

The CHANCES project was sponsored by an SBIR Phase II grant. The purpose of Phase II was to produce a 1-yr, 1-hr, 5-km resolution, global cloud/no cloud (CNC) database product (shown in Fig. 1) and to demonstrate the feasibility of producing a longer term (5-yr) climatological cloud database in Phase III.

The intent of the CHANCES project was not to produce new and innovative algorithms for cloud detection and analysis by remote sensing, but to use state-of-the-art, yet proven, techniques to demonstrate the feasibility of producing a usable high resolution cloud product from the very significant volume of satellite data available each day.

2. INPUT DATA

CHANCES input data are divided into two categories: digital satellite imagery and ancillary data. The objective of data acquisition was to build an archive on 8-mm data storage tapes that would serve as input to the Cloud/No Cloud processing. Ancillary data were obtained, primarily, from the USAF Combat Climate Center (AFCCC; formerly the Environmental Technical Applications Center - USAFETAC) on both 8-mm and nine-track magnetic tapes. Figure 2 is a graphical display of this information.

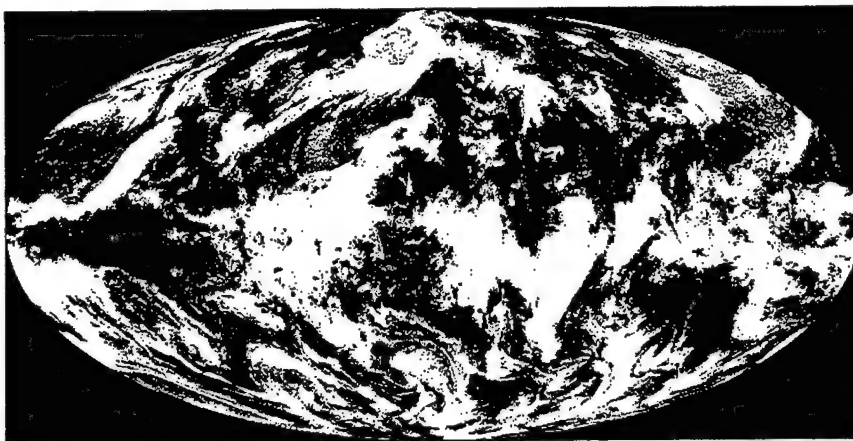


Figure 1. CHANCES global Cloud/No Cloud (CNC) image.

Raw satellite imagery that served as input to the CNC processing was archived on 8-mm tape. The geostationary satellite data were archived at the Cooperative Institute for Research in the Atmosphere (CIRA) at Colorado State University (CSU) in Fort Collins, Colorado. Polar orbiter data were archived by NOAA archive sites, in Boulder, Colorado and Asheville, North Carolina, using their respective platform specific formats.

2.1 GEOSTATIONARY SATELLITE IMAGERY

All of the geostationary image data are preprocessed to provide, as much as possible, a common format. Navigation headers, calibration tables, and additional documentation are taken from the original satellite image and reformatted into the CHANCES image header format. In addition, each image is "circularized" when it is archived to 8-mm tape to save storage space and cut the time required for archive and retrieval. Each full disk satellite image that is designed for display on a raster-based display system will contain a large amount of unusable space (in the corners of the rectangular image). When the geostationary satellite imagery is archived, only the Earth disc is saved. This reduces the storage requirement by about 40 percent (it varies from 36 percent to 44 percent depending on the vehicle and the start and stop scan lines).

2.2 POLAR ORBITER SATELLITE IMAGERY

The CHANCES project uses image data from both the Defense Meteorological Satellite Program (DMSP) and the National Oceanographic and Atmospheric Administration (NOAA) Advanced Very High Resolution Radiometer (AVHRR) satellites. These data were obtained on 8-mm tape from the NOAA/National Climatic Data Center (NCDC) in Asheville, North Carolina, and the NOAA/National Geophysical Data Center (NGDC) in Boulder, Colorado (see Fig. 2).

The AVHRR GAC data are archived at a resolution of 4 km. Data are written to tape as individual orbits, or partial orbits, with data from two vehicles included on each tape.

DMSP imagery were archived at a 2.7-km resolution. Data from F-10 and F-11 covered the period from the database start date, in February 1994, to

the data end date in January 1995. A smaller data set was received and processed from F-12 beginning in September 1994 and continuing until the end of the data period in January 1995. The F10 data were received intermittently from September 1994 until January 1995. The DMSP OLS data are written to tape chronologically, by full orbit, with approximately 36 hours of data from two vehicles on each tape. Both the visible and infrared channels are included for each orbit.

SATELLITE PLATFORM SENSORS AND RESOLUTIONS

Table 1 describes the detector characteristics for the meteorological satellite platforms that were used in the production of the CHANCES database.

ANCILLARY DATA

The three supportive databases used in this project are the USAF Surface Temperature database, the USAF Snow/Ice database, and the U.S. Navy ETOPO5 topography database. The topography database is static where as the Surface Temperature database and the Snow/Ice databases are analysis products that are built at the USAF Air Force Global Weather Central (AFGWC) and archived by AFCCC.

Table 1. Detector Characteristics for the Meteorological Satellite Platform.

	USAF DMSP	GMS	GOES	METEOSAT	NOAA AVHRR
Visible Wavelength (mm)	0.4-1.1	0.50-0.75	0.55-0.75	0.40-1.1	0.58-0.68
Infrared Wavelength (mm)	10.5-12.6	10.5-12.5	10.5-12.6	10.5-12.5	10.3-11.3
Infrared Wavelength AVHRR Channel 3 (mm)					3.55-3.93
Nominal subpoint res. of raw imagery processed for CHANCES (km)	2.7	5	VIS - 4 IR - 6.8	5	4
Approx. geo. sat. res. 55° from subpoint (km)		12	10	11	

USAF SURFACE TEMPERATURE DATABASE

The Surface Temperature database is a 46-km, 3-hr resolution database (built on the USAF RTNEPH grid that is based on a polar stereographic projection true at 60°). This database is built from a wide range of input data, and is quality controlled by AFGWC and AFCCC. The Surface Temperature database is built separately for each hemisphere and is provided on four 9-track tapes for each month. The northern hemisphere for days 1-16 are on the first tape, the southern hemisphere for the same period is on the second tape, and the remainder of the northern and southern hemisphere files for the month on the third and fourth tapes, respectively. The USAF publication, USAFETAC/UH-86/002, "Surface Temperature Analysis", contains additional information about this database.

SNOW AND ICE DATABASE

The Snow/Ice database is updated daily by AFGWC. This database is also on the RTNEPH 46 km grid, with one file per day. This database is stored as a single daily file which is accessed during CNC processing.

TOPOGRAPHY/GEOPOLITICAL MAPPING DATABASES

Topographic data is taken from the U.S. Navy ETOPO5 database. This database gives elevation data only and is on a 10-km resolution grid. This is the highest resolution topographic database that was available to STC-METSAT. This database was used to determine the elevation of the CHANCES grid points and also as an initial input to the land and water mask.

The final CHANCES land and water mask and geopolitical boundary map graphics used in the image alignment process were produced from the World Vector Shoreline database. This database (courtesy the Defense Mapping Agency) was produced at scale equivalents from 1:43,000,000 to 1:50,000. The vector shoreline data was provided by the National Geophysical Data Center in Boulder, Colorado.

3. DATA PROCESSING

Figure 3 shows the data processing flow for the CHANCES project. This figure may be referred to during the discussion of CHANCES data processing.

3.1 NAVIGATION AND REGISTRATION

Image alignment was required because the geographic navigation of many of the images received from the satellite operator is poor, and often the navigation parameters used to extract the images from tape are incorrect. The GOES-7 imagery, for example, was often in error by 15 pixels (75 km). The first step is to use an improved navigation algorithm that takes advantage of additional navigation parameters and adjustments that are available with the "raw" data files. The improved navigation is then used to extract points that are used in an automated image warping algorithm.

3.2 CLOUD/NO CLOUD AND QUALITY ANALYSIS PRODUCT GENERATION

The QA database is built for each independent platform and stored on the intermediate 8-mm tape for later ingest during the merge process. The format for the QA database allows information to be kept about satellite identification. This database also includes both the infrared and the visible CNC value as well as the final combined CNC that is considered the deliverable CNC product, and a flag to tell whether or not the visible data were used. A missing or filled flag is included to identify a point on the final output product that has been filled in due to missing or bad data.

An important feature of the CHANCES QA database is the inclusion of both a visible and infrared CNC flag. This provides a separate record of the CNC that was determined from both the infrared image and, when used, the visible image. This is important for two reasons. First, it is possible to use the QA database to identify thin cirrus (visible clear and infrared cloudy) and low stratus/stratocumulus or fog (visible cloudy, infrared clear) in non-snow/ice areas. It is also possible to do separate visible and

infrared statistics to determine the impact of using visible data and perhaps make an adjustment to nighttime CNC frequencies.

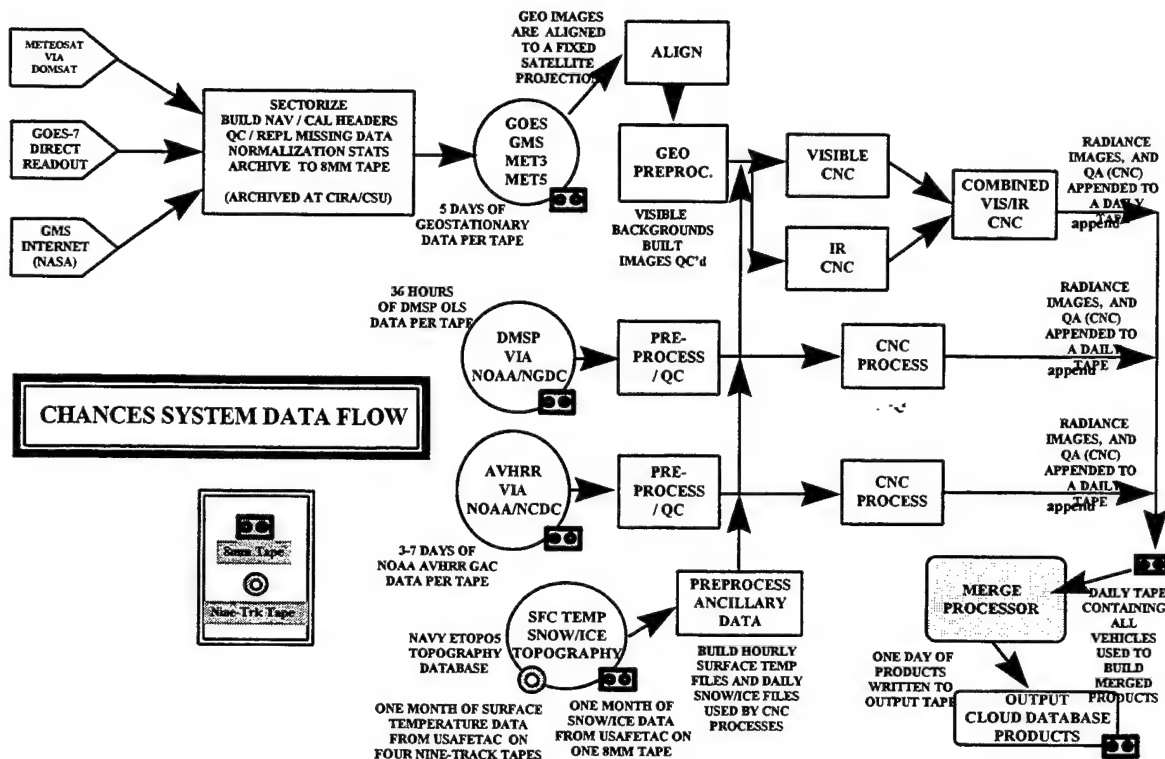


Figure 3. CHANCES System Data Flow.

Geostationary Visible Imagery Processing

The first step in the geostationary data preprocessing is to build "radiance backgrounds". These background images represent the cloud-free radiance scene that should be viewed for a specific time of day and viewing angle. Since the sun angle changes the background brightness as seen from the viewing satellite, a different background map was constructed for every hour that was processed. Quality control checks are made of each background, to remove shadows or cloud contaminated pixels. A further discussion of visible image processing can be found in Reinke et al. (1992). Shadows are removed with a geometric model that uses sun angle and cloud height to locate and remove cloud shadows. These shadows would contaminate the background with a very cold radiative temperature (dark in the visible) and produce false cloudy events in the CNC analysis.

Additional items that have been implemented specifically for the CHANCES project are modules to apply a terminator and sunglint mask to each background. The terminator is computed from the sun angle and the glint mask is applied over the background to identify the region of the image in which the visible data will not be used for CNC discrimination.

With the visible radiance background images constructed, classification of a pixel as cloudy or clear is easily automated. The process takes

advantage of the assumption that clouds are brighter (in the visible wavelengths) than the underlying background (the exceptions being snow and bright sand or sunglint over water). The image being operated on is compared to the cloud-free background, and all pixels with a count value higher (brighter) than the background by a threshold amount is assumed to be cloud-filled. The threshold will vary with each satellite platform and is determined empirically from independent tests run on data from each vehicle.

Snow covered data points (identified by the snow/ice database), bright desert, and sunglint region points are considered unreliable in the visible-only analysis and are flagged as such in the intermediate database. The infrared CNC decision will take precedence over each of these points during the combined visible and infrared processing. As in the visible background generation, a check is made for cloud shadows that will impact the CNC decision and the updating of the background image.

Cloud contamination occurs when there is not a day that is cloud free at a given pixel. In this case, the hottest background radiance value actually represents a cloud. These pixels are identified, then removed by using an area-weighted value taken from surrounding background points, or by simply reducing the radiance value at that point so that it will trigger a cloudy response in the CNC routine.

Geostationary Infrared Imagery Processing

Infrared image processing proceeds in a similar manner with all platforms, however, some additional tests are done in the case of the AVHRR GAC data to take advantage of the additional channels. The following tests are common to all of the platforms.

Infrared imagery is analysed by comparing each image to a radiance background. The significant difference is that the infrared background is very dynamic and must be built specifically for each hour that is processed.

The CHANCES project used the USAF Surface Temperature database as the initial background radiance image.

Combined Infrared and Visible CNC Processing

Each channel has its strengths and weaknesses in detecting clouds. The IR channel will often detect high, cold cirrus that is too thin to affect the visible scene radiance. Yet IR can miss low clouds whose temperatures are close or equal to the surface temperature. These low but bright clouds are detectable in a visible channel, especially over dark oceans. To make use of the each channel's strengths, CHANCES incorporates the cloud information from both channels during the daytime hours.

3.3 GLOBAL IMAGERY - MERGE PROCESSING

The merge processing takes place in stages with individual vehicles merged into the final output in a specific order. Polar data is processed for the entire polar orbit then remapped onto the global output image grid. DMSP is added first, followed by NOAA GAC, with the GAC data replacing the DMSP where it is available (due to the multispectral processing of the GAC data it is the preferred product). The geo data is then inserted onto the output image, replacing polar data where it is available.

Image Normalization

As infrared images are merged into the output global image file, a normalization correction is applied. This normalization is based on the Meteosat 4 and 5 satellite calibration. The normalization corrections are produced by analyzing co-located points on adjacent geostationary and overflying polar passes. Visible images are not normalized in the same manner, however visible radiances are converted to albedo. The effect of this conversion is to normalize the visible images to a common radiance measure and minimize the effect of limb darkening on the merged images.

3.4 MISSING DATA

One requirement of the CHANCES product is that missing data be filled-in. Missing data can be anywhere from a single data point to a large area encompassing a geo image. Missing data is filled in by applying a spatial or temporal interpolation of available data or, as the lowest priority, persistence (either forward or backward in time).

3.5 OUTPUT TO TAPE

Output tapes are built by writing compressed image files in hourly groups. Each group contains the visible, infrared, QA, and CNC image for one hour. One day of data (24 groups) is then written to a single tape. Each day of data is approximately 2.4 Gb, which is compressed to approximately 1.3 to 1.5 Gb using the LZW compression algorithm, then written to tape.

3.6 DATA QUALITY ASSESSMENT

Data quality assessment checks were performed at all stages of the CHANCES database processing. Much of the quality assessment was in the form of a manual inspection of images after each major step in the processing. The manual checks were used to identify and fix problems that are due to changes in the input data format. These basic quality checks require the examination of 368 images per data day. During the final production phase, STC-METSAT was processing 2 data days per calendar day, requiring the quality check of 736 images per day.

4. APPLICATIONS TO BATTLEFIELD ATMOSPHERICS

The CHANCES database is designed to be used for simulations applications, however, the unique nature of this new data set will provide input for a number of applications that are specific to the battlefield environment. The CHANCES database is (1) global in extent, and (2) the highest time- and space-resolution global radiance database ever produced. Products that can be built from the CHANCES database are not limited to clouds.

Examples of products that are of interest to all ground operations are the probability of encountering precipitation (trafficability), wind or temperature extremes, and limited field of view. The CHANCES database will allow, for the first time, the production of global maps of satellite derived fields such as wind, temperature, visibility, and cloud/aerosol obstruction. Much work has been done in the area of correlating cloud cover and cloud motion to the inference of these parameters. The limitation has always been the time and space resolution of the input data. The CHANCES database is an ideal source for input to such global high-resolution products. Table 2 is a

list of applications that have already been identified for the new CHANCES database.

Table 2. Applications of CHANCES data to Battlefield Atmospheric.

Application	Comment
EOTDA Backgrounds	Surface temperature and visible radiance
Mesoscale Winds	In the presence of complex terrain and weather
Optical Depth	Cloud-Free-Line-of-Sight
Acoustical Propagation	Diurnal cloud cycle tied to temperature inversion

5. FUTURE WORK

Future work by STC-METSAT will center around the production of an additional four years of the CHANCES database and two additional cloud products. The first product is a Global Layered Cloud called CHANCES Levels (CLVL) and the second is the CHANCES Global Cloud Climatology and Atmospheric Transmission (CCLIMAT) database. In addition, a spin-off global radiance background database and global optical depth database have been proposed for both the visible and infrared imagery portions of the CHANCES database.

5.1 LAYERED CLOUD PRODUCT - CLVL

This effort will investigate the feasibility of producing a reliable, high-resolution, global, layered cloud database from meteorological satellite imagery, upper air temperature and moisture fields, and surfaced-based cloud observations. The first phase will demonstrate how the CLVL product can be produced from the high-resolution CHANCES database and the subsequent work will focus on the production of a full year of the 5-km resolution CLVL product. This work is currently funded by USAF Phillips Lab to produce a one-month prototype product.

5.2 CLIMATOLOGY - CCLIMAT

An important follow-on to the initial CHANCES CNC database is the development of a global climatology for both clouds and optical depth. CHANCES visible and infrared satellite image data and CNC product will be used to produce global frequency-of-occurrence and conditional cloud climatologies and optical depth. The climatology product will include diurnal, monthly, and annual frequencies-of-occurrence of total cloud, cirrus, and low level (stratiform) clouds, as well as persistence probabilities and conditional cloud climatologies. The former will be conditioned on the initial cloud condition and also on other meteorological variables such as wind and temperature as well as topography. The optical depth analysis will take advantage of both the visible (when available) and infrared radiance databases to produce optical depth estimates for optically thick and thin (cirrus) clouds that are identified in the CHANCES database.

This proposed work will provide a one-month demonstration product that will be built for the entire globe for each point on the CHANCES 5-km grid. As additional years of CHANCES data are processed, the CCLIMAT project will

provide interannual variability statistics and multiyear cloud climatologies. This proposed work is currently unfunded.

6. ACKNOWLEDGMENTS

The STC team has delivered an innovative new cloud database product for the USAF under SBIR contract number F19628-93-C-0197. STC-METSAT acknowledges the support and helpful discussions provided during the course of this work by Dr. Kenneth Champion and Dr. Arnold Barnes, the USAF Technical Representatives. Special thanks are extended to USAF Maj. Steve Musto for assistance in the development of the CHANCES database specifications, and Dr. Garrett Campbell and Kelly Dean for their assistance with the geostationary satellite data ingest and archive.

7. REFERENCES

Gibson, H.M. and T.H. Vonder Haar, 1990: Cloud and Convection Frequency Over the Southeast United States as Related to Small-Scale Geographic Features. *Mon. Wea. Rev.*, **118**, 2215-2227.

Kidder, S.Q. and T.H. Vonder Haar, 1995: *Satellite Meteorology: An Introduction*. Academic Press, 456 pp.

Kiess, R.B. and W.M. Cox, 1988: The AFGWC Automated Real-Time Analysis Model. AFGWC/TN-88/001, AFGWC, Air Weather Service (MAC), Offutt AFB, NE, 82 pp.

Reinke, D.L., C.L. Combs, E.M. Tomlinson, and T.H. Vonder Haar, 1990a: *Persistence forecasts from high-resolution cloud composite climatologies*. Poster presentation at the Cloud Impacts on DoD Systems Conference, Monterey, CA, 9-11 January 1990.

Reinke, D.L., C.L. Combs, E.M. Tomlinson, and T.H. Vonder Haar, 1990b: *Interannual Variability in Cloud Frequency as Determined from GOES Satellite*. Presented at the Cloud Impacts on DoD Systems Conference, Monterey, CA, 9-11 January 1990.

Reinke, D.L., C.L. Combs, S.Q. Kidder, and T.H. Vonder Haar, 1992: Satellite Cloud Composite Climatologies: A New Tool in Atmospheric Research and Forecasting. *Bull. Amer. Meteor. Soc.*, **73**, 278-285.

Rossow, W.B., L.C. Gardner, J.P. Lu., and A.W. Walker. 1991: International Satellite Cloud Climatology Project (ISCCP): Documentation of Cloud Data WMO/TD - No. 266, World Meteorological Organization, Geneva, 76 pp. plus 3 Appendices.

PREDICTION OF INFRARED SCENES USING ARTIFICIAL NEURAL NETWORKS

Peter Soliz
Applied Sciences Laboratory, Inc.
Albuquerque, NM 87109, USA

Joseph Eicher
Air Force Phillips Laboratory
Hanscom AFB, MA, USA

George G. Koenig
Cold Regions Research and Engineering Laboratory
Hanover, NH, USA

ABSTRACT

Weather prediction models solve a set of complex dynamical and thermal-dynamical equations to extrapolate from initial conditions a set of future atmospheric parameters. In contrast, the most adroit weather forecasters are those who are able to recognize the key features in a weather pattern and associate them with a consequence which they have seen in the past. Whether starting from observed data or numerical forecasts, the human forecaster is ultimately the one to interpret the pattern and integrate the patterns with his expertise and knowledge of the physics and the shortfalls in the physics models to make the forecast for military operators. A study was performed using the Smart Weapons Operability Enhancement (SWOE) data to assess the capability of an Artificial Neural Network (ANN) to classify weather and make associations of these weather regimes with infrared (IR) scene characteristics. The ANN emulates human traits of pattern classification and associates present and antecedent weather patterns with an IR scene. It will be shown how an ANN approach may be used to "learn" error tendencies in physics models. A description of the ANN and results of the application of the ANN to SWOE data are presented.

1. BACKGROUND

This paper describes progress on a study of the application of the laterally primed adaptive resonance theory (LAPART) neural network model to weather impact decision aids for electro-optical weapon systems. The objective of the study was to demonstrate the feasibility of the LAPART neural network for inferring electro-optical scene parameters and weapon system performance using standard weather observations.

A number of candidate data collection efforts, such as the Geophysics Directorate's Air Combat Training/Electro-Optical Simulation (ACT/EOS) or the SWOE data from the CRREL, were assessed for applicability to the LAPART. The LAPART ANN was trained and its performance

tested on the SWOE meteorological data to demonstrate its thermal scene diagnostic and predictive capability.

The rationale for the selection of the LAPART, an implementation of ART by Healy, Caudell and Smith (1993), was given in an accompanying paper by Soliz and Caudell (1995). Details on the theory behind the LAPART and ART ANN may be found in the literature, including Healy et. al (1993), Caudell (1993a, 1993b), Grossberg (1986), Carpenter and Grossberg (1987) and others. The advantages and attributes of LAPART which we exploited are discussed below. The LAPART, like most ANNs, exhibits several characteristics not normally associated with traditional, serial computer algorithms.

The LAPART has several computational properties which are not generally found as a complete set in other neural networks.

- Abstraction of data occurs as a natural byproduct of the learning process. Explicit rule development is unnecessary, but can be extracted if desired by the user. Results which are presented show the "rules of thumb" that are produced by the LAPART:
- New classifications may be added without reprogramming the ANN. For the LAPART, learning can be done on-line (on the fly).
- The training process is less time consuming than that for many ANNs like the popular backpropagation.
- A vigilance parameter allows one to set the coarseness of the classification. This means one can train the LAPART class ANN to discover arbitrarily finer or coarser classes of EO performance. New categories are easily integrated into a trained network.
- Learning is assured to stabilize within a finite number of iterations. Long and often unsuccessful learning trials, as with the backpropagation ANN, can reduce the appeal and even impact the operational implementation of an ANN which does not have well behaved learning characteristics.

In the experiments using the SWOE weather data each of these LAPART attributes have been observed. Training times for the nearly 1000 weather observations over the 40 day period of the Grayling II SWOE test is usually on the order of seconds on the 90 Mhz Pentium which is being used for this development. Results show that indeed the effect on coarseness of classification and input data (observed or forecast) through the selection of the LAPART parameters, such as vigilance and parameter weighting can be observed. The LAPART ANN trains with normally two or three passes through the data set.

2. THE NEURAL NETWORK PARADIGM

Healy and Caudell's ART implementation employs the training of two ARTs simultaneously with a mapping of clusters between the two ARTs which results in an association of predictors and the event or parameter(s) being predicted, LAPART, for laterally primed ART. Another paper in these proceedings by Soliz and Caudell (1995) describes in detail the ART algorithm. It is sufficient to say that one of the ARTs is used to cluster the input data (predictor vector), data which will be used to predict an unknown parameter(s) related to the EO scene, for example. The second ART learns patterns or combinations of EO scene or target/scene characteristics. Running the two ARTs together, an association is developed between a given input vector of weather data and a EO vector. Once trained, the LAPART recalls the association for a given input weather vector to the EO vector. Figure 1 shows conceptually how the LAPART ANN is trained.

The selection of the SWOE data for this project was based on a number of factors. First, there is continuous and complete data for three episodes, two at Grayling and one at Yuma. In the case of the Grayling I and II data sets, a fall-winter and a winter-spring data set are available. This represents nearly a full cycle of seasons for one location. The data has all the elements required for performing the desired tests. The elements are defined as complete meteorological data, background data, soil data, 3 to 5- μm and 8-12 μm radiometric data, and target data at various operating conditions. Meteorological data includes standard instrument-based observations as frequent as every minute, human observations, upper air soundings, and non-standard meteorological data such as lidar ceilometer data and solar and sky flux measurements. Operationally some parameters are not available, such as background, soil, and solar/sky flux data. These were not used in the experiments which used the LAPART model.

The approach for using the LAPART to infer the nature of the IR scene was to characterize the IR scene with a number of statistics. A set of statistics was calculated for each image. These statistics include scene radiometric temperature statistics such as average total scene, mean, variance, sky average, foreground average, tree average and the difference between one of the trees and its surround ground radiometric temperature. Fractal dimensions were calculated to characterize the nature of the self-similarity scaling for the entire image. Co-occurrence statistics were also used to calculate entropy, contrast, and local contrast. These statistics are being used as the parameter(s) to be forecast using the corresponding meteorological data. Results of tests which have been conducted are discussed next.

4. LAPART TRAINING AND RESULTS

The goal of the study was to demonstrate and document the LAPART methodology for associating thermal scene characteristics from standard weather observations. In the application of the LAPART to the thermal scene characterization problem, a subset from the total set of meteorological parameters available in a given observation was selected as the independent variables. For this first experiment low, medium, and high cloud amounts were chosen as the input vector. LAPART_A clustered these into "similar" weather conditions. For the dependent variable (to be inferred), the temperature difference, ΔT , between one of the trees in the foreground and the "bare" ground just in front of the tree and entropy of the scene were used. These choices were made for convenience, since targets were not available throughout the Grayling II experiment. The preliminary LAPART training tests were designed to demonstrate capability of LAPART for inferring one of the critical factors affecting EO sensor performance, i.e. thermal scene characteristics, by categorizing the standard weather observations.

4.1 LAPART Learning Concept

It is instructive to depict how the LAPART operates on the data and how the classification of weather regimes is presented by LAPART. The large dimensionality of the input data vector makes it impossible to illustrate typical outputs on 2- or 3-dimensional charts. This fact does demonstrate the power of the LAPART to "sort out" the widely varying weather parameters into "hypercubes" of self consistent weather regimes. Figure 2 (left) illustrates the output of Weather Classes from one of the ART modules, ART-A, within the LAPART. ART-A discovers classes of weather regimes based on the combined values of the input vector. At the same time, ART-B produces output of the inferred parameters (right side). LAPART produces a mapping which associates weather regimes with operations-specific parameters. For this illustration, input weather classes are shown to be based on an input weather vector of dimension three. In reality, the cubes are hypercubes in N-space, where the input weather vector is of dimension N. The output vector is represented as 2-dimensional, but can be multi-dimensional where the operational requirement is for more than one output parameter.

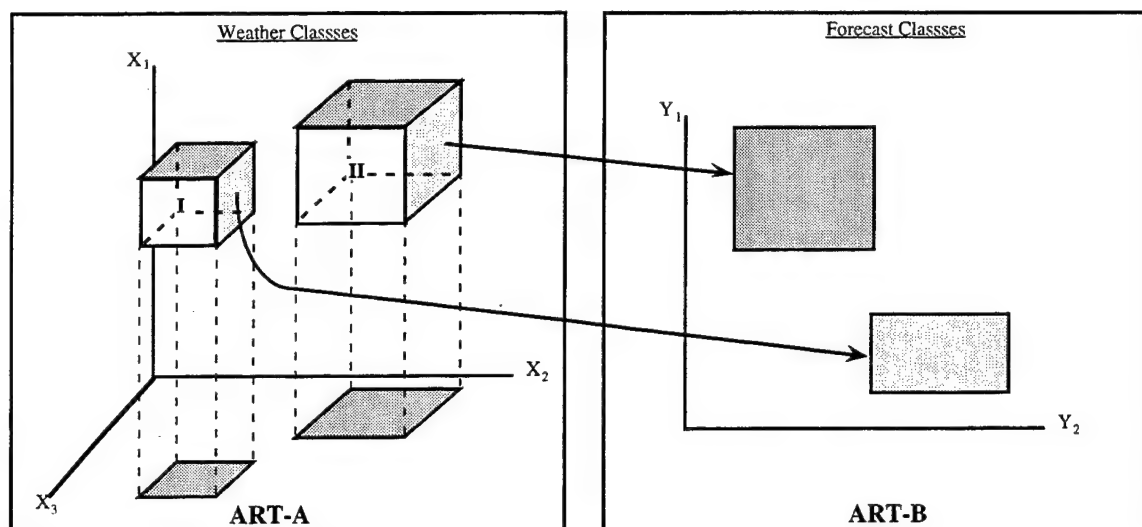


Figure 2. LAPART output in graphical representation.

The presentation of the weather impact decision aid model is in the format given in Figure 3. As one can see, large amounts of input data (like forecaster experience) is distilled to a few rules which are easily interpreted by the forecaster, yet can be applied consistently by all forecasters regardless of their level of experience.

Rule #13					
IF	(- 10.0 °	< Temp	< 0.0 °)	and	
	(75 %		< R.H. < 95 %)		and
	(2 m/s		< wind speed < 10 m/s)		and
	(etc.)				
THEN	(10	< output parameter	< 20)		

Figure 3. Sample output from ASL's Weather Impact Decision Aid System.

4.2 Analytical Tests Results

The focus of most of the testing was oriented toward assessing the LAPART's ability to produce associations between observed weather data and the scene characteristics. The goal of these tests was to develop something akin to an analytical model of thermal characteristics given observed data. The tests successfully showed that LAPART could learn an analytical-like association from the observed data. The tests also demonstrated that LAPART could be trained to any desired measure of precision in output and similarity in categorizing the weather regimes. This is done through the vigilance term.

Vigilance was adjusted so that in Test 1 eight ΔT regimes resulted. The associated ΔT s span an interval from -7.8° to $+8.1^\circ$ (values are scaled by $\times 10$ in output). The resolution is about 2° , which is consistent with the precision needed for many decision support systems. The output precision can be modified by adjusting the vigilance. Higher vigilance will result in more precision. Low vigilance will result in greater generalization of the input and output.

The output classes are generally plotted with the input parameters. A multi-dimensional plot, if it were possible, would show hypercubes which bound each of the weather classes (regimes). These would map to a second hyperspace where the hypercubes of the output (forecast)

parameter(s) would be plotted. The LAPART simply provides an algorithmic means for determining the boundary of these hypercubes using the training data. A solution to the problem of results presentation is to convert the hypercubes into sets of "rules of thumb".

The LAPART settings were varied on other tests to demonstrate certain aspects of the Grayling II data set. Table 1 below shows the parameters which were varied and the objective of each test. The reader can study the resulting rules (clustering) which resulted. Generally, one can see that the number of adjustments which one can make to "tune" the LAPART are minimal and intuitive. Vigilance adjustments can be made to increase or decrease the generalization.

Table 1. Showing Predicate settings (above) and bits per predicate (below) for several LAPART tests

Test #	Vigilance	Temp	R.H.	Wind Speed	Low amnt	Mid amnt	High amnt	Comments
1	A=0.75 B=0.90	0 0	0 0	0 0	40 2	40 2	10 2	Single output parameter was ΔT . 8 ΔT clusters were created. 58 weather classes.
2	A=0.75 B=0.90	0 0	0 0	0 0	40 2	40 2	10 2	Single output parameter was entropy. 8 entropy classes created. 60+ weather classes.
3	A=0.75 B=0.80	0 0	0 0	0 0	40 2	40 2	10 2	Same as Test 1, except that (B) vigilance is lowered. Output classes is six. 38 weather classes.
4	A=0.75 B=0.90	100 2	100 2	100 2	100 2	100 2	100 2	Inferred ΔT with six input weather parameters.
5	A=0.75 B=0.90	100 2	100 2	100 2	100 2	100 2	100 2	Inferred ΔT and scene entropy with six input weather parameters.

The difference between Test 3 and Test 1 illustrates the effect of changes in the vigilance. A high vigilance results in the LAPART which is less tolerant of differences between weather observations. A low vigilance allows the clustering of weather observations with greater differences. In the extreme a vigilance of 1.0 will only cluster weather observations which are exactly alike. A vigilance of 0.0 will cluster all weather observations in a single cluster. Neither extreme yields a useful result. The best value for this parameter is determined by the type of input and output desired. A vigilance which allows a certain amount of generalization can be determined by testing and analyzing results from different vigilance settings. This is easily implemented because of the rapid learning which allows multiple tests on a computer in relatively short times.

One can see from Tests 1-3 that clustering two or three parameters in some consistent manner is within the realm of a human. This may be the process which the human forecast goes through when assessing the effects of a weather situation on his/her forecast. If asked to consider more than the four parameters or tens of parameters, he will probably perform the analysis by comparing two at a time, then somehow integrating their combined effects to produce a forecast. In Test 4 six parameters are used to train the LAPART. The Test 5 adds further complication by asking LAPART to produce not one output parameter, but two simultaneously. The output calls for an inferred 'delta T' and 'scene entropy'. The latter statistic is one way of representing the clutter in the scene. This means that with a single training session, combinations of H-M-Low contrast and H-M-Low clutter scenes are mapped with the specified input weather parameters.

5. FUTURE DIRECTIONS

The Phillips Laboratory Geophysics Directorate is conducting experiments and collecting thermal and meteorological data for studying the TCM2 and EOTDA thermal contrast models. Presently

the TCM2 has given results which are in some cases different from those measured at the PL data collection site. Phillips Laboratory is attempting to isolate the source of these errors and apply corrections (or correct the physics) in the TCM2. Experiments will be designed to use the LAPART in analyzing thermal and meteorological data and TCM2 results. The application of LAPART will result in automatically-generated correction factors for TCM2 and offer insight into meteorological regimes which adversely affect TCM2 performance.

Figure 4 shows graphically how the LAPART will be trained in concert with the TCM2. Note that the basis for this approach is to train LAPART to "recognize" errors in the TCM2, not to "forecast" thermal parameters directly. This approach takes advantage of the fact that the TCM2 models may account for a large part of a parameter's variation as a function of meteorological inputs and time.

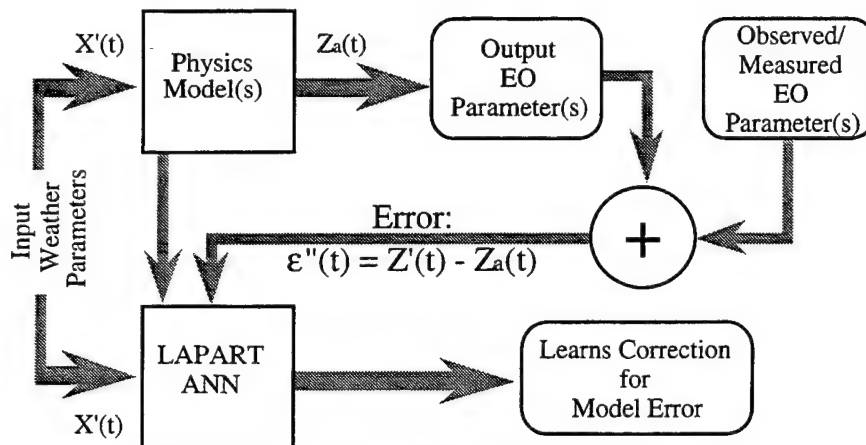


Figure 4. Concept for LAPART-based correction algorithm for physics models.

If stated as a time series problem, as in the equation below, the weather forecast models would be represented by the first term on the r.h.s. of Equation 1, X_d for deterministic contribution.

$$X(t) = X_d(t) + X_c(t) + X_r(t) \quad (1)$$

The effects of the chaotic, X_c , and random, X_r , terms represent aspects of the atmosphere which are non-deterministic (or at least indeterminable by our understanding of the physics). In general, as shown in Equation 2, there will be a difference, *i.e.*, an error, $e'(t)$, between the output from the weather forecast model, $X_d(t)$, and the measured or "actual" values of the parameters, $X'(t)$.

$$X'(t) = X_d(t) + e'(t) \quad (2)$$

For "perfect forecasts," *i.e.*, using observational data, $e'(t) = 0$. This implies that the input weather vector in Figure 6 going to the Physics Model has no forecast error, $e'(t) = 0$ and $X'(t) = X_d(t)$. The output from a "perfect" Physics Model, like the TCM2, may be given as the sum of the aspects of the physics for which an analytical model may be given, $Z_a(t)$, and those aspects of the physics which are not modeled, unknown, or modeled imperfectly, $Z_u(t)$.

$$Z(t) = Z_a(t) + Z_u(t) \quad (3)$$

In general there will be a difference or error, $e''(t)$, between calculated, $Z(t)$, and observed physics parameter, $Z'(t)$, given by Equation 4.

$$Z'(t) = Z_a(t) + e''(t) \quad (4)$$

Given training data composed of observed input parameters, the calculated physics model output, and the observed output parameter, the LAPART would "learn" an association between these variables and the difference between observed and calculated output parameter, that is, the error due to the deficiencies in the physics model.

A LAPART which is trained to correct errors in a physics-based model rather than attempting to implicitly (through "experience") learn the physics is conceptually applicable to any locale. Given this premise, a LAPART which is trained to apply error corrections to the physics model based on data collected at Hanscom AFB should be applicable anywhere in the world. In other words, if the physics does not change, then the physics model performs equally well or is equally deficient and the error corrections developed by LAPART apply anywhere. To test this hypothesis, LAPART will be trained and the TCM2 outputs (and errors) analyzed extensively using data collected at Hanscom. When data are available for other locations, the LAPART-corrected system, using data from Hanscom, will be tested with this new data. The results will be analyzed for applicability to new sites of a LAPART trained at the Hanscom site. Naturally, as more data are made available, the LAPART training will be updated, and data will be used for testing on yet other sites.

6. SUMMARY

The application of neural networks to weather impact decision aids has been demonstrated for a fairly small data set. The LAPART neural network which was selected is well suited for this application. In some respects it behaves like the human forecaster by learning weather regimes and to classify weather regimes by their characteristic features, such as temperature, humidity, cloud cover, etc. Like the human forecaster, LAPART then associates the weather regime with a certain consequence, such as low visibility, high thermal contrast, etc. Research using LAPART for weather impact decision aids is continuing and is being applied to commercial weather forecast problems and climatology categorization.

ACKNOWLEDGMENTS

Applied Sciences Laboratory, Inc. would like to thank Professor Tom Caudell from the Electrical Engineering and Computer Engineering Department, University of New Mexico, for his support in applying techniques in adaptive resonance theory which he has developed over the years. We also acknowledge the close relationship between ASL's ongoing independent research and development effort and a Phase I SBIR awarded to ASL by the Phillips Laboratory/Geophysics Directorate. Dr. Goeff Koenig, Cold Regions Research and Engineering Laboratory, has not only provided part of the data used in this development, but his encouragement is appreciated.

REFERENCES

- Carpenter, G. A., and S. Grossberg, 1987, "A massively parallel architecture for a self-organizing neural pattern recognition machine." *Computer Vision, Graphics, and Image Processing*, 37:54-115.
- Carpenter, G. A., S. Grossberg, and J. H. Reynolds, 1991, "ARTMAP: Supervised real-time learning and classification of nonstationary data by a self-organizing neural network." *Neural Networks*, 4:565-588.
- Caudell, T. P., and D. S. Newman, July 1993, "An adaptive resonance architecture to define normality and detect novelties in time series and databases." WCNN, pp IV-167-176.
- Caudell, T. P., and S. D. G. Smith, July 1991, "A data compressed ART-1 Neural Network Algorithm." *International Joint Conference for Neural Networks*, Seattle, WA.

- Field Activities Plan, Grayling II, Smart Weapons Operability Enhancement, Cold Regions Research & Engineering Laboratory, March-April 1994.
- Grossberg, S., 1986, *The Adaptive Brain I: Cognition, Learning, Reinforcement, and Rhythm, and the Adaptive Brain II: Vision, Speech, Language, and Motor Control*, Elsevier/North-Holland, Amsterdam.
- Healy, M. J., and T. P. Caudell, "Discrete stack interval representation and Fuzzy ART1." World Congress on Neural Networks, Portland, OR, II:82-91.
- Koenig, G. G. and J. P. Welsh, personal communication, December 15, 1994.
- Soliz, P., and T. P. Caudell, December 5-7, 1995, "Application of artificial neural networks to battlefield atmospherics." *Battlefield Atmospherics Conference*, Las Cruces, NM.

SCENE GENERATION INCLUDING MULTIPLY-SCATTERED DIFFUSE RADIANCE FROM FINITE CLOUDS

Donald W. Hoock Jr.
U.S. Army Research Laboratory
Battlefield Environment Directorate
White Sands Missile Range, NM 88002-5501

Sean G. O'Brien, John C. Giever
and Steven McGee
Physical Science Laboratory
New Mexico State University
Las Cruces, NM 88003

ABSTRACT

Diffuse multiple scattering from non-uniform aerosol clouds is one of the most challenging of modeling tasks. Radiance varies with viewing angle, cloud geometry, optical depth, and external incident radiance. At previous BAC conferences we have presented details of the development of the Battlefield Emission and Multiple Scattering Model (BEAMS) for computing this multiple scattering. Preliminary efforts to generalize the computed radiance from the obscurant clouds for reuse in time-dependent scenarios, first reported at last year's conference, are extended to actual applications of BEAMS in 3-D scene generation. Focus is on demonstration scenarios for the Joint Project Office for Special Technology Countermeasures, including plumes in the vicinity of a simulated airfield in realistic terrain. Effects of solar illumination and obscurant type on visual contrast of the cloud against its background and of partially obscured targets are illustrated, along with similar effects in the infrared.

1. INTRODUCTION

As constructive, virtual and semi-automated force models become integrated as Distributed Interactive Simulations (DIS), it is becoming clear that environmental representations and effects need to be more realistic and better quantified. This will allow better control and assessment of fidelity and correlation between separate simulators. Ultimately these models will also be integrated directly with outputs from detailed, item-level system performance models. However, an important requirement of DIS is real-time simulation. Thus, methods will need to be

developed for non real-time, high-fidelity, environmental effects model support. In this paper we report progress in this area for physics-based modeling of transmission and radiance from battlefield obscurants using the Battlefield Emission and Multiple Scattering (BEAMS) model.

2. MULTIPLE SCATTERING EFFECTS FOR SIMULATIONS

Multiple scattering effects are essential for both virtual and constructive simulations. Direct transmission (upper cloud in figure 1) is the fraction of energy surviving passage through the atmosphere. Transmission T ranges between one (clear) and 0 (opaque) through the equation:

$$T(R) = e^{-K_{\text{ext}} \cdot R} = e^{-\alpha \cdot CL} = e^{-\tau} \quad (1)$$

where τ is called the optical depth; R is distance along a path through an aerosol having volume extinction K_{ext} ; and CL is the path-integrated concentration (or "concentration-length") through an aerosol with mass extinction α (m^2/g), a wavelength-dependent aerosol optical constant.

Clouds characterized only by direct transmission always appear dark against their background. If we include a single scattering (middle of figure 1) by the angular scattering distribution (the phase function), then optically thin regions lighten due to scattered radiance. A complete description, however, requires that multiple scattering within the cloud also be taken into account (bottom of figure 1). This is the purpose of the BEAMS model. We parameterize this process as:

$$L_{\text{obs}}(R) = T(R) L_{\text{obj}}(0) + [1 - T(R)] L_s \quad (2)$$

where L_s is called the "limiting path radiance" since it is the cloud radiance when T goes to zero.

Those familiar with image generators for virtual simulations will recognize eq.(2) as the "blending equation" (figure 2). The image generator uses $(1-T)$, called the "opacity," and L_s , called the "source color value," to render one semi-transparent object in front of another. Usually these are graphics parameters assigned on "artistic" grounds. However, for rendering the atmosphere they can be, and should be, identified with the physical parameters T and L_s (figure 2). Note that the blending process is a simple linear interpolation between the object L_{obj} and the atmosphere L_s .

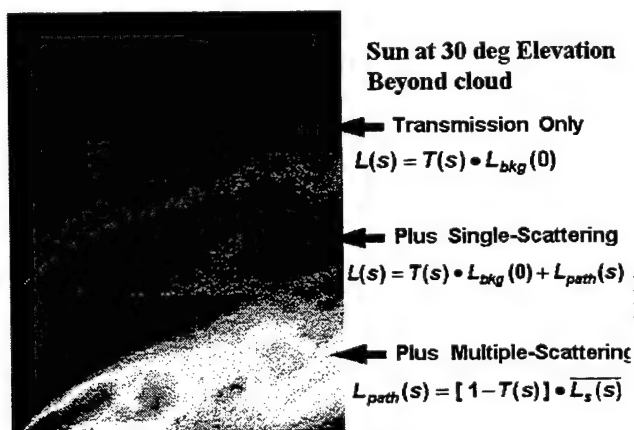


Figure 1. Importance of Multiple scattering.

Propagation "Blending" Equation

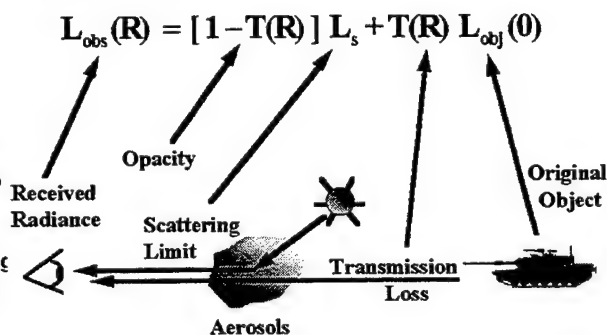


Figure 2. Physical Basis for Rendering Parameters.

In constructive simulations the contrast of an object against its background is closely related to eq. (2). Contrast is a ratio of difference in target and background radiance to background radiance:

$$C(R) = \frac{L_t(R) - L_b(R)}{L_b(R)} \quad (3)$$

If we use eq. (2) to substitute for the target radiance L_t and background radiance L_b as seen at range R , in terms of their values at range 0, then the contrast transmission equation is derived:

$$C(R) = \frac{C(0)}{1 + \left[\frac{L_s}{L_b(0)} \right] \left[\frac{1}{T(R)} - 1 \right]} \quad (4)$$

Thus, the same value of L_s used in virtual scene generation should also be used in constructive simulations such as JANUS and CASTFOREM. There the ratio of L_s to $L_b(0)$ is called the "sky-to-ground ratio" (Middleton, 1953).

Of course, L_s varies with observation angle, cloud optical depth and cloud geometry. Our goal is to parameterize L_s off-line (as in figure 3) and then to support real-time simulations via interpolation or table look-up (as in figure 4). The idea of this separation through parametric curves and tables is important, because it means that the physics-based models themselves need not be embedded directly into the simulations. The curves in figure 3 are from BEAMS outputs for fog oil clouds of roughly cubic shape and for a solar elevation of 30 deg. on a clear day.

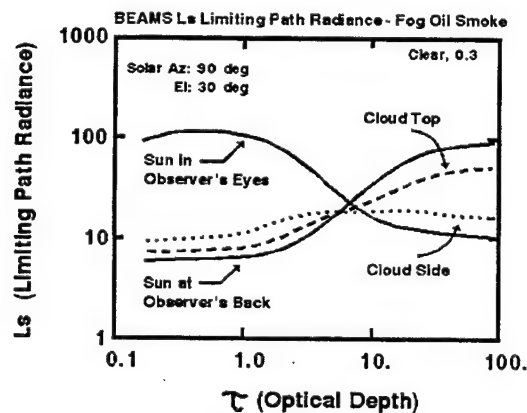


Figure 3. BEAMS Parameterization of L_s .

Concept of High-Fidelity Model
Applications to Analysis

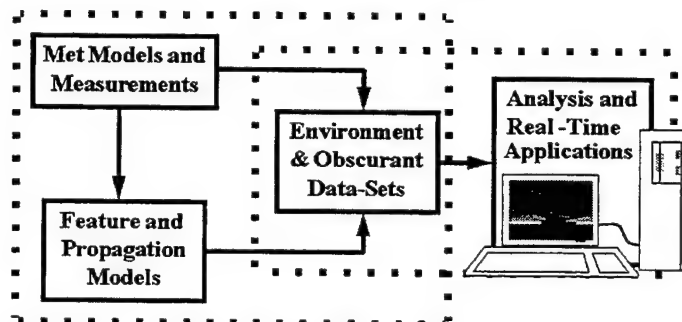


Figure 4. Coupling Simulations to High Fidelity Models.

3. BEAMS OVERVIEW

BEAMS has been described in detail in past BAC conferences (Hook, Giever and O'Brien 1993; Hook et al. 1994a; O'Brien 1993, 1994; O'Brien et al. 1995) and elsewhere (Hook, Giever and O'Brien 1993; Hook and Giever 1994b; Hook et al. 1995). Therefore we simply summarize the model's features here. BEAMS inputs a 3-D cubic grid of cloud concentrations (figure 5) from some source, for example: COMBIC, a model for mean gaussian puffs and plumes of battlefield smoke and dust (Ayres and DeSutter 1993); COMBIC/STATBIC, which textures COMBIC

concentrations with Kolmogorov statistics (MORS 1994); or dynamic simulations such as Large Eddy Simulation. Typical grids will contain from 10,000 to 100,000 elements.

Scattering, emission and extinction in each element are defined based on aerosol type. Single scattering "phase functions" are inputs. They describe the angular scattering by a single idealized particle which has the effective scattering properties of a weighted distribution of particle sizes at a monochromatic wavelength. The optical properties and phase function can be in terms of scalar power (hence BEAMS is a radiative transfer model) or as a polarization matrix. Separate versions of BEAMS exist for unpolarized and polarized cases.

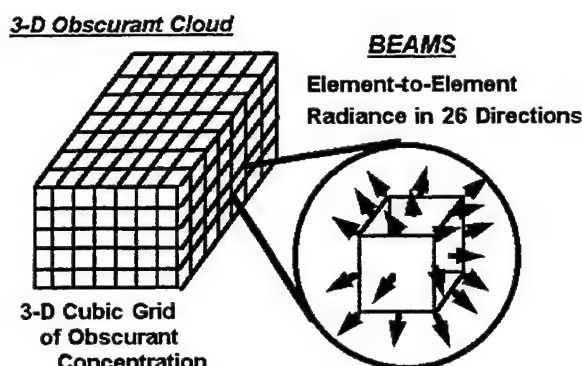


Figure 5. BEAMS Cloud Grid.

BEAMS redistributes radiance from each element to its nearest 26 neighbors, directionally averaged over each of the 26 solid angles. For elements which contain a significant concentration, BEAMS can use a "multiple-scattering phase function", built up off-line as transfer matrices for uniform concentration cubes based on the single-scattering phase function. External illumination fields on the cloud are held constant. Iterative transfer calculations among all elements within the cloud are computed to obtain a steady-state output radiance field. Figure 6 shows the modeled output for "chunks" of non-uniform fog oil smoke with sun overhead. The average optical depth for each cloud is given. Note that figure 3 shows a similar parameterization for 4 of the 26 beam directions, sampled at the centers of output faces. As the mean optical depth across the cloud is increased through about 7 to 9, the L_s curves cross-over. This marks the transition from a cloud that mainly passes light diffusely through it to one that mostly reflects light diffusely back. The latter case appears as the darkened cloud base in the lower right of figure 6.

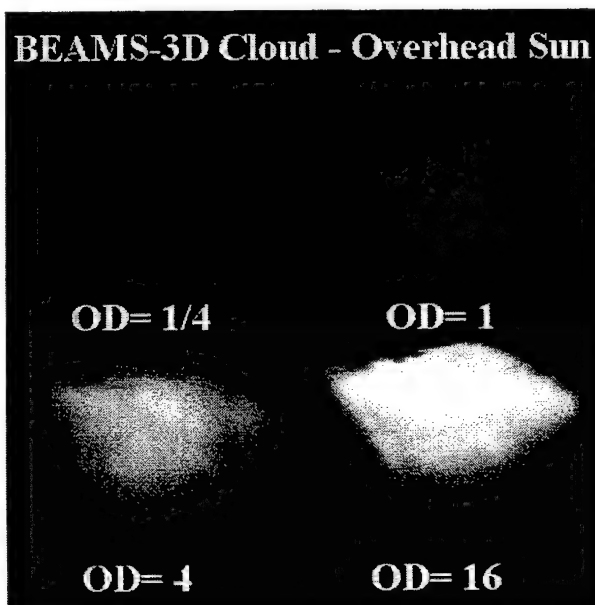


Figure 6. Cloud Radiance from L_s for Fog Oil Clouds.

BEAMS illumination sources can include: far-field direct (solar; lunar, ...); near-field direct (flares, including embedded point sources); limited-area direct (finite beams); diffuse skylight and terrain radiance; and internal thermal emission. These sources can be polarized.

Note that BEAMS is a steady-state radiative power model for the diffuse radiance from a cloud. We hope in future to address time-dependent multiple scattering for support to range-gating radar

sources. However, for some applications it could also require modeling of complex amplitude scattering to account for coherent interference effects. This would be beyond the scope of radiative transfer and standard phase-functions.

4. BEAMS APPLICATIONS EXAMPLES

As a high-fidelity model, BEAMS was produced as an obscuration effects analysis tool under sponsorship of the Joint Project Office for Special Technology Countermeasures. In addition, since physics-based cloud rendering requires the cloud L_s color value along with transmittance T or opacity $(1-T)$, it was clear that parameterized BEAMS outputs could also be useful in supporting scene visualization. Therefore, generation of such tables for simulation applications has been a project goal in the DMSO sponsored Environmental Effects for Distributed Interactive Simulation (E2DIS) program. This section presents several application examples of BEAMS.

Clouds are important cues in combat. Dust plumes from moving vehicles are often detected long before a vehicle itself is in view, for example. However, obscurants on the battlefield are highly non-uniform. Their "holes" and thick regions, generated by turbulence, can cause corresponding fluctuations in transmission, contrast and target acquisition of objects behind them. Few radiative transfer models can treat a finite 3-D medium, especially if it contains fluctuations in aerosol concentration. Monte Carlo methods are versatile, but usually require a fixed detector location and collection angle for each run. The BEAMS method is somewhat similar to a discrete ordinate method. Discrete ordinate methods treat interactions along two or more radiance streams through a cloud, with radiance "sampled" along fixed directions. However, it was decided to allow BEAMS to average diffuse radiance over several (26) solid angles to give more control over of flux conservation.

Figure 7 shows the simulation of cloud fluctuations using the Combined Obscuration Model for Battlefield Induced Contaminants (COMBIC) (Ayres and DeSutter 1993) and the Statistical Texture Application to Battlefield Induced Contaminants (STATBIC) (Hooek 1991; MORS 1994). The smooth COMBIC plume at the bottom of the figure is modified by the STATBIC texture, in the top of the figure. In both cases, the radiance is modified by the corresponding transmission through the cloud, and an L_s corresponding to that transmittance. Equation (2) is used to render the image for diffuse ambient radiation and for the sun 30 degrees above the horizon on the far side of the cloud.

Figure 8 shows an example of a 3-D scene for a point-illumination source. The cloud path radiance $[(1-T) L_s \text{ of eq. (2)}]$ output from BEAMS is rendered for fog oil smoke plumes

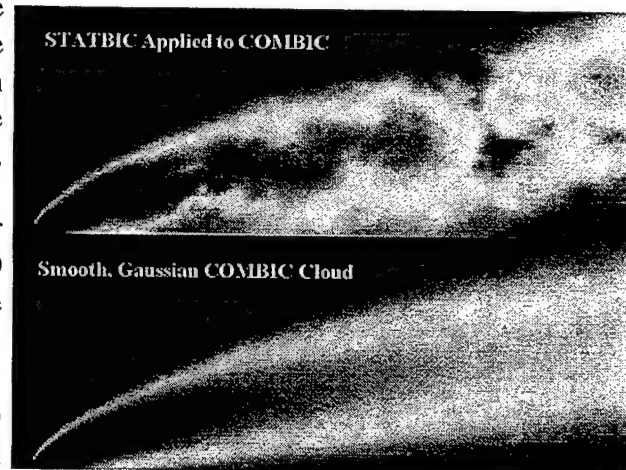


Figure 7. COMBIC/STATBIC Plume.

flowing over airfield hangars and around a control tower. The cloud is illuminated by a flare 100 m above ground level. The cloud concentration grid here is from Large Eddy Simulation calculations provided by Mr. Ronald Meyers of ARL/BED. (Several of his cases for plumes in near-laminar conditions and in fully-turbulent conditions are used in the examples in the rest of this paper.) This example is part of a current study to determine sky-to-ground ratios for nighttime conditions for use in constructive combat simulations.



Figure 8. BEAMS Radiance - Flare-Illumination.

Figures 9 through 11 show a polarization example. Aluminum chaff with an assumed fiber orientation of 30 deg rms with respect to the horizontal is input. A fixed point source 100 m above ground level of 94 Ghz radiation is fully polarized crosswind (figure 9). The chaff blows from left to right over the hangars. The co-polarized return is shown for a detector moving by at 60 deg elevation. Dark areas to the right of the hangars show stagnation zones in the plume. Figure 10 shows outputs for an incident beam on a rectangular block of chaff.

Polarized Radiance, Al Chaff 94 Ghz, Steady-State Source, 100m AGL



Received Co-Polarized Radiance , 60deg el

Figure 9. Chaff Over Hangar Area.

Figure 11 shows a scenario for nearly laminar chaff plumes. The MMW source moves left to right, 100 m above the center of the plumes, paralleling the detector.

The above are non real-time visualizations. Real-time scene generation can be provided by the Silicon Graphics Inc. (SGI) Performer software library. Performer accepts standard simulation data file formats, such as OpenFlight, Designer Workbench, SIF 2851, and others. These files store information on terrain elevation, photo-texture, polygonal objects and their level of detail as well as data object hierarchies to promote rapid sorting and culling in the field of view.

OD= 6.4 Long, 1.6 High; Al Chaff, 30 deg rms Orientation
94 GHz, Steady State, Top Down View

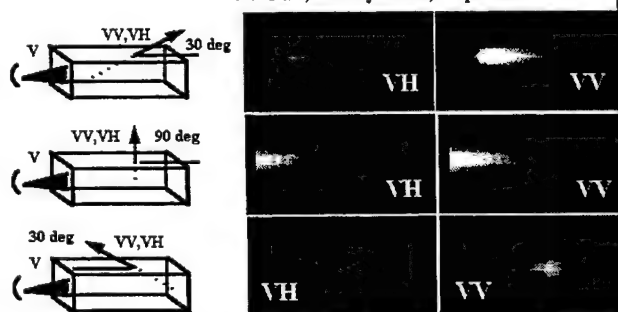


Figure 10. MMW Scattering in Box.

Uniform Source, 100 m AGL Above Cloud
Fully Polarized Cross-wind

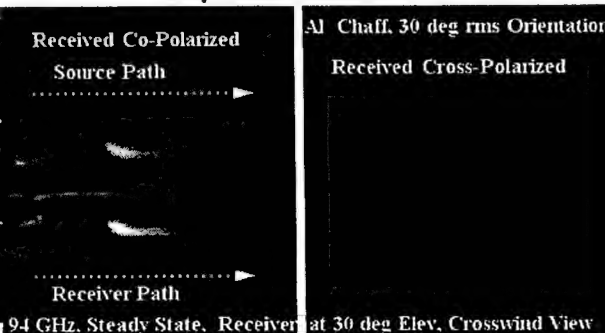


Figure 11. Laminar Chaff Flow.

As one of our projects, we developed an obscuration scenario. It consisted of an 8 km x 8 km section of terrain at Ft. Hunter Liggett (FHL), CA. Terrain elevations and textures were provided by the Pegasus 1-m posting data set produced originally by TEXCOM at FHL, and recently extended by the Georgia Technical Research Institute (GTRI). MultiGen, a simulation data set editor for use with OpenFlight, was used to incorporate and polygonalize the FHL terrain to a Triangularized Irregular Network (TIN) of polygons of about 100 m dimensions, and to overlay the terrain photo-texture. MultiGen was also used to produce a runway and apron to "pave" a dirt runway in the FHL scenario (figure 12), and to produce two hangars (figure 13) and a control tower. Performer then allows one to simply load the scenario and interactively "fly" through it at 30 frames per second.

Standard data set formats do not yet incorporate weather data or representations such as clouds. We therefore added on calls to our own software to render the BEAMS outputs. First, we added the capability to render the wind vector fields (figure 14) from the ARL/BED High Resolution Wind (HRW) model outputs provided by Mr. Ronald Cionco of ARL/BED for two weather scenarios. Scenario A is mid-morning (1045 LST) with mean winds at 5 m/s from the SE, air temperature 10 deg C, and terrain IR blackbody temperatures from 4.1 to 24.9 deg C. Scenario B is early morning (0745 LST) with wind at 3 m/s from the NW, air temperature 3 deg C, and terrain effective blackbody temperatures ranging from -4.9 to +4.0 deg C.

Mr. Ronald Meyers of ARL/BED provided plume concentration arrays for fog oil and carbon flake smoke releases over the airfield structures. BEAMS was run at visual and mid-IR (3.8-4.0 μm) wavelengths.

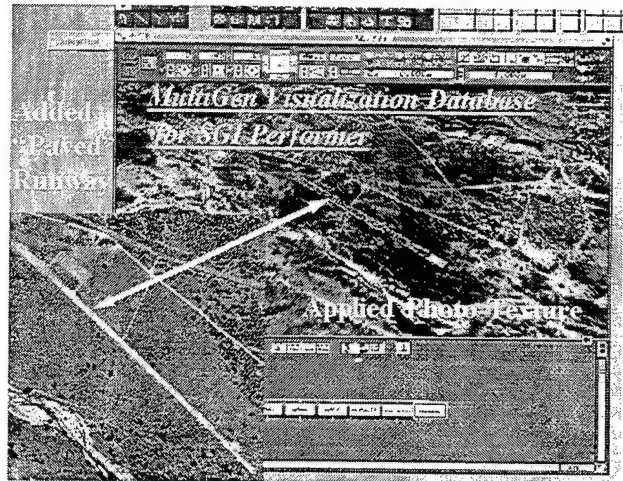


Figure 12. Pegasus Terrain in MultiGen.

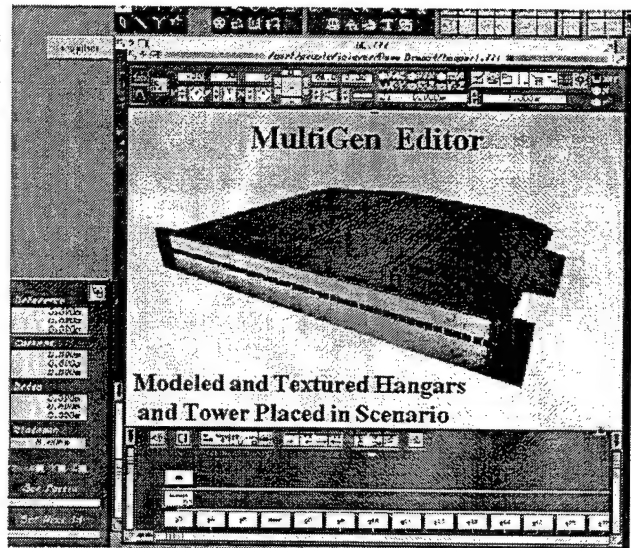


Figure 13. Hangar Structure Model in MultiGen.

Scenario Preparation

Performer Routines
Written to Display
Wind Field Vectors

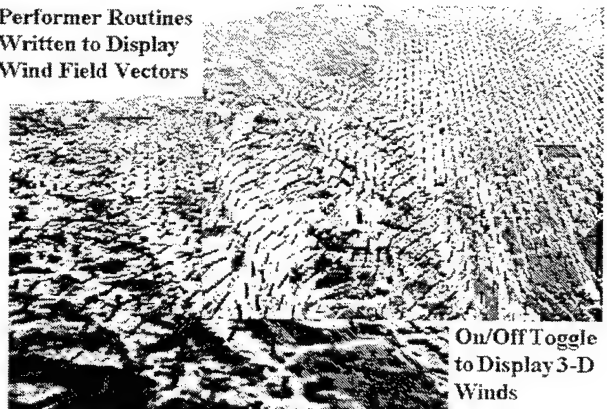


Figure 14. HRW Wind Field Vectors.

The BEAMS clouds were first rendered directly inside Performer as 30,000 cubic elements, using standard SGI Graphics Language (GL) calls (SGI 1991) implementing eq. (2) for each element. Obviously this slowed Performer down below real time (to about 0.3 Hz). As is common in real-time scene simulation, we then transformed the cloud elements into Performer "billboards". Billboards are simple textured objects (McGee 1995), usually 2-dimensional, which automatically turn to face the observer in the simulation. This sped up the scene generation rate, although performance is highly dependent on the number of billboards used to represent the plume. Figure 15 shows the rendered scenes for Scenario A using both techniques.

The GTRI infra-red terrain signature model GTSIG was applied to scenarios A and B. Figure 16 shows the clouds for scenario A using the GL-based rendering of cloud elements. The cloud thermal radiance is intermediate to the ranges in terrain radiance in this case. Cloud radiance shows some dependence on sun angle at these wavelengths. Figures 17 and 18 show both scenarios, with GL-based clouds (figure 17) and billboards (figure 18).

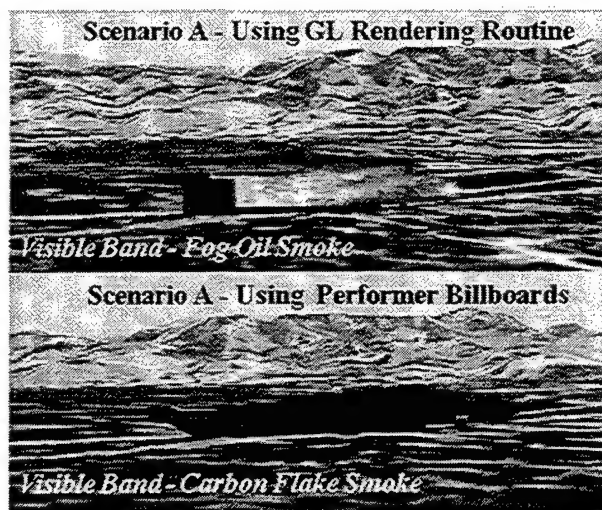


Figure 15. Visible - Scenario A.

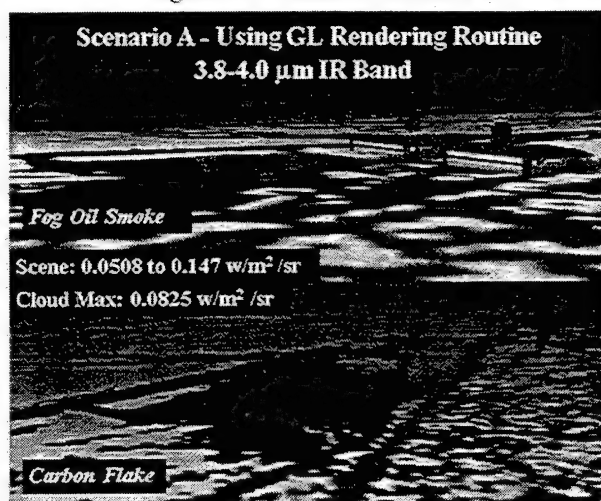


Figure 16. IR - Scenario A.

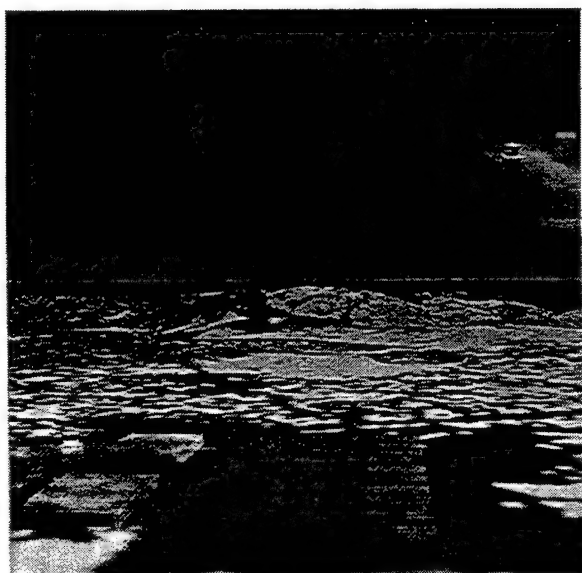


Figure 17. IR - GL-based Clouds.

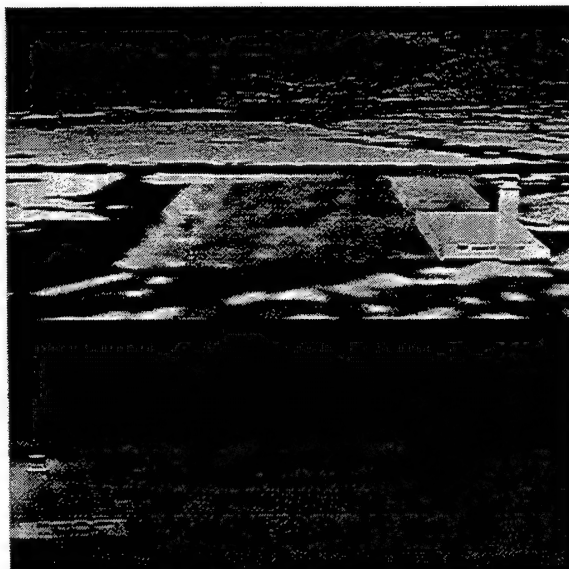


Figure 18. IR - Performer Billboards.

5. CONCLUSIONS

There is no doubt that virtual and constructive simulations will soon become interactive with more traditional RDT&E simulations. We feel that wider use of physics-based environment and effects parameters in these simulations will promote fidelity and correlation between them.. Objective procedures to compare simulated effects rather than to impose specific models themselves on the simulation community are a logical next step. This will allow simulators flexibility in choosing their own specific methods and implementations, as long as their simulated effects meet some (as yet unspecified) standards. To promote this goal, it will be important to establish standard data formats that connect non real-time physics-based models with those parameters directly needed by the real-time virtual and constructive simulations. Examples were given of how the BEAMS model, which is far from real-time, can provide parametric curves or tables of cloud limiting radiance L_s values. We have illustrated applications of BEAMS to visible, infrared and MMW wavebands, including both scalar and polarized radiance. Follow on work to BEAMS should be to extend the model to include time-dependent scattering for use in studies of range-gated (radar) incident radiation.

6. ACKNOWLEDGMENTS

Our thanks to Mr. Ronald Meyers of ARL/BED for providing outputs from his Large Eddy Simulation model.; and to Mr. Mario Torres of Science and Technology Corp. for his angular interpolation scheme and visibility comparisons. We acknowledge the support of the Defense Modeling and Simulation Office through the Environmental Effects on Distributed Interactive Simulation project which promotes tailoring of R&D environmental models to M&S applications. We particularly acknowledge the Joint Projects Office for Special Technology Countermeasures, Dahlgren, VA for their support of development of BEAMS and STATBIC.

7. REFERENCES

- Ayres, Scarlett and S. DeSutter, 1993. EOSAEL 92: Vol 14. Combined Obscuration Model for Battlefield-Induced Contaminants (COMBIC), U.S. Army Research Laboratory, ARL/BED Technical Report, White Sands Missile Range, NM 88002-5501.
- Hoock, Donald, 1991. "Modeling Time-Dependent Obscuration for Simulated Imaging of Smoke and Dust Clouds". In Proceedings of the SPIE, #1486, SPIE -- The International Society for Optical Engineering, Bellingham, WA, pp. 164-175.
- Hoock, Donald, J. Giever, and S. O'Brien, 1993. "Battlefield Emission and Multiple Scattering (BEAMS), a 3-D Inhomogeneous Radiative Transfer Model". In Proceedings of the SPIE, #1967, SPIE -- The International Society for Optical Engineering, Bellingham, WA, pp. 268-277.
- Hoock, Donald, J. Giever, S. McGee, and P. S. Hansen, 1994a. "Visualization of Obscuration and Contrast Effects Using the BEAMS Models". In Proceedings of the 1994 Battlefield

Atmospherics Conference, U.S. Army Research Laboratory, Battlefield Environment Directorate, White Sands Missile Range, NM.

Hoock, Donald and J. Giever, 1994b. "Modeling Effects of Terrain and Illumination on Visibility and the Visualization of Haze and Aerosols". In Proceedings of the SPIE, #2223, SPIE -- The International Society for Optical Engineering, Bellingham, WA, pp. 450-461.

Hoock, Donald, S. O'Brien., J. Giever., S. McGee and M. Torres, 1995. "Physics-Based Environmental and Embedded Process Models for Virtual Simulations". In Proceedings of the 17th I/ITSEC Conference, 15 Nov 1995, Albuquerque, NM; Interservice/ Industry Systems and Education Conferences, American Defense Preparedness Association, Arlington, VA 22101.

McGee, Steven, 1995. "Visual Simulation of Semi-Transparent Atmospheric Phenomena Using Silicon Graphics Performer 1.2: Some Lessons Learned". In Proceedings of the 1995 Interservice Test and Evaluation Association (ITEA) Conference on Modeling and Simulation: Today and Tomorrow, 12 Dec 1995, Las Cruces, NM, in process.

Middleton, W. K., 1953. Vision through the Atmosphere, Toronto, Canada: University of Toronto Press.

MORS Military Operations Research Society, 1994. MORS Military Operations Research Handbook (Vol 1), Olsen, Warren (Ed.), Alexandria VA.

O'Brien, Sean, 1993. "Comparison of the BEAMS 2.2 Radiative Transfer Algorithm with Other Radiative Transfer Methods". In Proceedings of the 1993 Battlefield Atmospherics Conference, U.S. Army Research Laboratory, Battlefield Environment Directorate, White Sands Missile Range, NM, pp. 421-435.

O'Brien, Sean, 1994. "A Multistream Simulation of Multiple Scattering of Polarized Radiation by an Ensemble of Non-spherical Particles". In Proceedings of the 1994 Battlefield Atmospherics Conference, Dec 1994, White Sands Missile Range, NM.

O'Brien, Sean, J. Giever, S. McGee and D. Hoock, 1995. "Visualization Tools for Artificial and Polarized Illumination of Obscurant Cloud". In Proceedings of the 1995 Battlefield Atmospherics Conference, Dec 1995, White Sands Missile Range, NM.

Silicon Graphics, Inc., 1991. Graphics Library Programming Guide, (No. 007-1201-040), Mountain View, CA.

Evaluation of WAVES Using Image Statistics

Patti Gillespie
US Army Research Laboratory
Battlefield Environment Directorate
White Sands Missile Range, NM 88002-5501

Michael Rollins
Science and Technology Corporation
Las Cruces, NM 88011

David Tofsted
US Army Research Laboratory
Battlefield Environment Directorate
White Sands Missile Range, NM 88002-5501

Abstract

The Weather and Atmospheric Effects for Simulation (WAVES) suite of models comprises BLIRB (Boundary Layer Illumination and Radiative Balance Model), ATMOS (a turbulence model), PIXELMOD (an image modifier), VIEW (a viewing geometry model), and CLOUDMASK (a cloud shadow mask model). This model can simulate a scene or can be used to modify an image. As part of the evaluation of WAVES suite, actual images of near field and far field target boards were split into the near and far field portions and the near field portion was modified by WAVES to simulate a far field image. Then image statistics were applied to each of the images to determine the degree of similarity of the images. The process used to obtain the near and far images is discussed in this paper. The modification of the near images is outlined. Finally, the conclusions drawn from the comparison of image statistics are analyzed.

1. Introduction

There is a military interest in generating realistic imagery for a variety of weather conditions on various computer systems. This visualization can be of the scattering and transmission properties of the atmosphere (in terms of cloud and aerosol types, locations, and densities) into the local, spectrally-dependent, three-dimensional directional radiances and transmittances for a horizontally-inhomogeneous atmosphere. These quantities are then used to determine, along the line-of-sight for each pixel in the image, the transmission, blurring, and path radiance effects.

The purpose of WAVES is to give the user the ability to modify images to include the effects of

weather and the atmosphere. There are two primary types of images WAVES deals with. The first is the real time computer generated visualizations; the second is the more traditional non-real time modification of images. For both of these image types, WAVES uses range-dependent, line of sight, transmission and path radiance effects to modify the images. Additionally, for the non-real time modifications, WAVES can include the effects of turbulence.

The heart of the WAVES suite of algorithms is an 8-stream radiative transfer model, BLIRB. Measurements of three-dimensional inhomogeneous scattering properties are not available in abundance. In fact, such data sets do not exist. In the past, a less direct approach was taken in this study to compare BLIRB to "data." Monte Carlo scattering calculations are often considered to be standards by which to judge other calculations (Davis, 1991), despite the fact that Monte Carlo models do not capture the generalized physics description of the scattering processes. In other words, statistical techniques (Monte Carlo models) are used to determine the path of each photon being followed in the experiment. The radiative transfer or illumination computed by BLIRB was compared for several geometries to a Monte Carlo radiative transfer algorithm, AGGIE (A Generalized Geometry Irradiance Estimator). [Tofsted and other, 1995] AGGIE, developed as a general purpose radiative transfer model for calculating radiative fluxes and distributions through an atmosphere, accounts in the cloud region for scattering and absorption by molecules and aerosols, the thermal emission of the atmosphere, clouds, and ground surface, and also the reflection of photons at surfaces in either a specular, isotropic, or Lambertian manner. The BLIRB algorithm is an 8-stream approach to radiative transfer, and is being expanded to a 32-stream algorithm. BLIRB accounts for the scattering in the atmosphere, and LOWTRAN is used for the molecular absorption. All comparisons were made for a wavelength of 0.45 micrometers.

Since comparisons to other models is not always very satisfying scientifically, comparison to data was sought. One method that can be used, and is used here, is to compare real to synthetic imagery and use a variety of tools that have been developed to give an indication of the similarity of the images. Our original intent was to generate entirely synthetic imagery based on Defense Mapping Agency (DMA) terrain and vegetation data and Silicon Graphics Inc. (SGI) Performer visualization software, scenes from Fort Hunter-Liggett, and use actual imagery obtained there during a field trial in 1995. Accompanying meteorological data and whole sky imager data were collected for this effort. Because of problems with registering the distance of objects in the image and the lack of calibrated targets in the images, data was collected at White Sands Missile Range during September and October of 1995 to make these comparisons. It was also determined that simulated imagery might lack detail that actual imagery might contain, and this would adversely impact the comparison of the simulated and actual imagery. Due to the level of effort required to actually simulate a scene at WSMR, and the lack of detail in a simulated image, a special scene was set up with which to make WAVES evaluation measurements. To this end, a calibrated target board was located in both the near and far parts of the image. WAVES was used to degrade the near image, and then comparisons of the two parts of the image, both before and after the degradation of the near part of the image were conducted. This paper details the comparisons made of these images, and thus evaluates the ability of the WAVES model to simulate the atmosphere.

As the model itself is new, the validation effort at this point is more of a calibration effort and a test of the methodology of using certain single-number metrics for characterization and comparison. The

model, having modules which account for turbulence, scattering, and attenuation, will probably perform better in some aspects than in others. It is expected that the model will have to be adjusted based on comparisons with test data and such adjustments may be made so as to minimize the difference in selected metrics between real images and their synthetic counterparts.

2. WAVES Overview

The main models in the simulation suite comprise BLIRB, a 3-D spectral radiative transfer code, VIEW, output database access code for line of sight path radiance/transmittance evaluations, PixelMod, for image spectral estimation and atmospheric effects modifications of images, ATMOS, a turbulence mode for evaluating the vertical profile of the refractive index structure parameter, and various related products. These latter products include a BLIRB front end for describing the inputs to BLIRB. A second module allows for a visualization of BLIRB inputs. This program is primarily designed to allow for determining the locations of clouds to be placed within the BLIRB space or modeled volume. The turbulence data calculated within ATMOS is then used within the VIEW model to evaluate the so-called receiver coherence diameter. This parameter is used to calculate the effects of turbulence blurring of images in the PixelMod code.

To perform the range-dependent calculations, WAVES uses line of sight radiative transfer calculations that generate the data for image modification. These line of sight calculations require a description of the radiation fluxes and extinction throughout the local environment. Radiation fluxes, turbulence parameters, and extinctions are calculated by the first phase of the WAVES models. The real-time image modification is done by PixelMod using data tables created by the FastVIEW program, which in turn uses databases created by the BLIRB model. The non-real time image modification is done by the PixelMod program using line-of-sight data created by the VIEW program created by three dimensional databases created by the BLIRB program.

BLIRB was developed for near-earth scenarios, and deals with a region up to 10 km in length and width and from the ground to either 5 or 12 kilometers AGL (above ground level). This allows most cloud related phenomena to be explored. BLIRB uses an iterative discrete-ordinates approach to calculate the direct solar (or lunar) flux, the directional radiances, and the total local extinction and scattering for all points on a grid with typical spacing of 250 meters. It performs these calculations for spectral bands defined as in LOWTRAN-7. These calculations allow complex inhomogeneous cloud fields to be used and the resulting complex radiations fields are produced. The extension beyond the one-dimensional vertical profiles available in LOWTRAN-7 is essential to realistic modeling of the battlefield. The directional effects allow for realistic changes in the appearance of scenes as the observer rotates, the inhomogeneity allows for clouds to engulf the observer or target, or pass between them, all in a self-consistent, radiometrically correct manner.

The results of the BLIRB model is a database of extinction, scattering and directional radiances, that depend on the wavelength and position in three-D space. These values are used for the viewing and imaging tools as they project lines-of-sight through space from the observing sensor to the elements that make up the scene.

The process starts with the analysis of the image, and conversion, pixel-by-pixel to a spectrally resolved element. This allows the creation of many spectral band images similar to the three RGB images from a common video source. Since each pixel represents a point in a 3-D geometry, based on observer position and look direction to a given pixel, the appropriate data from BLIRB can be applied to modifying the pixel's spectral content. The final step is to re-combine the spectrally resolved information into the three RGB signals for display. The general image processing approach is described by Tofsted (1993), and the spectral estimation process is described by Tofsted (1994). The general description of the currently used radiative transfer calculation process has been reported in Wetmore and Zardecki (1993).

3. Test Procedure

A set of test images was collected in the field to be used in the model validation. The purpose of generating the set of test images was two-fold, 1) to provide a reference scene for input into the WAVES model, and 2) to provide an atmosphere-degraded version of the same scene for comparison to WAVES output results.

In measuring atmospheric propagation of radiation, it is usually necessary to place a reference measurement device at one point, usually near a target object, and an identical measuring device directed at the target but farther away so that a specified amount of atmosphere exists between the two measuring devices. If the devices are visible-band imagers, the experimenter will expect to see a certain amount of degradation in the appearance of the target viewed from the far imager as compared to its appearance from the reference imager. The difference in appearance of the targets can be used to quantify some of the affects of the atmosphere on propagating visible radiation. This method is sound as long as there is a high degree of calibration between the two imagers. There are a number of things that can interfere with maintaining calibration in the field. If the imagers have automatic gain control, the gain setting will almost certainly differ between the two if they are in different locations due to varying ambient lighting conditions. Secondly, if the imagers are color, the color response curves will probably differ somewhat because of the sophistication of the signal stream.

To avoid the strict and difficult requirement of matching imagers, an alternative is to produce targets identical in their patterns and shading distributions but differing in scale corresponding to their respective distances from a single imager. This was the approach used in this testing. If a vacuum had been present, the appearance of the near and far target boards would have been virtually indistinguishable.

3.1 Turbulence Study

The first test of several planned was set up to study atmospheric turbulence. Generation of reference and corresponding degraded images from the field was accomplished as follows. A target board was built on which a 4'x4' black and white bar pattern was placed (see Figure 1). Two other target boards were then built and an 8'x8' bar pattern identical to the first but doubled in size scale was placed on them (see Figure 2). The first target board was placed an arbitrary distance from the imager and the

other two boards were placed at twice the distance from the imager along roughly the same line of sight. What appeared to the imager then were two identical patterns, the far one somewhat blurred and lower in contrast than the near one (see Figure 3). Images of the near pattern served as the reference image in the model. Images of the far pattern were compared to the images generated by the WAVES model from the input near pattern images. Descriptors and metrics used in the comparison between the images were the point spread function, gray-level co-occurrence statistics, and autocorrelation length. The co-occurrence statistics and autocorrelation length have been described in detail in (Bleiweiss and Rollins, 1994).

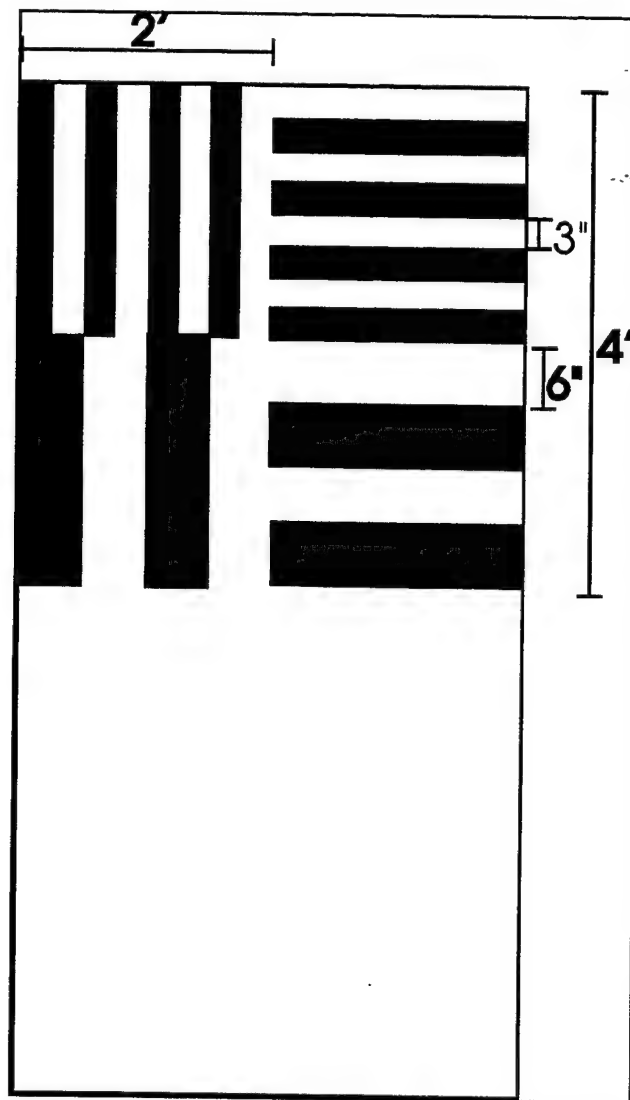


Figure 1

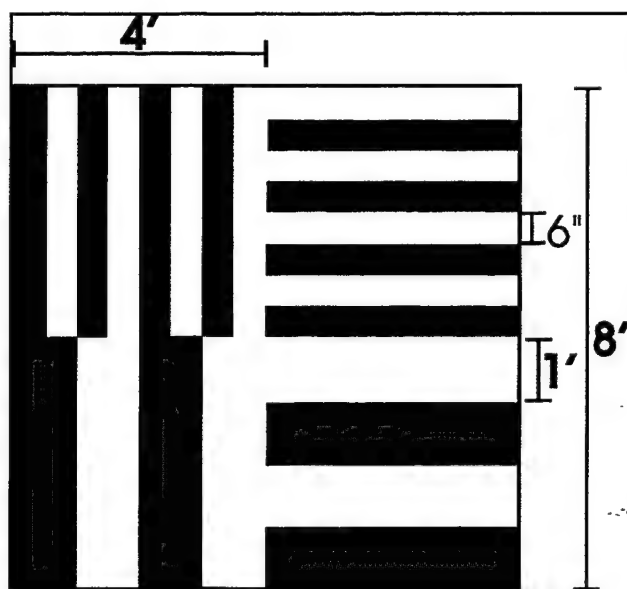


Figure 2

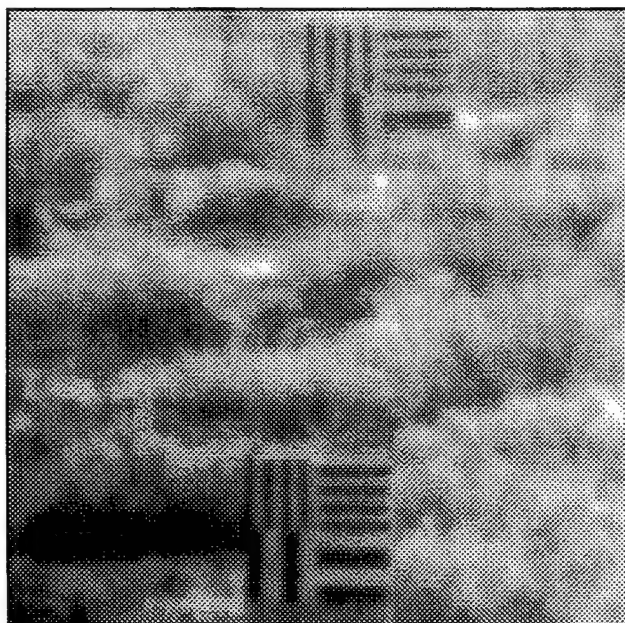


Figure 3

3.2 Equipment Used

The visible band imager used was a Photometrics Series 200 CCD computer-controlled camera. The camera has no automatic gain control, has variable exposure times over which it integrates the image, and supports image dimensions up to 384 rows by 576 columns. The CCD response is typical for silicon with a peak responsivity occurring at 670 nm.

Environmental measuring equipment included a scintillometer pair, a visibility meter, a barometer, a device for measuring wind speed and direction at two and ten meters above the ground, as well as temperature and humidity sensors at those two levels, and a radiometer.

The site chosen for the imager was at the 100-foot tower 3 miles east of the main post at White Sands Missile Range. The near and far target boards were placed along lines of sight radiating southeast from the tower (see figure 4). The tower provided elevation required for lessening the obscuration caused by vegetation. Figure 5 depicts this same layout, but from a side view.

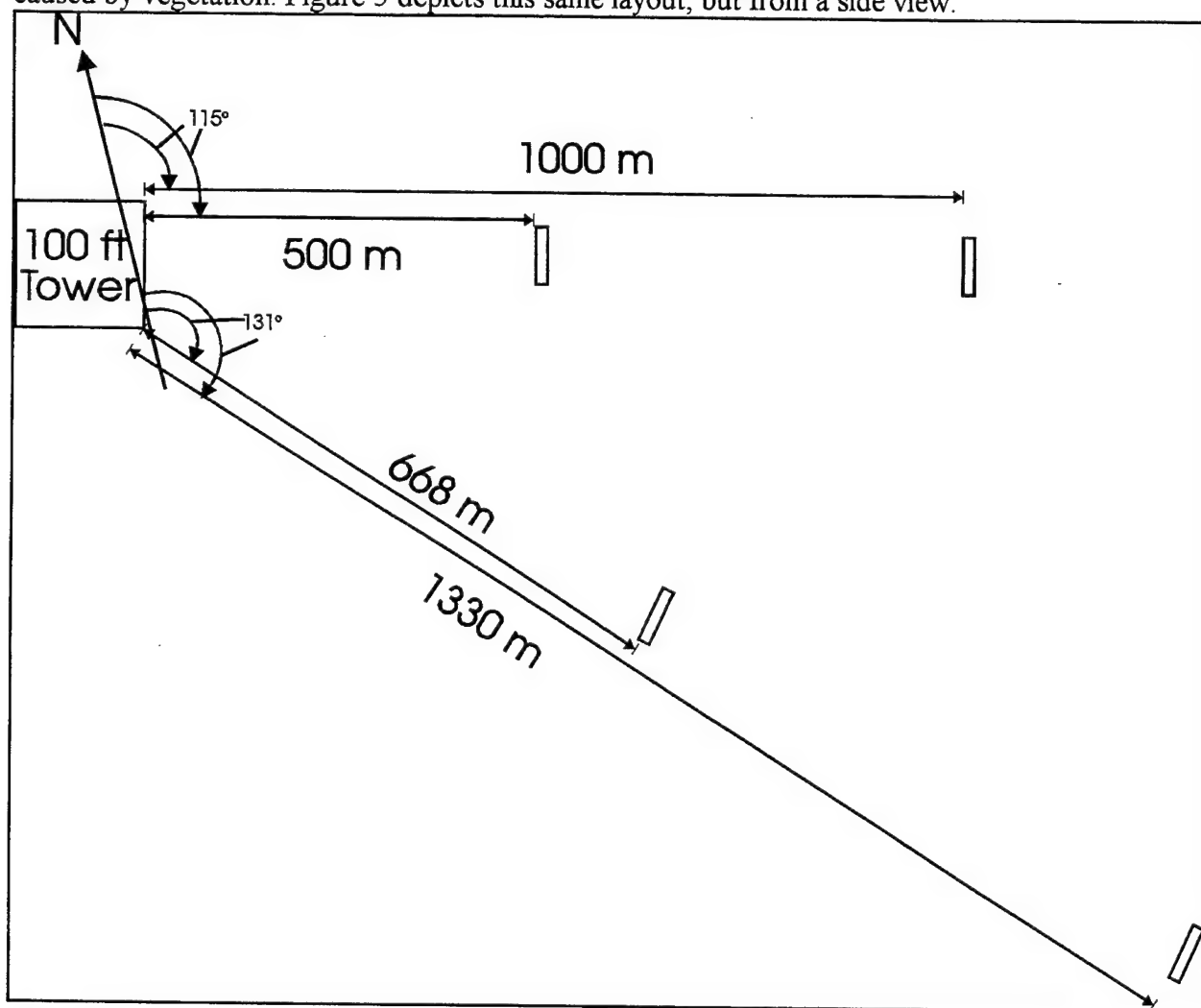


Figure 4

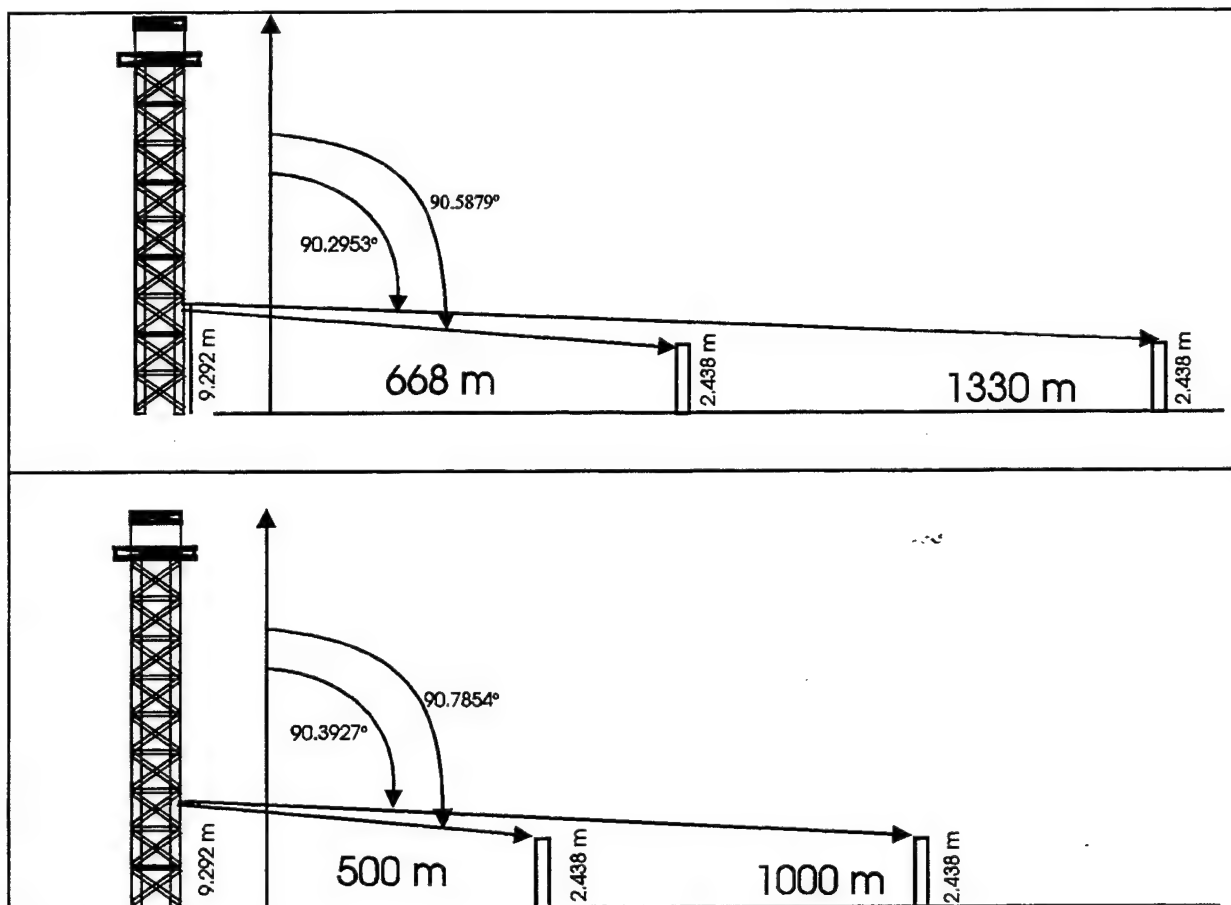


Figure 5

3.3 Phenomena Observed

The distances used in this study ranged from 0.5 to 1.3 kilometers. The distances were sufficient for observing significant distortion and spreading of the bar patterns by turbulence. Also seen in early morning imaging was forward scattering of solar radiation. This scattering into the viewing line of sight caused an offset increase in brightness of the far target board by as much as 15% greater than the near one. Of course both dark and light bands were brighter, diminishing the relative contrast.

4. Image Analysis Tools

4.1 The Modulation Transfer Function and Point-Spread Function

The Modulation Transfer Function (MTF) is the Fourier transform of the point spread function in optics.(Holst, 1993) The MTF is one of the chief means of assessing the effects of turbulence on the line of sight between the target and the imager.(Beland, 1993) When radiation passes through turbulence, it is refracted to a certain extent and changes path. Radiation from a scene which initially travels along parallel lines of sight can be refracted by the atmosphere to where the paths converge or diverge and a blurring is seen at the imager as a result. If a Fourier transform is calculated from

a distortion-free image and another one calculated for the same scene, but where atmospheric turbulence is present and blurring occurs, the Fourier coefficients will be seen to differ in the two transform images in accordance with the degree of blurring. Typically, the blurred image is a "low-pass" version of the undistorted image, where the low-frequency coefficients are proportionally stronger in the blurred image than in the undistorted one. If a ratio of each frequency coefficient is taken between the distorted and undistorted transform images, a map emerges which is the MTF. If the MTF is inverse transformed, the resulting map is the point-spread function (PSF).

For obtaining single numbers quantifying the degree of atmospheric distortion due to turbulence, the PSF is more convenient than the MTF. It is a real function (as opposed to a complex one) and it casts information in terms of a neighborhood of points in space as opposed to a neighborhood of spatial frequencies. The most interesting neighborhood of points in the PSF is about the (0,0) coordinate. If no atmospheric distortion is present, all of the energy in the entire PSF map will be located at (0,0). If slight distortion is present, most of the energy will be left in the (0,0) term, and the bulk of the remainder in the terms close to (0,0). If a point of light travels through a turbulent atmosphere and should only occupy a single pixel on an imager, the turbulence will cause the points image to occupy several neighboring pixels.

4.2 Measurements derived from MTF/PSF

As the modulation transfer function is the Fourier Transform of the point-spread function, they contain the same information. Being real-valued and widely used, the PSF was chosen as the framework from which to derive metrics. The first metric used was a measurement of the fraction of total energy remaining in the impulse at (0,0) upon inverse transforming the modulation transfer function. This metric is called the Impulse Remainder (IR) and is valued between 0 and 1. The second metric used is called the Point-Spread Entropy (PSE) and is a measure of how compact or distributed the energy is in the point spread function. If there is no spread and all energy is contained in a single point (i.e. the impulse at (0,0)) the PSE is 0. If the energy is spread out completely where a uniform distribution results, the PSE is a maximum of 5.5. The IR and PSE are simple and intuitive measures of the spreading of information. They gave stable and consistent results in this analysis.

For an NxN image with pixel intensities $I(m,n)$, the formula for Point-Spread Entropy was defined as

$$PSE = - \sum_{m=0}^{N-1} \sum_{n=0}^{N-1} \frac{I^2(m,n)}{E} \ln \left(\frac{I^2(m,n)}{E} \right)$$

where E is the total energy of the point-spread function calculated by

$$E = \sum_{m=0}^{N-1} \sum_{n=0}^{N-1} I^2(m,n)$$

and the Impulse Remainder is simply

$$IR = \frac{I^2(0,0)}{E}$$

The PSE is useful for understanding how spread out the energy is over a large number of PSF points while the IR only states how much energy is or is not in the (0,0) coordinate. Another common approach is to measure the width, in pixels, of the set of points about (0,0) whose energies are 50% of the maximum at (0,0) or more. For this study, there was never less than 85% of the energy at (0,0), leaving little energy for the surrounding points, so this width would always be just one pixel. This approach would not allow discernment of point-spread in our test cases.

4.3 Autocorrelation Length

The inverse Fourier transform of the power spectrum of an image gives the autocorrelation map, which is useful in determining how continuous or discontinuous the gray-scale distribution in an image is. It is also useful in specifying a typical "object length" within an image by providing the autocorrelation length. In this study, the autocorrelation length is determined by measuring the magnitude slope in the horizontal direction at position 0,0 according to (Ben-Yosef et. al., 1985).

The autocorrelation length is determined by computing the power spectrum of a region and taking its inverse Fourier Transform. Natural scenes are often modeled as Markov-I processes in which the intensity of a given pixel depends on the neighboring value and on an independent random variable. The autocorrelation function is a decaying exponential. The model is good when adjacent pixels are well correlated. For the binary target image, this is more true in the areas with the wider bands since the pixels differ appreciably only at the band boundaries.

$$ACF = e^{-\frac{x}{\alpha}}$$

The slope, calculated by taking the first derivative and evaluated at $x=0$ is then

$$-\frac{1}{\alpha}$$

and α itself is the correlation length. In this study, observing the fact that the correlation map has even periodic extensions, we take the eight nearest neighbors of 0,0 and calculate their intensity differences with $ACF(0,0)$ and compute an average, giving an average correlation length for all directions.

4.4 Gray-Level Co-occurrence Analysis

The Gray-Level Co-occurrence Matrix (GLCM) is a tabulation of the relative frequency that pairs of adjacent pixel values occur in an image. If a horizontal orientation is chosen, then the number of times a pixel has a value of 27 and its neighbor to the right or left has a value of 29 is recorded. That number is placed at position 27,29 in the matrix. Usually the numbers are divided by the total number of occurrences of all adjacent pixel pairs so that the matrix entries sum to one. The GLCM is a second-order distribution and therefore has some information about structure as well as grey-level content in an image. A number of statistics have been defined for the GLCM. Each specifies unique qualities about image features. The GLCM has been said (Wahl, 1987) to perform as well as Fourier Analysis in pattern description and segmentation. It is therefore employed here to observe how well ATMOS, in conjunction with PIXELMOD, renders distributions on the output images.

$$CONTRAST = \sum_{i=0}^{N-1} \sum_{j=0}^{N-1} (i-j)^2 g(i,j)$$

$$CORRELATION = \frac{1}{\sigma_m \sigma_n} \sum_{i=0}^{N-1} \sum_{j=0}^{N-1} (i-\bar{m})(j-\bar{n})g(i,j)$$

$$ENTROPY = - \sum_{i=0}^{N-1} \sum_{j=0}^{N-1} g(i,j) \text{LOG}(g(i,j))$$

$$HOMOGENEITY = \sum_{i=0}^{N-1} \sum_{j=0}^{N-1} g^2(i,j)$$

$$\overline{m} = \sum_{i=0}^{N-1} i \left(\sum_{j=0}^{N-1} g(i,j) \right)$$

$$\overline{n} = \sum_{j=0}^{N-1} j \left(\sum_{i=0}^{N-1} g(i,j) \right)$$

$$\sigma_m = \sum_{i=0}^{N-1} i \left(\sum_{j=0}^{N-1} g(i,j) \right)^2 - \overline{m}^2$$

$$\sigma_n = \sum_{j=0}^{N-1} j \left(\sum_{i=0}^{N-1} g(i,j) \right)^2 - \overline{n}^2$$

5. Test Results

Figures 6, 7, and 8 show sample near, far, and synthetic target images, respectively, for the same run. Numerical results are given in the tables that follow.

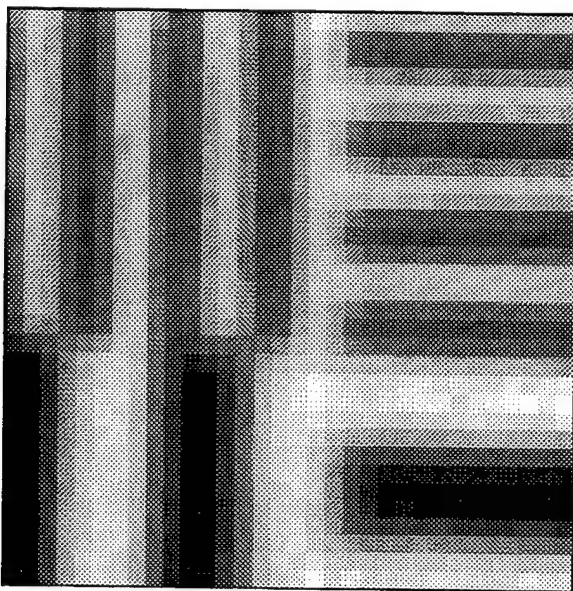


Figure 6 Near Target Image

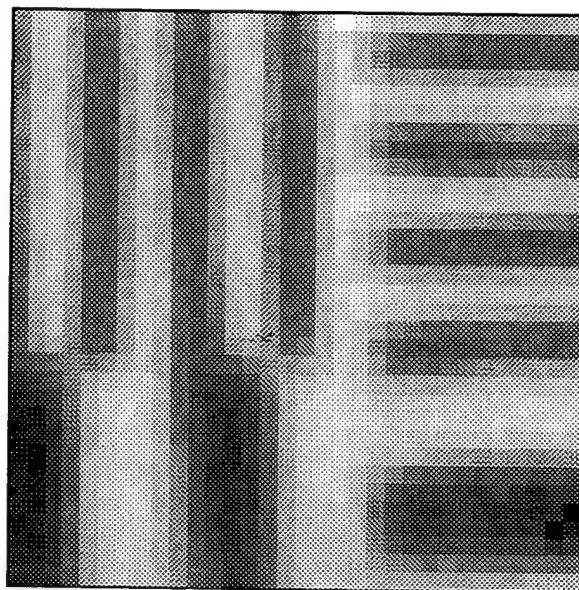


Figure 7 Far Target Image

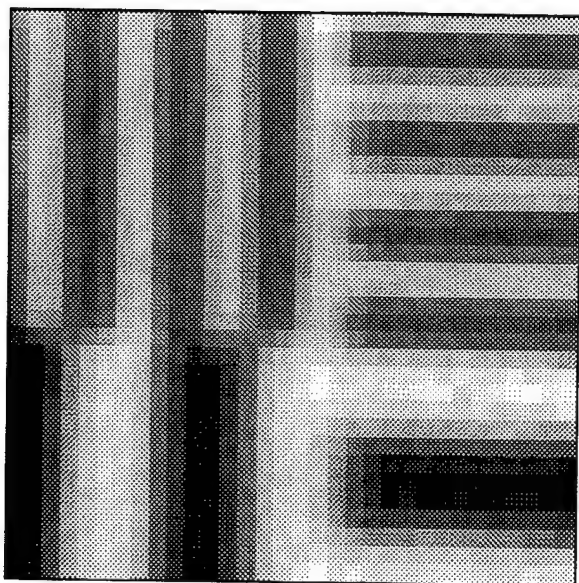


Figure 8 Synthetic Image Produced from Near Target.

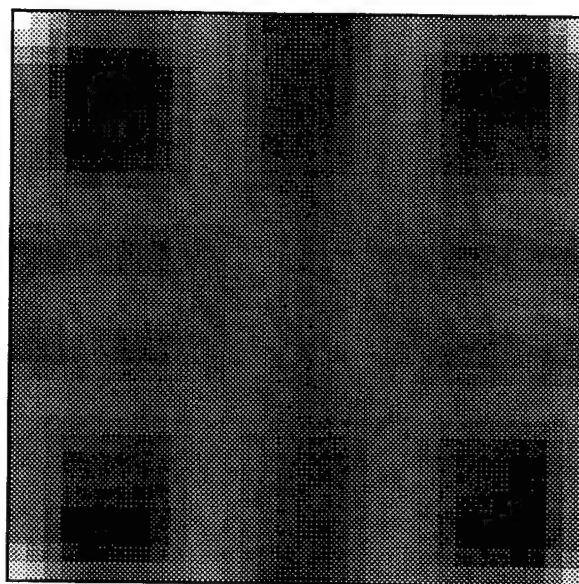


Figure 9 Autocorrelation Map of Near Target

6. Comparison Results

6.1 Results for Gray Level Co-occurrence Analysis

The results for the four GLCM metrics used in this test are presented in the following three tables. The contrast for the synthetic images is seen to be diminished compared to the other images.

Table 1. Near GLCM Results

Sequence #	Contrast	Correlation	Entropy	Homogeneity
1	1.0968	0.1486	2.5784	0.1082
2	1.7742	0.0928	2.9416	0.0796
3	1.6452	0.1434	2.6569	0.1020
4	3.2258	0.0929	2.6055	0.1545
5	4.1290	0.1257	2.7451	0.1446
6	3.9032	0.0961	2.4980	0.1951
7	32.8709	0.0561	3.5120	0.0411
8	4.6774	0.0936	2.6557	0.1498

Table 2. Far Image GLCM Results

Sequence #	Contrast	Correlation	Entropy	Homogeneity
1	.8387	0.1597	2.3019	0.1790
2	1.3226	0.1745	2.2033	0.1847
3	1.6774	0.0908	2.6388	0.1478
4	2.8387	0.1287	2.4309	0.1946
5	3.3226	0.0897	2.8103	0.1119
6	3.6452	0.0801	2.8117	0.1275
7	33.4839	0.0529	3.7470	0.0333
8	4.1935	0.0778	3.4194	0.0661

Table 3. Synthetic Image GLCM Results

Sequence #	Contrast	Correlation	Entropy	Homogeneity
1	0.6129	0.1746	2.3591	0.1587
2	0.4194	0.1477	1.9743	0.2081
3	0.6129	0.1328	2.1700	0.1852
4	1.6774	0.1019	2.6520	0.1358
5	2.5806	0.1234	2.8750	0.0952
6	2.5161	0.0898	3.0032	0.0671
7	17.4516	0.0637	3.4842	0.0421
8	5.2258	0.0987	2.8291	0.1410

6.2 Autocorrelation Lengths Comparison

The autocorrelation lengths obtained from the CCD images are given in the following table. The lengths were sensitive to time of day and sensitive to the target distance as would be expected. A sample autocorrelation map was given in Figure 9.

Table 4. Autocorrelation Length Comparison

Sequence #	Near Target ACL	Imaged Far Target ACL	Synthetic Far Target ACL
1	.2121	.2224	.2223
2	.2013	.2105	.2349
3	.1984	.2089	.2268
4	.1872	.1973	.2018
5	.1867	.1903	.1940
6	.1831	.1884	.1906
7	.1521	.1554	.1601
8	.1774	.1831	.1759

In view of the results for the GLCM contrast and the correlation lengths, it appears that there is a general trend in the model to excessively decrease contrast. Lack of contrast can cause greater correlation lengths as can blurring by turbulence. However, from the point-spread function results given next, this type of blurring is not observed as strongly in the synthetic imagery as in the acquired

images of the far target.

6.3 Point-Spread Function Results

Figures 10 and 11 show graphs of the point-spread function for test image sequence #5. Figure 10 is the point-spread function for the imaged near target to imaged far target case, and Figure 11 is the point-spread function for the imaged near target to the synthetic far target.

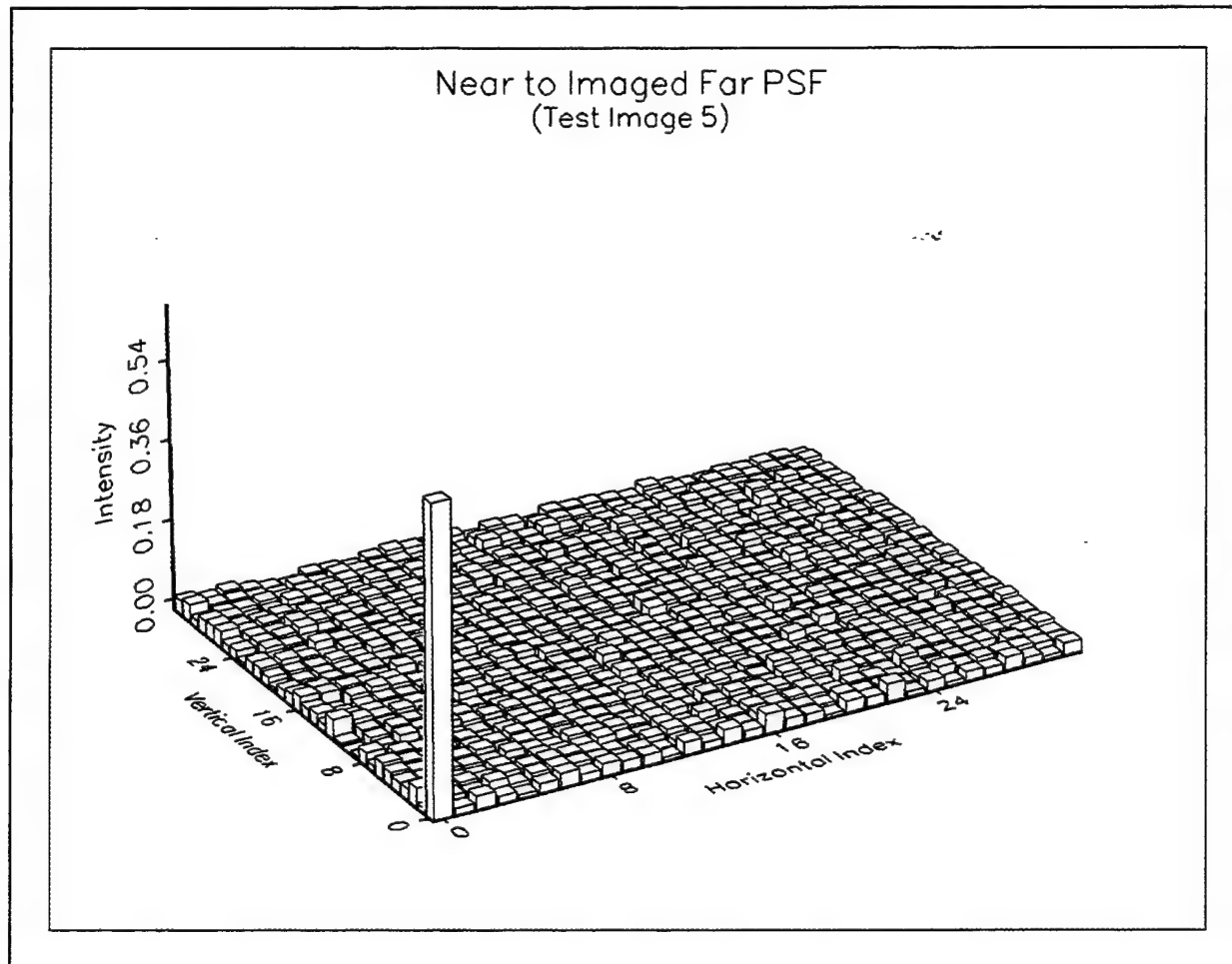


Figure 10 Real-real point spread function

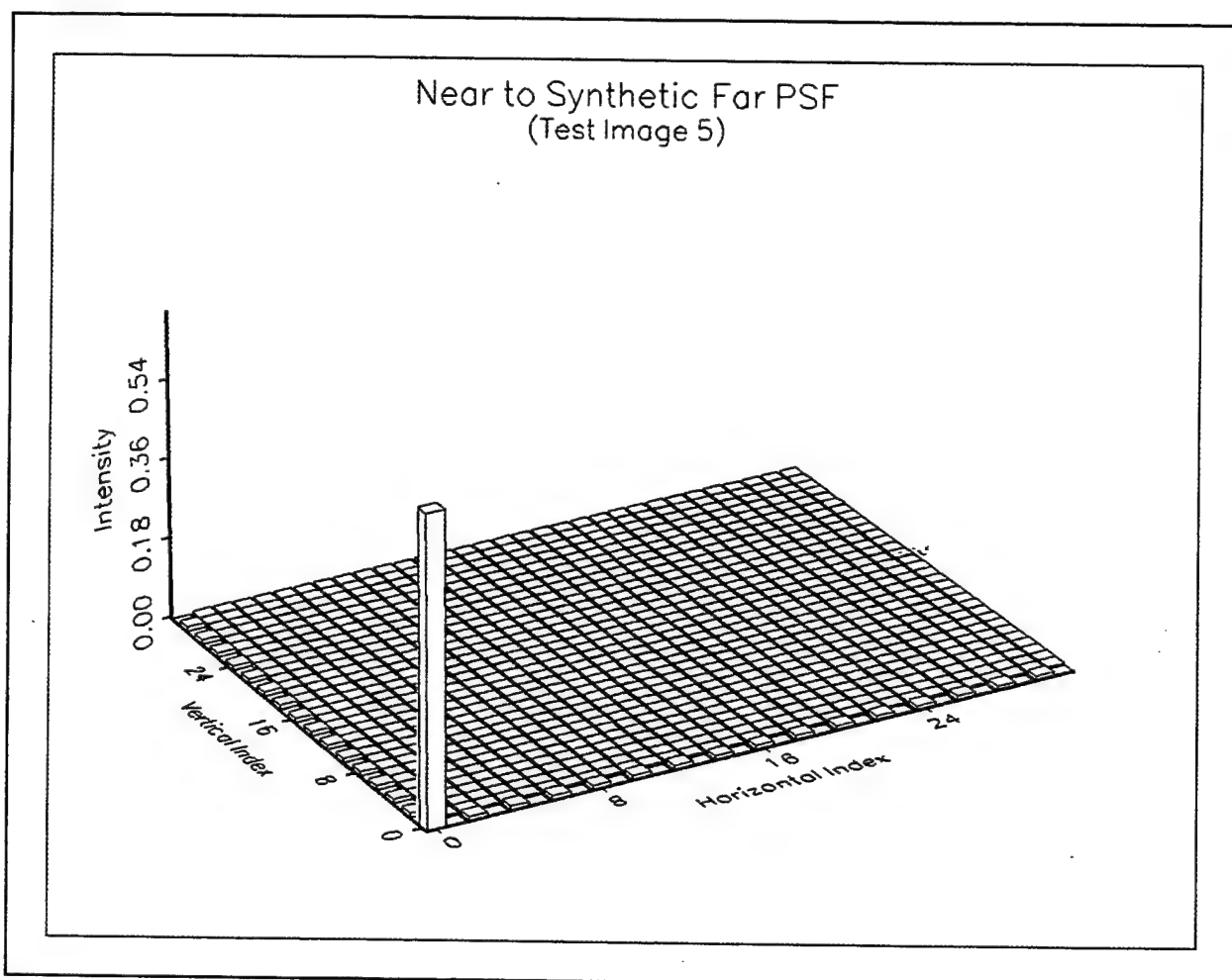


Figure 11 Real-synthetic Point Spread Function

Table 5. Point-Spread Entropy (scaled between 0 and 5.5)

Sequence #	near-to-imaged-far PSE	near-to-synthetic-far PSE
1	0.6082	0.0438
2	0.7026	0.7721
3	0.7656	0.5757
4	0.7372	0.1739
5	0.8237	0.0330
6	0.8496	0.0439
7	0.8518	0.1134
8	0.8017	0.0000

Table 6. Impulse Remainder (scaled between 0 and 1)

Sequence #	near-to-imaged-far IR	near-to-synthetic-far IR
1	.9381	.9959
2	.9275	.8952
3	.9201	.9255
4	.9240	.9809
5	.9142	.9970
6	.9102	.9959
7	.9102	.9882
8	.9152	1.0000

The point-spread function is not particularly sensitive to contrast. If turbulence causes the atmosphere to blur lines, the effect will be seen in the point-spread function. As seen earlier, the correlation length can be affected by lack of contrast as well as by blurring. These PSF metrics allow one to separate blurring caused by lack of contrast from that caused by turbulence.

7. Conclusions

7.1 Metric Performance

The metrics tested were GLCM metrics, autocorrelation length, and point-spread metrics. Each metric was stable so that small changes in position of a region of interest did not result in large changes in the metric. The metrics gave results agreeing with intuition and each provided unique information about image degradation caused by the atmosphere.

7.2 Test Setup

In view of the resemblance of metric values between the near and far imaged targets, it was seen that good duplication of scene characteristics can be expected when constructing near and far target boards of the same material. It is likely that in the case of visible imaging, it may sometimes be more reliable to use a near and a far target board with a single imager than a near and a far imager viewing the same board. The ability to "calibrate" the target boards to each other may be superior to the ability to calibrate imagers.

7.3 Model Performance

The WAVES model was able to impose blurring and contrast degradation of the same order of

magnitude observed in analysis of the field tests. From this initial test, the model seems to impose excessive contrast reduction due to scattering and attenuation and not enough blurring due to turbulence. It is believed that accuracy can be improved through testing and calibration using the metrics presented. Further comparisons are necessary to make final conclusions.

References

Beland, Robert R., "Propagation through Atmospheric Optical Turbulence," The Infrared & Electro-Optical Systems Handbook, Vol. 2, pp. 190-194, SPIE Press, 1993.

Ben-Yosef, N., Wilner, K., Simhony, S., Feigin G., "Measurement and Analysis of 2-D Infrared Natural Background," Applied Optics, Vol. 24, No. 14, pp. 2109-2113, 15 July, 1985.

Bleiweiss, Max P. and J. Michael Rollins, "Validation Results for SWOE Scene Generation Process," Proceedings of the Battlefield Atmospheric Conference, December 1994.

Davis, John, "An Evaluation of the Delta-Eddington Contrast Transmission Model," Atmospheric Environment, vol. 25A, No. 8, pp.1679-1687, 1991.

Holst, Gerald C., "Infrared Imaging System Testing," The Infrared & Electro-Optical Systems Handbook, Vol. 4, pp. 223-232, SPIE Press, 1993.

Tofsted, David, "Modifying Target Acquisition Images for Atmospheric Degradation Effects," Proceedings of the Cloud Impacts on DoD Operations and Systems 1993 Conference, PL-TR-94-2188, pp.213-218, Ft. Belvoir, VA, November 1993.

Tofsted, David, "Spectral Estimation and Processing of Imagery Data," Characterization and Propagation of Sources and Backgrounds, SPIE, Bellingham, WA, vol. 2223, pp. 511-520, Orlando, FL, April 1994.

Tofsted, David, Patti Gillespie, and Alan Wetmore, "The WAVES Modeling Suite: Extensions and Evaluation Update", Ground Target Modeling Vehicle Conference, August 1995.

Wahl, Friedrich M., "Digital Image Signal Processing", Artech House, Boston, 1987.

Wetmore, A. E., and Zardecki, A., "The Boundary Layer Illumination and Radiative Balance Model (BLIRB)," Proceedings of the Cloud Impacts on DOD Operations and Systems 1993 Conference, PL-TR-94-2188, pp. 201-206, Ft. Belvoir, VA, November 1993.

A HYBRID GIS AND 3-D INFRARED TARGET/BACKGROUND MODELING SYSTEM

G. P. Seeley
RADEX, Incorporated
Bedford, MA 01730, USA

S. A. Luker
Phillips Laboratory, USAF
Hanscom AFB, MA 01731, USA

ABSTRACT

Described is a system for 3-D IR scene simulation in the 8-12 micron range. A commercial GIS is used to integrate a wide variety of standard geographic data sources including DMA, USGS, and satellite data. Large regions of landuse data are rasterized at high resolutions and recoded to form a composite image representing georeferenced landuse/surface materials for a given area. Attribute data (e.g., slope, aspect) are computed by the GIS and associated with the composite image thus reducing computational time and data storage. With the GIS, subsets of large data regions are defined and three data layers (elevation, landuse, basemap) are clipped for export to 3-D IR models. Software for running the underlying thermal and radiance models from the exported GIS data has been constructed. The composite landuse grid is rendered, including atmospheric transmission effects, in the 8-12 micron IR region. Extensive use of texture mapping is made, including radiance model driven billboarded vegetation. The computed radiances from the physical models are used to determine the brightness for different surface materials of the composite texture map that overlays the elevation grid.

1. INTRODUCTION

Air Combat Targeting Electro-Optical Simulation (ACT/EOS) is a product of the Air Force Weather Impact Decision Aids (WIDA) Program based at Phillips Laboratory, Hanscom AFB, MA. The goal of ACT/EOS is to provide Air Force mission planners with predictions of infrared (IR) target scene radiances to aid in tactical decision making.

ACT/EOS focuses on integrating weather, target and geographic information with IR signature models such as the Smart Weapons Operability Enhancement Interim Thermal Model, SWOE ITM (Koenig, 1994), and the Thermal Contrast Model, TCM2 (Blakeslee and Rodriguez, 1994), for generation of realistic IR scenes. This effort has resulted in a demonstration prototype

enabling the user to select a geographic area of interest, appropriate weather data, and time of day to produce (8-12 micron) 3-D IR scenes containing targets on terrestrial backgrounds.

1.1 Project Objectives

ACT/EOS is a software product designed to predict the influence of weather conditions on IR weapons systems directed at high value targets. Mission planners and Weapons System Officers {WSO's} need IR weapons system performance information presented to them in terms that they can rapidly assimilate. A major component of this effort involves producing physically realistic 3-D imagery using predicted weather conditions and target information. The imagery is designed to enable WSO's to locate specific targets inside a mission footprint, which may be 20 km on a side. Mission planners need to identify combinations of time of day and weather conditions that will significantly degrade or enhance the performance of IR weapons systems so that they may select the most appropriate combination of sensors for a specific mission.

ACT/EOS is required to have reasonable computational demands. Scenes should be generated within a small number of minutes on a single high-performance UNIX workstation. ACT/EOS attempts to produce accurate predictions while operating within hardware, run-time and input data constraints. The goal is to provide the operational test and evaluation (T&E) community with a fully functional prototyped system using gridded weather data and standard spatial data products (e.g., DMA, USGS) with a user-friendly interface.

2. PHYSICAL MODELING

2.1 Model Approach

Modeling each element of a complex target scene is computationally expensive. Many elements of a scene have similar factors influencing their physical temperature. For example terrain areas that have similar slope, aspect and surface coverage have approximately the same factors driving their temperature. The computational burden can be substantially reduced by dividing the scene into thermally equivalent groups of objects. Thermally equivalent objects at different distances may have strongly different IR signatures due to optical properties and atmospheric transmission. A full transmission calculation for each unique sensor-to-object path would be very expensive. Sensor-to-object atmospheric paths can be divided into similar classes reducing the burden. Division into equivalence classes is performed at all levels of the physical modeling process to increase efficiency.

ACT/EOS relies on several previously developed physical models for predicting target/background signatures. The SWOE ITM and TCM2 are presently part of the ACT/EOS system and are undergoing preliminary validation. The atmospheric transmission model MODTRAN will be integrated and tested over the next few months.

The SWOE ITM is used to compute background facet temperatures. ITM is a multilayer 1-D heat flow model that can predict temperatures for a large number of surface material/soil combinations. Short, Medium and High generic vegetation, deciduous, coniferous and mixed

forest type surface coverages can be modeled. The vegetation model uses a canopy approach where the distribution of radiation through a canopy is treated statistically, rather than using exhaustive 3-D geometrical information on canopy structure. Bare surfaces include sand, various soil/subsoil combinations and asphalt. Currently asphalt is modeled as a user defined soil type. The model is being extended to incorporate various ages of asphalt and concrete. Slope, aspect, surface material and subsoil are used to segregate the terrain background into equivalence classes. A thermal calculation need only be run once for each equivalence class.

TCM2, based on the thermal analysis engine in the currently operational EOTDA, is used for target thermal and radiance computations. TCM2 divides a target into "thermal nodes", each node is connected with others with various types of linkages to account for conductive, convective and radiative heat transport modes. A radiosity approach is used to compute multi-bounce intra-target radiation interactions within the target. TCM2 uses a thermal and geometric target description, as well current meteorological data to compute zero-range radiance values for each facet of a target model.

MODTRAN is used for computing attenuation of IR radiation through the atmosphere. For scene generation applications many sensor-to-object paths need to be computed. The computational burden of running MODTRAN on each individual path is unacceptably high. Higgins *et. al.*, (1995) has developed an algorithm that runs MODTRAN on a grid of representative paths and interpolates between the grid points to allow more rapid computation of path transmission and path radiance.

Currently we are not performing calculations of BRDF, multiple bounce radiation paths, background shadowing by targets or other important physical effects. Only surface material temperature and emissivity are taken into account. Development of an efficient radiance code that includes more effects is ongoing.

2.2 Weather

IR scene prediction has a strong dependence on past and present weather conditions. ACT/EOS is constructing a link to the Air Force's Automated Weather Distribution System (AWDS) in order to automatically ingest weather data. AWDS provides global coverage observations and forecasts with continuous updates. The link software will have the capability to store weather data for a specific location until it is needed by the physical models. Uniform Gridded Data Field (UGDF) products will be used in the first version of the link software. Until the automated weather ingestion process is complete the ACT/EOS software runs from weather files produced from the Hanscom AFB test site.

2.3 Geographic Information System

Organizing the geographic data that drives the physical models is a formidable task. A complex geographic area is often comprised of multiple landuse/surface materials at widely differing scales and orientations. In order to characterize an area in detail many different data sources are often synthesized into an image representing the target/background. Vegetation types, surfaces

materials, soil types, target types, and elevation have to be quantified, or at least estimated, to model a scene. To meet the demands of assembling the variety of spatial data, ACT/EOS software integrates with a commercial geographic information system (GIS) which manages all geographic data required for modeling inputs.

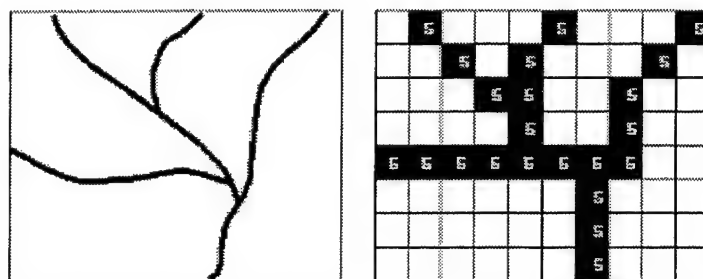
A GIS is a digital computer system for capturing, processing, managing, displaying, modeling, and analyzing geographically referenced spatial data, which are described by attribute data and location (Campbell, 1990). Encoded data usually follow either the polygon (vector) cartographic data structure, where spatial data are represented by points, lines, or polygons, or the grid (raster) cartographic data structure. In the raster structure points, lines, and polygons are encoded creating a matrix that is superimposed over the terrain such that the attribute information is collected within a systematic array of grid cells (Jensen, 1986).

A GIS is capable of analyzing multiple layers of data or overlays for a specific geographic region. The overlays may depict raw data (topography) or thematic data (land use, soils, or geology), but they must share common geographic qualities (including a geographic coordinate system), so that they can be merged into a single system that permits use of varied data as an integrated unit. An advantage of using GIS to manage a geographic data base is that GIS allows the user to quickly insert new data or respond to the most recent data changes. Because attribute data have preserved locations in space, it is easy to recode, combine, or isolate existing data.

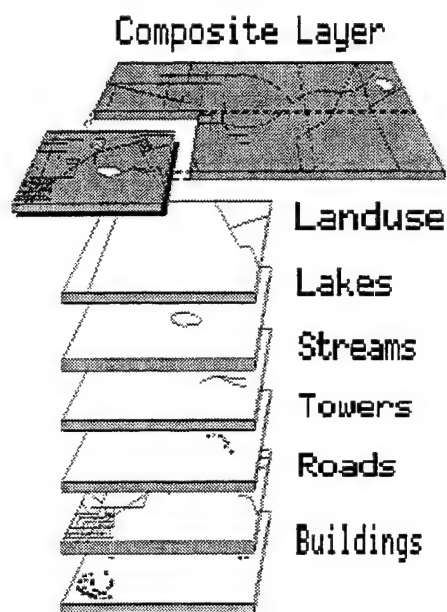
Arc/Info (ESRI, 1994), a commercial GIS, is used to store and manage all geographically referenced spatial data. Arc/Info imports a variety of standard geographic data formats including DMA, USGS, and commercial satellite data. DMA, the largest contributor of digital geographic data to DOD provides many different products including elevation data (DTED), feature data (DFAD), raster graphics and imagery (ADRG, CIB) which can be imported into Arc/Info. The standard DMA vector product format (VPF), developed by Earth Sciences Research Institute (ESRI), includes Digital Chart of the World (DCW) and Vector Smart Map (VMAP). Transportation, hydrography, and hypsography are also available through USGS in the form of Digital Line Graphs (DLG), while raster elevation data are stored as Digital Elevation Models (DEM). Many other standardized geographic data formats can be imported into Arc/Info including satellite data, scanned aerial photographs, and other government data such as soils data from the U.S. Department of Agriculture and land use/land cover from USGS.

All imported data (raster, including scanned imagery, and vector) are registered and georeferenced by transforming to a Universal Transverse Mercator (UTM) map projection using either a Clarke 1866, North American Datum of 1983, or World Geodetic System of 1972 and 1984 spheroid datum. DMA 1-degree DTED-1 has a spatial resolution of 90 meters, while some vector data may have spatial resolutions as low as 2.5 meters. The GIS resamples raster data sets quickly allowing for precise overlaying of multi-resolution grid data. Vector data are rasterized to a common cell size at fine resolutions to maintain data integrity. The overlays of individual raster grids representing land use/surface materials are then recoded ensuring that each land use/surface material receives a unique value Figure 1a. Recoded multi-layer grids are merged into a single composite grid Figure 1b consisting of various uniquely identified land use/surface materials. Attributes (e.g., slope, aspect) for each land use/surface material are stored along with

cell identification values in a value attribute table (VAT) that is exported to the 3-D thermal modeling software.



(a)



(b)

Figure 1. Rasterization of a stream vector (a) to a grid cell structure. Raster (grid) overlays forming a single raster composite layer (b).

Within the GIS a graphical menu system written in Arc Macro Language (AML) has been developed allowing the user to view and describe vector and raster data, perform vector/raster overlays, browse through a large region, and select geographical areas of interest for export to the 3-D thermal model software. Upon selection of an area of interest certain attribute data such as slope and aspect are calculated for export to the 3-D thermal model. In addition to categorized land use/surface materials and elevation data, registered georeferenced base maps are generated using either available commercial satellite data in the form of CIB or scanned aerial photographs. These thematic base maps provide the user an excellent visual frame of reference when selecting areas of interest. Three raster grid files (elevation, composite, and base map) are converted to floating point grids and are exported from Arc/Info to the 3-D thermal model.

2.4 Visualization

The first layer of data from the GIS to be processed is the elevation grid. The elevation data is the foundation on which all other data layers will be positioned. Normally we have a square gridpoint spacing of between 30 and 90 meters. These squares are then partitioned into a triangular network that constitutes the "frame" onto which all other data layers and objects in the scene are drawn onto. From the elevation data the modeling input quantities of slope and aspect for each triangular facet are derived. The height of surface targets is interpolated from the triangular network of elevation posts.

On each triangular facet there may be many different types of data describing surface conditions over the facet. These data may be at a much higher spatial resolution than the elevation grid itself. The data could include satellite imagery or aerial photography, rasterized vector products, or high resolution raster mapping data. In order to integrate the many resolutions of input data conveniently and render them in 3-D perspective a computer graphics technique known as texture mapping (Foley *et. al.*, 1990; Neider *et. al.*, 1993) is used.

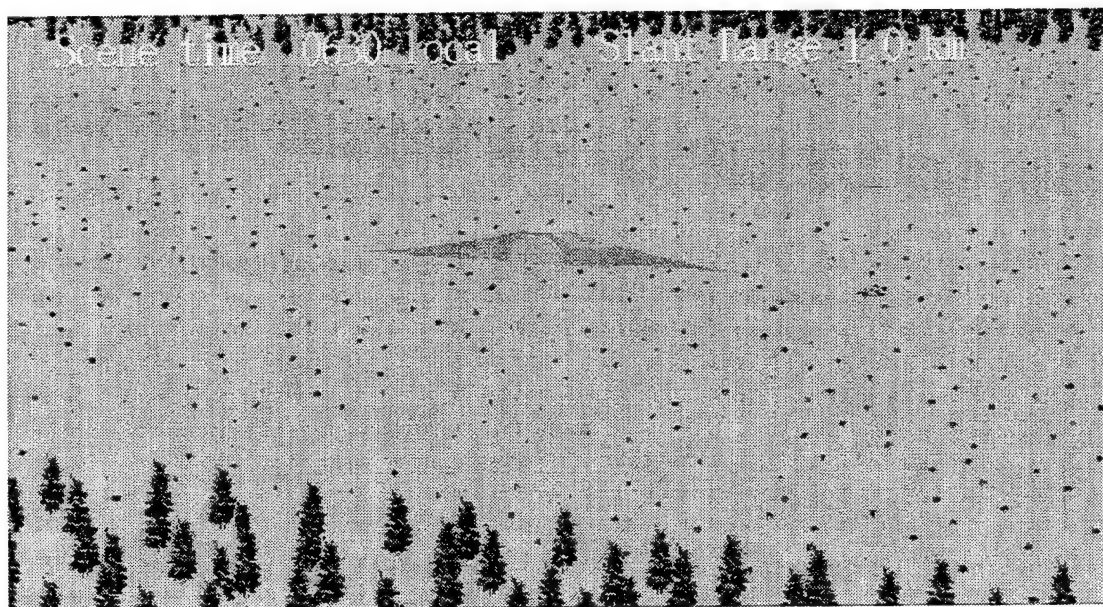
Texture mapping is used here as the basic mechanism for rendering diverse data over an elevation surface. Texture mapping enables one to "paint" the polygons defined by the elevation grid with a raster data map. The raster data used are not constrained to be at any particular length scale. Each data pixel in the texture map is known as a "texel". One texel may occupy many pixels or less than one pixel in a rendered image depending on the view distance and angle. The elasticity of texels is managed via texture mapping interpolation routines. Modern commercial three dimensional graphics libraries such as OpenGL (Neider *et. al.*, 1993) provide this interpolation functionality. The flexibility of the technique makes it ideal for combining data of multiple resolutions.

In the GIS data of multiple scales are rasterized to the scale of the smallest cell size data available. The composite grid layer is then applied to the elevation grid as a surface texture. The physical models needed to compute the scene radiances then read surface material codes from this composite layer in order to obtain the required thermal and optical properties. After the physical models have run the results are used to modify the appropriate texels in the image.

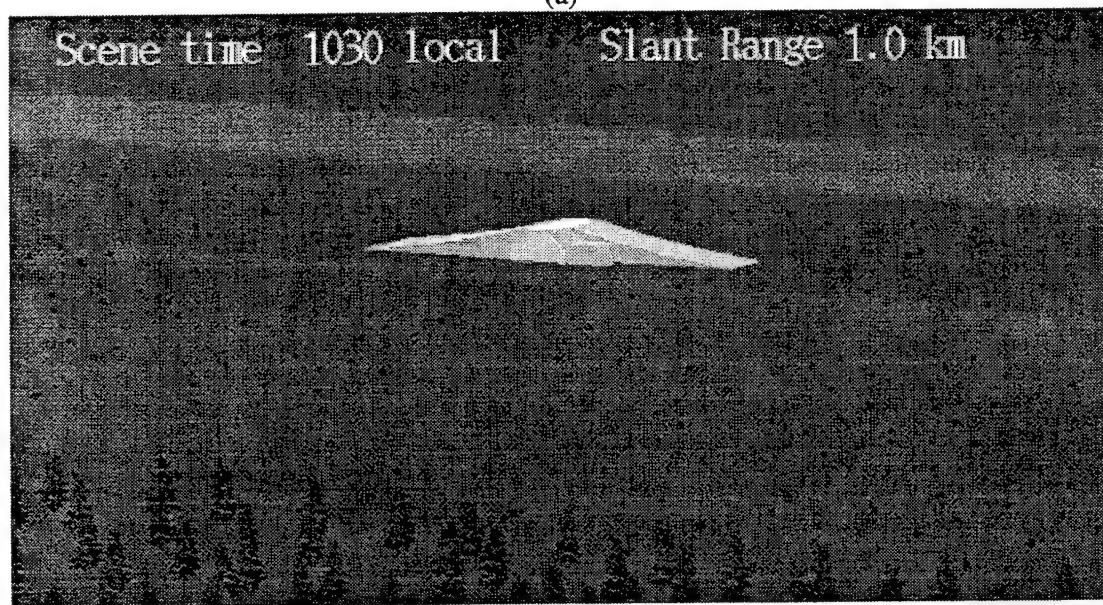
Texture mapping is also used to "billboard" vegetation into a scene by using a scanned image of a complex natural form leaving some pixels transparent. This enables one to construct fairly realistic looking vegetation scenes. The vegetation models are able to supply vegetation temperatures, which can be used to compute radiances for the vegetation. The pixels that make up the vegetation can then be appropriately modified to reflect the mean radiance of the vegetative item in question. This technique is compatible with a "canopy model" type of approach where the distribution of radiation through a vegetation is statistical, in contrast to a modeling effort that utilizes exhaustive full 3-D information on vegetative structure.

Figure 2 shows two 3-D scenes generated for a bunker target placed near an Eglin AFB runway at two different times. The scene at 630 am local (a) occurs before the sun has heated the bunker significantly. It is difficult to isolate the target from the background and WSOs would probably

have trouble locating the target if the mission were flown during this time. However, scene (b), generated at 1030 am local, depicts the target easily because solar loading has heated the bunker making it visible. Mission success is greatly increased if flown at the 9 am time. The atmospheric transmission in these scenes is a Beer's Law approximation. Billboarded trees are shaded based on ITM thermal model output. Terrain self-shadowing and BRDF effects are not presently modeled but would make important contributions to this scene.



(a)



(b)

Figure 2. 3-D LWIR scenes of a bunker model placed on USGS DLG /DTED background data for Eglin AFB

3. CONTINUING DEVELOPMENT AND VALIDATION

3.1 Near-Term Prototype Delivery

ACT/EOS has an active field validation program, 8-12 micron imagery of a test target and detailed meteorological data collection has been taking place at a Hanscom AFB test site since 3/95. A mobile sensor suite will begin observations at other sites in 3/96. Details on the validation program can be found in (Heckman, 1995) ACT/EOS will begin supporting PGM IR seeker field tests at Eglin AFB in 10/96 with a prototype system. Scene predictions will be provided to WSO's during test and evaluation activities. It is anticipated that the prototype system will be operated and imagery delivered via a world-wide-web page from a server housed at Hanscom AFB. Distributing predictions and imagery from a web page allows people using inexpensive computer systems trouble free access to the system's functionality. Currently operational mission planning and intelligence systems are already using the web to distribute information and imagery.

3.2 Improve Efficiency

Digital geographic information can be represented using various formats. Currently ACT/EOS stores geographic information in either a vector or raster data model. A third existing data model, the triangular irregular network or TIN, can possibly decrease model run times by reducing the number of polygons and therefore the number of calculations. The TIN model represents data by connecting nodes with irregular triangular facets. TINs are far superior to raster models when representing elevation data containing large flat regions. Although some data are stored in vector format, all calculations are performed on raster data. This is why linear feature such as roads and streams appear "blocky" and exaggerated. We plan to incorporate vector data into the actual modeling process by using GIS dynamic segmentation for coding prescribed distances along the vector. This will allow us to characterize features of the vector such as road slope/aspect, a crucial input to the models. Figure 3 illustrates how we plan to incorporate vector, raster, and TIN model structures to improve visualization and increase efficiency.

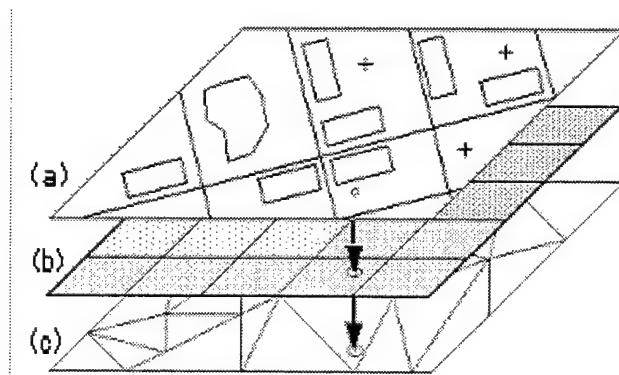


Figure 3. Using 3 model structures, linear features will be represented by vectors (a), landuse by raster (b), and elevation by TINs (c).

4. SUMMARY

The utility of the GIS in the management of geographic data is evident by: 1) reducing the time required to generate data sets suitable for IR modeling (regional coverage can be constructed in less than one day) by utilizing pre-existing (DMA, USGS) spatial data bases or by quickly changing land use/surface material categories, 2) calculating necessary attribute data (e.g., slope, aspect) for input into the thermal model, and 3) providing the user with a georeferenced 2-D map from which geographical areas of interest can be selected and exported to the 3-D thermal model software.

ACT/EOS has integrated several physical models for IR signature prediction and has constructed the infrastructure to efficiently run them using meteorological and geophysical data products. We plan extensive field testing and support of test mission in the coming year.

ACKNOWLEDGMENTS

Geoff Koenig of the Army Cold Regions Research Laboratory CRREL has been an immense help with the integration of the SWOE models into our own. Our in-house version of TCM2 has been developed by KRC under contract. Finally, we want to express our appreciation to the ACT/EOS program manager Lt. Col. Joseph Alleca and the rest of the ACT/EOS team (Stan Heckman, Tim Hiett, and 1st Lt. Dana Madsen) who have contributed their knowledge and expertise throughout the project.

REFERENCES

- Blakeslee, L., and L. Rodriguez, 1994. *Technical Reference Guide for TCM2*. WL-TR-94-1063
- Campbell, J.B., 1990: *Introduction to Remote Sensing*, The Guilford Press, New York.
- ESRI, 1994: *ARC/INFO Geographic Information System V 7.02*, Redlands, CA.
- Foley, J., Van Dam, A., Feiner, S., and J. Hughes, 1990: *Computer Graphics, Principles and Practice 2nd ed*, Addison Wellesley, Reading, MA, 1175 pp.
- Heckman, S. J., 1995. "Thermal Contrast Model Performance in Various Weather", In *Proceeding of the Battlefield Atmospherics Conference*, U.S. Army Atmospheric Research Laboratory, White Sands Missile Range, NM.
- Higgins, G. J., Gouvela, M. J., Hestand, P. D., and M. S. Seablom, 1995. *A Fast MODTRAN Interpolator for Scene Generation*, Target Modeling and Validation Conference, Houghton, MI.
- Jensen, J.R., 1986: *Introductory Digital Image Processing*, Prentice-Hall, Englewood Cliffs, NJ.

Koenig, G., 1994. *Smart Weapons Operability Enhancement Program Final Report*. Annex D
SWOE Models, Army Cold Regions Research and Engineering Laboratory, Hanover NH.

Neider, J., Davis, T., and M. Woo, 1993: *OpenGL Programming Guide*, Addison Wellesley.

Texture Generation for Use in Synthetic Scenes

Clem Z. Ota and J. Michael Rollins
Science and Technology Corporation
Las Cruces, New Mexico, USA

Max P. Bleiweiss
U.S. Army Research Laboratory
Battlefield Environment Directorate
White Sands Missile Range, New Mexico, USA

ABSTRACT

In the process of creating synthetic scenes for use in simulations/visualizations, texture is used as a surrogate to "high" spatial definition. For example, if one were to measure the location of every blade of grass and all of the characteristics of each blade of grass in a lawn, then in the process of composing a scene of the lawn, it would be expected that the result would appear "real"; however, because this process is excruciatingly laborious, various techniques have been devised to place the required details in the scene through the use of texturing. Experience gained during the recent Smart Weapons Operability Enhancement Joint Test and Evaluation (SWOE JT&E) has shown the need for higher fidelity texturing algorithms and a better parameterization of those that are in use. In this study, four aspects of the problem have been analyzed: texture extraction, texture insertion, texture metrics, and texture creation algorithms. The results of extracting real texture from an image, measuring it with a variety of metrics, and generating similar texture with three different algorithms is presented.

1. INTRODUCTION

The definition of texture is given by Haralick and Shapiro (1991) as that property of an image whereby small regions of that image experience "wide variation of tonal features". This is opposed to the "gray tone" property whereby small regions experience "little variation of discrete tonal features". These "small regions" make up the set of features and backgrounds in an image which can be resolved as unique portions of the image -- the textural properties are below this resolution threshold for definition of features. The real world properties which cause texture to exist are relief, and optical and thermal characteristics (e.g., emissivity, thermal conductivity, etc.)

of the various scene elements which exist on a small scale relative to the rest of the elements (features) in the scene.

An example of high resolution texture is the “map” shown in Figure 1. This image was obtained during the Smart Weapons Operational Enhancement Joint Test and Evaluation (SWOE JT&E) (Welsh et al. 1995) by the Waterways Experiment Station (WES) of the U.S. Army Corps of Engineers. It is a high spatial resolution image of a small region of natural terrain located at the Yuma I field test site (one of the locations used during the SWOE JT&E series of field tests). The data were obtained with a far infrared (8-12 μm) thermal imager configured with a narrow field of view lens. These kinds of texture images provided the raw material for the SWOE JT&E synthetic texture generation process which was one approach to the problem of creating fine detail synthetic texture without time-consuming, highly detailed modelling.

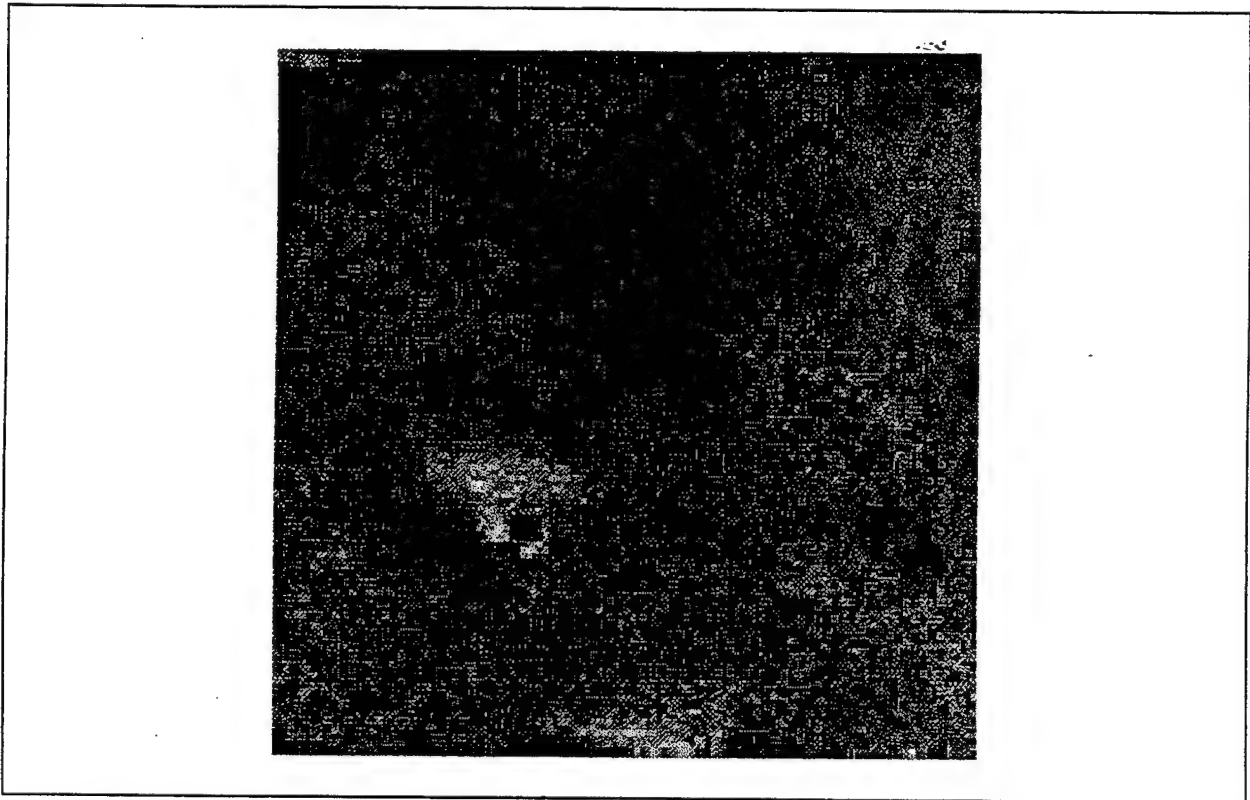


Figure 1. An example of a “texture” image, obtained during the SWOE JT&E for the purpose of defining a texture field for input to the SWOE image generating process. (The original image is an 8-bit gray scale which does not reproduce too well; however, the basic structure of the varying gray level can still be recognized.)

However, textural measures used to compare between real and synthetic imagery indicate that these procedures for introducing texture into a synthetic image may be flawed; at least, in some cases as indicated by the results of the analysis of the SWOE JT&E synthetic imagery (Bleiweiss et al. 1995). Figure 2 illustrates this problem. This figure consists of three panels: a “real” image, a synthetic image, and a “map” which defines regions of homogeneity within the field of view of the “imager”. Even in the synthetic image where an attempt has been made to introduce

texture to the various homogeneous regions, the result is very similar to the map of homogeneous regions -- not at all like the real image. There are other artifacts in these figures which should be ignored for the purposes of the discussion here (e.g., the relative contrast between trees and terrain do not match between the real and synthetic images).

The development of alternative texture generating algorithms and the comparison of the resulting synthetic textures among themselves and with "real" texture is the focus of this paper. The textural metrics and the texture generating algorithms used in this investigation are briefly discussed and then a comparison is made between the output of the algorithms and the real textures.

2. TEXTURE METRICS

The three "measures" discussed in this paper are:

1) correlation length: defined as the "lag" at which the spatial autocorrelation declines to $1/e$ of its maximum value -- lag, in this instance, is a distance measure defined by the sampling interval in space (i.e., a pixel)

2) a derivative of the gray level co-occurrence matrix (GLCM): The GLCM measures "the dependence between pairs of gray levels arising from pixels in a specified spatial relation" (Haralick and Shapiro 1991); for example, in an image, how many times do a given gray level pair occur side-by-side, relative to one another, at separations of 2 pixels, 3 pixels, ..., and so on. A variety of metrics (entropy, contrast, etc.) based on various moments of the GLCM have been developed which provide varying degrees of parameterization of the texture.

3) fractal dimension: for the purposes of the discussion here, the fractal dimension is defined as the parameter D in the following equation:

$$D = n + 1 - H \quad (1)$$

with $n = 2$, the dimension of the process (a line has a value of 1, a two-dimensional process, 2, and a three-dimensional process, 3) and

$$2H = \beta - n. \quad (2)$$

Under the assumption that the image gray level variation can be modelled as a "fractional Brownian 'noise'" ($0 < H < 1$), the value of β is determined from the slope of the power spectral density function of the image. The fractal dimension, then, measures the degree of roughness of the image (Fournier et al. 1982, Saupe 1988).

These metrics are used to compare the various synthetic textures. In addition, these metrics can also be used as "seeds" for algorithms to generate "texture".

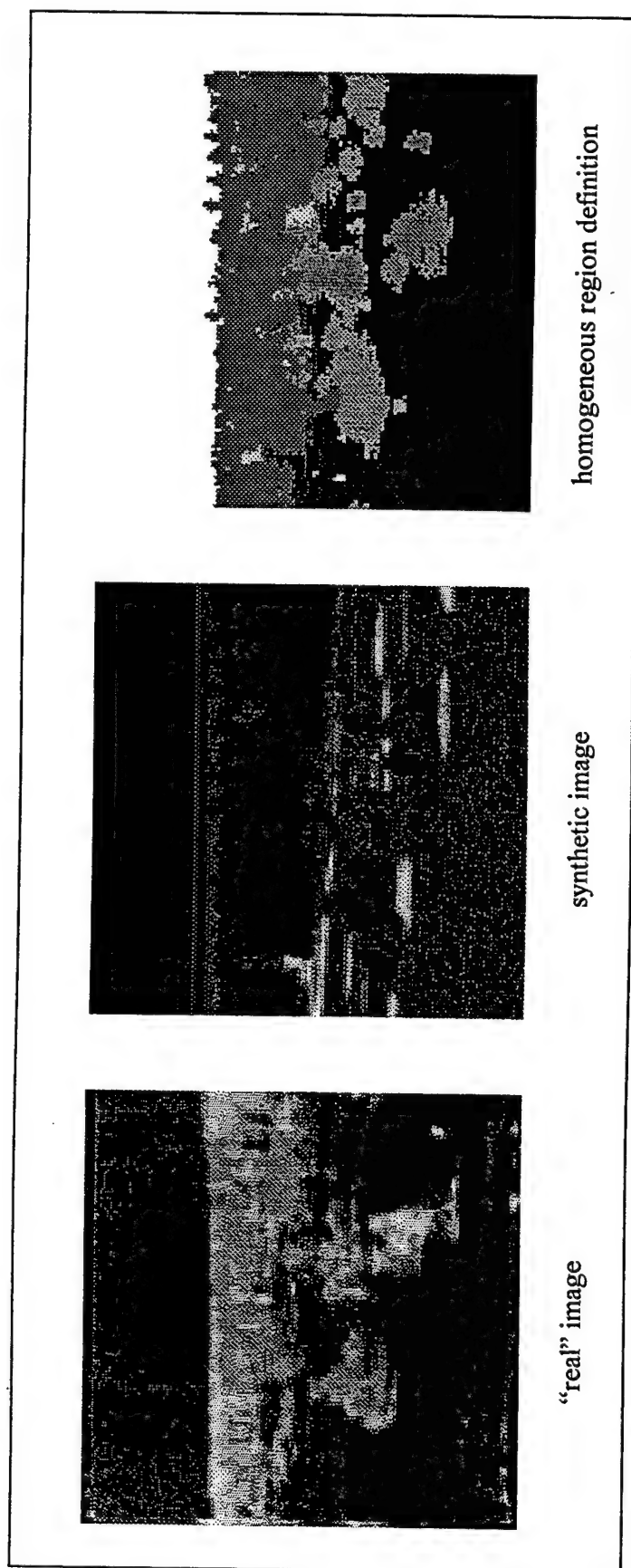


Figure 2. The three panels demonstrate the presence of texture in the real scene as indicated by variation in gray level within homogeneous regions (defined approximately by the panel on the right) and the relative lack of texture in the synthetic scene (except, perhaps, for the trees which, demonstrate texture because they are composed of many discrete elements whereas the rest of the scene has texture "painted" on regions of homogeneity. There are artifacts in the various panels which should be ignored for the purposes of the discussion here (e.g., the relative contrast between the trees and terrain for real and synthetic images, the border around the real image, etc.)

3. TEXTURE ALGORITHMS

It would be expected that a texture map generated from a fractal dimension algorithm would produce a measure which is just that same value of the fractal dimension. Furthermore, if that measure were capable of capturing all aspects of the real texture and, at the same time, the texture generating algorithm based on that measure is a capable algorithm, the other textural metrics (e.g., correlation length, etc.) would also provide the same measure for the real and synthetic textures. If some aspect of this expectation were not met, then further study would be suggested -- it really is not expected that any one of these algorithms will be successful 100% of the time. Hence, we have chosen three measures to use in three different algorithms to generate texture.

The mid-point replacement algorithm is a method of generating a two dimensional fractional Brownian "motion" or "noise". This approximate method is described in the book The Science of Fractal Images, by H. O. Peitgen and D. Saupe. The mid-point replacement algorithm produces an image that only approximates a fractional Brownian "motion". Another algorithm, based on this same concept, (Stoksik et al. 1995), which does a better job, is described in an appendix to a more complete version of this document (Ota et al. 1996).

The gray level co-occurrence matrix (GLCM) method for building textures presented here is based on the algorithm described in the paper by G. Lohmann (1995). In this algorithm, a set of four gray level co-occurrence matrices is used as feature vectors. Lohmann reports that the four primary co-occurrence matrices (horizontal, vertical, left- and right-diagonal) contain sufficient information to synthesize texture that very closely resemble textures from remotely sensed images of the Landsat/TM and ERS-1/AMI satellite-borne sensors. The idea here is to determine how well this algorithm performs on our type of imagery.

For a description of the correlation length algorithm used in this study, reference is made to paragraph 6.4 of Appendix G of the SWOE Final Report (Koenig 1995), where the basic methodology is laid out:

"Numerous approaches to texturing were reviewed and a simplified two-dimensional autoregressive (AR) model was selected. It uses correlation length in vertical and horizontal directions and brightness mean and standard deviation as input parameters for a kernel (process of order [1,1]. The model was developed from an AR model used in the US Air Force Infrared Modeling and Analysis (IRMA) image modeling system."

"An empirical approach was taken because of the lack of general theory or models on thermal IR texture. Using this approach "homogeneous" surfaces (grass, bare soil, trees, tree lines, etc.) of interest were imaged for the times (or under similar conditions) the synthetic scenes were to be generated. Textural features of these surfaces were measured and input to an autoregressive texture generator program which generated isotropic Gaussian texture maps. These maps were used by the rendering software to texture the polygons.

The raw output of the basic program, the isotropic Gaussian texture maps, is "smoothed" to reduce vertical and horizontal striation "artifacts" for long correlation lengths -- both maps (raw and smoothed) are used in the study reported here.

4. COMPARISONS AND DISCUSSION

The target texture which is the one to be duplicated by the various algorithms is shown in Figure 3(a). This map is a 32x32 image (segmented from the image/texture map of Figure 1) which has "texture" properties given in Table 1. For the correlation length technique, we present a typical raw image (unsmoothed) in Figure 3(b), in Figure 3(c) the midpoint displacement result, and in Figure 3(d), the gray level co-occurrence matrix technique output. Table 1 is a summary of the results of this study -- the application of the various metrics to the various texture maps. The table headings are acronyms for the metrics discussed in Section 2. With the exception of the mean and variance, these metrics measure the second order statistics of the images and all have been used in many studies of the textural properties of images. More details on the form and application of these metrics can be found in Bleiweiss et al. (1995). *MEAN* is the average grey level of the texture map (ranges from 0 to 128), *VAR* is the variance of the grey levels in the texture map, *FRAC D* is the fractal dimension, *ACL* is the autocorrelation length, *CONTR*, *CORR*, *ENTRPY*, and *HOMOG*, are GLCM metrics called "contrast", "correlation", "entropy", and "homogeneity", respectively -- the GLCM metrics are somewhat self-explanatory in meaning; in any case, the length of this paper will not allow detailed descriptions. Each algorithm was run 101 times, each with a different pick from the random number generator used in each algorithm -- a random number generator is used in each; however, the specific use is somewhat different from algorithm to algorithm (Ota et al. 1996).

TABLE 1. Texture Measure Values for Generated Textures. The column headings are defined in the text. The sources labeled IRMA and IRMA(SMOOTHED) are autocorrelation length algorithm output. The average and sample standard deviation are based on 101 samples for each texture type; i.e., each algorithm was run 101 times -- the variation is due to the variation introduced by the use of random number generators.

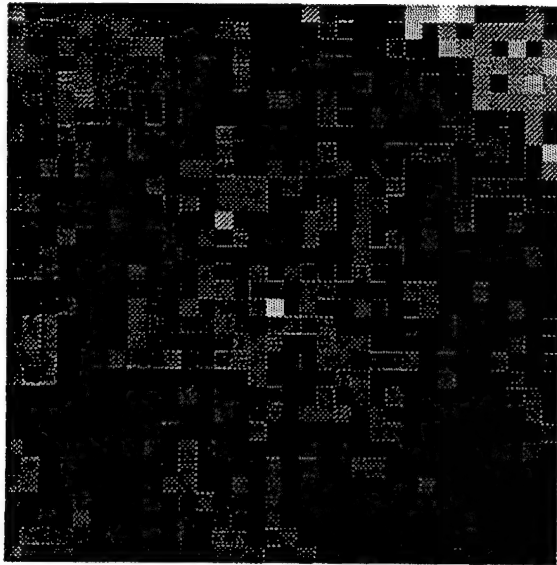
SOURCE		MEAN	VAR	FRAC D	ACL	CONTR	CORR	ENTRPY	HOMOG
TARGET TEXTURE		57.247	338.116	1.965	3.537	222.219	0.0667	4.544	0.014
MID-PT	average	56.756	336.775	1.920	11.116	14.393	0.978	6.419	0.002
REPLACE	std dev.	0.034	4.268	0.139	8.274	8.111	0.012	0.197	0.00052
GLCM	average	57.247	338.116	2.163	1.452	394.532	0.399	4.802	0.013
	std.dev.	0.000	0.000	0.134	0.402	20.833	0.032	0.015	0.00020
IRMA	average	56.027	327.618	2.159	3.055	160.203	0.748	7.126	0.001
	std.dev.	5.013	67.931	0.156	0.811	13.776	0.045	0.051	0.00010
IRMA	average	56.022	213.424	1.958	3.813	53.767	0.864	6.760	0.001
(SMOOTHED)	std.dev.	5.059	63.775	0.189	1.211	5.503	0.031	0.101	0.00017

Reference to Table 1, tells the story about the relative ability of the various algorithms to replicate the target texture as measured by the various metrics used in this study:

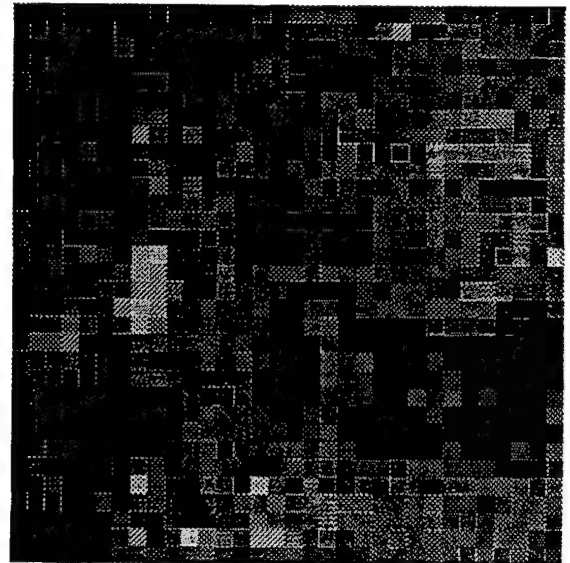
- mid-point replacement algorithm – The texture map created by this technique is similar to the target texture as measured by the fractal dimension (though not exact) but is “different” as measured by the other metrics.
- autocorrelation length (IRMA) algorithm – This texture map (unsmoothed) is close as measured by the autocorrelation length but is quite different as measured by the other metrics (with the possible exception of the fractal dimension which is similar to that of the target). The smoothed output presents an autocorrelation length much closer to the target. And, the fractal dimension is nearly the same as for the target; in fact, much closer than that of the mid-point replacement algorithm. The GLCM metrics all become worse under the action of the smoothing function.
- GLCM algorithm – The texture map created by this algorithm is about the same as the autocorrelation length algorithm as measured by the fractal dimension and, except for the entropy measure, which shows good agreement with the target entropy, all of the other GLCM metrics show that this map is different from the target map.

It would appear, then, that the autocorrelation-based technique (at least the smoothed version) is best able to create an image whose autocorrelation is nearly the same for target and synthetic while the other techniques seem to not be able to replicate “themselves” very well. A possible exception is the IRMA and GLCM ability to yield a “fractal dimension” close to that of the target. It remains to do a sensitivity study to determine the discrimination ability of these various metrics as their values change by small amounts (i.e., Is there much difference between a texture whose fractal dimension is 1.75 and one whose value is 1.85?, and so on.). Visual inspection may favor the GLCM algorithm though this may be due to the level of pixellation in the two maps and not truly comparable “texture”.

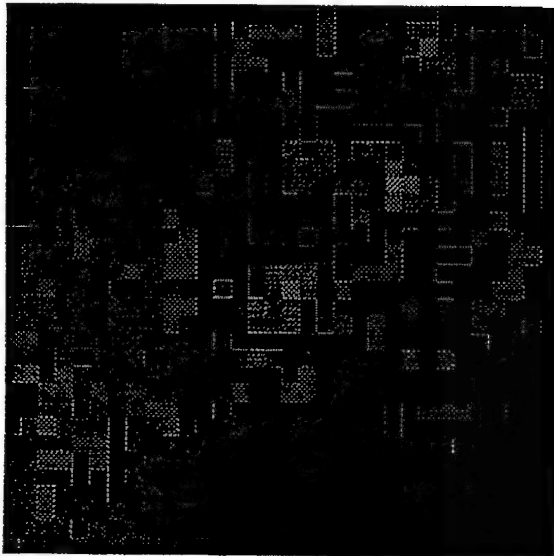
Why then, do the synthetic SWOE images have textural metrics, especially the autocorrelation length, so different (Bleiweiss et al. 1995) from the “real” images? More than likely, the answer lies in the way that texture was measured for input to the SWOE model, the way in which the texture was applied to the synthetic images, and the way in which the texture was measured in the real and synthetic images. For example, the scene which was imaged for textural characteristics was seen at a different perspective view and with a different spatial resolution than that of the “real” images and, the application of the synthetic texture is made to the scene elements as seen from the imager’s perspective (but with a texture as seen from a different perspective) and not to the scene elements before they are rendered into an image.



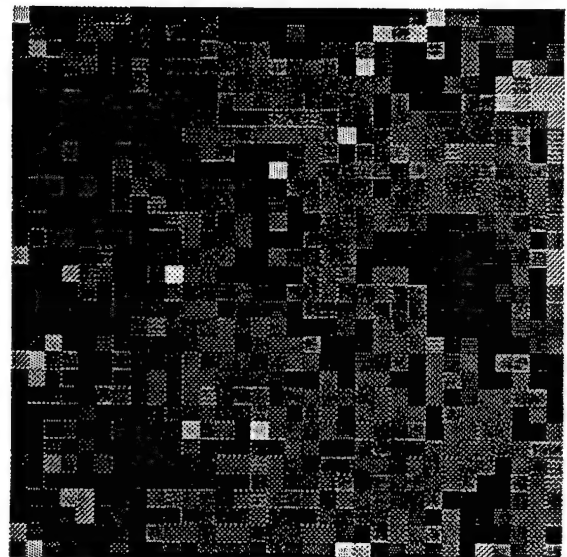
(a) Target



(b) Correlation Length



(c) Mid-Point Replacement



(d) GLCM

Figure 3. The “four” textures displayed in a common frame so as to better effect a visual comparison among them. It is not expected that there should be a one-to-one pixel comparability but that, instead, the “texture” should be the same.

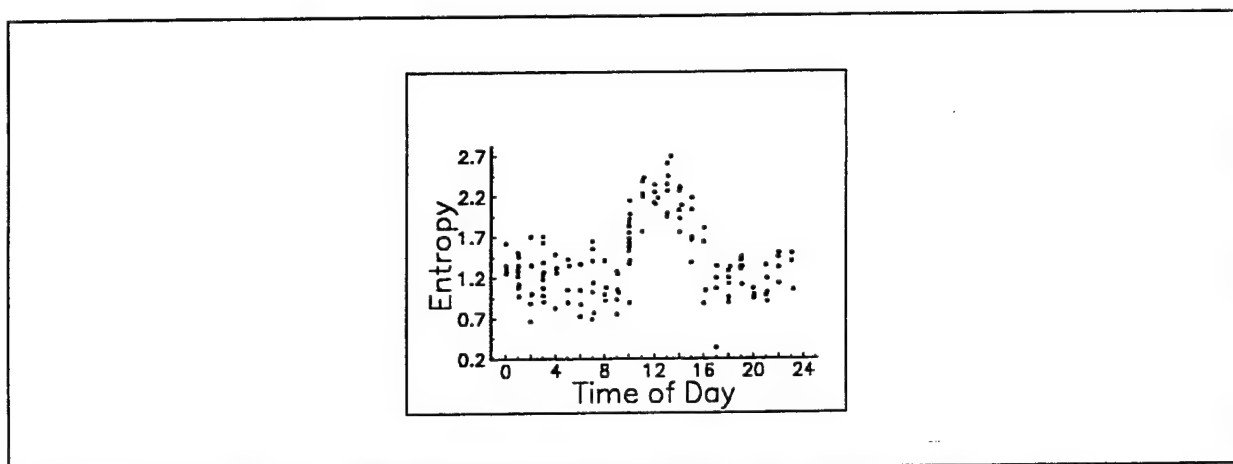


Figure 4. Plot of the "entropy", a GLCM metric, versus time of day to demonstrate the diurnal trend experienced by a metric such as this which could, possibly, be used in a parameterization of a "seed" to produce synthetic texture.

In fact, because the properties which create texture do not yield imagery that is invariant to the viewpoint, it is not at all clear that using such a simple approach would work at all -- the only exception regards a simple approach would be for the texture to be extracted from the real images and then pasted into the synthetic images and this then really becomes a hybrid technique, not a true synthetic technique. For an invariant approach, the texture should be applied as a variation of small scale relief and optical properties (assuming that the thermal properties are homogeneous at this scale) to the large scale relief. Then, when the scene is rendered into an image, the texture is properly mapped.

Future work may also look towards methods to parameterize texture based on some sort of environmental parameter. For example, one approach, but still one with many limitations, would be to parameterize the measure of texture for a particular imager view and then apply the correct texture based on the parameterization. An example of how this would work is suggested by Figure 4, a plot of a particular texture metric with time of day for the Yuma I field exercise of the SWOE JT&E. During that effort, the meteorological influences were quite even (day to day) so that diurnal trends in some of the textural metrics could be seen -- during the Grayling field exercises, the meteorological influences were so variable that this simple correlation was lost to ready viewing; though it may possibly be extracted through some sort of multivariate analysis.

5. SUMMARY

We have demonstrated the generation of texture using three different algorithms in an attempt to compare their various abilities to replicate a given texture. The results of that demonstration are mixed and, though the autocorrelation technique was certainly no worse than the rest of the algorithms, it may best suited for the task at hand (at least as far as this study has gone). We feel that the synthetic imagery (as judged by the metrics) generated in the SWOE process did not compare more favorably with real images regards the textural properties because of the way in which the texture was measured and then applied to the imagery -- no account was taken of the dependence of texture on view angle. Another possible reason is that the texture, as seen by the

real imagers (for the case studied in the SWOE effort) is not isotropic nor is it necessarily homogeneous over those scene elements thought to be homogeneous. Definitive answers remain until a more in depth study can be performed -- the first step has been taken (i.e., generation of the software and methodology to perform the study).

ACKNOWLEDGMENT

This effort was funded, in part, through the offices of the SWOE JT&E, Dr. J.P. Welsh, Director.

REFERENCES

- Bleiweiss, M.P., et al, 1995: *Appendix E of the SWOE JT&E Final Report -- Analysis of SWOE JT&E Infrared Imagery and Environmental Data* (see the reference below by Welsh, et al for more details).
- Fournier, A., D. Fussell, and L. Carpenter: "Computer Rendering of Stochastic Models", *Communication of the ACM*, Vol. 25, No. 6, 371-384.
- Haralick, R.M. and L.G. Shapiro, 1991: "Glossary of Computer Vision Terms", *Pattern Recognition*, Vol. 24, No. 1, 69-93.
- Koenig, G.K., 1995: *Appendix G of the SWOE JT&E Final Report -- The SWOE Modelling Process* (see the reference below by Welsh, et al for more details).
- Lohmann, G., 1995: "Analysis and synthesis of textures: a co-occurrence-based approach", *Comput. & Graphics*, Vol. 19, No. 1, pp. 29-36.
- Ota, C.Z., J.M. Rollins, and M.P. Bleiweiss, 1996: "Texture Generation for Use in Synthetic Scenes", ARL Technical Report, in preparation, U.S. Army Research Laboratory, Battlefield Environment Directorate, White Sands Missile Range, New Mexico.
- Saupe, D., 1988: "Algorithms for random fractals", in, *The Science of Fractal Images*, Pietgen, H.O. and D. Saupe, eds., Springer-Verlag, Berlin/New York.
- Sabol, B.M. and L.K. Balick, 1991: "Generating Textures for Synthetic Thermal Scenes", SWOE Report 91-3, U.S. Army Cold Regions Research and Engineering Laboratory, Hanover, NH 03755-1290.
- Stoksik, M.A., R.G. Lane, and D.T. Nguyen, 1995: "Practical Synthesis of Accurate Fractal Images", *Graphical Models and Image Processing*, Vol. 57, No. 3, pp. 206-219.
- Welsh, J.P., et al, :1995: "*SWOE JT&E Final Report*", U.S. Army Cold Regions Research and Engineering Laboratory, Hanover, NH 03755-1290.

ATMOSPHERIC EFFECTS INTERPOLATION ALGORITHM

Glenn J. Higgins, Melanie J. Gouveia, Paul D. Hestand, and Michael S. Seablom

TASC

Reston, VA 22090 USA

ABSTRACT

An interpolation algorithm has been developed to efficiently estimate atmospheric path transmission and radiance to support infrared scene visualization activities at PL/GPAA. The method uses MODTRAN to compute atmospheric path transmission and radiance for user-selected scenario parameters and for a limited number of geometries, dependent on the scenario parameters. Scaling laws and interpolation provide estimates of these quantities for other desired geometries corresponding to the locations of scene elements, yielding a significant time savings relative to executing MODTRAN for every desired geometry. Estimates of interpolation error for the atmospheric quantities as well as for apparent temperature are provided.

1. INTRODUCTION

The Phillips Laboratory, Geophysics Directorate is developing advanced decision aids to support the use of electro-optical weapons systems. This work is being conducted as part of the Air Combat Targeting/Electro-optical Simulation (ACT/EOS) program. Over the past few years, emphasis has been placed on developing the required physical models and tools needed to visualize three-dimensional thermal scenes in the 8 – 12 μm thermal band. An important component of the physical modeling is the treatment of atmospheric effects. The radiation emitted by a scene element is attenuated by the atmospheric volume along the path between the scene element and the sensor. At the same time, path emission along the same atmospheric path contributes to the radiance reaching the sensor. Both effects must be considered for realistic scene visualizations.

The MODTRAN atmospheric effects model is frequently used to estimate line-of-sight transmission and path radiance for specified scenario and atmospheric conditions. The amount of time required to execute MODTRAN in support of scene visualization can be very large, however, if MODTRAN is

used to compute path transmission and radiance for every scene element or every displayed pixel. For instance, if MODTRAN were executed for every pixel of a 1024x800 display, a total of 819,200 computations would be required.

Fortunately, a very large number of executions is not required in most cases. However, a sufficient number of runs is needed to properly "characterize" the scene. Figures 1a and 1b illustrate a visualized scene that includes terrain features, a POL storage tank, and the sky. From the perspective of executing MODTRAN, a wide range of viewing geometries and scenarios are present in this single scene. Some scene elements are located close to the sensor, while others are located a great distance away. Some paths intersect the ground, other paths do not. The atmospheric effects model must be capable of providing accurate estimates of path transmission and radiance for all of these paths.

2. APPROACH

The approach selected for ACT/EOS is to use MODTRAN to compute path transmission and radiance for a limited number of geometries, effectively sampling the scene spatially. Estimates for all other required geometries are obtained through interpolation. The premise is that the bulk of the execution time is consumed by executing MODTRAN. This is, in fact, the case.

There are two classes of interpolation. For sky (infinite) paths, MODTRAN is executed for a series of zenith look angles and estimates of path transmission and radiance for intermediate zenith angles are obtained by interpolation. For ground paths (paths intersecting scene elements on the ground), MODTRAN is executed for a series of paths starting at the sensor and terminating at gridpoint locations specified as a function of ground range from the sensor and altitude above mean sea level. Bi-linear interpolation is used to provide values at intermediate points as discussed in more detail below. It is assumed that atmospheric effects are independent of azimuth angle. Regardless of interpolation method, the interpolation step size for zenith angle and path endpoint ground range and altitude may be set by the user, depending on his or her accuracy requirements. The remainder of this paper focuses on the interpolation technique used for ground paths.

For ground path cases, interpolation is performed with scaled parameters rather than the MODTRAN-computed values of atmospheric path transmission and radiance (see Figure 2). The scale parameter used for atmospheric path transmission is defined as follows:

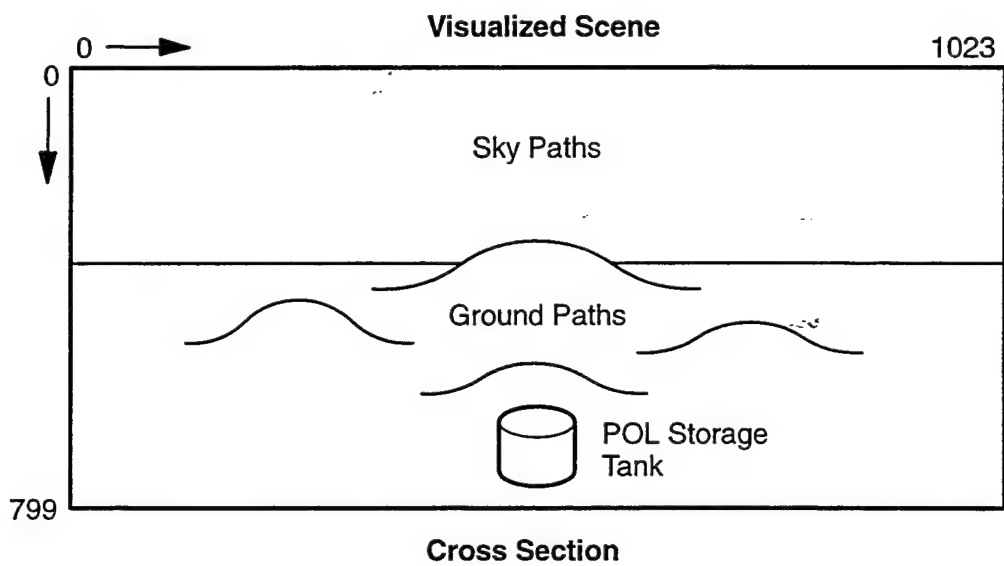


Figure 1a. Notional sketch of a visualized scene on a 1024 x 800 display.

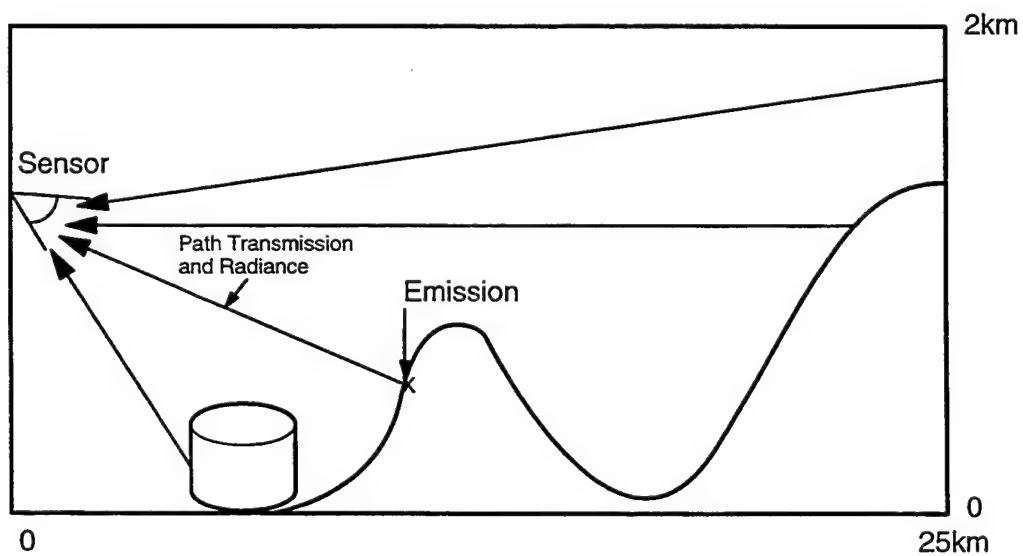


Figure 1b. Cross section depicting various sky and ground paths.

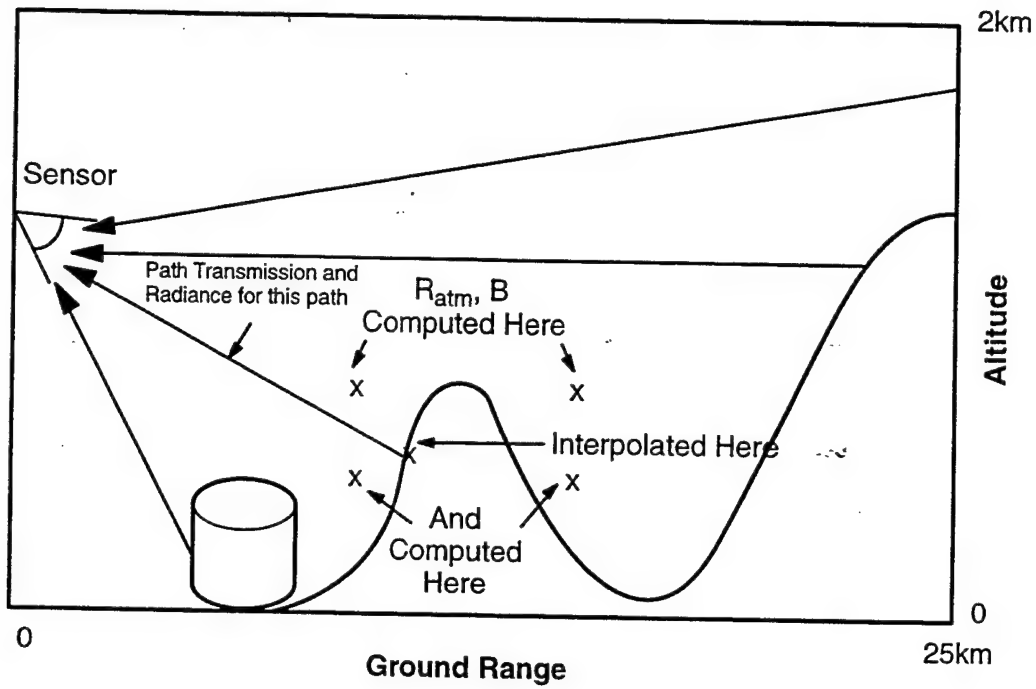


Figure 2. For ground paths, interpolation is performed using the scale parameters. The inverse relationships are used to recover path transmission and radiance.

$$B = \ln(\tau_{ave})/r \quad (1)$$

where

- B = scale parameter for path transmission
- τ_{ave} = atmospheric path transmission, averaged over sensor bandpass
- r = slant range

The scale parameter for path radiance is defined as follows:

$$R_{atm} = R_p/\epsilon_{atm} \quad (2)$$

where

- R_{atm} = scale parameter for path radiance
- R_p = path radiance, integrated over sensor bandpass
- $\epsilon_{atm} = (1 - \tau_{ave})$ (by definition)

The atmospheric transmission scale parameter, B , is essentially an average extinction coefficient for the path. The path radiance scale parameter, R_{atm} , is an estimate of the atmospheric blackbody radiance for the path, and is associated with thermal emission by the atmospheric volume along the path.

3. EXAMPLE RESULTS

Figures 3 and 4 provide examples of path transmission and radiance results for the MODTRAN mid-latitude winter and summer atmospheric profiles, respectively. In this wavelength region, water vapor and aerosol extinction dominate. As anticipated, path transmission decreases exponentially as the path length increases. The decrease is more pronounced in the summer case because absolute humidity is greater in the mid-latitude summer moisture profile. The slant path terminating lower in the atmosphere is attenuated more because absolute humidity and aerosol concentration are greater at lower altitudes. Path radiance increases as the path length increases because the emitting volume increases. Path radiance is larger for the mid-latitude summer case because air temperature and absolute humidity are greater in the mid-latitude summer profiles. Path radiance values are larger for the path terminating lower in the atmosphere because atmospheric temperature and emissivity are greater at lower altitudes.

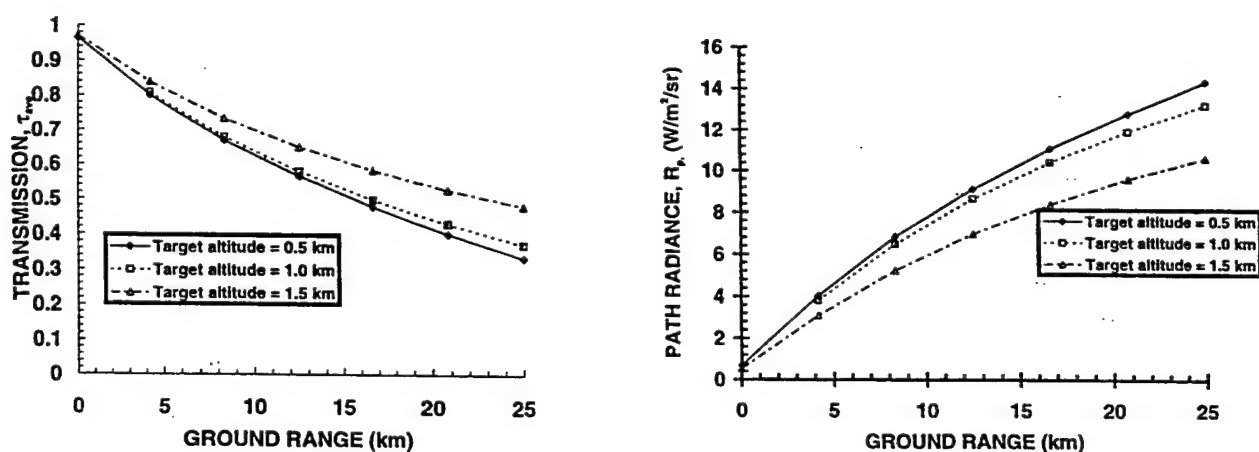


Figure 3. Path transmission and radiance for the mid-latitude winter case. The sensor altitude is 1 km.

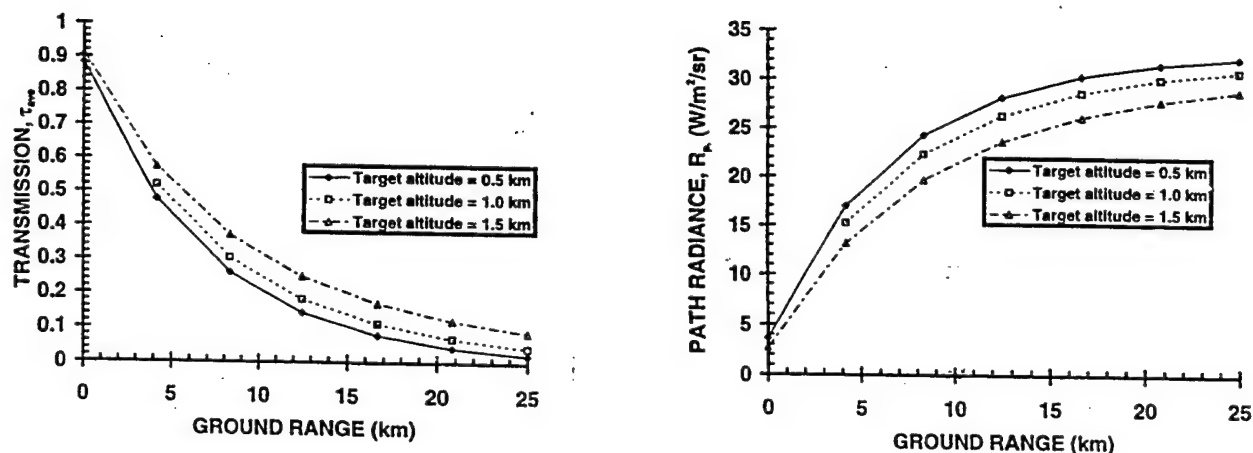


Figure 4. Path transmission and radiance for the mid-latitude summer case. The sensor altitude is 1 km.

Figures 5 and 6 depict the scale parameters for the two cases depicted in Figures 3 and 4. The scale parameters exhibit little change as functions of ground range and vary smoothly with altitude. The mid-latitude winter case for B, however, shows more non-linear variation with altitude than the other cases. Overall, these characteristics of the scale parameters suggest that bi-linear interpolation is reasonable.

Interpolated results were compared with direct MODTRAN computations for the midpoints between gridpoint locations. These comparisons were made for both path transmission and radiance. In addition, apparent blackbody radiance at the sensor was computed for paths between the sensor and each midpoint by assuming a 298K blackbody emission source at the midpoints. The following equation [(eq. (3))] was used to compute apparent radiance:

$$R_{ap} = \tau_{ave} \int \epsilon R_o d\lambda + R_p \quad (3)$$

where

- R_{ap} = apparent radiance at sensor
- ϵ = emissivity of the surface (1.0 assumed)
- R_o = surface blackbody radiance
- λ = wavelength

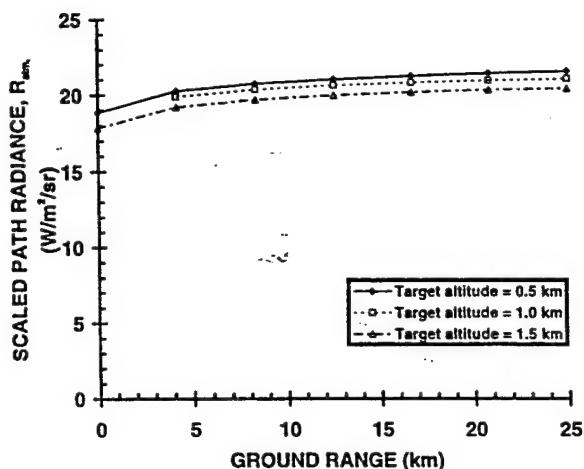
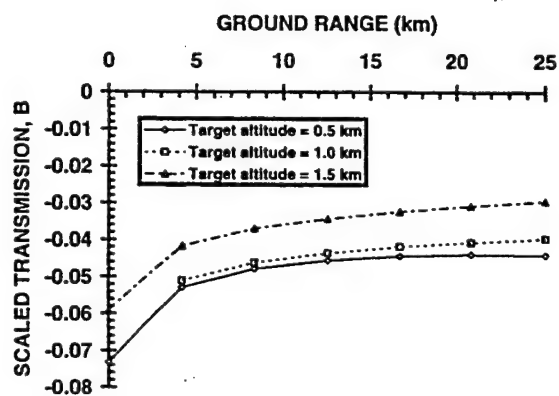


Figure 5. Scale parameters for the mid-latitude winter case.

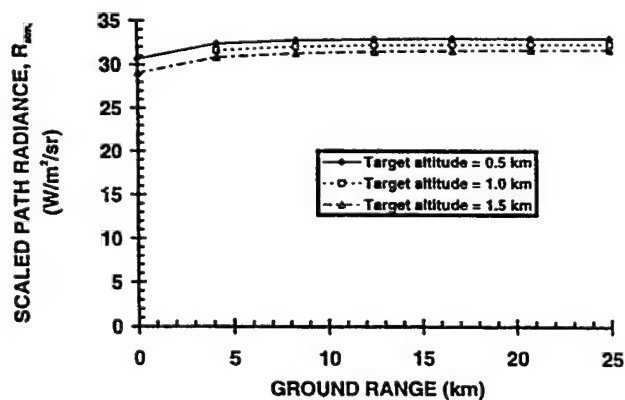
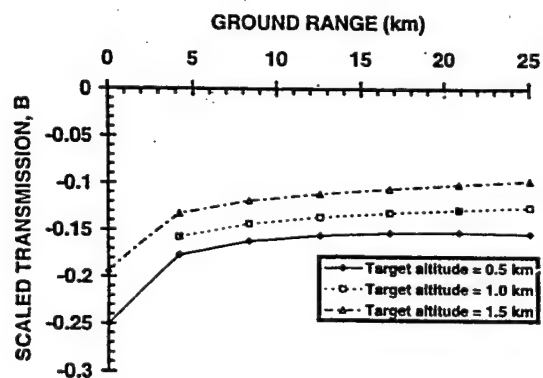


Figure 6. Scale parameters for the mid-latitude summer case.

Apparent blackbody radiance was converted to apparent blackbody temperature through application of Planck's equation.

Table 1 provides error statistics for the mid-latitude winter and summer cases, as well as run time estimates for a 66 Mhz Pentium class microcomputer. Two grid resolutions are shown. For the sake of comparison, the test locations for all cases were the midpoint locations of the higher resolution grid. Obviously, errors can be reduced by decreasing the sampling interval, but at the expense of execution time. The MODTRAN run times can be considered maximums, because the spectral resolution of the MODTRAN runs was the finest resolution possible (20 cm^{-1}).

We are in the process of comparing results for a wider variety of MODTRAN model atmospheres and aerosol models and for various grid resolutions. We are also considering the effects of cloud layers. A technical report is being prepared to describe all results.

Table 1 Error statistics and run time data for mid-latitude winter and summer cases. The sensor altitude is 1 km. The timing data allow comparison between the time required to interpolate MODTRAN results to a location vs. executing MODTRAN at the location.

RMSE and Run time data

Sampling domain: range 0 – 25 km; altitude 0 – 2 km

*MODTRAN runtime per point: 9 seconds

*Interpolation runtime per point: 0.005 seconds

Time savings per point: 8.995 seconds

Sampling interval: 4.0 km range; 0.17 km altitude; 91 gridpoints, 72 test locations

	RMSE EBBT	Percentage of points w/ $ \Delta T < 1 \text{ K}$	Mean relative error in τ_{ave}	Percentage of points w/relative error < 5%
Midlatitude Winter	1.2 K	82%	1.3%	93%
Midlatitude Summer	0.91 K	79%	3.9%	85%

Sampling Interval: 8.0 km range; 0.17 km altitude; 52 gridpoints, 72 test locations

	RMSE EBBT	Percentage of points w/ $ \Delta T < 1 \text{ K}$	Mean relative error in τ_{ave}	Percentage of points w/relative error < 5%
Midlatitude Winter	1.5 K	60%	1.9%	92%
Midlatitude Summer	1.5 K	63%	6.0%	67%

*Executed on 66 MHz Pentium

4. CONCLUDING REMARKS

The methods applied here can provide estimates of atmospheric path transmission and radiance to any desired accuracy. A flexible driver program is being developed in ANSI C to automatically execute MODTRAN over the interpolation grid. The user can select the desired atmospheric scenario, sensor position, and sampling domain and resolution. A separate program applies the scaling laws and performs interpolation for paths between the sensor and any desired location within the sampling domain.

A draft technical report is being prepared to accompany the software.

DYBETA - A PRACTICAL TOOL FOR BATTLEFIELD ENVIRONMENT ANALYSIS

S. Grossman, A. Katz, G. Sagi, D. Elial
Hancal System Engineering
Taas-Israel Industries Ltd
POB 1044/45, Ramat Hasharon 47100, Israel

ABSTRACT

Analysis of electro-optical systems performance and its degradation in battlefield environment needs integration of various data and models. The models involve operational scenarios, systems properties and their interaction with atmosphere and/or man-made obscurants. An integrated model (DYBETA) was built, and based on it, a friendly and flexible software tool that assists the analyst not familiar with the above detailed knowledge. The tool translates a given scenario (observation locations, systems and operational activities) to technical data in the DYBETA required format. Then, it computes and displays the spatial and temporal systems behavior. Performance is analyzed for given sector areas along a few hours' periods. The package is designed to minimize CPU time and is flexible enough to identify whether new input parameters require a whole new computation or not. Output consists of graphic mapping and alphanumeric results of statistical processing.

1. INTRODUCTION

For predicting effectiveness of systems and target acquisition ability in combat, one has frequently to consider battlefield environment influence during the battle period. Environment natural parameters include meteorological, solar and topographical data and induced ones include smoke, dust, artificial illumination. Techno operational parameters include systems features, observers and targets' nature, locations and tactics. There are several programs that deal with each of the above separately. In 1991, we presented the basic logic of and modeling of a comprehensive program that enables to deal with the dynamic ability to acquire targets during a battlefield scenario. The program was named DYBETA: Dynamic Battlefield

Environment Target Acquisition (Grossman et al., 1991). This paper presents the software package that runs the model, named also DYBETA. In the construction of the package, main efforts were concentrated in:

- Compatibility with large scale scenarios as well as "micro" situations
- Output related to large areas or specific points
- Fast sensitivity analyses with reduced CPU cost
- Compatibility with SUN computers
- Linkage with other programs

2. PROGRAMS AND SUBROUTINES

2.1 Main Programs: EOEXEC and COMBIC

In the present version a single DYBETA run can deal with several observation tasks in a single natural atmospheric situation and a given smoke/dust scenario. The methodology of integrating systems characteristics, obscuration and observation measures was described in BAC 91 (Grossman et al. 1991). The main programs are COMBIC and EOEXEC, EOEXEC being the main driver. The original version of EOEXEC was cut down to deal with DYBETA required subroutines only, but was extended to read all necessary inputs. Some necessary extensions and changes were made in COMBIC, most in or connected to COMBIC phase II:

- Scenario increased permissible number of source types (x2.5), source number (x10) and lines of sight (x40).
- Computation by dynamic allocation that yields optimal usage of memory resources.
- TLOC that referred to target location refers to target sector, defining angles, radii and their resolution. The program computes the necessary lines of sight to describe the whole sector.
- Integrating a numeric map to compute geometries of line of sight and obscurants. Concealed areas to the observation post are displayed. To avoid a conflict between variable terrain height and ground level as defined by COMBIC (blocking of the obscurants and reflection) DYBETA defines "sea level" ground reference.
- Threshold concentration was decreased and the distance to compute cloud geometry of a single cloud in the model was increased, as we deal with contribution of many sources.

2.2 Additional Models Applied

- "ILLUMA" to compute sun angles.
- "ACQUIS" is applied in DYBETA by aid of "lookup" tables to compute contrast thresholds needed by various acquisition devices and levels. Input data concerning the observation devices and target's characteristics is written in EOSAEL format in specific cards.
- "CONTRAST" is applied here by aid of "lookup" tables to yield upper limits of obscurant depth values to each acquisition event, derived from contrast attenuation through natural and obscured atmosphere, including effects of scattered solar radiation.

- "GRID" to read numeric map data and compute line of sight geometries.

2.3 User Interface

DYBETA can be run either directly with a given input file built externally or via a powerful user interface constructed on the SUN computer. The interface reads the operational scenario and user parameters, transforms it to a DYBETA input file and executes.

A DYBETA run, refers to a single given natural atmosphere. The input for a full run, comes in four main groups:

- Smoke/dust scenario (operational scenario)
- meteorological data
- Observation data (post, observed area, time of day, device)
- control parameters of computation and display

The interface operates menus of various operation modes and parameters and displays warning and error messages. After execution, it displays graphically the output results in a mode chosen through various output menus.

2.4 Operational Scenario Interface

An important subroutine of the interface is the operational scenario interface, built to serve the COMBIC unskilled user, not familiar with the detailed technical input required by COMBIC. The need for an interface of this kind arose also by the large size of data in a large scale scenario. The operational scenario interface translates the operational characteristics to technical data, applying "built-in" assumptions in regard to operating modes and technical data of the obscurant sources. The interface deals with six kinds of smoke/dust sources within up to three hours period:

- Artillery (nine types of munitions). The present interface assumes a single kind of smoke type for each munition and a single type of dust in the scenario area. Artillery barrage sources are batteries or battalions. Firing rates and targets locations are defined by the user, including guns attrition. Barrage dimension was assumed to depend on firing unit.
- Smoke pots
- Exhaust smokes
- Smoke candles
- Grenades

All the above can be activated in either of two modes: single and multi source operation. In a multi source operation, the interface approximates the overall effect to a single integrated cloud, according to predefined deployment rules. The center position is defined by the user. A mean velocity is derived from the positions defined every half hour.

3. DYBETA OPERATION MODES

The principal task of DYBETA, to manage a large scenario, inflicts on three parameters:

- scenario time length
- scenario area
- large number of smoke sources and events

COMBIC calculations of transmission are dominant in CPU consideration. DYBETA was therefore constructed modularly so that it can be run with previously calculated output data of smoke/dust, assuming the smoke/dust scenario is unchanged. In general, DYBETA can be run in three modes:

- Natural atmosphere only
- A run with unchanged smoke/dust parameters. This mode is useful mainly for displays of previous runs unchanged or for computation and display of updated output as a result of altering devices, targets or natural visibility.
- A comprehensive run which includes computation of smoke/dust data. Required when changing: scenario, observer post and meteorological parameters as wind velocity or humidity.

4. INTERFACE MENUS AND DATA BASE

4.1 Main & Secondary Menus

The main menu controls the graphical output, turns to secondary menus of input data and initiates a new run if needed. The menu refers to:

Input parameters or menus :

- Scenario
- Observation devices and targets (size and signatures)
- Basic input data
 - * Natural atmosphere meteorology
 - * Sub scenario period (in which sun position is fixed)
 - * Location, date, clock time , observation period and sector
 - * Computation resolution
- Additional basic input data for obscuration evaluation:
 - * Observation start relative to scenario
 - * Meteorology relevant to obscurants
 - * Smoke munition types to be active
 - * Observation sector

- * Temporal and spatial resolution
 - * Threshold of obscuration (time)
 - * Frequency of reports
 - * Output files
- Output control parameters or menus
 - * Dead areas display
 - * Period to be displayed
 - * Observation configurations to display (target & observer)

The **scenario** name in the main menu points to an operational scenario set of files prepared by the user. The files consist of separate files for each smoke munition type, artillery engagement scenario and files that describe deployment of targets along the course of the scenario.

Fig. 1 to Fig. 4. display the main menus. After completion of the menus, the interface creates an input file in the format of EOEXEC input cards. An example is shown in Fig.5 .

Execution

Smoke / Dust: yes ☒ no ☐

New Scenario: yes ☐ no ☒

Sub-Scenario

Display Configuration

Reset

Basic Data

Observation Location

Observation Configuration

Data Directory
 ↻ home3/smoke/results

Scenario Name
 ↻ demo

Figure 1: Primary Menu

Date	<input type="text" value="27"/> day	<input type="text" value="October"/> month	Time Steps	<input type="text" value="3"/>
"H" - hour	<input type="text" value="9"/> hour	<input type="text" value="0"/> minutes	Obscuration Threshold	<input type="text" value="80.00"/> percent
GMT offset	<input type="text" value="2"/> hours	<input type="text" value="0"/> minutes	* Wind Velocity	<input type="text" value="1.00"/> m/sec
* Observation Start	<input type="text" value="-150"/> minutes	<input type="text" value="0"/> hours	* Wind Direction	<input type="text" value="270.00"/> degrees
* Observation Duration	<input type="text" value="60"/> minutes	<input type="text" value="0"/> hours	* Atmospheric Pressure	<input type="text" value="940.00"/> mbar
Sub-Scenario Duration	<input type="text" value="30"/> minutes	<input type="text" value="0"/> hours	* PASQUILL Category	<input type="text" value="4.00"/>
Visibility	<input type="text" value="Clear (23)"/>		* Observed Sector:	
Latitude	<input type="text" value="31.80"/> degrees		* Start Angle	<input type="text" value="100.00"/> degrees
Longitude	<input type="text" value="-35.20"/> degrees		* End Angle	<input type="text" value="160.00"/> degrees
Radial Resolution	<input type="text" value="50.00"/> meters		* Angle Resolution	<input type="text" value="1.00"/> degrees
Angular Resolution	<input type="text" value="1.00"/> degrees		* Start Radius	<input type="text" value="3000"/> meters
* Temperature	<input type="text" value="20.00"/> centigrades		* End Radius	<input type="text" value="16000"/> meters
* Humidity	<input type="text" value="70.00"/> percent		* Radius Resolution	<input type="text" value="500"/> meters
			* Resolution of Obscuration	<input type="text" value="60"/> seconds
* A change in the in one of the marked parameters will cause recalculating the transmission file			<input type="button" value="Output Files"/> <input type="button" value="Smoke Munitions"/> <input type="button" value="Wavelengths"/> <input type="button" value="end"/>	

Figure 2: Basic Data Menu

Smoke Munitions

☒ Generators

☒ Pots

☒ Exhaust

☐ Candles

☒ Grenades

☒ Artillery

☐ End

Figure 3: Smoke Munitions Menu

Targets Dimension (cm)

☐ Other Size

☐ Tank Turret [90]

☐ Jeep [180]

☐ Truck [240]

☐ Tank [270]

☒ Tank Company [470]

☒ 5000.00

El-Op Signatures

☐ Add Contrast

☒ 0.300

Thermal Signatures

☐ Add Contrast

☒ 3.000

Observation Devices

☐ Binocular 20x120

☐ Binocular 8x30

☐ Binocular 15x80

☒ Binocular 25x150

☐ Binocular 7x50

☐ Eye

☐ Electro-Optical # 1

☐ Electro-Optical # 2

...

☐ Electro-Optical # n

☒ Thermal # 1

☐ Thermal # 2

...

☐ Thermal # n

Figure 4: Observation Configuration Menus: Devices & Target signatures

SCENARIO	300.000	4.500	30.000	2.000	31.800	-35.200	
METR	1.000	20.000	70.000	12.100			
ELOP	1.000	4.000					
THERMAL	1.000	34.000					
OUTPUT	3.000	80.000	1.000	1.000			
ACQUIS	1.000	50.000	1.000				
	4.000	4.000	0.000	0.300			
	34.000	4.000	0.000	3.000			
DEVICE	1.000	2.000	4.000	34.000			
COMBIC							
PHAS	1.000						
MET1	70.000	1.000	4.000	20.000	940.000	270.000	
MUNT	*	*	*	*			
DUST	*	*	*	*			
BARG	*	*	*	*			
/	*	*	*	*			
/	*	*	*	*			
/	*	*	*	*			
MUNT	*	*	*	*			
BURN	*	*	*	*			
CLOU	*	*	*	*			
SUBB	*	*	*	*			
GO							
PHAS	2.000						
ORIGIN	*	*	*	*			
TIME	*	*	*	*			
SLOC	*	*	*	*			
/	*	*	*	*			
/	*	*	*	*			
SLOC	*	*	*	*			
OLOC	*	*	*	*			
TLOC	-1.000	3000.000	16000.000	500.000	100.000	160.000	1.000
LIST	0.000	60.000	3600.000	60.000			
DONE							
END							

Figure 5: Example of an input file produced by the user interface after completion of menus

(* stand for various classified parameters)

5. OUTPUT

5.1 Output Files

The output is either graphical or alphanumeric. DYBETA produces output files applied both for graphic display and for statistical processing. The files are:

SEC - acquisition ranges in natural atmosphere for four levels of acquisition

OBSERVER - observation sector

LOS - line of sight grid in the observed sector

THRESH - obscurant transmittance thresholds

TRANS - results of obscurant transmittance data for the observed sector

SMOKE - dominant obscurants in connection to TRANS data

GRA - obscured grid cells (for graphic display)

SUM - detailed obscuration data

OUT - error messages of COMBIC

5.2 Graphic Output Display

In general, a single run can evaluate acquisition for several observer locations and observation configurations (devices and target signatures). The graphic output display refers to a single observer location and observation configuration. For natural atmosphere without obscurants, four acquisition envelopes (50% probability of moving target detection, detection, recognition and identification) are displayed on an area map for a given observation configuration. In the presence of obscurants, areas obscured to the observation are displayed for each level of acquisition separately.

5.3 Statistical Data

The data in the output files can be processed off line to yield statistical results in regard to various parameters. The results can be linked to systems performance measures thresholds as acquisition ranges or transmittance values.

5.4 Output Examples

The graphic output in figures 6, 7 & 8 refers to obscuration of 25X150 binoculars during a half hour period within a three hours complex smoke/dust scenario, containing: artillery smoke munitions and HE dust , smoke generators, pots, grenades and exhausts. Figure 6 displays acquisition envelopes in that half hour, while figures 7 & 8 display obscured target areas in a given sector for the 2nd and 3rd 10-minutes time steps. For a comparison between obscurance in the optical and thermal spectral domains, figure 9 displays acquired and relatively small obscured areas of a thermal device observing the same sector during the 3rd time step.

References

S.Grossman, A.Katz, D. Elial: "Transformation of COMBIC to Dynamic Battlefield Environment Target Acquisition model", Battlefield Atmospherics Conference 1991.

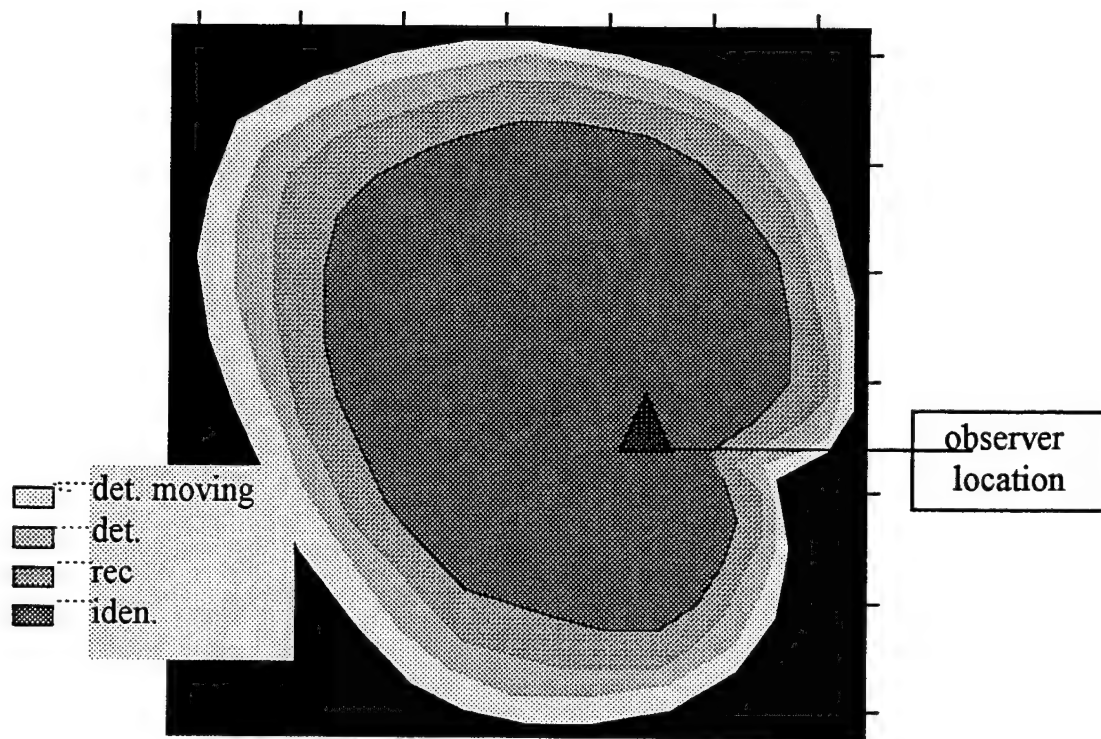


Figure 6: Acquisition envelopes (without obscurants)

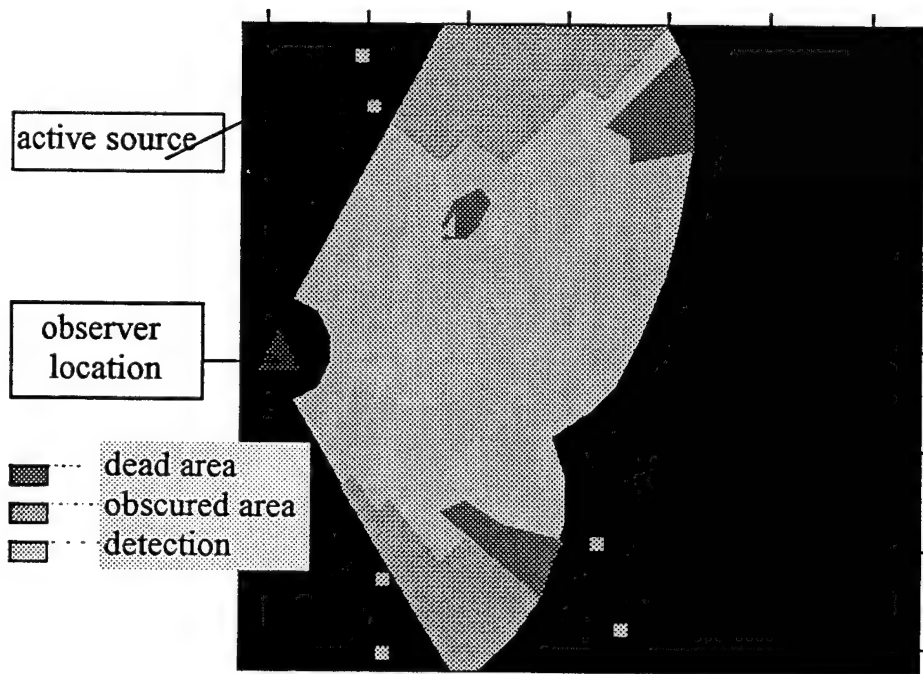


Figure 7: Obscuration of 25X150 binoculars, 2nd time step

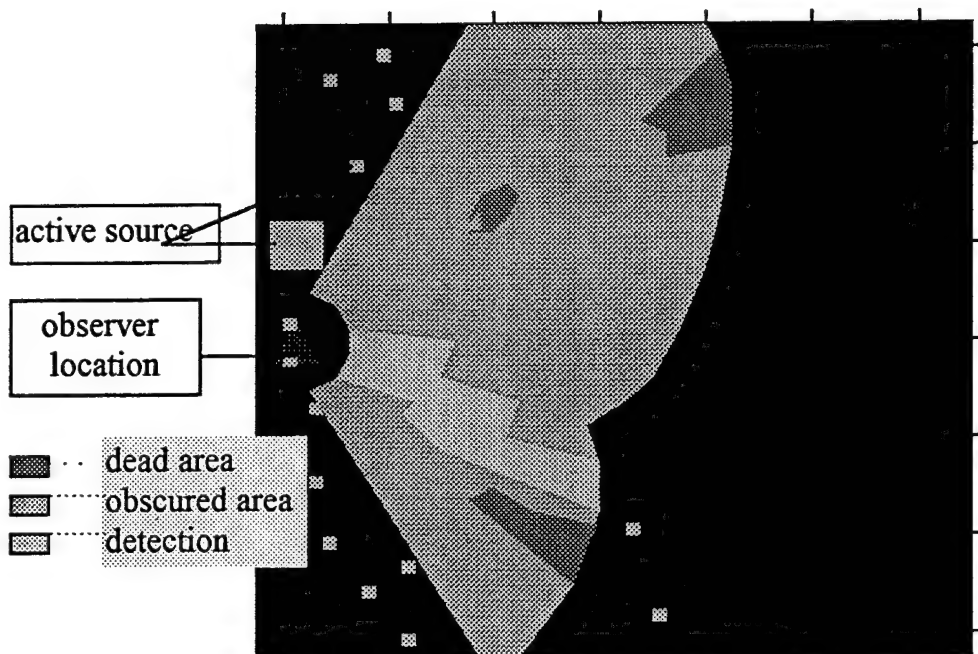


Figure 8: Obscuration of 25X150 binoculars, 3rd time step

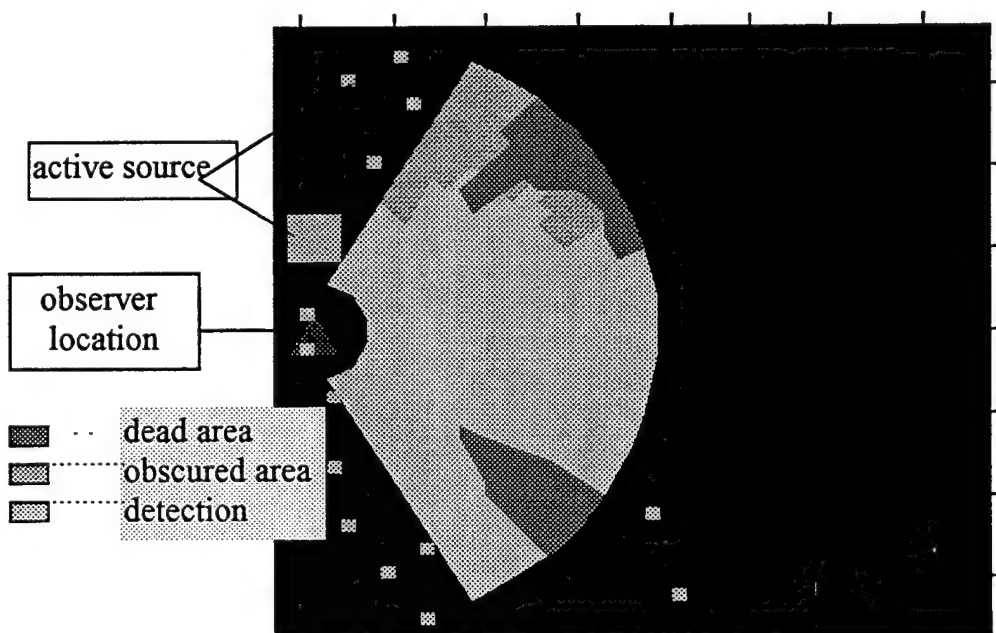


Figure 9: Obscuration of a thermal device, 3rd time step

Temporal Behavior of Natural Terrain Radiance at Infrared Wavelengths

Max P. Bleiweiss and Christopher D. Padilla
U.S. Army Research Laboratory
Battlefield Environment Directorate
White Sands Missile Range, New Mexico, USA

ABSTRACT

Because most infrared observations of natural terrain are made at infrequent or widely spaced time intervals, information on the high time resolution variation in background radiance is lacking. This is in spite of the fact that meteorological and other influences can cause apparent radiance to change by amounts equivalent to a few degrees Kelvin in seconds or tens of seconds. Infrared imagery acquired during the recent Smart Weapons Operability Enhancement Joint Test and Evaluation (SWOE JT&E) allows the investigation of the nature of IR radiance fluctuations with high time resolution under a variety of diurnal and meteorological conditions. Specifically, during the Grayling I deployment, images were acquired at the rate of 6.25 frames per second, for 10 seconds, every 5 minutes during each of the 2-hr mission periods. There were 107 mission periods during the 41 days of the test. A portion of these images have been segmented according to homogeneous features (determined independently of the image content) and histograms of apparent temperature within those features have been processed to allow studies of the temporal variation of radiance. The nature of the fluctuations as a function of meteorological, atmospheric, and diurnal conditions is discussed.

1. INTRODUCTION

Because most infrared observations of natural terrain are made at infrequent or widely spaced time intervals, information on the high time resolution variation in background radiance is lacking. This is in spite of the fact that meteorological and other influences can cause apparent radiance to change by amounts equivalent to a few degrees Kelvin in seconds or tens of seconds. In fact, most summaries of scene statistics consider only the spatial component -- no attempt has been made, to the authors' knowledge, to assemble statistics of the temporal component of scene

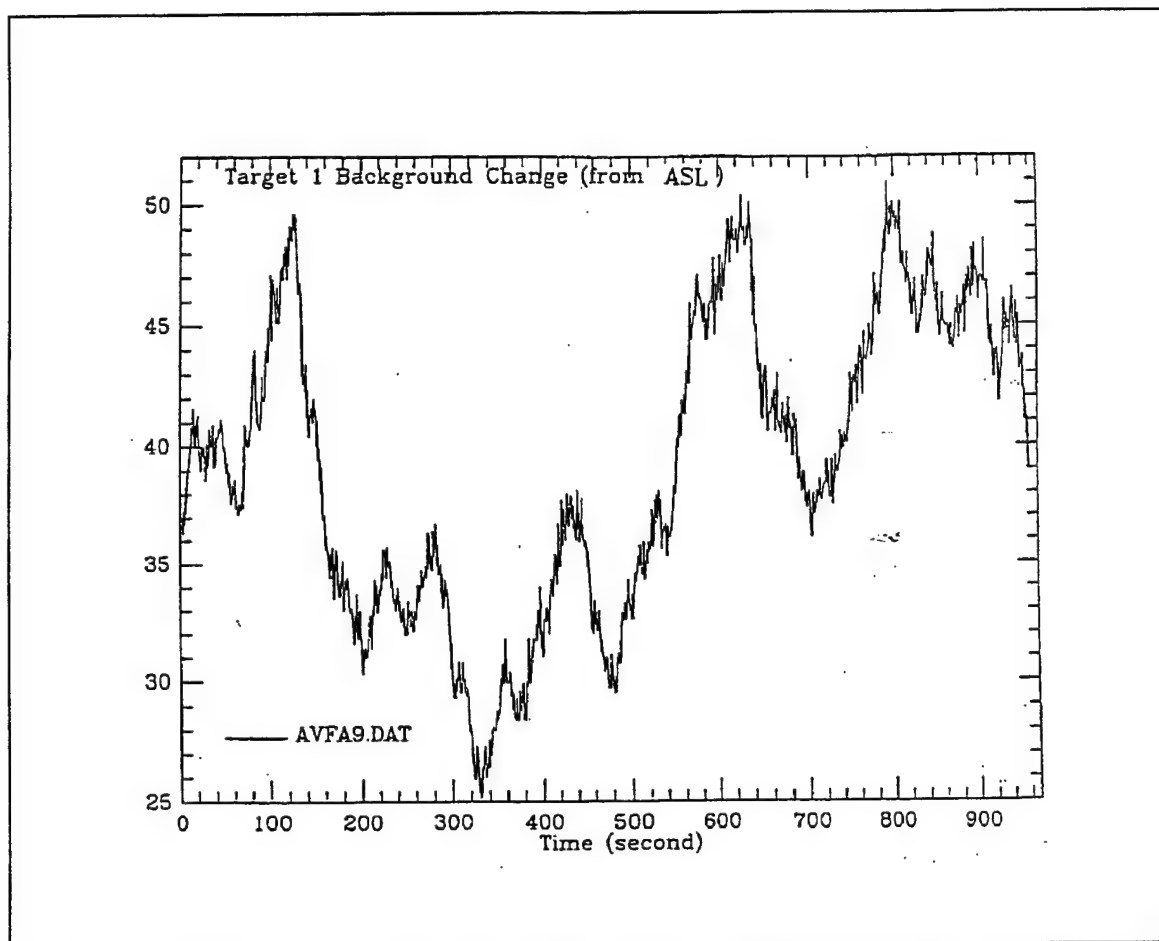


Figure 1. An example of the large and rapid variation of IR background radiance which has supplied a primary motivation for the study reported here. The amplitude scale is in units of an 8-bit gray scale so that the range of 256 units is scaled to approximately a 20 K delta T of apparent temperature -- ten units is approximately 0.8 K. This can, in turn, be related to radiance in a number of ways, the simplest is that the temperature is that which would be measured if the equivalent amount of radiance were due to a blackbody at that temperature.

variability. The phenomenon under discussion here is not necessarily the well known situation of a partly cloudy sky which then causes variation in radiance due to the crossing of the scene by shadows, though, certainly, this can be a factor. For example, while supporting a U.S. Army smoke test in the late Spring of 1989, observations were made that showed wide variation in IR background radiance. An example of these results is shown in Figure 1. (The significance of the existence of such phenomena is that "false targets" can come and go in infrared imagery -- these may replicate the appearance of real targets!) The meteorological and other pertinent conditions at the time during which these observations were made can be summarized:

- high elevation (about 7000 ft AGL) in Southern New Mexico so that the ambient atmospheric influences on attenuation, etc. would be expected to be minimal

- noon time so that period of slow change would be expected
- benign meteorological conditions:
 - clear sky, no clouds whatsoever
 - relatively calm wind conditions
 - low relative humidity
- many correlative measurements
 - variations were seen in only part of the image (equipment problems can be ruled out); in fact, the "disturbance" was seen to move across the field of view of the imager
 - transmission measurements along the same line of sight (no variation observed in either visible or IR bands)
 - visible color and black and white video observations along the same lines of sight (no obvious variation in the scene; e.g., no dust clouds observed, etc.).

This observation resulted in an extensive literature search in an effort to determine whether or not other similar observations had been made, whether or not there were existing databases which might be explored for such phenomena, and also whether the existence of such phenomena had been hypothesized and/or explained. The outcome of this effort culminated with a report by personnel of New Mexico State University's Physical Science Laboratory (NMSU/PSL) (Nolen and Bustamonte 1991). The results of that effort were that there were no known similar observations and existing databases (such as those at the Environmental Research Institute of Michigan (ERIM), Larocca (1990) and Eglin Air Force Base's (EAFB's) Target and Background Information Library System (TABILS), Simpson (1990)) contained no data capable of yielding similar observations. Yet, existing theory can explain these observations through known processes (e.g., phenomena such as variation in emissivity caused by reorientation of the leaves on a bush, caused by the wind, variation in transpiration of vegetation, etc.) though the definitive cause for these variations remains to be discovered because of a lack of "complete" information at the time the observations were made.

Furthermore, an extensive observational program of local terrain at WSMR was instituted to investigate these phenomena in more detail; however, overrun by events, (reorientation of effort and reduction of resources) those data remain to be reduced and analyzed. For the current investigation, recently acquired data which is in a format more amenable to study was used, instead. Infrared imagery (both mid-IR, 3-5 μm , and far-IR, 8-12 μm , bandpass) acquired during the recent Smart Weapons Operability Enhancement Joint Test and Evaluation (SWOE JT&E), though not obtained for long periods with high time resolution, was in digital format and did exist for short periods with high time resolution so that, at least, a beginning in making these types of studies could be made. Specifically, during the Grayling I deployment, images were acquired at

the rate of 6.25 frames per second, for 10 seconds, every 5 minutes during each of the 2-hr mission periods. The range to the mid-point of the scene was about 150 m so that with the nominal 20 degree field-of-view lenses, the spatial resolution was of the order of .4 m. There were 107 mission periods during the 41 days of the test.

Of those 107 missions, a smaller subset of observing periods was selected, primarily, because that smaller subset of images had previously been "registered" to the scene. This means that a region of interest (ROI) segmented from an image obtained during one mission period, can be assured of coming from the same portion of the scene for another mission period -- i.e., a given ROI always samples the exact same scene element (tree, ground, etc.). The reason that the registration procedures were required was that, as part of the servicing of the imagers, performing quality control checks, etc., the look angle of the imagers was not always exactly the same, mission-to-mission. This caused small variations in the content of the resultant field of view of the imager and resulted in small differences between ROIs from one mission to another. And, this would then result in comparisons between missions to not be consistent. The details of the image registration process can be found in the description of the analysis of the imagery performed for the SWOE JT&E final report (Bleiweiss et al. 1995).

For these mission periods, two divisions of the data were made. The first was to download the first ten second period from each of the missions -- this results in approximately 60 images per mission over a 10-s period to be available for further study. The other set was taken from the first hour of three mission periods which were chosen to span a wide range in diurnal conditions. This latter set consisted of 12 each, 10-s periods in order that some idea of variation over a one hour period could be obtained. This data set is a very limited subset of the total set obtained during the SWOE JT&E and though not the best for this study, it was the most accessible: there were times during the other two SWOE field exercises when more extensive data collection was experienced (e.g., during Yuma I, there was a 24-hr period when one image was acquired every one second, during Grayling II, during the non-mission periods, an image was acquired every 15 s during the whole test period -- about 40 days, etc.). Attempts will be made to access these data at a later date. The images have been segmented according to homogeneous features determined independently of the image content. Figure 2 shows an image with the ROIs indicated by boxes drawn on the sample image. Histograms of apparent temperature within those features were formed for further analysis.

The following discussion will begin with the details of the data reduction, based on these histograms, and is followed by a discussion of the nature of the fluctuations as a function of meteorological, atmospheric, and diurnal conditions. A summary and suggestions for further work concludes the report.

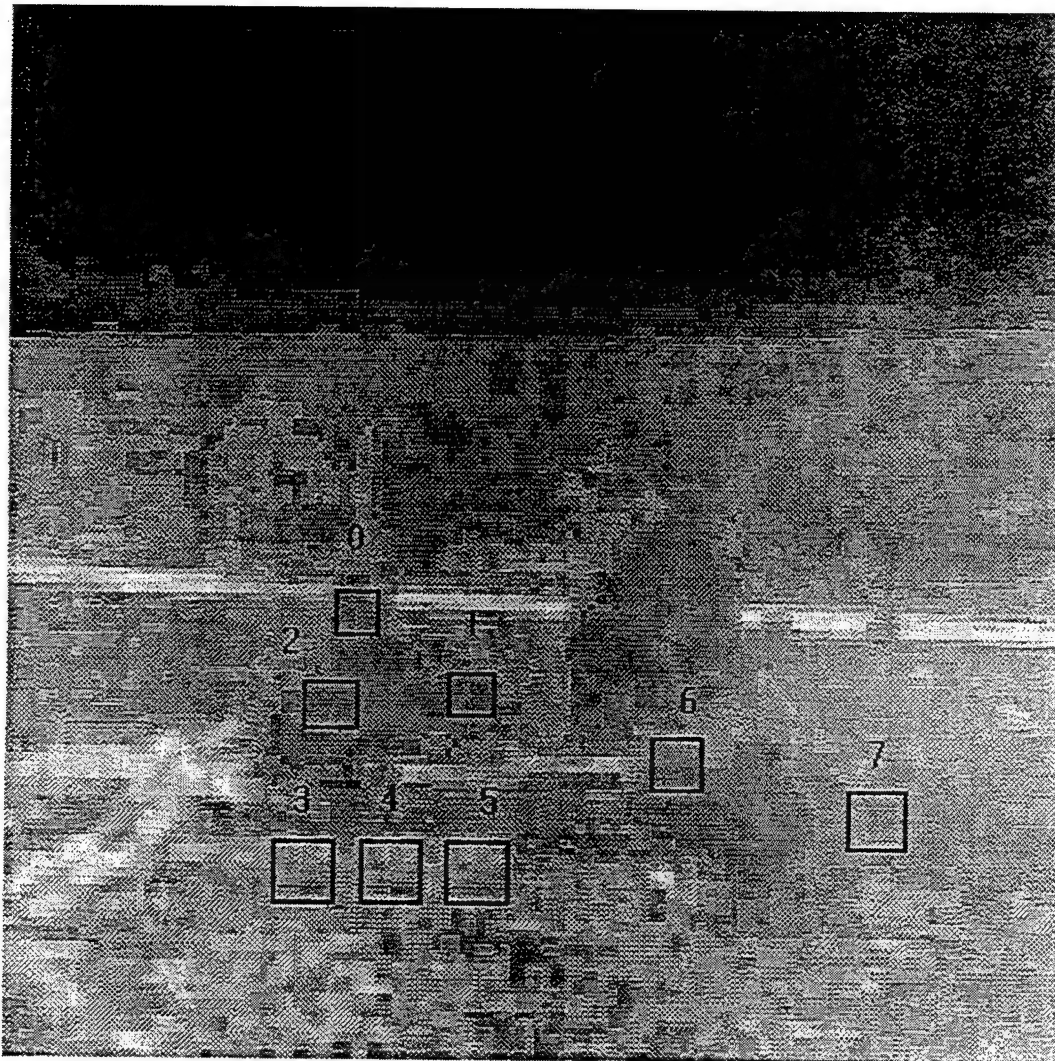


Figure 2. An example of the type of image under study along with notation showing the position of the AOIs.

2. DATA REDUCTION

The image of the scene under study was segmented to allow the investigation of the temporal evolution of individual scene elements: trees, bushes, ground, etc. In addition, some of the scene elements were duplicated to study whether those scene elements thought to be homogeneous were indeed so and hence, would respond similarly to the same stimulus. This resulted in eight areas of interest (ROIs) of varying square dimensions which were used to form histograms of the pixel apparent temperature. (The location of the ROIs is shown in Figure 2.) Table 1 lists the characteristics of the ROIs. ROI 0-2 and 6 were chosen to determine variation between like kinds of vegetation, ROI 3-5 were chosen to allow replication of the sampling (all three are relatively close to one another and cover "identical" patches of ground), and ROI 7, though thought to represent the same type of scene element as ROIs 3-5, appears to have a different apparent temperature and, consequently, might represent a different type of scene element.

Table 1. ROI Characteristics

Region Number	Region Size, pixels	Scene Element Type
ROI 0	3x3	coniferous tree
ROI 1	3x3	coniferous tree
ROI 2	4x4	coniferous tree
ROI 3	8x8	sparse grass
ROI 4	8x8	sparse grass
ROI 5	8x8	sparse grass
ROI 6	6x6	coniferous tree
ROI 7	8x8	sparse grass

The initial plan was to determine a variety of first order statistics based on the histograms of the apparent temperature within the ROI and to observe the temporal evolution of these parameters. This was accomplished; however, the variability of these parameters was so small that it was difficult to arrive at any conclusions. The next step was to determine the range of the integrated (weighted) apparent temperature -- this is another way of saying that the range (the difference between the maximum and minimum value) of the "average" within the ROI was determined and studied. The reason for the change in terminology is that "comparison of means" as is implied by the determination of the range of means or averages can only be effected if the distributions under study are normal distributions. It was not thought profitable to make this determination; instead, the weighted integral (an average) is very similar to (or nearly proportional to) what would be observed if the instantaneous field of view (IFOV) of the instrument were the same as the ROI in size and had a "point response function" which could be emulated by a rectangular response function. The data considered here was the set of one 10-s observations from the beginning of each of 40 of the mission periods, for each wave band. The number of pixels forming the average varied by ROI as is seen in Table 1 -- 9, 16, 36, or 64 depending on the size of the ROI.

For the 1-hr data sets, the results from the 12 each 10-s periods was similar to that obtained for the one 10-s period discussed above. These data were processed also to determine the weighted,

integrated (average) apparent temperature for each of the 10-s periods and to plot that as a function of time. It is understood that the proper way to sample a time series is to observe at a rate at least twice the Nyquist frequency for a band-limited signal -- in our case, that is impossible (we cannot band-limit mother nature) so it would be desirable to sample at a rate at least twice as fast as the expected or known variation in the background radiance. Furthermore, until we know more about this phenomena, we cannot go out and sample at some very high rate, for long periods, searching for the phenomena, because of the available resources and the inability to reduce such large amounts of data. This first attempt at analysis is to make an initial investigation and to begin to develop a methodology for such future studies as might be feasible.

3. RESULTS and DISCUSSION

The result of this study is that the range of variation within the 10-s period, for the 40 missions studied, is very small -- the largest range observed for any of the ROIs was 1 K. The bulk of the ranges fell at the noise level of the instruments (Berger and Bleiweiss 1994) -- the noise equivalent temperature difference (NETD) for the imagers is 0.3 K and 0.1 K for the mid- and far-IR, respectively). This is seen by inspection of the histograms of range, by ROI and wave band (page number constraints imposed by the conference committed preclude the insertion of several plots which would ease the interpretation). For the mid-IR band, the histograms show a maximum at 0.2 K or 0.3 K with a tail out to a maximum range of 0.5 K. The far-IR band peaks at 0.1 K and has a maximum range of 1 K. These results indicate that the mid-IR is marginally, more variable, temporally than the far-IR -- a result not unexpected because the mid-IR is more susceptible to variations in scattering of available radiation than is the far-IR; though the results can be clouded by the more noisy mid-IR system. In any case, the variation is small; whether or not it is insignificant remains to be determined as the results are compared to target/background differences (left for a later study).

A simple attempt at exploratory data analysis was made to see if there might be some relation between the observed meteorological conditions and these ranges of apparent temperature within the ROIs. This was accomplished by plotting the meteorological parameters (wind speed, visibility, air temperature, relative humidity, global flux, and time of day) versus the range -- with the exception of the global flux (which showed a small relationship), there were no obvious trends and there was no attempt to make a proper comparison because of the probable lack of meeting the assumptions required for correct statistical analysis.

The three mission periods examined show distinct differences over the 1-hr period studied. Mission 17 exhibits a trend during the period where the 10-s average changes by nearly 4 K from start to end with variation between 10-s periods as large as about 0.8 K. Mission 40 begins with an average apparent temperature 0.5 K higher than the hourly average, reaches a minimum of about 0.4 K below the average at 30 min into the hour and increases again near the end of the hour. The trends during Mission 48 show almost no variation in the average apparent temperature (10-s average) from one 5-min period to the next except near the end of the period when slight increases are noted -- ROI 0, 1, and 2 show less of an increase than the rest. It should be noted that the local time for the three mission periods was, 1100, 2300, and 0700, respectively. Thus, the trends noticed over the 1-hr periods can be attributed to the variation in,

or lack of, solar radiation. The wind speed was nominally 3.5, 1.5, and 0 m/s during these periods and may explain the period-to-period variation in average as it was greatest for the Missions 17 and 40 and least for Mission 48. There does not seem to be great differences between the mid-IR and far-IR. However, there are some; e.g., as the sun rises during Mission 48, the mid-IR seems to increase by larger amounts and the ground increases more than does the vegetation for the period-to-period change in average values. The range of variation during the 10-s period, for Mission 48, shows almost constant variation with the mid-IR having ranges of 0.15 to 0.4 K depending on scene element (the vegetation shows greater variation) while the far-IR is also constant with ranges of about 0.05 to 0.1 K with the vegetation only slightly more variable. Table 2 is a summary of some of the observations: the average apparent temperature experienced during the 1-hr period along with the range in the averages of the 10-s periods during the hour, by ROI.

Thus far, there have been no observations noted that approach the variability noticed in the WSMR observations described at the beginning of this paper. It may be that those observations are associated with phenomena not experienced during the Grayling Field Test. Certainly, the data on hand from the SWOE exercise has not been fully explored so that there may still be phenomena such as the WSMR results hidden there.

4. SUMMARY AND CONCLUSIONS

Infrared imagery acquired during the Grayling I field exercise of the SWOE JT&E have been processed to investigate some characteristics of the temporal variability of individual scene elements. The lack of continuous imagery for long periods has limited the scope of this study; instead of studying the apparent radiance over continuous periods, 10-s periods (sampled at 6.25 Hz) were segmented from the data set and one period from each of 40 different mission periods, for each of the mid- and far-IR wave bands, were processed. In addition, three 1-hr mission periods were also processed at the 5-min intervals that the instruments were turned on for -- this yields 12 each 10-s periods during each of the hours for investigation of the variation during a 1-hr period. The results of the 40 mission periods shows that the variation observed, during a 10-s period, was of the order of the instrumental noise and the largest variation observed during any of the 10-s periods was 1 K. This may be a significant result when these observations are compared to typical background scenes with targets. The three 1-hr periods seem to indicate that the variability seems to be more closely tied to wind speed than other meteorological factors though this has not been fully investigated and, the vegetation seems to show more variability than does the ground.

Future work should be directed towards the investigation of the additional SWOE data as well as the data acquired over the years at WSMR (that data taken during the observation of a scene local to the main post area of WSMR for which there is also a complete set of meteorological data acquired at 1-s intervals during the observations and at 15-min intervals during non observation periods during the last 5 years). The SWOE data should be first investigated in a similar manner for the Yuma I field exercise and then the continuous, high-time resolution data from both Yuma I and Grayling II should be analyzed.

Table 2. Summary of the Results for the 1-hr Mission Periods

Region	Mission 17 -IR		Mission 17 -IR		Mission 40 -IR		Mission 40 -IR		Mission 48 -IR		Mission 48 -IR	
	Average	Range	Average	Range	Average	Range	Average	Range	Average	Range	Average	Range
ROI 0	289.91	1.34	287.63	1.65	287.64	0.62	285.63	0.81	275.16	0.50	272.03	0.19
ROI 1	290.09	1.65	288.01	1.82	287.47	0.55	285.29	0.71	275.10	0.54	271.89	0.28
ROI 2	290.03	1.65	287.99	1.76	287.47	0.63	285.35	0.81	275.15	0.50	272.04	0.23
ROI 3	295.32	3.27	291.85	3.43	285.21	0.85	281.92	1.15	274.31	0.90	271.00	0.83
ROI 4	294.82	3.08	291.66	3.37	285.26	0.94	282.25	1.08	274.22	0.86	270.93	0.81
ROI 5	295.14	3.32	292.23	3.62	285.16	0.76	281.92	0.92	274.40	0.84	270.96	0.82
ROI 6	290.19	1.73	287.96	2.04	287.15	0.62	284.83	0.77	275.04	0.49	271.81	0.40
ROI 7	294.33	1.53	290.43	2.27	285.43	0.67	282.00	0.94	273.89	1.05	269.85	0.93

ACKNOWLEDGMENT

This effort was funded, in part, through funds provided by the SWOE JT&E office, Dr. J.P. Welsh, Director.

REFERENCES

Berger, R.H. and M.P. Bleiweiss, 1994: "Comparison of Infrared Radiometers Used to Gather Background Signature Data", 1994 SPIE International Symposium on Aerospace/Defense Sensing and Controls, Orlando, Florida

Bleiweiss, et al, 1995: "Appendix E: Analysis of the Imagery and Environmental Data" in the "Final Report for the SWOE JT&E", J.P. Welsh, et al, U.S. Army Cold Regions Research and Engineering Laboratory, Hanover, New Hampshire 03755.

Larocca, A.J. 1990: private communication.

Nolen, B. and D.D. Bustamante, 1991: "A Review of Thermal Models and Site Data for the High Temporal Resolution Characterization of Natural Terrain Radiance Fluctuations at the MIDAS/ATLAS Site", PSL-91/46, Physical Science Laboratory, New Mexico State University, Las Cruces, New Mexico 88003-0002.

Simpson, V., 1990: private communication

ACOUSTIC SENSORS AND SYSTEMS IN THE REAL WORLD: MODELING THE EFFECTS OF THE ENVIRONMENT ON ACOUSTIC PROPAGATION

David H. Marlin
U.S. Army Research Laboratory
Battlefield Environment Directorate
White Sands Missile Range, NM 88005, USA

ABSTRACT

Wind speed and direction, temperature, terrain, ground type, and turbulence all have a significant effect on outdoor sound propagation. It is not just surface data which are important; it is generally necessary to know the winds and temperature in the first several hundred meters above the ground. A change of wind speed or direction with altitude can produce significant directional dependence in the sound field. From a sensor point-of-view, this produces "blind" directions, where the sensor will not detect any acoustic activity, and "hyper-sensitive" directions, where distant sources may interfere with detection and classification of closer targets along the same azimuth. Propagation models can accurately predict this behavior, given accurate meteorological data. These models are of use in sensor and battlefield simulations, as well as operational applications such as tactical decision aids and mission planning aids. The limiting factor for operational use is the availability of meteorological data. With regard to simulations, many scenarios do not specify the upper air meteorological profiles. Furthermore, for most simulations, high-fidelity propagation models are far too slow to apply on-line, especially for broad spectrum acoustic signatures. Standard atmospheres and look-up-tables can aid in the incorporation of acoustic propagation into these simulations.

1. INTRODUCTION

One of the most important characteristics of a signature as received at the sensor is the signal to noise ratio (SNR). It is directly proportional to the detection probability and plays an important role in adaptive beam forming, used by many acoustic arrays. Furthermore, a good SNR for each of the spectral components of a signature is necessary for reliable identification and classification.

Between the source and sensor, the environment strongly affects propagation of those spectral components, and plays a major role in the overall system SNR. Temperature, humidity, wind speed and direction, terrain and ground type produce range, azimuth, frequency and time dependent variations of the signal power arriving at the sensor.

Accurate models of sensor performance, capabilities and limitations require accurate models of the environmental effects. There are a wide variety of acoustic propagation models available, with varying degrees of complexity. To choose the best model for a given application requires an understanding of the environmental effects, the models, and the application.

2. ENVIRONMENTAL EFFECTS

Wind and temperature induced sound-speed variations cause *refraction* of the acoustic field, redirecting energy upward or downward. This can result in *shadow zones*, where no direct energy propagates, and *ducts*, which tend to channel the energy for long ranges. On the scale of a few kilometers, these effects are primarily due to vertical variations in wind and temperature. Figure 1 shows some simple sound-speed profiles and the resulting propagation of acoustic energy.

Figure 2 demonstrates the sound field in a surface duct. It displays the attenuation of acoustic power, in dB, as a function of range and height, for a source frequency of 100 Hz. Note the long range channeling of sound in the surface duct. Figure 3 shows the sound field for an upward refracting atmosphere, with the resulting shadow zone.

Atmospheric *turbulence* can scatter a portion of the sound into a shadow zone, enabling

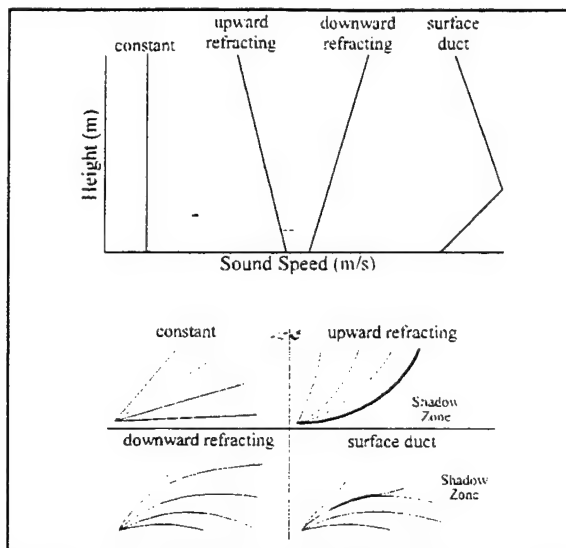


Figure 1 - Refraction of sound by simple sound speed profiles.

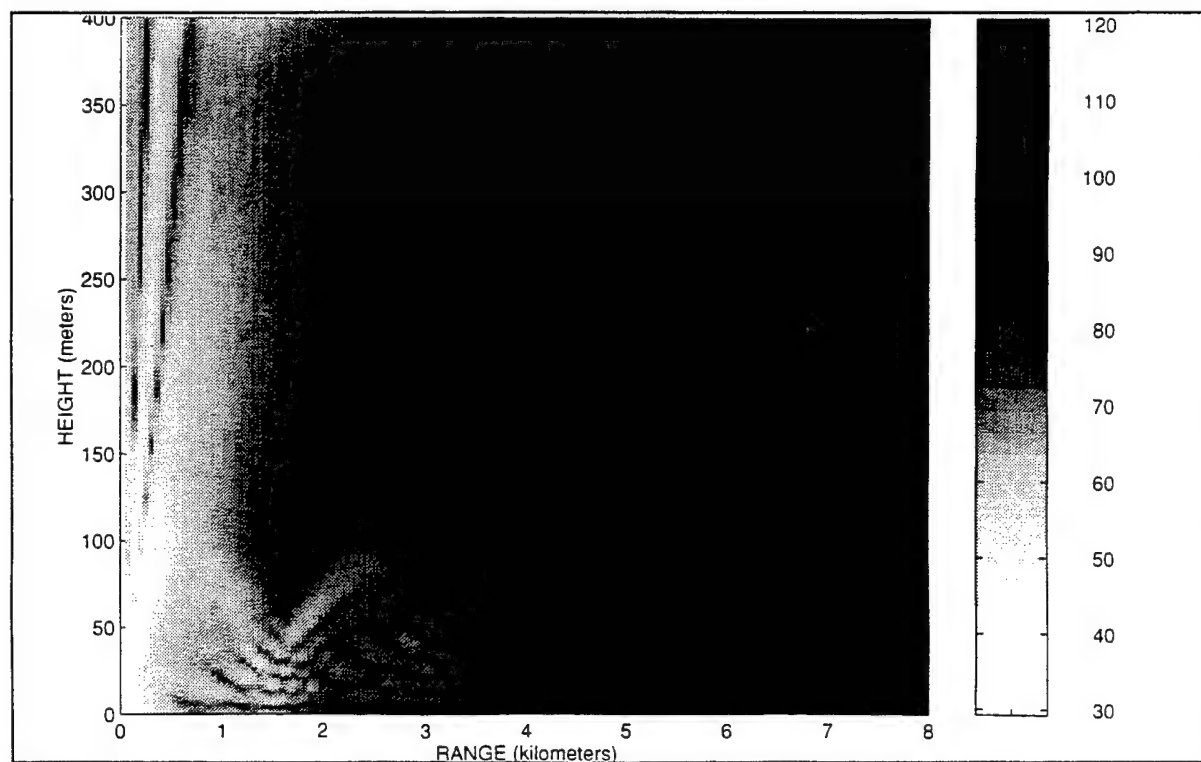


Figure 2 - Attenuation of acoustic power, in dB, in a surface duct. Source height is 5 m.

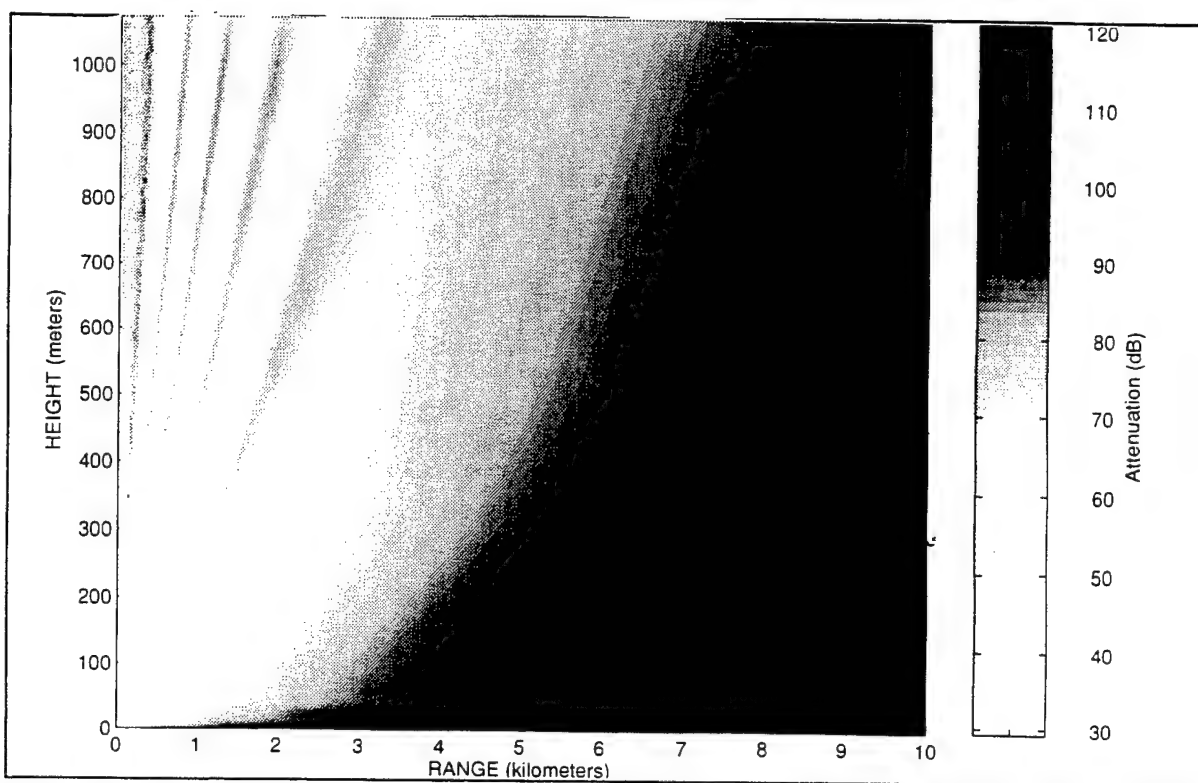


Figure 3 - Attenuation of acoustic power, in dB, in an upward refracting atmosphere. Source height is 5 m.

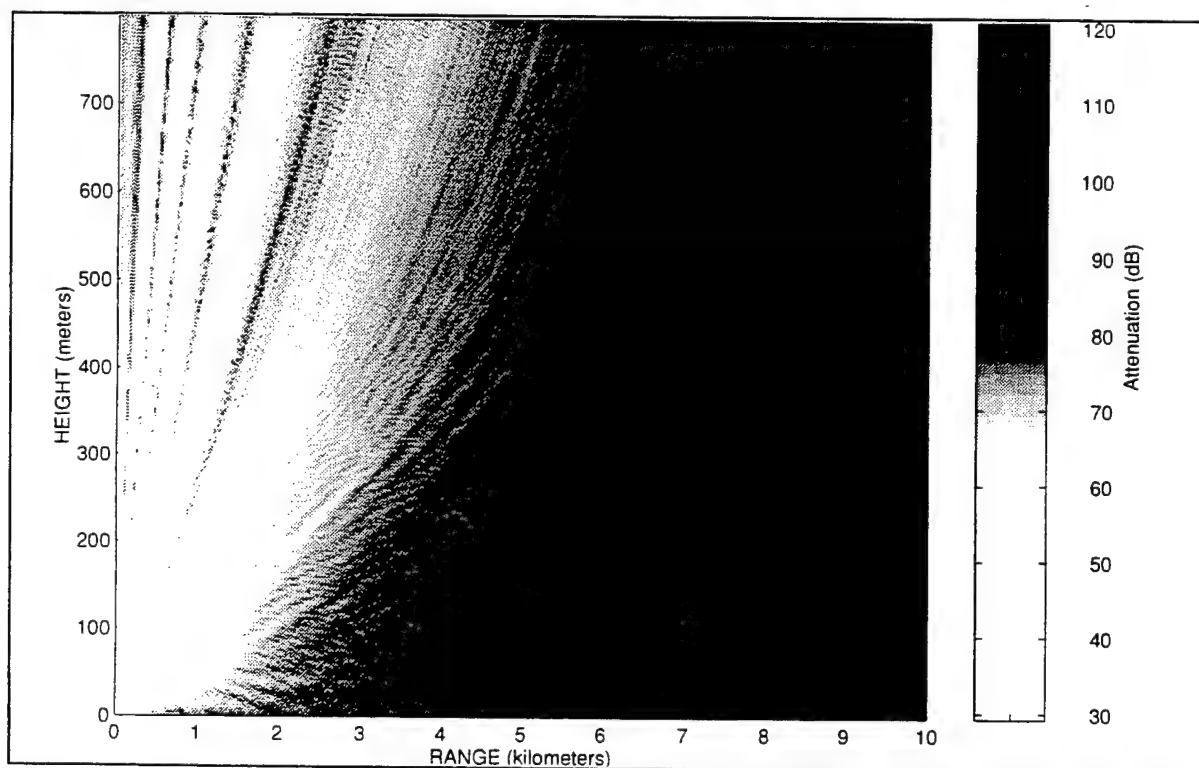


Figure 4 - Same as Figure 3, with the additional effect of scattering by atmospheric turbulence. Source frequency is 200 Hz.

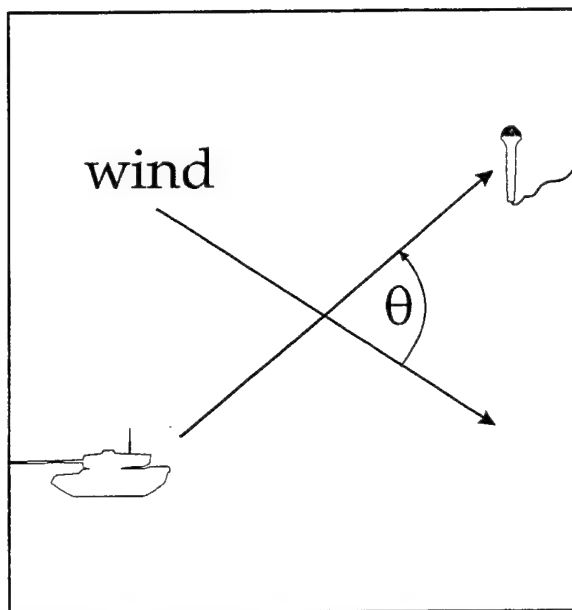


Figure 5 - Geometry of effective sound speed.

are pressure disturbances in the air, and their propagation is affected by relative motion of the air, i.e. the wind. Wind effects can be approximated in the wave equation¹ by using the effective sound speed, $c_{eff} = c + u \cos \theta$, where c is the actual temperature-dependent sound speed, u

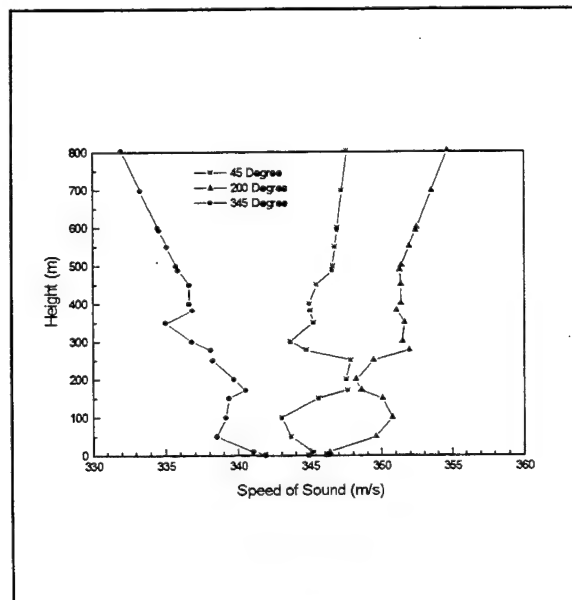


Figure 7 - Sound speed profiles, in selected directions, associated with meteorological profile of Figure 6.

detection, although with a somewhat lower SNR. This scattering can reduce coherence, affecting the accuracy of bearing estimates. Figure 4 shows the sound field of Figure 3 with the inclusion of turbulent scattering, at a source frequency of 200 Hz.

Temperature induced variations tend to produce a field which is symmetric in azimuth, at least within a few kilometers of the source. However, wind-induced variations are strongly dependent on the direction of propagation. Acoustic waves

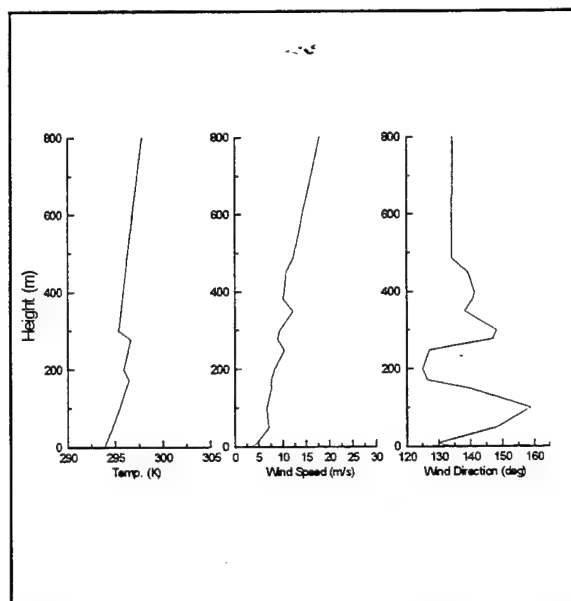


Figure 6 - Typical meteorological profile showing temperature, wind speed, and wind direction as a function of height.

is the wind speed, and θ is the angle between the direction of propagation and the wind (Figure 5). This results in a directional dependance of the sound speed, and an azimuth-dependent structure in the acoustic field.

Figure 6 shows an actual meteorological profile, with the resulting directional-dependent sound-speed profiles shown in Figure 7. Figure 8 is the power attenuation in the acoustic field resulting from the directional-dependent profiles. To the

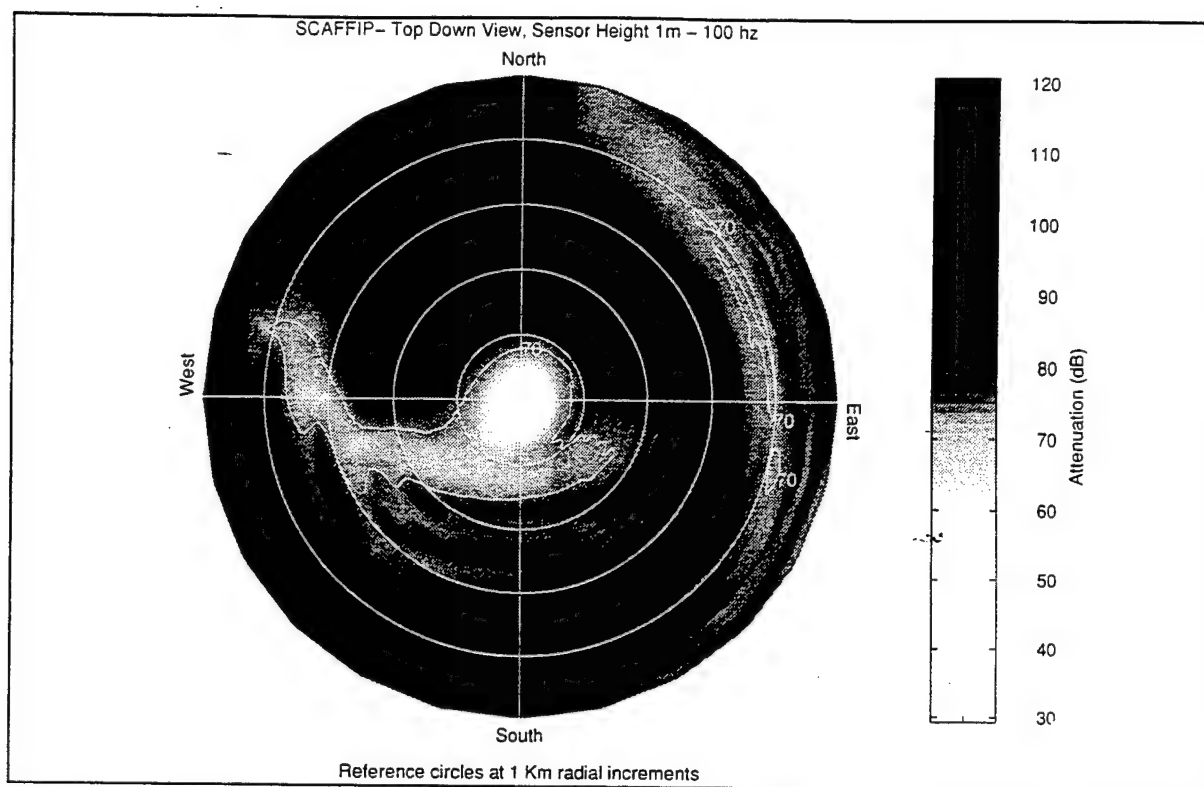


Figure 8 - Top-down view of attenuation, at a height of 1 m, from meteorological data of Figure 6. Source height is 5 m.

North-West is a strong shadow zone. The South-East through South-West predominantly see surface ducts. Upper air ducts occur in the Western and North-Easterly directions.

In addition to these atmospheric effects, the ground and terrain interact with the sound field in important ways. The *ground impedance* affects the way sound is reflected from the earth's surface. This is particularly important in a surface duct, where the sound is refracted downward and undergoes multiple ground reflections. Also, terrain features can produce shadow zones, depending on the refractive characteristics of the wind and temperature profiles.

Diffraction over a surface feature such as a hill can scatter sound into a shadow zone. This occurs at lower frequencies, while turbulent scattering tends to occur at higher frequencies. In general, one or the other will tend to scatter sound into any shadow zone that may exist behind a hill².

Molecular absorption causes the attenuation of acoustic energy with range. This attenuation is frequency dependent; higher frequency sound is attenuated more strongly. Below about 100 Hz, this effect is not significant for ranges less than 40-50 km. At 500 Hz, the sound is strongly attenuated beyond about three km. Propagation of signatures beyond four or five km is limited to frequencies of about 300 Hz or less.

Figure 9 graphically depicts several of the most important environmental effects discussed above.

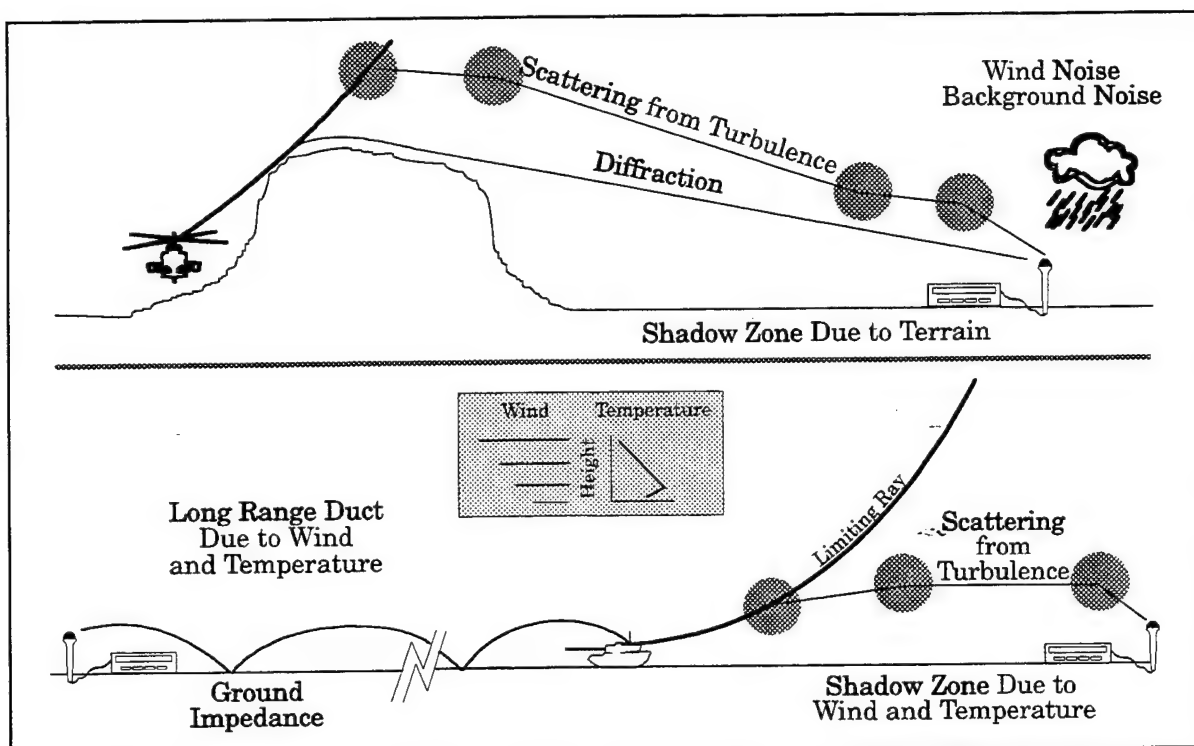


Figure 9 - Summary of environmental effects discussed above.

3. PROPAGATION MODELS

A number of outdoor sound propagation models exist which can model the phenomena discussed above. These models vary in complexity, ranging from simple spherical spreading models to full wave models, which numerically solve the wave equation. A hierarchy of models is given in table 1.

At the top of the table is the spherical spreading model, which incorporates only the $1/r^2$ decrease in power as sound radiates out from a point source. This decrease results from the increasing area of a spherical wavefront as it expands outward. This model doesn't incorporate refraction, terrain or turbulence effects, and generally works well only for short propagation ranges, less than about 500 meters. A simple improvement follows from incorporating a single hard-surface ground reflection, resulting in a dipole interference pattern. This can improve the usefulness of the model in some cases, but it is still limited to short ranges in general.

Ray tracing can incorporate the refractive effects of wind and temperature, but not terrain or turbulence. These models trace a ray or collection of rays radiating from a source at specified angles. They also track the amplitude of the sound field along the rays. Thus, they can give the sound power as well as the direction of propagation. Rays can be reflected upon hitting the ground, using Snell's law, but the ground can only be modeled as a hard surface, one which doesn't absorb any sound energy. This will not give good results for many ground types. Also, ray tracing models are not accurate at lower frequencies, and have trouble with caustics, regions where the rays tend to converge strongly.

Table I - Hierarchy of acoustic propagation models.

Model Complexity	Environmental Input Data
Spherical spreading - may include absorption and/or reflection from hard ground	Relative humidity for absorption
Ray tracing - incorporates refraction - may include absorption and/or reflection from hard ground	Temperature, wind, relative humidity
Full wave model - range independent - incorporates refraction, absorption, reflection from complex impedance ground	Temperature, wind, relative humidity, ground impedance
Full wave - turbulent scattering, flat terrain - incorporates refraction, turbulent scattering, absorption, reflection from complex impedance ground	Temperature, wind, relative humidity, ground impedance, c_n^2 or c_v^2 and c_t^2 (turbulence strength parameters)
Full wave - turbulent scattering, complex terrain - incorporates refraction, turbulent scattering, absorption, reflection from complex impedance ground, non-uniform surface topography	Temperature, wind, relative humidity, ground impedance, c_n^2 or c_v^2 and c_t^2 , surface topography (such as a DMA database)

In order to get more accurate results, it's necessary to go to full-wave models, so named because they numerically solve the reduced wave equation. Examples of this type are the Fast Field Program (FFP) and various versions of the Parabolic Equation (PE), including finite element PE's and FFT based split-step PE's. These models predict the attenuation of sound power, or *transmission loss*, as a function of range for a given azimuth and sensor height. Furthermore, most PE implementations also give the transmission loss at regularly spaced height intervals from the ground up to some maximum height. Figures 2 - 4 were generated by the Green's Function PE (GFPE), a version of the split-step PE.

The FFP and GFPE are also implemented in scanning versions, which give transmission loss vs. range at regularly spaced azimuth intervals to approximate a full two-dimensional, top-down look at the transmission loss at a given height. Figure 8 was generated by the Scanning Fast Field Program (SCAFFIP).

The FFP doesn't incorporate range dependent variations in the terrain or sound speed profile, hence it can't account for terrain variations. Furthermore, scattering by turbulence is difficult and cumbersome for the FFP and slows the model considerably. The PE is the only model to include complex terrain and turbulent scattering.

The cost of including more environmental effects is generally increased computation time and model complexity. Use of the FFP and PE generally requires expertise in propagation modeling

to ensure correct results. Furthermore, they can be quite slow, compared to the ray tracing and spherical spreading models. Both model propagation at a single frequency; determining environmental effects on a signature generally requires multiple runs of the propagation model at several frequencies. This can take from several minutes to several hours, depending on the computer, range, and bandwidth of the signature.

4. APPLICATIONS

Two important areas of application for propagation modeling are:

simulations and wargames, for sensor and weapon system evaluation, training and development of tactics, and

operational tools such as tactical decision aids and mission planning aids.

The latter is heavily dependent upon the availability of current, accurate meteorological data. In particular, the azimuth-dependent asymmetry displayed in Figure 8 is quite sensitive to wind direction. Most of the structure in that figure is due to changing wind direction with height. Without current wind and temperature profiles, it is virtually impossible to predict actual propagation conditions. This can be a formidable challenge, as conditions can change considerably over a period of hours or a distance of several kilometers. It is frequently not feasible to collect data at locations of interest, as they may be forward of enemy lines for example. Even if the location is available, it is difficult to collect data often enough.

Thus, it falls upon meteorological modeling and prediction to fill in the gaps, both by estimating profiles at locations where measurements aren't available, and predicting conditions in the future. This is generally computationally demanding, and still requires some type of accurate measurements to drive the model. Generally, the more measurements available, the better the model is at filling in the gaps. In any case, it can be quite difficult to accurately estimate or predict wind directions. This is not to say that tactical decision aids and mission planning aids are impossible. The point is simply that the availability of current meteorological data is the limiting factor. The Integrated Meteorological System (IMETS), with the Battlefield Forecast Model (BFM), is designed to provide measurements and forecasts of vertical meteorological profiles over a large horizontal grid. As this becomes operational, it will enable the use of acoustic propagation models on the battlefield.

The first application, to simulations and wargames, has a somewhat different problem. In many cases, the modelers are free to specify what meteorological conditions will be for a given scenario. The problem is not to predict actual conditions which *will* occur, but to choose realistic conditions which *might* be expected. This can be done using climatological data, for example.

Once the meteorological conditions are specified, the problem is one of computational speed. The full-wave models are simply too slow for most simulations, unless a supercomputer is used. One solution to this problem is to run the models off-line, before the simulation begins, and incorporate the results into look-up tables.

To date, most acoustic sensor simulations don't incorporate realistic environmental effects. There are several reasons for this. One is the misconception that environmental effects are negligible for ranges of a few km. In fact, shadow zones can occur at ranges less than one km, reducing the SNR considerably. Ducts can enable detection of sources beyond ten or even twenty km. These sources may appear to be much closer based on acoustic power alone. This can cause interference with other sources, making identification and classification more difficult. Also, a system which does not perform triangulation from multiple arrays may conclude these distant sources are nearby.

Another reason for the omission of environmental effects is the complexity of propagation modeling and meteorology. Most battlefield simulation and wargame developers do not have the necessary expertise in these subjects. This is not to fault them; it is the responsibility of the propagation modeling community to remedy the problem.

One area of current research is in the use of "standard acoustic atmospheres." This involves the creation of a small set of canonical sound speed profiles which incorporate a wide range of typical acoustic propagation conditions. Using these, a simulation developer or user will be able to choose from a catalog of standard atmospheres, based on criteria such as season, time of day, location, etc.

Another research topic is the development of more "user friendly" propagation models, which can help modelers glue environmental effects into battlefield simulations without requiring extensive acoustic propagation experience. This will be beneficial to the operational decision aids as well.

5. SUMMARY

The environment exerts considerable influence on propagating acoustic energy. This can have a significant effect on the probability of detection, accuracy of bearing estimates and tracking, and success of identification and classification algorithms. In particular, the wind can cause considerable azimuth-dependent variability in sensor performance. Propagation modeling can address these issues, given reliable meteorological data. Research is underway to improve the collection and estimation of meteorological profiles, and also to simplify the incorporation of propagation modeling into battlefield simulations and decision/planning aids.

For further study, there are several good books on acoustic propagation. Kinsler and Frey³ provide a good undergraduate introduction to acoustics and wave propagation. More advanced references for acoustic propagation include those of Pierce⁴, and Morse and Ingard⁵. An excellent reference for computational propagation modeling is by Jensen and Kuperman⁶. Although they specifically addresses underwater propagation modeling, the techniques are generally applicable to outdoor acoustics as well. Also, there are a number of good journal articles and technical reports dealing with spherical spreading⁷, ray tracing⁸, the FFP^{9,10}, SCAFFIP¹¹, and various implementations of the PE^{12,13,14,15}.

REFERENCES

1. Strictly speaking, the wave equation $\nabla^2 p - \frac{1}{c^2} \frac{\partial^2 p}{\partial t^2} = 0$ is only valid for a stationary medium. However, it is frequently applied to acoustics in a moving medium, by using the effective sound

speed. This is only an approximation, as it cannot account for crosswind effects.

2. It is important to note that shadow zones are not synonymous with non-line-of-sight. Refraction can direct sound into the region behind a hill, where there is no line-of-sight from source to sensor. In this case, there is no shadow zone. For example, this can occur in a surface duct, as discussed above. On the other hand, shadow zones can occur where there is line-of-sight, as in the case of an upward refracting atmosphere, also discussed above.

3. Lawrence. E. Kinsler, Austin R. Frey, et. al., *Fundamentals of Acoustics*, John Wiley and Sons, New York, 1982

4. Allan D. Pierce, *Acoustics: An Introduction to Its Physical Principles and Applications*, Acoustical Society of America, Woodbury, New York, 1989

5. Philip M. Morse, K. Uno Ingard, *Theoretical Acoustics*, Princeton University Press, Princeton, New Jersey, 1968

6. Finn B. Jensen, William A. Kuperman, et. al., *Computational Ocean Acoustics*, American Institute of Physics, New York, 1994

7. John M. Noble, "Evaluation of Simple Spherical Spreading Model for Near Vertical Acoustical Propagation," Technical Report ARL-TR-532, U.S. Army Research Laboratory, 1994

8. Terry L. Foreman, "Acoustic Ray Models Based on Eigenrays," ARL Report No. ARL-TR-1, Applied Research Laboratories, The University of Texas, Austin, TX, 1977

9. S. W. Lee, N. Bong, et. al., "Impedance formulation of the fast field program for acoustic wave propagation in the atmosphere," *J. Acoust. Soc. Am.*, **79**, 1986, pp. 628-634

10. S. J. Franke, G. W. Swenson, Jr., "A Brief Tutorial on the Fast Field Program (FFP) as Applied to Sound Propagation in the Air," *Applied Acoustics*, **27**, 1989, pp. 203-215

11. John M. Noble, David H. Marlin, "User's Manual for the Scanning Fast Field Program (SCAFFIP)", Technical Report ARL-TR-545, U.S. Army Research Laboratory, 1995

12. Kenneth E. Gilbert, Xiao Di, "A fast Green's function method for one-way sound propagation in the atmosphere," *J. Acoust. Soc. Am.*, **94**, 1993, pp. 2343-2352

13. Kenneth E. Gilbert, Michael J White, "Application of the parabolic equation to sound propagation in a refracting atmosphere," *J. Acoust. Soc. Am.*, **85**, 1989, pp. 630-637

14. M. West, K. Gilbert, R.A. Sack, "A Tutorial on the Parabolic Equation (PE) Model Used for Long Range Sound Propagation in the Atmosphere," *Applied Acoustics*, **37**, 1992, pp. 31-49

15. David H. Marlin, "Fast Parabolic Approximations for Acoustic Propagation in the Atmosphere," Technical Report ARL-TR-573, U.S. Army Research Laboratory, 1995

A High Spatial and Temporal Resolution Database
for
Synthetic Scene Generation and Validation

Max P. Bleiweiss¹, Thomas Cassidy², Forrest Scott², George G. Koenig³,
and James P. Welsh⁴

SWOE JT&E Program Office
72 Lyme Road
Hanover, NH 03755

ABSTRACT

The overall objective of the Smart Weapons Operability Enhancement (SWOE) Joint Test and Evaluation (JT&E) program sponsored by the Office of the Secretary of Defense is the enhancement of smart weapons performance through an effective application of knowledge of the environment. Specifically, the two objectives of the SWOE JT&E effort are to 1) validate the SWOE scene generation process and 2) collect a selected data set for use by the DoD community. This presentation provides an overview of the high spatial and temporal resolution environmental and imagery database collected during three SWOE field programs. These field programs were conducted during the summer-fall and winter-spring transition periods at Grayling, Michigan and the winter-spring transition at Yuma, Arizona.

¹U.S. Army Research Laboratory, Battlefield Environment Directorate, White Sands Missile Range, New Mexico

²Sensor Concepts and Applications, Inc., Phoenix, Maryland

³U.S. Army Cold Regions Research and Engineering Laboratory, SWOE JT&E Program Office, Hanover, New Hampshire

⁴Director, SWOE JT&E Program, U.S. Army Cold Regions Research and Engineering Laboratory, Hanover, New Hampshire

During the field programs, an extensive set of environmental parameters (e.g., air and soil temperature, solar and infrared fluxes, etc.) were collected at several locations over a fairly small test area. These parameters are required for synthetic scene generation and model evaluation, and have been used to investigate the "within" and "between" environmental variability. In addition to the collection of the environmental parameters, extensive infrared (IR) and millimeter wave (MMW) imagery were collected utilizing ground-based and airborne sensor systems. The IR imagery has been utilized in the validation of the SWOE generated synthetic scenes and to investigate the scene-to-scene and sensor-to-sensor thermal IR variability.

1. INTRODUCTION

The Smart Weapons Operability Enhancement (SWOE) program began as a Balanced Technology Initiative (BTI) in 1988. That effort was started at the Waterways Experiment Station (WES) of the U.S. Army Corps of Engineers in Vicksburg, Mississippi. Subsequently, the BTI effort developed to a Joint Test and Evaluation (JT&E) program under the JT&E program of the Office of the Director of Defense Research and Engineering (DDR&E), Office of the Secretary of Defense (OSD). The objectives of this JT&E were to validate the SWOE process of synthetic scene generation and to create a selected data set to both support the validation effort and to provide for future similar efforts as well as exist as a source of information for system developers. The guiding paragon of the synthetic scene generation process and resulting synthetic imagery has been fidelity to the real world based on physical models as opposed to the ability to generate scenes rapidly as might be required, for example, by the distributed interactive simulation community. This is not to say that the SWOE program cannot contribute to that effort but only to emphasize the direction of this effort.

To accomplish the objectives of the JT&E, it was required that the models be brought to a state of operability and that field exercises be planned and accomplished to provide both data with which to run the models and data for the select database. The field portion of the JT&E was accomplished in cooperation with, and under the aegis, of the Chicken Little Joint Program Office (CLJPO). The locale for the field exercise portion of the SWOE JT&E were Camp Grayling, Michigan (a Michigan Army National Guard facility) and U.S. Army Yuma Proving Ground, Arizona -- both established Chicken Little field sites. Other reasons for choosing these sites included the desire to chose widely disparate climates and those which emulated climates of strategic interest. The time periods chosen for the exercises were determined to be periods of wide variability in environmental parameters so the SWOE model could be stressed to a high degree. In addition, the data set would provide future capability to model these conditions.

A large body of documentation exists which further describes the SWOE effort and provides for it's future utility (e.g., Welsh et al. 1995). The purpose of this paper is to delineate the data sets acquired during the field exercises and to familiarize the reader with what may be available for their own purposes. The following paragraphs will group this data in a variety of ways to demonstrate some of the ways in which the data set would be useful (i.e.,

environmental/meteorological data, imagery, etc.) as well as describe the conduct of the field exercises and their impact on the data acquisition. The data requirements for model operation, for ground truth, and that data required for the validation process is identified. This then also describes the "select" data set, a portion of which has been placed on CD-ROM for distribution. Limited description of some of the analysis performed to date will also be presented.

2. DATA REQUIREMENTS⁵

In the simplest sense, a smart weapon system only needs to correctly distinguish targets; everything else in the scene is a non target. In a more complicated sense, the scene is composed of multiple scene elements, some of which may be mistaken for targets. In addition, the environment continually changes the signatures, and signature transmission, for both target and non target scene elements. The SWOE JT&E concentrated on the non target features and those effects of the environment that are the sources of false alarms. The goal is to exploit the knowledge of the environment in order to enhance the overall performance of the smart weapon system. This is not to say that the target issue is ignored because it is not -- limited resources could not allow everything to be considered in its smallest detail. Targets were included in some of the Yuma and Grayling data collection efforts and SWOE does have a capability to model targets in scenes.

To accomplish the JT&E objectives, the test scene and environment had to be characterized as realistically as possible. The goal of understanding the impact of the environment on the scene is to exploit this knowledge to improve smart weapon effectiveness. The goal of understanding the smart weapon system's sensor data is to determine the capability to detect, identify, and attack specified targets. This required the consideration of four categories of data: at-the-sensor data (i.e., imagery), documentation data (i.e., calibration, etc.), at-the-scene data (i.e., environmental, etc.), and back-up data

2.1 At-The-Sensor Data

At-the-sensor data describes the incident radiation field at the sensor. Such data are in units of energy per unit solid angle, per unit wavelength (or waveband), per unit sensor area (or pixel), per unit time. The SWOE technique to record this information was to acquire imagery at many different spectral bands.

2.2 Documentation Data

These data include sensor system characteristics; general scene, background, and environmental descriptions; instrumentation descriptions; and measurement system characteristics. More specifically:

⁵ (The bulk of the information in this section was derived from one of the SWOE planning documents prepared by Heaps 1991.)

EO Sensor Characteristics: The IR imaging sensors were, for the most part, commercially available devices whose spatial resolution and dynamic range were very good. The IR imagers were characterized by measurement at the Guided Weapons Evaluation Facility (GWEF) of the 46TW located at EAFB. The amplitude calibration was accomplished in a variety of ways depending on the organizations involved; in any case, extensive work was expended to ensure the highest quality data possible (e.g., Berger and Bleiweiss, 1995).

Scene Description or surface characterization: This information provides local area and terrain details. It can be further subdivided into three categories:

- Vegetation Mapping
- Soil Characterization
- Features.

Instrumentation Descriptions and Measurement System Specifications

2.3 At-The-Scene Data

These supporting data are measured at the scene in real time. They help recreate the scene as it was, or would be, seen by the sensor and are critical to the simulation effort. These data include scene element descriptors, background radiance, intervening atmospheric transmittance, additional environmental data, and locations of sensors, targets, and major scene elements. At-the-scene data also include the information needed to support (i.e., serve as input for) subsequent modeling.

This type of data can be further subdivided into five broad categories: scene element descriptors, scene element radiative properties, illumination, atmospheric transmittance, and environmental factors.

To meet these requirements, specific measurements were necessary as there was no source of information with sufficient details to accomplish the SWOE JT&E objectives. The next section will describe the field exercises conducted as well as the measurements made during those efforts.

3. FIELD EXERCISES AND SITE DESCRIPTION

3.1 General

Limitations of time and funding restricted the field exercise portion of the SWOE JT&E to three field trials: Grayling I, Yuma I, and Grayling II. Grayling I was conducted during September-October, 1992; Yuma I, during February-March-April, 1993; and Grayling II, during February-March-April, 1994. These periods corresponded, respectively, to the Fall/Winter, Winter/Spring, and Winter/Spring transition periods and, in fact, were times of wide variability in environmental conditions. Each field exercise consisted of two periods as concerns data acquisition; a preliminary effort to acquire the data required for the information database necessary for initialization of the model -- such things as terrain relief, feature inventory and location, etc. and

the actual exercise during which the meteorological, ground truth, and imagery data were acquired. The two test sites were chosen to emulate regions different in climate and topography: Grayling is reminiscent of Europe in both climate and terrain while Yuma is somewhat akin to Southwest Asia.

Each field exercise was conducted over a period of several weeks during which 1- or 2-hr mission periods (depending on the particular exercise) were "randomly" positioned in time for intensive data acquisition. The meteorological and some of the other data were acquired continuously; however, it was not possible, for example, to acquire imagery at the full data rates for the full duration of the test. Therefore, in the interest of meeting the requirements of statistical inference testing, imagery were acquired, primarily, during the mission periods and during those times, randomly selected images were downloaded for further analysis. A summary of this effort is given in Table 1 which lists, by field exercise, the test duration, mission length, number of missions, and the recording schedule required to fulfill the objectives of the JT&E. Depending on the particular exercise and mission, several sensors were scheduled to operate, simultaneously. For example, during Grayling II, three dual-band ground-based IR sensors, one MMW ground-based sensor, and an airborne platform with dual-band IR and a single-band MMW sensor were all observing the same scene (Site E) from the same (ARL/CRREL-IR), nearly the same (ARL-MMW), or different (46TW-IR and 46TW-ASETS/airborne) look angles. Simple arithmetic indicates an overwhelming amount of data -- terabytes were acquired during the three field exercises.

Table 1. Summary of Image Acquisition by Field Exercise

Field Exercise	Duration (days)	Mission Period (hours)	Number of Missions	Recording Schedule (see Note)
Grayling I	41	2	107	10s/5m (24X)
Grayling II	43	1	172	5s/1m (12X)
Yuma I	47	1	188	5s/1m (60X)

Note: In addition, where possible, other imagery were acquired. For example, during Grayling II, the ARL/CRREL IR sensor team were able to, by alternating sensor pairs, acquire 1 frame every 15s during the non-mission periods. The notation is read, for example: "record for 10s, every 5m (which happens 24 times during the 2-hr mission period)".

3.2 Instrumentation

Imaging: The purpose of the imaging portion of the test was to characterize the scene by way of a radiometric "snapshot" in the infrared portion of the spectrum and a backscatter "snapshot" for the MMW (active) portion of the spectrum. Calibrated imaging devices for the required wavebands (the "cameras") were placed at the same location or vantage point as would the smart weapon's sensor or its surrogate. These data were acquired in an attempt to capture the widest range of variability possible (and feasible) in order to both characterize the scenes and to provide data for verification of the synthetic scene generation process.

Imaging of the scenes, with and without targets, was accomplished by several teams using ground-based and airborne sensor systems. Groups from the Battlefield Environment Directorate of the U.S. Army Research Laboratory (ARL/BED), the U.S. Army Cold Regions Research and Engineering Laboratory (CRREL), the Waterways Experiment Station (WES) of the U.S. Army Corps of Engineers, and the 46th Test Wing (46TW) from Eglin Air Force Base (EAFB) were responsible for ground-based IR imaging systems while the U.S. Army S3I Directorate (ARL/S3ID) operated a ground-based MMW radar imaging system. The 46TW provided two airborne IR imaging systems: ASETS and BASES; C130-based and helicopter-based, respectively. In addition, the ASETS instrumentation package includes a 95 GHz MMW radar system. The airborne missions were a subset of the randomly selected mission schedule. Data received from each group varied as to media, formats, and content.

The airborne collection capability had state-of-the-art calibrated IR sensors in both the 3-5 and 8-12 micrometer bands and, in the MMW band, a fully polarimetric 94 GHz capability. There was also be a full color visual system. All of these were boresighted and mounted on a stabilized platform. This sensor system is owned and operated by the 46TW from Eglin Air Force Base in Florida.

Augmentation of the airborne measurements was necessary to ensure that periods which precluded flying were covered (i.e., hours of darkness -- by reason of noise abatement, inclement weather, etc.). This required both mid- and far-infrared measurements (3-5 and 8-12 micrometers) in a format similar to, if not identical with, the airborne measurements. Attempts were made (and were, for the most part, successful) to use the same spatial resolution and depression angles characteristic of the airborne measurements. In addition, the use of the ground-based measurements with identical systems allowed for the determination of the variability of "same" instruments. MMW radar measurements from the ground were made for the same reasons. Placement of the ground-based imaging systems was conducted to replicate at least one of the depression angles as experienced by the airborne sensors as closely as possible.

Environmental Parameters: At each site, which consisted of approximately a 1-2 square kilometer piece of "terrain", smaller regions representing the local extremes in micrometeorology or other characteristics (e.g., topography, vegetation coverage, etc.), were selected for more intense instrumentation. One or two of these sites (depending on the particular field exercise) were further defined to be regions of more intensive study than some of the others. (These regions were the ones chosen to be imaged by the ground-based sensors as well as the airborne systems.) This hierarchy of site selection allows the determination of the "within" and "between" variability for the various sensors -- both meteorological and imaging -- which then allows statements of homogeneity and degree of variation to be made and answers to questions such as the following to be found:

- Do we need to measure wind speed at several locations over the whole test site or will one station suffice?; What size site does this hold for?; Etc.

- Are the imagery measured from one "look angle" different than another?; Are the imagery from one site different than that from another site?; Etc.

And, though particular attention was paid to calibration of the various instruments (e.g., Berger and Bleiweiss, 1995), what variation can be expected between "identical" instruments and within "homogeneous" scene features. This, in particular, led to the definition of two smaller "sub-sites" within one of the primary Sites as a region determined, *a priori*, as being homogeneous. Thus, for example, measurements made on Site E1 and E2 (for Grayling I and E3/E4 for Grayling II) could be compared to get at instrumental variability and/or "within" variability and to then determine the effect which this has on the modelling effort and the resulting synthetic image.

The majority of the data acquired fall into two categories: imagery (IR and MMW/active) and environmental. Portions of these data sets were further subsampled for placement on CD-ROMs to allow ready access. These will be described in detail later. The discussion below will concentrate first on the imagery data set and then on the environmental data set.

3.3 Imagery Data

For Grayling I, during the two-hour mission period, IR imagery of Site E, both LWIR (8-12 μm) and SWIR (3-5 μm) were acquired at the rate of 6.25 frames per second, for 10 seconds, every five minutes. At Yuma I, two IR systems were used, simultaneously, to collect imagery of the "ARL" site at the rate of 6.25 frames per second, for five seconds, once per minute during the 1-hour mission period. And, during Grayling II, Site E was imaged by two IR systems, at the rate of 6.25 frames per second, for five seconds, every minute during the 1-hour mission period and during non-mission periods, one system or the other acquired one frame every 15 seconds. This was for the primary IR image collection systems; in addition, other IR systems were monitoring the same and other sites to allow other "look" angles and sites with other characteristics to be observed as well. During selected missions, for all three exercises, airborne imagery at a variety of elevations above ground level and with a variety of depression angles were acquired at IR wavelengths and, for Yuma I and Grayling II, MMW also.

High resolution imagery for a few discrete features were also acquired as part of the philosophy of acquiring data at a variety of scales (both temporal and spatial) for the "within" and "between" comparisons alluded to earlier. Some of this imagery was also used for the purpose of providing "textural" descriptors for use by the model.

3.4 Environmental Data

The environmental data, mainly meteorological parameters, were recorded at one minute intervals. These data were then averaged to produce 1-hr values for use by the SWOE model -- the model can use inputs with higher temporal resolution but for the purposes of this exercise, the 1-hr values was adequate. (The data saved for future studies and which was used in the data analysis described below, were the 1-min. values.) An example of the variation experienced with

one of the parameters (relative humidity) during one of the exercises (Grayling I) is shown in Figure 13 as a "synoptic" plot. Again, the detailed listing of these many parameters is given in Appendix A.

3.5 Scene Element Descriptors

In addition to the above parameters, a large number of descriptors, grouped, generally, as scene element descriptors were also obtained. Some of these were acquired on a one-time basis while others were required at regular and frequent intervals. Specifically, these are grouped and defined below:

- Terrain:
 - Topographic features
 - Soil
 - Vegetation
 - Hydrologic features
- Cultural features:
 - Roads
 - Structures

And, within each of these topics, there are several additional parameters to consider. In our situation, some of these were not present (e.g., structures); however, others caused extensive data collection efforts. For example, under hydrologic features, snow cover is a parameter -- during Grayling II, initially, the scene was totally covered with snow of varying characteristics. As the test progressed, the snow melted with different rates depending on the location on the scene and it would snow again and the cover would reform. In order that this be taken into account, the snow cover was mapped over the whole 1.7 square km area with a resolution of a few meters, on a daily basis or more often if demanded by the test schedule. It was efforts such as this which demonstrate the integrity of this "high spatial and temporal resolution database." Other parameters such as listed under topographic features were required to be obtained only once. Soil moisture measurements were made at several sites on a daily basis.

The length of this paper precludes detailed description of all of the parameters -- the model requires over a 100 different inputs. A large number of parameters can also be used as ground truth -- numbers which the model can calculate or use as input. Feature description is another case where a large number of details exist -- trees and bushes were located, their size and shape measured and recorded, and, in some instances, branch positions and dimensions logged. A large database of optical and thermal properties of natural materials accompanies the model.

3.6 Additional

Several steps of the field data flow procedures resulted in compilations of data logs; each with its own ordering criteria. The two sets developed by the SWOE representatives were basically divided into image related items and environmental measurement related items. Also during the

field test, several listings of personal notations and auxiliary information were assembled for the benefit of post-field analysis and documentation. These include photographs and planning meeting notes as well as daily journals of the SWOE Team Leaders.

4. CD-ROMS

One of the efforts to make the data more accessible was to place segments of the imagery and supporting information onto several CD-ROMs for distribution. The four CD-ROMs created to date are: 1) Grayling I, 2) Yuma I, 3) Grayling II, and 4) Target data from Grayling II. The sections below, by CD-ROM, describe the content of each disc.

Grayling I CD-ROM Data: These files are those which are associated with the critical frames selected through the random selection process and are primarily images of Site E. There are also images from the "Intersection" area from the airborne platforms [BASES or ASETS] where this area is defined as the intersection of the flight lines when flying between sites E-F and C-D. All image files are in the Automatic Target Recognition Working Group (ATRWG) format with Target and Background Information Systems (TABILS) header information included in the header.

Yuma I CD-ROM Data: This CD-ROM holds imagery associated with the "critical" frames. Also, there are 7 topographical files (in TIFF format). All image files are in ATRWG format with TABILS header information included in the header.

Grayling II CD-ROM Data: The Grayling II CD-ROM contains image files corresponding to the "critical" frames. There are also 816 ARL/S3I MMW radar files on the disc. These files are in TIFF format. All IR image files are in ATRWG format with TABILS header information included in the header.

Grayling II Target CD-ROM Data: The majority of images with targets in the field of view where for the TIPS imager. WES viewed the 2 targets (T72 tank and BTR70 armored personnel carrier) as the schedule allowed. All systems had the targets in the field of view for missions 167 and 168. The total number of IR images for each collector were: 16 ASETS, 482 TIPS, 4 ARL, 20 CRREL, and 65 WES files for a total of 587 files. There were also 12 ARL/S3I MMW radar files from missions 167 and 168. Table 5 shows the breakdown of these files. All IR image files are in ATRWG format with TABILS information included in the header. Note that in the TABILS information section of the header the slant range value shown is to the Center of Site E while the depression and bearing angles with respect to the collectors center of field-of-view. The ARL/S3I radar files are in TIFF format. The TIPS and CRREL data contain files whose time stamps match the ground and airborne critical frame times. The only airborne files are from Missions 167 & 168. Because these are TARGET files, target information was written to the TABILS section of the header. This target information was taken directly from the target files.

5. SUMMARY AND CONCLUSION

The SWOE JT&E effort has compiled a large body of data which can be used for a variety of purposes. The detailed attention which was paid to every aspect of the endeavor has allowed a database to be constructed which will be useful for the construction of scenarios to be used in future simulations, allows the validation of other simulation efforts, and can be used for further research efforts on the dynamics of natural terrain. The description presented above has attempted to outline the overall effort and describe some of the parameters measured and stored. The analyses made to date have attempted to determine the variability of many of the parameters and to determine homogeneity between sensors and sites; both from an imagery and environmental data perspective. The results of that analysis indicate that the scenes used in the SWOE study are homogeneous and that the sensor to sensor variability was sufficiently small to allow differentiation between real images and synthetic images.

ACKNOWLEDGMENT

Several different organizations participated in the SWOE JT&E effort. The main participants were (not necessarily in any special order and we hope that all are represented):

- U.S. Army Cold Regions Research and Engineering Laboratory
- U.S. Army Waterways Experiment Station
- U.S. Air Force 46TW
- Chicken Little Joint Projects Office
- U.S. Army Research Laboratory/Sensors Directorate/Battlefield Environment Directorate
- U.S. Air Force Phillips Laboratory
- NASA/Goddard Space Flight Center
- Sensor Concepts and Applications, Inc.
- VITRO Corp.
- The Analytical Sciences Corporation
- NMSU Physical Sciences Laboratory
- Science and Technology Corporation

REFERENCES

- Berger, R.H. and M.P. Bleiweiss, 1994: "Comparison of Infrared Radiometers Used to Gather Background Signature Data", 1994 SPIE International Symposium on Aerospace/Defense Sensing and Controls, Orlando, Florida.
- Heaps, M., 1991: *Interim SWOE Site Characterization Handbook*, SWOE Report 91-14, U.S. Army Cold Regions Research and Engineering Laboratory, Hanover, New Hampshire.
- Welsh, J.P., et al., 1995: *SWOE JT&E Final Report*, U.S. Army Cold Regions Research and Engineering Laboratory, Hanover, New Hampshire.

Atmospheric Experiments with an Imaging Spectral Radiometer

Patti Gillespie

Samuel Crow

David Tofsted

US Army Research Laboratory

Battlefield Environment Directorate

White Sands Missile Range, NM 88002-5501

Abstract

A state-of-the-art, high resolution, multispectral, imaging radiometer has been acquired by the Electro-Optics Team of the Battlefield Environment Directorate for use in various research projects. The first application of this unique instrument will be in the model evaluation of the Weather and Atmospheric Visualization Effects for Simulations (WAVES) model developed by the Electro-Optics Team. The Imaging Spectral Radiometer (ISR) is almost a one-of-a-kind capability, as the only other copy of this device was simultaneously procured by the Tank and Automotive Command (TACOM) Research Division. Potential joint experiments with TACOM have been discussed. This paper describes the ISR and its measurement capabilities, as well as, the initial experiments planned with the ISR. The ISR is a multispectral radiometer with up to 30 spectral channels spanning the visible and near-infrared wavebands. Color contrast, as depicted by WAVES, will be the first model component to be evaluated by the ISR. ISR radiometric measurement capabilities will be used to evaluate WAVES radiative transfer model results. ISR image sensing capabilities can be used in sensor performance comparisons and weather effects analysis, as well as, target and natural background characterization.

1. Introduction

In recent years high resolution or hyperspectral spectroscopy has become a popular topic. Multispectral imaging capability is an obvious extension to spectroscopy. The applications for this technology are various and diverse, however, this paper will only discuss the imaging spectroradiometer and two potential applications. We hope to use the imaging

spectroradiometer in a variety of measurements that will provide the Battlefield Environment Directorate with a unique experimental capability.

2. Apparatus Operational Specifications

The US Army Research Laboratory Battlefield Environment Directorate has recently obtained a Real-Time Imaging Spectroradiometer (RTISR) from the Surface Optics Corporation for experimental support of our electro-optics simulation program. This instrument is a powerful system for collecting and processing spectral images in near real-time. The RTISR can collect, calibrate, and process a set of 20 to 30 spectral images at a frame rate of up to 15 Hz, with each spectral image comprising 256x192 pixels in the wavelength range of 390 to 950 nm with a bandpass of approximately 10 nm. The images can cover the entire waveband or a subset of the waveband. The field of view can vary from 29°x22° to 1.9°x1.4°. The frame rate can be variable, and there is variable optical gain. This allows the instrument to operate in conditions varying from brighter than mid-day sunlight to low light level conditions (above moonlight levels).

Spectral images on a two-dimensional array are produced using refractive optics and continuously variable filter (CVF) technology. This technology then results in the simultaneous acquisition of spatial imagery, and near simultaneous acquisition of all spectra for each pixel. Furthermore, the technology is polarization insensitive. Other spectrometers, especially monochromators are highly sensitive to polarization effects.

The RTISR also spectro-radiometrically calibrates the data as it is collected. After the data are calibrated, the instrument applies six arbitrary spectral response functions to each pixel's spectral radiance. This permits the instrument to emulate any visible or near infrared sensor, such as the human eye. The default system response for the RTISR produces the CIE tristimulus integrals on three channels, and RGB on the three remaining channels. The instrument can also transform the tristimulus integrals, X, Y, and Z into the chromaticity integrals, x, y, and Y. Single band images are obtained using a delta function on the spectral content stored in the image data buffers. One may also convert to chromaticity coordinates x, y, and Y as well as R, G, and B values. The spectral response curves can be redefined to emulate any visible or near IR sensor.

The RTISR can be coupled to a computer and the controlling commands can be issued from the computer. The instrument can be set up to run in fully automatic mode or via manual operation. The frame update rate for the RTISR is dependent on the ambient light condition up to a maximum of 15 Hz. The radiometric range is from 0.01 to 10⁵ Cd/m². The RTISR specifications are summarized in Table 1 shown here.

RTISR Specifications

Spectral Range	390 - 950 nm
Spectral Bandwidth	2.5% of bandpass center wavelength
Spectral Selection	0.3 nm increments
Number of Frequency Bands (Images per Data Cycle)	20 or 30 center wavelengths only
Lens	1-10X Zoom w/ removable 1.55X telextender lens for 15.5X maximum
Field-of-View	29° x 22° max to 1.9° x 1.4° min
Instantaneous FOV	2 mr @ 1:1 to 0.13 mr @ 15.5:1 zoom
Number of Pixels H x V	256 x 192 staring array CCPD
Maximum Update Rate	15 Hz @ 20 point mode, 390-950 nm
Radiometric Dynamic Range	0.01 to 100,000 Candelas/square meter
Video Output	RGB and XYZ tristimulus integrals
Computer Input/Output	IEEE-488 or RS-232

Table 1. Specifications of the RTISR.

2.1 Equipment Description

The five parts of the RTISR are the imaging spectrometer, objective lens, continuously variable filters, intensifier, and the imaging array. A Cannon V10X15RDC motorized CCTV zoom lens passes light energy through the CVF to form images on the fiberoptic taper of the intensifier. The lens provides a variable focal length from 15 mm to 150 mm at a relative maximum aperture of F/1.8. A removable 1.55X tele-extender also allows for a maximum zoom of 15.5. The zoom, focus, and iris are all motorized with position feedback done by sensing potentiometers. The high-speed, CVF based imaging spectrometer generates spectral images for collection and processing by the rest of the system. At the point of acquisition in

the system the images are uncalibrated spectral images, thus the initial subsystem is a spectrometer, not a spectroradiometer. The spectral images are converted to true calibrated images within the electronics of the RTISR. The CVF is a narrow band variable filter that is immediately in front of the intensifier's input fiberoptic taper. The angular position of the CVF is monitored closely by the ISR electronics. User selected bands are accessed by gating on the system's microchannel plate intensifier system when the CVF is in the appropriate position. CVF rotation speed and gate times are used to control the collection of spectral data.

The microchannel plate (MCP)/CCD array forms a critical part of the image acquisition process. Photons bandpassed by the CVF are focussed onto a photocathode that emits electrons. There is a potential drop between the photocathode and the forward face of the MCP. Electrons entering tubes passing through the MCP experience a further potential drop, accelerating them into collisions with the tube walls. Additional electrons are liberated, leading to a cascade of up to several thousand electrons. A further 7000V potential accelerates the electrons onto a P47 phosphor screen. This screen is situated adjacent to the CCD array.

The system is designed to be self-adjusting to variations in light level, thus automatic adjustments are made in the iris, gate times, gate voltage, and CVF speed, to ensure maximum light gathering for the measurement conditions and system settings selected.

Over 400 million calculations per second must be performed by the RTISR because of the requirements on pixel resolution, frame-rate, and spectral resolution. Figure 1 depicts the RTISR instrument diagrammatically. The output from the detectors is digitized to a 12-bit resolution, electronically processed, and formatted for output to video. A calibrated, 12-bit set of digital images may be uploaded to a computer via the IEEE-488 interface for analysis. A precision iris allows operation under high light level conditions. Figure 2 is a more detailed diagram including the electronics.

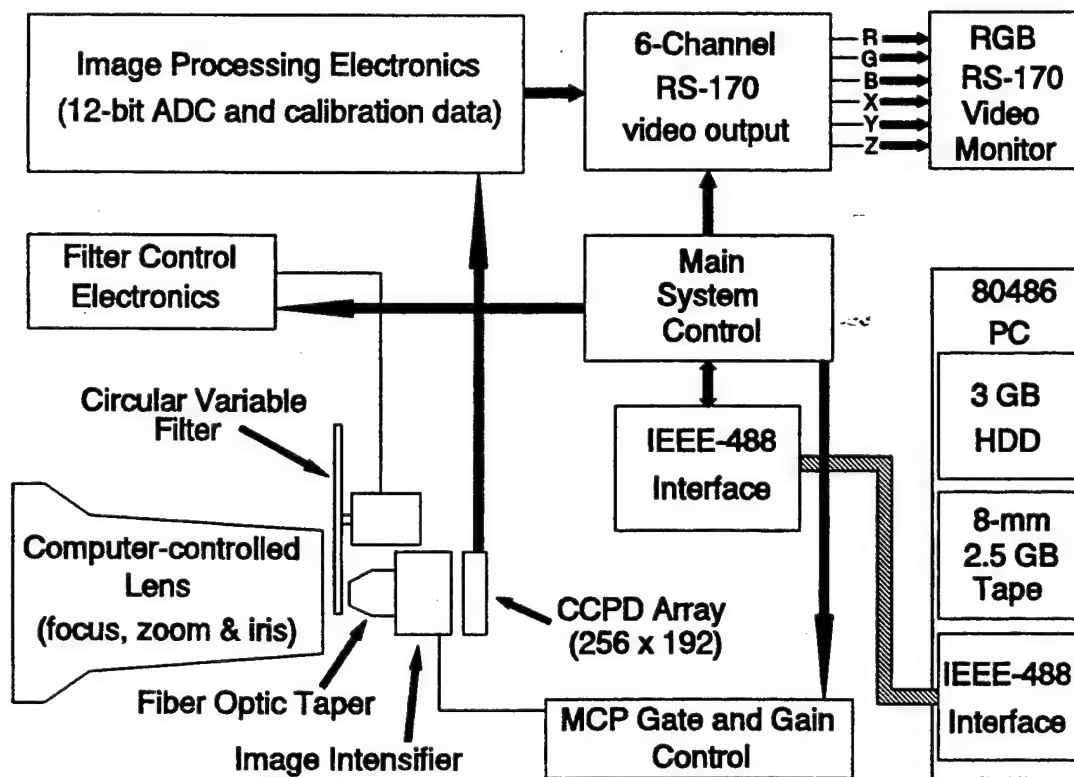


Figure 1. RTISR Subfunctions

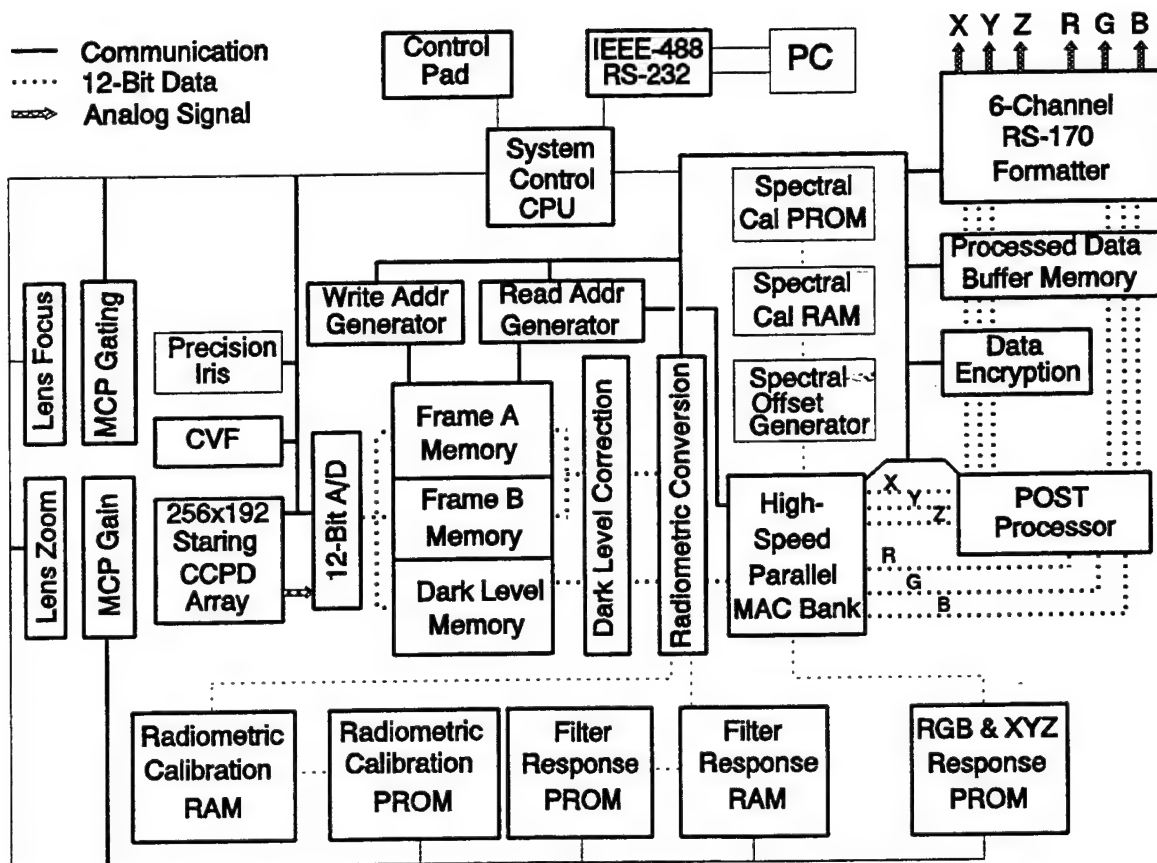


Figure 2. A detailed diagram of the electronics.

2.2 Sample Data

Shown here are samples of data for single color panels and for camouflage. No conclusions are drawn here for this data, as this presentation simply shows that this new instrument can give spectral information for two areas of interest for our group: spectral estimation for visualization and detection (or non-detection) of camouflage. Figure 3 is the data for the color panels, and Figure 4 is the data for camouflage and natural objects in a background.

Spectra of Color Panels

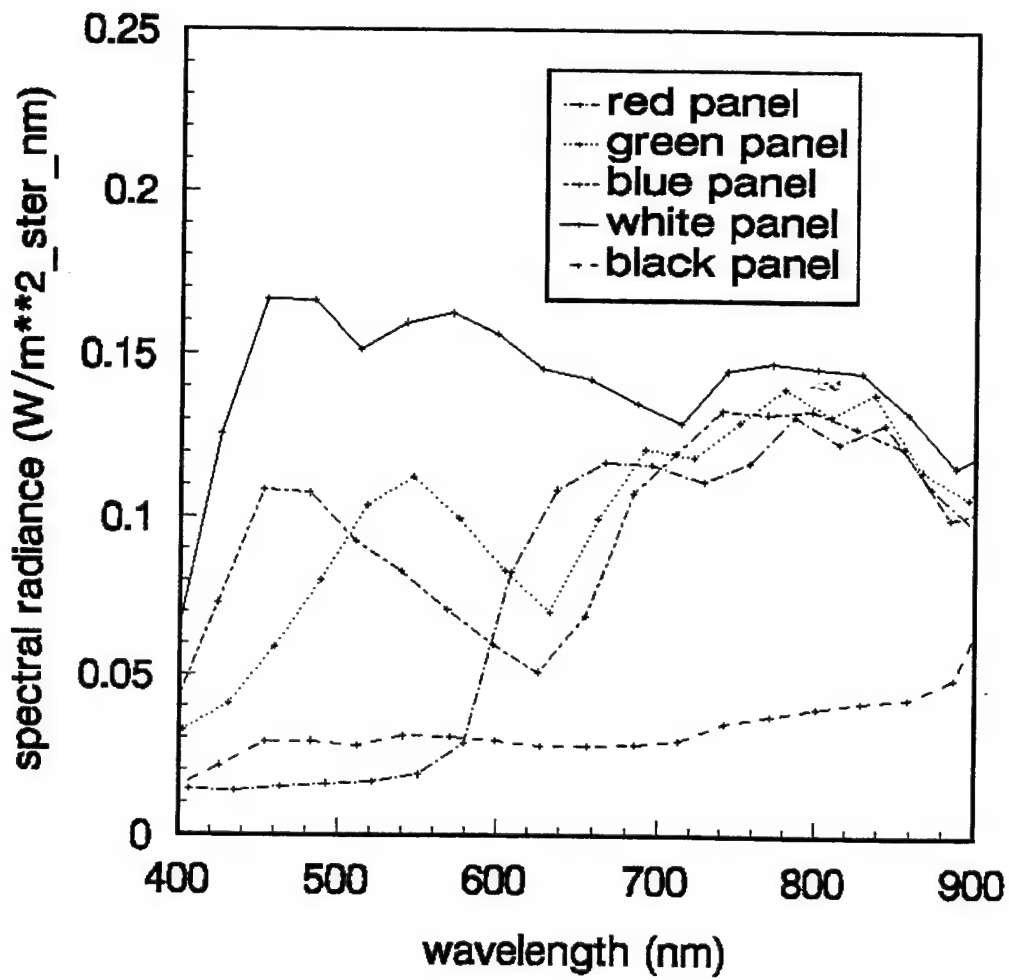


Figure 3. An example of data from color panels.

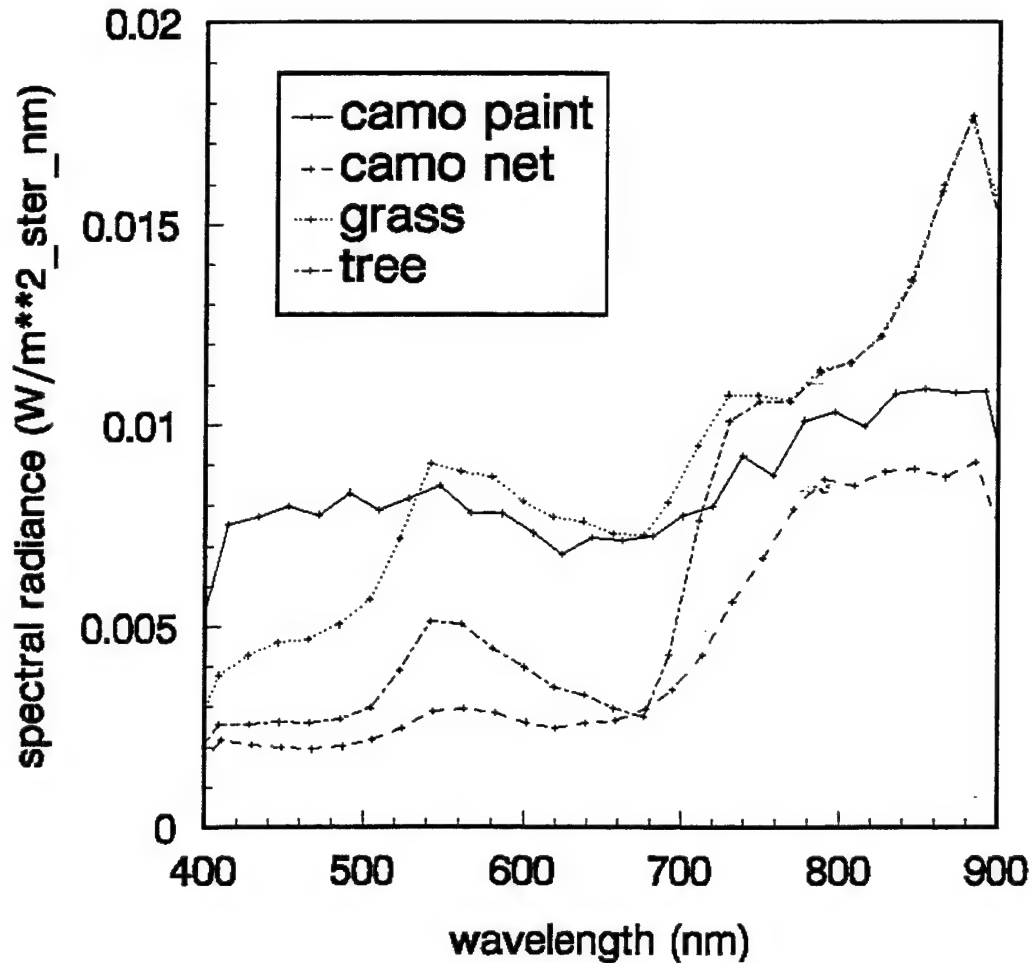


Figure 4. An example of data from a camouflage net and natural objects.

3. Summary

The Electro-Optics group at ARL-BE plans to fully investigate the use of this instrument in the coming months. This instrument should prove invaluable in evaluating our spectral estimation model that is used for visualization and simulation. This tool will also be important in the evaluation of camouflage and the effects of the atmosphere on camouflage.

References

Moore, Virgil L., Real Time Imaging Spectroradiometer (RTISR) - Users Manual Version 2.3, SOC-R832-004-0995, Prepared under Contract DAAL01-93-C-2017, 29 September 1995.

CROSS-PLATFORM DEMONSTRATION OF COMBIC GRAPHICAL USER INTERFACE (GUI)

Karen M. McLaughlin and Melanie M. Coakley
SPARTA, Inc.
Huntsville, AL 35805, USA

ABSTRACT

Cross platform demonstration of SBIR, Environmental Interaction for EOSAEL, Phase I final product. Purpose of Phase I effort was to prove the possibility of a GUI built into the Microsoft Windows operating system and interacting with the EOSAEL library. To show this, SPARTA implemented the GUI for the COMBIC module and successfully integrated it with the COMBIC FORTRAN code. We incorporated a comprehensive on-line help capability as well as context sensitive help. We used a cross platform development tool for the effort and have demonstrated this cross platform capability by installing and executing the COMBIC GUI on the Macintosh and SUN Unix platforms generating identical COMBIC input files to that produced by the PC/Windows compatible version used for development. Conference presentation will include demonstration of the COMBIC GUI on all three platforms.

1. INTRODUCTION

SPARTA, Inc., was one of six teams competing in a Phase I SBIR effort to prove the possibility of executing the Environmentally Oriented Systems Atmospheric Effects Library (EOSAEL) in the Microsoft Windows operating system. The results of SPARTA's effort are detailed below.

2. RESULTS OF THE PHASE I WORK

The primary objectives of the Phase I effort were to (1) develop a plan to interface all EOSAEL modules to a PC/Windows environment and (2) demonstrate the feasibility of that plan by developing a prototype interface for the Combined Obscuration Model for Battlefield Induced Contaminants (COMBIC) module and installing it on a CD ROM. A secondary objective was to provide cross-platform capability for the COMBIC prototype by using Neuron Data's Open Interface* toolkit to develop the Graphical User Interface (GUI).

These objectives were fully satisfied in our Phase I product. Specific accomplishments of the Phase I effort are as follows:

- (1) We designed and produced a graphical icon for each of the EOSAEL modules that visually portrays the physical phenomenon represented in the module.

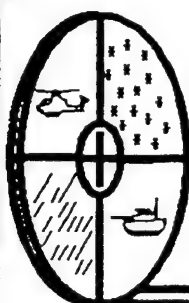
* Open Interface, Neuron Data Inc., 1310 Villa Street, Mountain View, CA 94041, (415) 528-3450

- (2) We designed GUIs for all the modules that organize the inputs into logically partitioned input screens and provide simple 'point and click' access to all the inputs.
- (3) We implemented the GUI for COMBIC and successfully integrated it with the COMBIC FORTRAN code, verifying that it produced output identical to that produced by the card-image input version of COMBIC.
- (4) We incorporated a comprehensive on-line help capability into COMBIC, including context sensitive help windows and a complete user's manual with hypertext for accessing topics of interest and pop-up windows for figures and equations. When the cursor is moved over an area for which context sensitive help is available, a visible change in the appearance of the cursor occurs as a signal to the user. Figures, tables and equations were regenerated in color where applicable and cleaned up for a clean finished appearance.
- (5) We demonstrated cross-platform capability of the COMBIC/GUI by installing and executing it on Macintosh and Sun UNIX platforms, generating identical COMBIC input files to that produced in the PC/Windows environment.
- (6) We recorded the enhanced COMBIC on a CD ROM and successfully executed the program from the CD ROM. The CD ROM setup includes a professional style install and uninstall routine. The install routine queries the user as to a preference to install the COMBIC application to the user's hard drive or running it from the CD.

COMBIC is among the most complex of the EOSAEL modules. Therefore, the success of the COMBIC/GUI development and CD ROM installation establishes the feasibility of GUI development for the entire EOSAEL suite, which is the objective of the planned Phase II effort.

Appendix A

AGENDA



1995
**Battlefield
Atmospherics
Conference**

5 - 7 December 1995

**WHITE SANDS MISSILE RANGE
NEW MEXICO**



AGENDA



Sponsored by
U.S. ARMY RESEARCH LABORATORY
Battlefield Environment Directorate
White Sands Missile Range, New Mexico

Tuesday, 5 December 1995

0730 **REGISTRATION** (Coffee & Tea)

0830 **Welcome**, BG Jerry L. Laws,
Commanding General, WSMR



0840 **Administrative Announcements**
Introduction of Keynote Speaker
Don R. Veazey, Director
Battlefield Environment Directorate (BED)

0900 **Keynote Address**, Brig. Gen. Thomas J. Lennon,
USAF Director of Weather

1000 **BREAK** (Refreshments)

SESSION I: OPERATIONAL WEATHER

Session Chair: John R. Erick, BED (ARL)
Invited Co-Chair: MAJ Robert L. Hamilton, Jr.,
HQ TRADOC

1030 **Introduction**

1040 **Navy/Air Force Cooperation (NAVAF Coop) Status Report**
Lt Col(S) Michael J. Buehl, USAF Naval
Meteorology and Oceanography Command,
Stennis Space Center, MS

1100 **Technical Validation of the Battlescale Forecast Model**
David I. Knapp and Robert E. Dumais, Jr., U.S.
Army Research Laboratory (BED), WSMR, NM

1120 **Pre-Operational Tests of the NRL Coupled Ocean/Atmosphere Mesoscale Prediction System (COAMPS)**
Richard M. Hodur, Naval Research Laboratory,
Monterey, CA

1140 **Standardized Climatological Support Package for Army Operations**
Kenneth R. Walters, Sr. and 2nd Lt Kenneth P. Cloys, Readiness Support Branch, USAF
Environmental Technical Applications Center,
Scott AFB, IL

1200 **LUNCH**

SESSION II: BATTLE WEATHER INTEGRATION

Session Chair: Edward M. Measure, BED (ARL)
Invited Co-Chair: (to be determined)

1300 **Introduction**

1310 **The UAV Dropsonde: Concept and Preliminary Results**
James L. Cogan, U.S. Army Research Laboratory
(BED), WSMR, NM; James Thomas, Thomas
Greenling, and S.A. Lucas, Physical Science
Laboratory, NMSU, Las Cruces, NM

1330 **The Battle Weather Test Bed: A System for Product Development for the Integrated Meteorological System**
John R. Erick, U.S. Army Research Laboratory
(BED), WSMR, NM

1350 **BFM Application to Artillery Meteorology**
Teizi Hanmi, and Abel J. Blanco, U.S. Army
Research Laboratory (BED), WSMR, NM; John
Spalding, Physical Science Laboratory, NMSU,
Las Cruces, NM

1410 **Validation of a Mass Consistent Wind Model at White Sands Missile Range**
John Sontowski, Robert M. Cox, Cathy
Dougherty, and Richard N. Fry, Jr. HQ,
DNA/SPWE, Alexandria, VA

- 1430 Weather Impact Decision Aids for E-O Weapons Support
Lt. Col. Joe Alleca, Phillips Laboratory/Geophysics Directorate, Hanscom AFB, MA
 Will be presented by 1st Lt. Dana M. Madsen

- 1450 "Knowing" the Weather for Army Battlefield Operations
Harold L. Massie, Jr., Ken Smith, Douglas Pearson, HQ USAF Directorate of Weather, Washington, DC, and *Richard Szymber*, U.S. Army Research Laboratory, Ft Huachuca, AZ

1510 Poster Introduction

1520 BREAK (Refreshments)

1550 Poster Session

1700 Adjournment

Wednesday, 6 December 1995

SESSION III: BOUNDARY LAYER RESEARCH

Session Chair: *Ronald Cionco*, BED (ARL)

Invited Co-Chair: *Dr. Joseph H. Shinn*
 Lawrence Livermore Laboratory

0800 Introduction

- 0810 Large Eddy Simulation Probability Density Function Modeling Over Complex Terrain and Structures
Ronald E. Meyers and *Keith S. Deacon*, U.S. Army Research Laboratory (BED), WSMR, NM

- 0830 Atmospheric Transport over White Sands Missile Range
Maj Robert M. Cox, John Sontowski, Richard N. Fry, Jr. and *Cathy Dougherty*, HQ DNA/SPWE, Alexandria, VA

- 0850 Analysis of Condensation Nuclei Counter Measurements in the Arabian Gulf and the Gulf of Oman
Andreas K. Goroch, Marine Meteorology Division, Naval Research Laboratory, Monterey, CA; *John W. Reay*, U.S. Army Research Laboratory (BED), WSMR, NM

- 0910 Measured Parameters of Puff Dispersion
Max P. Blalweis and *Christopher D. Padilla*, U.S. Army Research Laboratory (BED), WSMR, NM; *Kenneth C. Payne*, and *Donald Stogden*, Physical Science Laboratory, NMSU, Las Cruces, NM

0930 BREAK (Refreshments)

- 1000 High Resolution Urban Morphology Data for Urban Flow Modeling
Ronald M. Cionco, U.S. Army Research Laboratory (BED), WSMR, NM; *Richard Ellefsen*, San Jose State University, San Jose, CA

- 1020 High Resolution Wind Field Simulations Run Real-Time and with Other Inputs to Optimize Model Output
Ronald M. Cionco and *John H. Byers*, U.S. Army Research Laboratory (BED), WSMR, NM

- 1040 Solar Eclipse Effects Observed at the Atmospheric Profiler Research Facility
F.D. Eaton, J. R. Hines, W.H. Hatch, D. Schlegel, W. Parsons, R.M. Cionco, J. Byers, and *D. Garvey*, U.S. Army Research Laboratory (BED), WSMR, NM; *David R. Miller*, University of Connecticut, Storrs, CT

- 1100 A Discussion of Profiler Accuracies at the Atmospheric Profiler Research Facility
John R. Hines and *F. Eaton*, U.S. Army Research Laboratory (BED), WSMR, NM; *G. Hoidale*, W. Flowers and *L. Parker-Sedillo*, Science and Technology Corporation, Las Cruces, NM

- 1120 Forecasting Atmospheric Optical Turbulence Neutral Events-Part II
Gail Tirrell Vaucher and *Robert W. Endlich*, U.S. Army Research Laboratory (BED), WSMR, NM

1140 LUNCH

SESSION IV: ATMOSPHERIC PHYSICS

Session Chair: *Max Blalweis*, BED (ARL)

Co-Chair: *Thomas H. Vonder Haar*, Colorado State University

1300 Introduction

- 1310 Overview of DoD-Sponsored Research at the Cooperative Institute for Research in the Atmosphere (CIIRA)

Kenneth E. Ele, *Thomas H. Vonder Haar*, and *Donald L. Reinke*, Cooperative Institute for Research in the Atmosphere (CIIRA), Ft. Collins, CO

- 1330 The New Atmospheric Profiler Research Facility Barometer Network
W.H. Hatch, F.D. Eaton, J.R. Hines, and *W.S. Parsons*, U.S. Army Research Laboratory (BED), WSMR, NM

- 1350 First Results with a New Type of Radiometer
Edward M. Messers, U.S. Army Research Laboratory (BED), WSMR, NM

- 1410 Bi-Fractional Analysis: from 1D to 2D (with Wavelets)(Invited Paper)
Anthony Davis, Visiting Scientist from Canada, Goddard Space Flight Center, Greenbelt, MD

1435 BREAK (Refreshments)

- 1500 Radiative Properties of Fractal Clouds (Invited Paper)
Alexander Marshak, Visiting Scientist from FRU, Goddard Space Flight Center, Greenbelt, MD

- 1535 New Formulations for the Scattering of Sound in a Moving Random Medium
John M. Noble, U.S. Army Research Laboratory (BED), WSMR, NM and *V.E. Ostashev*, Fachbereich Physik, Universität Oldenburg, GE

- 1555 Obscure Mass Extinction Coefficient Determination by Least Absolute Deviation
Brian R. Bullard and *Roger E. Davis*, Science and Technology Corporation, Las Cruces, NM

- 1615 Detection of Optically-Active Particles by Laser Light Scattering Sensors
J. David Pendleton, David L. Rosen, and *James Gillespie*, U.S. Army Research Laboratory (BED), WSMR, NM

1635 Poster Introduction

1645 Poster Session

1715 Adjournment

1830 Banquet at the Hilton Hotel, Las Cruces, NM

Speaker - *Thomas H. Vonder Haar*
 Colorado State University

Thursday, 7 December 1995

SESSION V: ATMOSPHERIC SIMULATION AND ANALYSIS

Session Chair: Patti S. Gillespie, BED (ARL)

Invited Co-Chair: Major James Schaefer
AFCCC/MS, Scott AFB

0800 Introduction

0810 HADES: Hot and Dusty Environment Survey
(Invited Paper)
Andrew Tooth, British Aerospace, United Kingdom

0830 The Atmospheric Analysis Library
Young P. Yee, U.S. Army Research Laboratory (SLAD), WSMR, NM

0850 Multifractal Characterization as an Analytical Tool for Atmospheric Research
Thelma Chenault, Max P. Bleiweiss, and Rene Smith and Martin Bayang, U.S. Army Research Laboratory (SLAD) WSMR, NM

0910 Climatological and Historical Analysis of Clouds for Environmental Simulations (CHANCES) - Applications to Battlefield Atmospherics
Donald L. Reinke, Thomas H. Vonder Haar, and Kenneth E. Els, STC-METSAT, Fort Collins, CO

0930 Prediction of Infrared Scenes Using Artificial Neural Networks
Peter Soliz, Applied Sciences Laboratory, Inc., Albuquerque, NM; Joseph Eicher, Air Force Phillips Laboratory, Albuquerque, NM; George C. Koenig, Cold Regions Research and Engineering Laboratory, Hanover, NH

0950 **BREAK** (Refreshments)

1020 Scene Generation Including Multiply-Scattered Diffuse Radiance from Finite Clouds
Donald W. Hoock, U.S. Army Research Laboratory (BED), WSMR, NM; Sean G. O'Brien, John C. Giever and J. McGee, Physical Science Laboratory, NMSU, Las Cruces, NM

1040 Evaluation of WAVES Using Image Statistics
Patti Gillespie, U.S. Army Research Laboratory (BED), WSMR, NM and J. Michael Rollins, Science and Technology Corporation, Las Cruces, NM

1100 A Hybrid GIS and 3D Infrared Target/Background Modeling System
Guy Seeley, Radex Inc and Steve Luker, USAF, Phillips Laboratory/Geophysics Directorate, Hanscom AFB, MA

1120 Thermal Contrast Model Performance in Various Weather
Stan Heckman, Phillips Laboratory/Geophysics Directorate, Hanscom AFB, MA

1150 **LUNCH**

1310 Texture Generation for Use in Synthetic Scenes
Clem Z. Ota and J. Michael Rollins, Science and Technology Corporation, Las Cruces, NM; Max P. Bleiweiss, U.S. Army Research Laboratory (BED), WSMR, NM

1330 Atmospheric Effects Interpolation Algorithm
Glenn J. Higgins, Melanie J. Gouveia, P.D. Hestand, and Michael S. Seaborn, TASC, Reston, VA

1350 DVBETA - A Practical Tool for Battlefield Environment Analysis
Shlomit Grossman, A. Katz, G. Sagi, D. Elal, Hancel-System Engineering Division TAAS-Israel Industries Ltd., Ramat Hasharon, Israel

1410 Temporal Behavior of Natural Terrain Radiance at Infrared Wavelengths
Max P. Bleiweiss and Christopher D. Padilla, U.S. Army Research Laboratory (BED), WSMR, NM

1430 Acoustic Propagation and Detection Probabilities applied to Battlefield Simulations.
David H. Marlin, U.S. Army Research Laboratory (BED), WSMR, NM

1450 Shadow Zone Boundary Limitation of the Effective Acoustical Turbulence Scattering Volume using the Turbulence Ensemble Model
Harry J. Auvermann, U.S. Army Research Laboratory (BED), WSMR, NM and George H. Goedecke, Department of Physics, NMSU, Las Cruces, NM

1510 Poster Introduction--

1520 **BREAK** (Refreshments)

1540 Poster Session

1700 Adjournment

POSTER PRESENTATIONS

Tuesday, 5 December 1995

SESSION I: OPERATIONAL WEATHER

BFM Output as a Weather Forecasting Tool
Jeffrey Passner, U.S. Army Research Laboratory (BED), WSMR, NM

A Statistical Verification of the U.S. Army Battlescale Forecast Model: Case Study of Ft. Irwin, CA, April 1994
Robert E. Dumais, Jr., U.S. Army Research Laboratory (BED), WSMR, NM

Real-Time PC Interface and Applications of AWDS
Bruce L. Bauer, M. Noosh, and T. Myers, Mission Research Corporation, Huntsville, AL; R.M. Cox, Defense Nuclear Agency, Alexandria, VA

An Assessment of the Potential of the Meteorological Office Mesoscale Model to Produce Artillery Ballistic Messages, and Further Applications
Jonathan D. Turton and Peter F. Davies, Defence Projects, The Meteorological Office, United Kingdom

SESSION II: BATTLE WEATHER INTEGRATION

Survivability/Lethality and Battlefield Atmospherics: A Concept Paper
Robert A. Sutherland and Jill C. Thompson, U.S. Army Research Laboratory (SLAD), WSMR, NM; Robert C. Brown, U.S. Army Research Laboratory (BED), WSMR, NM; Louie Dominguez, U.S. Army TRADOC Analysis Center, WSMR, NM

Dual Technology Use for Coastal Maritime Search and Rescue
Marcos C. Sola and Glen Dockery, U.S. Army Research Laboratory, Adelphi, MD; Ken Miller and Jaime Gonzalez, Night Vision & Electronic Sensors Directorate (ARL), Adelphi, MD

The Processing, Databasing, and Displaying of AVHRR and DMSP Data for the Integrated Meteorological System
Stephen F. Kirby, U.S. Army Research Laboratory (BED), WSMR, NM

Automated Thermal Injury Risk Assessment for the Dismounted Soldier
Gary B. McWilliams and Eugene S. Barnes, U.S. Army Research Laboratory (BED), WSMR, NM; William T. Matthew, U.S. Army Research Institute of Environmental Medicine, Natick, MA

Programs for Access and Manipulation of Forecast Weather Data for the Purpose of Tactical Decision Aid Support on the Army Research Laboratory Weather Test Bed
Patrick V. Laybe, U.S. Army Research Laboratory (BED), WSMR, NM

Battlescale Forecast Model (BFM)
Teizi Henmi, Robert E. Dumaiz, Jr. and David I. Knapp, U.S. Army Research Laboratory (BED), WSMR, NM;
Danforth C. Weems, Physical Science Laboratory, NMSU, Las Cruces, NM

Evaluation of the EOTDA V3.1 at Naval Air Station Whidbey Island
Andreas K. Goroch, Steven B. Dreksler, and Gene Crain, Naval Research Laboratory, Monterey, CA

Ground Forces Weather Workstation and Trafficability Assessment Tool Based Upon Satellite Sensor Information and Forecast Weather Conditions
John B. Bolton, Christa Clynn, and Scott Risch, Sterling Software, ITD, Bellevue, NE

Selection of the Theater Forecast Model
Bruce L. Bauer, and C. Tremback, Mission Research Corporation, Ft. Collins, CO; R.M. Cox, Defense Nuclear Agency, Alexandria, VA; B.G. Shapiro, USAF Environmental Technical Application Center, Scott AFB, IL

Wednesday, 6 December 1995

SESSION III: BOUNDARY LAYER RESEARCH

Analysis of Signal Perturbations Measured by the BAT Acoustic Sensor Suite
John R. Fox, U.S. Army Research Laboratory (BED), WSMR, NM and Prasen Chintawongavanich, Physical Science Laboratory, NMSU, Las Cruces, NM

ARL Professional Exchange Program (APEX) to Israel for Meteorology
Arnold D. Tunick, U.S. Army Research Laboratory (BED), WSMR, NM

Putting Real Meteorology into Transport and Diffusion Models
Ronald E. Meyers, Keith S. Deacon and John Martin, U.S. Army Research Laboratory (BED), WSMR, NM

Boundary Layer Refractive Index Structure Parameter - Calibrating the APRF Sodar
John R. Hines, F. Eaton and W. Hatch, U.S. Army Research Laboratory (BED), WSMR, NM

The NOAA Boulder Atmospheric Observatory Boundary Layer Study - Clear Air or Not?
John R. Hines, F. Eaton and W. Hatch, U.S. Army Research Laboratory (BED), WSMR, NM; C. Riese, Radian Corporation, Austin, TX

Modelling and Measurements of Optical Turbulence in the Terrestrial Boundary Layer
D.L. Hutt and D. Stryckman, Defence Research Establishment Valcartier, Quebec, CANADA

SESSION IV: ATMOSPHERIC PHYSICS

Composite Profiles of Vertical Velocity Variance
W.H. Hatch, F.D. Eaton, and J.R. Hines, U.S. Army Research Laboratory (BED), WSMR, NM

Multifractal Analysis of Nonstationarity and Intermittency in Sodar Measured Wind
William A. Peterson, Thelma Chenault and Marie T. Madrid, U.S. Army Research Laboratory (SLAD), WSMR, NM

Number of Laser Wavelengths Limit Biodetection in Fluorescence Lidar
David Rosen and James Gillespie, U.S. Army Research Laboratory (BED), WSMR, NM

Thursday, 7 December 1995

SESSION V: ATMOSPHERIC SIMULATION & ANALYSIS

A High Spatial and Temporal Resolution Database for Synthetic Scene Generation and Validation
Max P. Bleiweis, U.S. Army Research Laboratory (BED), WSMR, NM; Thomas Cassidy, George G. Koenig and James P. Welsh, SWOE JT&E Program Office, Hanover, NH

Visualization Tools for Artificial and Polarized Illumination of Obscure Clouds
Sean G. O'Brien, John C. Giever and Steven J. McGee, Physical Science Laboratory, Las Cruces, NM; Donald W. Hock, U.S. Army Research Laboratory (BED), WSMR, NM

Atmospheric Experiments with an Imaging Spectral Radiometer
Patti Gillespie, David Tofsted and Samuel Crow, U.S. Army Research Laboratory (BED), WSMR, NM

Application of Artificial Neural Networks to Battlefield Atmospherics
Peter Soliz, Applied Sciences Laboratory, Inc., Albuquerque, NM; Thomas P. Caudell, University of New Mexico, Albuquerque, NM

Modeling Anisotropic Scatterers with the FFP-Based Acoustic Multi-Stream Propagation Program
Markku P. Kotiaho, U.S. Army Research Laboratory (BED), WSMR, NM

A Department of Defense Software Architecture
Frank O. Clark, Phillips Laboratory, Hanscom AFB, MA

The Atmosphere and Weather: PLEXUS
Dale Sinclair, Phillips Laboratory/Geophysics Directorate, Hanscom AFB, MA

Demonstration of a Windows-Based Weather Impact Decision Aid
John P. DiTuodi and Peter Soliz, Applied Sciences Laboratory, Inc., Albuquerque, NM; John M. Hickey, Cimarron Computer Engineering, Inc., Albuquerque, NM

Cross-Platform Demonstration of Combic Graphical User Interface (GUI)
Karen M. McLaughlin and Melanie M. Coakley, SPARTA, Inc., Huntsville, AL

Appendix B

ATTENDEE LIST

ATTENDEE LIST
1995 BATTLEFIELD ATMOSPHERICS CONFERENCE
5-7 DECEMBER 1995
WHITE SANDS MISSILE RANGE, NM

ALEXANDER, MR. MICHAEL S.
U.S. Army Test & Evaluation Command
Atmos Sciences Div, Meth & Proj Br
ATTN: AMSTE-TC-AA
White Sands Misl Range, NM 88002-5504
Phone: (505) 678-1316 DSN 258-1316

AUVERMANN, DR. HARRY J.
U.S. Army Research Laboratory
Battlefield Environment Directorate
ATTN: AMSRL-BE-S
White Sands Misl Range, NM 88002-5501
Phone: (505) 678-4224 DSN 258-4224

AYRES, MS. SCARLETT D.
U.S. Army Research Laboratory
Survivability/Lethality Analysis Dir
ATTN: AMSRL-SL-CA
White Sands Misl Range, NM 88002-5501
Phone: (505) 678-4350 DSN 258-4350

BACH, JR., DR. WALTER D.
U.S. Army Research Office
ATTN: SLCRO-GS
P.O.BOX 12211
Research Triangle Park, NC 27709-2211
Phone: (919) 549-4247 DSN 832-4247

BARNES, MR. EUGENE
Combat Weather Facility
Bldg 91027
ATTN: AMSRL-BE-W CWF/CWJ
595 Independence Road
Hurlburt Field, FL 32544-0000
Phone: (904) 884-5349 DSN 579-5349

BAUER, DR. BRUCE L.
MISSION RESEARCH CORPORTATION
6703 ODYSSEY DRIVE, SUITE 101
HUNTSVILLE, AL 35806-3301
Phone: (205) 922-5549

BAUGH, MR. WILLIAM C.
Environmental Technologies Group, Inc.
PO Box 9840
1400 Taylor Avenue
Baltimore, MD 21284-9840
Phone: (410) 321-5315

BENNETT, MR. WILLIAM H.
Aerojet Electro Systems, 1-1/7211
P.O. Box 296
1100 West Hollyvale Street
Azusa, CA 91702-0000
Phone: (818) 812-1321

BERNASCONI, MR. LOU
Aerojet
8511 Osuna NE
Albuquerque, NM 87111
Phone: (505) 292-2082

BILLINGSLEY, MR. DANIEL R.
U.S. Army Research Laboratory
Battlefield Environment Directorate
ATTN: AMSRL-BE-S
White Sands Misl Range, NM 88002-5501
Phone: (505) 678-4313 DSN 258-4313

BLANCO, MR. ABEL J.
U.S. Army Research Laboratory
Battlefield Environment Directorate
ATTN: AMSRL-BE-W
White Sands Misl Range, NM 88002-5501
Phone: (505) 678-3924 DSN 258-3924

BLEIWEISS, MR. MAX P.
U.S. Army Research Laboratory
Battlefield Environment Directorate
ATTN: AMSRL-BE-S
White Sands Misl Range, NM 88002-5501
Phone: (505) 678-3504 DSN 258-3504

BOLTON, MR. JOHN
Sterling Software, ITD Lead Engineer
1404 Fort Crook Road South
BellevueE, NE 68005
Phone: (402) 291-8300 DSN 294-8300

BRANO, MR. HARRY LEE
46 OSS/OSWT
601 W. Choctawhatchee Ave, Suite 60
Eglin AFB, FL 32542-5719
Phone: (904) 882-5960 DSN 872-5960

BROWN, DR. DOUGLAS R.
U.S. Army Research Laboratory
Battlefield Environment Directorate
ATTN: AMSRL-BE
White Sands Misl Range, NM 88002-5501
Phone: (505) 678-1225 DSN 258-1225

BROWN, PROF GARY S.
Virginia Polytechnical Institute
Department of Electrical Engineering
EMIL
Blacksburg, VA 24601-0111
Phone: (540) 231-4467

BROWN, MR. ROBERT C.
U.S. Army Research Laboratory
Battlefield Environment Directorate
ATTN: AMSRL-BE-W
White Sands Misl Range, NM 88002-5501
Phone: (505) 678-5424 DSN 258-5424

BRUCE, DR. DOROTHY A.
U.S. Army Research Laboratory
Battlefield Environment Directorate
ATTN: AMSRL-BE-S
White Sands Misl Range, NM 88002-5501
Phone: (505) 678-5524 DSN 258-5524

BUELL, LT COL(S) MICHAEL J.
Naval Meteorology and Oceanography Cmd
1020 Balch Blvd
Stennis Space Center, MS 39529-5005
Phone: (601) 688-5051 DSN 485-5051

BUIMER, MAJ A.R.
Royal Netherlands Army
Infantry Training Center
PO Box 853
3840 AW Harderwijk
NETHERLANDS

BULLARD, MR. BRIAN R.
Science and Technology Corporation
555 Telshor Boulevard, Suite 200
Las Cruces, NM 88011-0000
Phone: (505) 521-4353

BYERS, MR. JOHN H.
U.S. Army Research Laboratory
Battlefield Environment Directorate
ATTN: AMSRL-BE-S
White Sands Misl Range, NM 88002-5501
Phone: (505) 678-3951 DSN 258-3951

CARRILLO, MR. JESUS E.
Research Analysis and Maintenance, Inc
1790 Lee Trevino Drive
El Paso, TX 79936-0000

CHENAULT, MS. THELMA
U.S. Army Research Laboratory
Survivability & Lethality Directorate
ATTN: AMSRL-SL-CA
White Sands Misl Range, NM 88002-5501
Phone: (505) 678-6579 DSN 258-6579

CHIN, MR. KEN
U.S. Army CECOM/IEWD
ATTN: AMSEL-RD-IEW-TAM
Ft. Monmouth, NJ 07746-0000
Phone: (908) 427-5638 DSN 987-5638

CHRISTENSEN, MRS. CHARLOTTE
Danish Defence Command
Po Box 202
2950 Vedbaek
DENMARK

CHU, MR. PETER C.
Naval Postgraduate School
Department of Oceanography
Code OC/CU
833 Dyer Road
Monterey, CA 93943-5100
Phone: (408) 656-3688 DSN 878-3688

CIONCO, MR. RONALD M.
U.S. Army Research Laboratory
Battlefield Environment Directorate
ATTN: AMSRL-BE-S
White Sands Misl Range, NM 88002-5501
Phone: (505) 678-5210 DSN 258-5210

CLARK, CDR ROBERT
Chief of Naval Operations (CNO (NO96)
Oceanographer of the Navy
U.S. Naval Observatory Bldg 1
3450 Massachusetts Ave, NW
Washington, DC 20392-5421
Phone: (202) 762-1024 DSN 762-1024

CLOY, LT KENNETH P.
AF Combat Climatology Center
AFCCC/DOJ
BLDG 859, RM 509, Buchanan St.
Scott AFB, IL 62225-5116
Phone: (618) 256-3465 DSN 576-3465

COAKLEY, MRS. MELANIE M.
SPARTA Inc
4902 Corporate Drive
Hunstville, AL 35805-0000

COGAN, DR. JAMES L.
U.S. Army Research Laboratory
Battlefield Environment Directorate
ATTN: AMSRL-BE-W
White Sands Misl Range, NM 88002-5501
Phone: (505) 678-2094 DSN 258-2094

COREY, MR. THOMAS D.
Air Force Technical Applications Center
AFTAC/TXK
1030 S. Highway A1A
Patrick AFB, FL 32925-3002
Phone: (407) 494-7250 DSN 854-7250

COX, MAJ ROBERT M.
National Defense University
BLDG 62, RM 301C
Ft. McNair, WASH DC 22310-3398
Phone: (202) 287-9380/251 DSN 667-9330

CREEGAN, MR. EDWARD D.
U.S. Army Research Laboratory
Battlefield Environment Directorate
ATTN: AMSRL-BE-W
White Sands Misl Range, NM 88002-5501
Phone: (505) 678-4684 DSN 258-4684

CREMERS, MR. B.E.
TNO Prins Maurits Laboratory
PO Box 45
2280 AA Rijswijk
NETHERLANDS

CROW, MR. SAMUEL B.
U.S. Army Research Laboratory
Battlefield Environment Directorate
ATTN: AMSRL-BE-S
White Sands Misl Range, NM 88002-5501
Phone: (505) 678-4313 DSN 258-4313

CZARNIECKI, LTC JOSEPH
2nd Weather Flight
18th Air Support Operations Group
532 Swan Creek Road
Fort Washington, MD 20744-0000
Phone: (301) 292-3838 DSN 572-2520

DAVIDSON, DR. TOM
Physical Science Laboratory
New Mexico State University
Box 30002
Las Cruces, NM 88003

DAVIES, MR. PETER
The Meteorological Office
ROOM 117, Defence Projects
BRACKNELL
UNITED KINGDOM
Phone: 44-1344-856985

DAVIS, MR. ANTHONY
SSAI & NASA/GSFC
Goddard Space Flight Center
Code 913 (Anthony Davis)
Greenbelt, MD 20771

DAVIS, MR. JOHN
Colorado State University
Atmospheric Science
Foothills Campus
Fort Collins, CO 80523-0000

DAVIS, DR. ROGER E.
Science and Technology Corporation
555 Telshor Boulevard, Suite 200
Las Cruces, NM 88011-0000
Phone: (505) 521-4353

DEEPAK, DR. ADARSH
Science and Technology Corporation
101 Research Drive
Hampton, VA 23666-1340
Phone: (804) 865-1894

DEVORE, MR. JOHN G.
Visidyne, Inc.
5951 Encina Road, Suite 208
Goleta, CA 93117-2211
Phone: (805) 683-4277

DICKENSHIED, MR. ROBERT L.
U.S. Army Research Laboratory
Battlefield Environment Directorate
ATTN: AMSRL-BE-W
White Sands Misl Range, NM 88002-5501
Phone: (505) 678-1153 DSN 258-1153

DIXON, CAPT JAMES J.
MAWTS-1
ATTN: AGS Box 99200
Yuma, AZ 85369-9200
Phone: (520) 341-2534 DSN 951-2534

DREKSLER, MR. STEVEN B.
MAR, Inc.
Naval Research Laboratory
7 Grace Hopper Avenue
Monterey, CA 93940-0000
Phone: (408) 656-4838 DSN 878-4838

DUCHOW, MRS. LINDA
U.S. Army Research Laboratory
Battlefield Environment Directorate
ATTN: AMSRL-BE
White Sands Misl Range, NM 88002-5501
Phone: (505) 678-2672 DSN 258-2672

DUMAIS, JR., MR. ROBERT E.
U.S. Army Research Laboratory
Battlefield Environment Directorate
ATTN: AMSRL-BE-W
White Sands Misl Range, NM 88002-5501
Phone: (505) 678-4650 DSN 258-4650

DUNKEL, MR. MICHAEL D.
Optimetrix, inc.
1 Newport Drive, Suite H
Forest Hill, MD 21050-000

EATON, DR. FRANK D.
U.S. Army Research Laboratory
Battlefield Environment Directorate
ATTN: AMSRL-BE-E
White Sands Misl Range, NM 88002-5501
Phone: (505) 678-3956 DSN 258-3956

EIS, MR. KENNETH E.
Cooperative Institute for Research
in the Atmosphere (CIRA)
Foothills Campus, Colorado State Univ
Fort Collins, CO 80523-0000
Phone: (970) 491-8448

ELRICK, MR. JOHN R.
U.S. Army Research Laboratory
Battlefield Environment Directorate
ATTN: AMSRL-BE-W
White Sands Misl Range, NM 88002-5501
Phone: (505) 678-3691 DSN 258-3691

ENDLICH, MR. ROBERT W.
U.S. Army Research Laboratory
Battlefield Environment Directorate
ATTN: AMSRL-BE-W
White Sands Misl Range, NM 88002-5501
Phone: (505) 678-6297 DSN 258-6297

ESPARZA, MS. JOANNE M.
Physical Science Laboratory
New Mexico State University
P.O. Box 30002
Las Cruces, NM 88003-0002
Phone: (505) 522-9117

ESSENWANGER, DR. OSKAR M.
University of Alabama in Huntsville
Atmos & Environmental Science Dept
Research Institute, Room A-11
610 Mountain Gap Drive
Huntsville, AL 35803-1630
Phone: (205) 895-6296

FALTINOWSKI, MAJ GARY R.
Space and Naval Warfare Systems Command
SPAWARSSYSCOM
2451 Crystal Drive, PMW 175-1D RM 301
Arlington, VA 22245-5200
Phone: (703) 602-3891 DSN 332-3891

FRASIER, DR. JOHN T.
Associate Director for Science & Tech
U.S. Army Research Laboratory
ATTN: AMSRL-ST
2800 Powder Mill Rd.
Adelphi, MD 20783-1145
Phone: (301) 394-4152 DSN 290-4152

FREEMAN, DR. K. PATRICK
Science and Technology Corporation
555 Telshor Boulevard, Suite 200
Las Cruces, NM 88011-0000
Phone: (505) 521-4353

GAMSON, MR. JOSEPH
U.S. Army Research Laboratory
ATTN: AMSRL-CP-PE
2800 Powder Mill Road
Adelphi, MD 20783-1145
Phone: (301) 394-3557

GARVEY, DR. DENNIS
U.S. Army Research Laboratory
Battlefield Environment Directorate
ATTN: AMSRL-BE-S
White Sands Misl Range, NM 88002-5501
Phone: (505) 678-5677 DSN 258-5677

GIEVER, MR. JOHN C.
Physical Science Laboratory
New Mexico State University
P.O. Box 30002
Las Cruces, NM 88003-0002
Phone: (505) 678-3280

GILLESPIE, DR. PATTI L.
U.S. Army Research Laboratory
Battlefield Environment Directorate
ATTN: AMSRL-BE-S
White Sands Misl Range, NM 88002-5501
Phone: (505) 678-1817 DSN 258-1817

GOROCH, DR. ANDREAS K.
US Naval Oceanolgraphic and
Atmospheric Research Laboratory
7 Grace Hopper Avenue
Monterey, CA 93943-5006
Phone: (408) 656-4889 DSN 878-4889

GROSSMAN, MS. SHLOMIT
TAAS - Israel Industries Ltd
HANCAL-System Engineering Division
PO Box 1044/45
ISRAEL
Phone: 972 3 5484265

HAGERTY, DR. PATRICK E.
United Defense, L.P.
4800 E. River Road
Minneapolis, MN 55421-1498
Phone: (612) 572-4787

HALL, CDR CHRISTOPHER
COMDAVMETOCOM
1020 Balch Blvd
Stennis Space Center, MS 38529-5005
Phone: (601) 688-4840 DSN 485-4840

HALLIN, MR. STEPHEN C.
ESC/XRCW
50 Griffiss Street
Hanscom AFB, MA 01731-1624
Phone: (617) 271-8621 DSN 478-1186

HAMILTON, JR., MAJ ROBERT L.
HQ TRADOC
ATTN: ATDO-IW
Ft Monroe, VA 23651-5000
Phone: (804) 727-2319 DSN 680-2319

HARMS, MAJ DEWEY
HQ Air Weather Service/XOX
102 West Losey Street, Room 105
Scott AFB, IL 62225-5206
Phone: (618) 256-5631x443 DSN 576-5631

HARRELSON, MR. HAL
U.S. Army Research Laboratory
IS&T
2800 Powder Mill Road
Adelphi, MD 20783-1197
Phone: (202) 394-4362 DSN 290-4362

HARRIS, MR. JAMES E.
U.S. Army Research Laboratory
Battlefield Environment Directorate
ATTN: AMSRL-BE-W
White Sands Misl Range, NM 88002-5501
Phone: (505) 678-1339 DSN 258-1339

HARRISON, JR., DR. EDWARD J.
Computer Sciences Corporation
Ap 2, Suite 4000
2611 Jefferson Davis Hwy
Arlington, VA 22202-0000
Phone: (703) 418-8534

HASDAL, DR. JOHN A.
Teledyne Brown Engineering
300 Sparkman Drive NW (MS/50)
Huntsville, AL 35807-0000
Phone:

HATCH, MR. WILLIAM H.
U.S. Army Research Laboratory
Battlefield Enviroment Directorate
ATTN: AMSRL-BE-S
White Sands Misl Range, NM 88002-5501
Phone: (505) 679-9621 DSN 258-3956

HECKMAN, MR. STAN
SSAI/PL-GPAA
Phillips Lab, Geophysics Directorate
29 Randolph Road
Hanscom AFB, MA 01331

HEIMMER, MR. JOHN
Lockheed Martin (GES)
199 Borton Landing Road, MS137-110
Moorestown, NJ 08057-0927

HICKEY, MR. JOHN
Cimarron Computer Engineering, Inc.
1416 Caballero Drive, SE
Albuquerque, NM 87123-4465

HIGGINS, MR. GLENN J.
TASC
12100 Sunset Hills Road
Reston, VA 22090-0000
Phone: (703) 834-5000

HIMBROOK, MR. RICHARD F.
U.S. Army Research Laboratory
ATTN: AMSRL-SL-CA
White Sands Misl Range, NM 88002-5501
Phone: (505) 678-4917 DSN 258-4917

HINES, MR. JOHN R.
U.S. Army Research Laboratory
Battlefield Environment Directorate
ATTN: AMSRL-BE-S
White Sands Misl Range, NM 88002-5501
Phone: (505) 678-1561 DSN 258-1561

HODUR, DR. RICHARD M.
Naval Research Laboratory
BOX 2 NRL
7 Grace Hopper Ave
Monterey, CA 93943-5502
Phone: (408) 656-4788 DSN 878-4788

HOLBERG, MR. BENJAMIN
U.S. Army Research Laboratory
Foreign Intelligence
ATTN: AMSRL-MO-IF
White Sands Misl Range, NM 88002-5501
Phone: (505) 678-8846 DSN 258-8846

HOCK, DR. DONALD W.
U.S. Army Research Laboratory
Battlefield Environment Directorate
ATTN: AMSRL-BE-S
White Sands Misl Range, NM 88002-5501
Phone: (505) 678-5430 DSN 258-5430

HOWARD, III, MAJ GEORGE F.
U.S. Army Intelligence Center &
Ft. Huachuca
ATTN: ATZS-CDS-W
Ft. Huachuca, AZ 85613-6000
Phone: (520) 538-6472 DSN 879-6472

HUGHES, DR. ROY J.
Land Space & Optoelectronics Div
Defence Science & Technology Organ
PO Box 1500
Salisbury, SA 5108
AUSTRALIA
Phone: 61-8-259-5683

HUTT, MR. DANIEL L.
Defence Research Establishment
Valcartier
P.O. Box 8800
CANADA
Phone: (418) 844-4707

INTRONE, JR., MR. ROBERT E.
The Analytic Sciences Corporation(TASC)
55 Walkers Brook Drive
Reading, MA 01867-0000
Phone: (617)942-2000/2331

JAMESON, MR. TERRY C.
Commander
WSMR Meteorology Branch
ATTN: STEWS-NRO-DA
White Sands Misl Range, NM 88002-5113
Phone: (505)679-9106/9116 DSN 349-9106

JOHNSON, MR. ODELL M.
U.S. Army Research Laboratory
Battlefield Environment Directorate
ATTN: ATSF-CBL
Fort Sill, OK 73503-5600
1-800-284-1559 639-1559

JURCHENKO, MR. DANIEL
LOCKHEED MARTIN (GES)
199 Borton Landing Road (MS-137-110)
Moorestown, NJ 08057-0927

KANTROWITZ, MR. FRANK T.
U.S. Army Research Laboratory
Battlefield Environment Directorate
ATTN: AMSRL-BE-S
White Sands Misl Range, NM 88002-5501
Phone: (505) 678-1526 DSN 258-1526

KATZ, DR. DAVID
TAAS - Israel Industries Ltd.
Hancal-System Engineering Division
POB 1044/45
ISRAEL

KELLY, CAPT JOHNATHAN L.
ESC/WE
11 Eglin Street
Hanscom AFB, MA 01731-2122
Phone: (617) 377-3238 DSN 478-3238

KIRBY, MR. STEVE F.
U.S. Army Research Laboratory
Battlefield Environment Directorate
ATTN: AMSRL-BE-W
White Sands Misl Range, NM 88002-5501
Phone: (505) 678-7474 DSN 258-7474

KNAPP, DAVID I.
U.S. Army Research Laboratory
ATTN: AMSRL-BE-W
White Sands Misl Range, NM 88002-5501
Phone: (505) 678-8148 DSN 258-8148

KOHLER, MR. CHARLES R.
U.S. Army Research Laboratory
10235 Burbeck Road
Ft Belvoir, VA 22060-5838
Phone: (703) 704-3198 DSN 654-3198

KREISS, DR. WILLIAM T.
Georgia Institute of Technology
Georgia Tech Research Institute
EOEML/315 Baker Building
925 Dalney Street
Atlanta, GA 30332-0800
Phone: (404) 894-4392

LAMOTTE, MR. STEVEN J.
Physical Science Laboratory
New Mexico State University
P.O. Box 30002
Las Cruces, NM 88003-0002
Phone: (505) 522-9322

LEBLANC, MR. ROBERT E.
ASI Systems International
838 North Eglin Parkway, Suite 201
Fort Walton Beach, FL 32547-0000
Phone: (904) 862-4188

LEHNEIS, MR KIRK
WL/DOWA
2690 C Street, Suite 2
Wright-Patterson AFB, OH 45433-7409
Phone: (513) 255-1978 DSN 785-1978

LENNON, BG THOMAS J.
HQ, USAF/XOW
1490 Air Force Pentagon, Rm 4A1084
Washington, DC 20330-1490
Phone: (703) 614-7410 DSN 224-7410

LUKER, DR. STEVE
Phillips Lab/GPAA
29 Randolph Road
Hanscom AFB, MA 01731-0000
Phone:

MACKEY, CAPT J. BRYAN
12th Air Support Operations Squadron
Bldg 11210 Slewitzke Rd
Biggs AAF
Ft. Bliss AIN, TX 79918-5000
Phone: (915) 568-8702/8409 DSN 978-8702

MADDIX, MR. MAT V.
U.S. Army Missile Command
ATTN: AMSMI-RD-SS-AA
Redstone Arsenal, AL 35898-5000
Phone: (205) 876-2339 DSN 746-2339

MADSEN, 1ST LT DANA M.
Phillips Lab/GPAA
29 Randolph Rd.
Hanscom AFB, MA 01731-0000

MARLIN, MR. DAVID
U.S. Army Research Laboratory
Battlefield Environment Directorate
ATTN: AMSRL-BE-S
White Sands Misl Range, NM 88002-5501
Phone: (505) 678-5447 DSN 258-5447

MARSHAK, MR. ALEXANDER
SSAI and NASA/GSFC
Goddard Space Flight Center
Code 913
Greenbelt, MD 20771-0000

MARTENS, CAPT DAVID
607th Weather Squadron/DOF
UNIT #15173
KOREA

MASSIE, JR., LT COL HAROLD L.
HQ USAF/XOWX
1490 Air Force Pentagon
WASH, DC 20330-1490

MATSUMOTO, COL CLIFFORD R.
HQ AWS/XO
102 Losey Street, Room 105
Scott AFB, IL 62225-5206
Phone: (618) 256-3363x251 DSN 576-3363

MATTHEWS, LT PAUL E.
U.S. Special Operations Command
J-2 METOC, USSOCOM SOJ2-METOC
7701 Tampa Point Blvd
McDill AFB, FL 33621-5323
Phone: (813) 828-6041/2 DSN 968-6041

MCCLATCHEY, DR. ROBERT A.
Phillips Lab/Geophysics Lab
ATTN: AFGL/LY
29 Randolph Road
Hanscom AFB, MA 01731-5000
Phone: (617) 377-2975 DSN 478-2975

MC GEE, MR. STEVE J.
Physical Science Laboratory
New Mexico State University
PO Box 30002
Las Cruces, NM 88003-0002
Phone: (505) 522-3280

MCKINNEY, CAPT KRIS F.
Air Force Combat Climatology Center
859 Buchanan St, Room 306
Scott AFB, IL 62225-5116
Phone: (618) 256-4107 DSN 576-4107

MCLAUGHLIN, MRS. KAREN M.
SPARTA, Inc.
4901 Corporate Drive
Huntsville, AL 35805-0000
Phone: (205) 837-5282/1605

MEANOR, CDR DENIS
CNO N096
Oceanographer of the Navy N961E
3450 Massachusetts Ave, NW
Washington, DC 20392-5421
Phone: (202) 762-1024 DSN 762-1024

MEASURE, DR. EDWARD M.
U.S. Army Research Laboratory
Battlefield Environment Directorate
ATTN: AMSRL-BE-W
White Sands Misl Range, NM 88002-5501
Phone: (505) 678-3307 DSN 258-3307

MERRITT, CAPT ROY
HQ ACC/DOWR
205 Dodd Blvd, Ste 101
Langley AFB, VA 23665-2789
Phone: (804) 764-8445 DSN 574-8445

NILES, DR STANLEY
U.S. Army Research Laboratory
Battlefield Environment Directorate
ATTN: AMSRL-BE-S
White Sands Misl Range, NM 88002-5501
Phone: (505) 678-3834 DSN 258-3834

NOBLE, MR. JOHN M.
U.S. Army Research Laboratory
Battlefield Environment Directorate
ATTN: AMSRL-BE-S
White Sands Misl Range, NM 88002-5501
Phone: (505) 678-3751 DSN 258-3751

NOVLAN, MR. DAVID J.
WSMR Meteorology Branch
ATTN: STEWS-NRO-DA-E
White Sands Misl Range, NM 88002-5504
Phone: (505) 679-9115 DSN 349-9115

O'BRIEN, DR. SEAN G.
Physical Science Laboratory
New Mexico State University
PO Box 30002
Las Cruces, NM 88003-0002
Phone: (505) 521-9560

OTA, MR. CLEM
Science and Technology Corporation
555 Telshor Boulevard, Suite 200
Las Cruces, NM 88011-0000
Phone: (505) 521-4353

OWEN, MR. HANK
Lockheed Martin (GES)
199 Barton Landing Road
Moorestown, NJ 08057-0927

PACE, MR. JOHN
Atmospheric Release Advisory Capability
Lawrence Livermore National Laboratory
L-262 PO Box 808
Livermore, CA 94550-0000

PALACIOS, MR. FERNANDO R.
U.S. Army Research Laboratory
Battlefield Environment Directorate
ATTN: AMSRL-BE-S
White Sands Misl Range, NM 88002-5501
Phone: (505) 678-1493 DSN 258-1493

PASSNER, MR. JEFFREY E.
U.S. Army Research Laboratory
Battlefield Environment Directorate
ATTN: AMSRL-BE-W
White Sands Misl Range, NM 88002-5501
Phone: (505) 678-3193 DSN 258-3193

PEARSON, COL DOUGLAS C.
NASA Code ME
Space Shuttle Headquarters Office
300 E. St, SW
WASH, DC 20546-0000

PENDLETON, DR. DAVID
U.S. Army Research Laboratory
Battlefield Environment Directorate
ATTN: AMSRL-BE-S
White Sands Misl Range, NM 88002-5501
Phone: (505) 678-4488 DSN 258-4488

PENTECOST, DR. H.T.A.
Defence Research Agency Military Div
RARDE
Fort Halstead, Sevenoaks
UNITED KINGDOM
Phone: 1959514823

PETERSON, DR. WILLIAM A.
U.S. Army Research Laboratory
Survivability & Lethality Directorate
ATTN: AMSRL-SL-CA
White Sands Misl Range, NM 88002-5501
Phone: (505) 678-1533 DSN 258-1533

PICARD, MR. ROLAND (RON)
Fleet Numerical Meteorology
Oceanography Center
1 Grace Hopper Ave, Stop 1
Monterey, CA 93901-0000
Phone: (408) 656-4549 DSN 878-4549

PLATT, CMSGT ROBERT W.
Det 1, 335TRS
Combat Weather Training - CWT
595 Independence Road, Bldg 91027
Hurlburt Field, FL 32544-5618
Phone: (904) 884-5493 DSN 579-5493

POPE, MAJ LORI
Detachment 4, 617th Weather Squadron
Unit 7890
GE
Phone: 011-49-6541-18336 DSN 452-7336

RABY, MR. JOHN W.
U.S. Army Research Laboratory
Battlefield Environment Directorate
ATTN: AMSRL-BE-S
White Sands Misl Range, NM 88002-5501
Phone: (408) 656-2044 DSN 878-2044

REDING, CAPT PHIL
Combat Weather Facility
595 Independence Road, Bldg 91027
Hurlburt Field, FL 32544-5618
Phone: (904) 884-5730 DSN 527-5730

RICHTER, DR. JUERGEN H.
Naval Command, Control and Ocean
Surveillance Center RDT&E Division
53560 Hull Street (Code 54)
San Diego, CA 92152-5001
Phone: (619) 553-3053 DSN 553-3053

ROADCAP, LTC JOHN R.
PL/GPO
29 Randolph Street
Hanscom AFB, MA 01731-3010
Phone: (617) 377-2951 DSN 478-2951

ROLLINS, DR. J. MICHAEL
Science and Technology Corporation
555 Telshor Blvd., Suite 200
Las Cruces, NM 88011-0000

SAUTER, MRS. BARBARA J.
U.S. Army Research Laboratory
Battlefield Environment Directorate
ATTN: AMSRL-BE
White Sands Misl Range, NM 88002-5501
Phone: (505) 678-2840 DSN 258-2840

SAUTER, MR. DAVID P.
U.S. Army Research Laboratory
Battlefield Environment Directorate
ATTN: AMSRL-BE-W
White Sands Misl Range, NM 88002-5501
Phone: (505) 678-2078 DSN 258-2078

SCASNY, MAJ KEVIN D.
2nd Weather Flight/CC
Bldg 200, Hardee Ave
Ft. McPherson, GA 30330-6000

SCHAEFER, MAJ JAMES
AFCCC/MS
859 Buchanan St., Room 309
Scott AFB, IL 62225-5116
Phone: (618) 256-3902 DSN 576-3902

SCHROEDER, DR. JOHN
ONTAR Corporation
9 Village Way
North Andover, MA 01845-2000

SEELEY, MR. GUY
RADEX INC
Phillips Lab, Geophysics Directorate
29 Randolph Road
Hanscom AFB, MA 01731

SELSOR, MR. HARRY D.
Naval Research Laboratory
TOWS Program Office
Code 7406, Building 1105
Stennis Space Center, MS 39529-5004
Phone: (601) 688-4760 485-4760

SHAFFER, LTC ALAN R.
HQ USAF/XOWE
1490 Air Force Pentagon
Washington, DC 20330-1490
Phone: (703) 696-4021 DSN 226-4021

SHIRKEY, DR. RICHARD C.
U.S. Army Research Laboratory
Battlefield Environment Directorate
ATTN: AMSRL-BE-S
White Sands Misl Range, NM 88002-5501
Phone: (505) 678-5470 DSN 258-5470

SICKLER, LT COL GARY
Combat Weather Facility
595 Independence Road, Bldg 91027
Hurlburt Field, FL 32544-5618
Phone: (904) 884-5702 DSN 579-5702

SMITH, CPT BRADLEY P.
OSD/DDR&E
ATTN: E&LS (Rm 3D129)
3080 Defense Pentagon
WASH, DC 20301-3080
Phone: (703) 695-9604 DSN 225-9604

SNIDER, DR. DONALD E.
U.S. Army Research Laboratory
ARL Dir Staff Military Oper & Analysis
ATTN: AMSRL-MO-TB
2800 Powder Mill Road
Adelphi, MD 20783-1145
Phone: (301) 394-5166 DSN 290-4489

SOLIZ, DR. PETER
Applied Sciences Laboratory, Inc.
PO Box 21158
Albuquerque, NM 87154

SPALDING, DR. JOHN B.
Physical Science Laboratory
New Mexico State University
PO Box 30002
Las Cruces, NM 88003-0002
Phone: (505) 522-9298

STEINHOFF, MR. RALPH G.
U.S. Army Research Laboratory
Battlefield Environment Directorate
ATTN: AMSRL-BE-S
White Sands Misl Range, NM 88002-5501
Phone: (505) 678-4481 DSN 258-4481

SUTHERLAND, DR. ROBERT A.
U.S. Army Research Laboratory
Survivability/Lethality Directorate
ATTN: AMSRL-SL-CA
White Sands Misl Range, NM 88002-5501
Phone: (505) 678-4520 DSN 258-4520

SWIRBALUS, MR. ROBERT A.
PL/GPOL
Hanscom AFB, MA 01731-5000
Phone: (617) 377-3685

THOMPSON, MS. JILL C.
U.S. Army Research Laboratory
SLAD
ATTN: AMSRL-SL-CA
White Sands Misl Range, NM 88002-5501
Phone: (505) 678-2434 DSN 258-2434

TITLEY, CDR DAVID W.
Naval Oceanographic Office
1002 Balch Blvd
Stennis Space Center, MS 39522-5001
Phone: (601) 688-5152 DSN 485-5152

TOFSTED, MR. DAVID H.
U.S. Army Research Laboratory
Battlefield Environment Directorate
ATTN: AMSRL-BE-S
White Sands Misl Range, NM 88002-5501
Phone: (505) 678-3039 DSN 258-3039

TOLL, JR., CDR RAYMOND F.
Chief of Naval Operations NO96
Naval Observatory
2000 NAVY PENTAGON
WASHINGTON, DC 20350-2000
Phone: (202) 762-1005 DSN 762-1005

TOOTH, MR. ANDREW R.
British Aerospace (Operations) Ltd.
Sowerby Research Centre
FPC 267, P.O. Box 5
UNITED KINGDOM
Phone: 44-272-36-3095

TRAHAN, MR. BILL
Naval Surface Warfare Center
Dahlgren Division
17320 Dahlgren Rd, Code F44
Dahlgren, VA 22448-5100
Phone: (540) 653-7701 DSN 249-7701

TUNICK, MR. ARNOLD D.
U.S. Army Research Laboratory
Battlefield Environment Directorate
ATTN: AMSRL-BE-S
White Sands Misl Range, NM 88002-5501
Phone: (505) 678-4832 DSN 258-4832

TURTON, MR. JONATHAN D.
Meteorological Support Group
MoD DCS (R&T)
Main Building
WhiteHall
UNITED KINGDOM

TUTTLE, III, LTC CHARLES W.
Combined Army Command Staff Wx Officer
USACAC
ATTN: ATZL-CAW-E
415 Sherman Ave
Ft. Leavenworth, KS 66027-1344
Phone: (913) 684-4056 DSN 552-4056

ULMAN, CAPT JAMES C.
NAIC/TATW
4180 Watson Way
Wright-Patterson AFB, OH 45433-5648
Phone: (513) 257-7071 DSN 787-7071

VEAZEY, MR. DON R.
U.S. Army Research Laboratory
Battlefield Environment Directorate
ATTN: AMSRL-BE
White Sands Misl Range, NM 88002-5501
Phone: (505) 678-1225 DSN 258-1225

VIDAL, JR., MR. EDWARD
U.S. Army Research Laboratory
Battlefield Environment Directorate
ATTN: AMSRL-BE-W
White Sands Misl Range, NM 88002-5501
Phone: (505) 678-1184 DSN 258-1184

VONDER HAAR, DR. THOMAS H.
Colorado State University -CIRA
Foothills Campus
Fort Collins, CO 80523-0000
Phone: (970) 491-8448

WADE, MR. ARNOLD E.
U.S. Army Research Laboratory
Battlefield Environment Directorate
ATTN: AMSRL-BE-W
White Sands Misl Range, NM 88002-5501
Phone: (505) 678-1761 DSN 258-1761

WATKINS, MR. WENDELL
U.S. Army Research Laboratory
SLAD
ATTN: AMSRL-SL-CA
White Sands Missile Range, NM 88002-5501
Phone: (505) 678-4313

WEINGARTEN, MR. DEAN S.
U.S. Army Yuma Proving Ground
ASL Yuma Met Team
ATTN: STEYP-MT-LS-M (Met Team)
Yuma, AZ 85365-9102
Phone: (520) 328-6850 DSN 899-6850

WELLS, SMSGT LEONARD A.
3d Weather Squadron
Bldg 90049
Clarke Road
Fort Hood, TX 76544-5076
Phone: (817) 288-9166 DSN 738-9166

WELLS, MR. MICHAEL E.
Wells Consulting, Inc
3812 Glenmont Drive
Fort Worth, TX 76133-2956
Phone: (817) 292-2378

WESTERMEIER, MR. FRANZ E.
U.S. Army Engineer School
ATTN: ATSE-CD-TVC
Fort Leonard Wood, MO 65473-6640
Phone: (314) 596-0131/7350 DSN 676-7350

WHICKER, MAJ GEORGE A.
Air Weather Service
SYDC
102 W. Losey St, Rm 102
Scott AFB, IL 62225-5206
Phone: (618) 256-3268/312 DSN 576-3268

WILK, MR. WM. GLENN
MEVATEC Corporation
1525 Perimeter Parkway, Suite 500
Huntsville, AL 35806-0000
Phone:

WILSON, DR. KEITH
U.S. Army Research Laboratory
Battlefield Environment Directorate
ATTN: AMSRL-BE-S
White Sands Msl Range, NM 88002-5501
Phone: (505) 678-4006 258-4006

YEE, MR. YOUNG
U.S. Army Research Laboratory
SLAD
ATTN: AMSRL-SL-CA
White Sands Missile Range, NM 88002-5501

YEISLEY, CAPT MARK
Colorado State University -CIRA
CIRA, Foothills Campus
Fort Collins, CO 80523
Phone:

Author Index

- Alleca, Joe Lt. Col 77
- Barnes, Eugene S. 93
 Bauer, Bruce L. 22, 100
 Bayang, Martin 237
 Blanco, Abel 57
 Bleiweiss, Max P. 134, 237, 305, 334, 354
 Bullard, Brian R. 211
 Byers, John 144
- Cassidy, Thomas 354
 Chenault, Thelma 237
 Cionco, Ronald M. 144
 Coakley, Melanie M. 372
 Cogan, James 42
 Cox, R.M. 22, 64, 100, 114
 Crow, Samuel 364
- Davies, Peter F. 31
 Davis, Roger E. 211
 Dougherty, Cathy 64, 114
 Dumais, Robert Jr. 3, 12
- Eaton, Frank 163
 Eicher, Joseph 257
 Eis, Kenneth E. 184, 247
 Elial, D. 324
 Elrick, John R. 52
 Endlich, Robert W. 153
- Fry, Richard N. Jr. 64, 114
- Giever, John C. 266
 Gillespie, James 223
 Gillespie, Patti 276, 364
 Goroch, Andreas K. 126
 Gouvela, Melanie J. 315
 Greenling, Thomas 42
 Grossman, Shlomit 324
- Hatch, W. 163
 Henmi, Teizi 57
 Hestand, P.D. 315
 Higgins, Glenn J. 315
 Hines, John R. 163
 Hook, Donald W. 266
 Hutt, D.L. 173
- Katz, A. 324
 Kirby, Stephen F. 83
 Knapp, David I. 3
 Koenig, George 257, 354
- Lucas, S.A. 42
 Luker, Steve 295
- Marlin, David H. 344
 Marshak, Alexander 194
 Matthew, William T. 93
 McGee, Steven J. 266
 McLaughlin, Karen M. 372
 McWilliams, Gary B. 93
 Myers, T. 22
- Noah, M. 22
- O'Brien, Sean 266
 Ota, Clem Z. 305
- Padilla, Christopher D. 334, 134
 Payne, Kenneth C. 134
- Raby, John W. 126
 Reinke, Donald L. 184, 247
 Riese, C. 163
 Rollins, Michael 276, 305
 Rosen, David 223
- Sagi, G. 324
 Seabloom, Michael S. 315
 Seeley, Guy 295
 Shapiro, B.G. 100
 Smith, Rene 237
 Soliz, Peter 257
 Sontowski, John 64, 114
 Spalding, John 57
 Stogden, Donald 134
 Stryckman, D. 173
- Thomas, James 42
 Tofsted, David 364
 Tremback, C. 100
 Turton, Jonathan D. 31
- Vaucher, Gail Tirrell 153
 Vonder Haar, Thomas H. 184, 247
- Welsh, James P. 354